Physics of Atomic Nuclei, Vol. 67, No. 1, 2004, p. 1. Translated from Yadernaya Fizika, Vol. 67, No. 1, 2004, p. 3.

VERY HIGH MULTIPLICITY PHYSICS

Preface

The traditional purpose of the very high multiplicity physics workshops (VHMPW) is to highlight the present status and prospects of searches for new physics beyond the standard models of inelastic hadron interactions at intermediate and high energies. Various extensions of the existing theoretical approaches, including multiperipheral models, pQCD predictions, and fractal and wavelet analyses, were within the interest of the VHMPW held in the years 2000–2002 at JINR (Dubna).

The list of main topics at the VHMPW includes the following items: phenomenology of VHM processes, multiperipheral models, pQCD predictions in the VHM domain, low-x physics, statistical physics approaches, collective phenomena, multiparticle Bose–Einstein correlations, and perspectives of VHM experimental investigations.

The VHMPW was sponsored by the Joint Institute for Nuclear Research (Dubna) and the Russian Foundation for Basic Research.

The conference made a remarkable contribution to the fruitful exchange of ideas between theorists and experimentalists working in particle physics and high-energy nuclear physics.

The talks presented at the meetings are collected in the Proceedings, Dubna, JINR (2000–2002), and the present issue contains selected papers. We hope that the publication of them will contribute to a further development of theoretical concepts in multiparticle-production physics beyond the standard hadron physics. We believe that it will arouse interest of experimentalists in this important area of investigations.

A.N. Sissakian, J. Manjavidze

1063-7788/04/6701-0001$26.00

Physics of Atomic Nuclei, Vol. 67, No. 1, 2004, pp. 100–107. From Yadernaya Fizika, Vol. 67, No. 1, 2004, pp. 100–107.

Moments of the Very High Multiplicity Distributions*

V. A. Nechitailo**

Lebedev Institute of Physics, Russian Academy of Sciences, Leninskiĭ pr. 53, Moscow, 117924 Russia

Received April 30, 2003

Abstract—In experiment, the multiplicity distributions of inelastic processes are truncated due to finite energy, insufficient statistics, or special choice of events. It is shown that the moments of such truncated multiplicity distributions possess some typical features. In particular, the oscillations of cumulant moments at high ranks and their negative values at the second rank can be considered as ones most indicative of the specifics of these distributions. They allow one to distinguish between distributions of different type.

1. INTRODUCTION

The studies of multiplicity distributions of high-energy inelastic processes have produced many important and sometimes unexpected results (for reviews, see, e.g., [1–3]). The completely new region of very high multiplicities will be opened with the advent of the RHIC, LHC, and TESLA accelerators.

Theoretical approaches to the multiplicity distributions in high-energy processes usually have to deal with analytic expressions at (pre)asymptotic energies which only approximately account for the energy–momentum conservation laws or with purely phenomenological expressions of probability theory. The multiplicity range extends in this case from zero to infinity.

In experiment, however, one has to consider distributions truncated at some multiplicity values in one way or another. These cuts could appear due to energy limitations, low statistics of experimental data, or because of special conditions of an experiment. Energy limitations always impose the upper cutoff on the tail of the multiplicity distributions. Low statistics of data can truncate these distributions from both ends if they are insufficient to detect rare events with very low and/or very high multiplicity. Similar truncations appear in some specially designed experiments [4], when events within some definite range of multiplicities have been chosen.

It would be desirable even in these cases to compare the distributions within those limited regions with underlying theoretical distributions. The straightforward fits are sometimes not accurate enough to distinguish between various possibilities because the probability values vary by many orders of magnitude. A more rigorous approach is to compare different moments of the truncated distributions. The simple-minded χ^2 fits are less sensitive and provide less information. The cumulant moments K_q seem to be most sensitive to slight variations (and, especially, cuts and shoulders) of the distributions. They often reveal such tiny details of the distributions which otherwise are hard to notice.

In particular, QCD predicts quite peculiar behavior of cumulant moments as functions of their rank q. According to solutions to the equations for the generating functions of the multiplicity distributions in the asymptotic energy region, the ratio of cumulant moments K_q to factorial moments F_q usually denoted as $H_q = K_q/F_q$ behaves as q^{-2} and, at preasymptotic energy values, reveals the minimum [5] at $q \approx 5$ with subsequent oscillations at higher ranks [6, 7]. Such behavior has been found in experiment at presently available energies [8, 9]. The solutions to the corresponding equations for fixed-coupling QCD also indicate similar oscillations [10]. At asymptotics, the oscillations should disappear and H_q becomes a smoothly decreasing and positive definite function of q, as mentioned above.

Neither of the distributions of the probability theory possesses these features. Among them, the negative binomial distribution (NBD) happens to be one of the most successful ones in describing global features of the multiplicity distributions [11]. We recall that the negative binomial distribution is defined as

$$P_n = \frac{\Gamma(n+k)}{\Gamma(n+1)\Gamma(k)} a^n (1+a)^{-n-k}, \qquad (1)$$

where $a = \langle n \rangle / k$, $\langle n \rangle$ is the mean multiplicity, k is an adjustable parameter, and the normalization condi-

*This article was submitted by the author in English.

**e-mail: nechit@lpi.ru

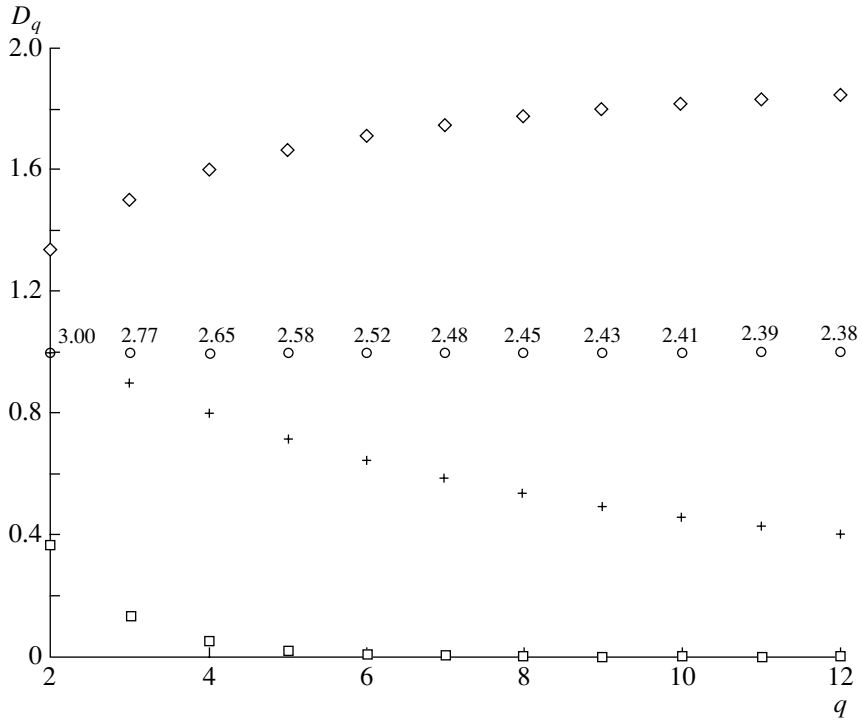

Fig. 1. $D_q = q^2 H_q$ are shown for asymptotic QCD by circles ($D_q^{\mathrm{QCD}} \equiv 1$) in comparison with NBD predictions at different values of the parameter $k = 2$ (diamonds), 3 (crosses), 10 (squares). The numbers near the QCD values show which values of k one would need to use for NBD to fit $D_q = 1$ at the corresponding q.

tion reads

$$\sum_{n=0}^{\infty} P_n = 1. \tag{2}$$

Its generating function is

$$G(z) = \sum_{n=0}^{\infty} P_n (1+z)^n = \left(1 - z\frac{\langle n\rangle}{k}\right)^{-k}. \tag{3}$$

The integer rank factorial and cumulant moments and their ratio are

$$F_q = \frac{1}{\langle n\rangle^q}\frac{d^q G(z)}{dz^q}\bigg|_{z=0} = \frac{\Gamma(q+k)}{\Gamma(k)k^q}, \tag{4}$$

$$K_q = \frac{1}{\langle n\rangle^q}\frac{d^q \ln G(z)}{dz^q}\bigg|_{z=0} = \frac{\Gamma(q)}{k^{q-1}}, \tag{5}$$

$$H_q = \frac{\Gamma(q)\Gamma(k+1)}{\Gamma(k+q)}. \tag{6}$$

H_q moments at the parameter $k = 2$ behave as $2/q(q+1)$, i.e., with a power-law decrease reminding one of QCD at large q, however, with a different weight factor. Therefore, at first sight, it could be considered as a reasonably good analytic model for asymptotic behavior of the multiplicity distributions. It has been claimed [12–15] that the superposition of two NBDs with different parameters and their cutoff at high multiplicities can give rise to oscillations of H_q and better fits of experimental data at preasymptotic energies. Nevertheless, the fits have not been perfect enough.

Let us compare first the asymptotic QCD predictions with NBD fits at different values of the adjustable parameter k. The values of $D_q = q^2 H_q$ plotted in Fig. 1 as functions of q for asymptotic QCD are identically equal to 1. For the NBD at $k = 2$, they exceed 1 tending to 2 at large q. At larger values of k, all D_q are less than 1 except $D_2 = 1$ at $k = 3$. Surely, the identity $D_1 \equiv 1$ is valid for any k due to the normalization condition.

To get asymptotic QCD results with all $D_q \equiv 1$ from expressions similar to the NBD, one would need to modify the NBD in such a way that the parameter k becomes a function of n. Thus, some effective values of k should be used to get QCD moments $D_q = 1$ at various q. They are obtained as the solutions to the equation

$$\prod_{n=1}^{q-1}\left(1 + \frac{k(q)}{n}\right) = q^2, \tag{7}$$

which follows from Eq. (6) for $H_q = q^{-2}$. They show that k decreases somewhat from 3 to some values exceeding 2 with an increase in q. This reflects the well-

known fact that the tails of distributions are underestimated in NBD fits [14] compared to experimental data in the preasymptotic region. Also, the amplitude of oscillations and their periodicity are not well reproduced by a single truncated NBD [14], and one has to use the sum of at least two NBDs to get a better fit. However, rather large values of k were obtained in these fits. It implies, in fact, that the fit is done with the help of two distributions very close to Poissonian shapes because the Poisson distribution is obtained from the NBD in the limit $k \to \infty$. Therefore, the tails are suppressed very strongly.

Here, we will focus our efforts on qualitative changes of moments when the NBD is truncated, especially, as applied to studies of very high multiplicities.

In QCD considerations based on the equations for the generating functions for quark and gluon jets, the preasymptotic (next-to-leading order, etc.) corrections give rise to oscillations of H_q. Even though they are of higher order in the coupling strength, they appear mainly due to account of energy conservation in the vertices of Feynman diagrams but not due to considering the higher order diagrams which are summed in the modified perturbation theory series (see [3]). In the phenomenological approach, this would effectively correspond to the cutoff of the multiplicity distribution at some large multiplicity. Therefore, we intend here to study how strongly such a cutoff influences the NBD moments, whether it produces oscillations of the cumulant moments, and how strong they are, and, as a more general case, consider the moments of NBD truncated at both low and high multiplicities. This would help answer the question whether the shape of the distribution in the limited region can be accurately restored from the behavior of its moments. It could become especially helpful if only events with very high multiplicities are considered in a given experiment because of the above-mentioned underestimation of tails in the NBD fits.

2. TRUNCATED NBD AND ITS MOMENTS

In real situations, the multiplicity distribution is sometimes measured in some interval of multiplicities and one can try to fit using the NBD the data available only in the restricted multiplicity range. Therefore, we shall consider the negative binomial distribution within the interval of multiplicities $m \le n \le N$ called $P_n^{(c)}$ and normalized to 1 so that

$$\sum_{n=m}^{N} P_n^{(c)} = 1. \tag{8}$$

Moreover, due to the reasoning above and to simplify formulas, we consider here only the case of $k = 2$. The generalization to arbitrary values of k is straightforward.

The generating function of the truncated distribution $G_c(z)$ can be easily found as

$$G_c(z) = \sum_{n=m}^{N} P_n^{(c)}(1+z)^n = G(z)(1+z)^m \frac{f(z)}{f(0)}, \tag{9}$$

where

$$f(z) = 1 + m(1-x) - [1 + (N+1)(1-x)]x^{N-m+1}, \tag{10}$$

$$x = b(1+z), \quad b = \frac{a}{1+a}. \tag{11}$$

Correspondingly,

$$f(0) \equiv f(z=0) \equiv f(x=b). \tag{12}$$

Using the above formulas for the factorial moments, one gets the following formula for the moments of the truncated distribution expressed in terms of the NBD moments (4):

$$F_q^{(c)} = \left(\frac{\langle n\rangle}{\langle n\rangle_c}\right)^q F_q \left\{ 1 + \frac{1}{f(0)(q+1)} \times \sum_{r=1}^{q} \frac{a^{-r}}{r!}(q+1-r) \left[\left(\frac{m}{1+a} + 1 - r \right) \times \theta(m+1-r) \prod_{i=1}^{r}(m+2-i) - \left(\frac{N+1}{a+1} + 1 - r \right) b^{N-m+1} \prod_{i=1}^{r}(N+3-i) \right] \right\}, \tag{13}$$

where $\langle n\rangle_c$ is the mean multiplicity of the truncated distribution. It is related to the mean multiplicity $\langle n\rangle$ of the original distribution as

$$\langle n\rangle - \langle n\rangle_c = \frac{(1-b)[(N+1)(N+2)b^{N-m+1} - m(m+1)]}{1 + m(1-b) + b^{N-m+1}[(N+1)b - N - 2]}. \tag{14}$$

These expressions can also be used for the distributions truncated on one side by setting $m = 0$ or $N = \infty$.

The cumulant moments can be calculated after the factorial moments are known from Eq. (13) according to the identities

$$F_q = \sum_{m=0}^{q-1} \frac{\Gamma(q)}{\Gamma(m+1)\Gamma(q-m)} K_{q-m} F_m. \tag{15}$$

This formula is a simple relation between the derivatives of a function and of its logarithm [see

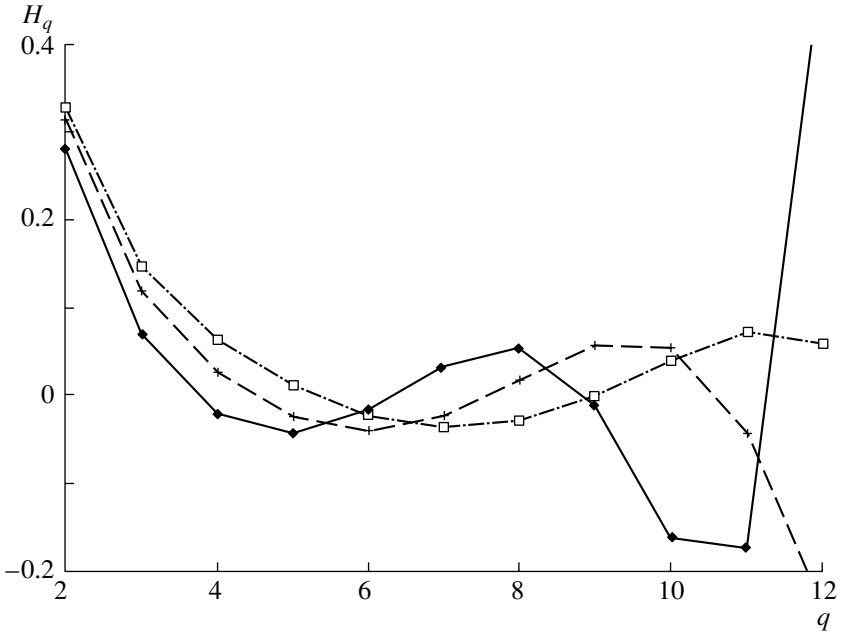

Fig. 2. H_q moments for NBD with $\langle n\rangle = 10$ truncated at $N = 30$ (diamonds), 40 (crosses), 50 (squares) at $m = 0$.

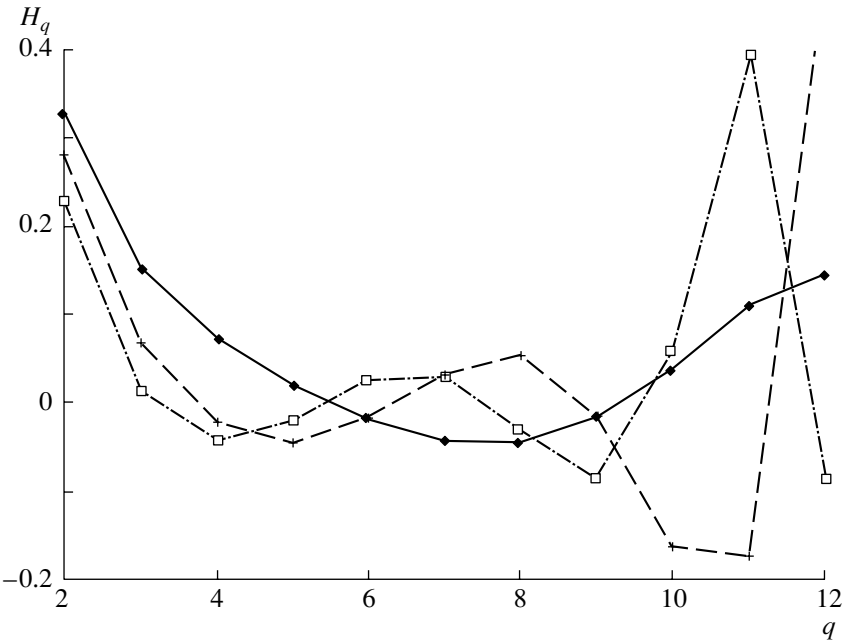

Fig. 3. H_q moments for NBD with $\langle n\rangle = 5$ (diamonds), 10 (crosses), 15 (squares) truncated at $N = 30$ at $m = 0$.

Eqs. (4) and (5)]. Therefore, it is valid for both original and truncated distributions.

For the Poisson distribution, the ratios H_q are identically equal to zero and are given by Eq. (6) for the NBD, while truncation induces new features. In the figures, we show the behavior of the ratios H_q as functions of the rank q for the truncated negative binomial distributions.

At the beginning, we consider the abrupt cutoff only of the very high multiplicity tail, i.e., the case $m = 0$ and $N > \langle n\rangle$. This mimics the energy–momentum conservation limits. In Figs. 2 and 3, it is shown that such a cutoff induces oscillations of H_q. The farther the cutoff from the mean multiplicity, the weaker the oscillations. This quite expected result is known from long ago [12, 13]. It is demonstrated in

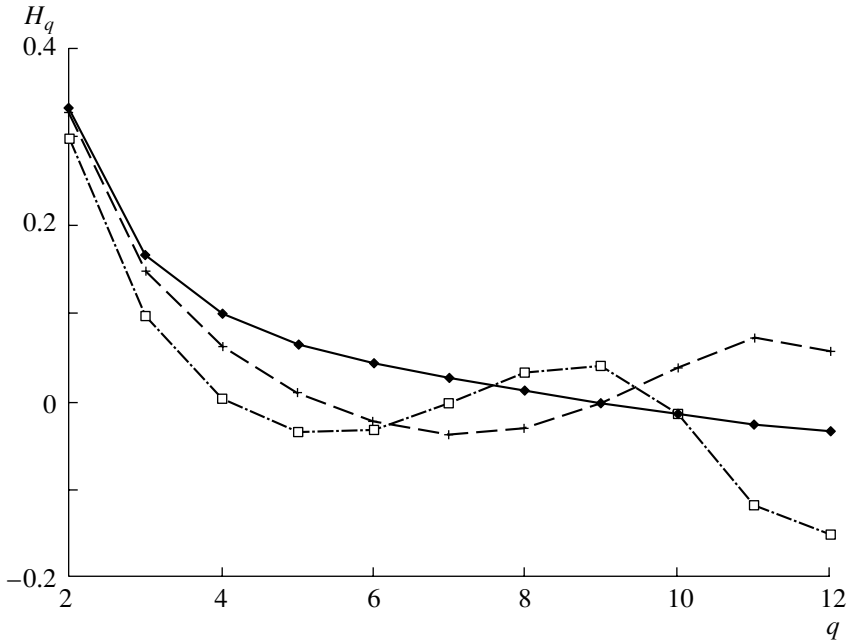

Fig. 4. H_q moments for NBD with $\langle n\rangle = 5$ (diamonds), 10 (crosses), 15 (squares) truncated at $N = 50$ at $m = 0$.

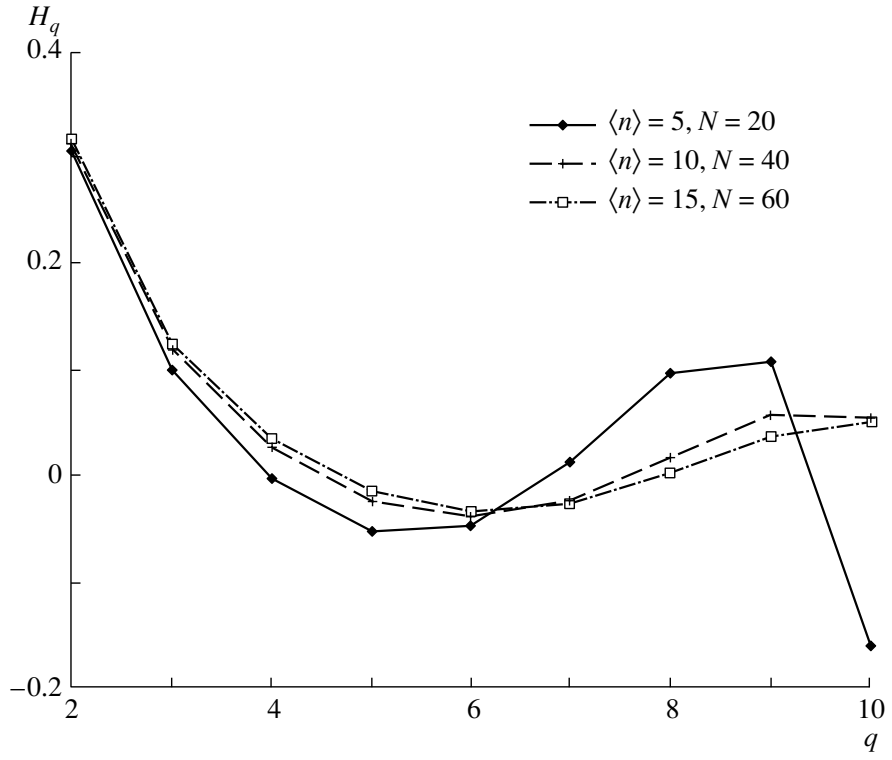

Fig. 5. Approximate scaling of H_q moments for NBD with $N/\langle n\rangle = \text{const}$ at $m = 0$.

Fig. 2 for $\langle n\rangle = 10$ and different cutoffs at $N = 30$, 40, 50. Another representation of the same result is seen in Fig. 3, where the constant cutoff $N = 30$ has been chosen for different $\langle n\rangle$ equal to 5, 10, and 15. The closer the cutoff to $\langle n\rangle$, the stronger the low-rank moments are damped. For the faraway cutoff $N = 50$, the period of oscillations increases. This increase is larger for lower mean multiplicity (see Fig. 4). At

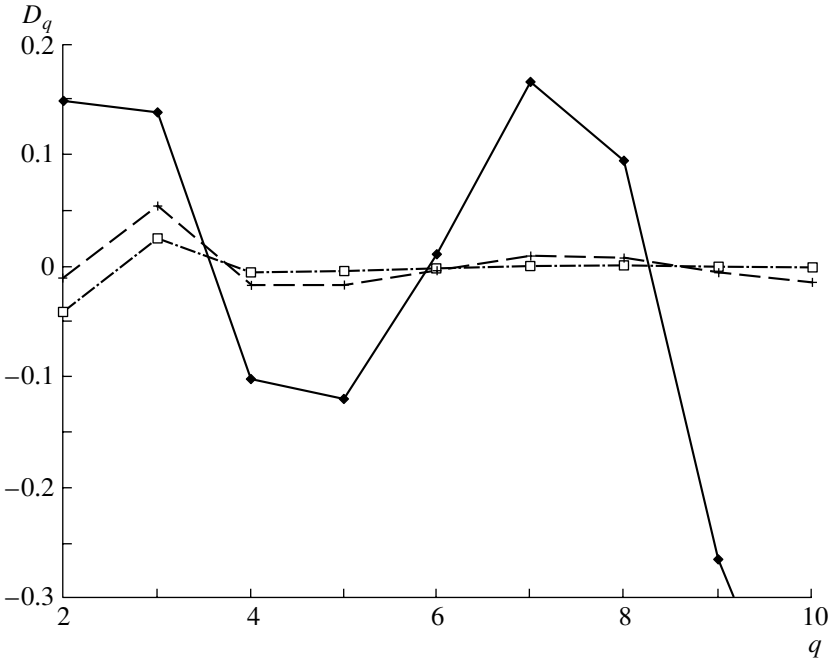

Fig. 6. D_q moments for NBD with $\langle n\rangle = 10$ truncated at $m = 10$, $N = 30$ (diamonds), 20–40 (crosses), 30–50 (squares).

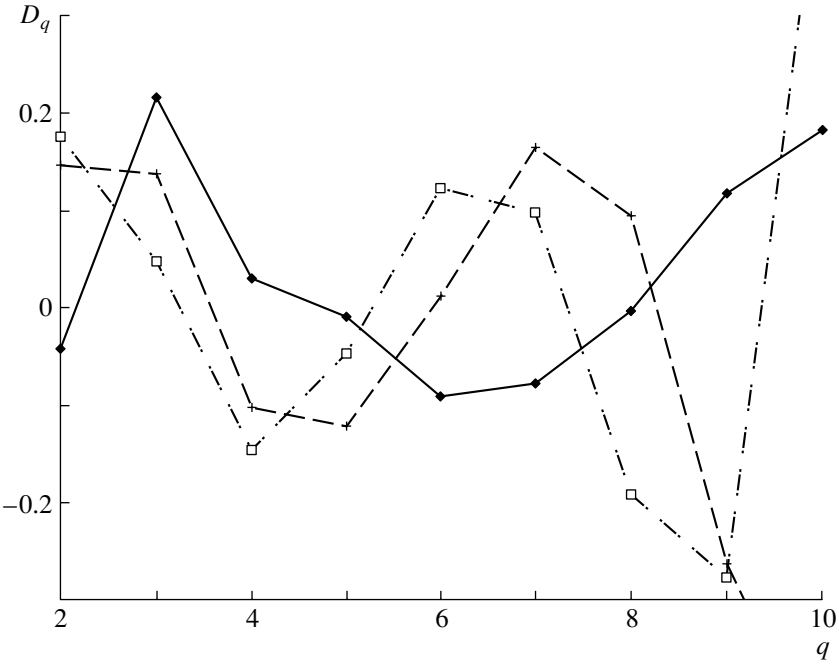

Fig. 7. D_q moments for NBD with $\langle n\rangle = 5$ (diamonds), 10 (crosses), 15 (squares) truncated at $m = 10$, $N = 30$.

$N/\langle n\rangle = \text{const}$, one observes the approximate scaling of H_q as seen in Fig. 5.

3. VERY HIGH MULTIPLICITIES

With the advent of RHIC, LHC, and TESLA, we are approaching the situation where average multiplicities become very high and the tails of multiplicity distributions reach values which are extremely large. These events with extremely high multiplicities at the tail of the distribution can be of special interest. The tails of particular channels usually die out very fast, and a single channel dominates at the very tail of the distribution. Mostly soft particles are created there. Thus, one hopes to get direct access to very low-x

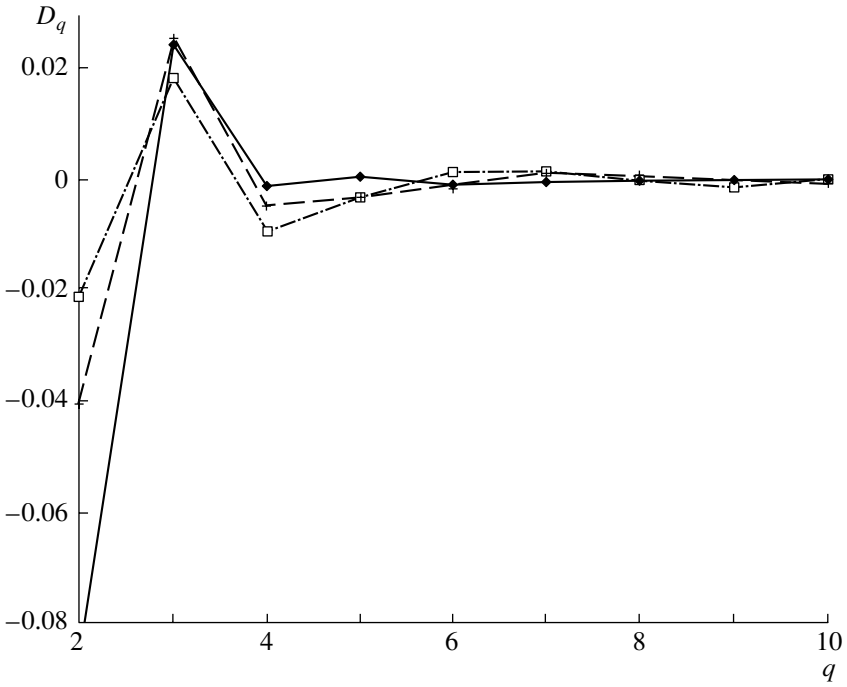

Fig. 8. D_q moments for NBD with $\langle n \rangle = 5$ (diamonds), 10 (crosses), 15 (squares) truncated at $m = 30$, $N = 50$.

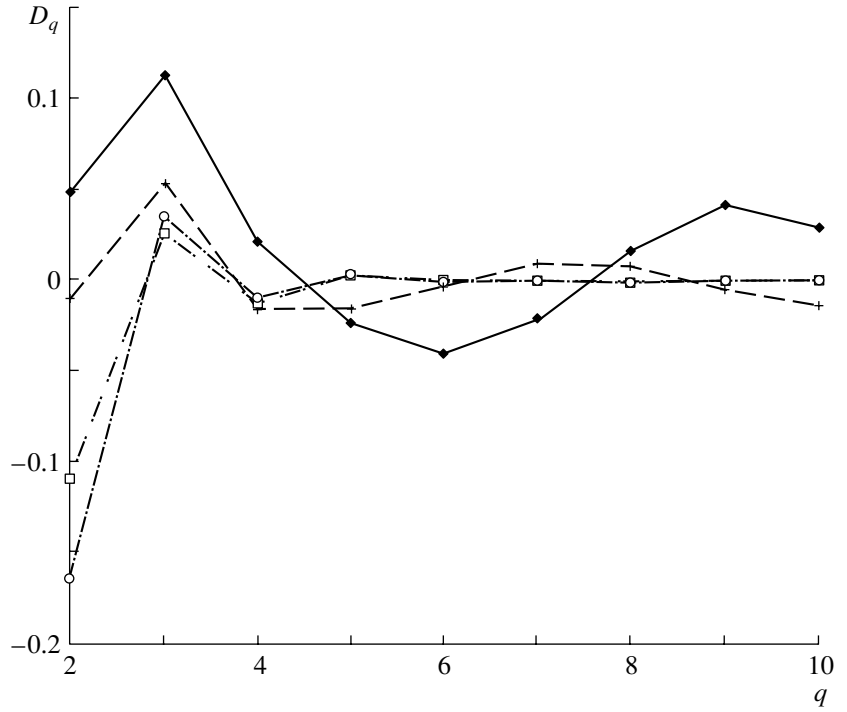

Fig. 9. D_q moments for NBD with $\langle n \rangle = 10$ truncated at $m = 20$, $N = 50$ (diamonds), 20–40 (crosses), 20–30 (squares), 20–25 (circles).

physics. QCD interpretation in terms of the BFKL equation (or its generalization) can be attempted. Also, the hadronic densities are rather high in such events, and the thermodynamic approach can be applied [16].

However, these events are rather rare and the experimental statistics have been quite poor until

now. The Poisson distribution has a tail which decreases mainly like an inverse factorial. According to NBD (1), the tail is exponentially damped with the power-increasing preexponential factor. At the same time, QCD predicts even a somewhat slower decrease as is seen in Fig. 1 from the behavior of the moments. This is important for future experiments in the very high multiplicity region.

To study these events within the truncated NBD with $k = 2$ according to Eq. (13), let us choose the multiplicity interval of constant length $N - m = 20$ and place it at various distances from the mean multiplicity $\langle n \rangle = 10$ as in Fig. 2. The resulting H_q are shown in Fig. 6.

The most dramatic feature is the negative values of H_2 and the subsequent change of sign of H_q at each q in the case where the lower cutoff m is noticeably larger than $\langle n \rangle$ ($m/\langle n \rangle \geq 2$). This reminds one of the behavior of H_q for the fixed multiplicity distribution and shows that the NBD tail decreases quite fast, so that the multiplicity m dominates in the moments of these truncated distributions.

The same features have been demonstrated in Figs. 7 and 8 for different average multiplicities and different positions of the fixed window $N - m = 20$. In Fig. 7, the window is rather close to $\langle n \rangle$ or even contains it inside (for $\langle n \rangle = 15$). Therefore, $H_2 < 0$ only for $\langle n \rangle = 5$. In Fig. 8, it is very far from $\langle n \rangle$. Thus, all H_2 are negative, the more the lower is $\langle n \rangle$. Again, the sign-changing characteristics remind one of those for the fixed multiplicity distribution.

Another possibility to study the tail of the distribution with the help of H_q ratios is their variation with the varying length of the tail chosen. At the same mean multiplicity $\langle n \rangle = 10$, we calculate moments for the intervals starting at $m = 20$ and ending at $N = 50$, 40, 30, 25. The values of H_q at rather low ranks $q = 2$, 3, 4, 5 are very sensitive to the interval length (as is shown in Fig. 9) and vary by an order of magnitude.

4. CONCLUSIONS

In connection with some experiments planned, our main concern here was to learn if H_q ratios can be used to judge the behavior of the tail of the multiplicity distribution. Using the NBD as an example, we have shown that H_q behaves in a definite way depending on the size of the multiplicity interval chosen and on its location. Comparing the corresponding experimental results with NBD predictions, one would be able to show whether the experimental distribution decreases slower (as predicted by QCD) or faster than the NBD.

In particular, the negative values of H_2 noted above are of special interest because they show directly how strong the decrease of the tail is. NBDs at different k values would predict different variations of H_2 with more negative H_2 for larger k. Also, the nature of oscillations of H_q moments at larger values of q reveals how steeply the tail drops down.

Let us stress that the choice of high multiplicities for such a conclusion could be better than the simple-minded fit of the whole distribution. As one hopes, in this case, there are fewer transitions between different channels of the reaction (e.g., from jets with light quarks to heavy quarks), and the underlying low-x dynamics can be revealed.

ACKNOWLEDGMENTS

This work is supported by the Russian Foundation for Basic Research, project nos. 00-02-16101 and 02-02-16779.

REFERENCES

1. I. M. Dremin, Usp. Fiz. Nauk **164** (8), 785 (1994) [Phys. Usp. **37**, 715 (1994)].
2. E. A. DeWolf, I. M. Dremin, and W. Kittel, Phys. Rep. **270**, 1 (1996).
3. I. M. Dremin and J. W. Gary, Phys. Rep. **349**, 301 (2001).
4. V. A. Nikitin, *Talk at III International Workshop on Very High Multiplicities, Dubna, Russia, 2002.*
5. I. M. Dremin, Phys. Lett. B **313**, 209 (1993).
6. I. M. Dremin and V. A. Nechitailo, Mod. Phys. Lett. A **9**, 1471 (1994); Pis'ma Zh. Éksp. Teor. Fiz. **58**, 881 (1993) [JETP Lett. **58**, 881 (1993)].
7. S. Lupia, Phys. Lett. B **439**, 150 (1998).
8. I. M. Dremin, V. Arena, G. Boca, *et al.*, Phys. Lett. B **336**, 119 (1994).
9. K. Abe *et al.* (SLD Collab.), Phys. Lett. B **371**, 149 (1996).
10. I. M. Dremin and R. C. Hwa, Phys. Rev. D **49**, 5805 (1994); Phys. Lett. B **324**, 477 (1994).
11. A. Giovannini, Nuovo Cimento A **15**, 543 (1973).
12. R. Ugoccioni, A. Giovannini, and S. Lupia, in *Proceedings of the XXIII International Symposium on Multiparticle Dynamics, Aspen, USA, 1993*, Ed. by M. M. Block and A. R. White (World Sci., Singapore, 1994), p. 297.
13. B. B. Levtchenko, in *Proceedings of the VIII Workshop on High Energy Physics, Zvenigorod, Russia, 1993*, Ed. by B. B. Levtchenko (Mosk. Gos. Univ., Moscow, 1994), p. 68.
14. A. Giovannini, S. Lupia, and R. Ugoccioni, Phys. Lett. B **388**, 639 (1996); **342**, 387 (1995).
15. R. Ugoccioni and A. Giovannini, Nucl. Phys. B (Proc. Suppl.) **71**, 201 (1999).
16. J. Manjavidze and A. Sissakian, Phys. Rep. **346**, 1 (2001).

Physics of Atomic Nuclei, Vol. 67, No. 1, 2004, pp. 108–114. From Yadernaya Fizika, Vol. 67, No. 1, 2004, pp. 108–113.

Proton–Proton Interaction with High Multiplicity at Energy of 70 GeV (Proposal)*

P. F. Ermolov[1], E. A. Kuraev, J. Manjavidze, A. P. Meschanin[2], V. A. Nikitin[**], I. A. Rufanov, and A. N. Sissakian

Joint Institute for Nuclear Research, Dubna, Moscow oblast, 141980 Russia

Received May 21, 2003

Abstract—The goal of the proposed experiment is to investigate the collective behavior of particles in the process of multiple hadron production in pp interaction $pp \to n_\pi\pi + 2N$ at the beam energy $E_{\rm lab} = 70$ GeV. The domain of high multiplicity $n_\pi = 30$–40, or $z = n/\bar{n} = 4$–6, will be studied. Near the threshold of reaction $n_\pi \to 69$, $z \to z_{\rm th} = 8.2$, all particles acquire small relative momentum $\Delta q < 1/R$, where R is the dimension of the particle production region. As a consequence of multiboson interference, a number of collective effects may show up: (a) a drastic increase in the partial cross section $\sigma(n)$ of production of n identical particles is expected, compared with commonly accepted extrapolation; (b) the formation of jets consisting of identical particles may occur as a result of the multiboson Bose–Einstein correlation (BEC) effect; (c) a large fluctuation of charged $n(\pi^+, \pi^-)$ and neutral $n(\pi^0)$ components and onset of centauros or chiral condensate effects are anticipated; (d) an increase in the rate of direct γ as a result of the bremsstrahlung in the partonic cascade and annihilation of $\pi^+\pi^- \to n\gamma$ in dense and cold pionic gas or condensate is expected. In the domain of high multiplicity $z \geq 5$, a major part of the c.m. energy $\sqrt{s} =$ 11.6 GeV is materialized, leading to a high-density thermalized hadronic system. Under this condition, a phase transition to cold quark–gluon plasma (QGP) may occur. The search for QGP signatures like large intermittency in the phase-space particle distribution and an enhanced rate of direct photons will be performed. The experimental setup is designed for detection of rare high-multiplicity events. The experiment is to be carried out at the extracted proton beam of the IHEP U-70 accelerator. The required beam intensity is $\sim 10^7$ s^{-1}. Under the assumption that the partial cross section $\sigma(n_\pi = 35) = 10$–1 nb, the anticipated counting rate is 10–1 events/h. The multiboson BEC enhancement may drastically increase the counting rate. © *2004 MAIK "Nauka/Interperiodica".*

1. INTRODUCTION

The investigation of multiple-particle production at high energy is one of the fundamental problems of hadron physics. It is essentially a nonperturbative process. QCD gives only a qualitative picture of this phenomenon: hadron collision initiates a partonic cascade. The gluon strings that arise between colored partons eventually break and produce quark–antiquark pairs. At the final stage of cascade development when the energy is exhausted, the partons join together creating hadrons. The mechanism of color confinement is unknown. As a consequence, at present, it is impossible to calculate theoretically even the main parameters of the process: multiplicity distribution, the energy and mass spectra of particles. Some features of the reaction are described by different models: thermodynamic, hydrodynamic, partonic cascade, Redge poles, and so on. But none of these approaches are complete and their substantiation is far from being rigorous.

There exists an extensive literature on this subject. The theoretical approaches based on statistics and thermodynamics are reviewed in [1, 2]. The grounds for the phase transition search are presented in [3, 4]. The importance of the investigation of multiparticle production for understanding the properties of hadron matter under extreme conditions, like high density and temperature, is stressed in [5]. A complete survey of the situation with particle correlation and intermittency can be found in [6]. Experimental data on multiplicity distribution and its phenomenological comprehension is given in [7].

The purpose of the proposed experiment "Thermalization" is to investigate the collective behavior of particles in the process of multiparticle production in

*This article was submitted by the authors in English.

[1]Skobeltsyn Institute of Nuclear Physics, Moscow State University, Vorob'evy gory, Moscow, 119992 Russia.

[2]State Science Center Institute of High-Energy Physics, Protvino, Moscow oblast, 142284 Russia.

**e-mail: nikitin@sunse.jinr.ru

pp (or pN) interactions

$$pp \to n_\pi \pi + 2N \qquad (1)$$

at the proton energy $E_{\rm lab} = 70$ GeV. At present, the multiplicity distribution at this energy is measured up to the number of charged particles $n_{\rm ch} = 20$ [8]. The corresponding scaling variable $z = n_{\rm ch}/\bar{n}_{\rm ch} = 3.5$. The kinematics limit is $n_{\pi,\rm th} = 69$, $z_{\rm th} = 8.2$. Here, $n_{\pi,\rm th}$ is the maximum number of charged and neutral pions allowed by energy–momentum conservation. We plan to study the events with multiplicity $n_\pi = 30$–45, $z = 5$–6. At large multiplicity and near the threshold of the process (1), where all particles have a small relative momentum, the high particle density $f = (2\pi)^3 d^6n/dp^3dr^3 \approx \pi^{3/2}N/(V_pV_r)$ in six-dimensional phase space is reached. Here, N is the number of particles in momentum–space volume V_pV_r. Note that, in the system $\hbar = c = 1$, the value f is dimensionless. The authors of [9–11] argue that the parameter f indicates the importance of multiparticle effects. The value f is the mean number of pions that interfere with one given pion and build the Bose–Einstein (BE) enhancement in the two-particle correlation function. Thus, if $f \ll 1$, only the two-particle correlation may be observed. Typically, $f \approx 0.1$ for the midrapidity region and $p_\perp \approx \bar{p}_\perp$. Even at LHC energy in Pb–Pb collisions, f is expected to be small in spite of huge multiplicity. This is due to large phase-space volume $V_pV_r \approx (4/3)^2\bar{p}^3\bar{r}^3$ occupied by secondary particles: $\bar{p} \approx 0.5$ GeV/c, $r \approx 10$ fm. In contrast to high-energy A–A collision, in our case of pp collision the volume V_pV_r is three orders of magnitude less, since we expect to have $\bar{p} \approx 0.07$ GeV/c, $r \approx 2$–3 fm. Therefore, we anticipate being able to reach a very high particle phase-space density, $f \gg 1$. As a consequence, one expects to observe the collective effects connected with multiboson interference: broadening of the multiplicity distribution, anomalous fluctuation of charged and neutral components, the formation of jets, and so on.

In the region $z \geq 4$, a major part of the c.m. energy $\sqrt{s} = 11.6$ GeV is transferred into the mass of particles produced. The density of the created hadron system may be rather high, $\rho/\rho_0 \approx 5$–10. Here, ρ_0 is the density of nuclear matter in the ground state. According to common belief, the system under such conditions is supposed to be a quark–gluon plasma (QGP). Figure 1 is taken from [12] to illustrate this statement.

The onset of QGP manifests itself, at least, by two signatures: large-particle intermittency in the phase space of rapidity–transverse momentum and an excess of direct photons and lepton pairs. We plan to search for both of these signatures. The unique feature of QGP in our case is its low temperature.

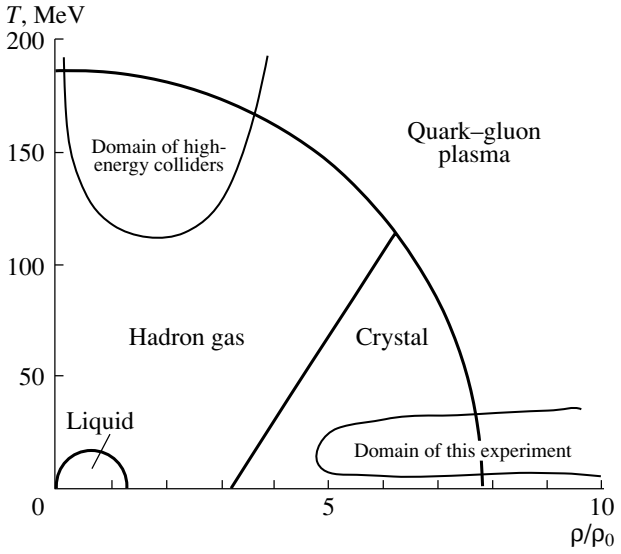

Fig. 1. Phase diagram of nuclear matter.

The closer we approach to the reaction threshold, the lower the temperature and the higher the density of the system. The lower the temperature, the longer the lifetime of the system. The latter is especially important: the system must come into equilibrium in order to reveal the QGP features.

Further progress in understanding the dynamics of the multiparticle production process will come from further development of the experiment.

For the purposes of this experiment, we plan to improve the setup Spectrometer with Vertex Detector (SVD) installed at the extracted proton beam of the IHEP (Protvino) U-70 accelerator. The beam intensity is 10^7 s^{-1}. It is incident on a hydrogen (or light nuclei) target and generates 10^4 s^{-1} pp (or pN) interactions. One should mention that it is difficult to make a reliable extrapolation of an experimentally measured multiplicity distribution from the region $0 \leq z \leq 3.5$ to the region $z \geq 5$. We expect that a partial cross section in the interval $4 \leq z \leq 5$ is about 10–1 nb. Then, we can collect about 1–10 events/h. However, there are theoretical arguments favoring BE enhancement of production of identical pions. Then, the counting rate will be much higher.

2. PHYSICS PROGRAM

2.1. Multiparticle Process near Kinematics Limit

Let us consider a high enough multiplicity $n_{\rm crit}$ when in c.m.s. no energy remains for formation of the leading particles. Then, all secondaries have equal energy $\sqrt{p_\perp^2 + p_l^2 + m^2}$, which we determine from the mean transverse momentum of pion $p_\perp \approx 0.3$ GeV/c,

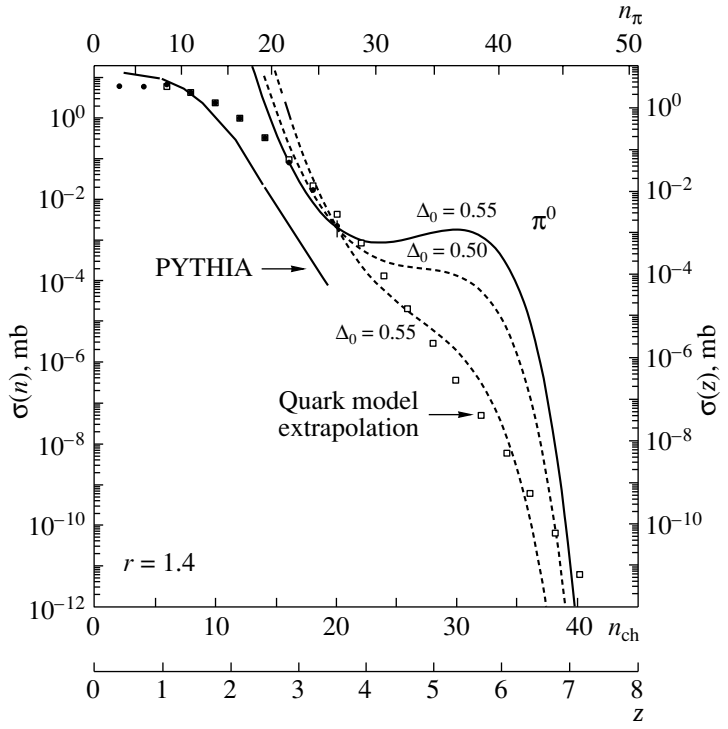

Fig. 2. Multiplicity distribution (partial cross section) in pp interaction. For details, see text.

as was measured in soft hadron reactions. The longitudinal momentum is $p_l = \dfrac{1}{\sqrt{2}} p_\perp$. The critical multiplicity is determined by relation $\sqrt{\bar{p}_\perp^2 + m_\pi^2} = (\sqrt{s} - 2m_N)/(n_{\text{crit}} + n_N)$. Here, $n_N = 2$ is the nucleon multiplicity. We get $n_{\text{crit}} = 23$. In the region $n \geq n_{\text{crit}}$, the particles in c.m.s. should have an isotropic angular distribution and their energy distribution is Maxwellian or BE. The corresponding temperature is $T = \dfrac{2}{3} E_{\text{kin}}$; $E_{\text{kin}} = (\sqrt{s} - 2m_N - n_\pi m_\pi)/(n_\pi + n_N)$. Here, n_π is pion multiplicity; T depends on pion multiplicity n_π and vanishes when $n_\pi \to n_{\text{th}}$. On this basis, we develop a Monte Carlo (MC) event generator and calculated the angular and momentum distribution of the pion and nucleons. These data are necessary for planning the experiment. An example: at multiplicity $n_\pi = 50$, the mean c.m. energy of all particles is 50 MeV and the mean lab. emission angle $\bar{\theta}_\pi = 90$ mrad, $\bar{\theta}_N = 40$ mrad. These numbers indicate the remarkable feature of this apparatus: having a very modest angular acceptance $\theta = 2\bar{\theta}_\pi = 200$ mrad, it will detect 95% of all secondary products.

There is experimental indication of the onset of the thermalization regime at multiplicity $n_{\text{ch}} = 18$ [13].

2.2. Multiplicity Distribution

The topological cross section $\sigma(n_{\text{ch}})$ in pp interaction at 70 GeV at the U-70 accelerator has been measured in two experiments [8] (see Fig. 2). The calculation by the MC PYTHIA code is shown. One can see that the standard generator predicts a value of cross section $\sigma(z)$ which is in reasonably good agreement with experimental data at $z < 2$ but it underestimates the value of $\sigma(z)$ by two orders of magnitude at $z \geq 3.5$.

An important task is the extrapolation of the function $\sigma(z)$ from the domain $z \leq 3.5$ to the domain of our interest $z \geq 5$. One successful approximation of the data at moderate energy is suggested in [14]. There, the authors make use of the additive quark model. It is assumed one quark–quark collision is described by a Poisson function. Two and three qq collision is represented by the convolution of Poisson functions.

The models mentioned above do not take into account the effect of interference of identical particles. Generally, the account of the multiboson effects is extremely difficult task. But there exists a simple analytically solvable model [9] allowing for a study of the characteristic features of multiboson systems under various conditions including those near the Bose condensation. The latter is even sometimes called a pion laser. The authors of [11] apply this model to study the influence of the Bose–Einstein correlation

(BEC) on pion multiplicity, spectra, and the two-pion correlation function. The prediction of this model is shown in Fig. 2. The free parameters are r for space dimension of the system and Δ for characteristic mean momentum of the particles. We see that the model strongly favors the production of π^0 (so-called anticentauro event).

2.3. Multiboson Jets

We considered the influence of the BE statistics on pion multiplicity distribution. There is another interesting BEC effect that is widely discussed in the literature. It is multiboson momentum (and angular) correlation. Preprint [15] is devoted to analysis of the multipionic system. It was found that the requirement of wave function symmetrization leads to the formation of an interference maximum with the momentum dispersion $d_{\rm cor}$ and the angular width $\theta_{\rm cor}$: $d_{\rm cor} = C/(r\sqrt{n})$; $\theta_{\rm cor} = d_{\rm cor}/p_0$, p_0 being the mean momentum of the pion. The meaning of these formulas is that, at $n \gg 1$, there is monochromatization in momentum space and angular collimation of the particles within the interference maximum.

A qualitatively similar effect is discussed in [16] but on rather different grounds. The authors point out the possibility that, at high enough energy density 3–6 GeV/fm^3 (which we hope will be easily achieved in our experiment), the produced pions can create a certain coherent state—a classical pion field, the analog of the classical electromagnetic field. Thus, one can expect a rather characteristic picture: a large number of pions may emerge with almost the same momentum, creating a jet pattern in concrete collision. There may be jets consisting predominantly of particles with only one sign (i.e., π^+, π^-, or π^0). These effects resemble a laser without an optical resonator. Another analogy is the electromagnetic coherent superemission in a spin-oriented system in a magnetic field.

2.4. Thermodynamics of the Hadron System

The emphasis of this proposal is the study of multiparticle process (1) at high multiplicity $n \geq n_{\rm crit}$, where the leading particles must vanish and it is reasonable to assume that the system approaches the thermodynamic equilibrium state. The onset of this regime may be checked directly by measuring the degree of isotropy of particle angular distribution in c.m.s. and by evaluating the temperature T_i corresponding to different species of the secondaries: $i = \pi$, K, p, $\bar{p}$, d. The difference of the quantities T_i gives another criterion of equilibrium. Thermodynamic analysis of hadron production has been widely used for a long time. The main features of the multiparticle process seem to be amenable to quantitative description. In particular, the abundance of different particle species is explained from relativistic quantum molecular dynamics. The application of this kind of theory and model to the data analysis of the proposed experiment have a sound basis since we plan to take special measures to detect a multiparticle system approaching the thermal equilibrium state. The deviation of the experimental observation from theoretical prediction will serve as a sign of new physics.

2.5. Intermittency

The secondary particles have a nonuniform distribution in momentum space. The particle density has statistical and dynamical fluctuations; i.e., the distribution has an intermittent character. The intermittency depends on the particle production mechanism. For instance, the resonances and the clusters in an intermediate state give rise to fluctuations in the final state of the system. The theoretical considerations show the rise of intermittency near the phase transition point. It also depends on the hadronization process (i.e., confinement) and QCD vacuum properties. Thus, experimental study of the intermittency may throw light on the complicated and hidden mechanism of particle production at high energy. The present project certainly has a direct connection with this topic, since high statistics of the high-multiplicity events make it possible to carry out a precise investigation of the intermittency effect.

One should distinguish stochastic and regular intermittency. The field source movement inside the medium with velocity greater than the phase velocity of the field quanta in this medium leads to wave production. In the case of electromagnetic interactions, it is the well-known Cherenkov effect. Generalization of Cherenkov radiation to scalar and vector field cases was developed in a number of papers. In particular, Cherenkov gluon radiation in QCD frames was devised in [17]. The existence of color current, necessary for this phenomena, is confirmed by studying hard processes. Cherenkov-type radiation can be emitted in the projectile and target particles. This leads to a distribution with two peaks of dense groups of particles (spikes) in rapidity phase space. At the same time, the particle distribution as a function of azimuthal angle is uniform. It is so-called ring events. Indication of the existence of such a phenomenon was reported in a number of papers (see, e.g., [18]). A double-peak shape in the pseudorapidity particle distribution for pp collisions has been observed in agreement with the coherent gluon-jet emission model. Therefore, high luminosity and high multiplicity trigger in "Thermalization" setup is very important

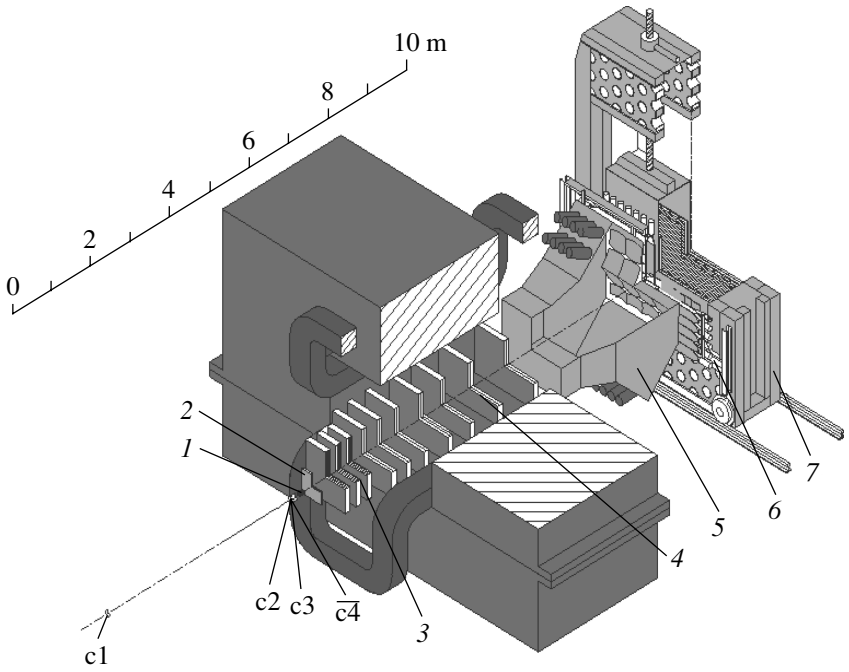

Fig. 3. Schematic of the experimental setup SVD: c1, c2—beam monitor; c3—nuclear and hydrogen targets; $\overline{\text{c4}}$—silicon vertex detector; *1*, *2* and *3*, *4*—tracker of the magnetic spectrometer, drift tubes, and proportional chambers; *5*—threshold Cherenkov counter; *6*—scintillation hodoscope; *7*—electromagnetic calorimeter.

to collect enough statistic for study the ring events. Accurate data will make it possible to determine the confinement radius and refractive index of hadron matter.

2.6. Direct Photons

Direct photons (DP) by definition are not a decay product of any known particles. In accordance with quantum electrodynamics, they may be emitted in the process of charged particle scattering. In particular, quark–quark and quark–gluon interaction leads to photon emission. The higher the density and the longer the system lifetime, the more DP it should emit. This simple picture explains why so many experimental and theoretical efforts are devoted to the study of DP. The phenomenon of DP was discovered, but, it seems, nothing unusual has been found up to now: the DP rate agrees with the general theoretical expectation. But there is one exception. They are low-energy photons $p_\perp \leq 0.1$ GeV/c, $x \leq 0.01$. One can cite at least three publications where the low-energy photon spectrum is measured and the photon rate exceeds the theoretical prediction by a factor of 5–7. It is K^+p and $p\bar{p}$ interaction at 70 GeV and π^+p and K^+p interaction at 250 GeV [19]. The excess of DP may be connected with some unknown physical process. It is especially interesting to investigate DP in the proposed experiment, since we are going to deal with a high-density system. The quark–gluon cascade leading to a high-multiplicity final state has a large number of steps (rescattering, loops, and so on) and each of them is connected with bremsstrahlung. Apart from this, at high density an additional source of γ is predicted [20]: the charged pion annihilation $\pi^+\pi^- \to n\gamma$. This process, if it is discovered, may serve as one of the tools of density and temperature measurement.

3. EXPERIMENTAL SETUP

The experiment will be carried out at the improved setup SVD installed at the extracted proton beam of the IHEP (Protvino) U-70 accelerator [21]. The physics program dictates the following requirements to the apparatus.

(i) The setup is capable of detecting, with high efficiency, events with large charge and (or) neutral multiplicity of 20–50 particles. Photon multiplicity is up to 100. The energy threshold of γ detection is 50 MeV.

(ii) The trigger system is capable of selecting rare events with multiplicity $n_\pi = 20$–50. The coefficient of suppression of low-multiplicity events $n_\pi < 20$ is 10^3.

(iii) The magnetic spectrometer has resolution $\delta p/p \approx 1\%$ in the momentum interval $p = 0.3$–4.0 GeV/c.

The setup schematic is presented in Fig. 3. The apparatus consists of the following main parts.

The position sensitive beam monitor.

The liquid hydrogen target has a diameter of 2 cm and length of 2.5 cm. The apparatus test and some data collection may be done with a nuclear target.

The vertex detector consists of ten planes of silicon strip detectors with space resolution of 2.5–5.0 μm.

The trigger solution is obtained from a combination of amplitude signals and number of hits in strip detectors and electromagnetic calorimeter signal.

The magnet has bending power equal to 1.5 T m and aperture $X \times Y = 130 \times 160$ cm.

The tracker of the magnetic spectrometer consists of 25 planes of drift tubes and proportional chambers.

4. CONCLUSION

The goal of the proposed experiment "Thermalization" is the investigation of collective behavior of particles in the process of multiple hadron production in pp (or pN) interaction $pp \to n_\pi\pi + 2N$ at the beam energy $E_{\rm lab} = 70$ GeV. The domain of high multiplicity $n_\pi = 30$–50, or $z = n/\bar{n} = 4$–6, will be studied. Near the threshold of reaction $n_\pi \to 69$, $z \to z_{\rm th} = 8.2$, all particles acquire small relative momentum $\Delta q < 1/R$, where R is the size of the particle production region. As a consequence of multiboson interference, a number of collective effects may show up.

The physics objectives of the experiment are as follows:

1. Search for new phenomena.

(a) Drastic broadening of the multiplicity distribution $\sigma(z)$ is expected due to effect of BEC. In the region $n_\pi \geq 40$, $z \geq 5$, the actual cross section $\sigma(z)$ may exceed by three orders of magnitude the extrapolated function $\sigma_{\rm extr}(z)$. The latter is calculated on the basis of QCD or qq-collision model without inclusion of the BEC effect.

(b) The BEC may manifest itself by formation of narrow jets of identical particles or "cold spots" in momentum space. The other notions for this effect are pion laser, classical boson field, and boson condensate.

(c) The particle sources may be of two types: chaotic and coherent. Precision measurement of the two-particle correlation function $R(q)$ makes it possible to determine the source parameters: chaoticity, spacetime size, primordial correlation length and time. The latter are dynamic characteristics of hadron matter.

(d) The large variation of the π^+, π^-, π^0 multiplicity is expected in the framework of BEC. The multiplicity fluctuations may also manifest classical pionic field production or onset of chiral condensate.

2. The systematic and precision study of known phenomena.

(a) The direct photons, especially with low energy $E_\gamma \leq 100$ MeV, may manifest new physics, in particular, existence of QGP.

(b) The study of stochastic intermittency is the instrument for phase transition search and also search for the BEC effect of the cold spot type.

(c) The existence of events with regular intermittency, so-called ring events, is published. This effect is referred as a gluonic Cherenkov radiation. It needs confirmation. If it really exists, it will be a genuine probe of hadronic matter properties.

(d) The measurement of the production rate of particles of different species π, K, p, d, $\bar{p}$ gives data for test and development of thermodynamics models. Simultaneous analysis of the differential cross section and BEC functions makes it possible to disentangle the hadronic system size, temperature, and expansion rate.

The experiment will be carried out at a 70-GeV proton beam of the IHEP U-70 accelerator. The apparatus design is essentially based on the fact that, at high multiplicity, all secondary particles have sharp forward collimation. In spite of the modest setup size, it is expected that at least 70% of all particles will drop into the aperture of the apparatus and will be detected.

The apparatus includes a liquid hydrogen target, silicon vertex detector, magnetic spectrometer, and electromagnetic calorimeter. The multilevel trigger system is designed to select the rare events with high charge and neutral multiplicity $n_\pi \geq 20$. The target luminosity is 10^{30} cm^{-2} s^{-1} at a beam intensity of 10^7s^{-1}.

The magnet spectrometer provides high momentum resolution $\delta p \leq 5$ MeV/c, which is crucially important for BEC investigation.

The counting rate of events with total multiplicity 40 is expected to be 10 events/h. If the scenario of BEC is realized, then counting rate will be substantially higher.

REFERENCES

1. R. Hagedorn, Riv. Nuovo Cimento **6** (10), 1 (1983).
2. J. D. Manjavidze, Fiz. Élem. Chastits At. Yadra **16**, 101 (1985) [Sov. J. Part. Nucl. **16**, 44 (1985)]; J. Manjavidze and A. Sissakian, Preprint No. E2-2000-217, JINR (Joint Inst. Nucl. Res., Dubna, 2000); Phys. Rep. **346**, 1 (2001).
3. J. D. Bjorken, Phys. Rev. D **27**, 140 (1983).
4. I. L. Rosental and Yu. A. Tarasov, Usp. Fiz. Nauk **163** (7), 29 (1993) [Phys. Usp. **36**, 572 (1993)].

5. E. L. Feinberg *et al.*, Usp. Fiz. Nauk **104**, 539 (1971) [Sov. Phys. Usp. **14** (4), 455 (1971)].
6. I. M. Dremin, Usp. Fiz. Nauk **164**, 785 (1994); A. E. De Wolf *et al.*, Phys. Rep. **270**, 1 (1996).
7. A. I. Golokhvastov, Preprint No. P2-98-181, JINR (Joint Inst. Nucl. Res., Dubna, 1998).
8. V. V. Babintsev *et al.,* Preprint No. M-25 (Inst. High Energy Phys., Protvino, 1976); M. Yu. Bogolyubsky *et al.,* Preprint No. 97-50 (Inst. High Energy Phys., Protvino, 1997).
9. S. Pratt, Phys. Rev. C **50**, 469 (1994).
10. G. F. Bertch, Phys. Rev. Lett. **72**, 2349 (1994).
11. R. Lednitsky *et al.*, Phys. Rev. C **61**, 034901 (2000).
12. V. G. Boiko *et al.*, Fiz. Élem. Chastits At. Yadra **22**, 675 (1991) [Sov. J. Part. Nucl. **22**, 326 (1991)].
13. P. F. Ermolov, in *Proceedings of the 21 Session of IHEP PAC, Serpukhov, 1977*, p. 67.
14. O. G. Chikilev and P. V. Shliapnikov, Yad. Fiz. **55**, 779 (1992) [Sov. J. Nucl. Phys. **55**, 432 (1992)].
15. M. I. Podgoretsky, Preprint No. P2-85-240 (Joint Inst. Nucl. Res., Dubna, 1985).
16. A. A. Anselm and M. G. Ryskin, Phys. Lett. B **266**, 482 (1991).
17. I. M. Dremin, Pis'ma Zh. Éksp. Teor. Fiz. **30**, 152 (1979) [JETP Lett. **30**, 140 (1979)]; Fiz. Élem. Chastits At. Yadra **18**, 31 (1987) [Sov. J. Part. Nucl. **18**, 31 (1987)].
18. I. M. Dremin *et al.*, Yad. Fiz. **52**, 840 (1990) [Sov. J. Nucl. Phys. **52**, 536 (1990)].
19. P. V. Chlapnikov *et al.*, Phys. Lett. B **141B**, 276 (1984); M. N. Ukhanov *et al.*, Preprint No. 86-195, IHEP (Inst. High Energy Phys., Protvino, 1986); F. Botterwerk *et al.*, Z. Phys. C **51**, 541 (1991).
20. M. K. Volkov and E. Kuraev, Phys. Lett. B **424**, 235 (1998); E. A. Kuraev and M. K. Volkov, Yad. Fiz. **62**, 133 (1999) [Phys. At. Nucl. **62**, 128 (1999)].
21. S. G. Basiladze *et al.*, Preprint No. 99-28/586, NIIYaF MGU (Inst. Nucl. Phys., Moscow State Univ., 1999).

Physics of Atomic Nuclei, Vol. 67, No. 1, 2004, pp. 11–20. From Yadernaya Fizika, Vol. 67, No. 1, 2004, pp. 13–22.

On Thermodynamic Description of Inelastic Hadron Collisions*

J. Manjavidze**

Institute of Physics, Georgian Academy of Sciences, Tbilisi, Georgia
Joint Institute for Nuclear Research, Dubna, Moscow oblast, 141980 Russia

Received May 21, 2003

Abstract—The S-matrix perturbation theory for the generating functional of Wigner functions at a finite temperature is derived. Two possible boundary conditions are considered. One of them is usual in a field theory vacuum boundary condition. The corresponding generating functional of Wigner functions can be used in particle physics. Another type of boundary condition assumes that the system under consideration is in an environment of blackbody radiation. This leads to the usual, in statistics, Kubo–Martin–Schwinger boundary condition at the equilibrium limit. The comparison of the S-matrix approach with the "nonstationary statistical operator" approach of Zubarev is considered. The range of applicability of the finite-temperature description of dissipation processes is discussed. © *2004 MAIK "Nauka/Interperiodica"*.

1. INTRODUCTION

The field-theoretical description of statistical systems at a finite temperature is usually based on the formal analogy between imaginary time and inverse temperature β ($\beta = 1/T$) [1]. This approach is productive [2] for the description of static properties of a system, but it requires a complicated mathematical formalism of the analytic continuation to real time [3] if we want to clear up the dynamical aspects of the statistical system.

The first important quantitative attempt to build up the real-time finite-temperature field theory [4] discovered a problem of the pinch singularities. Further investigations of the theory have allowed one to demonstrate the cancellation mechanism of these unphysical singularities [5]. This is attained by doubling the degrees of freedom [6, 7]: the Green's functions of the theory represent a 2×2 matrix. It surely makes the theory more complicated, but the operator formalism of the thermofield dynamics [8] shows the unavoidable character of this complication.

The Schwinger–Keldysh real-time finite-temperature field-theoretical description [6, 7] of statistical systems is based on the Kubo–Martin–Schwinger (KMS) [9, 10] boundary condition for a field:

$$\Phi(t) = \Phi(t - i\beta).$$

This formal trick introduces into the formalism the temperature $T = 1/\beta$ but without fail leads to equilibrium fluctuation–dissipation conditions [11] (see also [12]).

The multiple production may be considered as a process of dissipation of kinetic energy of colliding particles into the mass of produced particles [13]. The corresponding S-matrix approach to the finite-temperature description of inelastic particle collisions can be introduced (e.g., [14] and references cited therein) taking into account that, for instance,

$$d\Gamma_n = |a_{n,m}(\epsilon(q_1), \epsilon(q_2), \ldots, \epsilon(q_n))|^2 \times \prod_1^n \frac{d^3 q_i}{(2\pi)^3 \cdot 2\epsilon(q_i)}, \qquad \epsilon(q) = (q^2 + m_h^2)^{1/2},$$

is the differential measure of the final state, where $a_{n,m}(\epsilon(q_1), \epsilon(q_2), \ldots, \epsilon(q_n))$ is the corresponding amplitude. Then, following Gibbs [15], the state is characterized by the integral

$$Z_n = \int d\Gamma_n \delta\left(E - \sum_{i=1}^n \epsilon(q_i)\right).$$

We can define the temperature as the function of initial energy through the equation of state, i.e., proportional to the mean energy of created particles. Such introduction of temperatures as the Lagrange multiplier is obvious for the microcanonical approach [9]. The initial-state temperature will be introduced, if this is possible, in the same way. Using the standard terminology [10], we will deal in our approach with the "mechanical" perturbations only [16] and it will not be necessary to divide the perturbations into "thermal" and "mechanical" ones [17].

Introducing the temperature as the Lagrange multiplier, we should assume that the temperature fluctuations are small (Gaussian). In the opposite case, the notion of temperature loses its sense. The

*This article was submitted by the author in English.

**e-mail: joseph@nusun.jinr.ru

"working" idea concerning nonequilibrium processes is based on the assumption that evolution of a system goes through a few phases. In the first ("fast") phase, the s-particle distribution functions $\mathbf{D}_s$, $s > 1$, strongly depend on the initial conditions. But at the end of this phase, the system forgets the initial-state information. The second phase is "kinetic." One can expect that the spacetime fluctuations of thermodynamic parameters in this phase are large scaled, i.e., there are macroscopic domains in which the subsystems are in equilibrium with Gaussian fluctuations of thermodynamic parameters. In the last ("hydrodynamic") phase, the whole system is described by macroscopic parameters. We will see that the Schwinger–Keldysh [3, 6, 7] real-time finite-temperature formalism is applicable for the "hydrodynamic" phase only.

The described S-matrix finite-temperature approach can be realized not only for a uniform temperature distribution (we have done the first step in this direction, wishing to introduce initial and final temperatures separately). Thus, introducing cells of a measuring device (calorimeter) and introducing the energy–momentum shells of each cell separately, we can introduce the individual temperatures in each cell. This can be done since in the S-matrix theory the measurement is performed by free (mass-shell) particles, i.e., the measurement of energy (and momentum) can be performed in each cell separately. This allows one to capture the "kinetic" phase also (if the number of calorimeter cells is high enough). In this phase, multiparticle distribution functions $\mathbf{D}_s$, $s > 1$, are the functionals of the one-particle distribution function $\mathbf{D}_1$ only. This means the "shortened" description of the nonequilibrium medium [18]. We will return to this question considering the range of applicability of thermal descriptions of the dissipative processes.

Wigner proposed the function $W(q, R)$ for the phase space description of quantum states [19]:

$$W(q,R) = \int dr e^{iqr} \Psi(R + r/2)\Psi^*(R - r/2),$$

where $\Psi(x)$ is the wave function of state (see also [20]).

In the classical limit $\hbar = 0$, the function $W(q, r)$ coincides with the phase space probability distribution function. It obeys the equation [21]

$$\dot{W} = \{W, H\} + O(\hbar),$$

which coincides with the Liouville equation only in the classical limit $\hbar = 0$.

The extension of Wigner's idea on the relativistic case uses the connection between Wigner's approach and inclusive description of inelastic scattering processes [22, 23]. But the Wigner functions are not directly measurable quantities because of the quantum uncertainty principle $\Delta q \Delta r \sim \hbar$. This restriction leads to the impossibility of taking the 4-dimensional, of the cells of the measuring device (calorimeter) arbitrarily small (Δr).

Thus, in our terms, one can use the thermodynamic formalism if the "shortened" description of the nonstationary medium may be applied: in this case, a mean value of correlation functions over spacetime are negligible and the fluctuations of thermodynamic parameters are small (Gaussian).

In proposing [24] that the equilibrium in the nonuniform nonstationary medium may be attained in small regions more quickly than in the whole system, the entropy maximality in these restricted domains of a system can be used for the construction of the "local equilibrium density matrix" (LDM) [24]. But the LDM is applicable for description of processes in which dissipation may be disregarded [25]. Nevertheless, if the energy–momentum density of nonstationary flow is considerably smaller than the energy density of matter, then the first one can be taken into account perturbatively considering the LDM as the initial condition. This modifies the LDM into the "nonstationary density matrix" (NDM) of Zubarev [24] if an infinitesimal interaction with a heat bath is introduced to get increasing entropy.

2. S-MATRIX INTERPRETATION OF THERMODYNAMICS

2.1. Vacuum Boundary Conditions

The starting point of our calculations is the n-into-m-particles transition amplitude $a_{n,m}$, the derivation of which is a well-known procedure [26]. So, $a_{n,m}$ in the momentum representation has the form

$$a_{n,m}((q)_n;(p)_m) \tag{2.1}$$
$$= (-i)^{n+m} \prod_{k=1}^{m} \hat{\phi}(q_k) \prod_{k=1}^{n} \hat{\phi}^*(p_k) Z(\phi).$$

Here, we introduce the "annihilation" operator

$$\hat{\phi}(q) = \int dx e^{-iqx} \hat{\phi}(x), \quad \hat{\phi}(x) = \frac{\delta}{\delta \phi(x)}; \tag{2.2}$$

$\hat{\phi}^*(p_k)$ is the "creation" operator. The generating functional

$$Z(\phi) = \int D\Phi e^{iS(\Phi) - iV(\Phi+\phi)},$$

where $S(\Phi)$ is the free part of the action and $V(\Phi, \phi)$ describes the interactions. At the very end, one should set the auxiliary field $\phi = 0$.

To provide the convergence of the integral (2.1) over the scalar field, Φ, the action $S(\Phi)$ must contain a positive imaginary part. One may shift infinitesimally the time contour into the upper half plane [3, 27],

$$C_+ : t \to t + i\epsilon, \quad \epsilon > 0,$$

and after all calculations return the time contour to the real axis, $\epsilon \to +0$. In Eq. (2.1), the integration is performed over all field configurations with a standard vacuum boundary condition:

$$\int d^4x \partial_\mu (\Phi \partial^\mu \Phi) = \int\limits_{\sigma_\infty} d\sigma_\mu \Phi \partial^\mu \Phi = 0.$$

We introduce the probability

$$r(P) = \sum_{n,m} \frac{1}{n!m!} \int d\omega_n(q) d\omega_m(p) \tag{2.3}$$
$$\times\, \delta^{(4)}\left(P - \sum_{k=1}^{n} q_k\right) \delta^{(4)}\left(P - \sum_{k=1}^{n} p_k\right) |a_{n,m}|^2,$$

where

$$d\omega_n(q) = \prod_{k=1}^{n} d\omega(q_k) = \prod_{k=1}^{n} \frac{d^3 q_k}{(2\pi)^3 \cdot 2\epsilon(q_k)},$$
$$\epsilon = (q^2 + m_h^2)^{1/2},$$

is the Lorentz-invariant phase space element. It is evident that

$$r = \int d^4 P r(P)$$

is the imaginary part of the amplitude, $\langle \mathrm{vac}|\mathrm{vac}\rangle$. Therefore, for the computing of $r(P)$, the standard renormalization procedure can be applied and no new divergences will arise.

The Fourier transformation of δ functions in (2.3) allows one to write $r(P)$ in the form [28, 29]

$$r(P) = \int \frac{d^4\alpha_1}{(2\pi)^4} \frac{d^4\alpha_2}{(2\pi)^4} e^{iP(\alpha_1+\alpha_2)} \rho(\alpha),$$

where

$$\rho(\alpha) = \sum_{n,m} \frac{1}{n!m!} \int \prod_{k=1}^{n} \{d\omega(q_k) e^{-i\alpha_1 q_k}\} \tag{2.4}$$
$$\times \prod_{k=1}^{m} \{d\omega(p_k) e^{-i\alpha_2 p_k}\} |a_{n,m}|^2.$$

Inserting (2.1) into (2.4), we find that

$$\rho(\alpha) \tag{2.5}$$
$$= \exp\left\{ i \int dx dx' (\hat\phi_+(x) D_{+-}(x - x', \alpha_2) \hat\phi_-(x') - \hat\phi_-(x) D_{-+}(x - x', \alpha_1) \hat\phi_+(x')) \right\} Z(\phi_+) Z^*(\phi_-),$$

where D_{+-} and D_{-+} are the positive and negative frequency correlation functions;

$$D_{+-}(x - x', \alpha) = -i \int d\omega(q) e^{iq(x-x'-\alpha)}$$

describing the process of particle creation at the time moment x_0 and its absorption at x_0', $x_0 > x_0'$, and α is the center-of-mass (CM) 4-coordinate. The function

$$D_{-+}(x - x', \alpha) = i \int d\omega(q) e^{-iq(x-x'+\alpha)}$$

describes the opposite process, $x_0 < x_0'$. They obey the homogeneous equations

$$(\partial^2 + m^2)_x D_{+-} = (\partial^2 + m^2)_x D_{-+} = 0.$$

We suppose that $Z(\phi)$ may be computed perturbatively. For this purpose, the following transformations will be used:

$$e^{-iV(\phi)} = e^{-i\int dx \hat j(x) \hat\phi'(x)} e^{i \int dx j(x) \phi(x)} \tag{2.6}$$
$$\times\, e^{-iV(\phi')} = e^{\int dx \phi(x) \hat\phi'(x)} e^{-iV(\phi')}$$
$$= e^{-iV(-i\hat j)} e^{i\int dx j(x)\phi(x)},$$

where $\hat\phi$ was defined in (2.2) and at the end of calculations the auxiliary variables j, ϕ' should be taken equal to zero. Using the first equality in (2.6) we find that

$$Z(\phi) = e^{-i\int dx \hat j(x) \hat\Phi(x)} e^{-iV(\Phi+\phi)} \tag{2.7}$$
$$\times \exp\left\{ -\frac{i}{2} \int dx dx' j(x) D_{++}(x - x') j(x') \right\},$$

where D_{++} is the causal Green's function

$$(\partial^2 + m^2)_x G_{++}(x - y) = \delta(x - y).$$

Inserting (2.7) into (2.5) after simple manipulations with differential operators [see (2.6)], we find the expression

$$\rho(\alpha) = e^{-iV(-i\hat j_+) + iV(-i\hat j_-)} \tag{2.8}$$
$$\times \exp\left\{ \frac{i}{2} \int dx dx' (j_+(x) D_{+-}(x - x', \alpha_1) j_-(x') - j_-(x) D_{-+}(x - x', \alpha_2) j_+(x') - j_+(x) D_{++}(x - x') j_+(x') + j_-(x) D_{--}(x - x') j_-(x')) \right\},$$

where

$$D_{--} = (D_{++})^*$$

is the anticausal Green's function.

Considering the system with a large number of particles, we can simplify calculations choosing the CM frame $P = (P_0 = E, \mathbf{0})$. It is also useful [9, 14] to rotate the contours of integration over $\alpha_{0,k}$: $\alpha_{0,k} = -i\beta_k$, $\mathrm{Im}\beta_k = 0$, $k = 1, 2$. As a result, omitting an unnecessary constant, we will consider $\rho = \rho(\beta_1, \beta_2)$.

The integrals over β_k

$$r(E) = \int \frac{d\beta_1}{2\pi i}\frac{d\beta_2}{2\pi i} e^{(\beta_1+\beta_2)E} e^{-F(\beta_1,\beta_2)}, \qquad (2.9)$$

where

$$F(\beta_1, \beta_2) = -\ln \rho(\beta_1, \beta_2),$$

can be computed by the stationary phase method. This assumes that the total energy E is a fixed quantity. The solutions to the equations (of state)

$$E = \frac{\partial F(\beta_1, \beta_2)}{\partial \beta_k}, \quad k = 1, 2, \qquad (2.10)$$

give the most probable values of β_k at a given E. Equations (2.10) always have real solutions and, because of energy conservation law, both equations (2.10) have the same solution with the property [9]

$$\beta_k = \beta(E), \qquad \beta > 0.$$

Assuming that β is a "good" parameter, i.e., that the fluctuations of β_k are Gaussian, we can interpret $F(\beta_1, \beta_2)$ as the free energy and $1/\beta_k$ as the temperatures. Such a definition of thermodynamic parameters is in the spirit of microcanonical description. We will return to this question.

The structure of the generating functional (2.8) is the same as the generating functional of Niemi–Semenoff [5]. The difference lies in the definition of Green's functions assigned on the complex time contours $C_\pm$ ($C_- = C_+^*$) [7]. The doubling of the degrees of freedom is unavoidable since Green's functions D_{ij} are singular on the light cone.

2.2. Closed-Path Boundary Conditions

The generating functional $\rho(\alpha, z)$ has the important factorization property [see (2.5)]

$$\rho(\alpha) = e^{\hat{N}(\alpha;\phi)}\rho_0(\phi_\pm),$$

where the operator

$$\hat{N}(\alpha;\phi) \qquad (2.11)$$
$$= \int dx dx' (\hat{\phi}_+(x) D_{+-}(x - x', \alpha_2)\hat{\phi}_-(x') - \hat{\phi}_-(x) D_{-+}(x - x', \alpha_1)\hat{\phi}_+(x'))$$

acts on the generating functional

$$\rho_0(\phi_\pm) = Z(\phi_+)Z^*(\phi_-) \qquad (2.12)$$
$$= \int D\Phi_+ D\Phi_- \exp\{iS(\Phi_+) - iS(\Phi_-) - iV(\Phi_+ + \phi_+) + iV(\Phi_- + \phi_-)\}$$

of measurables. All external information was prescribed in the operator $\hat{N}(\alpha_1, \alpha_2; \phi)$ and interactions are hidden in $\rho_0(\phi_\pm)$.

By definition, the path integral (2.12) describes the closed path motion in the space of fields Φ. Hence, we can introduce the following boundary condition:

$$\int\limits_{\sigma_\infty} d\sigma_\mu \Phi_+ \partial^\mu \Phi_+ = \int\limits_{\sigma_\infty} d\sigma_\mu \Phi_- \partial^\mu \Phi_-. \qquad (2.13)$$

It requires that the fields Φ_+ and Φ_- (and their first derivatives) coincide on the boundary hypersurface σ_∞:

$$\Phi_\pm(\sigma_\infty) = \Phi(\sigma_\infty),$$

where, by definition, $\Phi(\sigma_\infty)$ is an arbitrary, "turning-point," field.

The existence of nontrivial field $\Phi(\sigma_\infty)$, in the absence of surface terms, has influence only on the structure of Green's functions G_{ij}. The general solution to equations for the Green's functions looks as follows:

$$G_{ii} = D_{ii} + g_{ii}, \quad G_{ij} = g_{ij}, \quad i \neq j. \qquad (2.14)$$

It contains the term g_{ij} which must obey the homogeneous equation

$$(\partial^2 + m^2)_x g_{ij}(x - y) = 0, \quad i, j = +, -. \qquad (2.15)$$

The general solution to these equations,

$$g_{ij}(x - x') = \int d\omega(q) e^{iq(x-x')} n_{ij}(q), \qquad (2.16)$$
$$q^2 = m^2,$$

is defined through the unknown functions n_{ij}. The latter are the functionals of "turning-point" field $\Phi(\sigma_\infty)$: if $\Phi(\sigma_\infty) = 0$, we must have $n_{ij} = 0$ and we must return to the theory of the previous section.

We should suppose that, on the infinitely far hypersurface σ_∞, only the free, i.e., mass-shell, particles may exist. This is natural in the S-matrix framework [30]. In other respects, the choice of the boundary condition is arbitrary.

Therefore, we describe evolution of the system in a background field of mass-shell particles. Let us assume that there are no any special correlations among them except the constraints of energy–momentum conservation laws. Then the derivation is the same as in [29].

After these preliminaries, it is easy to find that, in the CM frame, we have

$$n_{++}(q_0) = n_{--}(q_0) \tag{2.17}$$
$$= \left[\exp\left(\frac{\beta_1+\beta_2}{2}|q_0|\right)-1\right]^{-1} \equiv \tilde{n}\left(|q_0|\frac{\beta_1+\beta_2}{2}\right).$$

Computing n_{ij} for $i \neq j$, we must take into account that we have one additional particle:

$$n_{+-}(q_0) = \Theta(q_0)(1+\tilde{n}(q_0\beta_1)) \tag{2.18}$$
$$+ \Theta(-q_0)\tilde{n}(-q_0\beta_1)$$

and

$$n_{-+}(q_0) = \Theta(q_0)\tilde{n}(q_0\beta_2) \tag{2.19}$$
$$+ \Theta(-q_0)(1+\tilde{n}(-q_0\beta_2)).$$

Using (2.17), (2.18), and (2.19), as well as definition (2.14), we find the Green's functions (the matrix Green's functions in real-time finite-temperature field theories were first introduced in [31])

$$G_{ij}(x-x',(\beta)) = \int \frac{d^4q}{(2\pi)^4} e^{iq(x-x')}\tilde{G}_{ij}(q,(\beta)),$$

where

$$i\tilde{G}_{ij}(q,(\beta)) \tag{2.20}$$
$$= \begin{pmatrix} \dfrac{i}{q^2-m^2+i\epsilon} & 0 \\ 0 & -\dfrac{i}{q^2-m^2-i\epsilon} \end{pmatrix}$$
$$+ 2\pi\delta(q^2-m^2)$$
$$\times \begin{pmatrix} \tilde{n}\left(\dfrac{\beta_1+\beta_2}{2}|q_0|\right) & \tilde{n}(\beta_2|q_0|)a_+(\beta_2) \\ \tilde{n}(\beta_1|q_0|)a_-(\beta_1) & \tilde{n}\left(\dfrac{\beta_1+\beta_2}{2}|q_0|\right) \end{pmatrix}$$

and

$$a_\pm(\beta) = -e^{\beta(|q_0|\pm q_0)/2}.$$

The corresponding generating functional has the standard form

$$\rho_{\rm cp}(j_\pm) = \exp\{-iV(-i\hat{j}_+) + iV(-i\hat{j}_-)\} \tag{2.21}$$
$$\times \exp\left\{\frac{i}{2}\int dxdx' j_i(x)G_{ij}(x-x',(\beta))j_j(x')\right\},$$

where the summation over repeated indices is assumed.

Inserting (2.21) into the equation of state (2.10), we can find that $\beta_1 = \beta_2 = \beta(E)$. If $\beta(E)$ is a "good" parameter, then $G_{ij}(x-x';\beta)$ coincides with the Green's functions of the real-time finite-temperature field theory and the KMS boundary condition

$$G_{+-}(t-t') = G_{-+}(t-t'-i\beta), \tag{2.22}$$
$$G_{-+}(t-t') = G_{+-}(t-t'+i\beta)$$

is restored. Equation (2.22) can be deduced from (2.20) by direct calculations.

3. RANGE OF THE "HYDRODYNAMIC" APPROXIMATION

Let us return now to Eq. (2.4). To find the physical meaning of $\beta_{1(2)}$, we must show the way how they can be measured. If there is a nonequilibrium flow, it is hard to invent a thermometer (or thermodynamic calorimeter) which measures the temperatures of these dissipative processes spacetime locally. Another way is to define the temperatures through equations of state. This is possible in the accelerator experiments where the total energy E is fixed. The definition of temperature, both canonical and microcanonical, must coincide and, therefore, $\beta_{1(2)}$ must be "good" quantities; i.e., the fluctuations near solutions to Eqs. (2.10) must be Gaussian.

This assumption is the main problem facing nonequilibrium thermodynamics. The problem in our microcanonical terms looks as follows: the expansion near $\beta_{1(2)}(E)$ gives asymptotic series over

$$\int \mathbf{D}_s \sim \int \prod \{d\omega(k_i)dr_i\}\langle\epsilon(k_1)\epsilon(k_2)\cdots\rangle|_{(r_1,r_2,\ldots)},$$

where $\langle\,\rangle_{()}$ means the averaging over fields drawn on fixed points of phase space $(k,r)_i$. In other words, the fluctuations near $\beta_{1(2)}(E)$ are defined by the value of inclusive spectra familiar in particle physics. Therefore, $\beta_{1(2)}(E)$ are "good" quantities if these inclusive spectra are small. But this is too strong an assumption. A more careful analysis shows that having the factorization properties is enough [32]:

$$\int \prod \{d\omega(k_i)dr_i\}\langle\epsilon(k_1)\epsilon(k_2)\cdots\rangle|_{(r_1,r_2,\ldots)} \tag{3.1}$$
$$- \prod \int d\Omega(k_i)dr_i\langle\epsilon(k_i)\rangle|_{(r_i)} \sim 0.$$

It must be noted that this is the unique solution of the problem since the expansion near $\beta_{1(2)}(E)$ unavoidably leads to asymptotic series with zero radii of the convergence.

One can hope to avoid this problem working permanently in the energy–momentum representation, i.e., without the introduction of temperatures. Of course, this is possible in particle physics, but if $\beta_{1(2)}(E)$ is not a "good" parameter, this means that all correlations between created particles are sufficient, i.e., only the energy–momentum representation does not solve the problem.

Finally, the discussed factorization property of $\mathbf{D}_s$, $s > 1$, is the well known Bogolyubov condition of the

"shortened" description of nonequilibrium thermodynamic systems with s-particle distribution functions $\mathbf{D}_s$, $s>1$, expressed in terms of $\mathbf{D}_1$. It is the condition for the applicability of "hydrodynamic" descriptions since it assumes that the constant $\beta_1(E)=\beta_2(E)$ is a "good" parameter for the description of the whole system.

4. LOCAL EQUILIBRIUM HYPOTHESIS

4.1. Vacuum Boundary Condition

We start the consideration from the assumption that the temperature fluctuations are of large scale. In a cell whose dimension is much smaller than the fluctuation scale of temperature, we can assume that the temperature is a "good" parameter. (A "good" parameter means that the corresponding fluctuations are Gaussian.)

Let us surround the interaction region, i.e., the system under consideration, by N cells with known spacetime position and let us propose that we can measure the energy and momentum of groups of in- and outgoing particles in each cell. The 4-dimensional of cells cannot be arbitrarily small in this case because of the quantum uncertainty principle.

To describe this situation, we decompose δ functions on the product of $(N+1)$ δ functions:

$$\delta^{(4)}\left(P-\sum_{k=1}^{n}q_k\right)=\int\prod_{\nu=1}^{N}\left\{dQ_\nu\delta\left(Q_\nu-\sum_{k=1}^{n_\nu}q_{k,\nu}\right)\right\}\times\delta^{(4)}\left(P-\sum_{\nu=1}^{N}Q_\nu\right),$$

where $q_{k,\nu}$ is the momentum of the kth ingoing particle in the νth cell and Q_ν is the total 4-momentum of n_ν ingoing particles in this cell, $\nu=1,2,\ldots,N$. The same decomposition will be used for the second δ function. We must take into account the multinomial character of particle decomposition on N groups. This will give the coefficient

$$\frac{n!}{n_1!\cdots n_N!}\delta_{\mathrm{K}}\left(n-\sum_{\nu=1}^{N}n_\nu\right)\times\frac{m!}{m_1!\cdots m_N!}\delta_{\mathrm{K}}\left(m-\sum_{\nu=1}^{N}m_\nu\right),$$

where δ_{K} is the Kronecker δ function.

As a result, the quantity

$$r((Q)_N,(P)_N)=\sum_{(n,m)}\int|a_{(n,m)}|^2\times\prod_{\nu=1}^{N}\left\{\prod_{k=1}^{n_\nu}\frac{d\omega(q_{k,\nu})}{n_\nu!}\delta^{(4)}\left(Q_\nu-\sum_{k=1}^{n_\nu}q_{k,\nu}\right)\times\prod_{k=1}^{m_\nu}\frac{d\omega(p_{k,\nu})}{m_\nu!}\delta^{(4)}\left(P_\nu-\sum_{k=1}^{m_\nu}p_{k,\nu}\right)\right\} \tag{4.1}$$

describes the probability of measuring in the νth cell the fluxes of both ingoing particles with total 4-momentum Q_ν and outgoing particles with the total 4-momentum P_ν. The sequence of these two measurements is not fixed.

The Fourier transformation of δ functions in (4.1) gives

$$r((Q)_N,(P)_N)=\int\prod_{k=1}^{N}\frac{d^4\alpha_{1,\nu}}{(2\pi)^4}\frac{d^4\alpha_{2,\nu}}{(2\pi)^4}\times\exp\left\{i\sum_{\nu=1}^{N}(Q_\nu\alpha_{1,\nu}+P_\nu\alpha_{2,\nu})\right\}\rho((\alpha_1)_N,(\alpha_2)_N),$$

where $\rho((\alpha_1)_N,\ (\alpha_2)_N)=\rho(\alpha_{1,1},\ \alpha_{1,2},\ldots,\alpha_{1,N};\ \alpha_{2,1},\alpha_{2,2},\ldots,\alpha_{2,N})$ has the form

$$\rho((\alpha_1)_N,(\alpha_2)_N)=\int\prod_{\nu=1}^{N}\left\{\prod_{k=1}^{n_\nu}\frac{d\omega(q_{k,\nu})}{n_\nu!}e^{-i\alpha_{1,\nu}q_{k,\nu}}\times\prod_{k=1}^{m_\nu}\frac{d\omega(p_{k,\nu})}{m_\nu!}e^{-i\alpha_{2,\nu}p_{k,\nu}}\right\}|a_{(n,m)}|^2. \tag{4.2}$$

Inserting (2.1) into (4.2) we find

$$\rho((\alpha_-)_N,(\alpha_+)_N)=\exp\left\{i\sum_{\nu=1}^{N}\int dxdx'[\hat\phi_+(x)\times D_{+-}(x-x';\alpha_{2,\nu})\hat\phi_-(x')-\hat\phi_-(x)\times D_{-+}(x-x';\alpha_{1,\nu})\hat\phi_+(x')]\right\}Z(\phi_+)Z^*(\phi_-), \tag{4.3}$$

where ϕ_- is defined on the complex conjugate contour C_-: $t\to t-i\epsilon$ and $D_{+-}(x-x';\alpha)$ and $D_{-+}(x-x';\alpha)$ are the positive and negative frequency correlation functions, respectively.

We must integrate over sets $(Q)_N$ and $(P)_N$ if the distribution of fluxes of momenta over cells is not fixed. As a result,

$$r(P)=\int D^4\alpha_1(P)d^4\alpha_2(P)\rho((\alpha_1)_N,(\alpha_2)_N), \tag{4.4}$$

where the differential measure

$$D^4\alpha(P)=\prod_{\nu=1}^{N}\frac{d^4\alpha_\nu}{(2\pi)^4}K(P,(\alpha)_N)$$

takes into account the energy–momentum conservation laws

$$K(P,(\alpha)_N) = \int \prod_{\nu=1}^{N} d^4Q_\nu \exp\left\{ i\sum_{\nu=1}^{N} \alpha_\nu Q_\nu \right\} \times \delta^{(4)}\left(P - \sum_{\nu=1}^{N} Q_\nu \right).$$

Explicit integration gives

$$K(P,(\alpha)_N) \sim \prod_{\nu=1}^{N} \delta^{(3)}(\alpha - \alpha_\nu),$$

where α is the CM 3-vector.

To simplify the consideration, let us choose the CM frame and set $\alpha = (-i\beta, \mathbf{0})$. As a result,

$$K(E,(\beta)_N) = \int_0^\infty \prod_{\nu=1}^{N} dE_\nu \exp\left\{ \sum_{\nu=1}^{N} \beta_\nu E_\nu \right\} \times \delta\left(E - \sum_{\nu=1}^{N} E_\nu \right).$$

Consequently, in the CM frame,

$$r(E) = \int D\beta_1(E) D\beta_2(E) \rho((\beta_1)_N, (\beta_2)_N),$$

where

$$D\beta(E) = \prod_{\nu=1}^{N} \frac{d\beta_\nu}{2\pi i} K(E,(\beta)_N)$$

and $\rho((\beta)_N)$ was defined in (4.3) with $\alpha_{k,\nu} = (-i\beta_{k,\nu}, \mathbf{0})$, $\mathrm{Re}\beta_{k,\nu} > 0$, $k = 1, 2$.

4.2. Wigner Function Formalism

We will use the Wigner function approach in the formulation of Carruthers–Zachariasen [22]. In the previous section, the generating functional $\rho((\beta)_N)$ was calculated by means of dividing the "measuring device" (calorimeter) onto the N cell. It was assumed that the dimension of device cells tends to zero ($N \to \infty$). Now we will specify the cell coordinates using the Wigner description.

Let us introduce the distribution function F_n which defines the probability of finding n particles with definite momentum and with arbitrary coordinates. These probabilities (cross sections) are usually measured in particle physics. The corresponding Fourier-transformed generating functional can be deduced from (4.3):

$$F(z,(\beta_+)_N,(\beta_-)_N) \tag{4.5}$$
$$= \prod_{\nu=1}^{N} \prod_{i\neq j} \exp\left\{ \int d\omega(q) \hat{\phi}_i^*(q) e^{-\beta_{j,\nu}\epsilon(q)} \times \hat{\phi}_j(q) z_{ij}^\nu(q) \right\} Z(\phi_+) Z^*(\phi_-).$$

The variation of F over $z_{ij}^\nu(q)$ generates the corresponding distribution functions. One can interpret $z_{ij}^\nu(q)$ as the local activity: the logarithm of $z_{ij}^\nu(q)$ is conjugate to the number of particles in the cell ν with momentum q for the initial ($ij = 21$) or final ($ij = 12$) states. Note that $z_{ij}^\nu(q)\hat{\phi}_i^*(q)\hat{\phi}_j(q)$ can be considered as the operator of activity.

The generating functional (4.5) is normalized as follows:

$$F(z = 1, (\beta)) = R((\beta)), \tag{4.6}$$
$$F(z = 0, (\beta)) = |Z(0)|^2 = \rho_0(\phi_\pm)|_{\phi_\pm = 0},$$

where $\rho_0(\phi_\pm)$ is the "probability" of the vacuum-into-vacuum transition in the presence of external fields $\phi_\pm$. The one-particle distribution function

$$F_1((\beta_1)_N, (\beta_2)_N; q) = \frac{\delta}{\delta z_{ij}^\nu(q)} F|_{z=0} \tag{4.7}$$
$$= \{\hat{\phi}_i^*(q) e^{-\beta_i^\nu \epsilon(q)/2}\} \{\hat{\phi}_j(q) e^{-\beta_i^\nu \epsilon(q)/2}\} \rho_0(\phi_\pm)$$

describes the probability of finding one particle in the vacuum.

Thus,

$$F_1((\beta_1)_N, (\beta_2)_N; q) = \int dx dx' e^{iq(x-x')} \times e^{-\beta_{i,\nu}\epsilon(q)} \hat{\phi}_i(x) \hat{\phi}_j(x') \rho_0(\phi_\pm) \tag{4.8}$$
$$= \int dr \{ dy e^{iqy} e^{-\beta_{i,\nu}\epsilon(q)} \} \hat{\phi}_i(r + y/2) \times \hat{\phi}_j(r - y/2) \rho_0(\phi_\pm).$$

We introduce the one-particle Wigner function W_1 [22] using this definition:

$$F_1((\beta_1)_N, (\beta_2)_N; q) = \int dr W_1((\beta_1)_N, (\beta_2)_N; r, q).$$

Thus,

$$W_1((\beta_1)_N, (\beta_2)_N; r, q) = \int dy e^{iqy} e^{-\beta_{i,\nu}\epsilon(q)} \times \hat{\phi}_i(r + y/2) \hat{\phi}_j(r - y/2) \rho_0(\phi_\pm).$$

This distribution function describes the probability of finding in the vacuum a particle with momentum q at point r in cell ν.

Since the choice of the device coordinates is in our hands, it is natural to adjust the cell coordinate to the coordinate of measurement r:

$$W_1((\beta_1)_N, (\beta_2)_N; r, q) = \int dy e^{iqy} e^{-\beta_i(r)\epsilon(q)}$$

$$\times \hat{\phi}_i(r+y/2)\hat{\phi}_j(r-y/2)\rho_0(\phi_\pm).$$

This choice of the device coordinates leads to the following generating functional:

$$F(z,\beta) = \exp\left\{ i\int dydr[\hat{\phi}_+(r+y/2) \right. \quad (4.9)$$
$$\times D_{+-}(y;\beta_2(r),z)\hat{\phi}_-(r-y/2) - \hat{\phi}_-(r+y/2)$$
$$\left. \times D_{-+}(y;\beta_1(r),z)\hat{\phi}_+(r-y/2)]\right\}\rho_0(\phi_\pm),$$

where

$$D_{+-}(y;\beta(r),z)$$
$$= -i\int d\omega(q) z_{+-}(r,q)e^{iqy}e^{-\beta(r)\epsilon(q)},$$

$$D_{-+}(y;\beta(r),z)$$
$$= i\int d\omega(q) z_{-+}(r,q)e^{-iqy}e^{-\beta(r)\epsilon(q)}$$

are the modified positive and negative correlation functions.

The inclusive, i.e., partial, distribution functions are familiar in particle physics. These functions describe the distributions in the presence of an arbitrary number of other particles. For instance, the one-particle partial distribution function

$$P_{ij}(r,q;(\beta)) = \frac{\delta}{\delta z_{ij}(r,q)}F(z,(\beta))|_{z=1} \quad (4.10)$$
$$= \frac{e^{-\beta_i(r)\epsilon(q)}}{(2\pi)^3\epsilon(q)}\int dy e^{iqy}\hat{\phi}_i(r+y/2)$$
$$\times \hat{\phi}_j(r-y/2)\rho(\phi_\pm,(\beta)),$$

where Eq. (4.6) was used.

The mean multiplicity $n_{ij}(r,q)$ of particles in the infinitesimal cell Y with momentum q is

$$n_{ij}(r,q) = \int dq \frac{\delta}{\delta z_{ij}(r,q)} \ln F(z,(\beta))|_{z=1}.$$

If the interactions among fields are switched off, we can find that (omitting indices)

$$n(Y,q_0) = [e^{\beta(r)q_0}-1]^{-1}, \quad q_0 = \epsilon(q) > 0.$$

This is the mean multiplicity of the blackbody radiation.

4.3. Closed-Path Boundary Conditions

The developed formalism allows one to introduce more general "closed-path" boundary conditions. The presence of the external blackbody radiation flow will reorganize the differential operator $\exp\{\hat{N}(\phi_i^*\phi_j)\}$ only, and the new generating functional $\rho_{\rm cp}$ has the form

$$\rho_{\rm cp}(\alpha_1,\alpha_2) = e^{\hat{N}(\phi_i^*\phi_j)}\rho_0(\phi_\pm).$$

Introducing the cells, we will find that

$$\hat{N}(\phi_i^*\phi_j) = \int drdy\hat{\phi}_i(r+y/2)$$
$$\times \tilde{n}_{ij}(Y,y)\hat{\phi}_j(r-y/2),$$

where the occupation number $\tilde{n}_{ij}$ carries the cell index r:

$$\tilde{n}_{ij}(r,y) = \int d\omega(q)e^{iqy}n_{ij}(r,q),$$

and ($q_0 = \epsilon(q)$)

$$n_{++}(r,q_0) = n_{--}(r,q_0) = \tilde{n}(r,(\beta_1+\beta_2)|q_0|/2)$$
$$= [\exp((\beta_1+\beta_2)(r)|q_0|/2)-1]^{-1},$$

$$n_{+-}(r,q_0) = \Theta(q_0)(1+\tilde{n}(r,\beta_2 q_0))$$
$$+ \Theta(-q_0)\tilde{n}(r,-\beta_1 q_0),$$

$$n_{-+}(r,q_0) = n_{+-}(r,-q_0).$$

For simplicity, the CM system was used.

Calculating ρ_0 perturbatively, we will find that

$$\rho_{\rm cp}(\beta) = \exp\{-iV(-i\hat{j}_+) + iV(-i\hat{j}_-)\} \quad (4.11)$$
$$\times \exp\left\{ i\int drdy\hat{j}_i(r+y/2)G_{ij}(y,(\beta(r))) \right.$$
$$\left. \times \hat{j}_j(r-y/2)\right\},$$

where, using matrix notation,

$$iG(q,(\beta(r))) = \begin{pmatrix} \dfrac{i}{q^2-m^2+i\epsilon} & 0 \\ 0 & -\dfrac{i}{q^2-m^2-i\epsilon} \end{pmatrix} \quad (4.12)$$
$$+ 2\pi\delta(q^2-m^2)$$
$$\times \begin{pmatrix} n\left(\dfrac{(\beta_1+\beta_2)(r)}{2}|q_0|\right) & n(\beta_1(r)|q_0|)a_+(\beta_1) \\ n(\beta_2(r)|q_0|)a_-(\beta_2) & n\left(\dfrac{(\beta_1+\beta_2)(r)}{2}|q_0|\right) \end{pmatrix}$$

and

$$a_\pm(\beta) = -e^{\beta(|q_0|\pm q_0)/2}. \quad (4.13)$$

Formally, these Green's functions obey the standard equations in y space:

$$(\partial^2-m^2)_y G_{ii} = \delta(y), \qquad (\partial^2-m^2)_y G_{ij} = 0,$$
$$i \neq j,$$

since $\Phi(\sigma_\infty) \neq 0$ reflects the mass-shell particles. But the boundary conditions for these equations are not evident.

It should be emphasized that, in our consideration, r is the coordinate of measurement, i.e., r is regarded like the coordinate of calorimeter cells and there is no necessity to divide the interaction region of QGP into domains (cells). This means that L must be smaller than the typical range of fluctuations of QGP. But, on the other hand, L cannot be arbitrarily small since this will lead to the assumption of a local factorization property of correlators, i.e., to the absence of interactions.

Thus, changing $\beta \to \beta(r)$, we should assume that $\beta_{1(2)}(r)$ and $z_{+-(-+)}(r,k)$ are constants on interval L. This prescription adopts the Wigner function formalism for the case of high multiplicities. It describes the temperature fluctuations which are larger than L and the fluctuations smaller than L are averaged, leading to the absence, on average, of "non-Gaussian" fluctuations.

It is the typical "calorimetric" measurement since in a dominant number of calorimeter cells the measured mean values of energy, with exponential accuracy, are "good" parameters $\sim 1/\beta_2(r,E)$. We will assume that the dimension of calorimeter cells $L \ll L_{\rm cr}$, where $L_{\rm cr}$ is the dimension of characteristic fluctuations at the given n. In the deep asymptotics over n, we must have $L_{\rm cr} \to \infty$. This consideration shows that the proposed experiment with the calorimeter as the measuring device of particles energies is sufficiently informative in the domain of high multiplicities.

4.4. Nonstationary Statistical Operator

One cannot expect the evident connection between the above-considered S-matrix (microcanonical) and Zubarev's [24] approaches. The reason is the introduction of interaction with a heat bath in Zubarev's formalism. This interaction is crucial for the definition of NSL for the explanation of the trend to the maximal-entropy state starting evolution from the local-equilibrium state.[1)]

Therefore, in Zubarev's theory, the local-equilibrium state was chosen as the boundary condition. It is assumed that, in the suitably defined cells of the system at a given temperature distribution $T(\mathbf{x},t) = 1/\beta(\mathbf{x},t)$, where $(\mathbf{x},t)$ is the index of the cell, the entropy is maximal. The corresponding nonequilibrium statistical operator

$$\rho_z \sim \exp\left\{-\int d^3x \beta(\mathbf{x},t) T_{00}\right\} \tag{4.14}$$

describes evolution of a system in the time scale t. Here, $T_{\mu\nu}$ is the energy–momentum tensor. It is assumed that the system "follows" $\beta(\mathbf{x},t)$ evolution and the local temperature $1/\beta(\mathbf{x},t)$ is defined as the external parameter which is the regulator of systems dynamics. For this purpose, the special $i\epsilon$ prescription was introduced [24]. It brings the interaction with the heat bath.

The KMS periodic boundary condition cannot be applied to a nonstationary temperature distribution and for this reason the decomposition

$$\beta(\mathbf{x},t) = \beta_0 + \beta_1(\mathbf{x},t) \tag{4.15}$$

was proposed in [25]. Here, β_0 is the constant and the inequality

$$\beta_0 \gg |\beta_1(\mathbf{x},t)|$$

is assumed. Then,

$$\rho_z \sim e^{-\beta_0(H_0+V+B)}, \tag{4.16}$$

where H_0 is the free part of the Hamiltonian, V describes the interactions, and the linear term B over β_1/β_0 is connected with the deviation of temperature from the "equilibrium" value $1/\beta_0$. The presence of B perturbations creates "thermal" flows in the system to explain increasing entropy. Considering V and B as perturbations, one can calculate the observables averaging over equilibrium states, i.e., adopting the KMS boundary condition. Using the standard terminology, one can consider V as the "mechanical" and B as the "thermal" perturbations.

The quantization problem of the operator (4.16) is connected with the definition of the spacetime sequence of mechanical (V) and thermal (B) excitations. It is necessary since the mechanical excitations affect the thermal ones and vice versa. It was assumed in [25] that V and B are commuting operators, i.e., the sequence of V and B perturbations is not sufficient. The corresponding generating functional has the form [25]

$$\begin{aligned} Z(j) = \exp\Bigg\{ -i \int\limits_{C_\beta} d^4x \Bigg(V(-i\hat{j}(x)) \\ + \frac{\beta_1(\mathbf{x},\tau)}{\beta_0} T_{00}[-i\hat{j}(x)] \\ - \int\limits_{-\infty}^{0} dt_1 \frac{\beta_1(\mathbf{x},\tau+t_1)}{\beta_0} T_{00}[-i\hat{j}(\mathbf{x},t_1)] \Bigg) \Bigg\} \\ \times \mathrm{Tr}\left(e^{-\beta_0 H_0} T_C \exp\left\{ i \int\limits_C d^4y j(y)\Phi(y) \right\} \right), \end{aligned}$$

where the time contour C_β was described in Subsection 4.1 and τ is the measurement time.

[1)] This condition is not necessary in the S-matrix formalism since it is "dynamical" by its nature, i.e., it includes the notion of initial and final states as the boundary conditions.

It is evident that this solution leads to the renormalization by the interactions with the external field $\beta(\mathbf{x}, t)$ even without interactions among fundamental fields Φ. The source of these renormalizations is the kinetic term in the energy–momentum tensor T_{00}, i.e., follows from "thermal" interactions with the external heat bath. Note the absence of these renormalizations in the S-matrix formalism, see (2.21), where the interactions are generated by the V perturbations only.

The operators V and B are noncommuting ones [33] and B perturbations were switched on after V perturbations. In this formulation, nondynamical renormalizations are also present, but it is not unlikely that they may be canceled at the very end of calculations [34].

5. CONCLUSIONS

Finally, let us add that, as follows from the above conclusion, the very high multiplicity (VHM) process leads to a dense, cold, and equilibrium locally colored state, i.e., a "cold" plasma. Note that, if the parton system is "hot," the kinetic motion would rapidly separate the color charges and this must lead to strong polarization of the vacuum. This effect is absent in a QED plasma and this is why a QCD plasma must be cold. Just this is the VHM region.

ACKNOWLEDGMENTS

I would like to take the opportunity to thank Yu. Budagov, V. Kadyshevski, A. Korytov, E. Kuraev, L. Lipatov, V. Matveev, V. Nikitin, E. Sarkisyan, and A. Sissakian for fruitful discussions and constructive comments.

REFERENCES

1. F. Bloch, Z. Phys. **74**, 295 (1932).
2. T. Matsubara, Prog. Theor. Phys. **14**, 351 (1955).
3. N. P. Landsman and Ch. G. van Weert, Phys. Rep. **145**, 141 (1987).
4. L. Dolan and R. Jackiw, Phys. Rev. D **9**, 3320 (1974).
5. A. J. Niemi and G. Semenoff, Ann. Phys. (N.Y.) **152**, 105 (1984).
6. J. Schwinger, J. Math. Phys. A **9**, 2363 (1994).
7. L. V. Keldysh, Zh. Éksp. Teor. Fiz. **47**, 612 (1964) [Sov. Phys. JETP **20**, 1018 (1964)].
8. H. Umezawa, H. Matsumoto, and M. Tachiki, *Thermo-Field Dynamics and Condensed States* (North-Holland, Amsterdam, 1982).
9. M. Martin and J. Schwinger, Phys. Rev. **115**, 1342 (1959).
10. R. Kubo, J. Phys. Soc. Jpn. **12**, 570 (1957).
11. R. Haag, N. Hugengoltz, and M. Winnink, Commun. Math. Phys. **5**, 5 (1967).
12. H. Chu and H. Umezawa, Int. J. Mod. Phys. A **9**, 2363 (1994).
13. I. D. Manjavidze, Fiz. Élem. Chastits At. Yadra **16**, 101 (1985) [Sov. J. Part. Nucl. **16**, 44 (1985)].
14. E. Byuckling and K. Kajantie, *Particles Kinematics* (Wiley, London, 1973).
15. L. D. Landau, E. M. Lifshitz, and L. P. Pitaevskii, *Statistical Physics, Course of Theoretical Physics* (Butterworth–Heinemann, 1999), Vol. 5.
16. P. Kadanoff and P. C. Martin, Ann. Phys. (N.Y.) **24**, 419 (1963).
17. J. Manjavidze, hep-ph/9506424.
18. N. N. Bogolyubov, *Studies in Statistical Mechanics*, Ed. by J. de Boer and G. E. Uhlenbeck (North-Holland, Amsterdam, 1962).
19. E. P. Wigner, Phys. Rev. **40**, 749 (1932).
20. K. Hisimi, Proc. Phys. Math. Soc. Jpn. **23**, 264 (1940); R. J. Glauber, Phys. Rev. Lett. **10**, 84 (1963); E. C. G. Sudarshan, Phys. Rev. Lett. **10**, 277 (1963); R. E. Cahill and R. G. Glauber, Phys. Rev. **277**, 1882 (1969).
21. P. Carruthers and F. Zachariasen, Rev. Mod. Phys. **55**, 245 (1983).
22. P. Carruthers and F. Zachariasen, Phys. Rev. D **13**, 950 (1976).
23. E. Calsetta and B. L. Hu, Phys. Rev. D **37**, 2878 (1988).
24. D. N. Zubarev, *Nonequilibrium Statistical Thermodynamics* (Consultants Bureau, New York, 1974).
25. T. Bibilashvili and I. Pasiashvili, Ann. Phys. (N.Y.) **220**, 134 (1992).
26. A. N. Vasil'ev, *Functional Methods of Quantum Field Theory and Statistical Physics* (Leningrad Univ. Press, Leningrad, 1976).
27. R. Mills, *Propagators for Many-Particle Systems* (Gordon and Breach Science Publ., New York, 1970).
28. H. Matsumoto *et al.*, Prog. Theor. Phys. **70**, 559 (1983); H. Matsumoto, Y. Nakano, and H. Umezawa, J. Math. Phys. (N.Y.) **25**, 3076 (1984).
29. J. Schwinger, *Particles, Sources and Fields* (Addison-Wesley, 1970), Vol. 1.
30. L. Landau and R. Peierls, Z. Phys. **69**, 56 (1931).
31. P. M. Bakshi and K. T. Mahanthappa, J. Math. Phys. (N.Y.) **4**, 1, 12 (1963).
32. J. Manjavidze, hep-ph/9510360.
33. T. Bibilashvili, Phys. Lett. B **313**, 119 (1993).
34. T. Bibilashvili, private communication.

Physics of Atomic Nuclei, Vol. 67, No. 1, 2004, pp. 115–129. From Yadernaya Fizika, Vol. 67, No. 1, 2004, pp. 114–127.

Particle Correlations in $e^+e^- \to W^+W^-$ Events*

N. E. Pukhaeva**

University of Antwerpen, Antwerpen, Belgium
Joint Institute for Nuclear Research, Dubna, Moscow oblast, 141980 Russia

Received April 4, 2003

Abstract—Preliminary results are reported on the two-particle correlation function $R(Q)$ in hadronic Z decays, fully hadronic WW decays, and mixed hadronic–leptonic WW decays using data collected by the DELPHI detector at LEP at energies between 189 and 206 GeV. Evidence for Bose–Einstein correlations was observed in all three cases. The event mixing technique was used to determine correlations between particles arising from different W bosons in fully hadronic WW decays. An excess of like-sign particle pairs with low four-momentum difference in fully hadronic WW events is observed, consistent with the effect expected from correlations between identical particles from different W bosons. © *2004 MAIK "Nauka/Interperiodica".*

1. INTRODUCTION

The possible presence of color reconnection effects and Bose–Einstein correlations in hadronic decays of WW pairs has been discussed on a theoretical basis, in relation to the measurement of the W mass (see, for example, [1, 2] and references therein). These effects can induce a systematic uncertainty on the W-mass measurement in the fully hadronic channel [1] comparable with the expected accuracy of the measurement.

Bose–Einstein correlations (BEC) originate from the symmetrization of the production amplitude for identical bosons. The effects of BEC between identical bosons have been studied extensively in different types of reactions and for different boson species. Although many studies exist, there is still no complete understanding of the influence of this quantum mechanical effect on a multiparticle system generated in a high-energy collision. The description of a given multiparticle system itself is complicated by needing to know the amplitude for the system and symmetrize it.

The observable most often used for the investigation of BEC in multiparticle final states is the two-particle correlation function. It was also demonstrated that BEC considerably affect other observables in high-energy reactions [3]. A strong distortion of the $\rho^0(770)$ line shape due to BEC was observed in experimental data at LEP1 [4].

The $e^+e^- \to WW$ events allow a comparison of the characteristics of the W hadronic decays when both W decay hadronically in the reaction $e^+e^- \to W^+W^- \to q_1\bar{q}_2q_3\bar{q}_4$ (in the following, we shall often refer to this as the $(4q)$ mode) with the case in which one of the W decays leptonically in the reaction $e^+e^- \to W^+W^- \to q_1\bar{q}_2l\nu$ (denoted $(2q)$ mode for brevity). Since the distance between the W^+ and W^- decay vertices is considerably smaller than the typical hadronization distance, their decay products are expected to overlap in space and time and identical bosons from different W can be subject to BEC. In the framework of LUBOEI, the Bose–Einstein algorithm embedded in JETSET [5], the authors of [2] concluded that BEC between identical bosons from the decays of different W could strongly influence the measured mass of the W. On the other hand, some authors (see, e.g., [6]) argue that such inter-W correlations should not exist. It is therefore important to establish whether such correlations exist.

A rigorous mathematical treatment of correlations between pions from different W is given in [7]. BEC are incorporated in a spacetime parton-shower model for e^+e^- annihilation into hadrons in [8]. In the present paper, BEC are studied for W in $(4q)$ and in $(2q)$ events. Such a combined study allows us to extract information on BEC between decay products of the two hadronically decaying W. The data used for the analysis related to W were collected with the DELPHI detector [9, 10] at LEP in 1998, 1999, and 2000 at c.m. energies of 189–206 GeV with integrated luminosities of 155, 228, and 164 pb^{-1}, respectively, with total statistics of 547 pb^{-1}.

The layout of the paper is the following. Section 2 summarizes the general properties of BEC. Section 3 describes the particle and event selection

*This article was submitted by the author in English.

** e-mail: Nelli.Pukhaeva@cern.ch

criteria. Section 4 presents the measurements of correlation functions in Z and fully hadronic and mixed hadronic–leptonic WW events. Section 5 describes measurements of correlations between particles from different W in fully hadronic WW events. A summary is given in Section 6.

2. BOSE–EINSTEIN EFFECTS

BEC manifest themselves as an enhancement in the production of pairs of identical bosons close in phase space. To study the enhanced probability for emission of two identical bosons, the correlation function R is used. For pairs of particles, it is defined as

$$R(p_1, p_2) = \frac{P(p_1, p_2)}{P_0(p_1, p_2)}, \qquad (1)$$

where $P(p_1, p_2)$ is the two-particle probability density, subject to Bose–Einstein symmetrization; p_i is the four-momentum of particle i; and $P_0(p_1, p_2)$ is a reference two-particle distribution which, ideally, resembles $P(p_1, p_2)$ in all respects, apart from the lack of Bose–Einstein symmetrization.

If $f(x)$ is the spacetime distribution of the source, $R(p_1, p_2)$ takes the form

$$R(p_1, p_2) = 1 + |G[f(x)]|^2,$$

where $G[f(x)] = \int f(x) e^{-i(p_1 - p_2)x} dx$ is the Fourier transform of $f(x)$. Thus, by studying the correlations between the momenta of pion pairs, one can study the distribution of the points of origin of the pions. Experimentally, the effect is often described in terms of the variable Q, defined by $Q^2 = -(p_1 - p_2)^2 = M^2_{\pi\pi} - 4m^2_\pi$, where $M_{\pi\pi}$ is the invariant mass of the two pions. The correlation function can then be written as

$$R(Q) = \frac{P(Q)}{P_0(Q)}, \qquad (2)$$

which is frequently parametrized by the function

$$R(Q) = \gamma(1 + \delta Q)\left(1 + \lambda e^{-rQ}\right). \qquad (3)$$

In the above equation, in the hypothesis of a spherically homogeneous pion source, the parameter r gives the radius of the source and λ is the strength of the correlation between the pions.

BEC can be included in PYTHIA/JETSET [5] by using the LUBOEI code, where they are introduced as a final-state interaction [2, 5]. After the generation of the pion momenta, the values generated for all identical pions are modified by an algorithm that reduces their momentum vector differences according to Eq. (3). For the present analysis, the BE_{32} version of the LUBOEI code was used. For the comparison with the data, BEC were switched on in LUBOEI with a Gaussian parametrization for pions that are produced either promptly or as decay products of short-lived resonances (resonances with decay width less than 45 MeV were considered long-lived), with parameters set to $\lambda = \mathrm{PARJ}(92) = 1.35$ and $r = 0.58$ fm, which corresponds to model parameter $R = \mathrm{PARJ}(93) = 0.34$ GeV. It should be noted that the measured values for λ and r, corresponding to all particles, do not reproduce the above LUBOEI input values, which correspond to primary particles or particles from short lived resonance decays only.

Two scenarios were considered for the study of BEC in W pairs:

(i) BEC were included for particles from the same and from different W (hereafter called full BE). In this case, BEC between particles from different W are treated in the same way as BEC between particles from the same W.

(ii) BEC were included only for particles from the same W (hereafter called inside BE).

The correlation function was also studied in Z decays. Since the fraction of heavy-quark pairs initiating the hadronic final state differs in Z and in W events, and especially since b quarks are practically absent in W decays, a Z sample depleted in $b\bar{b}$ pairs has also been studied.

3. PARTICLE AND EVENT SELECTIONS

The present analysis relies on the information provided by the tracking detectors: the micro vertex detector, the inner detector, the time projection chamber as the main tracking detector, the outer detector, the forward chambers, and the muon chambers. The calorimeters were used for lepton identification and to detect neutral particles. All charged particles except those tagged as hard leptons in semileptonic events were taken to be pions and assigned the pion mass. Events were selected using a run quality flag, requiring all detectors essential for the analysis of the different decay channels of the W to be fully operational and efficient.

In the event selection, charged particles were selected if they had a polar angle between 10° and 170°, momentum between 0.2 GeV/c and the beam momentum, and good quality, i.e., track length greater than 15 cm, transverse and longitudinal impact parameters less than 4 cm (as measured from the nominal interaction point with respect to the beam direction), and error on the momentum measurement less than 100%. Neutral particles were considered if they were associated to an electromagnetic or hadron shower with energy greater than 0.5 GeV and had a relative error on the energy measurement less than 100%.

Electron identification in the polar-angle range between 20° and 160° used the characteristic energy deposition in the central and forward/backward electromagnetic calorimeters and demanded a nominal energy-to-momentum ratio consistent with unity. For this polar-angle range, the identification efficiency for high-momentum electrons was determined from simulation to be $(77 \pm 2)\%$, in good agreement with the efficiency determined using Bhabha events measured in the detector.

Tracks were identified as muons if they had at least one associated hit in the muon chambers or an energy deposition in the hadronic calorimeter consistent with a minimum ionizing particle. Muon identification was performed in the polar-angle range between 10° and 170°. Within this acceptance, the identification efficiency was determined from simulation to be $(92 \pm 1)\%$. Good agreement was found between data and simulation for high-momentum muons in $Z \to \mu^+\mu^-$ decays and for lower momentum muons produced in $\gamma\gamma$ reactions.

In the subsequent analysis, more restrictive cuts were used. The information from the time projection chamber of DELPHI was used to reconstruct the track, which gave an implicit track length cut of 25 cm. Only tracks with polar angle θ between 30° and 150° were accepted. The impact parameters in the transverse and longitudinal plane were required to be smaller than 0.4 cm and 1 cm/sin θ. The energetic isolated charged particle of the mixed decay channel was not included in the analysis.

3.1. Fully Hadronic Channel ($WW \to (4q)$)

The event selection criteria were optimized in order to ensure that the final state was purely hadronic and in order to reduce the residual background, for which the dominant contribution is radiative $q\bar{q}$ production, $e^+e^- \to q\bar{q}\gamma$, especially the radiative return to the Z peak, $e^+e^- \to \mathrm{Z}\gamma \to q\bar{q}\gamma$. For each event passing the above criteria, all particles were clustered into jets using the LUCLUS algorithm [5] with the resolution parameter $d_{\mathrm{join}} = 8$ GeV/c. At least four jets were required, with at least three particles in each jet.

Events from the radiative return to the Z peak were rejected by requiring the effective c.m. energy of the e^+e^- annihilation to be larger than $E_{\mathrm{c.m.}} \cdot 0.79$. The effective energy was estimated using either the recoil mass calculated from one or two isolated photons measured in the detector or, in the absence of such a photon, by forcing a two-jet interpretation of the event and assuming that a photon had been emitted collinearly to the beam line.

The remaining events were then forced into a four-jet $(4j)$ configuration. The four-vectors of the jets were used in a kinematic fit, which imposed conservation of energy and momentum. The variable D was defined as [11]

$$D = \frac{E_{\mathrm{min}}}{E_{\mathrm{max}}} \frac{\theta_{\mathrm{min}}}{(E_{\mathrm{max}} - E_{\mathrm{min}})}, \qquad (4)$$

where E_{min} and E_{max} are the minimum and maximum jet energies and θ_{min} is the smallest interjet angle after the constrained fit. Events were used only if the variable D was larger than 0.006 rad/GeV.

A total of 2807 events were selected.

The detector effects on the analysis were estimated using samples of WW events generated with EXCALIBUR [12] for all four-fermion final states. Background events were generated with PYTHIA 5.7 [5] with the fragmentation tuned to the DELPHI data at LEP1 [13]. The generated events were passed through the full detector simulation program DELSIM [10]. The purity and efficiency of the selection of $WW \to q\bar{q}q\bar{q}$, estimated using simulated events, were about 90 and 54%, respectively (see Table 1).

Table 1. The year of the run, the numbers of events selected, the purity of the samples, and the efficiency at different energies for $WW \to (4q)$

Year	$\sqrt{s}$, GeV	Number of events	Purity, %	Efficiency, %
1998	189	855	89.1	60.0
1999	192–200	1181	89.8	53.2
2000	202–206	771	90.5	49.6

3.2. Mixed Hadronic–Leptonic Channel ($WW \to (2q)l\nu$)

Events in which one W decays into a lepton plus neutrino $(l\nu)$ and the other one into quarks are characterized by two hadronic jets, one energetic isolated charged lepton, and missing momentum resulting from the neutrino. The main backgrounds to these events are radiative $q\bar{q}$ production and four-fermion final states containing two quarks and two charged leptons of the same flavor.

Events were selected by requiring six or more charged particles and a missing momentum of more than 5% of the nominal total c.m. energy. Electron and muon tags were applied to the events. In $q\bar{q}$ events, the selected lepton candidates are either leptons produced in heavy-quark decays or misidentified hadrons, which generally have rather low momenta and small angles with respect to the corresponding quark jet. The momentum of the selected muon or the energy deposited in the electromagnetic calorimeters by the selected electron was required to be greater

Table 2. The year of the run, the numbers of events selected, the purity of the samples, and the efficiency at the different energies for $WW \to (2q)$

Year	$\sqrt{s}$, GeV	Number of events	Purity, %	Efficiency, %
1998	189	630	95.2	51.8
1999	192–200	960	96.6	51.1
2000	202–206	643	97.2	48.0

than 17 GeV/c. The energy not associated to the lepton, but assigned instead to other charged or neutral particles in a cone of 10° around the lepton, is a useful measure of the isolation of the lepton; this energy was required to be less than 5 GeV for both muons and electrons. In addition, the isolation angle between the lepton and the nearest charged particle with a momentum greater than 1 GeV/c was required to be larger than 10°. If more than one identified lepton passed these cuts, the one with highest momentum was considered to be the lepton candidate from the W decay. The angle between the lepton and the missing momentum vector was required to be greater than 70°. All the other particles were forced into two jets using the LUCLUS algorithm [5]. Both jets had to contain at least one charged particle.

The radiative $q\bar{q}$ background was suppressed by looking for evidence of an initial-state radiation (ISR) photon. Events were removed if there was a cluster with energy deposition greater than 20 GeV in the electromagnetic calorimeters, and it could not be attributed to a charged particle. Events with ISR photons at small polar angles, where they would be lost inside the beam pipe, were suppressed by requiring the polar angle of the missing momentum vector to satisfy $|\cos\theta_{\rm miss}| < 0.96$.

The four-fermion neutral current background was reduced by applying additional cuts to events in which a second lepton of the same flavor as the first was detected. Such events were rejected if the energy in a cone of 10° around the second lepton direction was greater than 5 GeV.

If no lepton was identified, the most energetic particle which formed an angle greater than 25° with all other charged particles was considered as a lepton candidate. In this case, tighter cuts were applied. The lepton momentum had to be greater than 20 GeV/c, the amount of missing momentum greater than 20 GeV/c, and its polar angle $|\cos\theta_{\rm miss}| < 0.85$.

A kinematical fit was performed on the selected events. The four-vectors of the two jets, of the lepton, and of the missing momentum were used in the fit, which imposed conservation of energy and momentum and equality of the masses of the two-jet system and the lepton–neutrino system, attributing the missing momentum of the event to the undetected neutrino. Events were used only if the fit probability was larger than 0.1%. In total, 2233 events were selected. The purity and efficiency of the selection, estimated using simulated events, were about 96 and 50%, respectively (see Table 2).

4. CORRELATION FUNCTIONS FOR Z, $WW \to (4q)$, AND $WW \to (2q)l\nu$ EVENTS

To compute the correlation function $R(Q)$ (2), the two-particle probability density $P(Q)$ was calculated; the reference $P_0(Q)$ came from EXCALIBUR without BEC after full simulation of the DELPHI detector and after the same selection criteria as for real data. The $P_0(Q)$ reference distribution was normalized to the number of pairs in the $P(Q)$ distribution.

The presence of bin-to-bin and inside-bin correlations influences the errors on the $R(Q)$ distribution [14]. If there are N particles of given charge in an event, each one has $N-1$ entries in the two-particle density $P(Q)$, mostly contributing to different bins of the histogram. But due to the finite size of the bins, the same track can also contribute several times to the same bin, which is a source of inside-bin correlations. The covariance matrix technique was used to measure the parameters. The covariance matrix was calculated from the data themselves. The method is based on classical statistics (for details, see [15]). Let us consider the ith event from the set of n events and two-particle probability density P which is presented in the histogram h^i with N_p bins.

The histogram $H = \sum_{i=1}^{n} h^i$ and the values

$$c_{jk} = \sum_{i=1}^{n} (h_j^i - H_j/n)(h_k^i - H_k/n)(1 + 1/n)$$

were calculated event by event. Here, j and k are the bin numbers for the histograms. The correlations and errors for one event are not known, but the different events are uncorrelated. Considering bin values of the histogram made for one event as a random vector with unknown distribution, one has an uncorrelated ensemble of these vectors, and, hence, the covariance matrix can be estimated statistically.

For all events, the resulting histogram H for the two-particle probability density, the covariance matrix $P(Q)$, and $V_{jk} = c_{jk}n/(n-1)$ for this histogram were calculated. The fits below were performed using the inverted V_{jk} matrix.

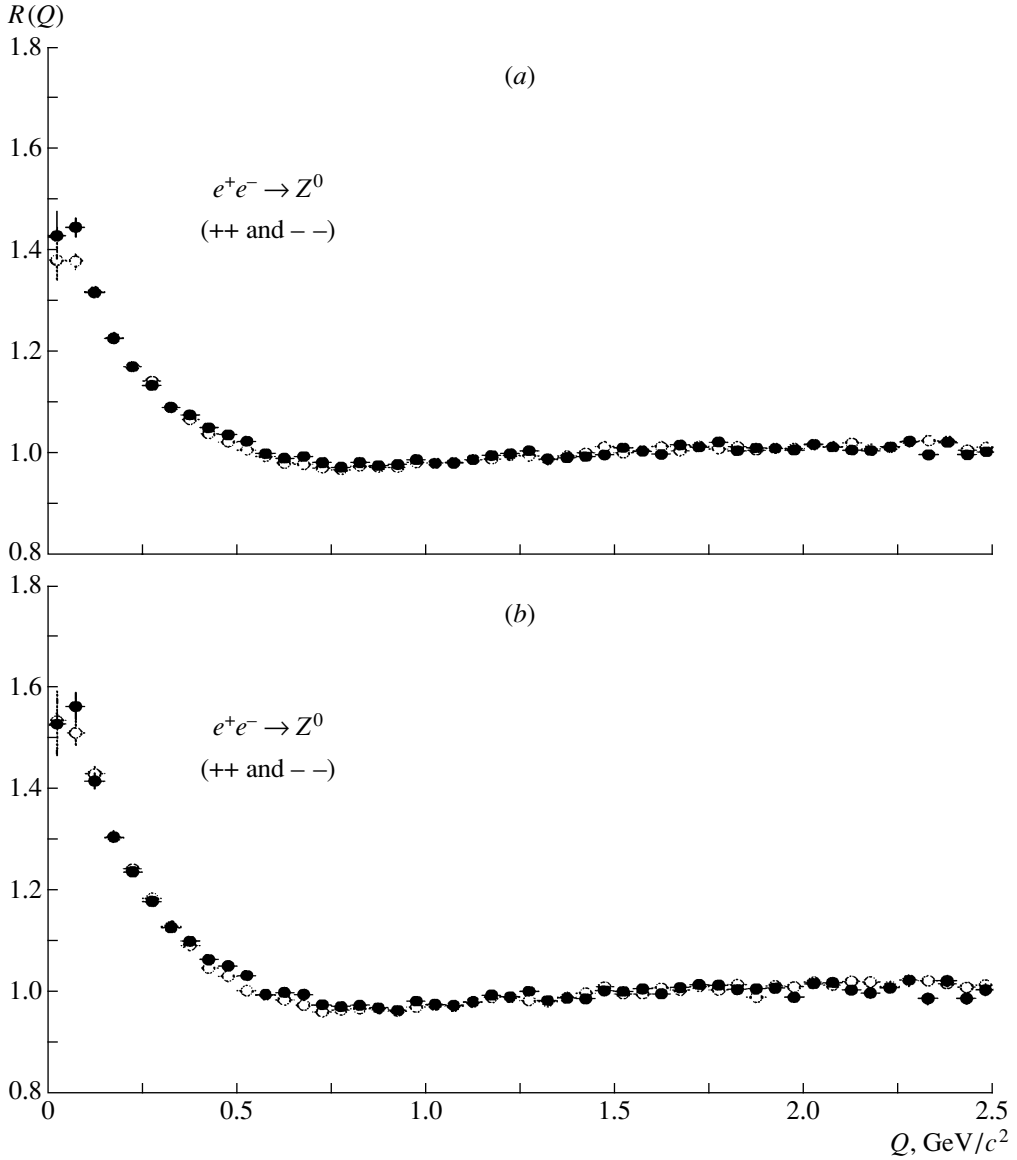

Fig. 1. (a) Measured correlation functions $R(Q)$ for like-sign pairs in Z decays for data (closed circles) and the PYTHIA Monte Carlo model tuned at the Z peak (open circles). (b) Same as in (a), but for Z events depleted in $b\bar{b}$ production.

4.1. Correlation between Particles in Z Events

Correlations between particles in Z events produced during the calibration runs were investigated. The track selection for the analysis was the same as above. The event selection was similar to the one in [16]. The number of selected events amounted to 24 681.

The $R(Q)$ distribution for like-sign combinations is shown in Fig. 1a. The fit using expression (3) yielded

$$\lambda_Z = 0.712 \pm 0.021(\text{stat.}), \quad (5)$$

$$r_Z = 0.888 \pm 0.040(\text{stat.})\ \text{fm}. \quad (6)$$

Since the fraction of heavy-quark pairs that initiated the hadron cascade is different in Z and in W decays, a light flavor-enriched Z sample has been used for comparison. The $b\bar{b}$ fraction has been reduced from the original 22% to about 2% by removing a large fraction of $b\bar{b}$ events using a b-event tagging procedure (see [10] for details). The correlation functions for this sample are shown in Fig. 1b for like-sign combinations. The results of the fit were

$$\lambda_{Z(\text{no } b\bar{b})} = 0.913 \pm 0.027(\text{stat.}), \quad (7)$$

$$r_{Z(\text{no } b\bar{b})} = 0.893 \pm 0.047(\text{stat.})\ \text{fm}. \quad (8)$$

The λ and r parameters in the LUBOEI BE_{32} code were tuned to the correlation function measured at the Z for like-sign pairs. The tuned parameters $\lambda = 1.35$ and $r = 0.58$ fm were obtained (PARJ(92) =

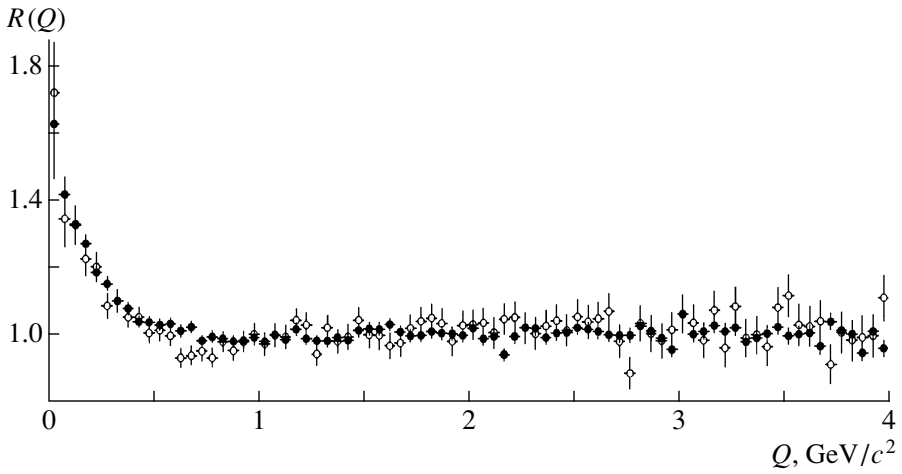

Fig. 2. Measured correlation functions $R_{2q}(Q)$ (open circles) and $R_{4q}(Q)$ (closed circles) for like-sign pairs.

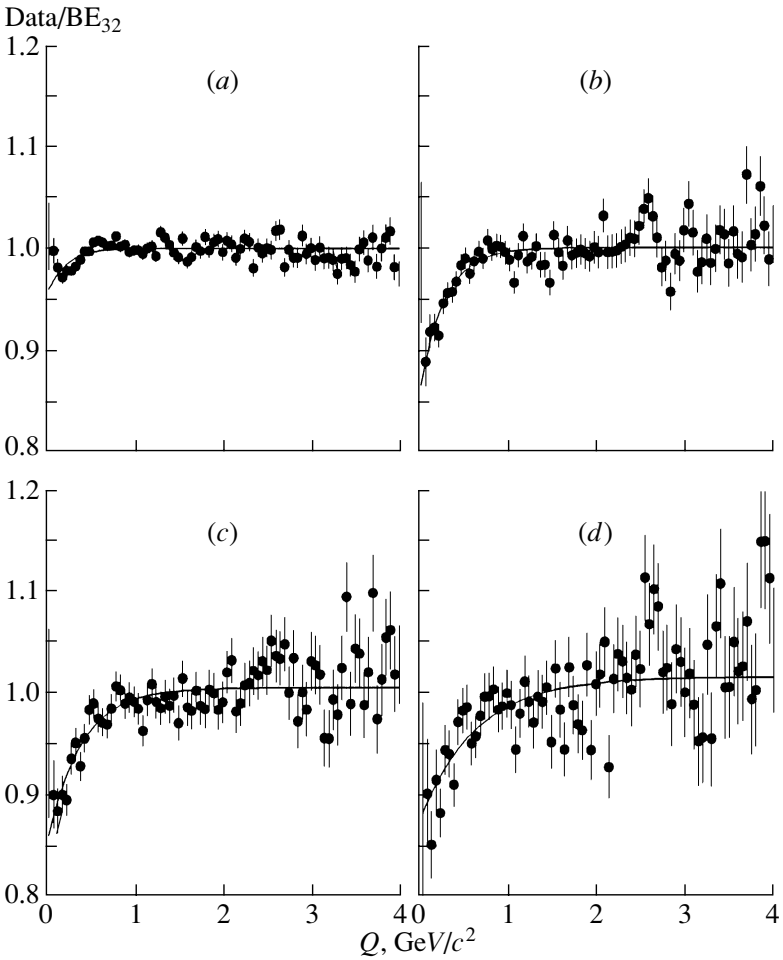

Fig. 3. The ratio of Q plots for real and simulated events in Z-decay data (a) for all Z events and for selected Z four-jet events with (b) $d_{\text{join}} > 4$ GeV/c, (c) $d_{\text{join}} > 5$ GeV/c, (d) $d_{\text{join}} > 6.5$ GeV/c. The model parameters were $\lambda = 1.35$ and $r = 0.58$ fm.

1.35 and PARJ(93) = 0.34 GeV). The $R(Q)$ distributions for the data for Z events are compared with the LUBOEI predictions in Figs. 1a and 1b. Good agreement between data and model was found.

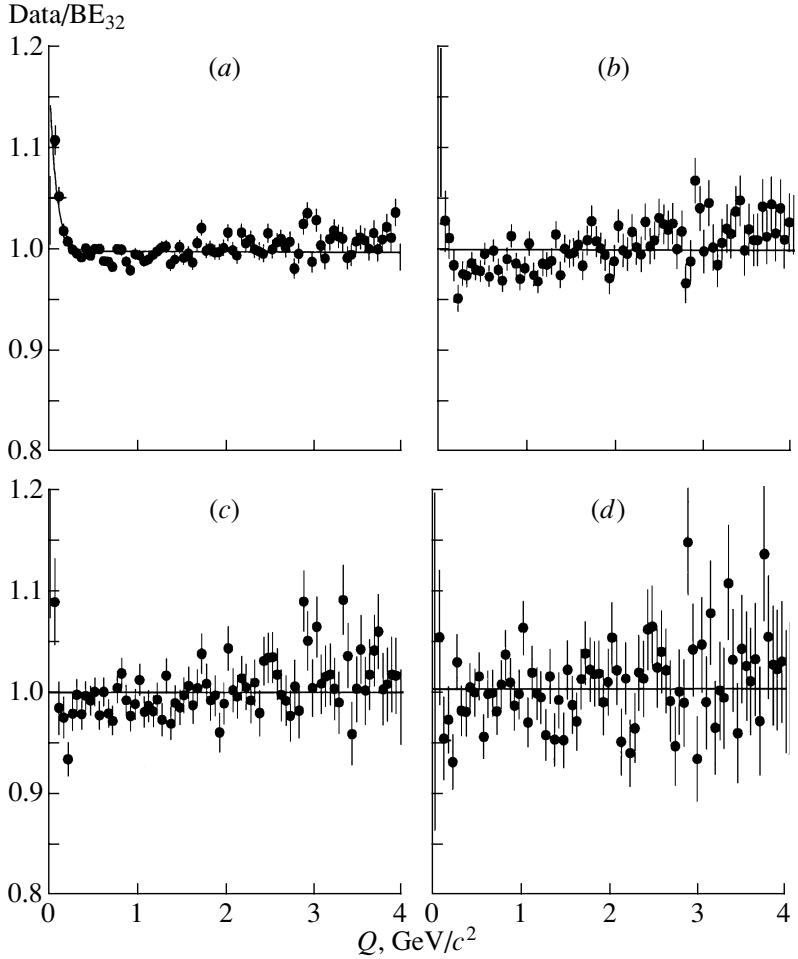

Fig. 4. Same as in Fig. 3, but for simulated events with parameters of $\lambda = 0.90$ instead of $\lambda = 1.35$.

4.2. Correlation between Particles from Any W in $WW \to (4q)$ and $WW \to (2q)l\nu$ Events

The $R_{2q}(Q)$ and $R_{4q}(Q)$ distributions for the data are shown in Fig. 2. A fit to the correlation functions $R(Q)$ using Eq. (3) yielded the values

$$\lambda_{2q} = 0.791 \pm 0.096(\text{stat.}), \quad (9)$$

$$r_{2q} = 1.177 \pm 0.121(\text{stat.})\ \text{fm} \quad (10)$$

for the mixed hadronic–leptonic channel and

$$\lambda_{4q} = 0.725 \pm 0.053(\text{stat.}), \quad (11)$$

$$r_{4q} = 1.117 \pm 0.070(\text{stat.})\ \text{fm} \quad (12)$$

for the fully hadronic decay channel.

4.2.1. Background subtraction in $WW \to (4q)$ events. Averaged over all energies, the selected WW fully hadronic events contained 10% $q\bar{q}$ events (Table 1). The correction for these background contributions to the fully hadronic sample was done in the following way.

A sample of $q\bar{q}$ events was generated with BEC included according to LUBOEI BE_{32} with parameters $\lambda = 1.35$ and $r = 0.58$ fm as was tuned at Z peak. These events were subjected to the same event and track selection criteria as the fully hadronic sample, and the Q distribution of the background was calculated from the events passing the selection.

The agreement between data and simulated events at Z peak for four-jet samples selected using the d_{join} requirement was then checked.

The comparison of Q distributions for data and simulated Z events are shown in Fig. 3 for all events (Fig. 3*a*) and for four-jet events (Figs. 3*b*, 3*c*, and 3*d* for $d_{\text{join}} > 4$ GeV/c, $d_{\text{join}} > 5$ GeV/c, and $d_{\text{join}} > 6.5$ GeV/c, respectively). The agreement for all events is satisfactory (as was shown also in Subsection 4.1), while the model strongly overestimates the correlations at low Q for selected four-jet samples.

We then used an alternative simulated sample at Z peak with reduced parameter of $\lambda = 0.90$ (instead of $\lambda = 1.35$). All other model parameters were the same. The comparison of Q distributions for data and these simulated Z events are shown in Fig. 4.

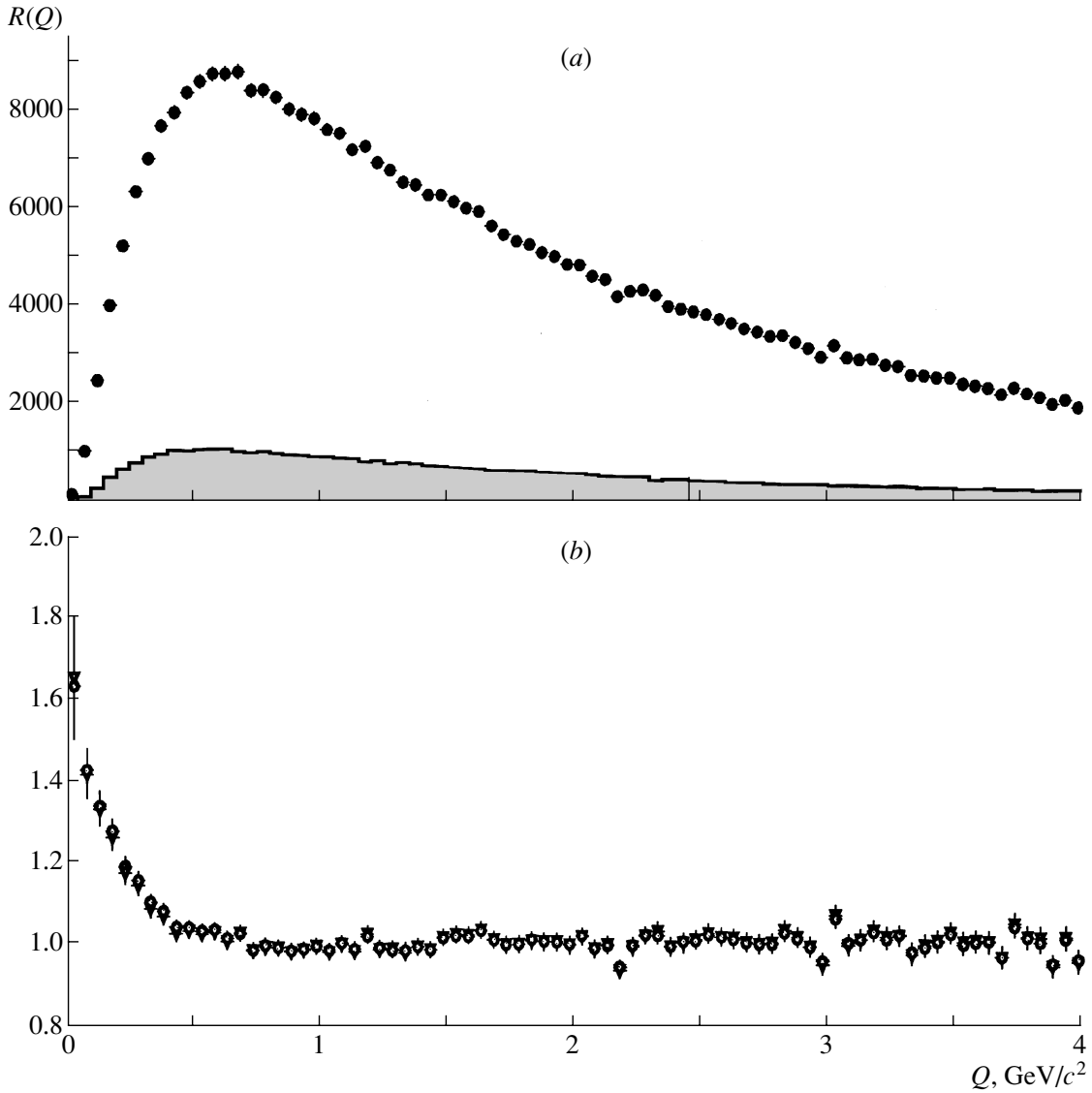

Fig. 5. (*a*) Q distributions for real ($4q$) events and for simulated ($4q$) background events for like-sign pairs (shaded area); (*b*) measured $R_{4q}(Q)$ distributions for ($4q$) events without and with background subtraction (circles and triangles, respectively).

The Q plot for simulated background $q\bar{q}$ events was corrected for the discrepancy between the data and the simulated sample at Z peak shown in Fig. 3*c*. This distribution, properly weighted by the percentage of the background, was subtracted from the experimental $WW \to (4q)$ distribution. Alternatively, the contribution of background $q\bar{q}$ events were subtracted using the simulated sample with parameter $\lambda = 0.90$ (without corrections). These two procedures yielded practically the same background-subtracted distributions.

The Q distributions for real WW fully hadronic events and for background events, calculated as described above, are shown in Fig. 5*a*. Figure 5*b* presents the $R(Q)$ distributions for $WW \to (4q)$ events without (circles) and with (triangles) background subtraction.

It can be seen that the background contribution hardly changes the Q distribution for ($4q$) events (Fig. 5*b*).

We note also that, for WW BEC analysis at LEP, the background contribution in the WW fully hadronic channel was usually estimated using the LUBOEI model tuned at the Z peak. As shown in this section, this can overestimate the correlations at low Q for four-jet samples. This problem is most important for selections with a high background contribution (which is up to 20% for some selections used at LEP).

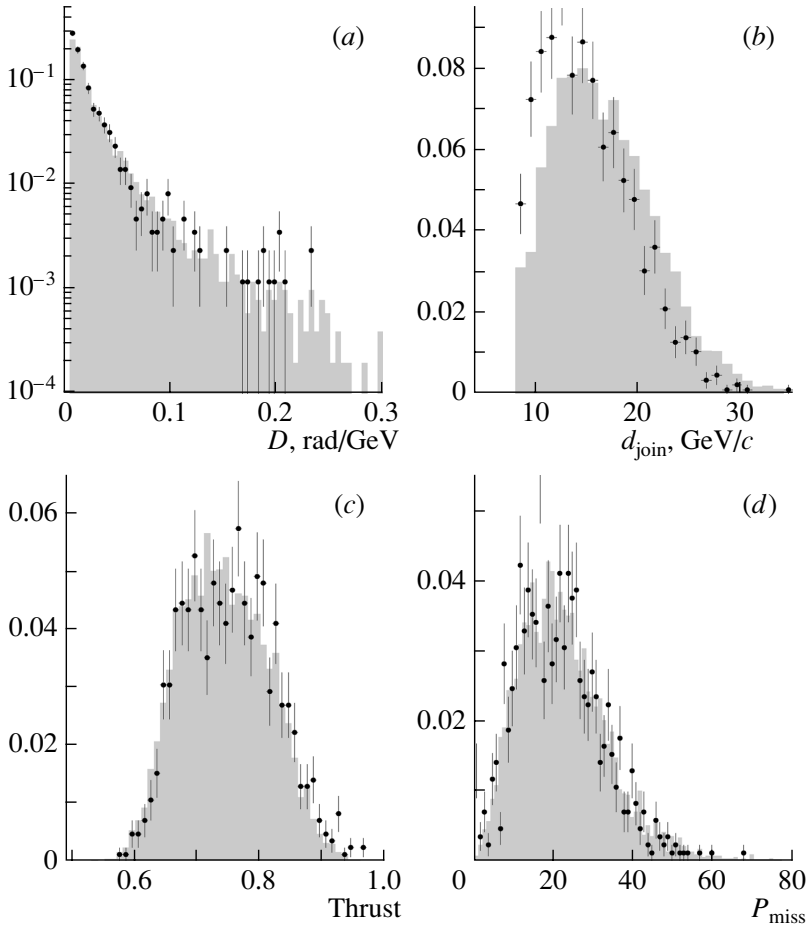

Fig. 6. Comparison of event shape variables for $(4q)$ (closed circles) and mixed events (shaded area) for real 1998 data.

A fit to the $R(Q)$ after the background subtraction with Eq. (3) yielded the values

$$\lambda_{4q} = 0.741 \pm 0.065(\text{stat.}), \quad (13)$$

$$r_{4q} = 1.199 \pm 0.088(\text{stat.})\ \text{fm}. \quad (14)$$

In the subsequent analyses the $R(Q)$ distributions after the background subtraction were used.

5. CORRELATIONS BETWEEN PARTICLES FROM DIFFERENT W

To perform a direct measurement sensitive to BEC between particles from different W, the analysis used a comparison sample which contained only BEC for particle pairs coming from a single W boson, but not for particle pairs from different W. This comparison sample of $(4q)$-like events was constructed by the mixing of two hadronic W from the different $(2q)$ events in the following way.

The pairs of W were accepted for mixing if they had momentum imbalance $|\mathbf{P}_1 + \mathbf{P}_2| < 25$ GeV. From each selected semileptonic event, the hadronic part was boosted to the rest frame of the W candidate. The rest frames of the W candidates were determined using the energy and momenta of the W obtained from the kinematical fits. The mixed event was then constructed from two W candidates by boosting the particles of the individual W in opposite directions. The boost vectors were determined taking into account energy–momentum conservation and the fitted mass of W candidate.

The fully hadronic event selections were applied to mixed events. Some event shape variables, multiplicities, and single-particle distributions for fully hadronic and mixed events for data and MC are shown in Figs. 6–10. In general, good agreement was found.

The expected R_{4q} when there are no correlations between W, constructed from the experimental values of P_{2q} (for pairs from same W) and from the mixed sample P_{mix} (for pairs from different W), can be written as

$$R_{4q}(Q)(\text{mixing}) \quad (15)$$

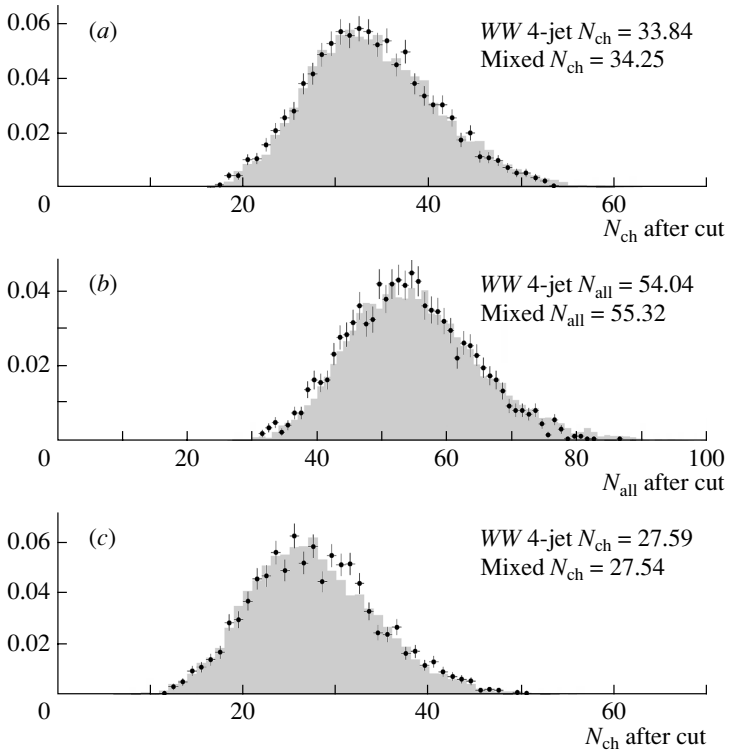

Fig. 7. Comparison of multiplicity distributions for ($4q$) and mixed events for real 1998 data for (a) all charged particles used for event selections, (b) all particles including neutrals, (c) charged particles used for analysis of Q distributions.

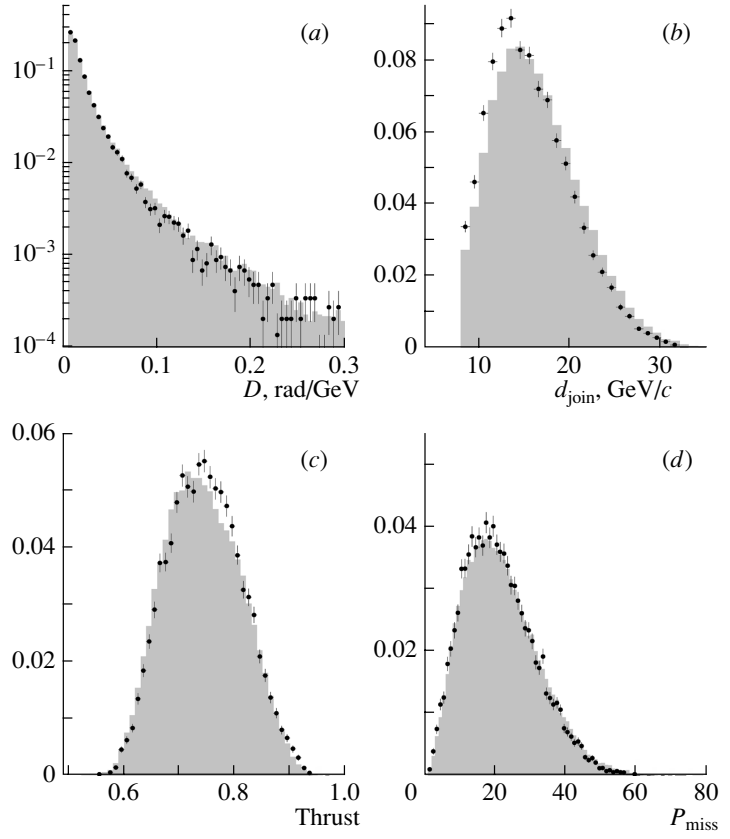

Fig. 8. Comparison of event shape variables for ($4q$) (closed circles) and mixed events (shaded area) for simulated data.

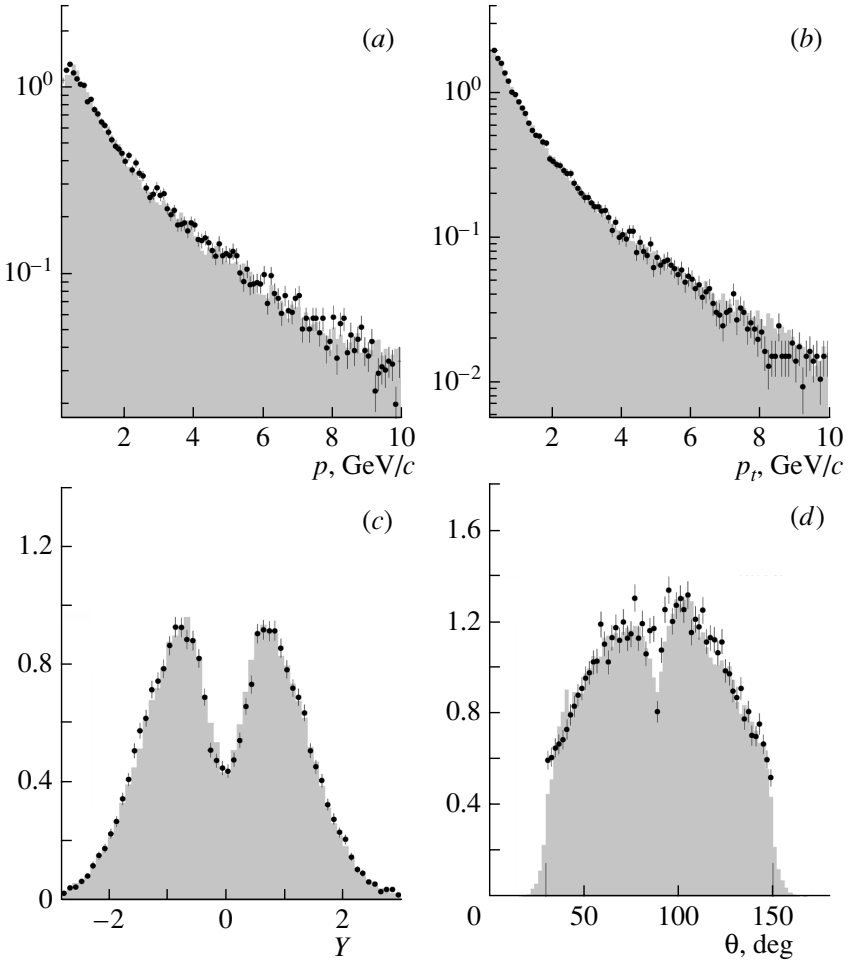

Fig. 9. Comparison of single-particle distributions for $(4q)$ (closed circles) and mixed events (shaded area) for real 1998 data.

$$= \frac{[P_{2q}(Q) + P_{\text{mix}}(Q)]_{\text{data}}}{[P_{2q}(Q) + P_{\text{mix}}(Q)]_{\text{DELSIM(no BEC)}}},$$

where $P_{\text{mix}}(Q)$ was obtained using the mixing of two $(2q)$ events as described above. The measured $R_{4q}(Q)$ and $R_{4q}(Q)$(mixing) are shown in Fig. 11 for like-sign pairs, indicating the correlations between particles from different W.

To perform model-independent measurements of correlations between particles from different W, the ratio, which is independent of any Monte Carlo model,

$$D(Q) \equiv \frac{P_{4q}(Q)}{P_{2q}(Q) + P_{\text{mix}}(Q)} \tag{16}$$

was used. This was fitted by the expression

$$D(Q) = N\,(1 + \delta Q)\left(1 + \Lambda e^{-RQ}\right). \tag{17}$$

The resulting plots are shown in Fig. 12.

The fit for the model with full BEC gave

$$\Lambda(\text{full BE}) = 0.227 \pm 0.026(\text{stat.}), \tag{18}$$

$$R(\text{full BE}) = 0.895 \pm 0.100(\text{stat.})\ \text{fm}, \tag{19}$$

$$\delta(\text{full BE}) = 0.000 \pm 0.002(\text{stat.}), \tag{20}$$

$$N(\text{full BE}) = 0.998 \pm 0.004(\text{stat.}). \tag{21}$$

Fixing the parameter R to the value obtained above ($R = 0.895$ fm) and repeating the fit for the model with inside BEC and for the data yielded

$$\Lambda(\text{inside BE}) = -0.002 \pm 0.016(\text{stat.}), \tag{22}$$

$$\delta(\text{inside BE}) = 0.001 \pm 0.001(\text{stat.}) \tag{23}$$

for the model with inside W BEC and

$$\Lambda(\text{data}) = 0.149 \pm 0.045(\text{stat.})^{+0.025}_{-0.020}(\text{syst.}), \tag{24}$$

$$\delta(\text{data}) = -0.003 \pm 0.004(\text{stat.}) \tag{25}$$

for data.

The systematic error quoted on the measured value of Λ(data) in (24) is the sum in quadrature of the following contributions.

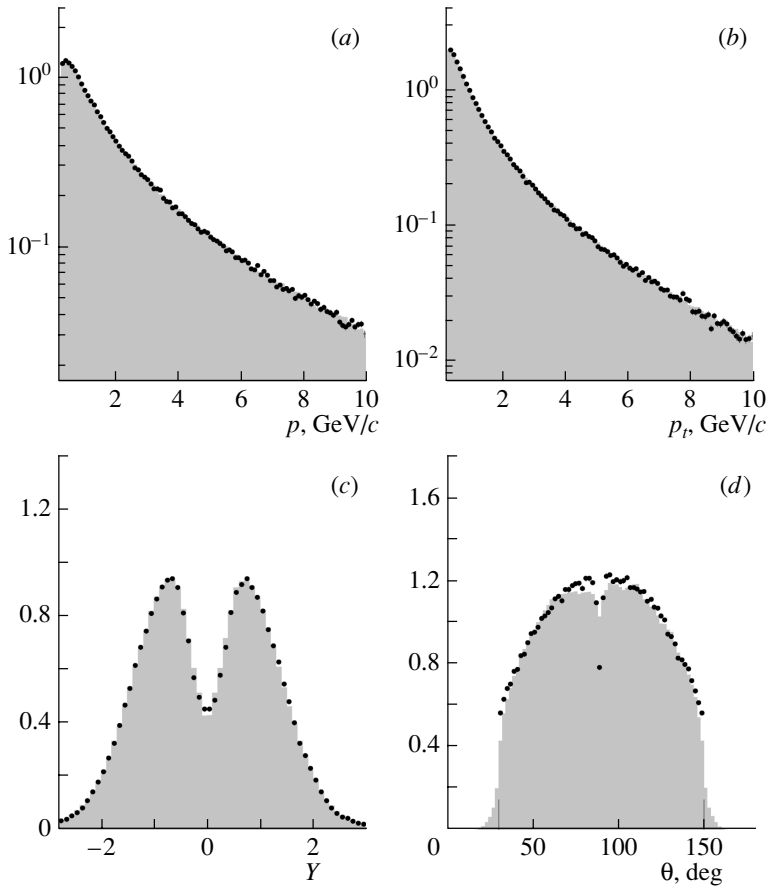

Fig. 10. Comparison of single-particle distributions for $(4q)$ (closed circles) and mixed events (shaded area) for simulated data.

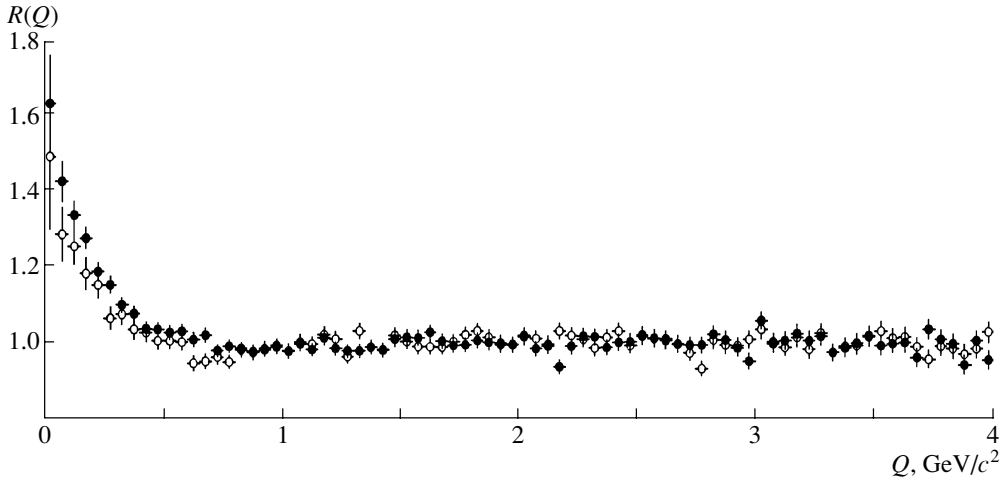

Fig. 11. Measured correlation functions $R_{4q}(Q)$ (closed circles) and $R_{4q}(Q)$ (constructed) (open circles) computed from $(2q)$ events using the mixing technique.

(i) Due to the event-mixing technique. Two estimated were made:

The model with BEC only inside W should give $\Lambda = 0.0$. The magnitude of the value Λ(inside BE) plus 1σ [Eq. (22)] is 0.018.

The effects of discrepancies between fully hadronic and mixed events were studied. Weights were assigned to the mixed events which were equal to the ratio of the event shape and single-particle distribu-

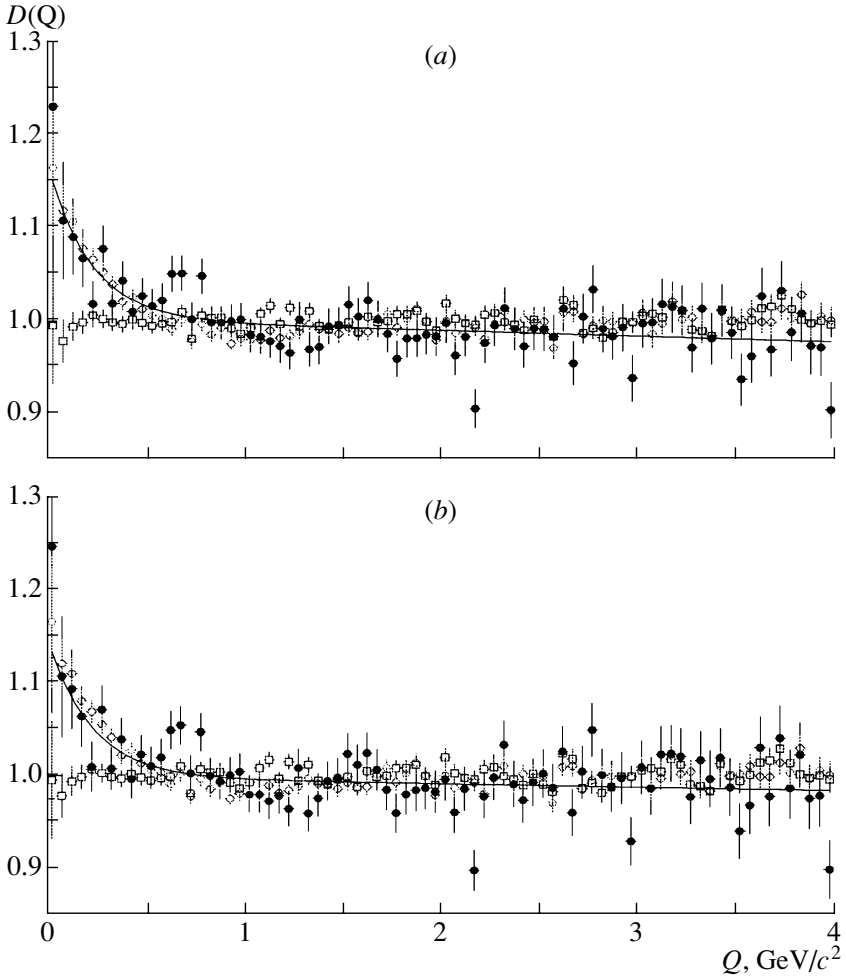

Fig. 12. (*a*) The ratio $D(Q)$ of full hadronic to mixed events for data (closed circles), for full BE (open circles), and for inside BE (open squares). (*b*) The same as (*a*), but after background subtraction from the data. The curves in figures show the best fit to expression (17) for data. The results of the fit quoted in the text were obtained using the full covariance matrix.

tion variables shown in Figs. 6–10. The maximum deviation obtained from the value (24) was 0.020.

The value ± 0.020, i.e., the larger of these two estimates, was used as a conservative systematic error due to the mixing technique.

(ii) Due to background events. The value of parameter Λ(data) without background subtraction was

$$\Lambda(\text{data}) = 0.164 \pm 0.043(\text{stat.}). \qquad (26)$$

The difference between the values of (24) and (26), i.e., $+0.015$, was used as an estimate of the systematic error.

(iii) The contribution due to other sources were found to be negligible.

The analysis was repeated using the requirement $\alpha > 3^\circ$, where α is the angle between pairs of particles. The corresponding $D(Q)$ plots are shown in Fig. 13. The fit for the prediction of the model with full BEC gave

$$\Lambda(\text{full BE}, \alpha \text{ cut}) = 0.292 \pm 0.037(\text{stat.}). \qquad (27)$$

Note that the $\alpha > 3^\circ$ requirement increases the sensitivity to inter-W correlations [values (18) and (27)].

The fitted values for the prediction of the model with inside BEC and for the data were

$$\Lambda(\text{inside BE}, \alpha \text{ cut}) = -0.002 \pm 0.021(\text{stat.}), \quad (28)$$

$$\Lambda(\text{data}, \alpha \text{ cut}) = 0.177 \pm 0.055(\text{stat.})^{+0.033}_{-0.023}(\text{syst.}). \qquad (29)$$

The value of Λ without background subtraction was $\Lambda(\text{data}, \alpha \text{ cut}) = 0.201 \pm 0.052$.

6. SUMMARY

The correlation functions for like-sign particles were measured in hadronic Z decays, in semilep-

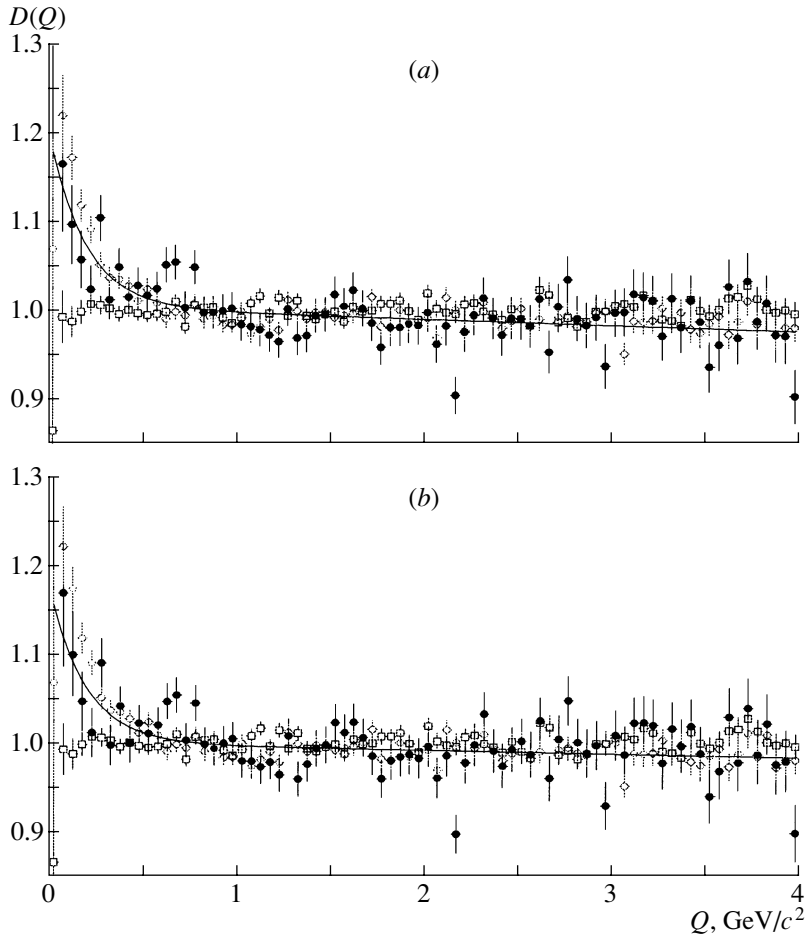

Fig. 13. Same as in Fig. 12, but for $\alpha > 3^\circ$ cut.

tonic and in fully hadronic WW channels using data collected with the DELPHI detector during the 1998, 1999, and 2000 runs with integrated luminosity of 547 pb^{-1} at c.m. energies of 189–206 GeV.

Measurements were performed to extract correlations between pions from different W. The event mixing technique was used to construct a comparison sample which contained only BEC for particle pairs coming from a single W boson.

The value of parameter $\Lambda(\mathrm{data})$ characterizing the correlations between particles from different W was found to be

$$\Lambda(\mathrm{data}) = 0.149 \pm 0.045(\mathrm{stat.})^{+0.025}_{-0.020}(\mathrm{syst.}).$$

The value using the $\alpha > 3^\circ$ requirement was found to be

$$\Lambda(\mathrm{data}, \alpha\ \mathrm{cut}) = 0.177 \pm 0.055(\mathrm{stat.})^{+0.033}_{-0.023}(\mathrm{syst.}).$$

Our overall conclusion is that our data support the hypothesis of correlations between like-sign pions coming from different W.

ACKNOWLEDGMENTS

I thank T. Sjöstrand for very useful discussions. I am greatly indebted to our technical collaborators and to the funding agencies for their support in building and operating the DELPHI detector, and to the members of the CERN-SL Division for the excellent performance of the LEP collider. I also thank the Organizing Committee of the VHMP Workshop.

REFERENCES

1. G. Altarelli, T. Sjöstrand, and F. Zwirner, CERN 96-01 (1996), Vol. 1.
2. L. Lönnblad and T. Sjöstrand, Eur. Phys. J. C **2**, 165 (1998); Phys. Lett. B **351**, 293 (1995).
3. G. Lafferty, Z. Phys. C **60**, 659 (1993).
4. P. D. Acton *et al.* (OPAL Collab.), Z. Phys. C **56**, 521 (1992); P. Abreu *et al.* (DELPHI Collab.), Z. Phys. C **63**, 17 (1994); P. Abreu *et al.* (DELPHI Collab.), Z. Phys. C **65**, 587 (1995); D. Buskulic *et al.* (ALEPH Collab.), Z. Phys. C **69**, 379 (1996).
5. T. Sjöstrand, Comput. Phys. Commun. **82**, 74 (1994); T. Sjöstrand *et al.*, Comput. Phys. Commun. **135**, 238 (2001); T. Sjöstrand, L. Lönnblad, and S. Mrenna, hep-ph/0108264.

6. J. Hakkinen and M. Ringner, Eur. Phys. J. C **5**, 275 (1998).
7. S. V. Chekanov, E. A. De Wolf, and W. Kittel, Eur. Phys. J. C **6**, 403 (1999).
8. K. Geiger, J. Ellis, U. Heinz, and U. A. Wiedemann, Phys. Rev. D **61**, 054002 (2000).
9. P. Aarnio *et al.* (DELPHI Collab.), Nucl. Instrum. Methods Phys. Res. A **303**, 233 (1991).
10. P. Abreu *et al.* (DELPHI Collab.), Nucl. Instrum. Methods Phys. Res. A **378**, 57 (1996).
11. P. Abreu *et al.* (DELPHI Collab.), Phys. Lett. B **456**, 310 (1999).
12. F. A. Berends, R. Kleiss, and R. Pittau, Nucl. Phys. B **424**, 308 (1994).
13. P. Abreu *et al.* (DELPHI Collab.), Z. Phys. C **73**, 11 (1996).
14. A. De Angelis and L. Vitale, Nucl. Instrum. Methods Phys. Res. A **423**, 446 (1999).
15. V. Perevoztchikov, M. Tabidze, and A. Tomaradze, DELPHI 2000-027 CONF 346.
16. P. Abreu *et al.* (DELPHI Collab.), Z. Phys. C **63**, 17 (1994).

Physics of Atomic Nuclei, Vol. 67, No. 1, 2004, pp. 130–139. From Yadernaya Fizika, Vol. 67, No. 1, 2004, pp. 128–137.

Soft and Hard Interactions in $p\bar{p}$ Collisions at $\sqrt{s} = 1800$ and 630 GeV*

F. Rimondi**
(for the CDF Collaboration)

Dipartimento di Fisica and Istituto Nazionale di Fisica Nucleare, Università di Bologna, Italy

Received May 21, 2003

Abstract—We present a study of $p\bar{p}$ collisions at $\sqrt{s} = 1800$ and 630 GeV collected using a minimum bias trigger by the CDF experiment in which the data set is divided into two classes corresponding to "soft" and "hard" interactions. For each subsample, the analysis includes measurements of the multiplicity, transverse momentum (p_T) spectrum, and the average p_T and event-by-event p_T dispersion as a function of multiplicity. A comparison of results shows distinct differences in the behavior of the two samples as a function of the center-of-mass (CM) energy. We find evidence that the properties of the soft sample are invariant as a function of CM energy. © *2004 MAIK "Nauka/Interperiodica".*

1. INTRODUCTION

Hadron interactions are often classified as either "hard" or "soft" [1, 2]. Although there is no formal definition for either, the term "hard interactions" is typically understood to mean high transverse energy (E_T) parton–parton interactions associated with such phenomena as high-E_T jets, while the soft component consists of everything else. Whereas perturbative QCD provides a reasonable description of high-E_T jet production, there is no equivalent theory for the low-E_T multiparticle production processes that dominate the inelastic cross section. Some QCD inspired models [2] attempt to describe these processes by the superposition of many parton interactions extrapolated to very low momentum transfers. It is not known, however, if these or other collective multiparton processes are at work.

The study of low-E_T interactions usually involves collecting data using minimum bias (MB) triggers, which, ideally, sample events in fixed proportion to the production rate—in other words, in their "natural" distribution. Lacking a comprehensive description of the microscopic processes [3] involved in low-E_T interactions, our knowledge of the details of low transverse momentum (p_T) particle production rests largely upon empirical connections between phenomenological models and data collected with MB triggers at many center-of-mass (CM) energies. Such comparisons are further complicated by the difficulty in isolating events of a purely soft or purely hard nature.

This paper adopts a novel approach in addressing this issue using samples of $p\bar{p}$ collisions at $\sqrt{s} =$ 1800 and 630 GeV collected with a MB trigger. The analysis first divides the full MB samples into two subsamples, one highly enriched in soft interactions, the other relatively depleted of soft interactions. We then compare inclusive distributions and final-state correlations between the subsamples and as a function of CM energy in order to gain insights into the mechanisms of particle production in soft interactions. The results in the isolated soft sample exhibit some interesting properties, in particular, an unpredicted invariance with CM energy. The results presented in this paper were published in [4].

2. DATA SET AND EVENT SELECTION

Data samples have been collected with the CDF detector at the Fermilab Tevatron Collider. The CDF apparatus has been described elsewhere [5]; here, only the parts of the detector utilized for the present analysis are discussed.

Data at 1800 GeV were collected with an MB trigger during runs 1A and 1B, and at 1800 and 630 GeV during run 1C. This trigger requires coincident hits in scintillator counters located at 5.8 m on either side of the nominal interaction point and covering the pseudorapidity ($\eta = -\log(\tan(\theta/2))$, where θ is the angle with respect to the proton direction) interval $3.2 < |\eta| < 5.9$, in coincidence with a beam-crossing signal.

*This article was submitted by the author in English.

**e-mail: Franco.Rimondi@bo.infn.it

1063-7788/04/6701-0130$26.00

The analysis uses charged tracks reconstructed within the central tracking chamber (CTC). The CTC is a cylindrical drift chamber covering a η interval of about three units with full efficiency for $|\eta| \leq 1$ and $p_T \geq 0.4$ GeV/c.

Inside the CTC inner radius, a set of time projection chambers (VTX) [6] provides r–z tracking information out to a radius of 22 cm for $|\eta| < 3.25$. The VTX is used in this analysis to find the z position of event vertices, defined as a set of tracks converging to the same point along the z axis. Reconstructed vertices are classified as either "primary" or "secondary" based upon a combination of the number of tracks pointing to the vertex and the forward–backward symmetry of these tracks. High-multiplicity vertices with highly symmetric topologies are considered to be primaries; low-multiplicity, highly asymmetric vertices are classified as secondaries.

The transverse energy flux was measured by a calorimeter system [7] covering from -4.2 to 4.2 in η.

The 1800-GeV data sample consists of subsamples collected during three different time periods. Approximately 1 700 000 events were collected in run 1A at an average luminosity of 3.3×10^{30} s^{-1} cm^{-2}, 1 500 000 in run 1B at an average luminosity of 9.1×10^{30} s^{-1} cm^{-2}, and 106 000 in run 1C at an average luminosity of 9.0×10^{30} s^{-1} cm^{-2}. The 630-GeV data set consists of about 2 600 000 events recorded during run 1C at an average luminosity of 1.3×10^{30} s^{-1} cm^{-2}.

Additional event selection conducted off-line removed the following events: (i) events identified as containing cosmic-ray particles as determined by time-of-flight measurements using scintillator counters in the central calorimeter; (ii) events with no reconstructed tracks; (iii) events exhibiting symptoms of known calorimeter problems; (iv) events with at least one charged particle reconstructed in the CTC to have $p_T > 400$ MeV/c, but no central calorimeter tower with energy deposition above 100 MeV; (v) events with more than one primary vertex; (vi) events with a primary vertex more than 60 cm away from the center of the detector (in order to keep full tracking efficiency in the CTC and avoid energy leakage through exposed cracks in the calorimeter); (vii) events with no primary vertices.

After all event selection cuts, 2 079 558 events remain in the full minimum bias sample at $\sqrt{s} =$ 1800 GeV (runs 1A + 1B + 1C) and 1 963 157 in that at $\sqrt{s} = 630$ GeV (run 1C).

The vast majority of rejected events failed the vertex selection. About 0.01% of selected events contain background tracks from cosmic rays that are coincident in time with the beam crossing and pass near the event vertex. The residual beam gas contamination is about 0.02%.

The systematic uncertainties that arise from the event selection criteria and other sources are discussed in Section 6.

3. TRACK SELECTION

Reconstructed tracks within each event must pass selection criteria designed to remove the main sources of background. Tracks must pass through a minimum number of layers in the CTC and have a minimum number of hits in each superlayer in order to reduce the number of tracks with reconstruction errors. Fake and secondary particle tracks are removed by requiring that tracks pass within 0.5 cm of the beam axis and within 5 cm along the z axis of the primary event vertex. Accepting only tracks with $p_T \geq 0.4$ GeV/c and within $|\eta| \leq 1.0$ ensures full efficiency and acceptance.

We define the charged track multiplicity in an event, $N^*_{\rm ch}$, as the number of selected CTC tracks in the event. The mean p_T of the event is defined as

$$\bar{p}_T = \frac{1}{N^*_{\rm ch}} \sum_i^{N^*_{\rm ch}} p_{T_i} \qquad (1)$$

unless stated otherwise.

4. SELECTION OF SOFT AND HARD INTERACTIONS

The identification of soft and hard interactions is largely a matter of definition [8]. In this analysis, we use a jet reconstruction algorithm to distinguish between the two classes. The algorithm employs a cone with radius $R = (\Delta\eta^2 + \Delta\phi^2)^{1/2} = 0.7$ to define "clusters" of calorimeter towers belonging to the jet. To be considered, a cluster must have a transverse energy (E_T) of at least 1 GeV in a seed tower, plus at least 0.1 GeV in an adjacent tower.

In the regions $|\eta| < 0.02$ and $1.1 < |\eta| < 1.2$, a track-clustering algorithm is used instead of the calorimeter algorithm in order to compensate for energy lost in calorimeter cracks. A track cluster is defined as one track with $p_T > 0.7$ GeV/c and at least one other track with $p_T \geq 0.4$ GeV/c in a cone of radius $R = 0.7$.

We define a soft event as one that contains no cluster with $E_T > 1.1$ GeV. All other events are classified as hard.

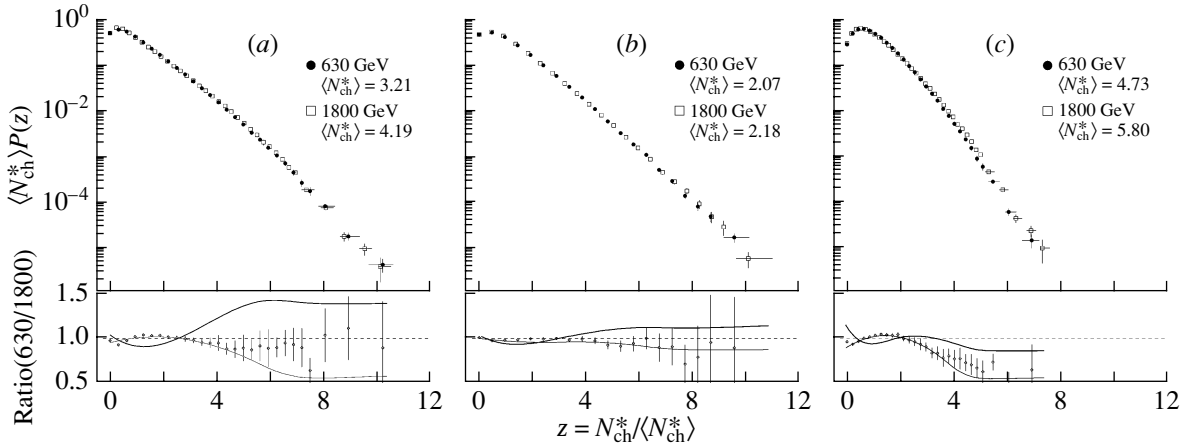

Fig. 1. Multiplicity distributions at 1800 and 630 GeV for (*a*) the full MB samples, (*b*) the soft samples, and (*c*) the hard samples; data are plotted in KNO variables for $|\eta| \leq 1.0$ and $p_T \geq 0.4$ GeV/*c*. In the bottom panel, the ratio of the above two distributions is shown. The two curves delimit the band of all systematic uncertainties (see Section 2).

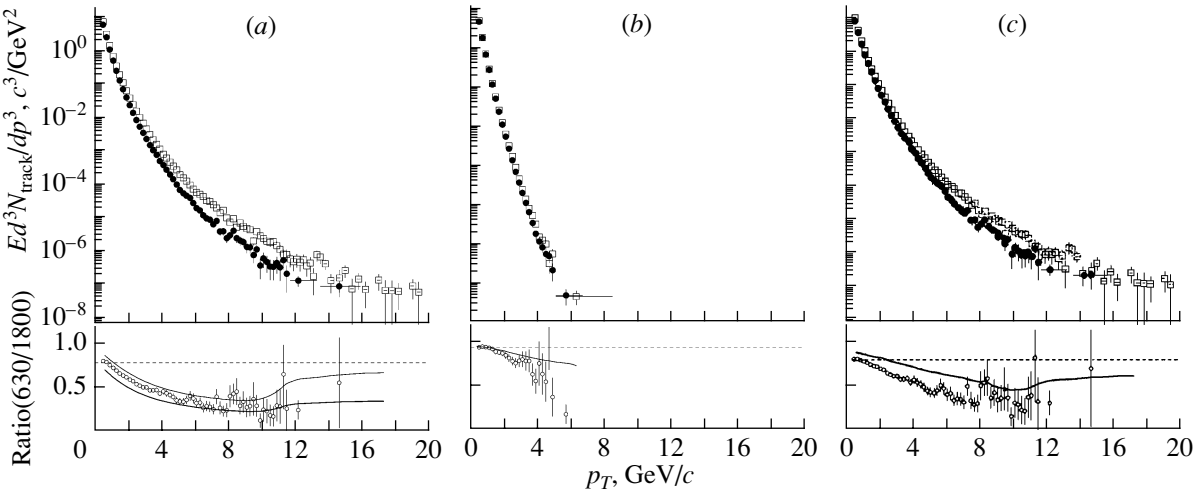

Fig. 2. Transverse momentum distributions at (□) 1800 and (●) 630 GeV ($|\eta| \leq 1.0$) for (*a*) the full MB samples, (*b*) the soft samples, and (*c*) the hard samples. In the bottom panel, the ratio of the two distributions is shown. The two curves delimit the band of all systematic uncertainties [see Section 2; for (*b*) and (*c*), the lower limit overlaps the data points]. N_{track} refers to the number of charged tracks in a unit η interval.

5. EFFICIENCY CORRECTIONS

The track reconstruction efficiency for the CTC has been investigated for several different analyses and under various conditions at CDF [9–11]. For this analysis, we have calculated a full-event track reconstruction efficiency using a parametric MC sample. Version 5.7 of the Pythia generator was used with the MB configuration tuned to match the inclusive multiplicity and p_T distributions of the 1800-GeV sample. For each inclusive distribution, a track-finding efficiency correction was computed by taking the ratio of the Pythia-generated distribution to the corresponding distribution from tracks traced through the apparatus. The efficiency for reconstructing the correct event charged multiplicity is about 95% up to a multiplicity of about 20, falling to about 85% at multiplicities above about 20.

The same Pythia MC sample was used to evaluate the background from gamma-ray conversions and charged and neutral particle decays. Correction factors due to these effects have been computed as a function of track p_T and the event multiplicity.

There exists a small contamination from diffractive events even in the restricted region of phase space examined in this study. We have evaluated this contamination with a special Pythia MC run in which only the diffractive generation algorithm was switched on. The data were then subjected to the full event and track

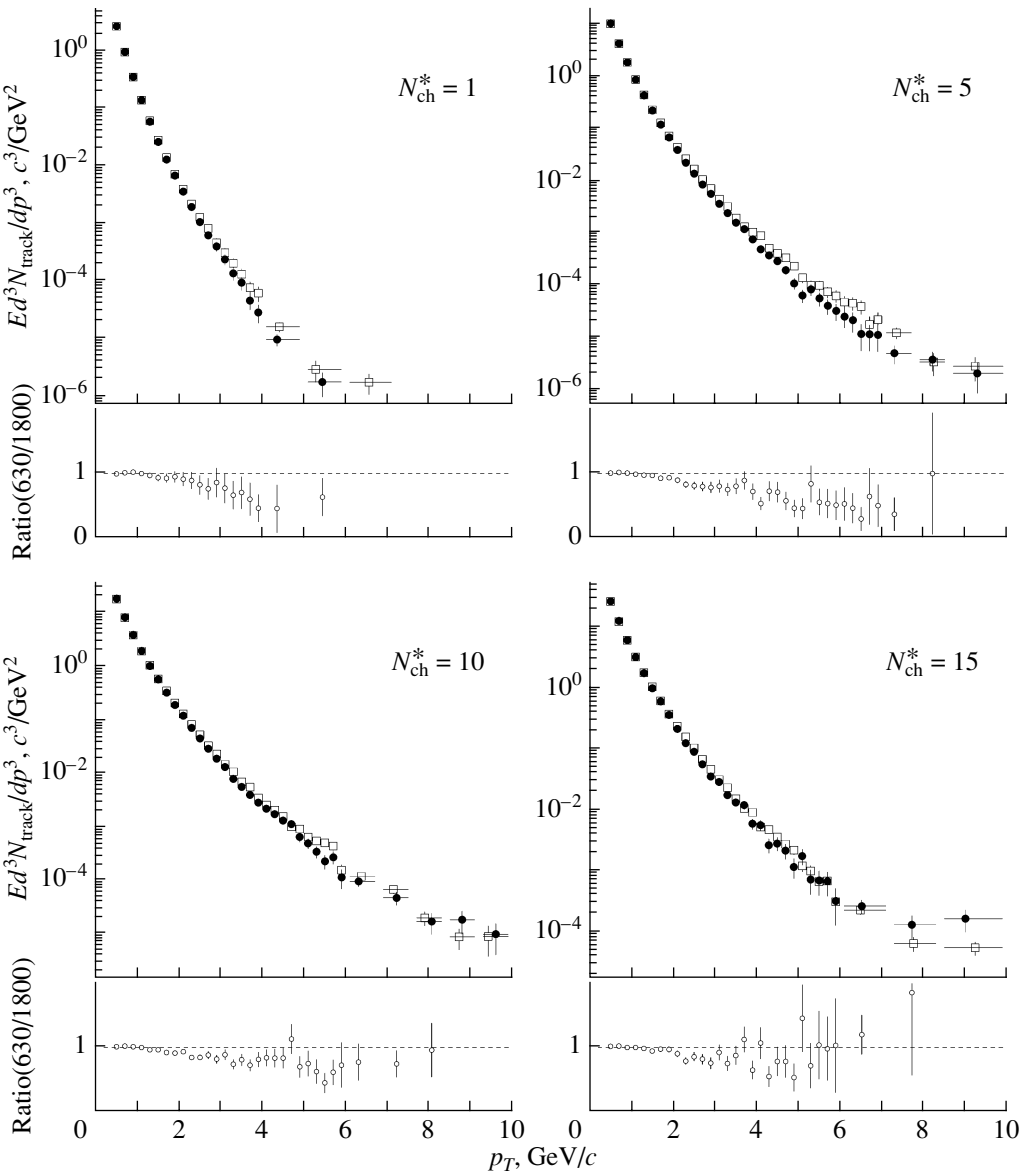

Fig. 3. Transverse momentum distributions at fixed multiplicity (multiplicity = 1, 5, 10, 15) for the full MB samples at (□) 1800 and (●) 630 GeV ($|\eta| \leq 1.0$). At the bottom of each plot, the ratio of the above two distributions is shown. Error bars represent statistical error only. Systematic error was found to be negligible and is not included.

selection procedure. The correction for this effect is estimated to be about 5% in the zero multiplicity bin, decreasing rapidly to zero for $N^*_{ch} \sim 4$. In the p_T distribution, the correction is between zero and 1% up to about 1 GeV/c.

6. SYSTEMATIC UNCERTAINTIES

Several sources of systematic errors have been investigated. The effect of each on the final distributions is discussed below.

Vertex selection. As discussed in Section 2, the vertex selection classifies vertices as either primary or secondary. The standard selection demands that primary vertices be highly isolated. Misclassification or identification of vertices can strongly influence the p_T and multiplicity distributions, particularly the latter. We set conservative bounds on the magnitude of this effect in the following way. Two samples of events are selected. In one, all vertices except the highest quality one are classified as secondaries. In the other sample, all vertices are classified as primary. Compared to results obtained using the standard vertex selection, the ratio of the multiplicity distribution at $\sqrt{s} = 630$ GeV to that at 1800 GeV varies by about 5% in the region between a multiplicity of 2 and 11, and reaches 40%

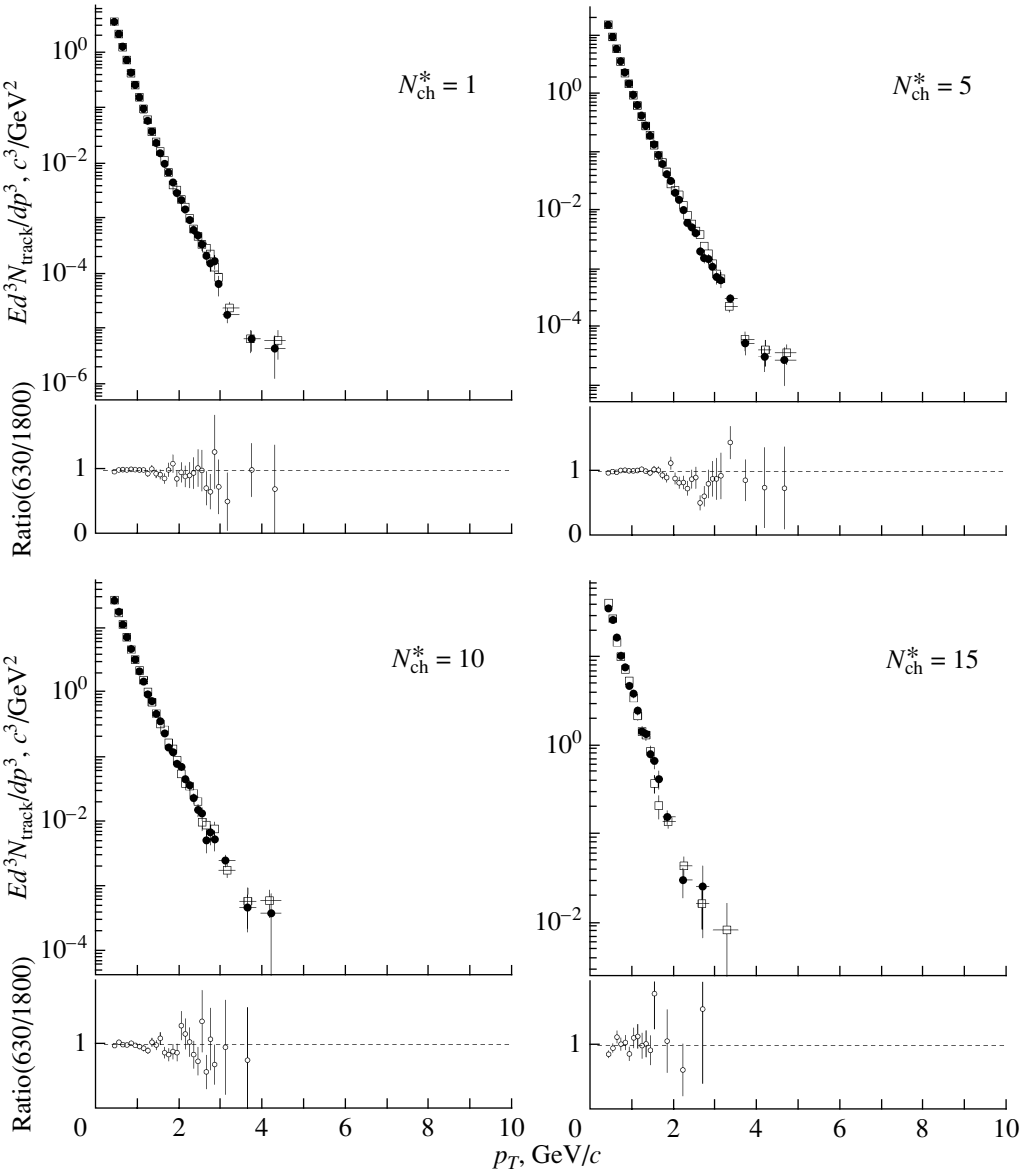

Fig. 4. Same as Fig. 3 for the soft samples.

for multiplicities in excess of 22. The deviation in the ratio of p_T distributions at the two energies is almost constant at about 10% up to a p_T around 11 GeV/c, increasing to 15% as p_T increases.

Vertices in some multiple interaction events remain unresolved and introduce a residual luminosity-dependent contamination. We estimate the systematic uncertainty from this source by comparing the results of the complete analysis on two subsamples of data, one at low luminosity ($<1.5 \times 10^{30}$ cm^{-2} s^{-1}) and the other at high luminosity ($>7 \times 10^{30}$ cm^{-2} s^{-1}). Differences range between 2% and 6% for multiplicities less than 20, increasing to about 16% for multiplicities in the range $20 < N^*_{ch} < 30$ and to 45% for multiplicities greater than 30. The effect on the ratios of the various distributions is negligible.

The selection of events identified with known calorimeter problems depends upon thresholds applied to classify the anomalous behavior. This selection removes $\lesssim$1% of the total sample. Changing the rejection factor causes no appreciable change in the distribution ratios.

Tracking efficiencies evaluated at CDF under various conditions and using different techniques obtain results that differ by as much as 8–10% in the low-p_T (below 1 GeV/c), high-p_T (above 2 GeV/c), or high-multiplicity regions. The impact of using widely different efficiency corrections on the multiplicity and

p_T distributions is—at most—as large as the statistical uncertainty. The effect on the distribution ratios is negligible.

The systematic uncertainty due to the correction for gamma conversions, secondary particle interactions, and particle decays is estimated to be about 1%, almost independent of multiplicity and p_T. The effect on the ratios of distributions is negligible.

The systematic uncertainty in the correction to the multiplicity distribution due to contamination from diffractive production is on the order of 1% and is limited to very low multiplicities ($0 \le N^{\star}_{\mathrm{ch}} \le 3$). No correction was applied to the p_T distribution, where the magnitude of the effect was less than 1% for all p_T. The effect is negligible on the distribution ratios.

The systematic uncertainty from the vertex selection dominates all other sources. The curves on the final inclusive distribution ratios are obtained as the ratios of the distributions originated by the extreme selections outlined above. They are not intended as point-to-point systematic uncertainties, but are included in the figures to show the approximate range over which the shape of the final distribution may be changed by altering the vertex selection.

Systematic effects cancel in the ratios of final-state correlations (see Subsections 7.2 and 7.3).

7. DATA ANALYSIS

7.1. Inclusive Distributions

We first examine the inclusive multiplicity and transverse momentum distributions. Figure 1*a* shows the multiplicity distributions for the full MB samples at 1800 and 630 GeV, plotted in KNO variables [12]. The distributions at the two energies show a weak violation of KNO scaling, as is expected in a limited phase-space region [13]. The same comparison is made in Figs. 1*b* and 1*c* for the soft and hard samples separately. The ratio of the multiplicity distributions at the two energies is plotted at the bottom of Fig. 1.

Transverse momentum distributions at the two energies are shown in Fig. 2*a* for the full MB sample. Figures 2*b* and 2*c* show the same distributions for the soft and hard sample, respectively. As for the multiplicity distributions, the ratios of the distributions at the two energies are shown in the bottom of these figures. The p_T spectrum in the soft sample falls more rapidly with increasing p_T than that of the hard sample. This difference is expected and reflects the absence of events with high-p_T jets in the soft sample.

A deeper insight into the dynamics of the interactions can be gained by comparing the p_T distributions for fixed charged multiplicity as a function of $\sqrt{s}$. Figure 3 shows fixed-multiplicity p_T distributions for the full MB sample at the two energies superimposed.

The same distributions are plotted in Figs. 4 and 5 for the soft and hard subsamples, respectively. For brevity, only multiplicities of 1, 5, 10, and 15 are shown.

We observe that, within uncertainties, the p_T distributions for a given multiplicity are the same at $\sqrt{s}$ equal to 1800 and 630 GeV—they are CM energy invariant. None of the current models predict or suggest such an invariance. The result suggests that, in purely soft interactions, the number of produced (charged) particles is the only global event variable changing with $\sqrt{s}$. The particle multiplicity may also fix other event properties independently of the energy of the reaction.

A further observation is worth noting. It is known that, for minimum bias samples, the slope of the inclusive p_T distribution increases steadily by some power of $\log s$ up to Tevatron energies [9, 14]. Such an increase is also visible for p_T distributions at fixed multiplicity for the full MB sample shown in Fig. 3. The result of the present analysis implies that the $\sqrt{s}$ dependence in the slope of the p_T distribution of the soft sample is due entirely to the change in the mean multiplicity. In contrast, the more pronounced change in the shape of the full MB and the hard samples as a function of $\sqrt{s}$ must be caused in part by the increasing cross section of hard parton interactions.

7.2. Dependence of Mean Track p_T on Charged Multiplicity

The correlation between mean p_T and charged multiplicity was first observed by UA1 [15] and then investigated at ISR [16] and Tevatron Collider energies [14, 17]. Although several different theoretical explanations have been proposed, such as geometrical models [18], thermodynamic models [19], and contributions from semihard parton scattering (minijets) [20], none provide satisfactory predictions for existing experimental results, leaving the real origin of the effect unexplained. Simulations performed with Pythia and Herwig generators do not show better agreement with data (see Fig. 6) [21]. In this analysis, the mean p_T (to be distinguished from the mean event p_T) is obtained by summing the p_T of all reconstructed charged tracks in all events with a given charged multiplicity, then dividing by the number of such tracks. The results are shown in Fig. 7*a* for the full MB sample at the two analyzed energies and in Figs. 7*b* and 7*c* for the soft and for the hard samples, respectively.

The event multiplicity is smeared by track-finding inefficiency. We correct the data points for the average track-finding efficiency at each multiplicity.

The mean p_T as a function of multiplicity for the soft sample (Fig. 7*b*) is nearly identical at the two

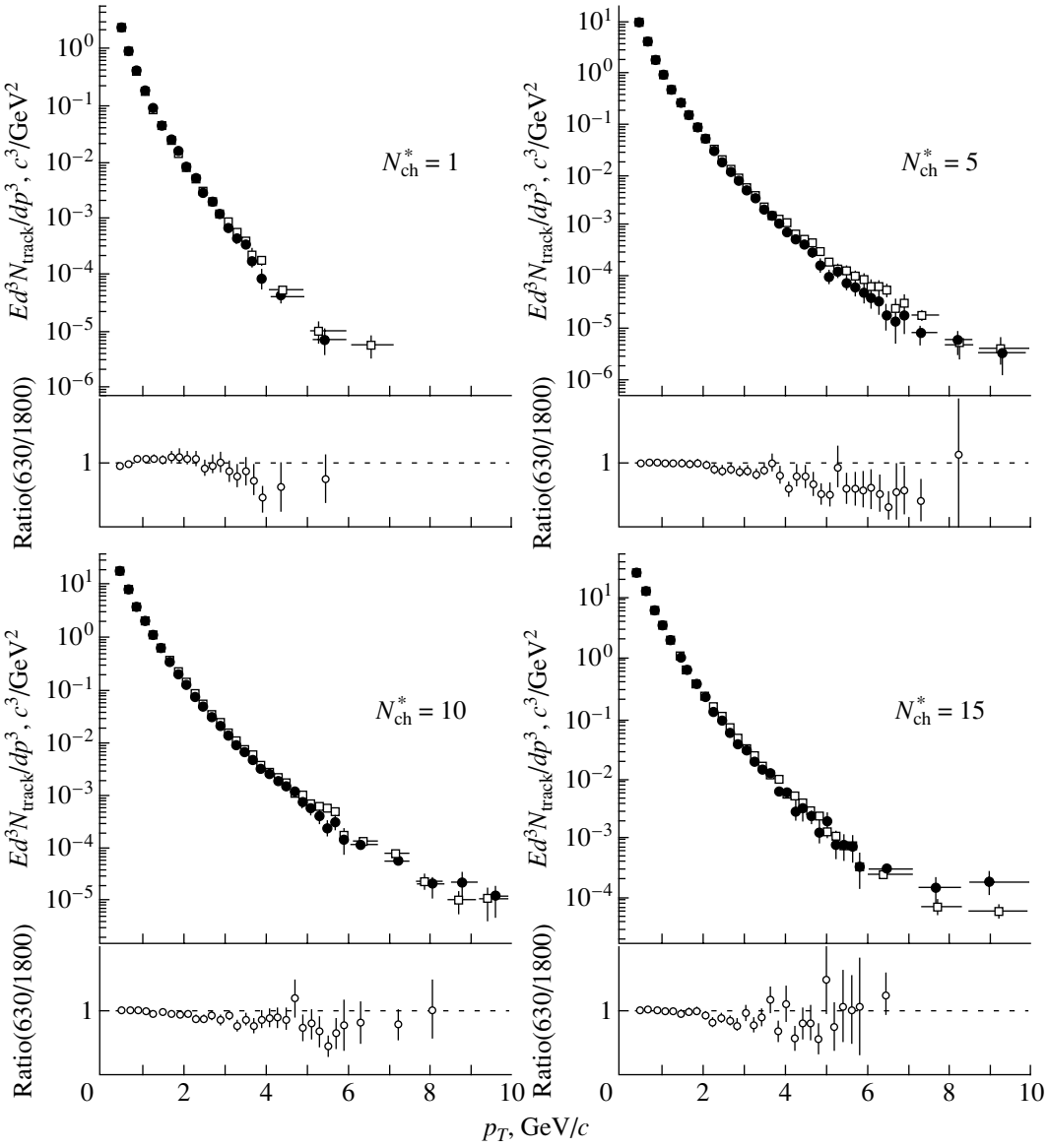

Fig. 5. Same as Fig. 3 for the hard samples.

energies. This invariance is a direct consequence and a confirmation of the invariance of the soft-p_T spectra at fixed multiplicities noted in the previous section.

Comparing Figs. 7*b* and 7*c*, we note a clear difference in the mean p_T correlation of the soft and hard samples. Interestingly, the mean p_T increases at low multiplicity even in the soft sample, which should be highly depleted in high-E_T events. This observation suggests that an increasing contribution from hard gluon production, as proposed in [20], is at least not the only mechanism responsible for the correlation at low multiplicity.

7.3. $\langle p_T \rangle_{ev}$ Dispersion versus Multiplicity

Event-by-event fluctuations of the mean event p_T have been shown to be a useful tool to investigate the collective behavior of soft multibody production and has been used to analyze experimental data in various different ways [22, 24]. Following the approach of [22], the dispersion D_m of the mean event p_T for events with multiplicity m is defined as

$$D_m(\bar{p}_T) = \frac{\langle \bar{p}_T^2 \rangle_m - \langle \bar{p}_T \rangle_m^2}{\langle \bar{p}_T \rangle^2_{\text{sample}}}. \qquad (2)$$

Brackets $\langle\ \rangle$ indicate an average over all events with the given multiplicity m, while $\bar{p}_T$ is the mean event p_T from Eq. (1).

The dispersion is expected to decrease with increasing multiplicity and to converge to zero when $m \to \infty$ if only statistical fluctuations are present. Conversely, an extrapolation to a nonzero value would

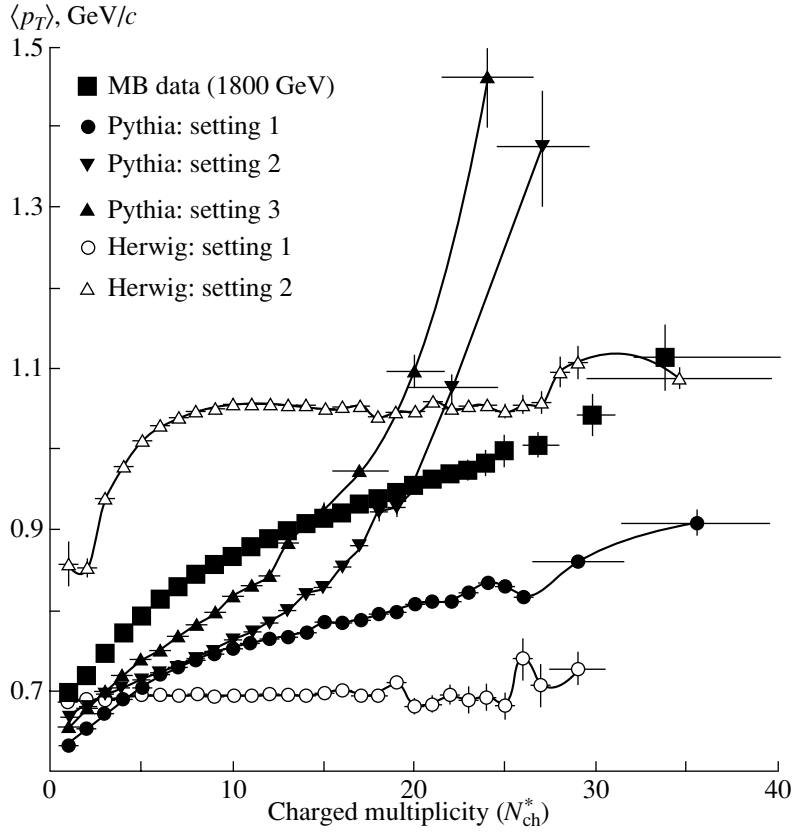

Fig. 6. Mean transverse momentum vs. multiplicity from Monte Carlo ($p_T \geq 0.4$ GeV/c, $|\eta| \leq 1.0$).

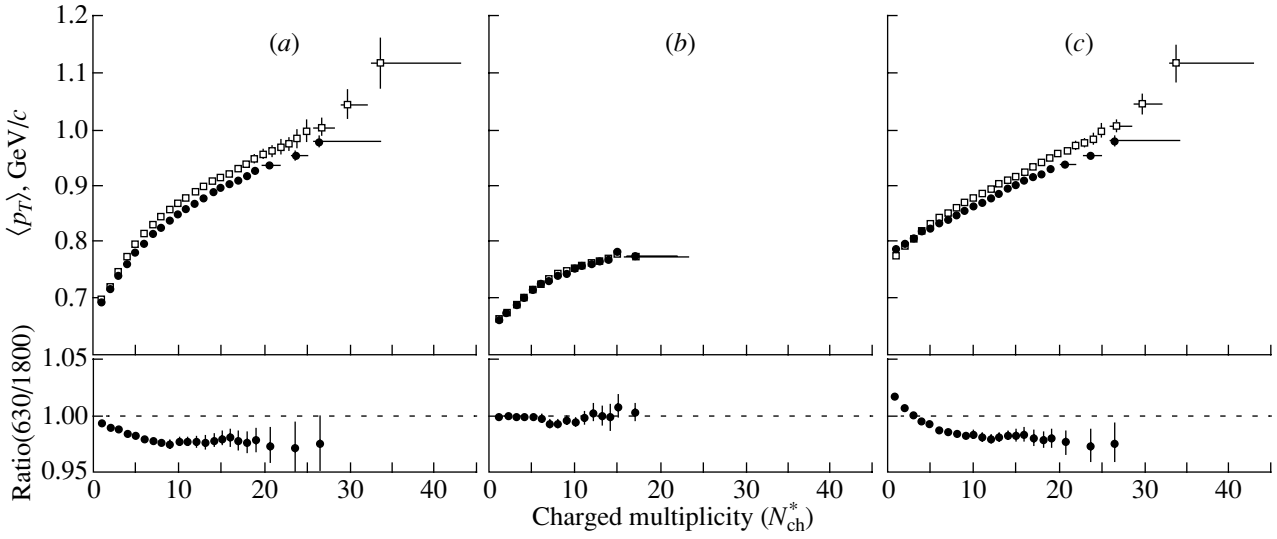

Fig. 7. Mean transverse momentum vs. multiplicity at (□) 1800 and (●) 630 GeV ($p_T \geq 0.4$ GeV/c, $|\eta| \leq 1.0$) for (*a*) the full MB samples, (*b*) the soft samples, and (*c*) the hard samples. On the bottom the ratio of the two curves is shown.

indicate the presence of nonstatistical fluctuations in $\bar{p}_T$ from event to event. This indeed is what was found in [22] and, in different ways, in [23] and [24]. Large nonstatistical fluctuations of the mean event p_T are a consequence of particle correlations in the multibody final state [25]. Figure 8*a* shows the present measurement of the dispersion as a function of the inverse multiplicity for the full minimum bias samples.

The correlation curve has a slope that varies across

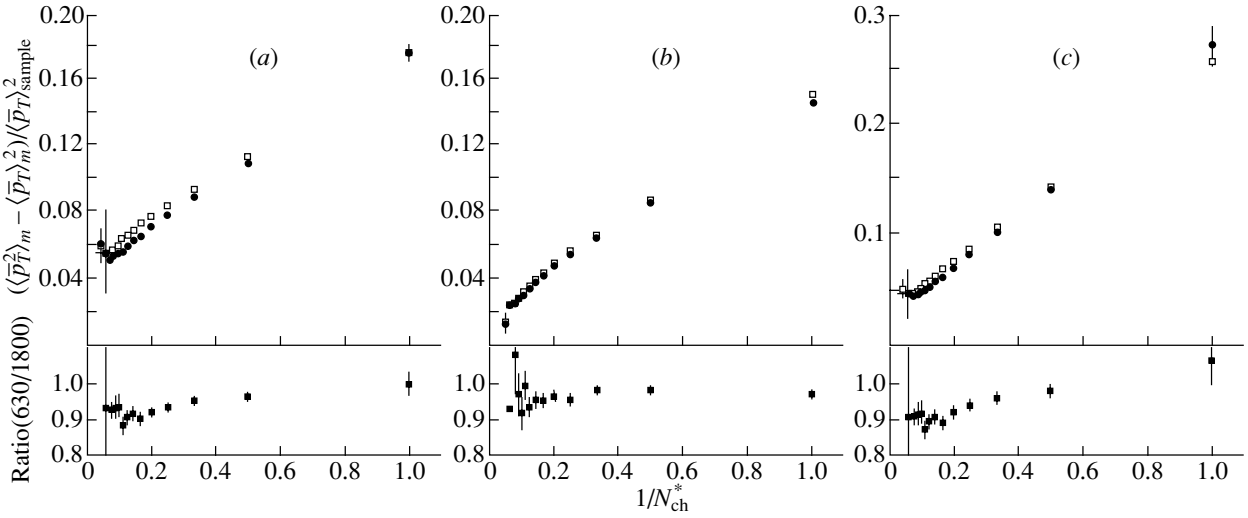

Fig. 8. Dispersion of the mean event p_T as a function of the inverse multiplicity at (□) 1800 and (●) 630 GeV ($p_T \geq 0.4$ GeV/c, $|\eta| \leq 1.0$) for (a) the full MB samples, (b) the soft samples, and (c) the hard samples. At the bottom, the ratio of the two curves is shown.

multiplicities, particularly at $\sqrt{s} = 1800$ GeV. The dispersion versus inverse multiplicity for the soft and hard samples, shown in Figs. 8*b* and 8*c*, confirms that this effect is related to the contribution of jet production, which, as discussed in [26], increases event-by-event fluctuations. The plots show only statistical uncertainties.

Comparing our soft sample results with the full MB results [22], where hard jet production has a much lower cross section than at Tevatron energies, we note that our points, unlike those in [22], drop at high multiplicity (multiplicity $\gtrsim$7). Since statistical fluctuations vary linearly with the multiplicity, the drop we observe indicates that final-state particle correlations change with multiplicity. Moreover the results plotted in Fig. 8*b* are consistent with an extrapolation to zero at infinite multiplicity. These observations support the idea that asymptotically the event mean p_T has no dynamical fluctuations.[1)]

Finally, the dispersion as a function of the inverse multiplicity for the soft samples has a constant ratio at the two energies, a fact which is not true for the hard samples.

8. CONCLUSION

Assuming that hard parton interactions in $\bar{p}p$ scattering eventually develop into final-state particles observable as clustered within jet cones and pushing the cluster identification threshold as low as possible, we separate minimum bias events into subsamples enriched in soft or hard collisions. Comparing the behavior of the two samples at two energies, we obtain the following results.

The multiplicity distributions of soft interactions follow KNO scaling going from $\sqrt{s} = 630$ to 1800 GeV. This is not true for those of the hard subsample. The p_T distribution at fixed multiplicity in the soft sample is also energy invariant, a property which was unexpected. By this, we mean that the momentum distribution in the soft sample is determined only by the number of charged particles in the final state, independently of the CM energy.

The mean p_T as a function of the charged multiplicity in the soft samples scales remarkably well with energy. In addition, the mean p_T increases with multiplicity even in the soft sample, where hard parton interactions are at most strongly suppressed. Neither feature is predicted by current theoretical or phenomenological models.

The dispersion of the $\langle p_T\rangle_{\text{ev}}$ shows a nonlinear dependence on the inverse multiplicity, an observation not previously reported. The rise at multiplicity greater than ~ 10 is essentially due to the presence of hard parton interactions. In the same multiplicity region, the slope of the dispersion in the soft sample extrapolates to zero at infinite multiplicity. This means that asymptotically there are no dynamical correlations in the event mean p_T. The ratio of the dispersion in the soft sample at the two energies is flat as a function of multiplicity, a feature not exhibited by the hard sample.

[1)] It has been observed [27] that this method cannot exclude the possibility of opposite sign correlations that perfectly cancel each other.

All the distributions and correlations studied using the soft subsample are compatible with the hypothesis of invariance with the CM energy, which is a new result. We conclude that the dynamical mechanism of inelastic multiparticle production in soft interactions, at least in this energy interval, is invariant with CM energy and that the properties of the final state are determined only by the number of (charged) particles.

REFERENCES

1. R. Ansari *et al.*, Z. Phys. C **36**, 175 (1987); X. Wang and R. C. Hwa, Phys. Rev. D **39**, 187 (1989); F. Ceradini *et al.* (UA1 Collab.), in *Proceedings of the International Europhysics Conference on High Energy Physics, Bari, Italy, 1985,* p. 0363.
2. T. Sjöstrand and M. van Zijl, Phys. Rev. D **36**, 2019 (1987), and references therein.
3. See [2] (summary of the references to these models).
4. D. Acosta *et al.*, Phys. Rev. D **65**, 072005 (2002).
5. F. Abe *et al.*, Nucl. Instrum. Methods Phys. Res. A **271**, 387 (1988), and references therein.
6. F. Snider *et al.*, Nucl. Instrum. Methods Phys. Res. A **268**, 75 (1988).
7. F. Balka *et al.*, Nucl. Instrum. Methods Phys. Res. A **267**, 272 (1988); S. R. Hahn *et al.*, Nucl. Instrum. Methods Phys. Res. A **267**, 351 (1988); K. Yasuoka *et al.*, Nucl. Instrum. Methods Phys. Res. A **267**, 315 (1988); R. G. Wagner *et al.*, Nucl. Instrum. Methods Phys. Res. A **267**, 330 (1988); T. Devlin *et al.*, Nucl. Instrum. Methods Phys. Res. A **267**, 24 (1988); S. Bertolucci *et al.*, Nucl. Instrum. Methods Phys. Res. A **267**, 301 (1988); Y. Fukui *et al.*, Nucl. Instrum. Methods Phys. Res. A **267**, 280 (1988); S. Cihangir *et al.*, Nucl. Instrum. Methods Phys. Res. A **267**, 249 (1988); G. Brandenburg *et al.*, Nucl. Instrum. Methods Phys. Res. A **267**, 257 (1988).
8. F. Abe *et al.*, Phys. Rev. D **56**, 3811 (1997); Phys. Rev. Lett. **79**, 584 (1997); X. Wang, Phys. Rev. D **46**, 1900 (1992); C. Albajar *et al.* (UA1 Collab.), Nucl. Phys. B **309**, 405 (1988).
9. F. Abe *et al.*, Phys. Rev. Lett. **61**, 1819 (1988).
10. F. Abe *et al.*, Phys. Rev. Lett. **76**, 2015 (1996).
11. F. Abe *et al.*, Phys. Rev. D **58**, 072001 (1998).
12. Z. Koba, H. B. Nielsen, and P. Oleson, Nucl. Phys. B **40**, 317 (1972).
13. R. E. Ansorge *et al.* (UA5 Collab.), Z. Phys. C **43**, 357 (1989); K. Alpgard *et al.*, Phys. Lett. B **121B**, 209 (1983).
14. T. Alexopoulos *et al.* (E735 Collab.), Phys. Lett. B **336**, 599 (1994); Phys. Rev. Lett. **60**, 1622 (1988); N. Moggi, Nucl. Phys. B (Proc. Suppl.) **71**, 221 (1999).
15. G. Arnison *et al.* (UA1 Collab.), Phys. Lett. B **118B**, 167 (1982).
16. A. Breakstone *et al.*, Phys. Lett. B **132B**, 463 (1983); **183**, 227 (1987); Z. Phys. C **33**, 333 (1987).
17. T. Alexopoulos *et al.* (E735 Collab.), Phys. Rev. D **48**, 984 (1993); Nucl. Phys. B (Proc. Suppl.) **25**, 40 (1992).
18. S. Barshay, Phys. Lett. B **127B**, 129 (1983).
19. L. Van Hove, Phys. Lett. B **118B**, 138 (1982); R. Hagedorn, Riv. Nuovo Cimento **6**, 10 (1983); J. D. Bjorken, Phys. Rev. D **27**, 140 (1983).
20. X. Wang and C. Hwa, Phys. Rev. D **39**, 187 (1989); M. Jacob, Preprint TH 3515, CERN (1983); F. W. Bopp, Phys. Rev. D **33**, 1867 (1986).
21. T. Sjöstrand, Comput. Phys. Commun. **82**, 74 (1994); G. Marchesini, B. R. Webber, G. Abbiendi, *et al.*, Comput. Phys. Commun. **67**, 465 (1992).
22. K. Braune *et al.*, Phys. Lett. B **123B**, 467 (1983).
23. H. Appelshäuser, Phys. Lett. B **459**, 679 (1999).
24. M. L. Cherry *et al.*, Acta Phys. Pol. B **29**, 2129 (1998).
25. M. Gaździcki, Eur. Phys. J. C **6**, 365 (1999), and references therein.
26. F. Liu, Eur. Phys. J. C **8**, 649 (1999).
27. T. A. Trainor, Nucl. Phys. B (Proc. Suppl.) **92**, 16 (2001); H. C. Eggers and K. Fialkowski, in *Proceedings of the ISMD 2000, Tihany, Ungary, 2000*.

Physics of Atomic Nuclei, Vol. 67, No. 1, 2004, pp. 140–144. From Yadernaya Fizika, Vol. 67, No. 1, 2004, pp. 138–142.

Law of Large Numbers and Asymptotic Behavior of Phase-Space Integral*

J. Manjavidze[1)], A. N. Sissakian[2)], and N. Shubitidze[1)***]**

Received June 11, 2003

Abstract—The law of large numbers is used for estimation of the longitudinal phase-space integral for big values of particle numbers. A fully completed analytic expression of the phase-space integral is obtained.

We propose a new method for estimating the phase-space integral at $n \to n_{\max} = \sqrt{s}/m$:

$$Z_n = \int \left\{ \prod_{i=1}^{n} \frac{d^3 k_i}{2\sqrt{k_i^2 + m^2}} \right\} \times \delta^4 \left(P - \sum k_i \right) f_n(k_1, \ldots, k_n), \quad (1)$$

where f_n is the amplitude module squire and $P \equiv (E, 0, 0, 0)$ is the total momentum. We work in the center-of-mass (CM) system. The integrals of such a type arise when the topological cross sections are calculated. We will examine the simplest case when f_n looks as follows:

$$f_n(k_1, \ldots, k_n) = \prod_{i=1}^{n} \exp\left(-r_0^2 k_{t,i}^2\right), \quad (2)$$

where $k_{t,i}$ is the transverse momentum of the ith particle and r_0 is the phenomenological transverse radius. This choice means the assumption that the secondaries are produced independently of each other. The transverse momentum cutoff is compatible with the present experimental data. Attempts to calculate the integrals (1) have a long history [1–10]. With the factorized amplitude (2), the dominant problem descended from the energy–momentum conservation δ function in (1). In order to avoid this difficulty, Kajantie and Karimaki [1] introduce the Fourier transformation for the δ function and use a saddle point method for calculating the Fourier transform. Lurcat and Mazur [2] use the Laplace transformation for the integrand, normalize it, and then interpret it as a frequency function. The latter was approximated by the Edgeworth series, retaining only the first few terms. An analogous technique with small modifications for a special case of f_n was used by Krzywicki as well as Bilash [3–5]. A number of attempts use the Monte Carlo (MC) method [8–10]. It is necessary to emphasize that all the aforementioned approaches present an algorithm of numerical calculations.

The basis of our method consists in the expansion of (1) in terms of universally independent functions. Then we will use the law of large numbers for their estimation. In this way, we find for (1) a completely analytic expression. It is important to build a fast generator of events if $n \to n_{\max} \gg 1$.

The produced particles have small momenta at $n \to n_{\max}$. One can neglect the motion of the CM frame in this limit. For this reason, we neglect the δ function for the law of conservation of momentum:

$$\delta^4 \left(P - \sum_{i=1}^{n} k_i \right) \to \delta \left(E - \sum_{i=1}^{n} \sqrt{k_i^2 + m^2} \right). \quad (3)$$

Performing integration over spherical angles, we come to the expression

$$Z_n(E) = (\pi/2)^n \times \int \left\{ \prod_{i=1}^{n} \frac{d(k_{t,i}^2) dk_z}{\sqrt{k_{t,i}^2 + k_{z,i}^2 + m^2}} e^{-r_0^2 k_{t,i}^2} \right\} \times \delta \left(E - \sum_{i=1}^{n} \sqrt{k_{t,i}^2 + k_{z,i}^2 + m^2} \right), \quad (4)$$

*This article was submitted by the authors in English.

[1)]Institute of Physics, Georgian Academy of Sciences, Tbilisi, Georgia, and Joint Institute for Nuclear Research, Dubna, Moscow oblast, 141980 Russia.

[2)]Joint Institute for Nuclear Research, Dubna, Moscow oblast, 141980 Russia; e-mail: sisakian@jinr.ru

**e-mail: joseph@nusun.jinr.ru

***e-mail: shubi@nusun.jinr.ru

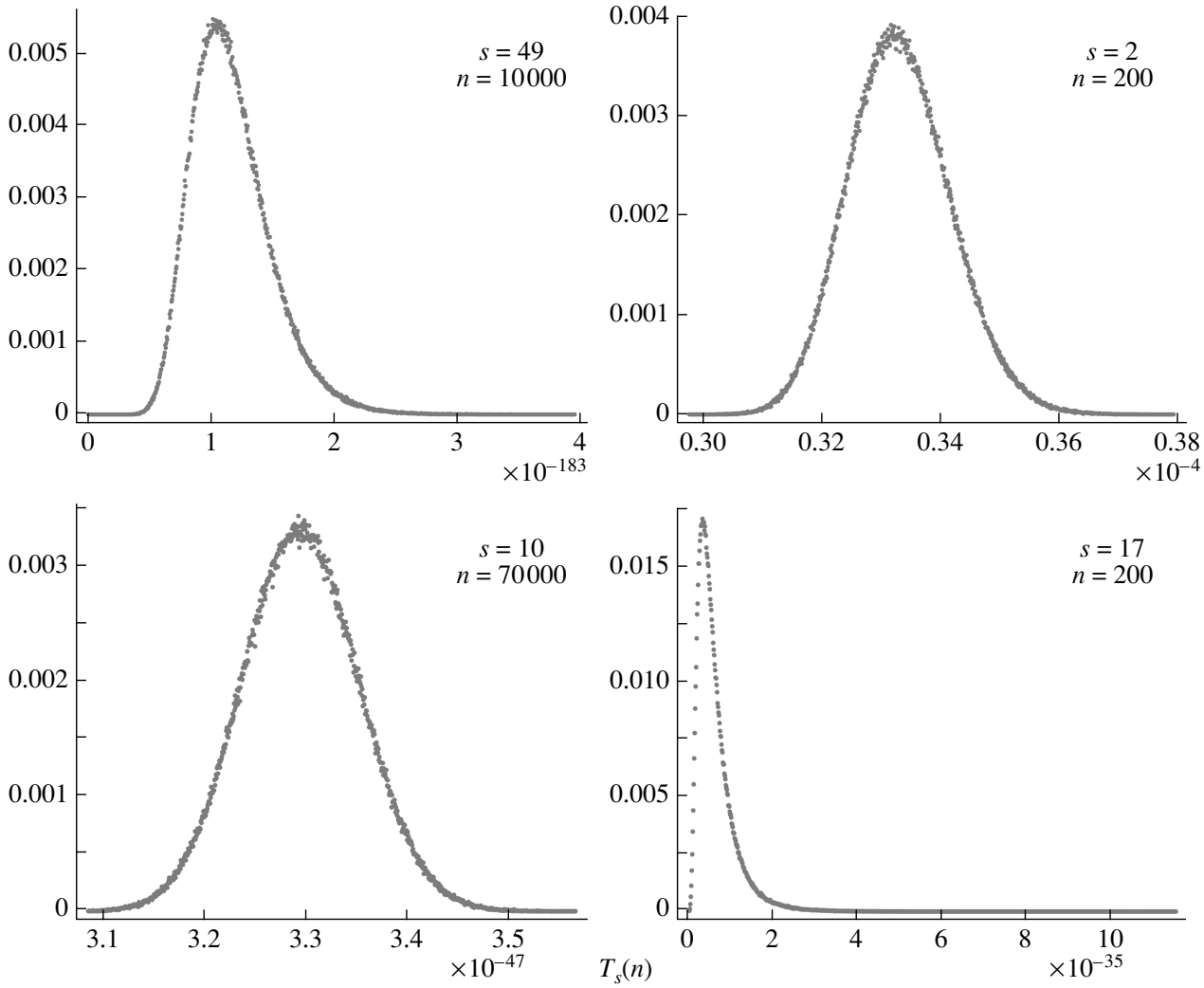

Fig. 1. Examples of statistical distribution of $T_s(n)$ functions.

where $k_{z,i}$ is the longitudinal and $k_{t,i}$ is the transverse momentum. Then we introduce the particle energy as the independent variable. As a result,

$$Z_n(E) = (\pi/r_0)^n [m(n_{\max} - n)]^{n-1} \times \left\{ \prod_{i=1}^{n} \int_0^1 dy_i F\left(r_0 m \sqrt{(n_{\max} - n) y_i ((n_{\max} - n) y_i + 2)} \right) \right\} \delta\left(1 - \sum y_i\right), \quad (5)$$

where $F(x)$ is the Dawson integral:

$$F(x) = e^{-x^2} \int_0^x e^{t^2} dt. \quad (6)$$

The Dawson integral can be presented in the following form:

$$F\left(r_0 m \sqrt{(n_{\max} - n) y ((n_{\max} - n) y + 2)} \right) = \sqrt{y} \exp\{a_0 + a_1 y + a_2 y^2 + \ldots\}, \quad (7)$$

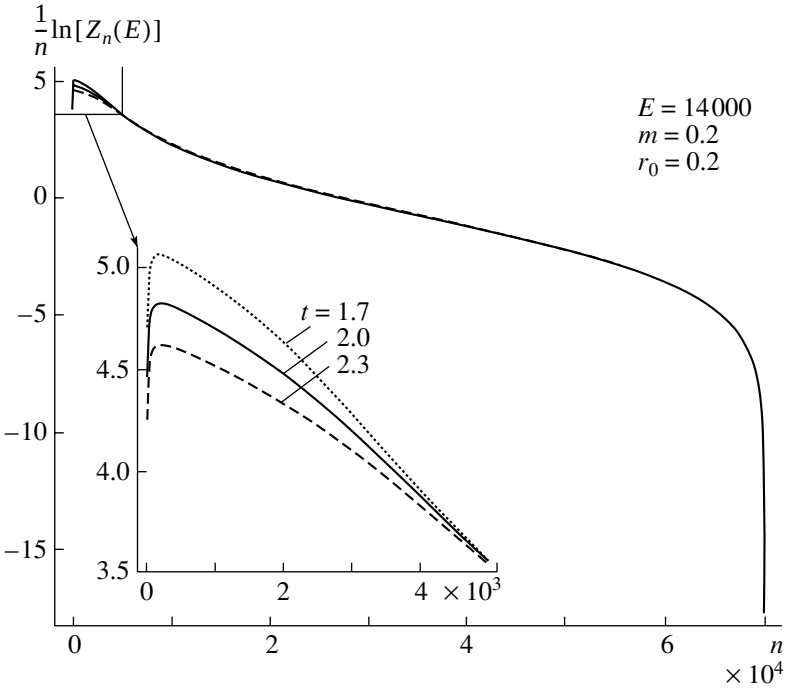

Fig. 2. Graphs of $(1/n)\ln[Z_n(E)]$ for various values of parameter t.

where the coefficients

$$a_s = \frac{1}{2\pi i}\int\limits_C d\zeta\zeta^{-s-1}\ln\left\{F\left(r_0 m\sqrt{(n_{\max}-n)\zeta((n_{\max}-n)\zeta+2)}\right)/\sqrt{\zeta}\right\}. \quad (8)$$

After the substitution of (7) into (5) we obtain

$$Z_n(E) = (\pi/r_0)^n[m(n_{\max}-n)]^{n-1} \quad (9)$$
$$\times\left\{\prod_{i=1}^{n}\int\limits_0^1 dy_i\sqrt{y_i}\right\}\delta\left(1-\sum y_i\right)$$
$$\times\exp\{n[a_0+a_1T_1(n)+a_2T_2(n)+\ldots]\},$$

where $T_s(n)$ is

$$T_s(n) = \frac{1}{n}\sum_{i=1}^{n} y_i^s. \quad (10)$$

Since we plan to calculate the integral (9) by the MC method, it is reasonable to investigate the statistical distributions of functions (10) with the constraint $\sum y_i = 1$. The calculations were performed for different values of s and n. As can be seen from Fig. 1, for relatively small values of s, the distribution tends to the normal type, but for relatively big values of s, the distribution tends to the Poissonian type.

We cannot find the exact expression for the distribution law of functions (10). Nevertheless, we can find an acceptable approximation for extremum points of the distribution of functions $T_s(n)$:

$$\frac{1}{s+1}\left(\frac{2}{n}\right)^s. \quad (11)$$

We also find the limits of the area where the most significant values of $T_s(n)$ are grouped:

$$\left(\frac{1}{s+1}\left(\frac{1.7}{n}\right)^s, \frac{1}{s+1}\left(\frac{2.3}{n}\right)^s\right). \quad (12)$$

Let us imagine that we calculate our integral (9) by the MC method. At every step, we must randomly select a group of nonnegative numbers $y_1, y_2, \ldots, y_n$ with the constraint $\sum y_i = 1$. Then one must substitute these numbers into (9). As a result, the maximal number of items would have the value of $T_s(n)$ coinciding with expression (11). Consequently, if we neglect small contributions, then one may change functions $T_s(n)$ in (9) by the corresponding value (11) and carry out the exponent from the integral (9).

After this procedure, the remaining integral has the form

$$\left\{\prod_{i=1}^{n}\int\limits_0^1 dy_i\sqrt{y_i}\right\}\delta\left(1-\sum_{i=1}^{n} y_i\right). \quad (13)$$

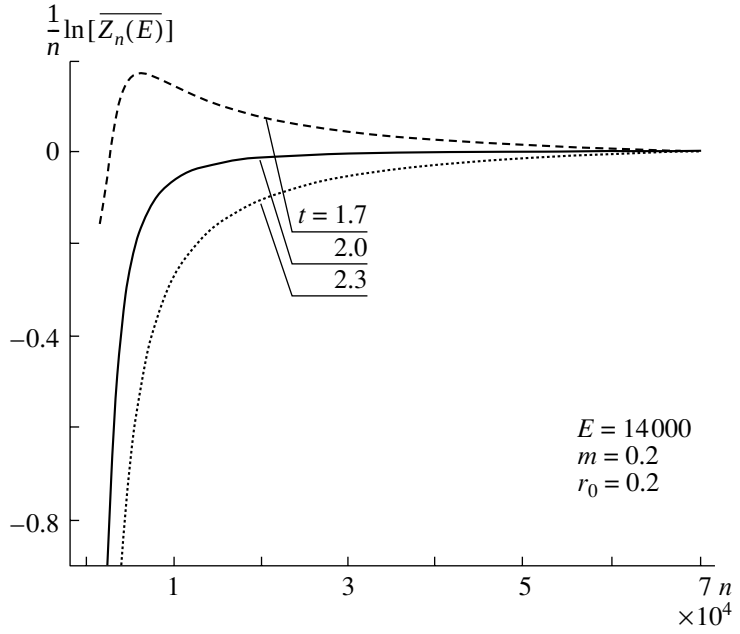

Fig. 3. Graphs of $(1/n)\ln[\overline{Z_n(E)}]$ for various values of parameter t.

It is easily calculable if the hyperspherical coordinates

$$\begin{aligned} y_1 &= \rho\cos^2(\varphi_{n-1})\ldots\cos^2(\varphi_2)\cos^2(\varphi_1), \\ y_2 &= \rho\cos^2(\varphi_{n-1})\ldots\cos^2(\varphi_2)\sin^2(\varphi_1), \\ &\vdots \\ y_{n-1} &= \rho\cos^2(\varphi_{n-1})\sin^2(\varphi_{n-2}), \\ y_n &= \rho\sin^2(\varphi_{n-1}) \end{aligned} \tag{14}$$

are introduced. As a result,

$$\left\{\prod_{i=1}^{n}\int_0^1 dy_i\sqrt{y_i}\right\}\delta\left(1-\sum_{i=1}^{n}y_i\right) \tag{15}$$

$$= \frac{(\Gamma(3/2))^{n-1}}{\Gamma(3n/2)}.$$

The final expression has the form

$$Z_n(E) = \frac{\pi^{(3n-1)/2}}{r_0\Gamma(3n/2)}\left[\frac{m(n_{\max}-n)}{2r_0}\right]^{n-1}e^{nW(2)}, \tag{16}$$

where

$$W(t) = \frac{n}{t}\int_0^{t/n}\ln\left[\frac{1}{\sqrt{y}}F\left(r_0 m\sqrt{(n_{\max}-n)y((n_{\max}-n)y+2)}\right)\right]dy. \tag{17}$$

Figure 2 shows three distributions of $(1/n)\ln[Z_n(E)]$ for various values of parameter t. As is seen from the graph, the differences are significant for small n (<5000). Thus, we find an area of validity of our Eq. (16).

Generalization for another form of f_n (2) is not a complicated procedure.

It is interesting to calculate the limit $r_0 \to 0$:

$$Q_n(E) = \lim_{r_0\to 0} Z_n(E). \tag{18}$$

For this purpose, Eq. (5) was used, and because of the property $\lim\limits_{x\to 0}F(x)/x = 1$, we obtain

$$\begin{aligned} Q_n(E) &= \pi^n m^{2n-1}(n_{\max}-n)^{3(n-1)/2} \\ &\times\left\{\prod_{i=0}^{n}\int_0^1 dy_i\sqrt{y_i((n_{\max}-n)y_i+2)}\right\} \\ &\times\delta\left(1-\sum y_i\right). \end{aligned} \tag{19}$$

Then we expand the square root in (19) into the series

$$\sqrt{y_i((n_{\max}-n)y_i+2)} = \exp\left\{\sum_{j=0}^{\infty} a_j y_j\right\}, \quad (20)$$

where

$$a_0 = \frac{1}{2}\ln 2, \quad a_j = (-1)^{j+1}\frac{1}{2j}\left(\frac{y}{2}\right)^j. \quad (21)$$

Using an analogous method, we obtain the following expressions for the "normalized" phase-space integral $\overline{Z_n(E)}$:

$$\overline{Z_n(E)} = Z_n(E)/Q_n(E) \quad (22)$$
$$= \left\{\frac{1}{r_0 m\sqrt{2(n_{\max}-n)}}\exp(W(2)-U(2))\right\}^n,$$

where

$$U(t) = \frac{1}{2}\left[\frac{(2-t)}{4}\frac{(n_{\max}-n)}{n}\right. \quad (23)$$
$$\left. + \left(1+\frac{2n}{t(n_{\max}-n)}\right)\ln\left(1+\frac{(n_{\max}-n)t}{2n}\right)-1\right].$$

In Fig. 3, you can see the behavior of $\overline{Z_n(E)}$ for various values of the parameter t.

The method for estimating the phase-space integral using the law of large numbers allows one to obtain an analytic expression. It is very significant when we build a fast event generator.

As would be expected, the dependence on the cutting parameter r_0 vanishes at the asymptotic on multiplicity $n \to n_{\max}$, but it is significant in the case where n has a finite value.

ACKNOWLEDGMENTS

We wish to express our appreciation to Dr. M. Mania from the Tbilisi Institute of Mathematics for many helpful discussions.

REFERENCES

1. K. Kajantie and V. Karimaki, Comput. Phys. Commun. **2**, 207 (1971).
2. F. Lurcat and P. Mazur, Nuovo Cimento **31**, 140 (1964).
3. A. Krzywicki, Nuovo Cimento **32**, 1067 (1964).
4. A. Krzywicki, J. Math. Phys. **6**, 485 (1965).
5. A. Bialas and T. Ruijgrok, Nuovo Cimento **39**, 1061 (1965).
6. E. H. de Groot, Nucl. Phys. B **48**, 295 (1972).
7. P. Pirala and E. Byckling, Comput. Phys. Commun. **4**, 117 (1972).
8. R. A. Morrow, Comput. Phys. Commun. **13**, 399 (1978).
9. R. Kleiss and W. J. Stirling, Comput. Phys. Commun. **40**, 359 (1986).
10. M. M. Block, Comput. Phys. Commun. **69**, 459 (1992).

Physics of Atomic Nuclei, Vol. 67, No. 1, 2004, pp. 145–155. From Yadernaya Fizika, Vol. 67, No. 1, 2004, pp. 143–152.

VERY HIGH MULTIPLICITY PHYSICS

Prospects of Experimental Measurements at LHC to Better Understand Cosmic Ray Induced Air Showers*

S. Tapprogge**

Helsinki Institute of Physics, Finland; c/o CERN, Geneva, Switzerland

Received May 28, 2003

Abstract—In a few years, the LHC will provide proton–proton and nucleus–nucleus collisions at the highest c.m. energies available so far in the laboratory, up to 14 TeV in the case of proton–proton collisions. This regime corresponds to energies of cosmic rays of about 10^{17} eV, above the so-called "knee region" in the cosmic-ray flux. A summary of main features of the machine will be presented, concentrating on the various running scenarios foreseen. An overview of the approved experiments and their baseline coverage, as well as possibilities for extensions, will be given. The latter could provide a better coverage of the forward region (small angles with respect to the beam direction) and might give valuable information to help in our understanding of extended air showers induced by cosmic rays in the atmosphere of the Earth.

1. INTRODUCTION

The LHC is designed to be a discovery machine, providing proton–proton collisions at the highest c.m. energy with a very large luminosity. Among the primary goals is the understanding of the origin of electroweak symmetry breaking, which could manifest itself in the observation of one (or more) Higgs boson(s). The LHC will also vastly extend the potential for discovery of new physics beyond the Standard Model, extending the mass scale up to several TeV for direct observations. In addition, the experiments are designed with the goal of performing precision measurements within the Standard Model (and of new processes as well—if found).

Due to its capability of colliding various beam species, the LHC will offer a unique possibility of studying strong interaction properties at the (future) energy frontier and probe further quantum chromodynamics (QCD) as the fundamental theory of strong interaction. These data are of importance (especially for *pp* collisions) to properly understand background processes for searches and precision measurements. They could also help in the understanding and interpretation of cosmic-ray-induced extended air showers, as discussed later in this contribution.

As shown in Fig. 1, *pp* collisions show the highest multiplicities in the central region ($|\eta| < 5$).[1)] However, the largest energies are found in the forward region (corresponding to very small scattering angles with respect to the beam direction; e.g., $|\eta| > 5$ implies $\theta < 10$ mrad). As will be shown later, it is this region that is of most interest and at the same time the most challenging for experimental instrumentation. It is worth noting that a c.m. energy of $\sqrt{s} = 14$ TeV for *pp* collisions corresponds to an incident proton energy of about 10^{17} eV in the laboratory frame.

The following section describes the layout and parameters of the LHC, including a discussion of the running scenarios presently foreseen. This is followed by a brief description of the five experiments,

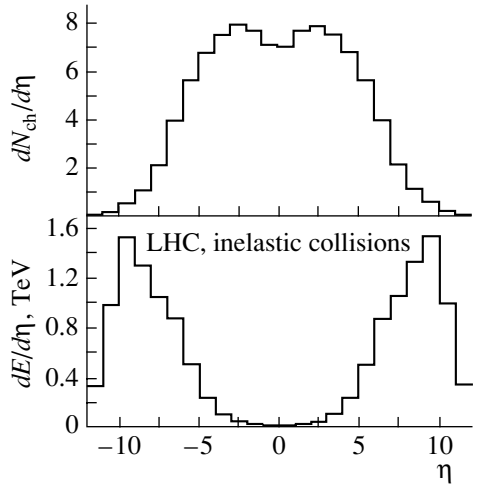

Fig. 1. Particle production in *pp* collisions at $\sqrt{s} =$ 14 TeV.

*This article was submitted by the author in English.

**e-mail: Stefan.Tapprogge@cern.ch

1)Pseudorapidity $\eta = -\log\tan(\theta/2)$, which for massless particles coincides with the rapidity $y = 0.5\log[(E + p_z)/(E - p_z)]$.

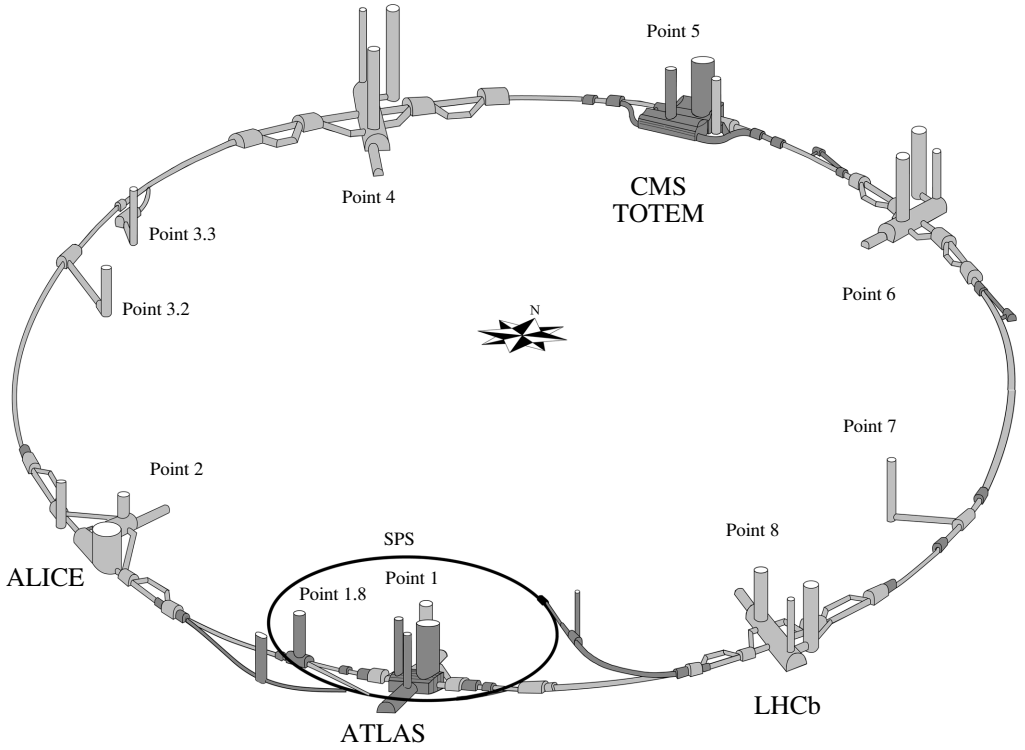

Fig. 2. Layout of the LHC, showing the underground caverns of the four interaction regions.

summarizing the baseline coverage. Next, a list of possible and important measurements at the LHC in the context of cosmic-ray-induced air showers is presented, followed by a discussion of instrumental aspects for extending the baseline coverage.

2. LHC MACHINE AND RUNNING SCENARIOS

The LHC (see Fig. 2) will be installed in the former LEP tunnel, which is located as far as 100 m below the surface and has a circumference of about 27 km. It will consist of two rings, where the beams can be brought into collision at four interaction points. In order to reach a c.m. energy of $\sqrt{s} = 14$ TeV for pp, more than 1200 superconducting dipole magnets with a nominal field strength of 8.3 T are needed to bend the protons. The design luminosity will be $\mathcal{L} = 10^{34}$ cm^{-2} s^{-1}, to be reached by filling the machine with 2835 bunches, each containing about 10^{11} protons. The separation between two bunch crossings will be 25 ns. It is feasible to run the machine at lower values of $\sqrt{s}$, down to about 2 TeV, and thus make it possible to obtain overlap with proton–antiproton collisions at Tevatron.

Furthermore, the LHC is designed to provide nucleus–nucleus collisions. In the case of Pb + Pb collisions, a c.m. energy of 1148 TeV (corresponding to an energy of 2.75 TeV per nucleon) can be reached at a luminosity of $\mathcal{L} = 10^{27}$ cm^{-2} s^{-1}. Collisions of lighter ions are possible as well, e.g., of Sn, Kr, Ar, and O. In addition, the LHC can operated in pA mode, colliding protons on nuclei. In this case, the c.m. system of the collision will not be at rest in the laboratory frame, but shifted by up to one unit in rapidity. Luminosities foreseen for pA collisions should range from $\mathcal{L} = 7.4 \times 10^{29}$ cm^{-2} s^{-1} for pPb up to $\mathcal{L} = 1.0 \times 10^{31}$ cm^{-2} s^{-1} for pO collisions.

Most of the time, the LHC is expected to be operated in pp mode. Approximately one month per year should be devoted to the studies of nucleus–nucleus and proton–nucleus collisions. Furthermore, shorter dedicated runs with special conditions should take place, e.g., for TOTEM to perform a precise measurement of the total cross section.

3. LHC EXPERIMENTS

Two big underground caverns (at interaction points 1 and 5) have been excavated for two general purpose experiments, ATLAS and CMS, which are optimized for high-p_T physics. The ALICE experiment will be situated at interaction point 2, dedicated to the study of heavy-ion collisions. Point 8 will be taken by LHCb, aiming at the study of b-hadron physics. Furthermore, the TOTEM experiment (to be installed at point 5) will measure the total cross section in pp collisions.

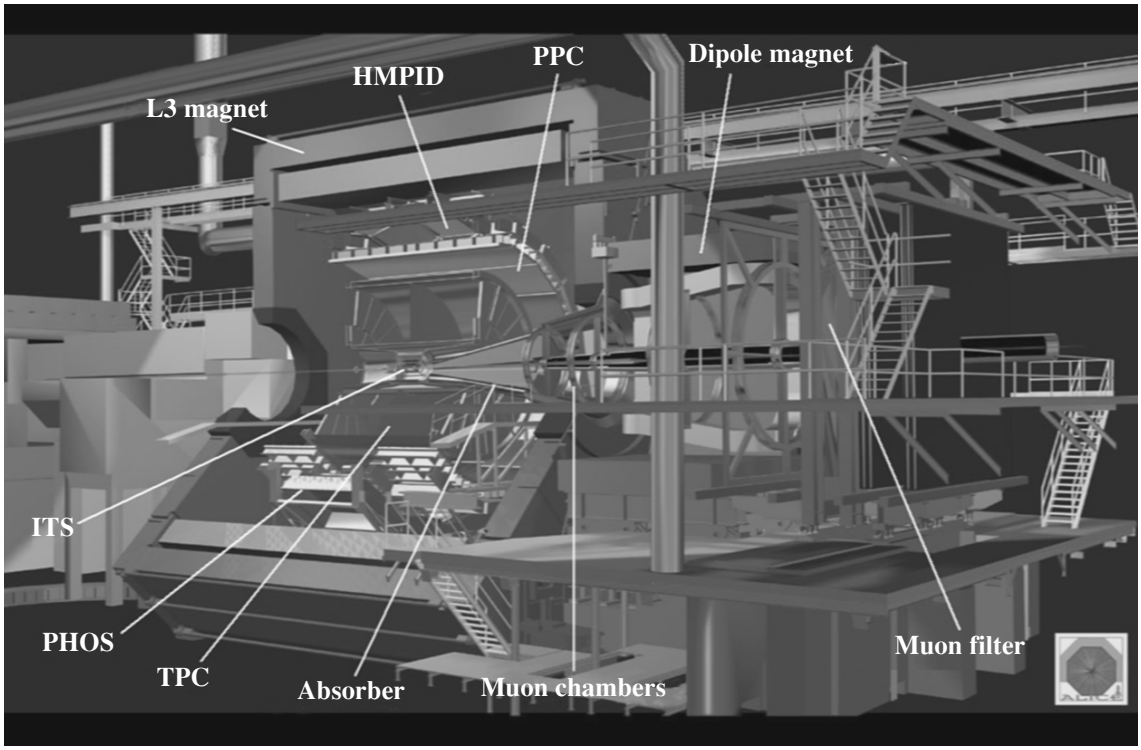

Fig. 3. The ALICE detector.

For most experiments, the design phase has been finished and the mass production of their components (especially in the case of ATLAS and CMS) is well under way, in some cases even close to completion. In the following, a brief overview of the main features of each experiment is given.

3.1. ALICE

The ALICE [1] detector, as shown in Fig. 3, will reuse the magnet of the L3 experiment. The central element of ALICE will be a huge time projection chamber (TPC), allowing precise tracking in the high-multiplicity environment of central heavy-ion collisions. Its coverage will be $|\eta| < 1$. Inside the magnet, further components are foreseen for photon detection, for electron–positron pair detection, and for multiplicity measurements (the latter using Si detectors covering the region of $-5.4 < \eta < 3.0$), as well as for particle identification (via time-of-flight and transition radiation).

Outside of the magnet, a dedicated muon spectrometer ($2.4 < \eta < 4.0$) with a separate dipole magnet is situated on one side of the experiment. ALICE will also have detectors in the machine tunnel: a zero-degree calorimeter to measure, e.g., the centrality of the heavy-ion collision.

3.2. ATLAS

ATLAS [2] is a general purpose experiment, shown in Fig. 4, optimized for high-p_T physics. Surrounding the interaction point, several tracking detectors will measure charged particles and reconstruct (primary and secondary) vertices. Closest to the beam, three layers of Si pixel sensors will be placed, followed by four layers of Si strip detectors. Further out, there will be a straw tube tracker (TRT), which can detect transition radiation to identify electrons. All these components are situated inside a solenoid magnet with a field of 2 T. The tracking detectors (inner detector) cover the region up to $|\eta| < 2.5$ and are surrounded by calorimetry, extending up to $|\eta| < 4.9$. In the barrel region, a fine-grained liquid argon (LAr) accordion calorimeter is foreseen as the electromagnetic part, followed by a tile scintillator calorimeter as the hadronic compartment. In the endcap and forward region, LAr technology is used again. Outside of the calorimeters, an open air-core toroid magnet system is situated, interleaved with muon detectors, to provide detection of muons and a stand-alone measurement of their momentum in the region $|\eta| < 2.7$.

The overall size of ATLAS is about 40×22 m and its weight will be about 7000 t. More details on the expected performance of ATLAS can be found in [3].

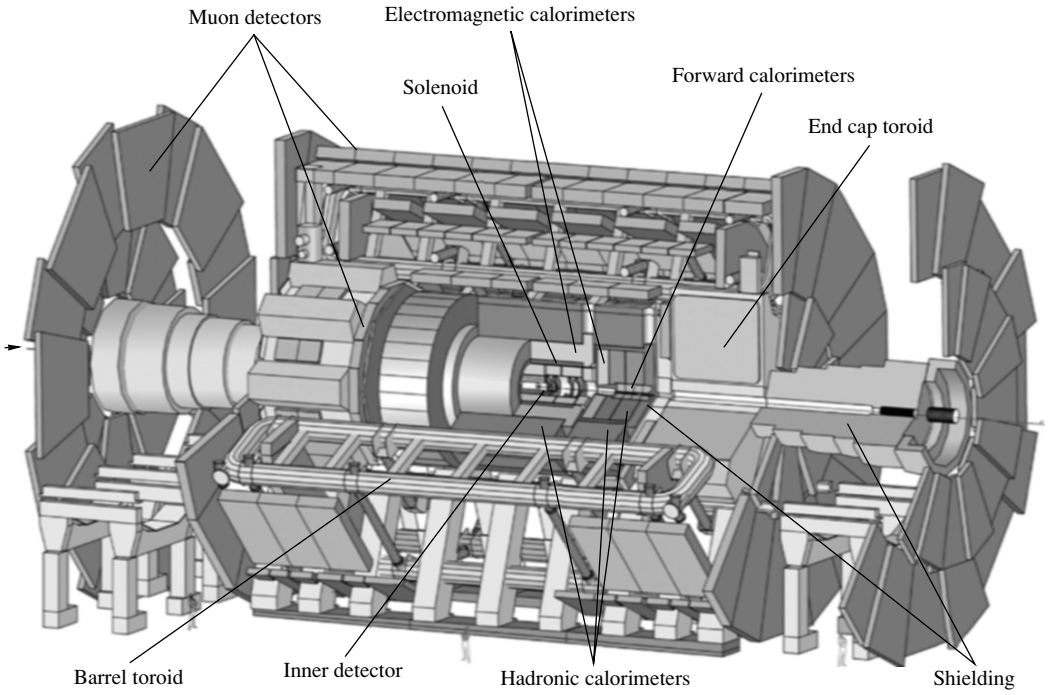

Fig. 4. The ATLAS detector.

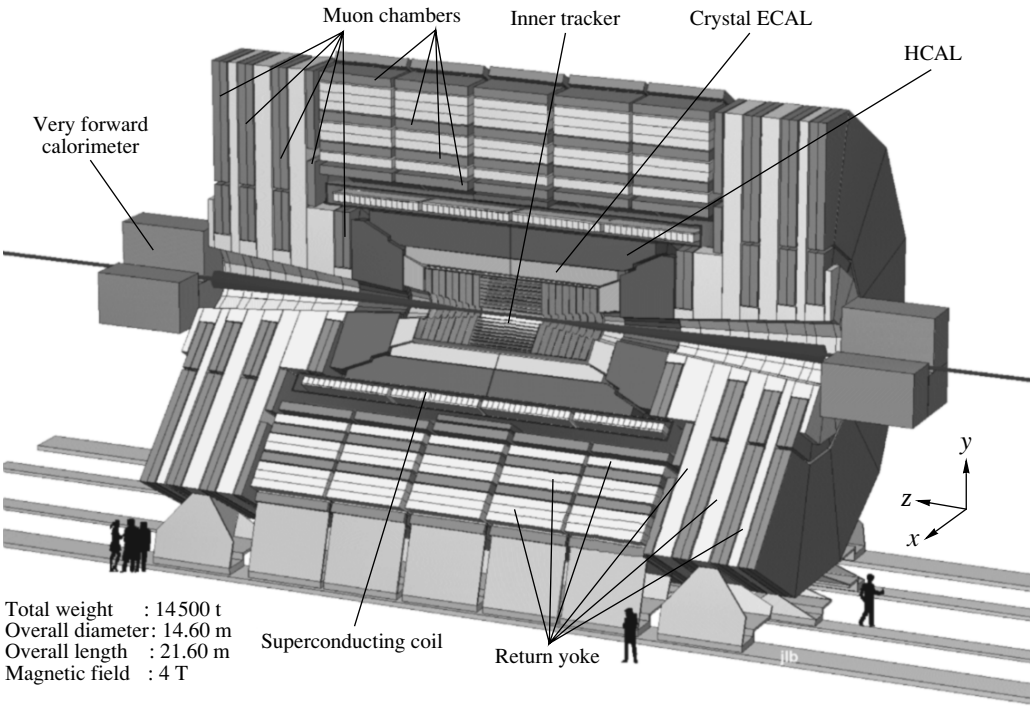

Fig. 5. The CMS detector.

3.3. CMS

CMS [4] is the other general purpose detector and is shown in Fig. 5. As ATLAS, it has been optimized for the detection of high-p_T leptons, photons, and jets (with and without b tagging) and measurement of missing transverse energy. The tracking is based on an all-silicon system, where the interaction point is surrounded with layers of pixel detectors. The remainder of the tracking volume is made of layers of Si

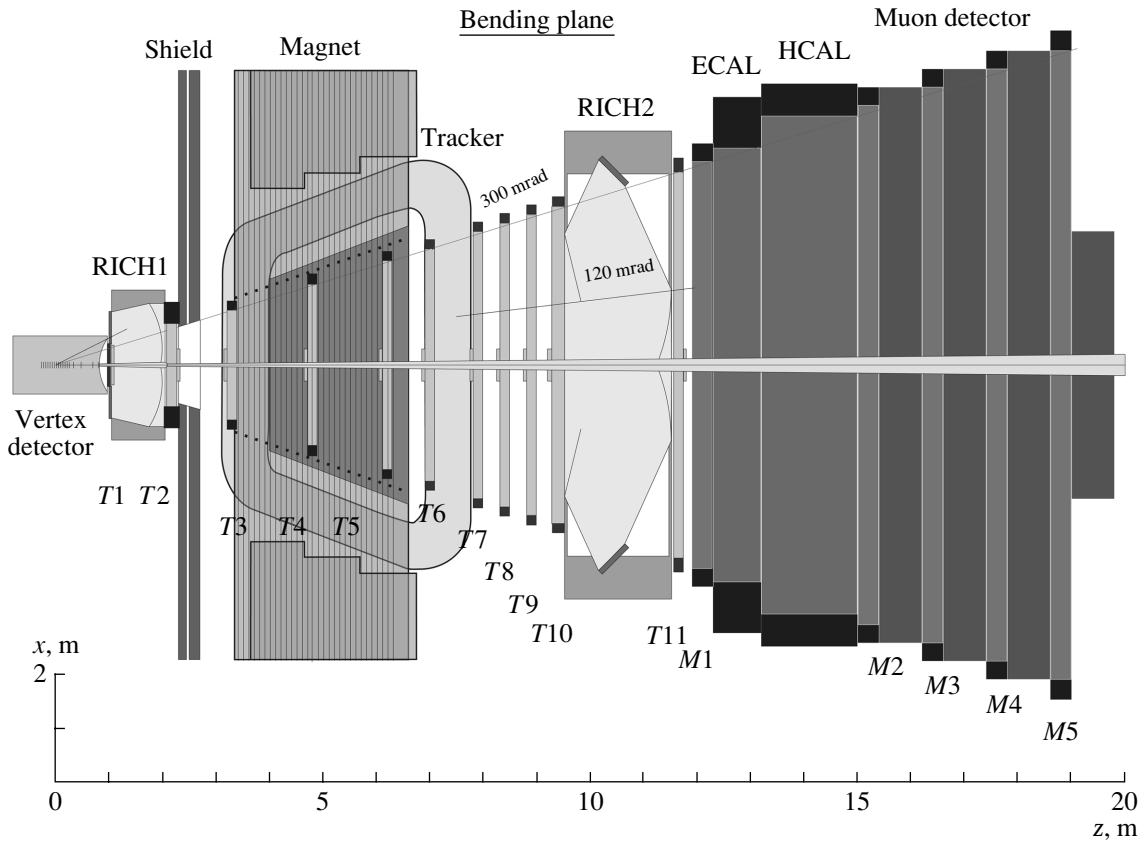

Fig. 6. The LHCb detector.

strip detectors. The tracking coverage extends up to $|\eta| < 2.5$. Surrounding the tracker, a $PbWO_4$ crystal electromagnetic calorimeter is situated, which is followed by a scintillator sandwich hadronic calorimeter. All of these components are located inside a large solenoid magnet, providing a field of 4 T. The calorimetric coverage is extended up to $|\eta| = 5$ by a forward calorimeter, instrumented with quartz fibers. The return yoke is instrumented for muon detection, covering the region $|\eta| < 2.5$.

CMS will have a size of 22×15 m and a weight of about 13 000 t.

3.4. LHCb

The LHCb [5] layout (as shown in Fig. 6) resembles a forward spectrometer, although LHCb will take data from colliding proton bunches. The interaction point will be surrounded by a precise vertex detector, followed by a tracking system, including a dipole magnet. LHCb will have various possibilities for particle identification, including two ring-imaging Čerenkov (RICH) detectors, electromagnetic and hadronic calorimetry, and a muon system. The acceptance region extends over $1.9 < \eta < 4.9$.

3.5. TOTEM

The primary goal of TOTEM is to measure the total cross section via the luminosity-independent method, which requires the simultaneous determination of elastic scattering (under small angles) and of the rate for inelastic interactions.

TOTEM will thus have two types of detectors (as shown in Figs. 7 and 8): firstly, detectors to measure charged particles from inelastic events in the region $3 < |\eta| < 7$, and, secondly, detectors to measure leading protons (e.g., from elastic scattering) at distances of 100–200 m from the interaction point in the machine tunnel (using so-called Roman pots). TOTEM will be installed at interaction point 5, and the inelastic detectors will be located inside the CMS experiment.

3.6. Summary on Phase-Space Coverage

The baseline design of the experiments, as described above, will allow one (although not always in the same experiment) to measure the production of identified particles in the region $-2.5 < \eta < 4.9$, where ATLAS and CMS should be able to reach p_T values of $\mathcal{O}(1\ \text{GeV})$ for the region of $|\eta| < 2.5$. Both ALICE and LHCb will extend this reach down

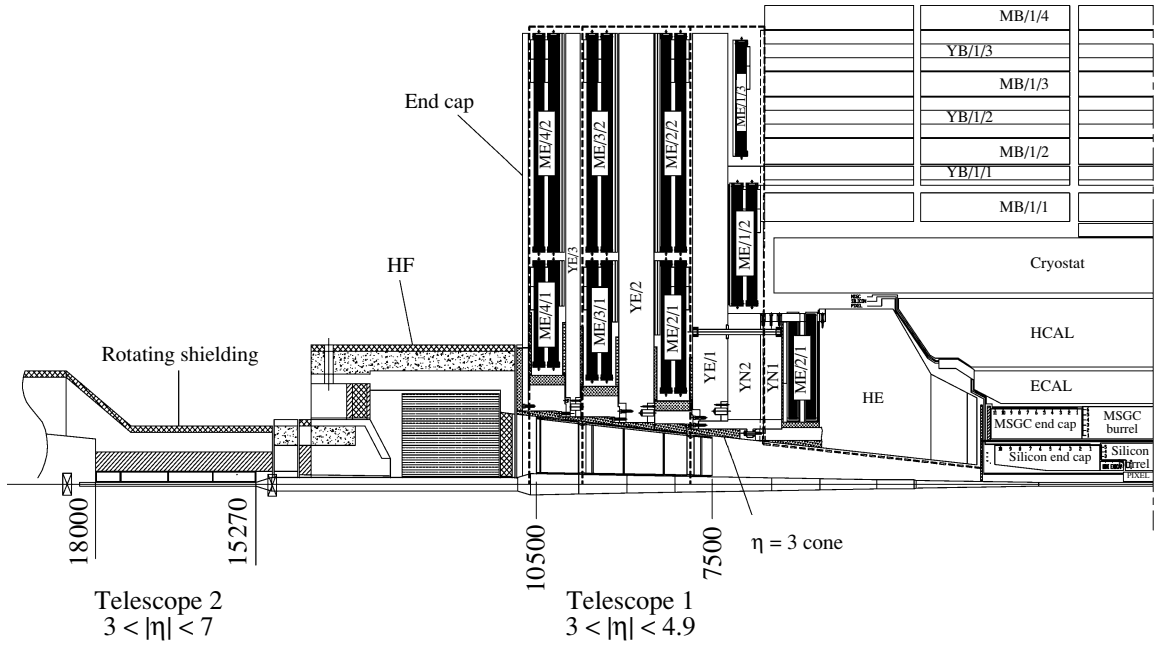

Fig. 7. The TOTEM layout of the two telescopes for measurement of particles from inelastic interactions within the CMS detector.

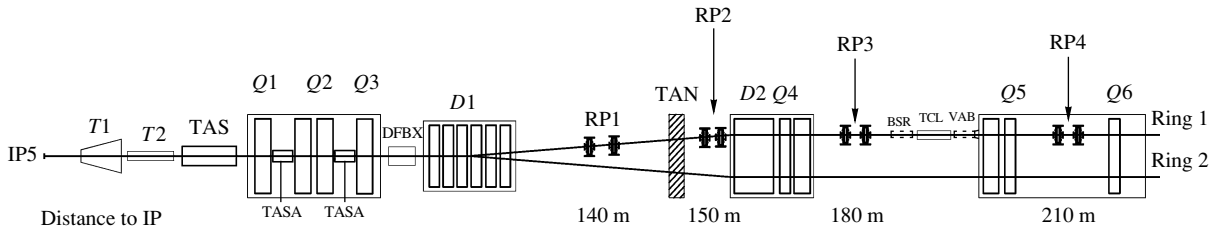

Fig. 8. The TOTEM layout for the leading proton measurements, showing four possible locations (RP1–RP4) for Roman pots.

to $\mathcal{O}(0.1$ GeV), although mostly only in the regions $|\eta| < 1$ (ALICE) and $1.9 < \eta < 4.9$ (LHCb).

Furthermore, the charged multiplicity will be measured by ALICE in the region $-5.4 < \eta < 3$ and by TOTEM in the region $3 < |\eta| < 7$. The energy flow will be covered by ATLAS and CMS for $|\eta| < 5$. ALICE will be able detect leading neutrons and TOTEM will measure (at least during dedicated runs) leading protons as well.

4. COSMIC-RAY-INDUCED AIR SHOWERS AND RELEVANT MEASUREMENTS AT LHC

In Fig. 9, the flux of cosmic rays is shown as observed from extended air showers created in the Earth's atmosphere. The observed spectrum extends in a power-law form over many orders of magnitude, more than 10 in energy and more than 30 in flux, without showing any clear structures. Of very special interest are events seen at the upper end of the spectrum, with energies of more than 10^{19} eV. The LHC will probe the energy region of about 10^{17} eV in pp collisions and about 10^{18} eV in Pb + Pb collisions, extending the reach by up to three orders of magnitude beyond the one of Tevatron. This will provide access to the energy region above the so-called "knee," where the spectrum changes its slope.

It is important to note that the available statistics at LHC will be enormous, in comparison to the observed rate of cosmic rays in this energy regime. For the region of the so-called "ankle" (about 10^{18} eV), only one cosmic-ray event is expected per km^2 per year, whereas at LHC a rate of 1 Hz of accepted events will provide a sample of 10^7 events per year.

The interpretation of the extended air showers observed on the Earth's surface aims at a precise determination of the energy and of the species of the incident particle creating the shower in the atmosphere. Figure 10 shows three examples of air show-

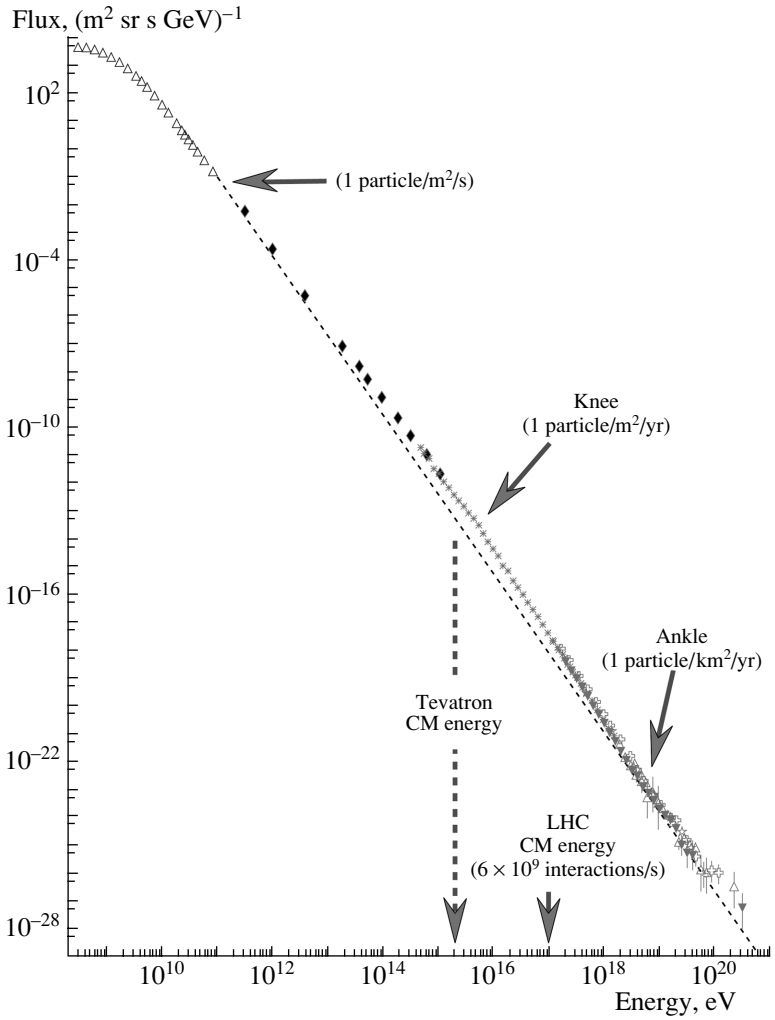

Fig. 9. Cosmic ray flux.

ers, one initiated by a photon, one by a proton, and one by an iron nucleus of the same energy (10^{14} eV). The differences in the shower development and in the composition of the observed particles are visible. The unfolding from the observed particles and their properties needs, however, precise models of hadronic interaction, which in turn rely on extrapolation from existing accelerator measurements. It is expected that the uncertainties will be reduced once the range of extrapolation becomes smaller.

As an example, the upper part of Fig. 11 shows the fractional energy $x_{\mathrm{lab}} = E/E_{\mathrm{lab}}$ of leading hadrons produced in $p\bar{p}$ collisions at a proton energy $E_{\mathrm{lab}} = 10^{17}$ eV. Clearly visible are the differences in the prediction of the four models shown. The lower part of this figure shows the predicted number of charged particles produced in inelastic interactions of protons ($E_{\mathrm{lab}} = 10^{19}$ eV) on a nitrogen nucleus for three models. Again, clear differences are observed, indicating that the existing data do not constrain the hadronic interaction models enough and that further measurements at higher energy are most welcome.

Some of the most important measurements to be performed at the LHC include

measurement of the total pp cross section,

measurement of the fraction of diffractive dissociation to the total cross section,

measurement of the forward (and also central) energy flow,

measurement of event multiplicities in the forward region,

momentum spectrum of leading particles.

Of special importance for these measurements is the forward region, since, e.g., the behavior of the inelastic interactions and the spectrum of leading particles in this region determines the energy transport through the atmosphere and thus strongly influences the air shower development. It is important to point out that present models indicate that measurements

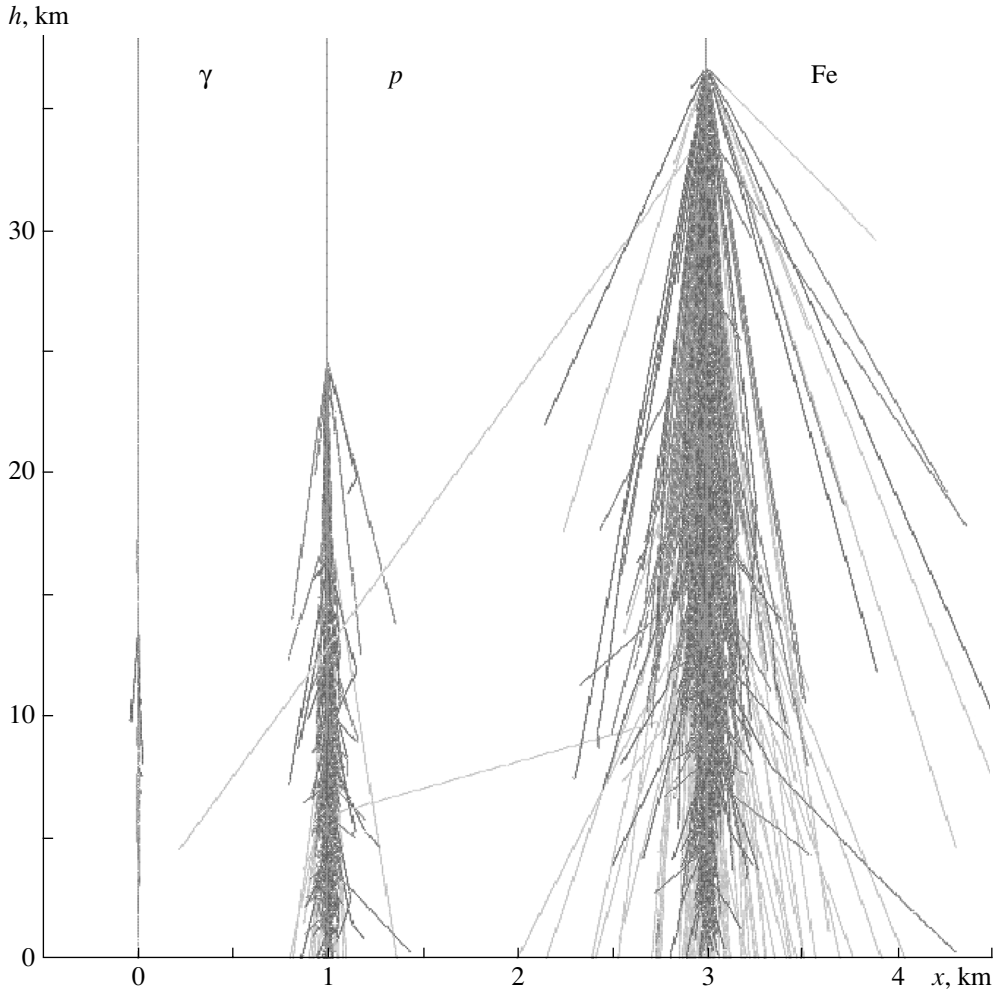

Fig. 10. Examples of air showers at an energy of $E = 10^{14}$ eV, induced by a photon, by a proton, and by an iron nucleus.

of only the central region (for properties such as energy flow and multiplicities of inelastic events) are not sufficient, as the models do not predict a consistent behavior between changes in the central region and the forward region. For a more detailed discussion of relevant measurements and their importance, see [6, 7].

5. INSTRUMENTAL ASPECTS

Although two types of possible extensions in the detector coverage can be distinguished, i.e., the measurement of leading particles and the detection and measurement of particles produced under small angles in inelastic interactions, several aspects regarding instrumentation details will be similar, as in both cases a detection close to the beam (pipe) is required. The measurement of leading particles has to occur at large distances from the interaction point, as these particles are either scattered under very small angles or lose only a small fraction of their momentum and thus leave the beam envelope only far away from their production point. An increase in the acceptance for particles from inelastic events has to happen mostly within the experimental caverns (before the first magnetic elements of the accelerator) and thus needs to be done very close to the beam, in order to have access to small scattering angles.

5.1. Leading Particle Measurements

The measurement of elastic scattering down to very small values of the momentum transfer $-t$ (which is necessary for a precise determination of the total cross section, as discussed in [8]) requires a special optics setup of the machine, where the beams are no longer strongly focused at the interaction point (to obtain the highest luminosity). The layout of the interaction regions 1 and 5 allows for instrumentation to be installed at distances of about 150 and 210 m from the interaction point (see Fig. 8). For this special optics setup, elastic scattering should be measurable

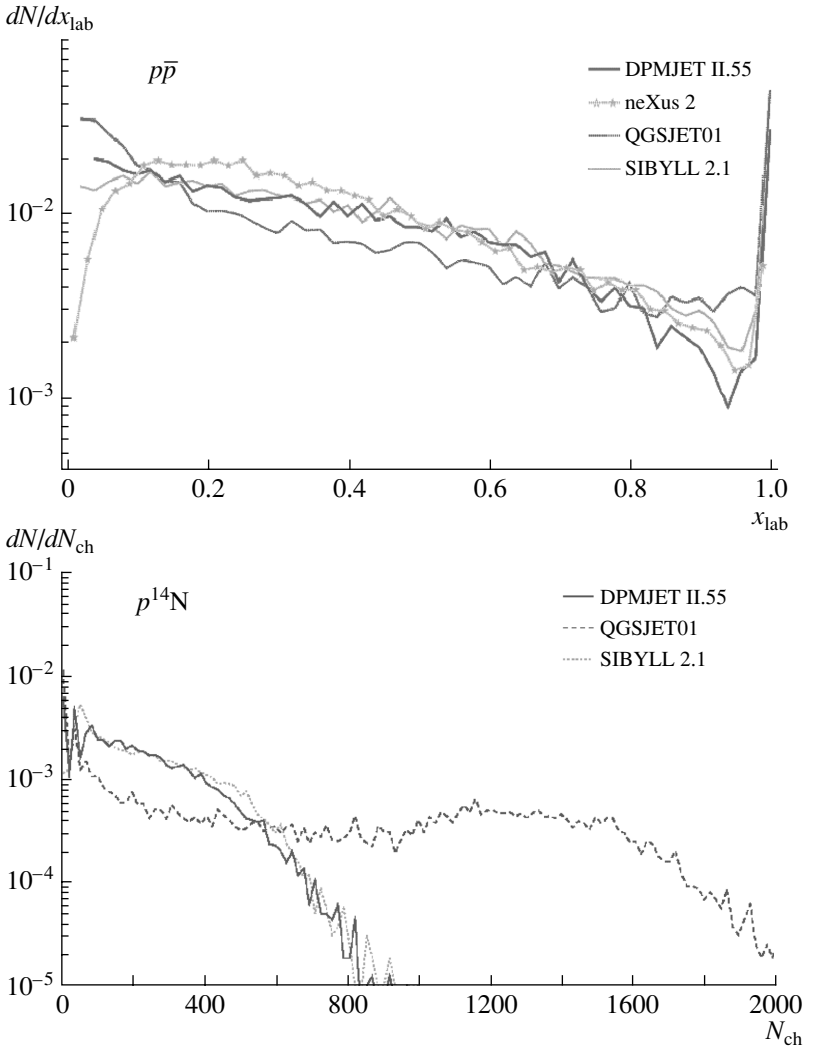

Fig. 11. Predictions of various models for properties of $p\bar{p}$ interactions at $E = 10^{17}$ eV (upper plot: distribution in the fractional energy $x_{\rm lab}$ of the leading hadron) and of $p^{14}N$ interactions at $E = 10^{19}$ eV (lower plot: charged particle multiplicity).

down to values of at least $-t \approx 10^{-2}$ GeV^2. In addition, the instrumentation in this region would give coverage for diffractively scattered protons with a momentum loss of about 2% or more. In order to reach smaller values of the momentum loss, one would have to go to distances of about 400 m, where presently no warm space for instrumentation is foreseen. The upper limit in momentum loss is—for a given location—determined by the apertures of the beam pipe and the machine element between the interaction point and the location of the Roman pot. For the positions mentioned above, momentum losses of up to about 20% should be detectable.

The detection of leading neutrons can be performed in a so-called "zero-degree" calorimeter, which would be installed after the beams are separated (to match to the two-beam pipe structure in the arcs of LHC). ALICE foresees having such a device, as mentioned above. For ATLAS and CMS, there are ongoing studies investigating the possibility of instrumenting an absorber (TAN) at a distance of about 140 m from the interaction point.

5.2. Inelastic Event Measurements

Besides the measurement of charged multiplicity, where the combination of all experiments should cover up to $|\eta| < 7$, an extended coverage for the measurement of the energy flow (up to $|\eta| < 8$) could be achieved by installing additional calorimeters inside the experimental cavern, e.g., of CMS. This would be done close to the beam pipe at a distance of about 18 m from the interaction point (or maybe by instrumenting the TAS absorber, which is situated at the transition between the experimental caverns of ATLAS or CMS and the machine tunnel). The availability of both a calorimeter and tracking detectors in

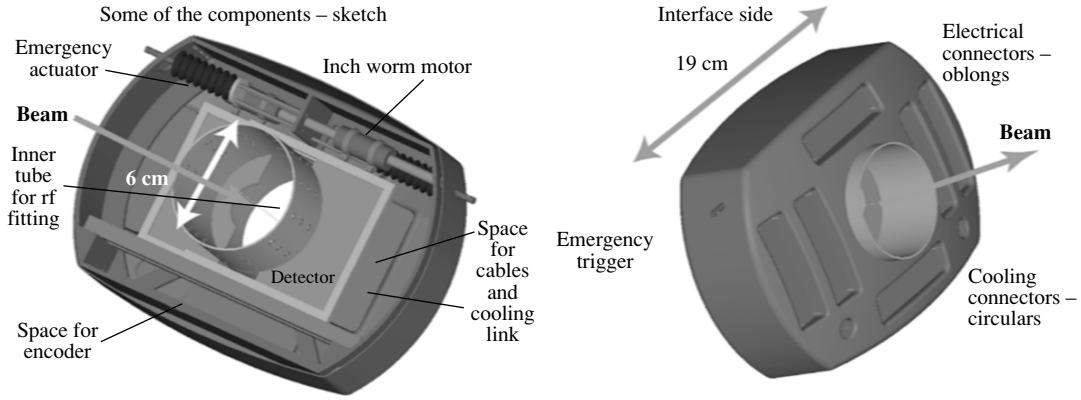

Fig. 12. Conceptual design of a microstation.

front of it would allow for limited particle identification capabilities, such as measurements of electrons and possibly photons.

5.3. Detector Concepts

Leading protons have been and are usually measured using silicon or scintillating fiber detectors, located in a movable casing (Roman pot), which also provides the separation from the beam vacuum. After stable beam conditions are reached, the pot is moved as close as possible to the circulating beam to provide the best acceptance for small-angle elastic scattering as well as for small-momentum-loss protons.

As the available space for additional instrumentation will often be very limited (e.g., inside the experimental caverns), a new detector concept has been developed, the microstation [9]. Its conceptual design is shown in Fig. 12. The basic idea is to perform the measurement inside the beam pipe, to obtain the closest possible approach of the sensor to the circulating beam. The design aims at a lightweight and very compact component (integrated with the beam pipe). It has to respect several requirements from the machine point of view, such as compatibility with the machine vacuum and no significant additional impedance to be introduced by the components. The sensor planes will be very precisely movable in a reproducible way, implemented by using inchworm motors built out of ceramic elements. This movement also has to be extremely reliable, as the microstation might be deployed in regions where access is difficult. The sensor is foreseen to be silicon based. Depending on the location and the type of measurement, it could be either of the Si strip type or of the Si pixel type, the latter in the case of larger particle densities (i.e., for measurements of inelastic event properties). For these sensors, special emphasis has to be given to a minimization of inactive areas close to the mechanical edge of the sensor, which would increase the effective distance to the beam center, from where onward measurements would be possible. A fully functional prototype for validation of the above requirements is presently under construction.

6. CONCLUSION

Starting in a few years, the LHC will offer excellent prospects for studies of strong interaction in proton and nucleus collisions at the future energy frontier. Its c.m. energy will extend the accelerator reach by up to three orders of magnitude in energy beyond what is available today, going up to equivalent energies of about 10^{17} eV for protons and about 10^{18} eV for lead ions in the laboratory frame.

Although the presently approved detectors cover a large part of the phase space for particle production, the truly forward region (small scattering angles with respect to the beam direction) is not yet addressed sufficiently well enough to be able to provide the maximal possible information. This information could be very useful to help in the understanding of extended air showers induced by cosmic rays. The ideas described in this contribution are presently being discussed within the experiments, with the aim to assess the feasibility of such extensions and to work towards sound technical designs. It has to be clear that such extensions cannot compromise the baseline detector performance for the high-p_T discovery and precision physics program. The experimental communities are open to additional suggestions and invite participation and contributions in this challenging enterprise.

It should not be forgotten that, so far, cosmic rays offer the only access to energies several orders of magnitude above what will be available in the foreseeable future from accelerator experiments. Improvements in the understanding of, e.g., cosmic-ray-induced air showers might thus also provide additional insight into particle physics.

REFERENCES

1. ALICE Technical Proposal, CERN/LHCC 95-71 (1995); http://alice.web.cern.ch/Alice/
2. ATLAS Technical Proposal, CERN/LHCC 94-43 (1994); http://atlas.web.cern.ch/Atlas/Welcome.html
3. ATLAS Detector and Physics Performance Technical Design Report, CERN/LHCC 99-14 and 99-15 (1999).
4. CMS Technical Proposal, CERN/LHCC 94-38 (1994); http://cmsdoc.cern.ch/cms/outreach/html/index.shtml
5. LHCb Technical Proposal, CERN/LHCC 98-4 (1998); http://lhcb.web.cern.ch/lhcb/
6. *NEEDS Workshop, Karlsruhe, April 2002*; http://www-ik.fzk.de/~needs
7. R. Engel, *Extensive Air Showers and Accelerator Data: the NEEDS Workshop, Karlsruhe, 2002*; hep-ph/0212340.
8. TOTEM Technical Proposal, CERN/LHCC 99-7 (1999); http://totem.web.cern.ch/Totem/
9. V. Nomokonov, in *Forward Physics and Luminosity Measurements at LHC*, Ed. by K. Huitu, R. Orava, S. Tapprogge, and V. Khoze (World Sci., Singapore, 2001).

Physics of Atomic Nuclei, Vol. 67, No. 1, 2004, pp. 156–162. From Yadernaya Fizika, Vol. 67, No. 1, 2004, pp. 153–159.

Wavelet Analysis of Angular Distributions of Secondary Particles in High-Energy Nucleus–Nucleus Interactions: Irregularity of Particle Pseudorapidity Distributions*

V. V. Uzhinsky[**], **V. Sh. Navotny**[1)], **G. A. Ososkov**, **A. Polanski**, and **M. M. Chernyavsky**[2)]

Joint Institute for Nuclear Research, Dubna, Moscow oblast, 141980 Russia

Received April 30, 2003

Abstract—Experimental data on interactions of sulfur and oxygen nuclei with photoemulsion nuclei at energies of 200 and 60 GeV/nucleon are analyzed with the help of a continuous wavelet transform. Irregularities in pseudorapidity distributions of narrow groups of the secondary shower particles in these interactions are observed upon application of the second-order derivative of a Gaussian as a wavelet. The irregularities can be interpreted as the existence of preference emission angles of groups of particles. Such an effect is expected during emission of Cherenkov gluons in nucleus–nucleus collisions. Some of the positions of the observed peculiarities on the pseudorapidity axis coincide with those found by Dremin *et al.* (I. M. Dremin *et al.*, Phys. Lett. B **499**, 97 (2001)). © *2004 MAIK "Nauka/Interperiodica"*.

In the last decade, a new type of mathematical analysis of data, so-called wavelet analysis, has become very popular in various branches of science and engineering [1–4]. Mainly, it is applied for analysis of time series coming from geophysics, meteorology, astrophysics, and so on (applications in aviation, medicine, and biology see in [5]).

The wavelet decomposition or wavelet transform of a function $f(x)$ is its decomposition on an orthogonal functional family of special form [6]:

$$W_\Psi(a,b)f = \frac{1}{\sqrt{C_\Psi}} \int_{-\infty}^{\infty} f(x)\Psi_{a,b}(x)dx, \qquad (1)$$

$$\Psi_{a,b}(x) \equiv a^{-1/2}\Psi\left(\frac{x-b}{a}\right).$$

Here, Ψ is called a wavelet, b is a translation parameter, a is a dilation parameter or a scale, and C_Ψ is a normalizing constant:

$$C_\Psi = 2\pi \int_{-\infty}^{+\infty} |\tilde{\Psi}(\omega)|^2 |\omega|^{-1} d\omega,$$

where $\tilde{\Psi}(\omega)$ is the Fourier transform of $\Psi(x)$.

The derivatives of the Gaussian function are often used as wavelets,

$$\Psi(x) \equiv g_n(x) = (-1)^{n+1}\frac{d^n}{dx^n}e^{-x^2/2},$$
$$n > 0, \qquad C_{g_n} = 2\pi(n-1)!.$$

The first two wavelets are well known:

$$g_1(x) = -xe^{-x^2/2}, \qquad g_2(x) = (1-x^2)e^{-x^2/2}.$$

The second one is called a Mexican hat wavelet (MHAT).

As can be seen, the wavelet transform puts a function of two variables, $W_\Psi(a,b)$, in correspondence to a function of one variable, $f(x)$. Until recently, a presentation and an analysis of a function of two variables was quite a difficult job, and only modern computers with their 3D graphics allowed one to implement completely the method of wavelet analysis.

There is a discrete analogy of the continuous wavelet transform (see [6]). It was used in elementary particle physics for the study of events of cosmic-ray interactions with matter—in the analysis of particle pseudorapidity distributions [7]. The wavelet coefficients ($W_\Psi(a,b)$) of energy distributions predicted by different models of multiparticle production were studied in [8]. The possibilities of wavelet analysis in searching for manifestation of the disoriented chiral condensate in the pseudorapidity distributions of the neutral particle fraction were considered in [9].

In [10], the wavelet transform was used for pattern recognition in Pb + Pb interactions at the energy of 158 GeV/nucleon. Structures were found in the

*This article was submitted by the authors in English.

[1)]FTI, Tashkent, Uzbekistan.
[2)]FIAN, Moscow, Russia.
[**]e-mail: uzhinsky@jinr.ru

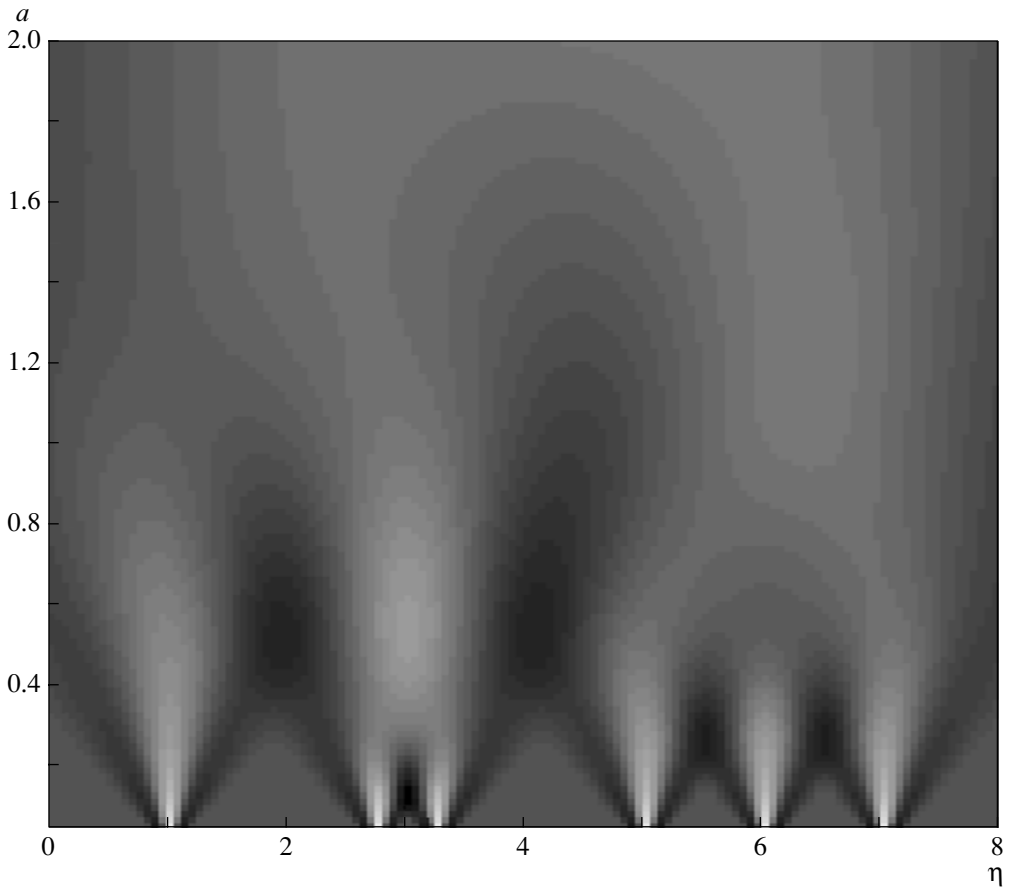

Fig. 1. Wavelet spectra of test example.

angular distributions of secondary particles that can be interpreted as irradiation of Cherenkov gluons. The last publications in this research are devoted to experimental search for the disoriented chiral condensate in nucleus–nucleus interactions [11].

Most of the aforementioned papers suffer from the apparent lack of quantitative results caused either by uniqueness of natural phenomenon or by low statistics of analyzed data. It is connected partly with specific properties of the wavelet analysis itself (see [12]). A regular method to apply wavelet analysis in particle physics is needed. Our paper presents experience in using the wavelet transform for analysis of more than 2000 interactions of nuclei with nuclei at high energies.

Experimental data were obtained during horizontal irradiation of NIKFI BR-2 nuclear photoemulsion with sulfur and oxygen nuclei with energies of 200 and 60 GeV/nucleon at the CERN SPS. The sensitivity of the emulsion was about 30 grains per unit length of 100 μm for single charged particles with minimal ionization.

Primary interactions were found by along-track double scanning: fast in the forward direction and slow in the backward direction. Fast scanning was performed at a velocity excluding any discrimination of events in the number of heavily ionizing tracks; slow scanning was carried out to find events, if any, with a little changed and unbiased projectile nucleus. Upon rejecting events of electromagnetic dissociation and purely elastic scattering in the total sample, 884 events of S + Em and 504 events of O + Em at the energy of 200 GeV/nucleon, and 884 O + Em interactions at the energy of 60 GeV/nucleon were selected for further analysis. In each event, the polar angles θ and azimuthal angles φ were measured.

Shower particles, or so-called s particles—single charged particles with a velocity $\beta = v/c \geq 0.7$—are considered in this study. The s particles consist mainly of produced particles and single charged nuclear fragments. A special separation of single charged fragments was not done.

According to [10], the distribution of secondary particles on the pseudorapidity $\eta = -\ln(\tan(\theta/2))$ in an event was given as

$$f(\eta) = \frac{dn}{d\eta} = \frac{1}{N}\sum_{i=1}^{N}\delta(\eta - \eta_i), \qquad (2)$$

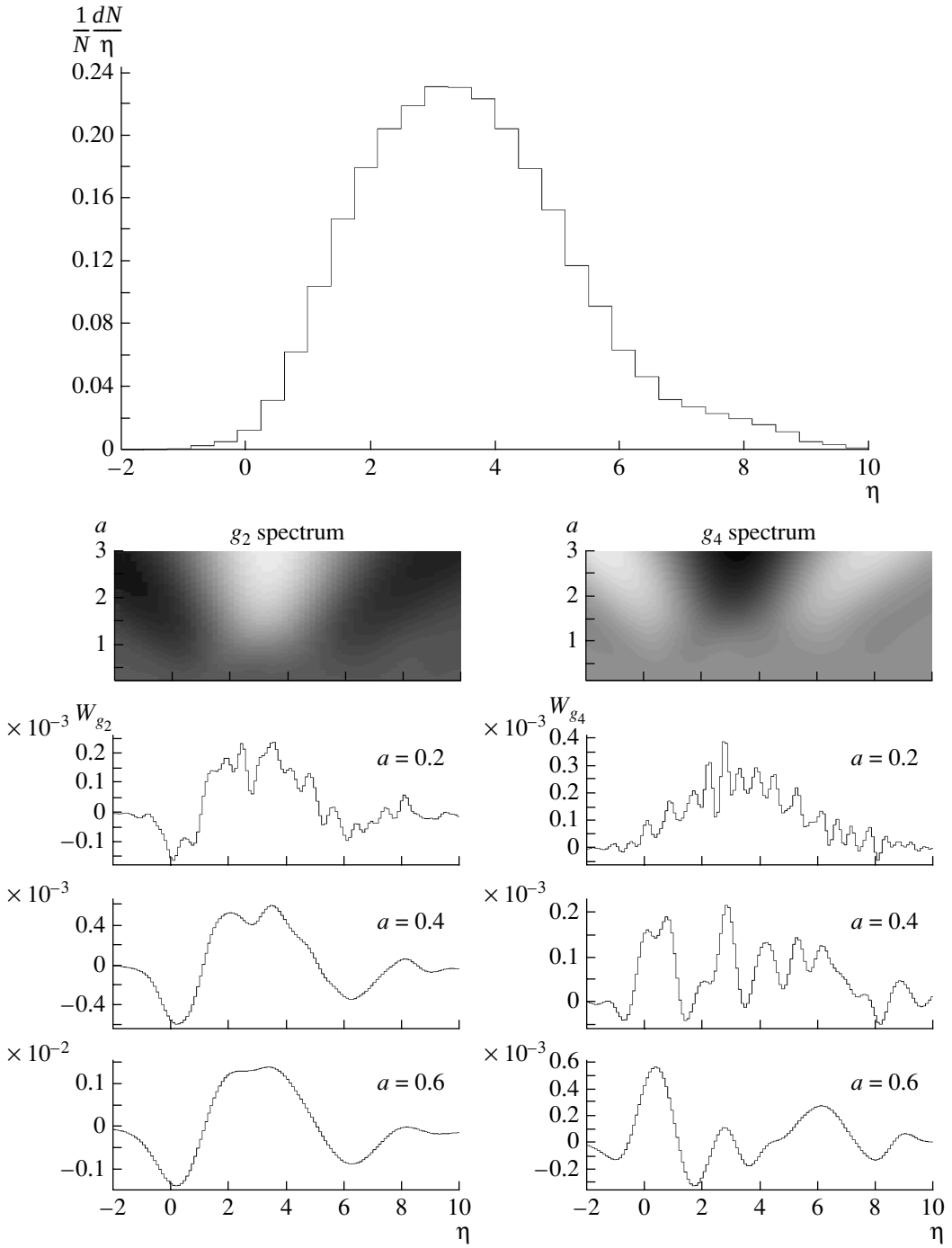

Fig. 2. Wavelet analysis of s-particle pseudorapidity distribution in S + Em interactions at the energy of 200 GeV/nucleon.

where N is the multiplicity of s particles in the event, and η_i is the pseudorapidity of the ith particle.

A wavelet transform of the function (2) gives

$$W_\Psi(a,b) = \frac{1}{N}\sum_{i=1}^{N} a^{-1/2}\Psi\left(\frac{\eta_i - b}{a}\right). \qquad (3)$$

Thus, the function of two variables is brought into correspondence with each particle. Wavelet spectra of the event ($W_\Psi(a,b)$) is a sum of such functions.

As an example, Fig. 1 presents wavelet spectra of an event with six particles having pseudorapidities $\eta_1 = 1$, $\eta_2 = 2.75$, $\eta_3 = 3.25$, $\eta_4 = 5$, $\eta_5 = 6$, and $\eta_6 = 7$. The values of translation parameter b (or η) are put on the X axis; dilation parameter a, on the Y axis. The values of the wavelet coefficients are

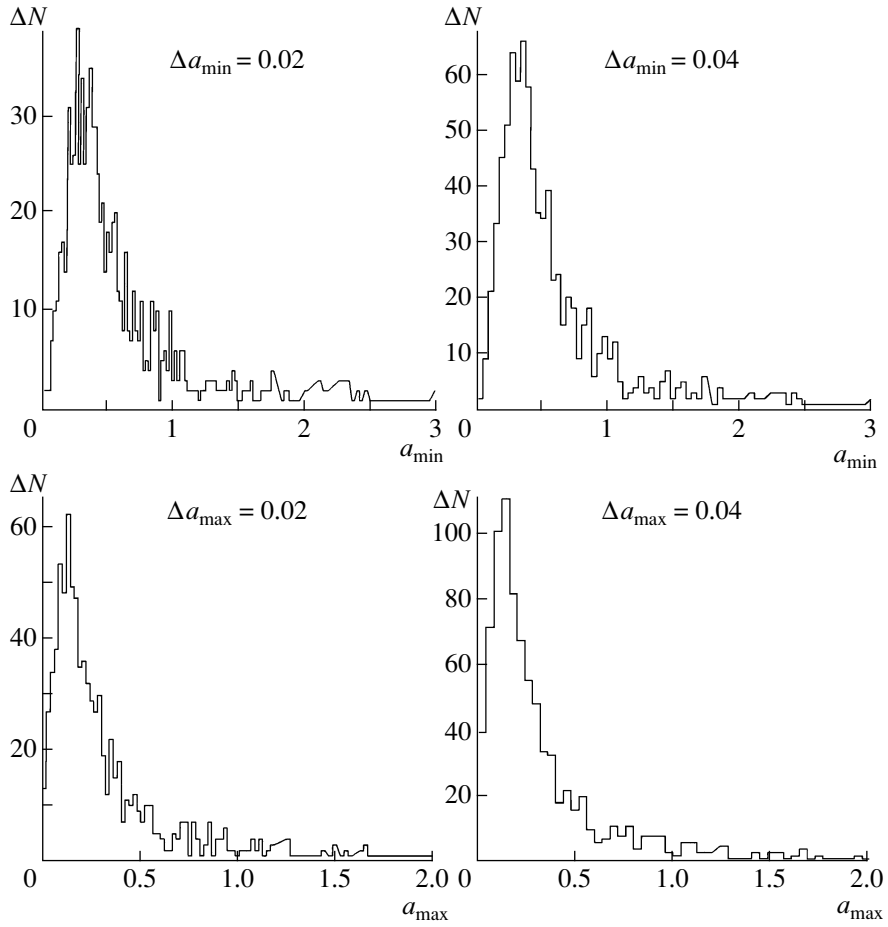

Fig. 3. Distributions of the extreme points of the scalograms of the S + Em events at the energy of 200 GeV/nucleon.

depicted using a gray-level scale: the high values of the coefficients are of light shade, while the lower ones are darker. As can be seen, in g_2 wavelet spectra at a scale lower than 0.3, all particles are distinguished. At a scale larger than 0.5, particles 2 and 3 cannot be resolved. At $a > 1$, particles 4, 5, 6 cannot be resolved. At $a > 2$, one could expect a fusion of particles 1, 2, and 3. However, this does not take place due to the small yield of particle 1 in the wavelet spectra at a large scale. Thus, the wavelet transform of g_2 allows one to study the particle clusterization.

Let us note that the positions of the local maxima of $W_\Psi(a, b)$ ($a \simeq 0.5$ and $b = 3$, $a \simeq 1$ and $b = 6$) on the b axis are connected with positions of the centers of the groups of particles 2, 3 and 4, 5, 6. The corresponding scales reflect the width of the groups on the pseudorapidity axis. Positions of the local minima give the centers of the pseudorapidity splits between the groups. Thus, the wavelet transform allows one to select a group of particles.

We started our analysis with study of the particle distribution on the pseudorapidities in all interactions. The histogrammed distribution for S + Em interactions at the energy of 200 GeV/nucleon is presented in Fig. 2. There are also g_2 and g_4 wavelet spectra at different scales. It should be noted that the wavelet transform was applied to raw experimental data, not to the histogrammed distribution. Thus, a fine structure of the spectra can be observed at small scales. The structure becomes more regular at large scales and turns into the wavelet function in the limit of large a. At $a \sim 0.4$, one can see three maxima in the g_2 spectra at $\eta \sim 2, 4$, and 8. It seems that the maximum at $\eta \sim 2$ is connected with the particle production in the target fragmentation region; the maximum at $\eta \sim 4$, with the particle production in the central region; and the maximum at $\eta \sim 8$, with spectator fragments of the projectile nucleus. In reality, the three maxima only reflect what can be seen with the naked eye—the left wing of the distribution is different from the right one. One can clearly see a change in the slope on the right wing at $\eta \sim 6$. At smaller scales, the structure is richer and does not allow such a simple interpretation. In order to find selected scales in the interactions and

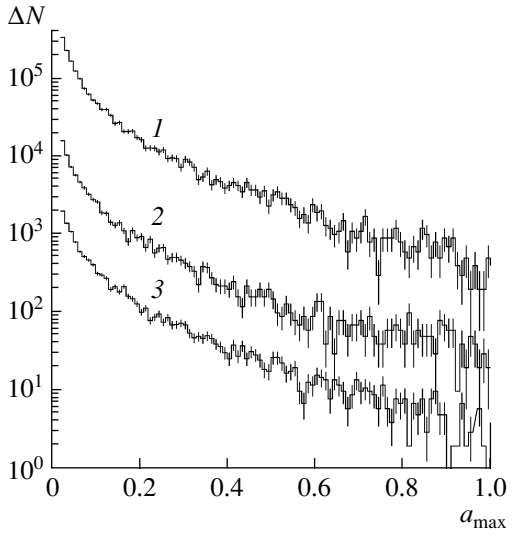

Fig. 4. $a_{\max}$ distributions in the S + Em and O + Em interactions at the energy of 200 GeV/nucleon and in the O + Em interactions at the energy of 60 GeV/nucleon (histograms *1*, *2*, and *3*, respectively). The distributions *1*, *2*, and *3* are multiplied by 10^2, 10^1, and 10^0, respectively.

to analyze the fine structure of the events, we turned to a study of the energy density and scalogram.

The spectrum of the energy density $(W_\Psi(a,b)^2)$ reflects peculiarities of the $W_\Psi(a,b)$ function and can be used for searching the particle group, though the definition of maxima and minima of the function is quite a complicated task. Therefore, at the first stage, we concentrated our attention on the energy distribution on scales, on scalogram $E_W(a) = \int W_\Psi(a,b)^2 db$ because it is a 1D function.

Scalograms reflect characteristic features of an event. For example, the scalogram of the g_2 spectrum for the test example has a minimum at $a \sim 1.1$, associated with an average distance between the groups of the particles 2, 3 and 4, 5, 6, and a maximum at $a \sim 0.5$, connected with the most compact group of particles 2, 3. It is possible to write an analytical expression for the scalogram using the g_2 wavelet and the distribution of the form (2):

$$S(a) = \frac{1}{32\sqrt{\pi}a^4} \times \sum_{ij=1}^{N} \left[\Delta_{ij}^4 - 12a^2\delta^2 - 12a^4\right] e^{-\Delta_{ij}^4/(4a^2)}, \quad (4)$$

$$\Delta_{ij} = \eta_i - \eta_j.$$

It is seen that the scalogram is a statistical averaged squared distance between particles. Thus, we expected that an analysis of the scalograms would allow us to find characteristic scales.

Distributions of local minimum and maximum positions in the scalograms of the events of S + Em interactions at the energy of 200 GeV/nucleon are given in Fig. 3. Though there are some irregularities in the distributions, we cannot say that they have a statistically guaranteed meaning. In addition, the analysis of connection between $a_{\min}$ and $a_{\max}$ and characteristics of the real events did not show any regularity. However, we believe that the study of a larger volume of experimental data will produce interesting results.

The next step of our study was a search for extremum points of function $W_\Psi(a,b)$ of the real events. Distributions of points on the dilation scale in our interactions are presented in Fig. 4. At first glance, the distributions have no characteristic peculiarities—bumps or pits. We can only remark that the distributions cannot be described by a simple exponential function. It is necessary to use at least two exponents in fitting the distributions. Simulation of *pp* interactions with the help of the HIJING program [13] has shown that the appearance of an exponent with a larger slope is connected with production of jets of particles. Thus, we consider our distributions as a manifestation of jet existence in nucleus–nucleus interactions.

Research on the distributions of the local maximum of $W_\Psi(a,b)$ on b gives more interesting results. Figure 5 shows the distributions of all our interactions at $a_{\max} \geq 0.05$ (*1*), $a_{\max} \geq 0.1$ (*2*), $a_{\max} \geq 0.2$ (*3*), and $a_{\max} \geq 0.3$ (*4*). As can be seen, the peculiarities of the distributions at $\eta \sim 1.5$, $\eta \sim 2$, $\eta \sim 3$, $\eta \sim 3.5$, and $\eta \sim 5$ are located at the same positions for different interactions. The peculiarities, as can be seen, are connected with narrow groups, where $a_{\max} < 0.05$. We interpret them as the existence of preferred emission angles of the groups of particles. Let us note that the positions of some irregularities found by us coincide with those observed early in [10] in the study of Pb + Pb interactions at the energy of 158 GeV/nucleon. Unlike [10], where 5 mostly central events were analyzed, we present the results for more than 2000 events.

Research on narrow groups of particles with help of traditional methods was the third step. Figure 6 shows a distribution on a pseudorapidity interval between neighboring particles in an event. It was observed that there were pairs of particles with close pseudorapidities, $\Delta < 10^{-5}$! Their number increases statistical fluctuations. The distribution of the centers of the pairs on η has two bumps at $\eta \sim 3$ and 4. Thus, we can conclude that the peculiarities of the wavelet spectra observed by us at small scales are connected with the narrow groups of particles.

One can suppose that such pairs occur due to data input error when two or three entries in the event

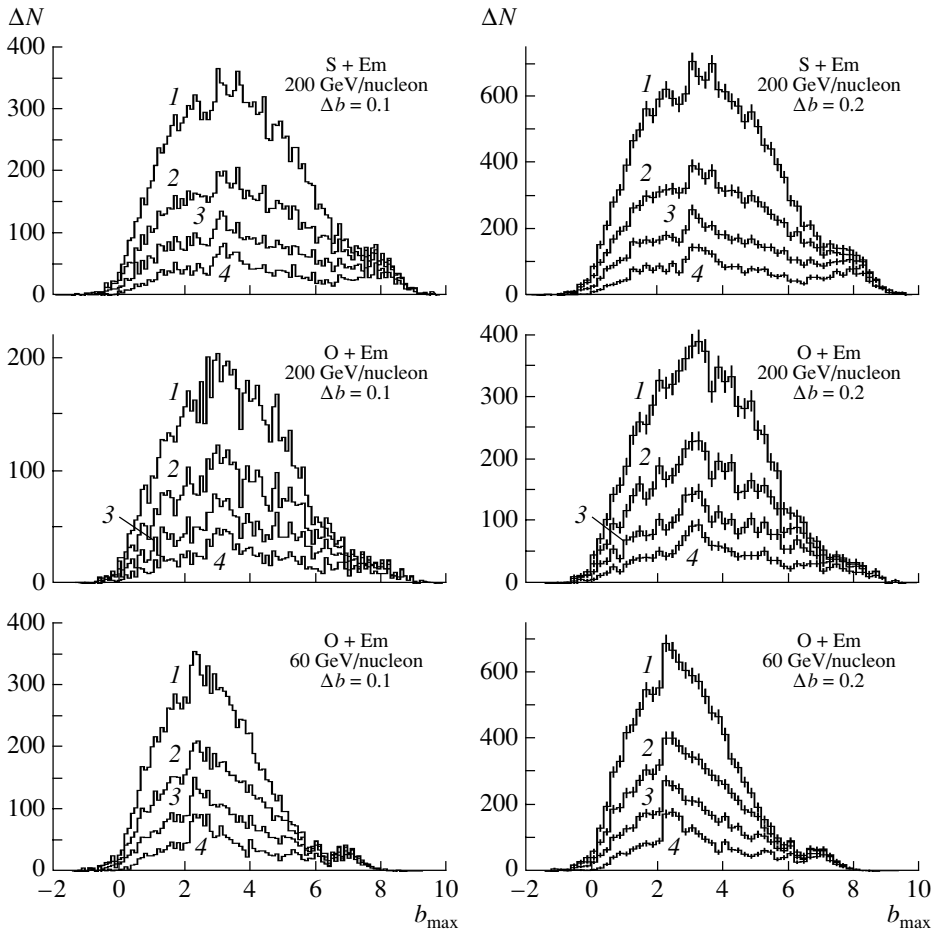

Fig. 5. b_{max} distributions in the S + Em and O + Em interactions at the energy of 200 GeV/nucleon and in the O + Em interactions at the energy of 60 GeV/nucleon. Δb is the step of the histogramming. The distributions *1–4* are obtained at $a_{max} \geq 0.05$, $a_{max} \geq 0.1$, $a_{max} \geq 0.2$, and $a_{max} \geq 0.3$, respectively.

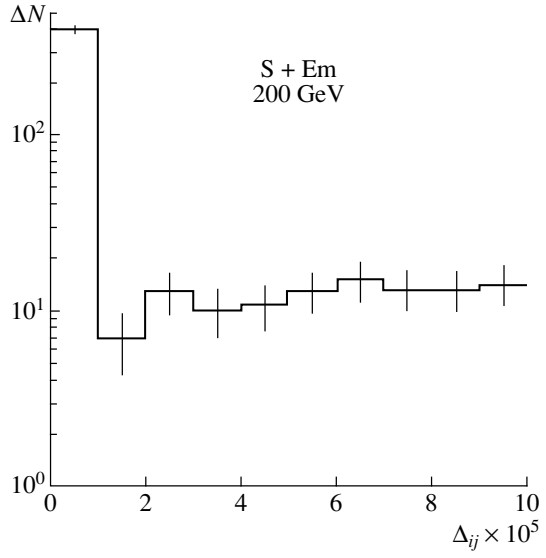

Fig. 6. Distribution on the pseudorapidity interval between the neighboring particles in all studied interactions.

record correspond to the same particle. In this case, such ghost "particles" must have identical η and φ. The fraction of these pairs is lower than 20% among all the observed narrow pairs. The other pairs have different values of azimuthal angles. The distribution of the particles of the narrow groups on φ has no clear peculiarities and reflects the methodological drawback of the photoemulsion experiments—a poor identification of particles flying perpendicularly to the emulsion plate (at $\varphi \sim 0°$ and 180°). The distribution of the azimuthal angle difference of the particles of the narrow group has no irregularities either. Therefore, these pairs cannot belong to a jet of particles. The nature of such pairs is not clear to us.

SUMMARY

(i) The continuous wavelet transform has been used for the analysis of more than 2000 events of nucleus–nucleus interactions at high energies (S + Em and O + Em interactions at energies of 200 and 60 GeV/nucleon).

(ii) It is shown that the maxima of $W_\Psi(a,b)$ obtained with the help of the g_2 wavelet are associated with the groups of particles.

(iii) It has been found that the distribution of the group of particles on scales in the interactions under study is heterogeneous, which can be caused by jet production.

(iv) It is observed that the distributions of the groups on pseudorapidities have irregularities; there are preferences of emission angles of the groups.

(v) Pairs of particles with close pseudorapidities, $\Delta < 10^{-5}$, have been found for the first time.

The nature of the peculiarities observed by us is not yet clear.

ACKNOWLEDGMENTS

We are grateful to the members of the EMU-01 Collaboration for their kind permission to employ the experimental data analyzed in this paper.

The authors (V.V.U. and M.M.C.) thank the Russian Foundation for Basic Research (project nos. 00-01-00307 and 03-02-17079) and INTAS (grant no. 00-00366) for their financial support.

REFERENCES

1. H. Weng and K.-M. Lau, J. Atmos. Sci. **51**, 2523 (1994).
2. P. Kumar and E. Foufoula-Georgio, Rev. Geophys. **235**, 385 (1997).
3. N. M. Astafyeva and G. A. Bazilevskaya, Phys. Chem. Earth C **25**, 129 (1999).
4. K. Kudela *et al.*, Solar Phys. **199**, 200 (2001).
5. I. M. Dremin, Usp. Fiz. Nauk **170**, 1235 (2000).
6. I. Daubechies, *Ten Lectures on Wavelets* (Soc. Ind. Appl. Math., Philadelphia, 1992), p. 357.
7. N. Suzuki, M. Biyaima, and A. Oksawa, Prog. Theor. Phys. **94**, 91 (1995).
8. D. Huang, Phys. Rev. D **56**, 3961 (1997).
9. Z. Huang, I. Sarcevic, R. Thews, and X.-N. Wang, Phys. Rev. D **54**, 750 (1996).
10. N. M. Astafyeva, I. M. Dremin, and K. A. Kotelnikov, Mod. Phys. Lett. A **12**, 1185 (1997); I. M. Dremin *et al.*, Phys. Lett. B **499**, 97 (2001); hep-ph/0007060.
11. M. L. Kopytine *et al.*, nucl-ex/0104002.
12. C. Torrence and G. P. Compo, Bull. Am. Meteorol. Soc. **79**, 61 (1998).
13. M. Gyulassy and M. Plumer, Phys. Lett. B **243**, 432 (1990); X.-N. Wang and M. Gyulassy, Phys. Rev. D **44**, 3501 (1991).

Physics of Atomic Nuclei, Vol. 67, No. 1, 2004, pp. 163–169. From Yadernaya Fizika, Vol. 67, No. 1, 2004, pp. 160-166.

VERY HIGH MULTIPLICITY PHYSICS

Toward Very High Multiplicity Event Generator*

J. Manjavidze[1)] and **V. V. Voronyuk**

Joint Institute for Nuclear Research, Dubna, Moscow oblast, 141980 Russia

Received April 30, 2003

Abstract—The generating functional for probabilities is derived for the scalar model of Yang–Mills fields in terms of functional integrations. The example of $2 \to 2$ scattering is shown and problems that arise are mentioned. © *2004 MAIK "Nauka/Interperiodica".*

1. INTRODUCTION

The aim of the paper is to describe the first attempts to construct the event generator for very high multiplicity hadron processes. It will be based on a newly developed approach, namely, so-called topological QCD [1].

The method of derivation of the generating functional for probabilities will be illustrated by the scalar model of Yang–Mills fields. It is known (see review paper [2]) that the ansatz $B^\mu(x) = i\sigma^{\mu\nu}\partial_\nu \ln u(x)$ reduces the Yang–Mills theory to the scalar conformal field theory. For this reason, we will consider the theory with Lagrangian

$$\mathcal{L} = \left[\frac{1}{2}(\partial_\mu u)^2 - \frac{g}{4}u^4\right] + \left[\frac{1}{2}(\partial_\mu \varphi)^2 - \frac{m^2}{2}\varphi^2\right] - \kappa u\varphi^2. \quad (1)$$

The field φ corresponds to external particles, and for simplicity we restrict ourselves to the lowest order over it. In some sense, (1) represents the scalar Yang–Mills theory, where u is the "gauge" field and φ is the "quark" field. We will suppose, therefore, that the asymptotic states are composed from pairs of the field φ.

The quantization is performed in the vicinity of nontrivial classical solution u_c. The corresponding perturbation theory (the scalar version of topological QCD) describes the expansion over the inverse coupling constant, $1/g$. For this purpose, the transformation to "collective variables" (they will have the meaning of action–angle variables) will be realized. The idea of such transformation of quantum variables has been widely discussed (see, e.g., [3]).

In Section 2, we define the generating functional. Section 3 presents quantization in terms of the collective variables. The explicit expression of the generating functional for probabilities and the example of $2 \to 2$ scattering are shown in Section 4. In conclusion, Section 5 presents a brief discussion of results.

2. GENERATING FUNCTIONAL

We will derive in this section the explicit formulas for the generating functional. The formalism of the generating functional was used by number of authors and it will be important for us.

2.1. Generating Functional for Multiple Production Phenomena

We will consider the quantity

$$\rho(z,\alpha) = \sum_{m,n=1}^{\infty} \frac{1}{m!n!}\int d\omega_m(p; z_i, \alpha_i) \times d\omega_n(q; z_f, \alpha_f)|a_{m,n}(p,q)|^2, \quad (2)$$

where

$$d\omega_m(p; z, \alpha) = \prod_{k=1}^{m} \frac{d^3p_k e^{i\alpha p_k} z(p_k)}{(2\pi)^3 2\varepsilon(p_k)},$$

$$\varepsilon(p) = \sqrt{\mathbf{p}^2 + m^2},$$

is the Lorentz-covariant phase-space element, $z(p)$ is some "good" weight function, and $a_{m,n}(p,q)$ is the m-into-n-particles transition amplitude.

The generating functional $\rho(z,\alpha)$ can be used as the event generator for the description of accelerator experiments. For example, if

$$\rho_{m\to n}(p,q;\alpha)$$

*This article was submitted by the authors in English.

[1)]Institute of Physics, Tbilisi, Georgia; Joint Institute for Nuclear Research, Dubna, Moscow oblast, 141980 Russia.

**e-mail: joseph@nusun.jinr.ru

***e-mail: vadimv@nusun.jinr.ru

$$= \prod_{k=1}^{m} \frac{\delta}{\delta z_i(p_k)} \prod_{k=1}^{n} \frac{\delta}{\delta z_f(q_k)} \rho(z,\alpha)\Big|_{z=0},$$

then the total cross section can be written as

$$\sigma_n(a_1 + a_2 \to f) = \frac{1}{J(s)} \times \sum_n \int \frac{d^4\alpha_i}{(2\pi)^4} \frac{d^4\alpha_f}{(2\pi)^4} e^{iP(\alpha_i+\alpha_f)} \times \rho_{2\to n}(p_1,p_2;q_1,\ldots,q_n;\alpha) \prod_{k=1}^{n} d^3q_k,$$

where $J(s)$ is the standard normalization factor.

The reduction formula for the amplitude looks as follows:

$$a_{m,n}(p_1,\ldots,p_m;q_1,\ldots,q_n) \qquad (3)$$

$$= (-i)^{m+n} \prod_{k=1}^{m} \hat{\phi}(p_k) \prod_{k=1}^{n} \hat{\phi}^*(q_k) Z[\phi]\Big|_{\phi=0}.$$

Here, the symbol "$\wedge$" denotes the variational derivative:

$$\hat{\phi}(p) = \int d^4x e^{-ipx} \frac{\delta}{\delta\phi(x)},$$

$$Z[\phi] = \int D\varphi e^{iS_{C_+}(\varphi) - iV_{C_+}(\varphi+\phi)},$$

where C_+ is the Mills complex time contour [4],

$$t \to t + i\epsilon, \quad \epsilon \to +0, \quad -\infty \le t \le +\infty.$$

Inserting (3) into (2), one finds

$$\rho(z,\alpha) = \sum_{m,n}^{\infty} \frac{1}{m!n!} \prod_{k=1}^{m} \left[\int \frac{d^3p_k e^{i\alpha_i p_k} z_i(p_k)}{(2\pi)^3 2\varepsilon(p_k)} \hat{\phi}_+(p_k) \hat{\phi}^*_-(p_k) \right] \times \prod_{k=1}^{n} \left[\int \frac{d^3q_k e^{i\alpha_f q_k} z_f(q_k)}{(2\pi)^3 2\varepsilon(q_k)} \hat{\phi}^*_+(q_k) \hat{\phi}_-(q_k) \right] Z[\phi_+] Z^*[\phi_-]\Big|_{\phi_\pm=0}.$$

Summation over m and n can be done. As a result,

$$\rho(z,\alpha) = e^{N_+(\hat{\phi};\alpha_i,z_i) + N_-(\hat{\phi};\alpha_f,z_f)} \rho_0[\phi]\Big|_{\phi_\pm=0}, \quad (4)$$

where

$$N_+(\hat{\phi};\alpha_i,z_i) = \exp\left[\int \frac{d^3p e^{i\alpha_i p} z_i(p)}{(2\pi)^3 2\varepsilon(p)} \hat{\phi}_+(p) \hat{\phi}^*_-(p) \right],$$

$$N_-(\hat{\phi};\alpha_f,z_f) = \exp\left[\int \frac{d^3q e^{i\alpha_f q} z_f(q)}{(2\pi)^3 2\varepsilon(q)} \hat{\phi}^*_+(q) \hat{\phi}_-(q) \right],$$

$$\rho_0[\phi] = Z[\phi_+] Z^*[\phi_-].$$

2.2. Unitarity Condition

Our basic idea consists in considering the probability instead of the amplitude. It is useful because of the existence of the unitary condition $SS^+ = I$. Indeed, the amplitude A must satisfy the condition

$$S = I + iA \quad \Rightarrow \quad iAA^* = A - A^*.$$

Therefore, since the observables are $\sim \langle \text{in}|A|\text{out}\rangle\langle\text{out}|A^*|\text{in}\rangle$, there is no necessity to know the phase of $\langle \text{in}|A|\text{out}\rangle$ or, what it is the same, there is no necessity to calculate the real part of the amplitude $\langle \text{in}|A|\text{out}\rangle$.

We will consider the scalar gu^4 conformal field theory with Lagrangian (1). Therefore,

$$\rho_0[\phi] = \int Du_+ D\varphi_+ \exp\left[iS_{C_+}(u_+) + iS_{0C_+}(\varphi_+) - iV_{C_+}(u_+, \varphi_+ + \phi_+) \right] \times \int Du_- D\varphi_- \exp\left[-iS_{C_-}(u_-) - iS_{0C_-}(\varphi_-) + iV_{C_-}(u_-, \varphi_- + \phi_-) \right],$$

where

$$S_C(u) = \int_C d^4x \left[\frac{1}{2}(\partial_\mu u)^2 - \frac{g}{4}u^4 \right],$$

$$S_{0C}(\varphi) = \int_C d^4x \left[\frac{1}{2}(\partial_\mu \varphi)^2 - \frac{m^2}{2}\varphi^2 \right],$$

$$V_C(u,\varphi) = \kappa \int_C d^4x u(x)\varphi(x).$$

For the sake of simplicity, let us consider the low-

est order over φ:

$$\rho_0[\phi] = \int Du_+ e^{iS_{C_+}(u_+) - iV_{C_+}(u_+,\phi_+)} \times \int Du_- e^{-iS_{C_-}(u_-) + iV_{C_-}(u_-,\phi_-)}. \quad (5)$$

Since the choice of contour $C_\pm$ unambiguously defines the choice of $\phi_\pm$, we will consider one quantity ϕ such that $\phi = \phi_+(t \in C_+)$ and $\phi = \phi_-(t \in C_-)$.

Instead of the two independent fields u_+ and u_-, we introduce

$$u_\pm = u \pm e$$

with the boundary condition

$$\int\limits_{C_+} dx \partial_\mu (u_+ \partial^\mu u_+) = \int\limits_{C_-} dx \partial_\mu (u_- \partial^\mu u_-).$$

We extract a linear term with respect to e in the exponent

$$S_{C_+}(u+e) - S_{C_-}(u-e) - V_{C_+}(u+e,\phi) + V_{C_-}(u-e,\phi) = 2\mathrm{Re} \int\limits_{C_+} dx \frac{\delta S(u)}{\delta u} e + \tilde{S}(u,e).$$

We will assume that terms $\sim i\mathrm{Im}\int_{C_+} dx$ are proportional to $\epsilon \to +0$, and therefore they will be omitted.

The expansion over e looks as follows:

$$\exp[iS_{C_+}(u+e) - iS_{C_-}(u-e) - iV_{C_+}(u+e,\phi) + iV_{C_-}(u-e,\phi)] = \exp\left[-i\left(\int\limits_{C_+} dx \hat{j}(x)\hat{e}'(x) + \int\limits_{C_-} dx \hat{j}(x)\hat{e}'(x)\right)\right] \exp\left[2i\mathrm{Re}\int dx j(x)e(x)\right] \times \exp\left[2i\mathrm{Re}\int dx \frac{\delta S(u)}{\delta u} e(x)\right] \exp[i\tilde{S}(u,e')],$$

where, as usual, $\hat{j}(x)$ and $\hat{e}'(x)$ are the corresponding variational derivatives. The auxiliary variables $j(x)$ and $e'(x)$ must be set to zero at the end of all calculations.

Inserting this expansion into (5), one has

$$\rho_0[\phi] = e^{-i\hat{K}(j,e')} \int DuDe \times \exp\left[2i\mathrm{Re}\int dx \left(\delta S(u)/\delta u + j(x)\right) e(x)\right] e^{i\tilde{S}(u,e')},$$

where the power series over the operator

$$\hat{K}(j,e) = \int\limits_{C_+} dx \hat{j}(x)\hat{e}(x) + \int\limits_{C_-} dx \hat{j}(x)\hat{e}(x)$$

gives the quantum perturbation series.

Performing the integration over De, we obtain

$$\rho_0[\phi] = e^{-i\hat{K}(j,e)} \int DM(u) e^{i\tilde{S}(u,e)}\Big|_{j,e=0}, \quad (6)$$

$$DM(u) = \prod_x du \delta\left(\partial_\mu^2 u + gu^3 - j\right). \quad (7)$$

By means of the evident identity

$$1 = \int Dp \delta(p - \dot{u}),$$

the measure (7) can be rewritten as

$$DM(u) = DM(u,p) = \prod_x du(x)dp(x)\delta\left(\dot{u} - \frac{\delta H_j}{\delta p}\right)\delta\left(\dot{p} + \frac{\delta H_j}{\delta u}\right), \quad (8)$$

where H_j is the total Hamiltonian

$$H_j(u,p) = \int d^3x \left(\frac{1}{2}p^2 + \frac{1}{2}(\nabla u)^2 - \frac{g}{4}u^4 - ju\right).$$

3. FACTOR SPACE

As is seen from (8), the integral over u is defined by the strict, regular, and real solution of the inhomogeneous Hamiltonian equation. The latter presents a definite problem and it is useful to construct the perturbation theory in terms of the collective variables [3]. In the present section, we will show our realization of this idea.

3.1. Classical Solution

In accordance with topological QCD, the largest contribution is given by those field configurations that maximally violate the symmetry of the action.

The conformal invariant equation

$$-\frac{\delta S(u)}{\delta u} \equiv \Box u + gu^3 = 0$$

has the $O(4) \times O(2)$ invariant solution [2]. The $O(4) \times O(2)$ group is the maximal compact subgroup of the Minkowski conformal group and, therefore, this is the solution that gives the largest contribution. It is regular everywhere in Minkowski space and it possesses finite energy and action.

In our parametrization, it looks as follows:

$$\sqrt{-g}u_c(x) = \left[4a^2/((x-x_0)^2 - a^2)^2 + 4a^2((x-x_0)_\mu \lambda^\mu)^2\right]^{1/2}, \qquad g < 0,$$

where x_0 is an initial position, $a > 0$ is a scale factor, and λ_μ is the restricted constants of integration: $\lambda_\mu \lambda^\mu = 1$.

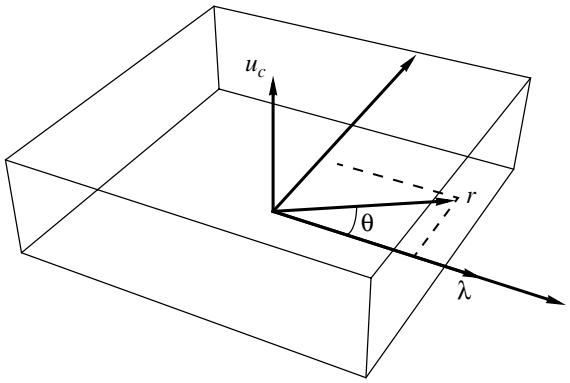

Fig. 1.

The Lorentz transformation can be written as

$$\begin{cases} t' = |\lambda_0| t - \mathrm{sgn}(\lambda_0)\lambda_k x_k, \\ x_i' = x_i + \mathrm{sgn}(\lambda_0)\lambda_i \left(\dfrac{\mathrm{sgn}(\lambda_0)\lambda_k x_k}{|\lambda_0|+1} - t \right), \end{cases} \qquad (9)$$

where the primed frame is the CM frame of u_c, where $\lambda_i = 0$, and the unprimed one is moving with velocity $v_i = \lambda_i/\lambda_0$.

The classical energy and momentum can be easily calculated with the help of the transformation (9):

$$E = \int d^3x \left\{ \frac{1}{2}(\dot{u}_c)^2 + \frac{1}{2}(\nabla u_c)^2 + \frac{1}{4} g u_c^4 \right\} = \frac{\pi^2}{2|g|a}|\lambda_0| = \frac{\pi^2}{2|g|a}\sqrt{1+\lambda_i^2},$$

$$P_i = \int d^3x \dot{u}_c \partial_i u_c = \frac{\pi^2}{2|g|a}\mathrm{sgn}(\lambda_0)\lambda_i.$$

For a better conception of u_c, let us show some graphics. The classical solution depends on $\mathbf{x}^2$ and $(\mathbf{x}\cdot\boldsymbol{\lambda})$. It is an invariant function under rotations about the direction of the vector $\boldsymbol{\lambda}$. So it is convenient to plot u_c against $r = \sqrt{\mathbf{x}^2}$ and angle $\theta = \widehat{\boldsymbol{x}\boldsymbol{\lambda}}$, as is shown in Fig. 1. Figure 2 presents time evolution of the solution in the CM frame, $\boldsymbol{\lambda} = 0$. Figure 3 presents the time evolution of the solution with $\lambda \neq 0$.

3.2. Explicit $O(4) \times O(2)$ Invariance

In the CM frame, u_c looks as follows:

$$u_c(x) = \sqrt{\frac{-4a^2/g}{(x^2-a^2)^2 + 4a^2t^2}}.$$

Let us introduce new variables

$$\zeta_0 = x_0, \quad \zeta_1 = x_1, \quad \zeta_2 = x_2, \quad \zeta_3 = x_3,$$
$$\zeta_5 = \frac{1}{2a}(a^2+x^2), \quad \zeta_6 = \frac{1}{2a}(a^2-x^2).$$

They define a six-dimensional hypertorus [5]

$$\begin{cases} \zeta_1^2 + \zeta_2^2 + \zeta_3^2 + \zeta_5^2 = \zeta_0^2 + \zeta_6^2, \\ \zeta_5 + \zeta_6 = 1. \end{cases}$$

In these variables, the classical solution has explicitly $O(4) \times O(2)$ invariant form

$$\sqrt{-g}u_c = (\zeta_0^2 + \zeta_6^2)^{-1/2}.$$

To obtain these variables for general case, one should use the Lorentz transformation (9):

$$\zeta_0 = x_\mu \lambda^\mu, \quad \zeta_1 = \frac{x_1\lambda_0 - x_0\lambda_1}{\sqrt{1+\lambda_2^2+\lambda_3^2}},$$
$$\zeta_2 = \frac{x_2 + \lambda_3(x_2\lambda_3 - x_3\lambda_2) - \lambda_2 x_\mu \lambda^\mu}{\sqrt{1+\lambda_2^2+\lambda_3^2}\sqrt{1+\lambda_3^2}},$$
$$\zeta_3 = \frac{x_3 - \lambda_3 x_\mu \lambda^\mu}{\sqrt{1+\lambda_3^2}},$$
$$\zeta_5 = \frac{1}{2a}(a^2+x^2), \quad \zeta_6 = \frac{1}{2a}(a^2-x^2),$$

where

$$\lambda_0^2 = 1 + \lambda_1^2 + \lambda_2^2 + \lambda_3^2.$$

3.3. Mapping

The measure (7) contains the equation of motion with arbitrary quantum source $j(x)$. It is hard to find the general solution to this equation if u_c is the nontrivial function, $u_c = u_c(x)$. For this reason, we will map our quantum problem into the flat and homogeneous manifold. It is the factor space of the variables $(a, \lambda, x_0) \equiv (\xi, \eta)$.

In order to do the mapping

$$u_c: \quad (u,p)(\mathbf{x},t) \to (\xi,\eta)(t),$$

we start from the integral

$$\rho_0[\phi] = e^{-i\hat{K}(j,e)} \int DM(u,p) e^{i\tilde{S}(u,e)} \Big|_{j,e=0}, \qquad (10)$$

where the measure

$$DM(u,p) = \prod_x du(x)dp(x)\delta\left(\dot{u} - \frac{\delta H_j}{\delta p}\right) \times \delta\left(\dot{p} + \frac{\delta H_j}{\delta u}\right). \qquad (11)$$

Inserting the identity

$$1 = \frac{1}{\Delta(u_c,p_c)} \int \prod_t d\xi(t) d\eta(t) \times \delta\left(u(x) - u_c(\xi(t),\eta(t))\right) \delta\left(p(x) - p_c(\xi(t),\eta(t))\right), \qquad (12)$$

into (10), where $(u,p)_c$ are some given functions, we must assume that the determinant $\Delta(u_c,p_c) \neq 0$. It

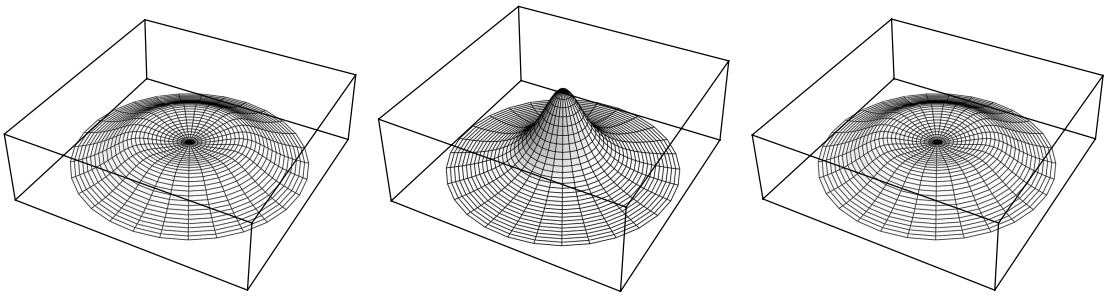

Fig. 2. Time evolution, $\lambda = 0$.

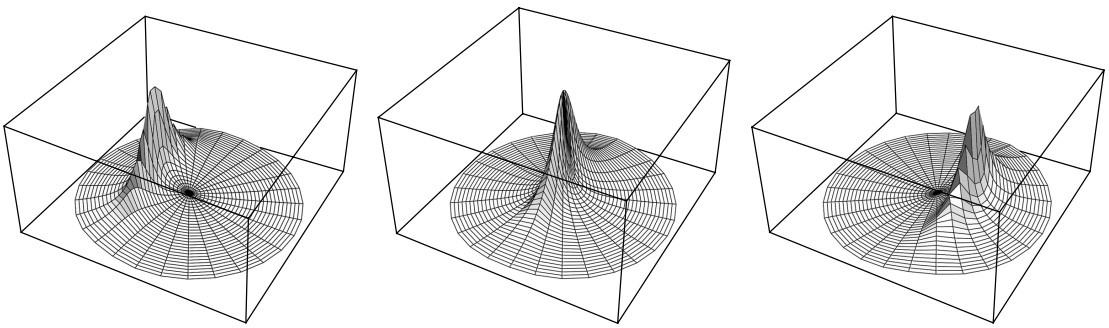

Fig. 3. Time evolution, $\lambda \neq 0$.

is important to take into account that both measures (10) and (12) are δ-like. This allows us to change the integration order and first to perform the integration over (u, p):

$$DM(\xi,\eta) = \frac{1}{\Delta(u_c,p_c)}\prod_t d\xi(t)d\eta(t) \qquad (13)$$
$$\times\,\delta\left(\dot{u}_c - \frac{\delta H_j(u_c,p_c)}{\delta p_c}\right)\delta\left(\dot{p}_c + \frac{\delta H_j(u_c,p_c)}{\delta u_c}\right).$$

The δ functions can be rewritten identically in the form

$$\prod_t \delta\left(\dot{u}_c - \frac{\delta H_j}{\delta p_c}\right)\delta\left(\dot{p}_c + \frac{\delta H_j}{\delta u_c}\right) \qquad (14)$$
$$= \prod_t \delta\left(\frac{\partial u_c}{\partial\xi}\dot{\xi} + \frac{\partial u_c}{\partial\eta}\dot{\eta} - \frac{\delta H_j}{\delta p_c}\right)$$
$$\times\,\delta\left(\frac{\partial p_c}{\partial\xi}\dot{\xi} + \frac{\partial p_c}{\partial\eta}\dot{\eta} + \frac{\delta H_j}{\delta u_c}\right)$$
$$= \int\prod_t d\bar{\xi}d\bar{\eta}\delta\left(\bar{\xi} - \left\{\dot{\xi} - \frac{\delta h_j}{\delta\eta}\right\}\right)$$
$$\times\,\delta\left(\bar{\eta} - \left\{\dot{\eta} + \frac{\delta h_j}{\delta\xi}\right\}\right)\delta\left(\frac{\partial u_c}{\partial\xi}\bar{\xi} + \frac{\partial u_c}{\partial\eta}\bar{\eta}\right.$$
$$+\left\{\frac{\partial u_c}{\partial\xi}\frac{\delta h_j}{\delta\eta} - \frac{\partial u_c}{\partial\eta}\frac{\delta h_j}{\delta\xi}\right\} - \frac{\delta H_j}{\delta p_c}\Big)\delta\left(\frac{\partial p_c}{\partial\xi}\bar{\xi}\right.$$
$$\left.+\frac{\partial p_c}{\partial\eta}\bar{\eta} + \left\{\frac{\partial u_c}{\partial\xi}\frac{\delta h_j}{\delta\eta} - \frac{\partial u_c}{\partial\eta}\frac{\delta h_j}{\delta\xi}\right\} + \frac{\delta H_j}{\delta u_c}\right).$$

Here, we introduce the function $h_j = h_j(\xi,\eta)$ defined by the equalities

$$\{u_c, h_j\}_{\xi,\eta} = \frac{\delta H_j(u_c,p_c)}{\delta p_c}, \qquad (15)$$
$$\{p_c, h_j\}_{\xi,\eta} = -\frac{\delta H_j(u_c,p_c)}{\delta u_c},$$

where the Poisson brackets are

$$\{X,Y\}_{\xi,\eta} = \frac{\partial X}{\partial\xi}\frac{\partial Y}{\partial\eta} - \frac{\partial X}{\partial\eta}\frac{\partial Y}{\partial\xi}.$$

We will assume that

$$h_j(\xi,\eta) = H_j(u_c,p_c). \qquad (16)$$

Just in this case, $u_c(\mathbf{x},\xi,\eta)$ is the classical solution and, as a result, (ξ,η) would be the factor manifold.

Then, using (14) and (15), we obtain

$$\prod_x \delta\left(\dot{u}_c - \frac{\delta H_j}{\delta p_c}\right)\delta\left(\dot{p}_c + \frac{\delta H_j}{\delta u_c}\right)$$
$$= \prod_x d\bar{\xi}d\bar{\eta}\delta\left(\bar{\xi} - \left\{\dot{\xi} - \frac{\delta h_j}{\delta\eta}\right\}\right)$$
$$\times\,\delta\left(\bar{\eta} - \left\{\dot{\eta} + \frac{\delta h_j}{\delta\xi}\right\}\right)\delta\left(\frac{\partial u_c}{\partial\xi}\bar{\xi} + \frac{\partial u_c}{\partial\eta}\bar{\eta}\right)$$
$$\times\,\delta\left(\frac{\partial p_c}{\partial\xi}\bar{\xi} + \frac{\partial p_c}{\partial\eta}\bar{\eta}\right).$$

Under the assumption that $\Delta(u_c,p_c) \neq 0$, the last two δ functions would give only solutions $\bar{\xi} = 0$ and

$\bar{\eta}=0$. Therefore,

$$\prod_x \delta\left(\dot{u}_c-\frac{\delta H_j}{\delta p_c}\right)\delta\left(\dot{p}_c+\frac{\delta H_j}{\delta u_c}\right) \tag{17}$$
$$=\Delta_c(\xi,\eta)\delta\left(\dot{\xi}-\frac{\delta h_j}{\delta\eta}\right)\delta\left(\dot{\eta}+\frac{\delta h_j}{\delta\xi}\right),$$

where

$$\Delta_c(\xi,\eta)=\int d\bar{\xi}d\bar{\eta}\delta\left(\frac{\partial u_c}{\partial\xi}\bar{\xi}+\frac{\partial u_c}{\partial\eta}\bar{\eta}\right)$$
$$\times\,\delta\left(\frac{\partial p_c}{\partial\xi}\bar{\xi}+\frac{\partial p_c}{\partial\eta}\bar{\eta}\right).$$

As a result, using (13) and (17), we obtain

$$DM(u,p)=DM(\xi,\eta) \tag{18}$$
$$=\prod_t d\xi d\eta\delta\left(\dot{\xi}-\frac{\delta h_j}{\delta\eta}\right)\delta\left(\dot{\eta}+\frac{\delta h_j}{\delta\xi}\right),$$

where $h_j(\xi,\eta)$ is defined by Eq. (16).

Strictly speaking, performing a transformation, one must conserve the dimension of the measure, i.e.,

$$\dim D(u,p)=\dim D(\xi,\eta).$$

This means that $D(\xi,\eta)\sim D\Omega$, where $D\Omega$ is the differential measure of none of the dynamical variables [1]. The absorption of the integral over $D\Omega$, in a sense, is equivalent to the renormalization procedure of the canonical quantization schemes of the field theories. For this reason, we omit $D\Omega$ in (18).

3.4. Quantization Scheme

We will introduce the pair of conjugate parameters

$$\begin{cases}\xi(t)=t+x_0,\\ \eta(t)=\dfrac{\pi^2}{2a}|\lambda_0|\end{cases} \tag{19}$$

as the collective variables. While the other parameters (λ_i,x_{0i}) will be the C-number parameters. The integration over them gives the zero-mode volume.

From Eq. (6), using Eq. (18), we obtain

$$\rho_0(\phi)=e^{-i\hat{K}(j,e)}\int d\Omega\prod_t d\xi d\eta\delta\left(\dot{\xi}-\frac{\delta h_j}{\delta\eta}\right)$$
$$\times\,\delta\left(\dot{\eta}+\frac{\delta h_j}{\delta\xi}\right)e^{i\tilde{S}(u_c,e)},$$

where $d\Omega=d^3\lambda d^3x_0$. This choice of dynamical variables (19) gives the following total transformed Hamiltonian:

$$h_j=\eta-\int d^3x u_c(x;\xi,\eta;\lambda)j(x,t).$$

It is useful to introduce the projection of j onto the ξ and η axes. The result looks as follows:

$$\rho_0(\phi)=e^{-i\hat{K}(j_\xi,e_\xi)}e^{-i\hat{K}(j_\eta,e_\eta)} \tag{20}$$
$$\times\int d\Omega\prod_t d\xi d\eta\delta\left(\dot{\xi}-1\right)\delta\left(\dot{\eta}\right)e^{i\tilde{S}(u_c,e_c)},$$

where

$$e_c=e_\eta\frac{\partial u_c}{\partial\xi}-e_\xi\frac{\partial u_c}{\partial\eta},$$

$$u_c=u_c\Big(\mathbf{x};\xi(t)+t+\int dt'\theta(t-t')j_\xi(t'),\eta(t)$$
$$+\int dt'\theta(t-t')j_\eta(t');\lambda\Big).$$

Noting that

$$\int\prod_t dX(t)\delta(\dot{X})=\int dX(0)\equiv\int dX_0,$$

one may perform the remaining integrations:

$$\rho_0(\phi)=e^{-i\hat{K}(j_\xi,e_\xi)}e^{-i\hat{K}(j_\eta,e_\eta)} \tag{21}$$
$$\times\int d\Omega d\xi_0 d\eta_0 e^{i\tilde{S}(u_c,e_c)},$$

where

$$u_c=u_c\Big(\mathbf{x};\xi_0+t+\int dt'\theta(t-t')j_\xi(t'),\eta_0$$
$$+\int dt'\theta(t-t')j_\eta(t');\lambda\Big),$$

and in our case

$$\tilde{S}(u_c,e_c)=-2\kappa\mathrm{Re}\int dx\phi^2e_c$$
$$-2g\mathrm{Re}\int dx u_c e_c^3.$$

4. PARTICLE PRODUCTION

4.1. Generating Functional in the Factor Space

Now, let us insert (21) into (4):

$$\rho(z,\alpha)=e^{N_+(\hat{\phi};\alpha_i,z_i)+N_-(\hat{\phi};\alpha_f,z_f)}$$
$$\times\,e^{-i\hat{K}(j_\xi,e_\xi)}e^{-i\hat{K}(j_\eta,e_\eta)}\int d\Omega d\xi_0 d\eta_0$$
$$\times\exp\left[-2i\kappa\mathrm{Re}\int dx\phi^2e_c-2ig\mathrm{Re}\int dx u_c e_c^3\right].$$

We suppose that the observables are the pairs produced from one point and, therefore, we make the

replacement $\phi^2(x) \to \phi(x)$. Then we obtain the generating functional for pair production probabilities:

$$\rho(z,\alpha) = e^{-i\hbar\hat{K}(j_{\xi,\eta},e_{\xi,\eta})} \times \int d\Omega d\xi_0 d\eta_0 e^{-N(\alpha_i,z_i)-N(\alpha_f,z_f)} \times e^{(-2ig/\hbar)\mathrm{Re}\int dx u_c e_c^3}\Big|_{j_{\xi,\eta},e_{\xi,\eta}=0}, \quad (22)$$

where

$$N(\alpha_i,z_i) = 4\hbar^2\kappa^2 \times \int \frac{d^3p e^{i\alpha_i p} z_i(p)}{(2\pi)^3 2\varepsilon(p)} \left|\int\limits_{C_+} dx e^{-ipx} e_c(x)\right|^2,$$

$$N(\alpha_f,z_f) = 4\hbar^2\kappa^2 \times \int \frac{d^3q e^{i\alpha_f q} z_f(q)}{(2\pi)^3 2\varepsilon(q)} \left|\int\limits_{C_+} dx e^{iqx} e_c(x)\right|^2.$$

4.2. Elastic Scattering

Let us show an example: $2 \to 2$ scattering. Using (22), we get

$$\rho_{2\to2}(p_1,p_2;q_1,q_2) = \frac{4^4\hbar^{16}\kappa^8 e^{i\alpha_i(p_1+p_2)} e^{i\alpha_f(q_1+q_2)}}{(2\pi)^{12}2\varepsilon(p_1)2\varepsilon(p_2)2\varepsilon(q_1)2\varepsilon(q_2)} e^{-i\hat{K}(j_{\xi,\eta},e_{\xi,\eta})} \times \int d^3x_0 d\xi_0 d\eta_0 d^3\lambda |\Gamma(p_1,e_c)|^2 |\Gamma(p_2,e_c)|^2 \times |\Gamma^*(q_1,e_c)|^2 |\Gamma^*(q_2,e_c)|^2 \times e^{-2i\hbar^2 g\mathrm{Re}\int dx u_c e_c^3}\Big|_{j_{\xi,\eta},e_{\xi,\eta}=0}. \quad (23)$$

Here, the quantum-perturbation-generating operator is

$$\hat{K}(j_{\xi,\eta},e_{\xi,\eta}) = \int\limits_{C_\pm} dt \left(\hat{j}_\xi \hat{e}_\xi + \hat{j}_\eta \hat{e}_\eta\right)$$

and

$$\Gamma(p,e_c) = \int\limits_{C_+} d^4x e^{-ipx} e_c(x),$$

$$\Gamma^*(q,e_c) = \int\limits_{C_+} d^4x e^{iqx} e_c(x),$$

$$e_c = e_\eta \frac{\partial u_c}{\partial \xi_0} - e_\xi \frac{\partial u_c}{\partial \eta_0},$$

$$u_c = u_c\Big(\mathbf{x}+\mathbf{x_0}; \xi_0 + t + \int dt' \theta(t-t') j_\xi(t'), \eta_0 + \int dt' \theta(t-t') j_\eta(t'); \lambda\Big),$$

$$\sqrt{-g}u_c(\mathbf{x},\xi,\eta,\lambda) = \left\{4h^2\varrho^2/[(\eta^2(\xi^2-\mathbf{x}^2)-\varrho^2)^2 + 4\eta^2\varrho^2(\xi\sqrt{1+\lambda^2} - x_i\lambda^i)^2]\right\}^{1/2},$$

where $\varrho = \dfrac{\pi^2}{2}\sqrt{1+\lambda^2}$.

It is evident from (23) that

$$u_c \sim \frac{1}{\sqrt{g}} \quad \Rightarrow \quad \rho_{2\to2} \sim \frac{\hbar^{16}}{g^4}C_1 + \frac{\hbar^{18}}{g^5}C_2 + \frac{\hbar^{20}}{g^6}C_3 + \ldots.$$

5. CONCLUSION

The compact expression (22) for the generating functional is analytically strict and allows us to deal with an arbitrary number of particles in the initial and final states. It has the form of a perturbation series that is generated by the operator $\exp(-i\hat{K})$.

As has already followed from $2 \to 2$ scattering, the lowest order over $\hat{K}$ in expression (23) has a large, factorially increasing, number of integrals. We analyze these terms in order to divide the problem into computable elementary parts that can be used for the fast evaluation of contributions.

In addition, we suppose that, within the limit of a high number of produced particles when equilibrium occurs, it is possible to make a good approximation and substantially simplify the expression.

REFERENCES

1. J. Manjavidze and A. Sissakian, Theor. Math. Phys. **130**, 153 (2002).
2. A. Actor, Rev. Mod. Phys. **51**, 461 (1979).
3. N. H. Christ and T. D. Lee, Phys. Rev. D **12**, 1606 (1975); E. Tomboulis, Phys. Rev. D **12**, 1678 (1975); L. Faddeev and R. Jackiw, Phys. Rev. Lett. **60**, 1692 (1988); M. Alvarez, hep-th/9702040.
4. R. Mills, *Propagators for Many-Particle Systems* (Gordon and Breach, New York, 1970).
5. B. M. Schechter, Phys. Rev. D **16**, 3015 (1977).

Physics of Atomic Nuclei, Vol. 67, No. 1, 2004, pp. 170–182. Translated from Yadernaya Fizika, Vol. 67, No. 1, 2004, pp. 167–179.

80th ANNIVERSARY OF THE BIRTH OF SPARTAK TIMOFEEVICH BELYAEV

Mechanisms of Binary and Ternary Low-Energy Fission of Nuclei with Allowance for Nonsphericity Effects

S. G. Kadmensky*

Voronezh State University, Universitetskaya pl. 1, Voronezh, 394693 Russia

Received January 13, 2003

Abstract—Within the quantum-mechanical theory of fission, wave functions for fragments of binary nuclear fission and amplitudes of partial fission widths are constructed with allowance for a strong nonsphericity of fragment-interaction potentials. It is shown that, in the strong-coupling approximation, the symmetry axes of fission fragments are oriented along the symmetry axis of a fissile nucleus. The structure of the fragment-interaction potentials is analyzed, and the mechanism that is responsible for the alignment of the spins and relative orbital angular momenta of fission fragments and which explains the emergence of high fragment-spin values in experiments is substantiated. The mechanisms in question are generalized to the case of ternary nuclear fission. The fragment-interaction potentials and fragment wave functions are investigated, along with the partial fission widths with respect to the ternary fission of nuclei.

1. INTRODUCTION

A quantum-mechanical theory of the spontaneous and low-energy induced fission of nuclei was developed in [1, 2]. This theory treats fission as the decay of a quasistationary state of a fissile nucleus within a time-independent formalism that is based on the theory of nuclear reactions [3], the unified theory of the nucleus [4], and the theory of open Fermi systems [5] and which was successfully tested in describing the protonic, alpha, and cluster decays of nuclei (see [6, 7], [8], and [9], respectively). This theory of fission relies on A. Bohr's concept of transition fission states [10] and on the application of the adiabatic approximation [1, 2, 6] to states of the nucleus that has already undergone disintegration. In the theory, the amplitudes of partial fission widths and fission phases depending on the spins, relative orbital angular momenta, and intrinsic states of fission fragments are introduced in a natural way, the law of conservation of the total fissile-nucleus spin being rigorously taken into account.

The angular distributions of fragments originating from low-energy photofission were analyzed within the proposed theory of binary fission, and it was found that these distributions deviate from the distributions predicted by A. Bohr's formula [10]. This result made it possible to substantiate [11] the appearance of high values of relative orbital angular momenta and spins of fission fragments in the experiment reported in [12]. By using experimental data on the binary fission of some nuclei, the values of P-even and P-odd asymmetries in the angular distributions of a third particle emitted in the ternary fission of the same nuclei in (n, f) reactions induced by polarized cold neutrons were predicted in [13, 14] on the basis of the theory of ternary fission [2]. The structure of the potential of the interaction between a third particle and fission fragments originating in ternary nuclear fission was analyzed in [15], and the angular distributions of a third particle with respect to the direction of light-fission-fragment emission were investigated there.

In the strong-coupling approximation [10] and with the aid of the fact that A. Bohr's formula [10] describes well the experimental angular distributions of fragments originating from binary nuclear fission, the developed theory of fission [1, 2] made it possible to conjecture, with allowance for the quantum-mechanical uncertainty principle for orbital angular momenta and the angles of particle emission, that the symmetry axes of fission fragments are aligned with the symmetry axis of the nucleus undergoing fission and that fission fragments are emitted predominantly along or against the direction of the symmetry axis of this nucleus.

In analyzing, in the present study, the wave functions for fragments from binary and ternary nuclear fission, a strong nonsphericity of fragment-interaction potentials is taken consistently into account in order to validate the ideas formulated above and to introduce the mechanism of orientation pumping of high values of relative orbital angular momenta and spins of fission fragments.

*e-mail: kadmensky@phys.vsu.ru

1063-7788/04/6701-0170$26.00

2. FISSILE-NUCLEUS WAVE FUNCTION IN THE ASYMPTOTIC REGION OF BINARY FISSION

Let us consider the binary fission of an axisymmetric nucleus, which, in the case of equilibrium deformations, is described by the wave function $\Psi^{J\pi M}_{\sigma K}$, where J is the nuclear spin; M and K are the spin projections onto, respectively, the z axis in the laboratory frame and the nuclear-symmetry axis, which coincides with the z' axis in the intrinsic coordinate frame; π is parity; and σ stands for other quantum numbers, including the atomic weight A and the charge Z of the nucleus. The asymptotic behavior of this wave function in the vicinity of the point where the nucleus disintegrates into fission fragments can be represented as [13, 14]

$$\Psi^{J\pi M}_{\sigma K} \to \sum_{tq} b^{J\pi}_{t\sigma K} c^{J\pi}_{qtK} \Psi^{J\pi M}_{qK}, \tag{1}$$

where $b^{J\pi}_{t\sigma K}$ is the amplitude describing the transition of the wave function $\Psi^{J\pi M}_{\sigma K}$ in the process of fissile-nucleus evolution associated with the variation of the deformation parameters of the nucleus to the wave function $\Psi^{J\pi M}_{tK}$ for the transition fission state defined at the saddle point of the deformation potential of the fissile nucleus [10] and $c^{J\pi}_{qtK}$ is the amplitude of the transformation of the transition fission state tK into the fission mode qK defined in the vicinity of the point where the nucleus disintegrates into fission fragments [16] and characterized by the wave function $\Psi^{J\pi M}_{qK}$. Since, for the fission process that is asymmetric in the charges and masses of nascent fission fragments, the corresponding fission mode is associated with an axisymmetric pearlike shape of the fissile nucleus at finite values of static octupole-deformation parameters, the wave function $\Psi^{J\pi M}_{qK}$ can be represented in the form [10]

$$\Psi^{J\pi M}_{qK} = \sqrt{\frac{2J+1}{16\pi^2}}[(1-\delta_{K,0})\{D^J_{MK}(\omega)\chi^\pi_{qK}(\xi) + (-1)^{J+K} D^J_{M-K}(\omega)\chi^\pi_{\overline{qK}}(\xi)\} + \delta_{K,0}\sqrt{2} D^J_{M0}(\omega)\chi^\pi_{qn}(\xi)], \tag{2}$$

where $D^J_{MK}(\omega)$ is a generalized spherical harmonic depending on the Euler angles $(\alpha, \beta, \gamma) \equiv \omega$ characterizing the orientation of the axes of the fissile nucleus with respect to the axes of the laboratory frame. For the fissile nucleus, the intrinsic functions $\chi^\pi_{qn}(\xi)$ for $K = 0$ and $\chi^\pi_{qK}(\xi)$ for $K \neq 0$, which depend on the intrinsic coordinates of the nucleus, ξ, are given by

$$\chi^\pi_{qn}(\xi) = \frac{1}{\sqrt{2}}(\psi_{qn}(\xi) + \pi\hat{p}\psi_{qn}(\xi))i^{(1-\pi)/2}, \tag{3}$$

$$\chi^\pi_{qK}(\xi) = \frac{1}{\sqrt{2}}(\psi_{qK}(\xi) + \pi\hat{p}\psi_{qK}(\xi))i^{(1-\pi)/2},$$

where $\hat{p}$ is the operator of reflection of spatial coordinates and the functions $\psi_{qn}(\xi)$ and $\psi_{qK}(\xi)$ are not parity eigenstates and correspond to a pearlike shape of the fissile nucleus. We have $\chi_{\overline{qK}}(\xi) = \tau\chi_{qK}(\xi)$, where τ is the time-inversion operator and the function $\chi_{qn}(\xi)$ is an eigenfunction of the operator τ for the eigenvalue $n = (-1)^J$ [10].

Upon the scission of the fissile nucleus and the formation of binary-fission fragments, the fission-mode wave function $\Psi^{J\pi M}_{qK}$ (2) goes over to the wave function $(\Psi^{J\pi M}_{qK})^{\rm as}$, which, by using the methods of the unified theory of the nucleus [4] and of the theory of open Fermi systems [5], can be recast into the form

$$(\Psi^{J\pi M}_{qK})^{\rm as} = \left\langle G^{J\pi M}(x, R; x', R') \left| \hat{Q}(H-E)\hat{P} \right| \Psi^{J\pi M}_{qK}(x', R') \right\rangle, \tag{4}$$

where R is the absolute value of the radius vector $\mathbf{R} = \mathbf{R}_1 - \mathbf{R}_2$ characterizing the relative motion of fission fragments, $\mathbf{R}_i$ being the c.m. coordinate of the ith fragment ($i = 1, 2$; $A_1 \leq A_2$), and x stands for the set of all coordinates of the fissile nucleus, with the exception of the coordinate R.

Formula (4) involves the divergent Green's function $G^{J\pi M}(x, R; x', R')$, which is a solution to the equation

$$\hat{Q}(H-E)\hat{Q}G^{J\pi M}(x, R; x', R') = \delta(x-x')\delta(R-R'), \tag{5}$$

where H and E are, respectively, the total Hamiltonian of the fissile nucleus and its energy and the projection operator $\hat{Q}$ has the form $\hat{Q} = 1 - \hat{P}$, with the operator $\hat{P}$ being given by

$$\hat{P} = \sum_s \left|\Psi^{J\pi M}_s\right\rangle \left\langle \Psi^{J\pi M}_s \right|.$$

The wave functions $\Psi^{J\pi M}_s$ form a complete orthonormalized basis of multiparticle shell functions that participate in the formation of stationary and quasistationary states of the fissile nucleus (including the $\sigma\pi JMK$ state under study) in the shell region of

the configuration space spanned by the coordinates (x, R), where the fissile nucleus has a compact shape and has not yet undergone a transition to fission channels.

If use is made of the orthogonal-projection method [17], the operators $\hat{Q}(H-E)\hat{P}$ and $\hat{Q}(H-E)\hat{Q}$ appearing in (4) and (5) can be replaced, by respectively, the operator H and the operator $(\tilde{H}-E)$, where $\tilde{H} = H_0 + \tilde{V}$ with $\tilde{V} = V + \chi\hat{P}$; here, V is the fission-fragment-interaction potential, H_0 is the Hamiltonian for noninteracting fragments, and $\chi \to +\infty$. In this case, one can introduce the complete orthonormalized basis of eigenfunctions $\Psi_a^{J\pi M\pm}(x, R)$ of the Hamiltonian $\tilde{H}$ that correspond to continuous energies E_a,

$$(\tilde{H} - E_a)\Psi_a^{J\pi M\pm}(x, R) = 0, \tag{6}$$

and represent the solution to Eq. (5) in the form [3]

$$G^{J\pi M}(x, R; x', R') = \sum_a \int \frac{dn_a}{dE_a} dE_a \tag{7}$$
$$\times \frac{\Psi_a^{J\pi M+}(x, R)\Psi_a^{*J\pi M-}(x', R')}{E_a - E + i\delta},$$

where the addition of $(+i\delta)$ in the denominator on the right-hand side of Eq. (7) results in that only divergent spherical waves appear in the asymptotic expression for the Green's function (7) and where integration with respect to E_a is performed with allowance for the energy density dn_a/dE_a of states a. The action of the operator $\chi\hat{P}$ in Eq. (6) results in that the wave functions $\Psi_a^{J\pi M\pm}$ become orthogonal to the fission-mode wave functions $\Psi_{qK}^{J\pi M}$ and undergo damping in the shell region of the fissile nucleus. These functions describe the potential scattering of fission fragments on each other, in which case there can arise only quasimolecular optical resonances (but not multiparticle resonances corresponding to nuclear states in the shell region).

The solution to Eq. (6) can in turn be represented in the form [3]

$$\Psi_a^{J\pi M\pm}(x, R) = \varphi_a^{J\pi M}(x, R) + \sum_b \int dE_b \frac{dn_b}{dE_b} \tag{8}$$
$$\times \frac{\varphi_b^{J\pi M}(x, R)\left\langle \varphi_b^{*J\pi M}(x', R')\left|T^{\pm}\right|\varphi_a^{J\pi M}(x', R')\right\rangle}{E_b - E_a \pm i\delta},$$

where $\varphi_a^{J\pi M}(x, R)$ is an eigenfunction of the unperturbed Schrödinger equation $(H_0 - E_a) \times \varphi_a^{J\pi M}(x, R) = 0$ and $T^{\pm}$ denotes the T matrix that satisfies the equation

$$T^{\pm} = \tilde{V} + \tilde{V}\frac{1}{E_a - H_0 \pm i\delta}T. \tag{9}$$

Following the method proposed in [3], we first construct the wave function $\varphi_a(x, R)$ that is not pure in the total spin J and which is normalized to a delta function of energy. It is taken in the form

$$\varphi_a(x, R) \equiv \varphi_{\mathbf{k}_c c\beta M_F}(x, R) \tag{10}$$
$$= \frac{1}{(2\pi)^{3/2}}\sqrt{\frac{k_c M_c}{\hbar^2}}e^{i\mathbf{k}_c\cdot\mathbf{R}}U_{c\beta M_F},$$

where $\mathbf{k}_c$ is the wave vector of the relative motion of fission fragments in the $c \equiv \sigma_1\pi_1 K_1\sigma_2\pi_2 K_2$ channel with $k_c = \sqrt{2M_c Q_c/\hbar^2}$, Q_c and M_c being, respectively, the energy and the reduced mass of fragments; $\beta \equiv J_1 J_2 F$; and $U_{c\beta M_F}$ is the channel-spin function having the form

$$U_{c\beta M_F} = \left\{\Psi_{\sigma_1 K_1}^{J_1\pi_1 M_1}(\omega_1, \xi_1)\Psi_{\sigma_2 K_2}^{J_2\pi_2 M_2}(\omega_2, \xi_2)\right\}_{FM_F}. \tag{11}$$

Here, $\Psi_{\sigma_i K_i}^{J_i\pi_i M_i}(\omega_i, \xi_i)$ is the wave function for the ith axisymmetric fission fragment; it does not involve static odd (including octupole) deformations and has the form (2) [10], where one must replace the subscripts $JMq\pi K\omega\xi$ by the subscripts $J_i M_i\sigma_i\pi_i K_i\omega_i\xi_i$ and the intrinsic wave functions χ_{qK}^{π}, $\chi_{\overline{qK}}^{\pi}$, and χ_{qn}^{π} by the corresponding intrinsic wave functions $\chi_{\sigma_i K_i}^{\pi_i}$, $\chi_{\overline{\sigma_i K_i}}^{\pi_i}$, and $\chi_{\sigma_i n_i}^{\pi_i}$ for fission fragments.

Expanding the exponential function $e^{i\mathbf{k}_c\cdot\mathbf{R}}$ in a series in spherical harmonics, we recast the wave function (10) into the form

$$\varphi_{\mathbf{k}_c c\beta M_F} = \sqrt{\frac{2}{\pi}}\sqrt{\frac{k_c M_c}{\hbar^2}}\sum_L i^L Y_{LM_L}^*(\Omega_{\mathbf{k}_c}) \tag{12}$$
$$\times Y_{LM_L}(\Omega_{\mathbf{R}})j_L(k_c R)U_{c\beta M_F},$$

where $j_L(k_c R)$ is a spherical Bessel function and the solid angle $\Omega_{\mathbf{R}} \equiv (\theta_{\mathbf{R}}, \varphi_{\mathbf{R}})$ determines the direction of the radius vector $\mathbf{R}$ in the laboratory frame.

Substituting expression (12) into Eq. (8), performing integration with respect to E_b and $\Omega_{\mathbf{k}_b}$ with allowance for the relation $dn_b/dE_b = M_b k_b d\Omega_{\mathbf{k}_b}$, and using the technique developed in [3], we can then obtain the function $\Psi_a^{J\pi M\pm}(x, R)$ that is pure in spin and which is normalized to a delta function of energy. The result is

$$\Psi_\alpha^{J\pi M\pm}(x, R) = \sum_{\alpha'} U_{\alpha'}^{J\pi M}(x)\frac{f_{\alpha'\alpha}^{J\pi\pm}(R)}{R}, \tag{13}$$

where the channel function $U_\alpha^{J\pi M}(x)$ characterized by a specific value of the total spin J of fission fragments has the form

$$U_\alpha^{J\pi M}(x) = \left\{U_{c\beta M_F} i^L Y_{LM_L}(\Omega_{\mathbf{R}})\right\}_{JM}, \tag{14}$$

with $\alpha \equiv c\beta L$, the set of coordinates x being defined as $x \equiv \omega_1, \xi_1, \omega_2, \xi_2, \Omega_{\mathbf{R}}$. The amplitude $f^{J\pi\pm}_{\alpha'\alpha}(R)$ appearing in Eq. (13) satisfies the set of coupled radial equations

$$\left(\frac{d^2}{dR^2} - \frac{L'(L'+1)}{R^2} + k_{c'}^2\right) f^{J\pi\pm}_{\alpha'\alpha}(R) - \frac{2M_{c'}}{\hbar^2}\sum_{\alpha''} \tilde{V}^{J\pi M}_{\alpha'\alpha''}(R) f^{J\pi\pm}_{\alpha''\alpha}(R) = 0, \tag{15}$$

$$\tilde{V}^{J\pi M}_{\alpha'\alpha''}(R) = \langle U^{J\pi M}_{\alpha'} | \tilde{V} | U^{J\pi M}_{\alpha''} \rangle \tag{16}$$

with the boundary conditions $f^{J\pi\pm}_{\alpha'\alpha}(R) \to 0$ for $R \to 0$ and

$$f^{J\pi\pm}_{\alpha'\alpha}(R) \to \mp\frac{1}{2i}\sqrt{\frac{2}{\pi\hbar v_c}} \times \left\{\exp\left[\mp i\left(k_c R - \frac{L\pi}{2}\right)\right]\delta_{\alpha'\alpha} \mp S^{J\pi\pm}_{\alpha'\alpha}\exp\left[\pm i\left(k_{c'}R - \frac{L'\pi}{2}\right)\right]\right\} \tag{17}$$

for $R \to \infty$; here, $v_c = \hbar k_c/M_c$. In formula (17), $S^{J\pi\pm}_{\alpha'\alpha}$ are the S-matrix elements that describe the scattering of fission fragments on each other and which are related to the operators $T^{\pm}$ (9) by the equation [3]

$$S^{J\pi\pm}_{\alpha'\alpha} = \delta_{\alpha'\alpha} \mp 2\pi i \left\langle \tilde{j}_{L'}(k_{c'}R) U^{J\pi M}_{\alpha'} \left| T^{\pm} \right| \tilde{j}_L(k_c R) U^{J\pi M}_{\alpha} \right\rangle, \tag{18}$$

where $\tilde{j}_L(k_c R) = \sqrt{2k_c M_c/\pi\hbar^2}\, j_L(k_c R)$. Upon the substitution of the wave function (13) into formula (7) and performing integration with respect to the energy E_a, we can obtain the Green's function $G^{J\pi M}(x, R; x', R')$ in the asymptotic region $R \to \infty$. The result is

$$G^{J\pi M}(x, R; x', R') = \sum_{\alpha} U^{J\pi M}_{\alpha}(x)\sqrt{\frac{M_c}{\hbar^2 k_c}} \times \frac{\exp\left[i\left(k_c R - \frac{L\pi}{2}\right)\right]}{R} \sum_{\alpha'} \left\langle U^{J\pi M}_{\alpha'}(x') \frac{\tilde{f}^{J\pi-}_{\alpha'\alpha}(R')}{R'} \right|. \tag{19}$$

In the limit $R \to \infty$, the wave function $(\Psi^{J\pi M}_{qK})^{\mathrm{as}}$ (4) is then given by

$$(\Psi^{J\pi M}_{qK})^{\mathrm{as}} = \sum_{\alpha} U^{J\pi M}_{\alpha}(x) \times \frac{\exp\left[i\left(k_c R - \frac{L\pi}{2}\right)\right]}{R}\sqrt{\frac{\Gamma^{J\pi}_{qK\alpha}}{\hbar v_c}}, \tag{20}$$

where the partial-fission-width amplitude $\sqrt{\Gamma^{J\pi}_{qK\alpha}}$ is defined as

$$\sqrt{\Gamma^{J\pi}_{qK\alpha}} = \sqrt{2\pi}\sum_{\alpha'} \left\langle U^{J\pi M}_{\alpha'} \frac{\tilde{f}^{J\pi-}_{\alpha'\alpha}(R)}{R} |H| \Psi^{J\pi M}_{qK} \right\rangle. \tag{21}$$

Formula (21) takes into account the character of fission-fragment interaction more correctly than the analogous formula for the partial-width amplitude $\sqrt{\Gamma^{J\pi}_{qK\alpha}}$ in [1].

3. MECHANISM OF ALIGNMENT OF THE SYMMETRY AXES OF FISSION FRAGMENTS WITH THE SYMMETRY AXIS OF THE FISSILE NUCLEUS

In order to obtain deeper insight into the relationship between the orientation of the symmetry axes of axisymmetric fission fragments and the orientation of the symmetry axis of the axisymmetric fissile nucleus, we use the method proposed in [1].

The structure of formula (21), which determines the partial-fission-width amplitude, leads to a serious problem. This formula involves an integral with respect to all $(3A-3)$ coordinates ω, ξ of a fissile nucleus; the wave function $\Psi^{J\pi M}_{qK}(\omega, \xi)$ depends on these coordinates, but the function $U^{J\pi M}_{\alpha'} \tilde{f}^{J\pi-}_{\alpha'\alpha}(R)/R$, which also appears in the integral in question, corresponds to already formed fission fragments and depends on the $(3A-3)$ coordinates ω_1, ξ_1, ω_2, ξ_2, and $\mathbf{R}$, which do not include the coordinate ω. In order to overcome this difficulty, we can go over, in the functions $D^{J_1}_{M_1K_1}(\omega_1)$ and $D^{J_2}_{M_2K_2}(\omega_2)$, which appear in the fission-fragment wave functions $\Psi^{J_1\pi_1 M_1}_{\sigma_1 K_1}$ and $\Psi^{J_2\pi_2 M_2}_{\sigma_2 K_2}$, to the intrinsic coordinate frame of the fissile nucleus by using the Wigner transformation

$$D^{J_i}_{M_iK_i}(\omega_i) = \sum_{K_i'} D^{J_i}_{M_iK_i'}(\omega) D^{J_i}_{K_i'K_i}(\omega_i'), \tag{22}$$

where ω_i' are the Euler angles determining the orientation of the symmetry axis of the ith fragment with respect to the symmetry axis of the fissile nucleus. Substituting formula (22) into the channel function $U^{J\pi M}_{\alpha}$ (14) and multiplying it by a continuous function $\varphi(\omega_{21})$ depending on the Euler angles ω_{21} of the second fragment with respect to the symmetry axis of the first fragment and satisfying the condition $\varphi(0) = 1$, one can obtain a new channel function $U^{J\pi M}_{\alpha}(x_1)$, which, upon the multiplication by the function $\tilde{f}^{J\pi-}_{\alpha'\alpha}(R)/R$, becomes dependent on

the set of coordinates x_1, $R \equiv \omega$, ω_{21}, ω'_1, ω'_2, ξ_1, ξ_2, and $\mathbf{R}$. With an eye to performing integration in formula (21) with respect to the coordinates ω and ξ and under the assumption that, for the spontaneous and low-energy induced fission of nuclei, the main contribution to the partial-width amplitude (21) comes from the components of the fissile-nucleus Hamiltonian H that are diagonal in the intrinsic wave functions for fission fragments, it is natural to represent the set of intrinsic coordinates ξ of the fissile nucleus in the form $\xi \equiv \omega_{21}, \xi_1, \xi_2, \mathbf{R}$, where the coordinates ξ_1 and ξ_2 correspond to the intrinsic coordinates of fission fragments in the channel function $U_\alpha^{J\pi M}(x_1)$. In this case, the set of coordinates on which the channel function $U_{\alpha'}^{J\pi M}(x_1)\tilde{f}_{\alpha'\alpha}^{J\pi-}(R)/R$ depends will include two extra (with respect to the set of coordinates ξ) coordinates ω'_1 and ω'_2, which, in performing integration involving this function in formula (21), can be considered as parameters on which the partial-width amplitude $\sqrt{\Gamma_{qK\alpha}^{J\pi}(\omega'_1,\omega'_2)}$ obtained in this case depends. Upon the substitution of the channel functions $U_\alpha^{J\pi M}(x_1)$ and the amplitudes $\sqrt{\Gamma_{qK\alpha}^{J\pi}(\omega'_1,\omega'_2)}$ into formula (20), the resulting wave function $(\Psi_{qK}^{J\pi M}(\omega,\omega_{12},\omega'_1,\omega'_2,\xi_1,\xi_2,\mathbf{R}))^{\mathrm{as}}$ will then also become dependent on two extra variables ω'_1 and ω'_2. In order to compensate this dependence, it is necessary, in going over [1] from the multidimensional flux density $\mathbf{j}_{qK}^{J\pi M}(\omega,\omega_{12},\omega'_1,\omega'_2,\xi_1,\xi_2,\mathbf{R})$ obtained by using the wave function in the asymptotic form $(\Psi_{qK}^{J\pi M}(\omega,\omega_{12},\omega'_1,\omega'_2,\xi_1,\xi_2,\mathbf{R}))^{\mathrm{as}}$ to the observed fission-fragment flux density $\mathbf{j}_{qK}^{J\pi M}(\mathbf{R})$ in the direction of the radius vector $\mathbf{R}$, to perform integration with respect to the extra coordinates ω'_1 and ω'_2 in addition to the integration with respect to the variables ω, ω_{12}, ξ_1, and ξ_2.

Before performing the aforementioned integration, we explicitly isolate, in the partial-fission-width amplitude $\sqrt{\Gamma_{qK\alpha}^{J\pi}(\omega'_1,\omega'_2)}$ (21), the overlap integral A_{qKc}^{π} of the intrinsic functions for fission fragments and a fissile nucleus; that is,

$$A_{qKc}^{\pi}(\omega,\omega_{12},\omega'_1,\omega'_2,\mathbf{R}) \qquad (23)$$
$$= \int d\xi_1 d\xi_2 \chi_{\sigma_1 K_1}^{*\pi_1}(\xi_1(\omega_1))\chi_{\sigma_2 K_2}^{*\pi_2}(\xi_2(\omega_2))\chi_{\sigma K}^{\pi}(\xi(\omega)),$$

where the relation between the intrinsic coordinates ξ_1, ξ_2, and ξ and the symmetry axes of the corresponding nuclei that is associated with the use of the strong-coupling approximation in constructing the intrinsic wave functions for axisymmetric deformed nuclei on the basis of the generalized model of the nucleus [10] is present in an explicit form. If the atomic weights (A_i) of fission fragments are rather large ($A_i \gg 1$), it can be stated that, even in the presence of a neck in the prescission configuration of a fissile nucleus, the overlap integral (23) will have, to a high degree of precision, the form

$$A_{qKc}^{\pi}(\omega,\omega_{12},\omega'_1,\omega'_2,\mathbf{R}) \qquad (24)$$
$$= A_{qKc}^{\pi}(\mathbf{R})\delta^{1/2}(\omega'_1)\delta^{1/2}(\omega'_2)\delta^{1/2}(\omega_{12}),$$

where $\delta^{1/2}(x)$ is the amplitude of the delta function $\delta(x)$.

Upon the substitution of this overlap integral into the integral in (21), the partial-width amplitude $\sqrt{\Gamma_{qK\alpha}^{J\pi}(\omega'_1,\omega'_2)}$ takes the form

$$\sqrt{\Gamma_{qK\alpha}^{J\pi}(\omega'_1,\omega'_2)} = \sqrt{\Gamma_{qK\alpha}^{J\pi}(0,0)}\delta^{1/2}(\omega'_1)\delta^{1/2}(\omega'_2). \qquad (25)$$

The presence of the delta-function amplitudes in (25) makes it possible to calculate the observed flux density $\mathbf{j}_{qK}^{J\pi M}(\mathbf{R})$ in a simplified form by using the modified channel functions $U_\alpha^{J\pi M}(\bar{x})$ and the modified partial-width amplitudes $\sqrt{\bar{\Gamma}_{qK\alpha}^{J\pi}}$. The functions $U_\alpha^{J\pi M}(\bar{x})$, which depend on the set of coordinates $\bar{x} \equiv \omega, \xi_1, \xi_2, \mathbf{R}$, are obtained from the channel functions $U_\alpha^{J\pi M}(x)$ (14) under the condition $\omega_1 = \omega_2 = \omega$. The amplitudes $\sqrt{\bar{\Gamma}_{qK\alpha}^{J\pi}}$ are given by formula (21), where integration is performed with respect to the set of variables ω, ω_{12}, ξ_1, ξ_2, and $\mathbf{R}$; the modified channel functions $U_\alpha^{J\pi M}(\bar{x})$ and the function $\delta^{1/2}(\omega_{12})\Psi_{qK}^{J\pi M}(\omega,\xi)$ are used instead of the channel functions $U_\alpha^{J\pi M}(x)$ (14) and the wave function $\Psi_{qK}^{J\pi M}(\omega,\xi)$, respectively; and the fissile-nucleus Hamiltonian $H(\omega_1,\xi_1,\omega_2,\xi_2,\mathbf{R})$ is replaced by the same Hamiltonian at $\omega_1 = \omega_2 = \omega$. The radial functions $\tilde{f}_{\alpha'\alpha}^{J\pi-}(R)$ entering into the integral in (21) are now calculated by solving a set of coupled equations that belongs to the type in (15), but in which the fission-fragment-interaction potential $V(\omega_1,\xi_1,\omega_2,\xi_2,\mathbf{R})$ is replaced in the matrix element $\tilde{V}_{\alpha'\alpha''}^{J\pi M}(R)$ (16) by the same potential at $\omega_1 = \omega_2 = \omega$.

The physical meaning of the result obtained in this way is as follows. Because of the effect of the strong-coupling approximation [10], the fission-fragment axes are oriented strictly along the symmetry axis of a fissile nucleus. The presence of a neck in the prescission configuration of a fissile nucleus can lead to some small deviations of the Euler angles ω_1 and ω_2 from the Euler angles ω. However, the stiffness coefficients for these deviations at $A_1, A_2 \gg 1$ are very large, which leads to very high energies of bending

vibrations in the prescission configuration of a fissile nucleus. Because of the condition $\omega_1 = \omega_2 = \omega$, there are virtually no similar vibrations in the region of already formed fission fragments as well. Since the condition $\omega_1 = \omega_2 = \omega$ was used in [1], the results of that study remain in force.

4. STRUCTURE OF THE POTENTIAL DESCRIBING THE INTERACTION OF BINARY-FISSION FRAGMENTS

The potential $V_c(\mathbf{R}, \omega_1, \omega_2)$ that describes the interaction of fragments originating from the binary fission of nuclei and which is diagonal in the channel index c can be represented as the sum of the Coulomb potential $V_c^{\mathrm{Coul}}(\mathbf{R}, \omega_1, \omega_2)$ and the nuclear potential $V_c^{\mathrm{nucl}}(\mathbf{R}, \omega_1, \omega_2)$. For the nuclear potential $V_c^{\mathrm{nucl}}(\mathbf{R}, \omega_1, \omega_2)$, one can use the real part of the averaged optical nuclear potential of fission-fragment interaction. As was shown within the theory of open Fermi systems [5], this potential coincides with the generalized Hartree–Fock potential. The respective expression was constructed in [18] on the basis of the theory of finite Fermi systems [19] for zero-range effective interactions in the particle–hole channel. The result can be written as

$$V_c^{\mathrm{nucl}}(\mathbf{R}, \omega_1, \omega_2) = A_1 A_2 C_0 \left[\frac{F_{\mathrm{in}} - F_{\mathrm{ex}}}{\rho_0}\right. \quad (26)$$
$$\times \left(\int \rho_1^2(\mathbf{r})\rho_2(\mathbf{R}+\mathbf{r})d\mathbf{r} + \int \rho_1(\mathbf{r})\rho_2^2(\mathbf{R}+\mathbf{r})d\mathbf{r}\right)$$
$$\left. + F_{\mathrm{ex}} \int \rho_1(\mathbf{r})\rho_2(\mathbf{R}+\mathbf{r})d\mathbf{r}\right],$$

where C_0, F_{in}, F_{ex}, and ρ_0 are constants [19] and the vectors $\mathbf{r}$ and $(\mathbf{R}+\mathbf{r})$ are drawn from the centers of mass of the corresponding fragments.

Let us represent the single-particle nucleon density in an axisymmetric deformed fragment as

$$\rho_i(\mathbf{r}) = \rho_0 \left[1 + \exp\left(\frac{r - R_{A_i}(\mathbf{r}, \omega_i)}{a}\right)\right]^{-1}, \quad (27)$$

where

$$R_{A_i}(\mathbf{r}, \omega_i) = R^0_{A_i}\left[1 + \beta_2^{(i)} B(\mathbf{r}, \omega_i)\right]. \quad (28)$$

If use is made of the Wigner transformation from the intrinsic coordinate frame of the respective fragment to the laboratory frame, the quantity $B(\mathbf{r}, \omega_i)$ is given by

$$B(\mathbf{r}, \omega_i) = Y_{20}(\theta_i) = \sum_m D^{*2}_{m0}(\omega_i) Y_{2m}(\Omega_{\mathbf{r}}), \quad (29)$$

where θ_i is the angle between the vector $\mathbf{r}$ and the symmetry axis of the ith fragment. Considering that the deformation parameters $\beta_2^{(i)}$ of fission fragments are rather small, we expand the functions $\rho_i(\mathbf{r})$, $\rho_i^2(\mathbf{r})$, $\rho_i(\mathbf{R}+\mathbf{r})$, and $\rho_i^2(\mathbf{R}+\mathbf{r})$ in series in these parameters to the first-order terms. By way of illustration, we present the expansion of the function $\rho_i(\mathbf{R}+\mathbf{r})$:

$$\rho_i(\mathbf{R}+\mathbf{r}) = \rho_i^0(|\mathbf{R}+\mathbf{r}|) \quad (30)$$
$$+ \frac{\partial \rho_i^0(|\mathbf{R}+\mathbf{r}|)}{\partial R^0_{A_i}} R^0_{A_i} \beta_2^{(i)} B(\mathbf{R}+\mathbf{r}, \omega_i) + \ldots.$$

For the function $Y_{2m}(\Omega_{\mathbf{R}+\mathbf{r}})$ appearing in the definition of the quantity $B(\mathbf{R}+\mathbf{r}, \omega_i)$, we can use the formula [20]

$$Y_{2m}(\Omega_{\mathbf{R}+\mathbf{r}}) = \frac{1}{|\mathbf{R}+\mathbf{r}|^2}$$
$$\times \sum_{LM} S_L R^{2-L} r^L (-1)^L Y_{LM}(\Omega_{\mathbf{r}}) Y_{2-L,m-M}(\Omega_{\mathbf{R}}),$$

where

$$S_L = \left[\frac{(4\pi)5!}{(2L+1)(5-2L)!}\right]^{1/2} C^{2m}_{(2-L)L(m-M)M}.$$

By expanding functions of $|\mathbf{R}+\mathbf{r}|$ that enter into formulas of the type in (30) in series in the spherical harmonics

$$Y_{l0}(\theta_{\mathbf{rR}}) = \sum_m Y_{lm}(\Omega_{\mathbf{R}}) Y^*_{lm}(\Omega_{\mathbf{r}}) \sqrt{\frac{4\pi}{2l+1}}$$

and substituting the resulting expansions into formula (26), we can represent the potential $V_c^{\mathrm{nucl}}(\mathbf{R}, \omega_1, \omega_2)$ in the form

$$V_c^{\mathrm{nucl}}(\mathbf{R}, \omega_1, \omega_2) = V_{c0}^{\mathrm{nucl}}(R) \quad (31)$$
$$+ \sum_{i=1}^{2} V_{ci}^{\mathrm{nucl}}(R) \beta_2^{(i)} B(\mathbf{R}, \omega_i)$$

($\theta_{\mathbf{rR}}$ is the angle between the vectors $\mathbf{r}$ and $\mathbf{R}$).

The Coulomb potential of fission-fragment interaction, $V_c^{\mathrm{Coul}}(\mathbf{R}, \omega_1, \omega_2)$, is given by

$$V_c^{\mathrm{Coul}}(\mathbf{R}, \omega_1, \omega_2) = Z_1 Z_2 e^2 \quad (32)$$
$$\times \iint \frac{\rho_1(\mathbf{r}_1)\rho_2(\mathbf{r}_2)}{|\mathbf{R}+\mathbf{r}_1-\mathbf{r}_2|} d\mathbf{r}_1 d\mathbf{r}_2.$$

Since the condition $R > |\mathbf{r}_1 - \mathbf{r}_2|$ is satisfied upon the scission of a fissile nucleus into fission fragments, the function $|\mathbf{R}+\mathbf{r}_1-\mathbf{r}_2|^{-1}$ can be expanded in a series in powers of $|\mathbf{r}_1 - \mathbf{r}_2|/R$. To the second-order terms inclusive, we have

$$|\mathbf{R}+\mathbf{r}_1-\mathbf{r}_2|^{-1} = \frac{1}{R} + \frac{\mathbf{R}(\mathbf{r}_1-\mathbf{r}_2)}{R^3} \quad (33)$$
$$+ \frac{3(\mathbf{R}, \mathbf{r}_1-\mathbf{r}_2)^2 - R^2(\mathbf{r}_1-\mathbf{r}_2)^2}{2R^5} + \ldots.$$

Substituting the expansion in (33) into (32), considering that the fragment densities possess the property $\rho(\mathbf{r}_i) = \rho(-\mathbf{r}_i)$ because of parity conservation, and using expansions of the type in (30), we can reduce the potential $V_c^{\mathrm{Coul}}(\mathbf{R}, \omega_1, \omega_2)$ to a form that is similar to that which was previously obtained in [18]. The result is

$$V_c^{\mathrm{Coul}}(\mathbf{R}, \omega_1, \omega_2) = \frac{Z_1 Z_2 e^2}{R} + \frac{3}{5}\frac{Z_1 Z_2 e^2}{R^3}\sum_{i=1}^{2}\beta_2^{(i)}(R_{A_i}^0)^2 B(\mathbf{R}, \omega_i). \quad (34)$$

5. MECHANISM OF ALIGNMENT OF SPINS AND RELATIVE ORBITAL ANGULAR MOMENTA OF FISSION FRAGMENTS

The nonspherical part of the fission-fragment-interaction potential $V_c(\mathbf{R}, \omega_1, \omega_2)$ given by (31) and (34) does not depend on the quantities

$$N^I(\omega_1, \omega_2) = \sum_m D_{m0}^I(\omega_1) D_{m0}^{*I}(\omega_2),$$

which are associated with the direct interaction of the fission-fragment spins with each other. In the potential $V_c(\mathbf{R}, \omega_1, \omega_2)$, such dependences arise only in small terms of second and higher orders in the deformation parameter $\beta_2^{(i)}$. This means that the structure of the fission-fragment-interaction potential cannot lead to the appearance of the mechanism considered in [21], where the orientation pumping of the fission-fragment spins was due to the emergence of terms depending on structures of the form $N^I(\omega_1, \omega_2)$.

The nonsphericity of the fission-fragment-interaction potential $V_c(\mathbf{R}, \omega_1, \omega_2)$ is entirely due to terms that linearly depend on the quantities $B(\mathbf{R}, \omega_i)$ given by (29) with the substitution of $\mathbf{R}$ for $\mathbf{r}$, which describe the coupling of the relative angular momenta and spins of fission fragments.

In order to obtain deeper insight into this coupling, we will investigate in greater detail the properties of the quantity $B(\mathbf{R}, \omega_i)$, which does not change the projection of the spin of a fission fragment onto its symmetry axis, because it involves the Wigner function $D_{m0}^{*2}(\omega_i)$ corresponding to zero value of this projection. Since the quantity $B(\mathbf{R}, \omega_i)$ is a scalar (that is, it remains invariant upon going over from one coordinate frame to another) because of a scalar character of the fission-fragment-interaction potential $V_c(\mathbf{R}, \omega_1, \omega_2)$, it does not change the total spin of the system undergoing fission. Indeed, the quantity $B(\mathbf{R}, \omega_i)$ can be represented in the form

$$B(\mathbf{R}, \omega_i) = \sqrt{4\pi} \times \sum_{mJ} C_{22-mm}^{J0} Y_{2-m}(\beta_i, \alpha_i) Y_{2m}(\theta_{\mathbf{R}}, \varphi_{\mathbf{R}}) \delta_{J,0}, \quad (35)$$

where β_i and α_i are the Euler angles appearing in the definition of ω_i. It directly follows from the representation in (35) that the total spin J related to the quantity $B(\mathbf{R}, \omega_i)$ is equal to zero. Therefore, the nonspherical terms of the potential $V_c(\mathbf{R}, \omega_1, \omega_2)$, which are associated with the quantity $B(\mathbf{R}, \omega_i)$, can change the relative orbital angular momentum $\mathbf{L}$ of fission fragments by the positive-parity quantity $\Delta\mathbf{L}_i$, provided that the spin of the ith fragment, $\mathbf{J}_i$, changes simultaneously by the quantity $\Delta\mathbf{J}_i = -\Delta\mathbf{L}_i$, the projections of the spin $\Delta\mathbf{J}_i$ and of the relative orbital angular momentum $\Delta\mathbf{L}_i$ onto the symmetry axis of the ith fragment being equal to zero. The inclusion of nonspherical terms of the potential $V_c(\mathbf{R}, \omega_1, \omega_2)$ may lead to the emergence of a mechanism that generates high values of the relative orbital angular momentum and spins of fission fragments. In order to understand the nature of this mechanism, we make use of the results presented in the preceding section, where we have shown that, because of the effects of the strong-coupling approximation for the intrinsic wave functions of fission fragments and a fissile nucleus, the symmetry axes of the fission fragments are aligned with the symmetry axis of the nucleus undergoing fission. It immediately follows that the fission-fragment-interaction potential must be calculated under the condition $\omega_1 = \omega_2 = \omega$, in which case one can represent this potential in the form $V_c(R, \theta_\omega)$ (where θ_ω is the angle between the direction of the radius vector $\mathbf{R}$ and the symmetry axis of the nucleus undergoing fission) and determine it with the aid of formulas (31) and (34), where the quantity $B(\mathbf{R}, \omega)$ is substituted for $B(\mathbf{R}, \omega_i)$. But in this case, the mechanism generating relative orbital angular momenta and spins of fragments that was proposed in [18] and which is associated with the emergence of bending vibrations of fission fragments with respect to the radius vector $\mathbf{R}$, whose direction is actually assumed to be coincident with the direction of the symmetry axis of the nucleus undergoing fission, cannot be realized in principle. Instead of this mechanism, there arises a mechanism aligning the relative orbital angular momentum and spins of fission fragments that is associated with oscillations of the radius vector $\mathbf{R}$ about the symmetry axis of the nucleus undergoing fission.

The above alignment mechanism may be due to the nonsphericity of the Coulomb barrier that, upon the summation of the nuclear potential $V_c^{\mathrm{nucl}}(R, \theta_\omega)$ and the Coulomb potential $V_c^{\mathrm{Coul}}(R, \theta_\omega)$ of fission-fragment interaction, emerges at minimal values of the modulus of the radius vector $R = R_m(\theta_\omega)$ (which

are dependent on the angle θ_ω), where the nuclear potential $V_c^{\rm nucl}(R,\theta_\omega)$ virtually vanishes,

$$R_m(\theta_\omega) = R^0_{A_1}(1+\beta_2^{(1)}Y_{20}(\theta_\omega)) + R^0_{A_2}(1+\beta_2^{(2)}Y_{20}(\theta_\omega)) + s. \quad (36)$$

Here, the quantity s is associated with the presence of a neck in the prescission configuration of the nucleus undergoing fission and is estimated [18] at $s = 0.5$ fm and the radius $R^0_{A_i}$ can be represented as $R^0_{A_i} = 1.4A_i^{1/3}$ fm. Expanding the spherical harmonic $Y_{20}(\theta_\omega)$ in a series in the angles θ_ω to first-order terms, we recast the quantity $R_m(\theta_\omega)$ (36) into the form

$$R_m(\theta_\omega) = R_m - \sqrt{\frac{5}{4\pi}}\frac{3}{2}\sum_{i=1}^{2} R^0_{A_i}\beta_2^{(i)}\theta_\omega^2.$$

Upon substituting this value of $R_m(\theta_\omega)$ into expression (34) for the potential $V_c^{\rm Coul}(R,\theta_\omega)$ at $\omega_1 = \omega_2 = \omega$ and expanding the respective potential in powers of θ_ω^2 to first-order terms, we can derive an expression for the maximum of the Coulomb barrier $B^{\rm Coul}(\theta_\omega)$ as a function of the angle θ_ω. The result is

$$B^{\rm Coul}(\theta_\omega) = B_0^{\rm Coul} + \frac{C\theta_\omega^2}{2}, \quad (37)$$

where

$$B_0^{\rm Coul} = \frac{Z_1Z_2e^2}{R_m} \times \left\{1 + \frac{1}{R_m^2}\sum_{i=1}^{2}(R^0_{A_i})^2\left(\frac{9}{20\pi}\right)^{1/2}\beta_2^{(i)}\right\}, \quad (38)$$

$$C = \frac{Z_1Z_2e^2}{R_m}\sqrt{\frac{5}{4\pi}}\sum_{i=1}^{2}\beta_2^{(i)}\left[\frac{3R^0_{A_i}}{R_m} - \frac{9}{5}\frac{(R^0_{A_i})^2}{R_m^2}\right]. \quad (39)$$

Relating the atomic weights A_i and the nuclear charges Z_i to the mass and charge asymmetries ($\Delta A = A_2 - A_1$ and $\Delta Z = Z_2 - Z_1$, respectively) of fission fragments as

$$A_1 = \frac{A-\Delta A}{2}, \quad A_2 = \frac{A+\Delta A}{2}, \quad Z_1 = \frac{Z-\Delta Z}{2}, \quad Z_2 = \frac{Z+\Delta Z}{2}, \quad (40)$$

we can expand the functions in (37) in powers of $\Delta Z/Z$ and $\Delta A/A$. Considering that the maximum values of $\Delta Z/Z$ and $\Delta A/A$ for the spontaneous and low-energy induced fission of $A \approx 240$ nuclei are about 0.2, one can retain, in this expansion, only terms of zeroth order of smallness, whereupon, for the quantities C and R_m, one obtains the values of $C \approx 100$ MeV and $R_m = 17$ fm at $A_1 = A_2 = A/2 \approx 120$, $Z_1 = Z_2 = Z/2 \approx 46$, and $\beta_2^{(1)} \approx \beta_2^{(2)} \approx 0.3$.

For small angles θ_ω, the Schrödinger equation for the relative orbital motion of fission fragments in the intrinsic coordinate frame of a fissile nucleus can be represented, by analogy with [21], in the form

$$\left[-\frac{\hbar^2}{2MR_m^2}\frac{1}{\theta_\omega}\frac{\partial}{\partial\theta_\omega}\left(\theta_\omega\frac{\partial}{\partial\theta_\omega}\right) - \frac{\hbar^2}{2MR_m^2}\frac{1}{\theta_\omega^2}\frac{\partial^2}{\partial\varphi_\omega^2} + \frac{C\theta_\omega^2}{2} - \varepsilon\right]\Psi_\varepsilon(\theta_\omega,\varphi_\omega) = 0, \quad (41)$$

where M is the reduced mass of fission fragments, $M = mA/4 \simeq 60m$, m being the nucleon mass. Solutions to Eq. (41) describe oscillations of the direction of the radius vector $\mathbf{R}$ about the symmetry axis of a fissile nucleus in the angles θ_ω. For the ground state of these oscillations, the energy is $\varepsilon = \varepsilon_0$, the corresponding wave function $\Psi_0(\theta_\omega,\varphi_\omega)$ normalized with respect to the phase-space element $\sin\theta_\omega d\theta_\omega d\varphi_\omega$ being given by

$$\Psi_0(\theta_\omega,\varphi_\omega) = \sqrt{\frac{\gamma}{\pi}}\exp\left[-\frac{\gamma\theta_\omega^2}{2}\right], \quad (42)$$

where $\gamma = M\varepsilon_0R_m^2/\hbar^2 = 196$ and $\varepsilon_0 = \hbar\sqrt{C/M} = 0.5$ MeV.

For the Schrödinger Eq. (41) at the fixed radius vector $R = R_m$ to be applicable to the problem being considered, it is necessary that, over a time period commensurate with the period of oscillations $T = \hbar/\varepsilon_0$, the distance R between the centers of mass of fission fragments whose relative velocity is $v(R)$ change by a quantity much less than R_m, this corresponding to fulfillment of the condition

$$\frac{\hbar}{\varepsilon_0}\frac{v(R_m)}{R_m} = \frac{E^{\rm kin}(R_m)}{\varepsilon_0\,[k(R_m)R_m]} \ll 1, \quad (43)$$

where $E^{\rm kin}(R_m)$ and $k(R_m)$ are, respectively, the kinetic energy and the wave vector of the relative motion of fragments at $R = R_m$ [$E^{\rm kin}(R_m) = (Q_c - B_0^{\rm Coul} - \varepsilon_0)$, with Q_c being the energy of the relative motion of fragments for the fission channel c being investigated]. If, for the quantity $E^{\rm kin}(R_m)$, one uses the estimate from [22], $E^{\rm kin}(R_m) \le 10$ MeV, the left-hand side of the inequality in (43) assumes a value not exceeding 0.2, which is quite sufficient for fulfillment of condition (43).

Expanding the function in (42) in terms of spherical harmonics $Y_{L0}(\theta_\omega,\varphi_\omega)$, one can obtain [23]

$$\Psi_0(\theta_\omega,\varphi_\omega) = \sum_L b_L Y_{L0}(\theta_\omega,\varphi_\omega), \quad (44)$$

where

$$b_L = \frac{(2L+1)}{\gamma}\frac{(2L+0.5)^4}{\gamma^2}\exp\left\{-\frac{(2L+0.5)^2}{\gamma}\right\}, \quad (45)$$

with $\sum_L b_L^2 = 1$. It follows that the angular component of the wave function for the relative motion of fragments can be represented in the form (44), which reflects the fact that, in the case where the radius vector **R** is aligned with the symmetry axis of the nucleus undergoing fission, the relative orbital angular momenta **L** of fission fragments have vanishing projections K_L onto this symmetry axis ($K_L = 0$).

The wave function (44) was used in constructing fission widths and angular distributions of binary-fission fragments in [1, 13–15], where it was corrected to take into account the law of parity-conservation in fission. For a pearlike shape of a fissile nucleus described by the wave function (4), this law leads to the selection rule $(-1)^L = \pi$, whence it follows that, instead of the function in (44), it is necessary to use a function of the form

$$\Psi_0(\theta_\omega, \varphi_\omega) = \sum_L b_L Y_{L0}(\theta_\omega, \varphi_\omega)\left[\frac{1+\pi(-1)^L}{2}\right]. \quad (46)$$

In order to describe the normalized (to unity) amplitude of the angular distribution of nuclear-fission fragments in the intrinsic coordinate frame, use was made in [1] of a function $\Psi_0(\theta_\omega, \varphi_\omega)$ that differs from that in (46) only by the sharp-cutoff approximation; that is,

$$\Psi_0(\theta_\omega, \varphi_\omega) \quad (47)$$
$$= \sum_L \tilde{b}_L \Theta(L_m - L) Y_{L0}(\theta_\omega, \varphi_\omega)\left[\frac{1+\pi(-1)^L}{2}\right],$$

where $\Theta(L_m - L)$ is the Heaviside step function and

$$\tilde{b}_L = \sqrt{2L+1} \quad (48)$$
$$\times \left[\sum_L (2L+1)\Theta(L_m - L)\left[\frac{1+\pi(-1)^L}{2}\right]\right]^{1/2}.$$

If the maximum value L_m in formula (47) is found from the condition requiring the coincidence of the expectation values $\langle L\rangle$ and $\langle L(L+1)\rangle$ calculated by the formulas

$$\langle L\rangle = \sum_L L b_L^2, \quad \langle L(L+1)\rangle = \sum_L L(L+1) b_L^2$$

for the distributions in (46) and (47), there arises, for L_m, the estimate $L_m \approx 2\sqrt{\gamma} \approx 30$. So large a value of L_m is rather close to that which lies in the range $20 < L_m < 25$ and which was found in [11] from an analysis of the deviations of the angular distributions of photofission fragments from the distributions predicted by A. Bohr's formula [10], which arises if use is made of the wave functions (46) and (47) for $\gamma, L_m \to \infty$. As was indicated in [11], the values obtained above for L_m make it possible to substantiate an approximate validity of A. Bohr's formula [10] and to explain the origin of high values observed experimentally in [12] for the average spins of fission fragments. It should be noted that the values found for L_m may increase somewhat upon taking into account nonzero temperatures T_0 for the prescission fissile-nucleus configuration occurring in a thermodynamic equilibrium [18]. For the spontaneous and low-energy induced fission of nuclei, however, the temperature T_0 must be much less than 1 MeV, which is not expected to change the values obtained above for L_m strongly.

With the aid of these results, one can consistently substantiate the computational formulas used in [1, 13–15] to describe the properties of binary fission of nuclei and to confirm the ideas of nuclear fission that were developed in [24].

6. STRUCTURE OF WAVE FUNCTIONS AND PARTIAL-WIDTH AMPLITUDES FOR TERNARY FISSION OF NUCLEI

By using the methods of the unified theory of the nucleus [4], the theory of open Fermi systems [5], and the theory of three-body nuclear reactions [25, 26] and the results presented in [2], the asymptotic form $(\Psi_{qK}^{J\pi M})^{\text{as}}$ of the wave function $\Psi_{qK}^{J\pi M}$ for the fission mode of ternary fission in the region where two fragments and a third particle (below, we take an alpha particle for a third one) have already been formed can be represented, as in the case of binary fission, by formula (4), where the divergent Green's function $G^{J\pi M}(\tilde{x}, \rho; \tilde{x}', \rho')$ now depends on the three-particle set of coordinates $\tilde{x}$ and ρ. The coordinates $\tilde{x} \equiv \omega_1, \xi_1, \omega_2, \xi_2, \Omega_{\mathbf{r}}, \Omega_{\mathbf{R}}, \varepsilon$ and ρ take into account the appearance of the radius vector **r** characterizing the motion of the alpha particle with respect to the center of mass of two ternary-fission fragments and having the form

$$\mathbf{r} = \mathbf{R}_3 - \frac{A_1\mathbf{R}_1 + A_2\mathbf{R}_2}{A_1 + A_2}.$$

The coordinates ρ and ε are given by [25, 26]

$$R = \sqrt{\frac{M_c}{M_a}}\rho\sin\varepsilon, \quad r = \sqrt{\frac{M_c}{M_b}}\rho\cos\varepsilon,$$

where the angle ε varies within the range $0 \le \varepsilon \le \pi/2$ and the quantities M_a, M_b, and M_c have the form

$$M_a = \frac{A_1A_2}{A_1 + A_2}m, \quad M_b = \frac{A_3(A_1 + A_2)}{A}m,$$

$$M_c = \sqrt{M_a M_b}.$$

All of the results obtained above for the binary fission of nuclei and given in formulas (13)–(21) can now be generalized to the case of ternary nuclear fission if, instead of the two-particle channel function $U_\alpha^{J\pi M}(x)$ (14), we use the three-particle channel function $U_{\tilde\alpha}^{J\pi M}(\tilde x)$ in the form

$$U_{\tilde\alpha}^{J\pi M}(\tilde x) = \left\{\left\{\left\{\Psi_{\sigma_1 K_1}^{J_1\pi_1 M_1}(\omega_1,\xi_1)\Psi_{\sigma_2 K_2}^{J_2\pi_2 M_2}(\omega_2,\xi_2)\right\}_{FM_F} i^L Y_{LM_L}(\Omega_{\mathbf{R}})\right\}_{J_0M_0} i^l Y_{lM_l}(\Omega_{\mathbf{r}})\right\}_{JM} \frac{Y_{c\lambda Ll}(\varepsilon)}{\sin\varepsilon\cos\varepsilon}, \tag{49}$$

where the subscript $\tilde\alpha$ is defined as $\tilde\alpha = \alpha l\lambda$; l is the relative orbital angular momentum of the third particle; the subscript λ takes the values of $\lambda = 0, 1, 2...$; and the function $Y_{c\lambda Ll}(\varepsilon)$, which is normalized in the space of the angles ε, is expressed in terms of Jacobi orthogonal polynomials [25, 26]. Instead of the function $f_{\alpha'\alpha}^{J\pi-}(R)/R$ (15), it is then necessary to use the function $\tilde f_{\tilde\alpha'\tilde\alpha}^{J\pi-}(\rho)/\rho^{5/2}$ that is normalized to a delta function of energy and which, at $k_c = \sqrt{2M_cQ_c/\hbar^2}$ and $v_c = \hbar k_c/M_c$ (where Q_c is the total energy of the relative motion of fission fragments in the channel c), is obtained by solving the set of coupled equations

$$\left(\frac{d^2}{d\rho^2} + k_{c'}^2\right)\tilde f_{\tilde\alpha'\tilde\alpha}^{J\pi-}(\rho) - \frac{2M_{c'}}{\hbar^2}\sum_{\tilde\alpha''}\tilde V_{\tilde\alpha''\tilde\alpha'}^{J\pi M}(\rho)\tilde f_{\tilde\alpha''\tilde\alpha'}^{J\pi-}(\rho) = 0, \tag{50}$$

with the boundary condition $\tilde f_{\tilde\alpha'\tilde\alpha}^{J\pi-}(\rho) \to 0$ for $\rho \to 0$ and the boundary condition

$$\tilde f_{\tilde\alpha'\tilde\alpha}^{J\pi-}(\rho) \to \frac{1}{2i}\left\{\exp\left[i\left(k_c\rho - \frac{L_0\pi}{2}\right)\right]\delta_{\tilde\alpha'\tilde\alpha} + \exp\left[-i\left(k_{c'}\rho - \frac{L_0'\pi}{2}\right)\right]S_{\tilde\alpha'\tilde\alpha}^{J\pi-}\right\} \tag{51}$$

for $\rho \to \infty$, where $L_0 = L + l + 2\lambda + 3/2$. In formula (51), $S_{\tilde\alpha'\tilde\alpha}^{J\pi-}$ is an element of the three-particle S matrix. The matrix element $\tilde V_{\tilde\alpha''\tilde\alpha'}^{J\pi M}(\rho)$ in (50) is given by formula (16), where it is necessary to replace the two-particle channel functions $U_\alpha^{J\pi M}(x)$ by the three-particle functions $U_{\tilde\alpha}^{J\pi M}(\tilde x)$ and the two-particle potentials $V(x,R)$ by the corresponding three-particle fission-fragment-interaction potentials $V(\tilde x,\rho)$. In this case, the asymptotic expression $(\Psi_{qK}^{J\pi M})^{\mathrm{as}}$ for the fission-mode wave function $\Psi_{qK}^{J\pi M}$ in the limit $\rho \to \infty$ can be represented in the form

$$(\Psi_{qK}^{J\pi M})^{\mathrm{as}} = \sum_{\tilde\alpha} U_{\tilde\alpha}^{J\pi M}(\tilde x) \times \frac{\exp\left[i\left(k_c\rho - \frac{L_0\pi}{2}\right)\right]}{\rho^{5/2}}\sqrt{\frac{\Gamma_{qK\tilde\alpha}^{J\pi}}{\hbar v_c}}, \tag{52}$$

where the partial-fission-width amplitude $\sqrt{\Gamma_{qK\tilde\alpha}^{J\pi}}$ for the three-body fission channel $\tilde\alpha$ is given by (21) with the above substitutions.

7. STRUCTURE OF THE INTERACTION OF FRAGMENTS ORIGINATING FROM THE TERNARY FISSION OF NUCLEI

If one employs the method of extra coordinates, which was applied above to the case of binary nuclear fission, it can be shown that, because of the effect of the strong-coupling approximation [10], the symmetry axes of fragments originating from ternary fission are aligned with the symmetry axis of the fissile nucleus—that is, $\omega_1 = \omega_2 = \omega$, as in the case of binary fission. The potential $V_c(R,\theta_\omega)$ representing the interaction of ternary-fission fragments coincides with the analogous potential $V_c(R,\theta_\omega)$ of the interaction of binary-fission fragments, the latter being given by Eqs. (31) and (34) at $\omega_1 = \omega_2 = \omega$; upon going over to three-particle variables, it becomes dependent on the quantities ρ and ε via the relation $R = \sqrt{M_c/M_a}\rho\sin\varepsilon$.

The potential $V_\alpha(\mathbf{R},\mathbf{r},\omega)$ describing the interaction of an alpha particle and two ternary-fission fragments can be represented as the sum of the Coulomb potential $V_\alpha^{\mathrm{Coul}}(\mathbf{R},\mathbf{r},\omega)$ and the nuclear potential $V_\alpha^{\mathrm{nucl}}(\mathbf{R},\mathbf{r},\omega)$. In the c.m. frame of the fissile nucleus, where its c.m. coordinate is

$$\mathbf{R}_0 = \frac{4\mathbf{R}_\alpha + A_1\mathbf{R}_1 + A_2\mathbf{R}_2}{A} = 0,$$

there arise simple relations between the relative coordinates $\mathbf{R}$ and $\mathbf{r}$ and the c.m. coordinates $\mathbf{R}_1$, $\mathbf{R}_2$, and $\mathbf{R}_\alpha$ of fission fragments; that is,

$$\mathbf{R}_1 = \mathbf{R}_{01} - \frac{4\mathbf{r}}{A}, \quad \mathbf{R}_2 = -\mathbf{R}_{02} - \frac{4\mathbf{r}}{A}, \quad \mathbf{R}_\alpha = \frac{A_1 + A_2}{A}\mathbf{r}, \tag{53}$$

$$\mathbf{R}_{01} = \frac{A_2}{A_1+A_2}\mathbf{R}, \quad \mathbf{R}_{02} = \frac{A_1}{A_1+A_2}\mathbf{R},$$
$$\mathbf{R}_\alpha - \mathbf{R}_1 = \mathbf{r} - \mathbf{R}_{01}, \quad \mathbf{R}_\alpha - \mathbf{R}_2 = \mathbf{r} + \mathbf{R}_{02}.$$

In the approximation where an alpha particle is treated as a pointlike object, the Coulomb potential $V_\alpha^{\mathrm{Coul}}(\mathbf{R},\mathbf{r},\omega)$ describing the interaction of the alpha particle with ternary-fission fragments can then be represented in the form [15]

$$V_\alpha^{\mathrm{Coul}}(\mathbf{R},\mathbf{r},\omega) = 2e^2\sum_i Z_i \int \frac{\rho_i(\mathbf{r}_i)d\mathbf{r}_i}{|\mathbf{R}_i - \mathbf{R}_\alpha + \mathbf{r}_i|}, \quad (54)$$

where $\mathbf{r}_i$ is the proton coordinate reckoned in the ith fission fragment from its c.m. coordinate and $\rho_i(\mathbf{r}_i)$ is the normalized (to unity) proton density in the ith fragment. Since the alpha particle is emitted from the small neck of the prescission configuration of a fissile nucleus, the conditions $r_i/R < 1$ and $r/R < 1$ are satisfied in the region of intense alpha-particle interaction with ternary-fission fragments after their formation. Expanding the potential (54) in a series in powers of r_i/R and r/R to second-order terms inclusive and in a series in powers of the charge and mass asymmetries of fission fragments, $\Delta Z/(Z-2)$ and $\Delta A/(A-4)$, to the first nonvanishing terms and using the expansions of the densities of fission fragments in powers of their deformation parameters $\beta_2^{(i)}$ to first-order terms of smallness of the form (30), we can arrive at [15]

$$V_\alpha^{\mathrm{Coul}}(R,r,\theta_{\mathbf{rR}}) = \frac{2(Z-2)e^2}{R} \quad (55)$$
$$+ \frac{8(Z-2)e^2}{R^2} r\sqrt{\frac{4\pi}{3}}Y_{10}(\theta_{\mathbf{rR}})\left(\frac{\Delta Z}{Z-2} + \frac{2\Delta A}{A-4}\right)$$
$$+ \frac{16(Z-2)e^2}{R^2} r^2\sqrt{\frac{4\pi}{5}}Y_{20}(\theta_{\mathrm{rR}})$$
$$- \frac{(Z-2)e^2}{R^3}\frac{24}{5}\sum_{i=1}^{2}(R_{A_i}^0)^2\beta_2^{(i)}Y_{20}(\theta_\omega),$$

where $\theta_{\mathbf{rR}}$ is the angle between the vectors $\mathbf{r}$ and $\mathbf{R}$.

The first and the fourth term in the potential (55) are independent of the coordinate $\mathbf{r}$ and can be added, as small corrections, to the potential $V_c(R,\theta_\omega)$ describing the interaction of ternary-fission fragments. As to the second and the third term in formula (55), which are dependent on the coordinate $\mathbf{r}$, they specify the true Coulomb potential $V_\alpha^{\mathrm{Coul}}(r,R,\theta_{\mathbf{rR}})$ of the interaction between the alpha particle and ternary-fission fragments in the region of r values being considered.

In order to construct the nuclear potential $V_\alpha^{\mathrm{nucl}}(\mathbf{R},\mathbf{r},\omega)$ of alpha-particle interaction with ternary-fission fragments, we can make use of the method that was proposed in [18, 19] and which was previously employed to construct the nuclear potential $V_c^{\mathrm{nucl}}(R,\theta_\omega)$ of interaction of these fragments. This yields

$$V_\alpha^{\mathrm{nucl}}(\mathbf{R},\mathbf{r},\omega) = 4C_0 \quad (56)$$
$$\times\left\{\frac{F_{\mathrm{in}}-F_{\mathrm{ex}}}{\rho_0}\left[\rho_1^2(\mathbf{r}-\mathbf{R}_{01}) + \rho_2^2(\mathbf{r}-\mathbf{R}_{02})\right]\right.$$
$$\left. + F_{\mathrm{ex}}\left[\rho_1(\mathbf{r}-\mathbf{R}_{01}) + \rho_2(\mathbf{r}-\mathbf{R}_{02})\right]\right\}.$$

Expanding the potential (56) in a series in powers of r/R and retaining terms to second order of smallness inclusive, we can isolate, in the resulting potential $V_\alpha^{\mathrm{nucl}}(\mathbf{R},\mathbf{r},\omega)$, the term $V_\alpha^{\mathrm{nucl}}(\mathbf{R},0,\omega)$, which arises in (56) at $\mathbf{r}=0$ and which is a small correction to the nuclear fission-fragment-interaction potential $V_c(R,\theta_\omega)$. We can expand, in a series in the angle θ_ω, terms in the potential (56) that depend on the coordinate r and discard terms proportional to θ_ω^2 because they are small corrections to the term $C\theta_\omega^2/2$ for the nonspherical Coulomb barrier (37). In this case, the true nuclear potential that describes alpha-particle interaction with ternary-fission fragments and which is associated with the coordinate r proves to be independent of the angle θ_ω and assumes the form

$$V_\alpha^{\mathrm{nucl}}(r,R,\theta_{\mathbf{rR}}) = r\sqrt{\frac{3}{4\pi}}Y_{10}(\theta_{\mathbf{rR}}) \quad (57)$$
$$\times\left\{4C_0\frac{(F_{\mathrm{in}}-F_{\mathrm{ex}})}{\rho_0}\right.$$
$$\times\left[-\frac{\partial(\bar\rho_1(R_{01}))^2}{\partial R_{01}} + \frac{\partial(\bar\rho_2(R_{02}))^2}{\partial R_{02}}\right]$$
$$\left. + 4F_{\mathrm{ex}}C_0\left[-\frac{\partial\bar\rho_1(R_{01})}{\partial R_{01}} + \frac{\partial\bar\rho_2(R_{02})}{\partial R_{02}}\right]\right\}$$
$$+ \frac{1}{6}r^2\left[\sqrt{\frac{5}{\pi}}Y_{20}(\theta_{\mathbf{rR}}) + 1\right]\left\{4C_0\frac{(F_{\mathrm{in}}-F_{\mathrm{ex}})}{\rho_0}\right.$$
$$\times\left[\frac{\partial^2(\bar\rho_1(R_{01}))^2}{\partial R_{01}^2} + \frac{\partial^2(\bar\rho_2(R_{02}))^2}{\partial R_{02}^2}\right]$$
$$\left. + 4F_{\mathrm{ex}}C_0\left[\frac{\partial^2\bar\rho_1(R_{01})}{\partial R_{01}^2} + \frac{\partial^2\bar\rho_2(R_{02})}{\partial R_{02}^2}\right]\right\},$$

where $\bar\rho_i(R)$ is the density of the spherical ith fragment of radius $\bar R_{A_i} = R_{A_i}^0(1+\sqrt{5/4\pi}\beta_2^{(i)})$. If one expands the resulting potential (57) in a series in the charge- and mass-asymmetry parameters of fission fragments, $\Delta Z/(Z-2)$ and $\Delta A/(A-4)$, to the first nonvanishing terms, then that term in this potential which involves $Y_{10}(\theta_{\mathbf{rR}})$ will be a linear function of the parameters $\Delta Z/(Z-2)$ and $\Delta A/(A-4)$,

while the term featuring $Y_{20}(\theta_{\mathbf{rR}})$ can be treated as that which is independent of these parameters. In this case, the potential $V_\alpha^{\rm nucl}(r, R, \theta_{\mathbf{rR}})$ (57) will have symmetry that is coincident with the symmetry of the Coulomb potential $V_\alpha^{\rm Coul}(r, R, \theta_{\mathbf{rR}})$ (55), which was constructed above, apart from the fact that, in $V_\alpha^{\rm nucl}(r, R, \theta_{\mathbf{rR}})$, there arises a spherically symmetric term that is proportional to r^2, which is independent of $\theta_{\mathbf{rR}}$, and which is due to the presence of unity in the sum $\left[\sqrt{5/\pi}Y_{20}(\theta_{\mathbf{rR}}) + 1\right]$ appearing in expression (57).

The appearance of an alpha particle introduces virtually no changes in the potential $V_c(R, \theta_\omega)$ of ternary-fission-fragment interaction in relation to the analogous potential describing the interaction of binary-fission fragments; the potentials $V_\alpha^{\rm Coul}(r, R, \theta_{\mathbf{rR}})$ and $V_\alpha^{\rm nucl}(r, R, \theta_{\mathbf{rR}})$ are independent of the angles θ_ω and change only slightly as the radius vector $\mathbf{R}$ changes by a small quantity that is necessary for the realization of condition (43), under which the mechanism of alignment of the vector $\mathbf{R}$ along the symmetry axis of a fissile nucleus comes into play. In view of this, the above mechanism of alignment will be realized, nearly without any distortions, for ternary nuclear fission as well. In this case, the motion of the alpha particle emitted in ternary fission can be treated, to a high degree of precision, as its motion in the field of the "dumbbell" that is formed by elongated fission fragments, whose intrinsic symmetry axes coincide with the symmetry axis of the parent nucleus, and which becomes more extended with time. By using the ideas developed above, the angular component of the wave function describing the relative motion of the three fragments in ternary fission in the intrinsic coordinate frame of a fissile nucleus, $\Psi(\Omega_{\mathbf{r}}, \Omega_{\mathbf{R}}, \omega)$, can be represented, in the asymptotic region $\rho \to \infty$, in the form of the product of the wave function $\Psi_0(\theta_\omega, \varphi_\omega)$ (46) describing the relative angular motion of the fragments, which is virtually undistorted by the emergence of the alpha particle, and the wave function $\Psi_\alpha(\theta_{\mathbf{rR}})$ describing the angular motion of the alpha particle with respect to the direction of fragment motion; that is,

$$\Psi_\alpha(\theta_{\mathbf{rR}}) = \sum_l b_l(\varepsilon) Y_{l0}(\theta_{\mathbf{rR}}), \qquad (58)$$

where the coefficients $b_l(\varepsilon)$ depend on the angles ε, which determine the energy of the alpha particle in the asymptotic region [25, 26]. A similar representation of the wave function $\Psi(\Omega_{\mathbf{r}}, \Omega_{\mathbf{R}}, \omega)$ for $\rho \to \infty$ was used previously in [2] in describing the experimental angular distributions of alpha particles [27] originating from the ternary fission of unpolarized nuclei and in calculating the coefficients of P-odd and P-even asymmetries (see [13] and [14], respectively) in the ternary fission of nuclei.

8. CONCLUSION

This study has demonstrated the potential of the quantum-mechanical theory of fission for describing the mechanisms and properties of the spontaneous and low-energy induced binary and ternary fission of nuclei. The results obtained here, together with the results reported in [1, 2, 13–15], make it possible to trace fission dynamics after the scission of a fissile nucleus into fragments, including the derivation of information about the neutron and radiative modes of fission-fragment decay.

ACKNOWLEDGMENTS

I am grateful to V.E. Bunakov, W.I. Furman, A.L. Barabanov, F. Goennenwein, and G.A. Petrov for stimulating discussions. Special thanks are due to L.V. Rodionova for assistance in performing numerical estimations.

This work was supported by INTAS (project no. 99-00229) and by the Russian Foundation for Basic Research (project no. 03-02-17469).

REFERENCES

1. S. G. Kadmensky, Yad. Fiz. **65**, 1424 (2002) [Phys. At. Nucl. **65**, 1390 (2002)]
2. S. G. Kadmensky, Yad. Fiz. **65**, 1833 (2002) [Phys. At. Nucl. **65**, 1785 (2002)].
3. M. Goldberger and K. Watson, *Collision Theory* (J. Wiley and Sons, New York, 1964; Mir, Moscow, 1967).
4. K. Wildermuth and Y. C. Tang, *A Unified Theory of the Nucleus* (Vieveg, Braunshweig, 1977; Mir, Moscow, 1980).
5. S. G. Kadmensky, Yad. Fiz. **62**, 236 (1999) [Phys. At. Nucl. **62**, 201 (1999)]; Yad. Fiz. **64**, 478 (2001) [Phys. At. Nucl. **64**, 423 (2001)].
6. S. G. Kadmensky, Yad. Fiz. **63**, 613 (2000) [Phys. At. Nucl. **63**, 551 (2000)]; Yad. Fiz. **65**, 863 (2002) [Phys. At. Nucl. **65**, 831 (2002)].
7. S. G. Kadmensky and A. A. Sanzogni, Phys. Rev. C **62**, 054601 (2000).
8. S. G. Kadmensky and W. I. Furman, *Alpha Decay and Related Nuclear Reactions* (Énergoatomizdat, Moscow, 1985).
9. S. G. Kadmensky, W. I. Furman, and Yu. M. Chuvilsky, Izv. Akad. Nauk SSSR, Ser. Fiz. **50**, 1786 (1986).
10. A. Bohr and B. Mottelson, *Nuclear Structure* (Benjamin, New York, 1969, 1975; Mir, Moscow, 1971, 1977), Vols. 1, 2.
11. S. G. Kadmensky and L. V. Rodionova, Yad. Fiz. **66**, 1259 (2003) [Phys. At. Nucl. **66**, 1219 (2003)].

12. Yu. N. Kopach *et al.*, Phys. Rev. Lett. **82**, 303 (1999).
13. S. G. Kadmensky, Yad. Fiz. **66**, 1739 (2003) [Phys. At. Nucl. **66**, 1691 (2003)].
14. S. G. Kadmensky, Yad. Fiz. **66** (2003, in press).
15. S. G. Kadmensky, Izv. Ross. Akad. Nauk, Ser. Fiz. **67**, 30 (2003).
16. P. O. Hess, S. Misicu, and W. Greiner, J. Phys. G **26**, 957 (2000).
17. V. I. Kukulin, V. G. Neudatchin, and Yu. F. Smirnov, Fiz. Élem. Chastits At. Yadra **10**, 1236 (1979) [Sov. J. Part. Nucl. **10**, 492 (1979)].
18. T. M. Scneidman *et al.*, Phys. Rev. C **65**, 064302 (2002).
19. A. B. Migdal, *Theory of Finite Fermi Systems and Applications to Atomic Nuclei* (Nauka, Moscow, 1975; Interscience, New York, 1967, transl. of 1st Russ. Ed.).
20. D. M. Brink and G. R. Satchler, *Angular Momentum* (Oxford Univ. Press, Oxford, 1968).
21. I. N. Mikhailov and P. Quentin, Phys. Lett. B **462**, 7 (1999).
22. W. I. Furman, in *Proceedings of FJ/OM Spring Session* (Geel, Belgium, 1999), p. 248.
23. J. O. Rasmussen *et al.*, Nucl. Phys. A **136**, 465 (1969).
24. A. Barabanov and W. Furman, Z. Phys. A **357**, 441 (1997).
25. L. M. Delves, Nucl. Phys. **20**, 275 (1960).
26. N. F. Mott and H. S. W. Massey, *The Theory of Atomic Collisions* (Clarendon, Oxford, 1965; Mir, Moscow, 1969).
27. M. Mutterer and J. P. Theobald, *Dinuclear Decay Modes* (JOP Publ., Bristol, 1996), Chap. 12.

Translated by A. Isaakyan

Physics of Atomic Nuclei, Vol. 67, No. 1, 2004, pp. 183–194. Translated from Yadernaya Fizika, Vol. 67, No. 1, 2004, pp. 180–190.

80th ANNIVERSARY OF THE BIRTH OF SPARTAK TIMOFEEVICH BELYAEV

Green's Function Method in the Problem of Complex Configurations in Fermi Systems with Pairing

S. P. Kamerdzhiev and E. V. Litvinova*

Institute of Physics and Power Engineering, pl. Bondarenko 1, Obninsk, Kaluga oblast, 249020 Russia

Received March 19, 2003

Abstract—The Green's function method is used to derive general equations for describing effects of pairing in Fermi systems where there are two types of interaction, two-particle and quasiparticle–phonon interaction. These equations generalize Bardeen–Cooper–Schrieffer theory to the case of complex configurations involving "strong" phonons. In the approximation of weak coupling to phonons, realistic equations that make it possible to describe excited states of nonmagic even–even nuclei with allowance for a single-particle continuum and complex configurations of the *two quasiparticles* ⊗ *phonon* type are formulated for the first time. These equations are solved for an isovector $E1$ resonance in the stable isotope ^{120}Sn and in the unstable isotopes ^{104,132}Sn. It is shown that complex configurations must be taken into account in order to describe $E1$ excitations—in particular, in a broad energy region around the nucleon binding energy.

1. INTRODUCTION

In the majority of S.T. Belyaev's studies devoted to nuclear physics, he considered nuclei that involve pairing and, in almost all of them, consistently employed the Green's function method, which, as could have been seen even from those studies and as was confirmed later on, proved to be quite seminal for a further development of the microscopic theory of the nucleus [1–4].

The inclusion of complex configurations is one of the main trends in the development of the modern theory of the nucleus.[1)] The development of nuclear-physics experiments—first of all, the improvement of the experimental resolution—and the need for explaining the widths of giant resonances and other features of nuclei required taking into account complex configurations in the microscopic theory of the nucleus (for an overview, see [5–7]). The quasiparticle–phonon model [5], which relies on the Hamiltonian formalism, proved to be the most advanced in the quantitative aspect. Over the past decade, the Green's function method has been used as a basis for developing a quantitative approach for magic nuclei [7] that takes simultaneously into account all three mechanisms of giant-resonance formation—namely, those that are associated with $1p1h$ configurations (RPA), a single-particle continuum, and complex configurations of the $1p1h \otimes$ *phonon* type. It was shown that this approach (generalized theory of finite Fermi systems), which is a direct generalization of Migdal's theory of finite Fermi systems [8] to the case of the aforementioned complex configurations, describes successfully not only the total widths of resonances but also their gross structure. There naturally arises the question of generalizing such an approach to the case of nuclei where pairing effects are present.

Complex configurations were taken into account in quite a general form in the studies of Belyaev and Zelevinsky [2, 4], where the corresponding general formulas were obtained for calculating the properties of both even–even and odd nuclei involving effects of pairing. Those studies appeared well ahead of their time. In particular, those authors showed that it is necessary to take complex configurations into account explicitly (see, for example, [4]), in contrast to what was done in the theory of finite Fermi systems [8], where complex configurations were included effectively in an integral form through phenomenological parameters of the theory. On the other hand, experience gained in theoretical analyses and, what is more important, experiments revealed that, in order

* e-mail: litva@aport.ru

[1)] By complex configurations in nuclei involving effects of pairing, we mean, for the sake of definiteness, those that are more complicated than $1qp \otimes$ phonon configurations in odd nuclei and those that are more complicated than one-phonon or $2qp$ configurations in even–even nuclei, these three types being taken into account in the quasiparticle (qp) random-phase approximation (QRPA). We imply here, above all, complex configurations featuring phonons, since the analysis of phonon-free complex configurations, which are obtained by means of the substitution *phonon* → $2qp$, is more complicated and less clear physically.

to explain specific experimental data, it is necessary to single out and consider particular complex configurations and, when possible, to invoke available additional approximations.

The present article reports on a continuation of the studies described in [9–12] and devoted to generalizing the theory of finite Fermi systems in such a way as to take explicitly into account complex configurations in nuclei where pairing is present. The emergence of a second, quasiparticle–phonon, mechanism of pairing [9], in addition to the usual Bardeen–Cooper–Schrieffer mechanism, is one of the most interesting results that are obtained upon consistently taking into account complex configurations in the particle–particle channel. This mechanism owes its existence to the appearance of a second, quasiparticle–phonon, interaction in the problem and is similar to the pairing mechanism studied by Eliashberg [13] in solid-state physics, albeit the nature of phonons in nuclear matter is totally different from that in solid bodies. The mechanism considered by Eliashberg corresponds to the case of strong coupling to phonons and reduces to the usual Bardeen–Cooper–Schrieffer mechanism in the limit of weak coupling. In nuclei featuring unfilled shells, the case of strong coupling is realized in both nucleon subsystems (see [14]). Therefore, it is necessary to consider this mechanism. Moreover, an analog of the Migdal–Eliashberg approximations used in Eliashberg's theory should probably be abandoned in dealing with such nuclei. An analysis of this type may be of interest for other strongly interacting Fermi systems as well.

The ensuing exposition is organized as follows. In Section 2, we consider some general relations for Fermi systems containing an odd number of particles and featuring two types of interaction. Relevant equations for even–even nuclei involving effects of pairing are derived in Section 3 with allowance for $2qp \otimes phonon$ configurations. These equations are solved for the isovector $E1$ resonance in the stable nucleus ^{120}Sn and in the unstable nuclei ^{104,132}Sn.

2. GENERAL RELATIONS

2.1. General Solutions for Odd Nuclei: "Purification" and Effective Mass

Excited states of an odd Fermi system where pairing effects are present are determined by solving the set of equations for the normal (causal) Green's functions G and G^h and the anomalous Green's functions $F^{(1)}$ and $F^{(2)}$, these equations involving the mass operators Σ and Σ^h for the former and the mass operators $\Sigma^{(1)}$ and $\Sigma^{(2)}$ for the latter (for the sake of simplicity, we will use a unified notation in the following—for example, Σ^i). Each of the operators symbolized as Σ^i can be represented as the sum of two terms such that the energy dependence is completely absorbed in one of them (M^i) [10–12]:

$$\Sigma(\epsilon) = \widetilde{\Sigma} + M(\epsilon), \quad \Sigma^{(1)}(\epsilon) = \widetilde{\Sigma}^{(1)} + M^{(1)}(\epsilon), \quad (1)$$
$$\Sigma^h(\epsilon) = \widetilde{\Sigma}^h + M^h(\epsilon), \quad \Sigma^{(2)}(\epsilon) = \widetilde{\Sigma}^{(2)} + M^{(2)}(\epsilon).$$

It is then convenient to write formal solutions to the set of equations for the above Green's functions in the form (in the diagonal approximation in the single-particle index of the λ representation)

$$\eta = \pm\sqrt{\epsilon_{\lambda n}^2 + \Delta_{\lambda n}^2}, \quad (2)$$
$$\epsilon_{\lambda n} = \frac{\tilde{\epsilon}_\lambda + M_{ev\lambda}(\eta)}{1 + q_\lambda(\eta)}, \quad \Delta_{\lambda n}^{(2)} = \frac{\tilde{\Delta}_\lambda^{(2)} + M_\lambda^{(2)}(\eta)}{1 + q_\lambda(\eta)},$$

where $q_\lambda(\eta) = -M_{odd\lambda}(\eta)/\eta$; $M_{ev}(\epsilon)$ and $M_{odd}(\epsilon)$ are, respectively, the even and the odd part of the single-hole mass operator $M(\epsilon)$; and η is a root of the corresponding secular equation, this root being, in general, characterized by two indices, λ and n (number of solution).

The quantities $\tilde{\Sigma}^i$ and M^i in relations (1) and (2) are not specified. We only assume that the operators M^i involve quasiparticle–phonon interaction, although, in other cases, M^i may contain an effective or a bare two-particle interaction. The case of weak coupling in nuclei that feature pairing—it corresponds to the presence of a small parameter in the system, $g^2 < 1$, where g is the dimensionless phonon-production amplitude—was quantitatively studied in [9, 10]. But in the general case of strong coupling to phonons, all single-particle Green's functions appearing in $\tilde{\Sigma}^i$ and M^i must be exact. Apart from this complication, there arises the well-known problem of taking into account corrections to the corresponding vertex. As was indicated by Belyaev and Zelevinsky [2, 4], each correction to the vertex involves a $6j$ coefficient such that, for a first approximation, one can disregard all corrections, with the exception of the first-order correction containing one $6j$ coefficient (this correction was written explicitly in [12]). By applying the technique of matrix Green's functions that were employed in [1], we can easily find that, in this approximation, the quantities M^i assume the form (here and below, we present only M and $M^{(2)}$ and disregard pair phonons)

$$M(\epsilon) = M^r(\epsilon) + M^v(\epsilon), \quad (3)$$
$$M^{(2)}(\epsilon) = M^{(2)r}(\epsilon) + M^{(2)v}(\epsilon),$$

where the rainbow diagrams and corrections to the vertex are denoted by M^{ir} (rainbow) and M^{iv} (vertex), respectively. The equivalent graphical form of these relations is

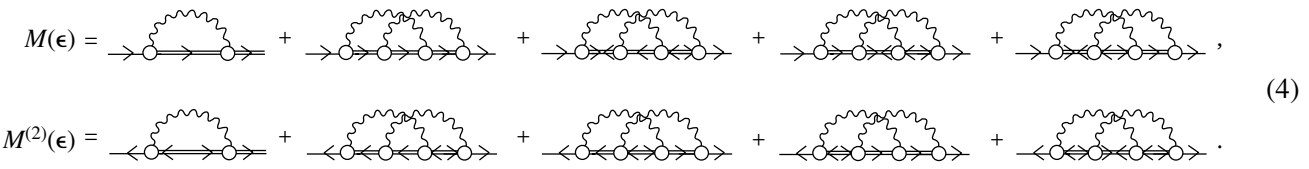

(4)

These relations are also valid for other strongly interacting Fermi systems both at zero and at nonzero temperature (up to the temperature T_c of a phase transition from a superconducting to a normal state)—for example, for fullerides (see the study of Grimaldi *et al.* [15], who considered the case of $\tilde{\Sigma}^i = 0$ and who presented diagrams for M^i at $T = T_c$).

In a similar form, relations (2) were obtained in [16] in the approximation $M^i = M^{ir}$ (rainbow diagrams). For an infinite system treated in the same approximation and for the case of $\tilde{\epsilon}_\lambda = \tilde{\Delta}_\lambda = 0$, such relations were derived in Eliashberg's study [13], which was seminal for the development of the microscopic theory of conventional superconductors. For nuclei, Hahne *et al.* [17] constructed a procedure for isolating, in an effective particle–particle interaction, a phonon term that leads to the emergence of the quantity $M^{(2)} = M^{(2)r}$ and implemented this procedure numerically for the ^{18}O nucleus.

The inclusion of corrections to the vertex means that one goes far beyond Eliashberg's theory. For nuclei, the role of these corrections (crossed graphs) in the formation of features of low-energy neutron–nucleus scattering was quantitatively estimated (without allowance for pairing) by Samoilov and Urin [18], who found that the relative contribution of the two-phonon crossed graph does not exceed 25–50%, as a rule, but that it may amount to 100% in some rare cases. In their later study [19], however, those authors reproduced previous qualitative arguments in favor of disregarding crossed graphs. Since it is very difficult to assess crossed graphs quantitatively, the corresponding three-level model with pairing was studied in [20], and the distribution of the single-particle strength for the $j = 11/2$ state was calculated there. It was found that the two-phonon correction to the vertex makes a noticeable contribution—in particular, the spectroscopic factor for the dominant level decreases from 0.49 to 0.40.

For an analysis of pairing, that solution to the set of equations for the Green's functions is of greatest interest which has the form (2) and which corresponds to low-lying single-particle levels in an odd nucleus where pairing effects are present. These levels, which are referred to as dominant ones, have the greatest spectroscopic factor. They are given by Eqs. (2) for fixed ("dominant") n [9, 10]; that is,

$$E_\lambda = \pm\sqrt{\epsilon_\lambda^2 + \Delta_\lambda^2}, \tag{5}$$

$$\epsilon_\lambda = \frac{\tilde{\epsilon}_\lambda + M_{\mathrm{ev}\lambda}(E_\lambda)}{1 + q_\lambda(E_\lambda)}, \quad \Delta_\lambda^{(2)} = \frac{\tilde{\Delta}_\lambda^{(2)} + M_\lambda^{(2)}(E_\lambda)}{1 + q_\lambda(E_\lambda)},$$

where $q_\lambda(E_\lambda) = -M_{\mathrm{odd}\lambda}(E_\lambda)/E_\lambda$. Using these relations and knowing observed $\{\epsilon_\lambda, \Delta_\lambda\}$, one can find the "purified" values $\{\tilde{\epsilon}_\lambda, \tilde{\Delta}_\lambda\}$, which determine the purified single-particle basis in all equations featuring complex configurations. This procedure for determining $\{\tilde{\epsilon}_\lambda, \tilde{\Delta}_\lambda\}$ makes it possible to avoid the double counting of that part in the quasiparticle–phonon interaction which appears in the quantities M^i. As can be seen from Eqs. (5), the observed gap $\Delta_\lambda^{(2)}$ involves contributions both from the two-particle interaction (in $\tilde{\Delta}_\lambda^{(2)}$) and from the quasiparticle–phonon interaction (in $\tilde{\Delta}_\lambda^{(2)}$ and in $M_\lambda^{(2)}$)—that is, there are in general two pairing mechanisms (see also Subsection 2.2).

A general description of pairing makes it possible to single out its role in various physical quantities and its mechanisms more clearly. By way of example, we will consider general formulas for the effective nucleon mass. As is well known, it is convenient to represent this quantity in the form [8, 21]

$$\frac{m^*(\epsilon)}{m} = \frac{m_k(\epsilon)}{m}\frac{m_\omega(\epsilon)}{m}, \tag{6}$$

so that, at the Fermi boundary ($\epsilon = \mu, p = p_{\mathrm{F}}$), we have

$$\frac{m_\omega(\mathbf{r})}{m} = \left[1 - \frac{\partial\Sigma(\mathbf{r}, p, \epsilon)}{\partial\epsilon}\right]_{\mathrm{F}}, \tag{7}$$

$$\frac{m_k(\mathbf{r})}{m} = \left[1 + 2m\frac{\partial\Sigma(\mathbf{r}, p, \epsilon)}{\partial p^2}\right]_{\mathrm{F}}^{-1},$$

where Σ is the quantity to which the single-particle mass operator reduces in the mixed representation [8] and which determines the exact Green's function G. As was shown in [12], the general equation for G in nuclei that involve pairing can be recast into the form (diagonal approximation)

$$G = \tilde{G} + \tilde{G}(M + M_{\mathrm{el}})G, \tag{8}$$

where $M_{\rm el}$,

$$M_{\rm el} = -(\Sigma^{(1)}\bar{G}^h\Sigma^{(2)} - \tilde{\Sigma}^{(1)}\tilde{G}_0^h\tilde{\Sigma}^{(2)}), \qquad (9)$$

is the general expression for the mass operator responsible for the pairing mechanism additional to the mechanism described by the term $\tilde{\Sigma}^{(1)}\tilde{G}_0^h\tilde{\Sigma}^{(2)}$, which, in the limit $M^i = 0$, corresponds to the Bardeen–Cooper–Schrieffer mechanism (see also the next section). The Green's functions $\bar{G}^h$ and $\tilde{G}_0^h$ were defined in [12].

It can be seen from Eq. (8) that $\Sigma = M + M_{\rm el}$ in nonmagic nuclei. From this relation and from (7), we then obtain, under the assumption that $M_{\rm el}(\Delta = 0) = 0$, the contribution of pairing to the effective mass in the form

$$\frac{m_\omega^{\rm pair}}{m} = \frac{m_\omega}{m} - \frac{m_\omega(\Delta=0)}{m} = \frac{\partial M}{\partial\epsilon_{\rm F}} \qquad (10)$$
$$- \frac{\partial M(\Delta=0)}{\partial\epsilon_{\rm F}} + \frac{\partial M_{\rm el}}{\partial\epsilon_{\rm F}},$$

$$\frac{m_k^{\rm pair}}{m} = \frac{m_k}{m} \qquad (11)$$
$$- \frac{m_k(\Delta=0)}{m} = \left[1 + 2m\frac{\partial(M+M_{\rm el})}{\partial p_{\rm F}^2}\right]^{-1}$$
$$- \left[1 + 2m\frac{\partial M(\Delta=0)}{\partial p_{\rm F}^2}\right]^{-1}.$$

In magic nuclei, we have $M_{\rm el} = 0$; therefore, one can calculate the quantities m_ω and m_k by the formulas

$$\frac{m_\omega}{m} = 1 - \frac{\partial M(\Delta=0)}{\partial\epsilon_{\rm F}}, \qquad (12)$$
$$\frac{m_k}{m} = \left[1 + 2m\frac{\partial M(\Delta=0)}{\partial p_{\rm F}^2}\right]^{-1}.$$

With the aid of these formulas, one can calculate, for each nucleus, the observed effective nucleon mass, which is phenomenologically defined at the Fermi surface as a quantity that is close to the free nucleon mass.

2.2. Case of Rainbow Diagrams

Let us consider the case of $M^i = M^{ir}$ and $M^{iv} = 0$; in contrast to the linearized version studied in [9, 10], this case is essentially nonlinear. In this approximation, we will derive a few equations for $\tilde{\Delta}_\lambda$ and Δ_λ.

By definition, the quantities $\tilde{\Sigma}^i$ in (1) are independent of the energy variable ϵ; therefore, the quantity $\tilde{\Sigma}^{(2)}$, for example, can be represented in the form (diagonal approximation)

$$\tilde{\Sigma}_\lambda^{(2)} = \tilde{\Delta}_\lambda = \sum_{\lambda'} W_{\lambda\bar{\lambda}\lambda'\bar{\lambda}'}\int\frac{d\epsilon}{2\pi i}F_{\lambda'}^{(2)}(\epsilon), \qquad (13)$$

where W is a new ϵ-independent particle–particle interaction that is different from the well-known phenomenological particle–particle interaction appearing in the standard Bardeen–Cooper–Schrieffer equation.

In order to derive an equation for $\tilde{\Delta}_\lambda$, we make use of a spectral representation for the function $F^{(2)}$ [22]; that is,

$$F_\lambda^{(2)}(\epsilon) = \sum_n\sqrt{S_{\lambda n}^+ S_{\lambda n}^-} \qquad (14)$$
$$\times\left(\frac{1}{\epsilon - E_{\lambda n} + i\delta} - \frac{1}{\epsilon + E_{\lambda n} - i\delta}\right),$$

where $S_{\lambda n}^\pm$ are the residues corresponding to the particle and hole components of the Green's function G,

$$S_{\lambda n}^\pm = \frac{(1+q_{\lambda n})(E_{\lambda n} \pm \epsilon_{\lambda n})}{\dot{\Theta}_\lambda(E_{\lambda n})}. \qquad (15)$$

Here,

$$\Theta_\lambda(\epsilon) = (\epsilon - \tilde{\epsilon}_\lambda - M_\lambda(\epsilon))(\epsilon + \tilde{\epsilon}_\lambda + M_\lambda^h(\epsilon)) \qquad (16)$$
$$- (\tilde{\Delta}_\lambda + M_\lambda^{(2)}(\epsilon))^2,$$

and an overdot denotes differentiation with respect to energy (see also [10]). From (13) and (14), we find for $\tilde{\Delta}_\lambda$ that

$$\tilde{\Delta}_\lambda = \sum_{\lambda' n} W_{\lambda\bar{\lambda}\lambda'\bar{\lambda}'}\sqrt{S_{\lambda' n}^+ S_{\lambda' n}^-} \qquad (17)$$
$$= \sum_{\lambda' n} W_{\lambda\bar{\lambda}\lambda'\bar{\lambda}'}\frac{\Delta_{\lambda' n}(1+q_{\lambda' n})}{\dot{\Theta}_{\lambda'}(E_{\lambda' n})},$$

which is a generalization of the Bardeen–Cooper–Schrieffer equation to the case of strong coupling and which, in the limit where all $M^{(i)}$ vanish, reduces to the Bardeen–Cooper–Schrieffer equation (in that case, $\dot{\Theta}_\lambda = 2E_{\lambda n} = 2E_\lambda$). It should be emphasized that, in the absence of phonon exchange in the particle–particle channel ($M^{(2)} = 0$), the relation $\Delta_\lambda = \tilde{\Delta}_\lambda(1 + q_\lambda(E_\lambda))^{-1}$ follows from (5) for the observed gap; that is, both factors involve a contribution of the quasiparticle–phonon interaction.

The role of the quasiparticle–phonon interaction and of the corresponding two pairing mechanisms can be analyzed in an alternative way. In the approximation of rainbow diagrams that is considered here, the Green's function $F^{(2)}$ satisfies the equation [10]

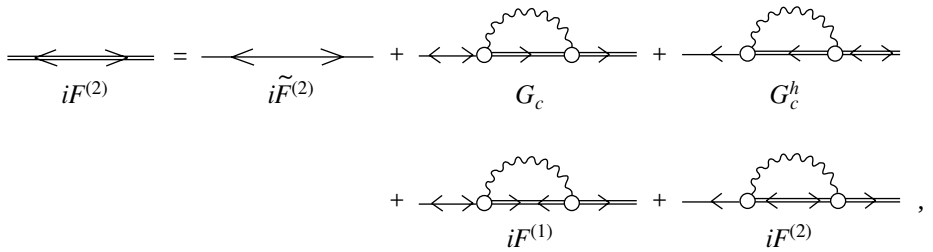

(18)

where G_c stands for the Green's function allowing for pair correlations. Substituting Eq. (18) into (13), we can isolate, in $\tilde{\Delta}_\lambda$, the contributions of two mechanisms, the Bardeen–Cooper–Schrieffer and the quasiparticle–phonon mechanism; that is,

$$\tilde{\Delta}_\lambda = \tilde{\Delta}_\lambda^{(0)} + \tilde{\Delta}_\lambda^{\text{phon}}, \tag{19}$$

where $\tilde{\Delta}_\lambda^{(0)}$ corresponds to the Bardeen–Cooper–Schrieffer mechanism for the renormalized ("purified") interaction,

$$\tilde{\Delta}_\lambda^{(0)} = \sum_{\lambda'} W_{\lambda\bar{\lambda}\lambda'\bar{\lambda}'} \int \frac{d\epsilon}{2\pi i} \tilde{F}_{\lambda'}^{(2)}(\epsilon) \tag{20}$$

$$= \sum_{\lambda'} W_{\lambda\bar{\lambda}\lambda'\bar{\lambda}'} \frac{\tilde{\Delta}_{\lambda'}^{(0)}}{2\sqrt{\tilde{\epsilon}_{\lambda'}^2 + (\tilde{\Delta}_{\lambda'}^{(0)})^2}},$$

and where $\tilde{\Delta}_\lambda^{\text{phon}}$ involves the contribution of the quasiparticle–phonon interaction. In the weak-coupling approximation ($g^2 < 1$), a calculation of these quantities for ^{120}Sn was performed in [9], where it was found that the averaged contributions of the quantities $\tilde{\Delta}_\lambda^{(0)}$ and $\tilde{\Delta}_\lambda^{\text{phon}}$ amount to 74 and -5%, respectively, of the observed value of the pairing gap; therefore, the contribution of the term involving $M^{(2)}$ in (5) and corresponding to phonon exchange in the particle–particle channel is 31% of the observed gap. A value that is quantitatively close to the last one was obtained for the same nucleus in [23], where the nonlinear problem formulated above has already been addressed. This similarity comes as no surprise, since the case of weak coupling ($g^2 < 1$) is realized in the ^{120}Sn nucleus [10].

Let us now derive an equation for observed Δ_λ with the aid of the spectral representation (14). Substituting Eq. (14) into (2) and employing Eq. (17), we obtain

$$\Delta_\lambda = \frac{1}{1 + q_\lambda(E_\lambda)} \sum_{\lambda' n'} \sqrt{S_{\lambda' n'}^+ S_{\lambda' n'}^-} \tag{21}$$

$$\times \left\{ W_{\lambda\bar{\lambda}\lambda'\bar{\lambda}'} + \sum_s |g_{\lambda\lambda'}^s|^2 \frac{2(E_{\lambda' n'} + \omega_s)}{E_\lambda^2 - (E_{\lambda' n'} + \omega_s)^2} \right\},$$

where $E_\lambda = \sqrt{\epsilon_\lambda^2 + \Delta_\lambda^2}$, $g_{\lambda\lambda'}^s$ is the amplitude describing the production of an s phonon, and ω_s is its energy.

The formulas obtained above for $\tilde{\Delta}_\lambda$ and Δ_λ are of interest for the case of strong coupling to phonons—for example, this is so for nuclei involving doubly unfilled shells, in which case there exist "strong" 2_1^+ phonons with $g > 1$.

To conclude this section, we emphasize once again that, according to our definition, "purification" consists in eliminating, from observables, only those terms in the exact mass operators Σ^i that are dependent on the energy variable ϵ. It is possible to define $\tilde{\Sigma}^i$ in (1) in an alternative way—for example, to include the observables ϵ_λ and Δ_λ in $\tilde{\Sigma}^i$ (this is precisely what is done in the non-self-consistent QRPA approach, where $M^i = 0$ by definition). But upon the inclusion of complex configurations, double counting can then be avoided only via subtracting that contribution from M^i which is contained in the observables ϵ_λ and Δ_λ. Our version is more convenient if for no other reason than the fact that our purified basis $\{\tilde{\epsilon}_\lambda, \tilde{\Delta}_\lambda\}$ is a phenomenological analog of the Hartree–Fock–Bogolyubov basis. Concurrently, the procedure of deriving $\{\tilde{\epsilon}_\lambda, \tilde{\Delta}_\lambda\}$ from $\{\epsilon_\lambda, \Delta_\lambda\}$ (see [10]) is quantitatively more satisfactory, since, from the observables $\{\epsilon_\lambda, \Delta_\lambda\}$, one extracts the contribution of precisely those—and only those—phonons that are explicitly taken into account in complex configurations. Within the existing approach that involves self-consistency [23, 24], where this self-consistency is ensured at the RPA level and where complex configurations are calculated on the basis of the same self-consistent scheme, it remains unclear which complex configurations are contained in the single-particle scheme obtained in this way. In all probability, this problem could only be solved upon formulating and implementing a self-consistent approach that would take complex configurations into account explicitly.

3. INCLUSION OF COMPLEX CONFIGURATIONS IN NONMAGIC EVEN–EVEN NUCLEI IN THE APPROXIMATION OF WEAK QUASIPARTICLE–PHONON COUPLING

A method for taking into account *two quasiparticles* $\otimes$ *phonon* configurations in nonmagic even–even nuclei was formulated in [11]. This method makes it possible to calculate the contribution to the resonance width from the fragmentation of simple excitations over such configurations. A numerical implementation of the method in question is hindered primarily by the fact that the expressions for the multicomponent propagator contain second-order poles, in which case there arise nonphysical results for relevant cross sections. In the same study ([11]), a procedure was proposed for eliminating such poles, and this procedure was implemented for a simple schematic model. In calculations for actual nuclei, it turned out, however, that this procedure is not always sufficient. In the present section, we propose a somewhat different approach to solving the problem in question. It will be shown that, by consistently considering "hazardous" diagrams of each type, one can sum them in all orders in the phonon-production amplitude.

3.1. Basic Relations

We will calculate the cross section for electric L-pole photoabsorption. We have

$$\sigma_L(E) = \frac{8\pi^3(L+1)e^2}{L[(2L+1)!!]^2}\left(\frac{E}{\hbar c}\right)^{2L-1} S_L(E),$$

where the strength function

$$S_L(E) = -\frac{2L+1}{\pi}\mathrm{Im}\sum_{S,\tau}\delta_{S0}e_\tau \qquad (22)$$
$$\times \int_0^\infty dr r^{J+2}\delta\rho_{S,\tau}(r;\omega),$$
$$\omega = E + i\eta, \qquad \eta \to +0,$$

is expressed in terms of the change $\delta\rho$ in the density matrix for the nuclear system under study in an external field, L is the orbital angular momentum of the electric excitation being considered, S is the spin index ($S = 0, 1$), τ is the isotopic index ($\tau = n, p$), $J = L$ for $L \geq 1$, and e_τ is the local nucleon charge.

For the quantity $\delta\rho$, one solves a set of equations in the coordinate representation. Upon separating the coordinate dependence, this set of equations assumes the form

$$\delta\rho_{S,\tau}(r_1;\omega) = \delta\rho^{(0)}_{S,\tau}(r_1;\omega) \qquad (23)$$
$$-\sum_{S',\tau'}\int_0^\infty dr_2\, r_2^2 A^{(\tau)L}_{LS,LS'}(r_1,r_2;\omega)$$
$$\times \mathcal{F}^{\tau\tau'}_{S'}(r_2)\delta\rho_{S',\tau'}(r_2;\omega),$$
$$\delta\rho^{(0)}_{S,\tau}(r_1;\omega) = -e_\tau\int_0^\infty dr_2 r_2^{J+2}A^{(\tau)L}_{LS,L0}(r_1,r_2;\omega),$$

(24)

where $\mathcal{F}$ is the amplitude of effective particle–hole interaction. This amplitude is parametrized according to the theory of finite Fermi systems; that is,

$$\mathcal{F}^{\tau\tau'}_S(r) = \delta_{\tau\tau'}\, C_0\left[\delta_{S,0}(f+f') + \delta_{S,1}(g+g')\right] \qquad (25)$$
$$+ (1-\delta_{\tau\tau'})\, C_0\left[\delta_{S,0}(f-f') + \delta_{S,1}(g-g')\right],$$

where $f(r)$ and $f'(r)$ are given by interpolation formulas involving the parameters f_{ex}, f_{in}, f'_{ex}, and f'_{in}.

In the problem being considered, the radial part of the particle–hole (ph) propagator, $A^{(\tau)L}_{LS,LS'}(r_1,r_2;\omega)$, has the form

$$A^{(\tau)L}_{LS,LS'}(r_1,r_2;\omega) = A^{\mathrm{cont}(\tau)L}_{LS,LS'}(r_1,r_2;\omega) \qquad (26)$$
$$+ A^{\mathrm{disc}(\tau)L}_{LS,LS'}(r_1,r_2;\omega),$$

where A^{cont} is that part of the propagator which describes transitions from paired levels of the discrete spectrum to the continuum, pairing being disregarded in the continuum itself,

$$A^{\mathrm{cont}(\tau)L}_{LS,LS'}(r,r';\omega) = -\sum_1 \delta_{\tau\tau_1}v_1^2R_1(r)R_1(r') \qquad (27)$$
$$\times \sum_{l_2j_2} T_{12}^{LSS'}\left[G^\tau_{l_2j_2}(r,r';\mu_\tau - E_1 + \omega)\right.$$
$$\left. + (-1)^{S+S'}G^\tau_{l_2j_2}(r,r';\mu_\tau - E_1 - \omega)\right].$$

Here, the partial-wave components G^τ_{lj} of the radial part of the Green's function without pairing are calculated exactly, which makes it possible to take fully into account the single-particle continuum at the RPA level. The quantity A^{disc} is that part of the propagator which includes pairing corrections to A^{cont} near the Fermi surface—that is, in that part of the spectrum where the Cooper gap does not vanish—and components that describe more complicated configurations involving phonons, A^{phon}:

$$A^{\mathrm{disc}(\tau)L}_{LS,LS'}(r,r';\omega) = \sum_{12}^{\mathrm{disc}}\delta_{\tau\tau_1}\delta_{\tau\tau_2}R_1(r) \qquad (28)$$
$$\times R_2(r')R_1(r')R_2(r)T_{21}^{LSS'}\left[\frac{v_1^2(1-v_2^2)}{\omega + E_1 + E_2}\right.$$

$$- \frac{(1-v_1^2)v_2^2}{\omega - E_1 - E_2} + \frac{v_2^2}{\omega + \mu_\tau - \epsilon_1 - E_2}$$
$$- \frac{v_1^2}{\omega - \mu_\tau + \epsilon_2 + E_1} + (-1)^S \frac{\Delta_1\Delta_2}{4E_1E_2}$$
$$\times \left(\frac{1}{\omega + E_1 + E_2} - \frac{1}{\omega - E_1 - E_2} \right) \Bigg]$$
$$+ A^{\mathrm{phon}(\tau)L}_{LS,LS'}(r, r'; \omega).$$

Here, the symbol $\sum_{12}^{\mathrm{disc}}$ denotes summation over the discrete part of the single-particle basis; $1 \equiv (\tau_1, n_1, l_1, j_1)$ is the set of single-particle quantum numbers in a spherical nucleus, the projection of the total angular momentum being excluded from this set; v_1^2 are the occupation numbers of quasiparticle states; and $T_{12}^{LSS'}$ are the products of the reduced matrix elements of spherical tensor operators,

$$T_{12}^{LSS'} = \frac{1}{2L+1} \times \langle j_1 l_1 || T_{LLS} || j_2 l_2 \rangle \langle j_1 l_1 || T_{LLS'} || j_2 l_2 \rangle. \quad (29)$$

Let us now consider the quantity A^{phon}. The general expressions for this quantity were presented in [11]. Here, we will address a realistic particular case of the general approach, disregarding nonpole terms in single-quasiparticle Green's functions and, hence, ground-state correlations caused by quasiparticle–phonon coupling. It will be shown that, in this case, one can eliminate, from the propagator, second-order poles by summing infinite series of Feynman diagrams of each class.

Without allowance for the ground-state correlations, the total propagator in the λ representation has the form

$$\mathcal{A}_{121'2'}(\omega) = \frac{u_1 v_2}{\omega - E_{12}} \Bigg\{ \delta_{11'}\delta_{22'} + \frac{1}{\omega - E_{1'2'}} \quad (30)$$
$$\times \Bigg[\delta_{22'} \sum_{3,s} \frac{g^s_{13}(g^s_{1'3})^*}{\omega - E_{23} - \omega_s} \mathcal{X}_{11'33}$$
$$+ \delta_{11'} \sum_{3,s} \frac{g^s_{2'3}(g^s_{23})^*}{\omega - E_{13} - \omega_s} \mathcal{X}_{22'33} - \sum_s g^s_{11'}(g^s_{22'})^*$$
$$\times \left(\frac{1}{\omega - E_{1'2} - \omega_s} + \frac{1}{\omega - E_{12'} - \omega_s} \right) \mathcal{X}_{121'2'} \Bigg] \Bigg\}$$
$$\times (u_{1'} v_{2'} + v_{1'} u_{2'} \hat{P}),$$

where $u_1 = \sqrt{1 - v_1^2}$ and $E_{12} = E_1 + E_2$. It can be seen from (30) that, in the approximation where there is no dynamical coupling to the particle–particle channel, this propagator consists of two terms, a normal and an anomalous one. The latter involves the operator $\hat{P}$ transforming the vertex V into V^h. The factors

$$\mathcal{X}_{121'2'} = u_1 u_2 u_{1'} u_{2'} + u_1 v_2 u_{1'} v_{2'} + v_1 u_2 v_{1'} u_{2'} + v_1 v_2 v_{1'} v_{2'} \quad (31)$$

arise upon summation of four diagrams of each type (that is, those that differ from one another only in the quasiparticle occupation numbers and which have the same pole structure), whereby one takes into account all $2qp$ combinations that are possible within our approximations. Further, we rewrite the normal term of the propagator in (30), isolating terms containing second-order poles; that is,

$$\mathcal{A}^{\mathrm{norm}}_{121'2'}(\omega) = \delta_{11'}\delta_{22'} \Bigg\{ \frac{u_1^2 v_2^2}{\omega - E_{12}} \quad (32)$$
$$+ \frac{u_1^2 v_1^2}{(\omega - E_{12})^2} \Bigg[\sum_{3,s} \frac{|g^s_{13}|^2}{\omega - E_{23} - \omega_s} \mathcal{X}_{1133}$$
$$+ \sum_{3,s} \frac{|g^s_{23}|^2}{\omega - E_{13} - \omega_s} \mathcal{X}_{2233}$$
$$- 2 \sum_s \frac{g^s_{11}(g^s_{22})^*}{\omega - E_{12} - \omega_s} \mathcal{X}_{1212} - \sum_s g^s_{12}(g^s_{21})^* \frac{u_2 v_1}{u_1 v_2}$$
$$\times \left(\frac{1}{\omega - E_{22} - \omega_s} + \frac{1}{\omega - E_{11} - \omega_s} \right) \mathcal{X}_{1221} \Bigg] \Bigg\}$$
$$- (1 - \delta_{11'}\delta_{22'})(1 - \delta_{12'}\delta_{1'2})$$
$$\times \frac{u_1 u_1' v_2 v_2' \mathcal{X}_{121'2'}}{(\omega - E_{12})(\omega - E_{1'2'})} \sum_s g^s_{11'}(g^s_{22'})^*$$
$$\times \left(\frac{1}{\omega - E_{1'2} - \omega_s} + \frac{1}{\omega - E_{12'} - \omega_s} \right).$$

Four terms in the bracketed expression on the right-hand side of (32) represent the components of the propagator that involve a right- and a left-hand insertion and two phonon-exchange components. They obviously correspond to the graphs in which $1 = 1'$, $2 = 2'$, $1 = 2'$, and $2 = 1'$ and always involve second-order poles if we restrict our consideration to the g^2 approximation. We now examine such graphs in the next order in the phonon-production amplitude. In the fourth order in g, or, which is equivalent, in the second order in M, the graph involving the left-hand insertion yields

$$\mathcal{D}^{l;1}_{2;12} = \int \frac{d\epsilon}{2\pi i} G_1^+(\epsilon) M_1^+(\epsilon) G_1^+(\epsilon) M_1^+(\epsilon) \quad (33)$$
$$\times G_2^-(\epsilon - \omega) = \frac{u_1^2 v_2^2}{(\omega - E_{12})^3} \sum_{3,s} \frac{|g^s_{13}|^2 u_1^2 u_3^2}{\omega - E_{23} - \omega_s}$$
$$\times \sum_{4,s} \frac{|g^s_{14}|^2 u_1^2 u_4^2}{\omega - E_{24} - \omega_s}.$$

Similar expressions can be obtained for all other $\mathcal{D}_2^{l;i}$ involving anomalous Green's functions. Performing summation over all possible $2qp$ configurations, we find for left-hand insertions that

$$\mathcal{D}^l_{2;12} = \sum_{i=1,4} \mathcal{D}^{l,i}_{2;12} = \frac{u_1^2 v_2^2}{(\omega - E_{12})^3} \times \sum_{3,s} \frac{|g^s_{13}|^2 \mathcal{X}_{1133}}{\omega - E_{23} - \omega_s} \sum_{4,s} \frac{|g^s_{14}|^2 \mathcal{X}_{1144}}{\omega - E_{24} - \omega_s}. \quad (34)$$

In the third order in M, we have

$$\mathcal{D}^l_{3;12} = \frac{u_1^2 v_2^2}{(\omega - E_{12})^4} \sum_{3,s} \frac{|g^s_{13}|^2 \mathcal{X}_{1133}}{\omega - E_{23} - \omega_s} \times \sum_{4,s} \frac{|g^s_{14}|^2 \mathcal{X}_{1144}}{\omega - E_{24} - \omega_s} \sum_{5,s} \frac{|g^s_{15}|^2 \mathcal{X}_{1155}}{\omega - E_{25} - \omega_s}, \quad (35)$$

and so on. We can see that the infinite sum

$$\mathcal{D}^l_{12} = \mathcal{D}^l_{0;12} + \mathcal{D}^l_{1;12} + \mathcal{D}^l_{2;12} + \ldots \quad (36)$$
$$= \frac{u_1^2 v_2^2}{\omega - E_{12}} \left[1 + \frac{1}{\omega - E_{12}} \sum_{3,s} \frac{|g^s_{13}|^2 \mathcal{X}_{1133}}{\omega - E_{23} - \omega_s} + \left(\frac{1}{\omega - E_{12}} \sum_{3,s} \frac{|g^s_{13}|^2 \mathcal{X}_{1133}}{\omega - E_{23} - \omega_s} \right)^2 + \left(\frac{1}{\omega - E_{12}} \sum_{3,s} \frac{|g^s_{13}|^2 \mathcal{X}_{1133}}{\omega - E_{23} - \omega_s} \right)^3 + \ldots \right]$$

is formally a power series that converges for

$$|q| = \left| \frac{1}{\omega - E_{12}} \sum_{3,s} \frac{|g^s_{13}|^2 \mathcal{X}_{1133}}{\omega - E_{23} - \omega_s} \right| < 1. \quad (37)$$

It follows that, within the region of convergence, the sum in question has the form

$$\mathcal{D}^l_{12} = \frac{u_1^2 v_2^2}{\omega - E_{12} - \sum_{3,s} \frac{|g^s_{13}|^2 \mathcal{X}_{1133}}{\omega - E_{23} - \omega_s}}. \quad (38)$$

Similar results are obtained for the infinite sums of the components involving right-hand insertions and the components involving a transverse phonon. Thus, we are able to take into account, in all orders, the propagator components involving all possible combinations of insertions and transverse phonons and depending on two indices. With allowance for the aforesaid, the normal part of the propagator assumes the form

$$\mathcal{A}^{\text{norm}}_{121'2'}(\omega) = \delta_{11'}\delta_{22'} \frac{u_1^2 v_2^2}{\omega - E_{12} - \mathcal{C}_{12}} - (1 - \delta_{11'}\delta_{22'})(1 - \delta_{12'}\delta_{1'2}) \times \frac{u_1 u'_1 v_2 v'_2 \mathcal{X}_{121'2'}}{(\omega - E_{12})(\omega - E_{1'2'})} \sum_s g^s_{11'} (g^s_{22'})^* \times \left(\frac{1}{\omega - E_{1'2} - \omega_s} + \frac{1}{\omega - E_{12'} - \omega_s} \right), \quad (39)$$

where

$$\mathcal{C}_{12} = \sum_{3,s} \frac{|g^s_{13}|^2 \mathcal{X}_{1133}}{\omega - E_{23} - \omega_s} + \sum_{3,s} \frac{|g^s_{23}|^2 \mathcal{X}_{2233}}{\omega - E_{13} - \omega_s} - 2 \sum_s \frac{g^s_{11} (g^s_{22})^* \mathcal{X}_{1212}}{\omega - E_{12} - \omega_s} - \sum_s g^s_{12} (g^s_{21})^* \frac{u_2 v_1}{u_1 v_2} \times \left(\frac{1}{\omega - E_{22} - \omega_s} + \frac{1}{\omega - E_{11} - \omega_s} \right) \mathcal{X}_{1221}. \quad (40)$$

The anomalous part of the propagator is obtained in a similar way by means of the simultaneous substitutions $u_{1'} \to v_{1'}$ and $v_{1'} \to u_{1'}$ and a multiplication by the corresponding phase coefficient.

3.2. Calculation of the Isovector E1 Resonance in the ^{104,120,132}Sn Isotopes

In our calculations, we took into account the $J^\pi = 2^+$, 3^-, 4^+, 5^-, and 6^+ collective low-lying phonons, whose properties were determined by solving the set of equations of the theory of finite Fermi systems in the λ representation. The single-particle continuum was taken into account at the QRPA level according to the method developed in [25].

We employed the effective Landau–Migdal particle–hole interaction, whose parameters are well known and quite universal for medium-mass and heavy nuclei. This makes it possible to describe giant multipole resonances in unstable nuclei. For these parameters, we took the following well-known values (for more details, see [7]):

$$f_{\text{in}} = -0.002, \quad f'_{\text{in}} = 0.76, \quad f'_{\text{ex}} = 2.30, \quad (41)$$
$$g = 0.05, \quad g' = 0.96, \quad C_0 = 300 \text{ MeV fm}^3.$$

In calculating the features of low-lying phonons, the parameter f_{ex} was chosen in such a way as to obtain the best fit to their positions known experimentally for the ^{120,132}Sn nuclei. As a result, it turned out that f_{ex} values range between -3.3 and -4.9. For the unstable nucleus ^{104}Sn, we set $f_{\text{ex}} = -4.0$.

In calculating the dipole-photoabsorption cross section, the additional forced-matching procedure developed in [25] to eliminate and suppress the ghost dipole state associated with the motion of the center of mass was used for effective particle–hole interaction.

The single-particle wave functions and levels for ^{104}Sn were calculated with the standard Woods–Saxon potential. For ^{120}Sn, we made a rough fit of

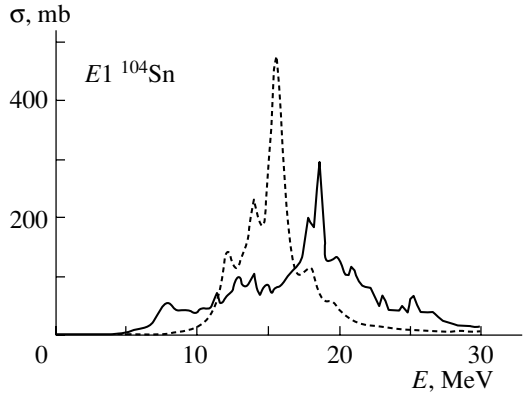

Fig. 1. Cross section for dipole photoabsorption in ^{104}Sn: (solid curve) results of the full calculation with allowance for complex configurations and (dashed curve) results of the QRPA calculation with allowance for a continuum.

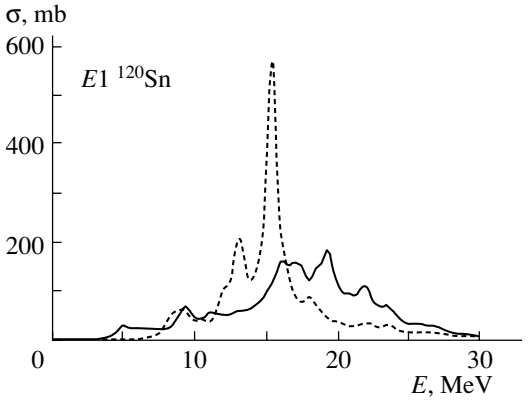

Fig. 2. As in Fig. 1, but for ^{120}Sn.

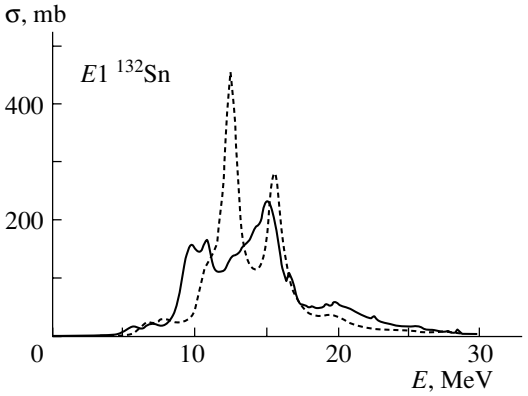

Fig. 3. As in Fig. 1, but for ^{132}Sn.

the parameters of the mean-field potential to single-particle levels known from experiments. These levels were obtained by using data reported in [26]. The energies of single-particle levels in ^{132}Sn were fitted to values quoted in [27].

Taking into account the law of particle-number conservation and using the diagonal-pairing approximation, we calculated the matrix elements of the Cooper gap Δ_ν according to the equation

$$\hat{j}_\nu \Delta_\nu = -\sum_{\nu'} \Gamma^\xi_{\nu\nu'} \frac{\hat{j}_{\nu'} \Delta_{\nu'}}{2E_{\nu'}}, \qquad (42)$$

where $\hat{j}_\nu = \sqrt{2j+1}$, ν standing for the set of single-particle quantum numbers that does not include the projection of the angular momentum. The matrix elements of the quantity obtained by renormalizing, according to the theory of finite Fermi systems, the local amplitude of interaction in the two-particle channel are given by

$$\Gamma^\xi_{\nu\nu'} = \gamma_0^\xi (-1)^{l_\nu + l_{\nu'}} \frac{\hat{j}_\nu \hat{j}_{\nu'}}{4\pi} \int_0^\infty dr r^2 R^2_\nu(r) R^2_{\nu'}(r),$$

$$\gamma_0^\xi = \frac{C_0}{\ln(c_p/\xi)}, \quad \xi = \sqrt{\xi_1 \xi_2}, \qquad (43)$$

where $C_0 = 300$ MeV fm^3 and c_p is a phenomenological parameter that was set to 1 MeV in our calculations. The quantities ξ_1 and ξ_2 determine the boundaries of the basis in which one solves the gap equation and which includes states in the unfilled (valence) shell (in the case of nuclei featuring effects of pairing), as well as states in two shells below the valence shell and states in two shells above it.

In Figs. 1–3, the solid curves represent the dipole-photoabsorption cross sections calculated with allowance for complex configurations. Also shown there for the sake of comparison are the results of the corresponding CQRPA (continuum quasiparticle random-phase approximation) calculations. Both types of calculation were performed by using the smearing-parameter value of 400 keV. The calculations revealed that the use of the propagator where terms corresponding to ground-state correlations are discarded leads to a sum rule that is nearly coincident with its CQRPA value. The resonance width was computed as the width of a Lorentz distribution that approximates a model strength function [28]. The mean resonance energy $\bar{E}$ was defined as $\bar{E} = \sqrt{m_1/m_{-1}}$, where m_k is the kth moment of the strength function.

The integrated features of the calculated curves are compiled in the table. From Figs. 1–3 and from the table, it can be seen that, for all nuclei studied here, the resonance width increases by a factor of 2 to 3 upon the inclusion of complex configura-

Integrated features of the isovector $E1$ resonance in tin isotopes

Isotope	^{104}Sn		^{120}Sn		^{132}Sn	
Method	1	2	1	2	1	2
EWSR [%]	108.5	108.2	99.9	99.2	94.4	94.3
$\bar{E}$ [MeV]	13.5	15.2	14.8	14.2	14.1	13.0
Γ [MeV]	5.7	1.7	4.7	2.1	3.6	2.1
σ_0 [mb]	187	668	238	512	309	541
σ_{int} (0–15 MeV) [%]	32	38	26	39	52	55
σ_{int} (0–12 MeV) [%]	17	8	16	13	27	21
$\sigma_{\text{int}}(0-\bar{E})$ [%]	23	44	25	29	43	36
$\sigma_{\text{int}}(0-\bar{E}/2)$ [%]	1.7	0.26	3.9	0.40	1.9	0.76

Note: The following notation is used in the table: EWSR is σ_{int} divided by the value of the classical model-independent sum rule, $\sigma_{\text{cl}} = 60\dfrac{NZ}{A}$ mb MeV; $\bar{E}$ is the mean resonance energy; Γ is the resonance width; σ_0 is the maximum of the Lorentz distribution; and $\sigma_{\text{int}}(0-E)$ stands for the relevant cross sections integrated over the corresponding energy intervals. Columns 1 and 2 present the results of, respectively, the full calculation with allowance for complex configurations and the CQRPA calculation.

tions and agrees well with the experimental value of $\Gamma_{\text{expt}} = 4.9$ MeV for ^{120}Sn from [30]. This is one of the main results of the present study. Within the energy interval 0–30 MeV, which was investigated here, the degree to which the Thomas–Reiche–Kuhn sum rule is exhausted for ^{120}Sn and ^{132}Sn is 99.9 and 94.4%, respectively, and this is quite a satisfactory and natural result, since, in contrast to the approach used in [7], our present calculations disregard ground-state correlations caused by complex configurations. For the nuclei being investigated, the mean resonance energy also increases upon the inclusion of complex configurations; for ^{120}Sn, the result for it with allowance for them agrees satisfactorily with experimental data: $\bar{E}_{\text{theor}} = 14.8$ MeV versus $\bar{E}_{\text{expt}} = 15.4$ MeV [29]. The above trends for the energy-weighted sum rule (EWSR) and for $\bar{E}$ are not observed in ^{104}Sn, and this may be due to some flaws in the single-particle scheme, which, in contrast to the cases of ^{120}Sn and ^{132}Sn , could not be fitted here to experimental data.

In connection with the general interest in low-lying $E1$ excitations (pygmy dipole resonance), we have calculated the integrated contributions of the $E1$ strength within various intervals over the low-lying slope of an $E1$ resonance with and without allowance for complex configurations (see table). As can be seen from the figures and from the table, complex configurations lead to a very sizable and irregular increase in the strength within the intervals 0–12 MeV and 0–$\bar{E}/2$. This means that it is necessary to take complex configurations into account in the energy region of a presumed pygmy dipole resonance.

4. CONCLUSION

In Section 2, we have performed a general analysis of the case where a Fermi system in which pairing may occur is governed by interactions of two types, two-particle interaction in the particle–particle channel and quasiparticle–phonon interaction that corresponds to strong coupling to phonons. Attention has been given primarily to the particle–particle channel and to a description of pairing in the case of any complex configurations involving phonons. The relations derived in the course of this analysis are not closed, at least in the sense that the problem of formulating equations for phonons has been skipped. Even if one could formulate such equations for superfluid systems, an implementation of this scheme at the nonlinearity level adopted in the present study would hardly be a realistic task (for magic nuclei, an attempt at formulating such a scheme was undertaken in [30]). Therefore, it seems reasonable to extract the properties of "strong" phonons from experimental data.

We have been able to isolate, in a general form, the contributions to the observable pairing gap from two

mechanisms, a mechanism of the Bardeen–Cooper–Schrieffer type and the quasiparticle–phonon mechanism. Among other things, we have shown that, even if quasiparticle–phonon interaction is absent in the particle–particle channel ($M_\lambda^{(2)} = 0$), there is a contribution from the quasiparticle–phonon interaction both to the observable gap, Δ_λ, and to its purified counterpart, $\tilde{\Delta}_\lambda$, so that the analysis of the problem in the general, nonlinear, case remains quite involved under these conditions inclusive.

In Section 3, the Green's function method has been used to formulate realistic equations in the weak-coupling approximation ($g^2 < 1$) for describing excitations in an even–even Fermi system that may exhibit pairing effects. On the basis of these equations, one can in principle calculate the features of states in such a systems up to energies of 25 to 30 MeV, simultaneously taking into account the continuous spectrum, QRPA configurations, and complex configurations of the *two quasiparticles* $\otimes$ *phonon* type. After some simplifications (nondiagonal phonon-exchange graphs and ground-state correlations induced by the quasiparticle–phonon interaction were disregarded, and the procedure for purifying single-particle properties was not implemented), the isovector $E1$ resonance in the stable isotope ^{120}Sn and the unstable isotopes ^{104,132}Sn has been calculated on the basis of this approach. In summary, all three mechanisms of giant-resonance formation—decay into simple configurations of the discrete spectrum, particle emission into the continuous spectrum, and fragmentation over complex configurations—have been simultaneously taken into account for the first time ever in our approach for nuclei that involve pairing. Reasonably good agreement with experimental data has been obtained, which demonstrates the validity of our approach. In connection with keen interest in low-lying $E1$ excitations, we have studied the behavior of the $E1$ strength function at energies below the resonance maximum. By means of a direct comparison with the results of the CQRPA calculations performed within the identical scheme, it has been shown that complex configurations must be taken into account in order to describe $E1$ excitations over a broad energy region around the nucleon binding energy.

ACKNOWLEDGMENTS

We are grateful to V.I. Tselyaev for generous assistance in solving the CQRPA problem in the coordinate representation.

REFERENCES

1. S. T. Belyaev, Yad. Fiz. **1**, 3 (1965) [Sov. J. Nucl. Phys. **1**, 3 (1965)].
2. S. T. Belyaev and V. G. Zelevinskiĭ, Yad. Fiz. **1**, 13 (1965) [Sov. J. Nucl. Phys. **1**, 10 (1966)].
3. S. T. Belyaev, Yad. Fiz. **2**, 51 (1965) [Sov. J. Nucl. Phys. **3**, 35 (1966)].
4. S. T. Belyaev and V. G. Zelevinskiĭ, Yad. Fiz. **2**, 615 (1965) [Sov. J. Nucl. Phys. **2**, 442 (1966)].
5. V. G. Soloviev, *Theory of Complex Nuclei* (Nauka, Moscow, 1971; Pergamon, Oxford, 1976); *Theory of Atomic Nuclei: Quasiparticles and Phonons* (Énergoatomizdat, Moscow, 1989).
6. G. F. Bertsch, P. F. Bortignon, and R. A. Broglia, Rev. Mod. Phys. **55**, 287 (1983).
7. S. P. Kamerdzhiev, G. Ya. Tertychny, and V. I. Tselyaev, Fiz. Élem. Chastits At. Yadra **28**, 333 (1997) [Phys. Part. Nucl. **28**, 134 (1997)]; S. Kamerdzhiev, J. Speth, and G. Tertychny, Phys. Rep. (in press).
8. A. B. Migdal, *Theory of Finite Fermi Systems and Applications to Atomic Nuclei* (Nauka, Moscow, 1965; Interscience, New York, 1967).
9. A. V. Avdeenkov and S. P. Kamerdzhiev, Pis'ma Zh. Éksp. Teor. Fiz. **69**, 669 (1999) [JETP Lett. **69**, 715 (1999)].
10. A. V. Avdeenkov and S. P. Kamerdzhiev, Yad. Fiz. **62**, 610 (1999) [Phys. At. Nucl. **62**, 563 (1999)]; Phys. Lett. B **459**, 423 (1999).
11. S. P. Kamerdzhiev, E. Litvinova, and D. Zawischa, Eur. Phys. J. A **12**, 285 (2001).
12. S. P. Kamerdzhiev and E. V. Litvinova, Yad. Fiz. **64**, 686 (2001) [Phys. At. Nucl. **64**, 627 (2001)].
13. G. M. Éliashberg, Zh. Éksp. Teor. Fiz. **38**, 966 (1960); J. P. Carbotte, Rev. Mod. Phys. **62**, 1027 (1990).
14. A. Bohr and B. R. Mottelson, *Nuclear Structure*, Vol. 2: *Nuclear Deformations* (Benjamin, New York, 1975; Mir, Moscow, 1977).
15. C. Grimaldi, L. Petronero, and S. Strässler, Phys. Rev. B **52**, 10530 (1995).
16. S. G. Kadmenskiĭ and P. A. Luk'yanovich, Yad. Fiz. **49**, 384 (1989) [Sov. J. Nucl. Phys. **49**, 238 (1989)].
17. F. J. W. Hahne, W. D. Heiss, and C. A. Engelbreht, Ann. Phys. (N.Y.) **104**, 251 (1977); Phys. Lett. B **66B**, 218 (1977).
18. V. V. Samoĭlov and M. G. Urin, Izv. Akad. Nauk SSSR, Ser. Fiz. **55**, 2272 (1991); Yad. Fiz. **55**, 2041 (1992) [Sov. J. Nucl. Phys. **55**, 1133 (1992)].
19. V. V. Samoilov and M. H. Urin, Nucl. Phys. A **567**, 237 (1994).
20. A. V. Avdeenkov and S. P. Kamerdzhiev, in *Proceedings of the 7th International Spring Seminar on Nuclear Physics "Challenges of Nuclear Structure"* (Maiori, 2001), Ed. by A. Covello (World Sci., 2002), p. 283.
21. C. Mahaux, P. F. Bortignon, R. A. Broglia, and C. H. Dasso, Phys. Rep. **120**, 1 (1985).
22. A. V. Avdeenkov, Candidate's Dissertation in Physics and Mathematics (Inst. Phys. Power Eng., Obninsk, 1999).

23. J. Terasaki, F. Barranco, P. F. Bortignon, *et al.*, nucl-th/0109056.
24. G. Colo, Nguen Van Giai, P. F. Bortignon, *et al.*, Phys. Rev. C **50**, 1496 (1994).
25. S. Kamerdzhiev, R. Liotta, E. Litvinova, and V. Tselyaev, Phys. Rev. C **58**, 172 (1998).
26. A. H. Wapstra and K. Bos, At. Data Nucl. Data Tables **19**, 177 (1977); Nucl. Data Sheets **67**, 2 (1992); **64**, 2 (1991).
27. S. Kamerdzhiev, J. Speth, G. Tertychny, and J. Wambach, Z. Phys. A **346**, 253 (1993).
28. V. I. Tselyaev, Izv. Akad. Nauk, Ser. Fiz. **64**, 541 (2000).
29. S. S. Dietrich and B. L. Berman, At. Data Nucl. Data Tables **38**, 199 (1988).
30. S. P. Kamerdzhiev and V. I. Tselyaev, Yad. Fiz. **44**, 336 (1986) [Sov. J. Nucl. Phys. **44**, 214 (1986)].

Translated by A. Isaakyan

Physics of Atomic Nuclei, Vol. 67, No. 1, 2004, pp. 195–198. From Yadernaya Fizika, Vol. 67, No. 1, 2004, pp. 191–194.

80th ANNIVERSARY OF THE BIRTH OF SPARTAK TIMOFEEVICH BELYAEV

Anapole Moment of an Exotic Nucleus*

K. E. Arinstein, V. F. Dmitriev, and I. B. Khriplovich**

Budker Institute of Nuclear Physics, Siberian Division, Russian Academy of Sciences, pr. Akademika Lavrent'eva 11, Novosibirsk, 630090 Russia
Novosibirsk State University, ul. Pirogova 2, Novosibirsk, 630090 Russia

Received March 3, 2003

Abstract—We consider the anapole moment of ^{11}Be and demonstrate that the contribution to it of the $1p_{1/2}$ level, which is anomalously close to the ground state, is essentially compensated for by the contribution of the continuum. Our estimate for this anapole moment is $\kappa(^{11}\mathrm{Be}) \simeq (0.07{-}0.08)g_n$.

1. The anapole moment (AM) is a special magnetic multipole arising in a system that has no definite parity [1]. The corresponding magnetic field looks like that created by a current in a toroidal winding.

For many years, the anapole remained only a theoretical curiosity. The situation has changed due to the studies of parity nonconservation (PNC) in atoms. Since these tiny PNC effects increase with the nuclear charge Z, all the experiments are performed with heavy atoms. The main contribution to the effect is independent of nuclear spin and caused by the parity-violating weak interaction of electron and nucleon neutral currents. This interaction is proportional to the so-called weak nuclear charge Q which is numerically close (up to the sign) to the neutron number N. Thus, in heavy atoms, the nuclear-spin-independent weak interaction is additionally enhanced by about two orders of magnitude. Meanwhile, the nuclear-spin-dependent effects due to neutral currents not only lack the aforementioned coherent enhancement, but are also strongly suppressed numerically in the electroweak theory. Therefore, the observation of nuclear-spin-dependent PNC phenomena in atoms had looked absolutely unrealistic.

However, it was demonstrated [2, 3] that these effects in atoms are dominated not by the weak interaction of neutral currents, but by the electromagnetic interaction of atomic electrons with nuclear AM. Since the magnetic field of an anapole, like that of a toroidal winding, is completely confined inside the system, the electromagnetic interaction of an electron with the nuclear AM occurs only as long as the electron wave function penetrates the nucleus. In other words, this electromagnetic interaction is as local as the weak interaction itself, and in this sense they are indistinguishable. The nuclear AM is induced by PNC nuclear forces and is therefore proportional to the same Fermi constant $G = 1.027 \times 10^{-5} m^{-2}$ (we use the units $\hbar = 1$, $c = 1$; m is the proton mass), which determines the magnitude of the weak interactions in general and that of neutral currents in particular. The electron interaction with the AM, being of an electromagnetic nature, introduces an extra small factor into the effect discussed, the fine-structure constant $\alpha = 1/137$. Then, how does it appear that this effect is dominating?

The answer follows from the same picture of a toroidal winding. It is only natural that the interaction discussed is proportional to the magnetic flux through such a winding, and hence in our case it is proportional to the cross section of the nucleus, i.e., to $A^{2/3}$, where A is the atomic number. Indeed, a simple-minded model calculation leads to the following analytical result for the dimensionless effective constant κ which characterizes the anapole interaction in units of G [3]:

$$\kappa = \frac{9}{10} g \frac{\alpha\mu}{m r_0} A^{2/3}. \qquad (1)$$

Here, g is the effective constant of the P-odd interaction of the outer nucleon with the nuclear core, μ is the magnetic moment of the outer nucleon, and $r_0 = 1.2$ fm. In heavy nuclei, the enhancement factor $A^{2/3}$ is close to 30 and compensates essentially for the smallness of the fine-structure constant α. As a result, κ is not so small in heavy atoms; it is numerically close to 0.3.

The nuclear AM was experimentally discovered in 1997 [4]. This result for the total effective constant

*This article was submitted by the authors in English.

** e-mail: khriplovich@inp.nsk.su

of the PNC nuclear-spin-dependent interaction in ^{133}Cs is

$$\kappa_{\rm tot}(^{133}{\rm Cs}) = 0.44(6). \quad (2)$$

If one subtracts from this number the nuclear-spin-dependent contribution of neutral currents, as well as the result of the combined action of the "weak" charge Q and the usual hyperfine interaction, the answer for the anapole constant is

$$\kappa_{\rm exp}(^{133}{\rm Cs}) = 0.37(6). \quad (3)$$

Thus, the existence of an AM of the ^{133}Cs nucleus is reliably established.

This result provides valuable information on PNC nuclear forces. Of course, to this end, it should be combined with reliable nuclear calculations. The most detailed theoretical predictions for this AM can reasonably be summarized, at the so-called "best values" for the parameters of P-odd nuclear forces [5], as follows [6, 7]:

$$\kappa_{\rm theor}(^{133}{\rm Cs}) = 0.15{-}0.21. \quad (4)$$

There are good reasons to consider this prediction sufficiently reliable, at the accepted values of the P-odd nuclear constants.

The comparison of the theoretical value (4) for the cesium AM with the experimental result (3) indicates that the "best values" of [5] somewhat underestimate the magnitude of P-odd nuclear forces. In no way is this conclusion trivial. The point is that the magnitude of parity-nonconserving effects found in some nuclear experiments is much smaller than that following from the "best values" (see review [8]). In all these experiments, however, either the experimental accuracy is not high enough, or the theoretical interpretation is not sufficiently convincing. The experiment [4] looks much more reliable in both respects. Still, further experimental investigations of nuclear AMs are certainly of great interest.

2. In principle, the AM can be enhanced not only due to large A, but also in the case when, anomalously close to the ground state of a nucleus, there is an opposite-parity level of the same angular momentum. In this connection, attention was attracted in [9, 10] to exotic halo nuclei. In particular, the exotic neutron-rich halo nucleus ^{11}Be was considered therein. In this nucleus, the outer odd neutron is in the state $2s_{1/2}$, its only bound excited level being $1p_{1/2}$ (the well-known "inversion of levels"). The anomalously small energy separation between these two levels of opposite parity,

$$|\Delta E| = E(1p_{1/2}) - E(2s_{1/2}) = 0.32\ {\rm MeV}, \quad (5)$$

enhances by itself their P-odd mixing and, thus, the AM of this nucleus. As pointed out in [9, 10], the small binding energy of the odd neutron,

$$|\Delta E_0| = 0.50\ {\rm MeV}, \quad (6)$$

affects the AM additionally, but in two opposite directions. On the other hand, it suppresses the overlap of the odd-neutron wave function with the core and thus suppresses the mixing of the $2s_{1/2}$ and $1p_{1/2}$ levels due to the weak-interaction operator, which has the form

$$W = \frac{G}{\sqrt{2}}\frac{g_n}{2m}\{\boldsymbol{\sigma}\cdot\mathbf{p}, \rho(r)\}; \quad (7)$$

here g_n is the effective constant of the P-odd interaction of the outer neutron with the nuclear core, $\boldsymbol{\sigma}$ and $\mathbf{p}$ are the momentum and spin operators of the outer neutron, and $\rho(r)$ is the spherically symmetric core density. On the other hand, the small binding energy enhances the matrix element of $\mathbf{r}$ in the anapole operator of the neutron,

$$\mathbf{a} = \frac{\pi e\mu_n}{m}\mathbf{r}\times\boldsymbol{\sigma}, \quad (8)$$

where $\mu_n = -1.91$ is the neutron magnetic moment.

The detailed calculation which takes into account the P-odd mixing of the ground state only with the $1p_{1/2}$ level results in the following value for the effective anapole constant [10]:

$$\kappa_1(^{11}{\rm Be}) = 0.17 g_n. \quad (9)$$

Indeed, this value is 15 times larger than that given by the estimate (1) for $A = 11$ (the neutron constant g_n is poorly known by itself, most probably $g_n \lesssim 1$). Certainly, this enhancement of an AM in a light nucleus would be of serious interest even if its possible experimental implications are set aside.

However, such a strong enhancement of AM, as given in (9), in a loosely bound nucleus does not look natural. In particular, nothing of the kind happens in the deuteron. Even in the limit of vanishing binding energy, when the energy interval between the deuteron s state and the continuum p states tends to zero, the deuteron AM in no way is enhanced [11] (see also [12]). As to the problem of ^{11}Be discussed here, we argue below that a strong cancellation between the contribution of the bound $1p_{1/2}$ state [accounted for in (9)] and that of the continuum (omitted therein) takes place, resulting in a serious suppression of the estimate (9).

3. We start with the general expression for the AM, as induced by operators (7) and (8):

$$\langle 0|\mathbf{a}|0\rangle = \frac{G}{\sqrt{2}}\frac{\pi e\mu g}{2m^2}\sum_n \frac{\langle 0|\mathbf{r}\times\boldsymbol{\sigma}|n\rangle\langle n|\{\boldsymbol{\sigma}\cdot\mathbf{p},\rho(r)\}|0\rangle + \langle 0|\{\boldsymbol{\sigma}\cdot\mathbf{p},\rho(r)\}|n\rangle\langle n|\mathbf{r}\times\boldsymbol{\sigma}|0\rangle}{E(2s_{1/2}) - E_n}. \quad (10)$$

To estimate the sum, we use at first the closure approximation, which is facilitated here by the same (negative) sign of all energy denominators. After extracting some average value of denominators, $-\bar{\Delta}$ ($\bar{\Delta} > 0$), and using the completeness relation, the sum (10) reduces to

$$\langle 0|\mathbf{a}|0\rangle = -\frac{G}{\sqrt{2}}\frac{\pi e\mu g}{2m^2\bar{\Delta}}\langle 0|\{[\mathbf{r}\times\boldsymbol{\sigma}],\{\boldsymbol{\sigma}\cdot\mathbf{p},\rho(r)\}\}|0\rangle. \quad (11)$$

Thus, the arising effective operator transforms as follows:

$$\{[\mathbf{r}\times\boldsymbol{\sigma}],\{\boldsymbol{\sigma}\mathbf{p},\rho(r)\}\} = 4(\mathbf{l}+\boldsymbol{\sigma})\rho(r), \quad (12)$$

where $\mathbf{l}$ is the orbital angular momentum of the valence nucleon. (It is rather amusing that we arrive here at the same combination $\mathbf{l}+\boldsymbol{\sigma}$ which enters the expression for the magnetic moment of a bound electron.)

In our case of ^{11}Be, $\mathbf{l} = 0$ and $\boldsymbol{\sigma} = 2\mathbf{I}$, where $\mathbf{I}$ is the spin of the nucleus. Thus, here the expression for AM reduces to

$$\langle 0|\mathbf{a}|0\rangle = -\frac{G}{\sqrt{2}}\frac{4\pi e\mu_n g_n}{m^2\bar{\Delta}}\langle 0|\rho(r)|0\rangle\mathbf{I}. \quad (13)$$

With the standard prescription (see [3]) of deleting from the expression for $\langle 0|\mathbf{a}|0\rangle$ the factors $(G/\sqrt{2})\mathbf{I}$ and multiplying the rest by $eI(I+1)(-1)^{I+1/2-l}/(I+1/2)$, we arrive finally at the following expression for the effective anapole constant:

$$\kappa = \frac{3\pi\alpha\mu_n g_n}{m^2\bar{\Delta}}\langle 0|\rho(r)|0\rangle. \quad (14)$$

The expectation value $\langle 0|\rho(r)|0\rangle$ was calculated by us with the same ground-state wave function

$$R_{2s}(r) = \frac{2^{3/2}a^2[1-(r/a)^2]\exp(-r/r_0)}{r_0^{3/2}\sqrt{45r_0^4+2a^4-12a^2r_0^2}},$$
$$r_0 = 1.45\ \text{fm}, \qquad a = 2\ \text{fm},$$

and core density

$$\rho(r) = \rho_0\exp(-r^2/R_c^2), \qquad \rho_0 = 0.20\ \text{fm}^{-3},$$
$$R_c = 2\ \text{fm},$$

as those used in [10]. Thus, the obtained expectation value is

$$\langle 0|\rho(r)|0\rangle = 0.052\rho_0 = 0.01\ \text{fm}^{-3}. \quad (15)$$

Now, if $\bar{\Delta}$ is identified with the smallest energy interval $E(1p_{1/2}) - E(2s_{1/2}) = 0.32$ MeV, the numerical result is

$$\kappa(\bar{\Delta} = 0.32\ \text{MeV}) = -0.036g_n. \quad (16)$$

The comparison of (16) with (9) demonstrates that, in the last estimate, the negative contribution of continuum states outweighs the positive one of $1p_{1/2}$, with a small net result which only slightly exceeds, if at all, the typical value of κ as given by (1).

As expected, the small binding energy strongly suppresses $\langle 0|\rho(r)|0\rangle$ as compared to ρ_0 itself [see (15)]. However, the expected enhancement of the matrix element of $\mathbf{r}$ in the anapole operator (8) is not operative in (16) since on average this $\mathbf{r}$ is eaten up by $\mathbf{p}$ in the weak-interaction operator (7). And the strong suppression of $\langle 0|\rho(r)|0\rangle$ compensates in (16) for the enhancement due to small energy intervals.

Estimate (16) can be improved considerably in the following way. Its comparison with (9) demonstrates that, with $\bar{\Delta} = 0.32$ MeV, the contribution of the continuum to κ constitutes

$$\kappa_c(\bar{\Delta} = 0.32\ \text{MeV}) = -0.036g_n - 0.17g_n \quad (17)$$
$$= -0.206g_n.$$

With the continuum threshold at $\bar{\Delta} = |\Delta E_0| = 0.50$ MeV, the continuum contribution is certainly overestimated by (17). However, κ_c can be easily recalculated for more reasonable values of $\bar{\Delta}$ just by multiplying (17) by $0.32/\bar{\Delta}$.

Combining the thus obtained improved values of κ_c with (9), we arrive at the following estimates for the anapole moment of ^{11}Be:

$\bar{\Delta}$, MeV	$\kappa(^{11}\text{Be})$
0.6	$0.060g_n$
0.7	$0.076g_n$
0.8	$0.088g_n$.

(18)

We believe that, with all the uncertainties of our estimates (18) for the anapole moment of ^{11}Be, they are more reliable than (9). Most probably, the real value of $\kappa(^{11}\text{Be})$ is around $(0.07-0.08)g_n$; i.e., it is 2–3 times smaller than (9).

ACKNOWLEDGMENTS

The investigation was supported by the Russian Foundation for Basic Research, project no. 03-02-17612, and through a grant for Leading Scientific Schools.

REFERENCES

1. Ya. B. Zel'dovich, Zh. Éksp. Teor. Fiz. **33**, 1531 (1957) (the paper contains also the mention of the analogous results obtained by V. G. Vaks).
2. V. V. Flambaum and I. B. Khriplovich, Zh. Éksp. Teor. Fiz. **79**, 1656 (1980) [Sov. Phys. JETP **52**, 835 (1980)].
3. V. V. Flambaum, I. B. Khriplovich, and O. P. Sushkov, Phys. Lett. B **146B**, 367 (1984).
4. C. S. Woods *et al.*, Science **275**, 1759 (1997).
5. B. Desplanques, J. F. Donoghue, and B. R. Holstein, Ann. Phys. (N.Y.) **124**, 449 (1980).
6. V. F. Dmitriev and V. B. Telitsin, Nucl. Phys. A **674**, 168 (2000).
7. W. C. Haxton, C.-P. Liu, and M. J. Ramsey-Musolf, Phys. Rev. C **65**, 045502 (2002).
8. E. G. Adelberger and W. C. Haxton, Annu. Rev. Nucl. Part. Sci. **35**, 501 (1985).
9. M. S. Hussein, A. F. R. de Toledo Piza, O. K. Vorov, and A. K. Kerman, Phys. Rev. C **60**, 064615 (1999).
10. M. S. Hussein, A. F. R. de Toledo Piza, O. K. Vorov, and A. K. Kerman, Nucl. Phys. A **686**, 163 (2001).
11. I. B. Khriplovich and R. V. Korkin, Nucl. Phys. A **665**, 365 (2000).
12. M. J. Savage and R. P. Springer, Nucl. Phys. A **644**, 235 (1998); **657**, 457 (E) (1999).

Physics of Atomic Nuclei, Vol. 67, No. 1, 2004, pp. 199–208. From Yadernaya Fizika, Vol. 67, No. 1, 2004, pp. 195–204.

80th ANNIVERSARY OF THE BIRTH OF SPARTAK TIMOFEEVICH BELYAEV

Evolution of Baryon-Free Matter Produced in Relativistic Heavy-Ion Collisions*

V. N. Russkikh[1)], Yu. B. Ivanov[1)], E. G. Nikonov[2)], W. Nörenberg***, and V. D. Toneev[2)]*****

Gesellschaft für Schwerionenforschung mbH, Darmstadt, Germany

Received February 14, 2003

Abstract—A three-fluid hydrodynamic model is introduced for simulating heavy-ion collisions at incident energies between a few and about 200 A GeV. In addition to the two baryon-rich fluids of two-fluid models, a new model incorporates a third, baryon-free (i.e., with zero net baryonic charge), fluid, which is created in the midrapidity region. Its evolution is delayed due to a formation time τ, during which the baryon-free fluid neither thermalizes nor interacts with the baryon-rich fluids. After formation, it thermalizes and starts to interact with the baryon-rich fluids. It is found that, for $\tau = 0$, the interaction strongly affects the baryon-free fluid. However, at reasonable finite formation time, $\tau \simeq 1$ fm/c, the effect of this interaction turns out to be substantially reduced, although still noticeable. Baryonic observables are only slightly affected by the interaction with the baryon-free fluid. © *2004 MAIK "Nauka/Interperiodica".*

1. INTRODUCTION

Nearly fifty years have passed since the paper "Relativistic Kinetic Equation" by Belyaev and Budker was published [1]. The proposed relativistic formulation of the distribution function and the kinetic equation with small-angle scattering have been included in many textbooks and found numerous applications in atomic physics and electron–positron plasma. Recently, a generalized relativistic kinetic equation of this type was implemented for describing the partonic evolution in very early stages of a heavy-ion collision at ultrarelativistic RHIC energies [2]. In the present paper, we address more moderate, but nevertheless highly relativistic, energies, i.e., up to those reached at the CERN SPS. The relativistic kinetic equation is used in a peculiar way, namely, to derive a coupling term for three-fluid hydrodynamic equations.

Two-fluid hydrodynamics with free-streaming radiation of pions was advanced first in [3, 4]. The initial stage of heavy-ion collisions definitely is a highly nonequilibrium process. Within the hydrodynamic approach, this nonequilibrium is simulated by means of a two-fluid approximation, which takes care of the finite stopping power of nuclear matter [5, 6], and simultaneously describes the entropy generation at the initial stage. The radiated pions form baryon-free matter in the midrapidity region, while two baryon-rich fluids simulate the propagation of leading particles. The pions are the most abundant species of the baryon-free matter which may contain any hadronic and/or quark–gluon species including baryon–antibaryon pairs.

The first applications of the two-fluid model [7, 8] to the description of heavy-ion collisions in a wide range of incident energies, from those of SIS to SPS, were quite successful. One of the advantages of the hydrodynamic models is that they directly address the equation of state (EoS) of nuclear matter, which is of prime interest for this domain of physics. In particular, we have shown [9] recently that the experimental excitation function of the directed flow is well described by the mixed-phase EoS in contrast to earlier predictions of the two-phase bag-model EoS. In these 3D hydrodynamic simulations, we describe the whole process of the reaction, i.e., the evolution from the formation of a hot and dense nuclear system to its subsequent decay. This is in contrast to numerous other simulations, which treat only the expansion stage of a fireball formed in the course of the reaction, while the initial state of this dense and hot nuclear system is constructed from either kinetic simulations or more general, albeit model-dependent, assumptions (e.g., see [10, 11]).

However, the approximation of free-streaming pions, produced in the midrapidity region, was still irritating from the theoretical point of view, in partic-

*This article was submitted by the authors in English.

[1)]Russian Research Centre Kurchatov Institute, pl. Kurchatova 1, Moscow, 123182 Russia.

[2)]Joint Institute for Nuclear Research, Dubna, Moscow oblast, 141980 Russia.

**e-mail: Y.Ivanov@gsi.de

***e-mail: W.Nrnbrg@gsi.de

****e-mail: Toneev@gsi.de

ular, because the relative momenta of the produced pions and the leading baryons are in the range of the Δ resonance for the incident energies considered. This would imply that the interaction between the produced pions and the baryon-rich fluids should be strong. The free-streaming assumption relies on a long formation time of produced pions. Indeed, the proper time for the formation of the produced particles is commonly assumed to be on the order of 1 fm/c in the comoving frame. Since the main part of the produced pions is quite relativistic at high incident energies, their formation time should be long enough in the reference frame of calculation to prevent them from interacting with the baryon-rich fluids. However, this argument is qualitative rather than quantitative and, hence, requires further verification. The first attempt to do this was undertaken by the Frankfurt group [12], which started to explore an opposite extreme. They assumed that the produced pions immediately thermalize, forming a baryon-free fluid (or a "fireball" fluid, in terms of [12]), and interact with the baryon-rich fluids. No formation time was allowed, and the strength of the corresponding interaction was guessed rather than microscopically estimated. This opposite extreme, referred to as a $(2+1)$-fluid model and not quite being justified either, yielded results substantially different from those of the free-streaming approximation. This was one of the reasons why in subsequent applications the Frankfurt group neglected the interaction between baryon-free and baryon-rich fluids, while keeping the produced pions thermalized [13], thus effectively restoring the free-streaming approximation. However, the assumed immediate thermalization of the fireball fluid together with the lack of interaction with baryon-rich fluids still was not a consistent approximation.

In this paper, we would like to return to the problem of verification of the free-streaming approximation for the produced pions. To do this, we extend the two-fluid model of [3, 4, 7–9] to a three-fluid model, where the created baryon-free fluid (which we call a "fireball" fluid, according to the Frankfurt group) is treated on equal footing with the baryon-rich ones. However, we allow a certain formation time for the fireball fluid, during which the constituents of the fluid propagate without interactions. Furthermore, we estimate the interaction between fireball and baryon-rich fluids by means of a relativistic kinetic equation and elementary cross sections.

In this paper, we consider incident energies in the range from a few to about 200 A GeV (i.e., from AGS to SPS energies). The interest in this energy range was recently revived in connection with the project of the new accelerator facility at GSI SIS200 [14]. The goal of the research program on nucleus–nucleus collisions at this planned facility is the investigation of nuclear matter in the region of incident energies ($E_{\rm lab} \simeq 10$–40 A GeV), in which the highest baryon densities and highest relative strangeness at moderate temperatures are expected. Here, the QCD phase diagram is much less explored, both experimentally and theoretically, as compared to the higher energy region characterized by higher temperatures, but lower net baryon densities, where lattice QCD calculations [15] and a large body of experimental data from SPS (CERN) [16] and RHIC (BNL) [17] are available by now.

2. THREE-FLUID HYDRODYNAMIC MODEL

Unlike the one-fluid hydrodynamic model, where local instantaneous stopping of projectile and target matter is assumed, a specific feature of the dynamic three-fluid description is a finite stopping power resulting in a counterstreaming regime of leading baryon-rich matter. Experimental rapidity distributions in nucleus–nucleus collisions support this counterstreaming behavior, which can be observed for incident energies between a few and 200 A GeV. The basic idea of a three-fluid approximation to heavy-ion collisions [3, 4, 18] is that, at each spacetime point $x = (t, \mathbf{x})$, the distribution function of baryon-rich matter, $f_{\rm br}(x,p)$, can be represented as a sum of two distinct contributions,

$$f_{\rm br}(x,p) = f_p(x,p) + f_t(x,p), \qquad (1)$$

initially associated with constituent nucleons of the projectile (p) and target (t) nuclei. In addition, newly produced particles, populating the midrapidity region, are associated with a fireball (f) fluid described by the distribution function $f_f(x,p)$. Note that both baryon-rich and fireball fluids may consist of any type of hadrons and/or partons (quarks and gluons), rather than only nucleons and pions. However, here and below, we suppress the species label on the distribution functions for the sake of transparency of the equations.

With the above-introduced distribution functions f_α ($\alpha = p, t, f$), the coupled set of relativistic Boltzmann equations looks as follows:

$$p_\mu \partial_x^\mu f_p(x,p) = C_p(f_p, f_t) + C_p(f_p, f_f), \qquad (2)$$

$$p_\mu \partial_x^\mu f_t(x,p) = C_t(f_p, f_t) + C_t(f_t, f_f), \qquad (3)$$

$$p_\mu \partial_x^\mu f_f(x,p) = C_f(f_p, f_t) + C_f(f_p, f_f) + C_f(f_t, f_f), \qquad (4)$$

where C_α denote collision terms between the constituents of the three fluids. We have omitted intrafluid collision terms, like $C_p(f_p, f_p)$, since below they will be canceled anyway. The displayed interfluid collision

terms have a clear physical meaning: $C_{p/t}(f_p, f_t)$, $C_{p/t}(f_{p/t}, f_f)$, and $C_f(f_{p/t}, f_f)$ give rise to friction between p, t, and f fluids, and $C_f(f_p, f_t)$ takes care of particle production in the midrapidity region. Note that, up to now, we have made no approximation, except for hiding intrafluid collision terms.

Let us proceed to approximations which justify the term "fluids" already used. We assume that constituents within each fluid are locally equilibrated, both thermodynamically and chemically. In particular, this implies that the intrafluid collision terms are indeed zero. This assumption relies on the fact that intrafluid collisions are much more efficient in driving a system to equilibrium than interfluid interactions. As applied to the fireball fluid, this assumption requires some additional comments, related to the concept of a finite formation time. During the formation proper time τ after production, the fireball fluid propagates freely, interacting neither with itself nor with the baryon-rich fluids. After this time period, the fireball matter thermalizes locally and starts to interact with both itself and the baryon-rich fluids. Being heated up, these three fluids may contain not only hadronic but also deconfined quark–gluon species, depending on the EoS used.

The above assumption suggests that interaction between different fluids should be treated dynamically. To obtain the required dynamic equations, we first integrate the kinetic Eqs. (2)–(4) over momentum and sum over particle species with the weight of baryon charge. This way, we arrive at equations of the baryon-charge conservation

$$\partial_\mu J^\mu_\alpha(x) = 0 \tag{5}$$

for $\alpha = p$ and t, where $J^\mu_\alpha = n_\alpha u^\mu_\alpha$ is the baryon current defined in terms of baryon density n_α and hydrodynamic 4-velocity u^μ_α normalized as $u_{\alpha\mu}u^\mu_\alpha = 1$. Equation (5) implies that there is no baryon-charge exchange between p and t fluids, as well as that the baryon current of the fireball fluid is identically zero, $J^\mu_f = 0$. Integrating kinetic Eqs. (2)–(4) over momentum with weight of 4-momentum p^ν and summing over all particle species, we arrive at equations of the energy–momentum exchange for energy–momentum tensors $T^{\mu\nu}_\alpha$ of the fluids

$$\partial_\mu T^{\mu\nu}_p(x) = -F^\nu_p(x) + F^\nu_{fp}(x), \tag{6}$$

$$\partial_\mu T^{\mu\nu}_t(x) = -F^\nu_t(x) + F^\nu_{ft}(x), \tag{7}$$

$$\partial_\mu T^{\mu\nu}_f(x) = F^\nu_p(x) + F^\nu_t(x) - F^\nu_{fp}(x) - F^\nu_{ft}(x), \tag{8}$$

where the F^ν are friction forces originating from interfluid collision terms in kinetic Eqs. (2)–(4). F^ν_p and F^ν_t in Eqs. (6) and (7) describe energy–momentum loss of baryon-rich fluids due to their mutual friction. A part of this loss $|F^\nu_p - F^\nu_t|$ is transformed into thermal excitation of these fluids, while another part $(F^\nu_p + F^\nu_t)$ gives rise to particle production in the fireball fluid [see Eq. (8)]. F^ν_{fp} and F^ν_{ft} are associated with friction of the fireball fluid with the p and t fluids, respectively. Note that Eqs. (6)–(8) satisfy the total energy–momentum conservation

$$\partial_\mu(T^{\mu\nu}_p + T^{\mu\nu}_t + T^{\mu\nu}_f) = 0. \tag{9}$$

As described above, the energy–momentum tensors of the baryon-rich fluids ($\alpha = p$ and t) take the conventional hydrodynamic form

$$T^{\mu\nu}_\alpha = (\varepsilon_\alpha + P_\alpha)\, u^\mu_\alpha\, u^\nu_\alpha - g^{\mu\nu} P_\alpha \tag{10}$$

in terms of the proper energy density ε_α and pressure P_α. For the fireball, however, only the thermalized part of the energy–momentum tensor is described by this hydrodynamic form:

$$T^{(\mathrm{eq})\mu\nu}_f = (\varepsilon_f + P_f)\, u^\mu_f\, u^\nu_f - g^{\mu\nu} P_f. \tag{11}$$

Its evolution is defined by an Euler equation with a retarded source term

$$\partial_\mu T^{(\mathrm{eq})\mu\nu}_f(x) = \int d^4x' \delta^4\left(x - x' - U_F(x')\tau\right) \times \left[F^\nu_p(x') + F^\nu_t(x')\right] - F^\nu_{fp}(x) - F^\nu_{ft}(x), \tag{12}$$

where τ is the formation time, and

$$U^\nu_F(x') = \frac{F^\nu_p(x') + F^\nu_t(x')}{|F_p(x') + F_t(x')|} \tag{13}$$

is a free-streaming 4-velocity of the produced fireball matter. In fact, this is the velocity at the moment of production of the fireball matter. According to Eq. (12), the energy and momentum of this matter appear as a source in the Euler equation only later, at time $U^0_F\tau$ after production, and in different space point $\mathbf{x}' - \mathbf{U}_F(x')\tau$, as compared to the production point $\mathbf{x}'$. At first glance, one can immediately simplify the right-hand side of Eq. (12) by performing integration with the δ function. However, this integration is not that straightforward, since the expression under the δ function, $x - x' - U_F(x')\tau = 0$, may have more than one solution with respect to x'. The latter would mean that the matter produced at several different spacetime points x' simultaneously thermalizes at the same spacetime point x. This is possible due to the nonlinearity of the hydrodynamic equations.

The residual part of $T^{\mu\nu}_f$ (the free-streaming one) is defined as

$$T^{(\mathrm{fs})\mu\nu}_f = T^{\mu\nu}_f - T^{(\mathrm{eq})\mu\nu}_f. \tag{14}$$

The equation for $T_f^{(\mathrm{fs})\mu\nu}$ can easily be obtained by taking the difference between Eqs. (8) and (12). If all the fireball matter turns out to be formed before freeze-out, then this equation is not needed. Thus, the three-fluid model introduced here contains both the original two-fluid model with pion radiation [3, 4, 7–9] and the $(2+1)$-fluid model [12, 13] as limiting cases for $\tau \to \infty$ and $\tau = 0$, respectively.

The nucleon–nucleon cross sections at high energies are strongly forward–backward peaked. In this case, the Boltzmann collision term can be simplified significantly, since the involved 4-momentum transfer is small. The small-angle-scattering expansion of the collision integral results in the relativistic Fokker–Planck equation, as first derived by Belyaev and Budker [1]. Precisely this equation was used in [5] to estimate the friction forces, F_p^ν and F_t^ν, proceeding from only NN elastic scattering. Later, these friction forces were calculated [19] on the basis of (both elastic and inelastic) experimental inclusive NN cross sections

$$F_\alpha^\nu = \rho_p \rho_t \left[(u_\alpha^\nu - u_{\bar{\alpha}}^\nu)\, D_P + \left(u_p^\nu + u_t^\nu\right) D_E \right], \quad (15)$$

$\alpha = p$ and t, $\bar{p} = t$ and $\bar{t} = p$. Here, ρ_α denotes the scalar densities of the p and t fluids,

$$D_{P/E} = m_N\, V_{\mathrm{rel}}^{pt}\, \sigma_{P/E}(s_{pt}), \quad (16)$$

where m_N is the nucleon mass, $s_{pt} = m_N^2 \left(u_p^\nu + u_t^\nu\right)^2$ is the mean invariant energy squared of two colliding nucleons from the p and t fluids, $V_{\mathrm{rel}}^{pt} = [s_{pt}(s_{pt} - 4m_N^2)]^{1/2}/(2m_N^2)$ is the mean relative velocity of the p and t fluids, and $\sigma_{P/E}(s_{pt})$ are determined in terms of nucleon–nucleon cross sections integrated with certain weights (see [3, 4, 7, 8, 19] for details). It was found in [19] that a part of these friction terms, which is related to the transport cross section, may be well parametrized by an effective deceleration length λ_{eff} with a constant value $\lambda_{\mathrm{eff}} \approx 5$ fm. However, there are reasons to consider λ_{eff} as a phenomenological parameter, as was pointed out in [7]. Indeed, as is seen from Eq. (16), this friction is estimated only in terms of nucleon–nucleon cross sections, while the excited matter of baryon-rich fluids certainly consists of a great number of hadrons and/or deconfined quarks and gluons. Furthermore, these quantities may be modified by in-medium effects. In this respect, $D_{P/E}$ should be understood as quantities that give a scale of this interaction.

Equations (5)–(7) and (12), supplemented by a certain EoS and expressions for friction forces F^ν, form a full set of equations of the relativistic three-fluid hydrodynamic model. To make this set closed, we still need to define the friction of the fireball fluid with the p and t fluids, F_{fp}^ν and F_{ft}^ν, in terms of hydrodynamic quantities and some cross sections.

3. INTERACTION BETWEEN FIREBALL AND BARYON-RICH FLUIDS

Our aim here is to estimate the scale of the friction force between the fireball and baryon-rich fluids, similar to that done before for baryon-rich fluids [19]. To this end, we consider a simplified system where all baryon-rich fluids consist only of nucleons, as the most abundant component of these fluids, and the fireball fluid contains only pions.

For incident energies from 10 (AGS) to 200 A GeV (SPS), the relative nucleon–pion energies are in the resonance range dominated by the Δ resonance. To estimate this relative energy, we consider a produced pion, being at rest in the center of mass (c.m.) of the colliding nuclei, $q_\pi = \{m_\pi, 0, 0, 0\}_{\mathrm{c.m}}$. Baryon-rich fluids decelerate each other during their interpenetration. This means that the nucleon momentum should be smaller than the incident momentum, $|p_N| < |\{m_N \gamma_{\mathrm{c.m}}, \mathbf{p}_{\mathrm{c.m}}\}|$, where $\gamma_{\mathrm{c.m}}$ is the gamma factor of the incident nucleon in the c.m. frame. Calculating the invariant relative energy squared $s = (p+q)^2$ at $E_{\mathrm{lab}} = 158\ A$ GeV, we obtain $s^{1/2} < 1.8$ GeV. This range of s precisely covers the resonance region, $1.1 < s^{1/2} < 1.8$ GeV [20]. At $E_{\mathrm{lab}} = 10\ A$ GeV, we arrive at $s^{1/2} < 1.3$ GeV, which is also within the resonance region. At even lower incident energies, the strength of the fireball fluid becomes so insignificant, as compared with thermal mesons in the p and t fluids, that the way of treating its interaction with the baryon-rich fluids does not significantly affect the observables. For the same reason, we do not apply any special prescription for the unification of the fireball fluid with the baryon-rich fluids, since this may happen only at relatively low incident energies $E_{\mathrm{lab}} < 10\ A$ GeV.

The resonance-dominated interaction implies that the essential process is absorption of a fireball pion by a p- or t-fluid nucleon with formation of an R resonance (most probably Δ). This produced R resonance still belongs to the original p or t fluid, since its recoil due to absorption of a light pion is small. Subsequently, this R resonance decays into a nucleon and a pion already belonging to the original p or t fluid. Symbolically, this mechanism can be expressed as

$$N^\alpha + \pi^f \to R^\alpha \to N^\alpha + \pi^\alpha.$$

As a consequence, only the loss term contributes to the kinetic equation for the fireball fluid.

Proceeding from the above consideration, we write the collision term between fireball-fluid pions and α-fluid nucleons ($\alpha = p$ or t) as follows:

$$C_f(f_\alpha, f_f) \quad (17)$$
$$= -\int \frac{d^3q}{q_0} W^{N\pi\to R}(s) f_f^{(\mathrm{eq})}(x,p) f_\alpha(x,q),$$

where $s = (p+q)^2$,

$$W^{N\pi\to R}(s) = (1/2)[(s - m_N^2 - m_\pi^2)^2 - 4m_N^2 m_\pi^2]^{1/2} \sigma_{\rm tot}^{N\pi\to R}(s)$$

is the rate of producing a baryon R resonance, and $\sigma_{\rm tot}^{N\pi\to R}(s)$ is the parametrization of experimental pion–nucleon cross sections [20]. Here, only the distribution function of formed (and, hence, thermalized) fireball pions, $f_f^{(\rm eq)}$, enters the collision term, since the nonformed particles did not participate in the interaction by assumption.

Integrating $C_f(f_\alpha, f_f)$ weighted with the 4-momentum p^ν over momentum, we arrive at

$$F_{f\alpha}^\nu(x) = \int \frac{d^3q}{q_0}\frac{d^3p}{p_0} p^\nu W^{N\pi\to R}(s) \times f_f^{(\rm eq)}(x,p) f_\alpha(x,q) \simeq \frac{W^{N\pi\to R}(s_{f\alpha})}{m_\pi u_f^0}\left(\int \frac{d^3q}{q_0} f_\alpha(x,q)\right) \times \left(\int \frac{d^3p}{p_0} p^0 p^\nu f_f^{(\rm eq)}(x,p)\right) = D_{f\alpha}\frac{T_f^{(\rm eq)0\nu}}{u_f^0}\rho_\alpha, \quad (18)$$

where we replaced p^0 and s with their mean values, $\langle p^0\rangle = m_\pi u_f^0$ and $s_{f\alpha} = (m_\pi u_f + m_N u_\alpha)^2$, and introduced the transport coefficients

$$D_{f\alpha} = W^{N\pi\to R}(s_{f\alpha})/(m_N m_\pi) = V_{\rm rel}^{f\alpha}\sigma_{\rm tot}^{N\pi\to R}(s_{f\alpha}). \quad (19)$$

Here, $V_{\rm rel}^{f\alpha} = [(s_{f\alpha} - m_N^2 - m_\pi^2)^2 - 4m_N^2 m_\pi^2]^{1/2} \times (2m_N m_\pi)^{-1}$ denotes the mean invariant relative velocity between the fireball and the α fluids. Thus, we have expressed the friction $F_{f\alpha}^\nu$ in terms of the fireball-fluid energy–momentum density $T_f^{0\nu}$, the scalar density ρ_α of the α fluid, and a transport coefficient $D_{f\alpha}$. Note that this friction is zero until the fireball pions are formed, since $T_f^{(\rm eq)0\nu} = 0$ during the formation time τ.

In fact, the above treatment is an estimate of the friction terms rather than their strict derivation. This peculiar way of evaluation is motivated by the form of the final result (18). An advantage of this form is that m_π and any other mass do not appear explicitly, and hence this form allows a natural extension to any content of the fluid, including deconfined quarks and gluons, under the assumption that $D_{f\alpha}$ represents just a scale of the transport coefficient.

4. SIMULATIONS OF NUCLEUS–NUCLEUS COLLISIONS

The relativistic 3D code for the above-described three-fluid model was constructed by means of modifying the existing two-fluid 3D code of [3, 4, 7–9]. In actual calculations, we used the mixed-phase EoS developed in [21–23]. This phenomenological EoS takes into account a possible deconfinement phase transition of nuclear matter. The underlying assumption of this EoS is that unbound quarks and gluons may coexist with hadrons in the nuclear environment. In accordance with lattice QCD data, the statistical mixed-phase model describes the first-order deconfinement phase transition for pure gluon matter and crossover for one with quarks [21–23].

We performed simulations of nucleus–nucleus collisions Pb + Pb at $E_{\rm lab} = 158\ A$ GeV and Au + Au at $E_{\rm lab} = 10.5\ A$ GeV. The general dynamics of heavy-ion collisions is illustrated in Fig. 1 by the energy-density evolution of the baryon-rich fluids ($\varepsilon_b = \varepsilon_p + \varepsilon_t$, in the c.m. frame of colliding nuclei) in the reaction plane of the Pb + Pb collision. Different stages of interaction at relativistic energies are clearly seen in this example: two Lorentz-contracted nuclei (note the different scales along the x and z axes in Fig. 1) start to interpenetrate through each other, reach a maximal energy density by the time $\sim$ 1.1 fm/c, and then expand predominantly in the longitudinal direction, forming a "sausage-like" freeze-out system. At this and lower incident energies, the baryon-rich dynamics is not really disturbed by the fireball fluid and hence the cases $\tau = 0$ and 1 fm/c turn out to be indistinguishable in terms of ε_b.

In Fig. 2, the dynamic evolution of the fireball energy density (ε_f, in the c.m. frame of the colliding nuclei) in the reaction plane of the Pb + Pb collision at impact parameter $b = 2$ fm is shown for two values of the formation time, $\tau = 0$ (the left column of panels) and 1 fm/c (the right column of panels). It starts to form near the time moment when the maximal energy density ε_b is reached. The f-fluid evolution indeed looks like that for an expanding fireball; its density depends significantly on the formation time.

To quantitatively reveal the role of the interaction between fireball and baryon-rich fluids, we followed the evolution of the total energy released into the fireball fluid,

$$E_f^{(\rm released)}(t) = \int_0^t dt' \int d^3x' \left(F_p^0(x') + F_t^0(x')\right) \quad (20)$$

[cf. Eq. (8)], and the total energy retained in the fireball fluid (both thermalized and nonthermalized) after

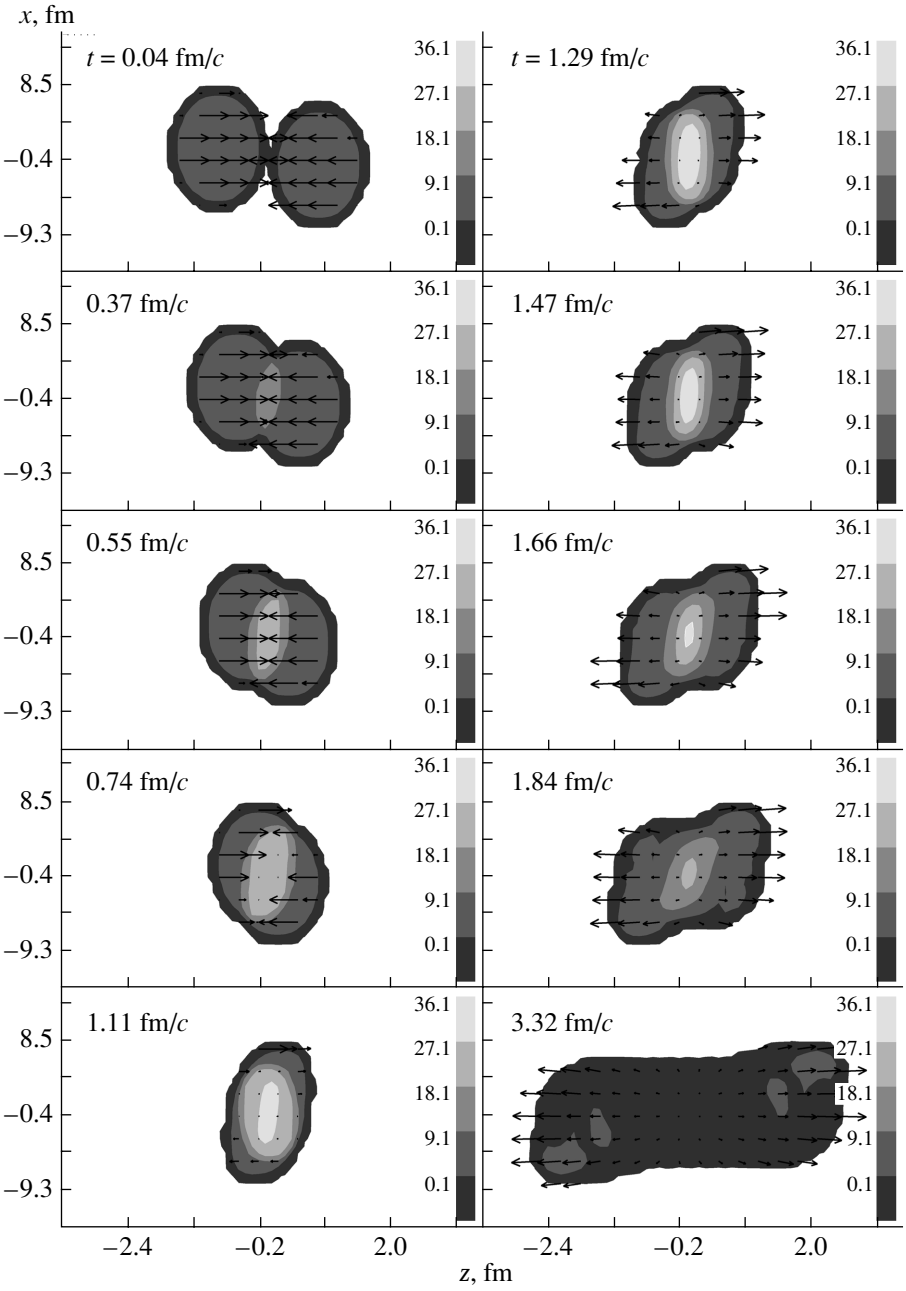

Fig. 1. Time evolution of the energy density, $\varepsilon_b = \varepsilon_p + \varepsilon_t$, for the baryon-rich fluids in the reaction plane (xz plane) for the Pb + Pb collision ($E_{\rm lab} = 158\ A$ GeV) at impact parameter $b = 2$ fm. Shades of gray represent different levels of ε_b as indicated at the right side of each panel. Numbers on this palette show the ε_b values (in GeV/fm^3) at which the shades change. Arrows indicate the hydrodynamic velocities of the fluids.

interaction,

$$E_f^{(\rm tot)}(t) = \int d^3x T_f^{00}(t,\mathbf{x}) = \int\limits_0^t dt' \int d^3x' \quad (21)$$
$$\times \left(F_p^0(x') + F_t^0(x') - F_{fp}^0(x') - F_{ft}^0(x')\right)$$

[cf. Eq. (8)], in the c.m. frame of two colliding nuclei. Results of the calculation are presented in Fig. 3. To provide a common scale, the quantity $E_f^{(\rm released)}$ calculated with the formation time $\tau = 100$ fm/c is presented in all the panels. The $\tau = 100$ fm/c case practically implies absence of interaction between the fireball and baryon-rich fluids and the equality $E_f^{(\rm tot)} = E_f^{(\rm released)}$, because $T_f^{(\rm eq)00} = 0$ and hence $F_{fp}^0 = F_{ft}^0 = 0$ [cf. Eq. (18)].

First, we see that the energy release into in the

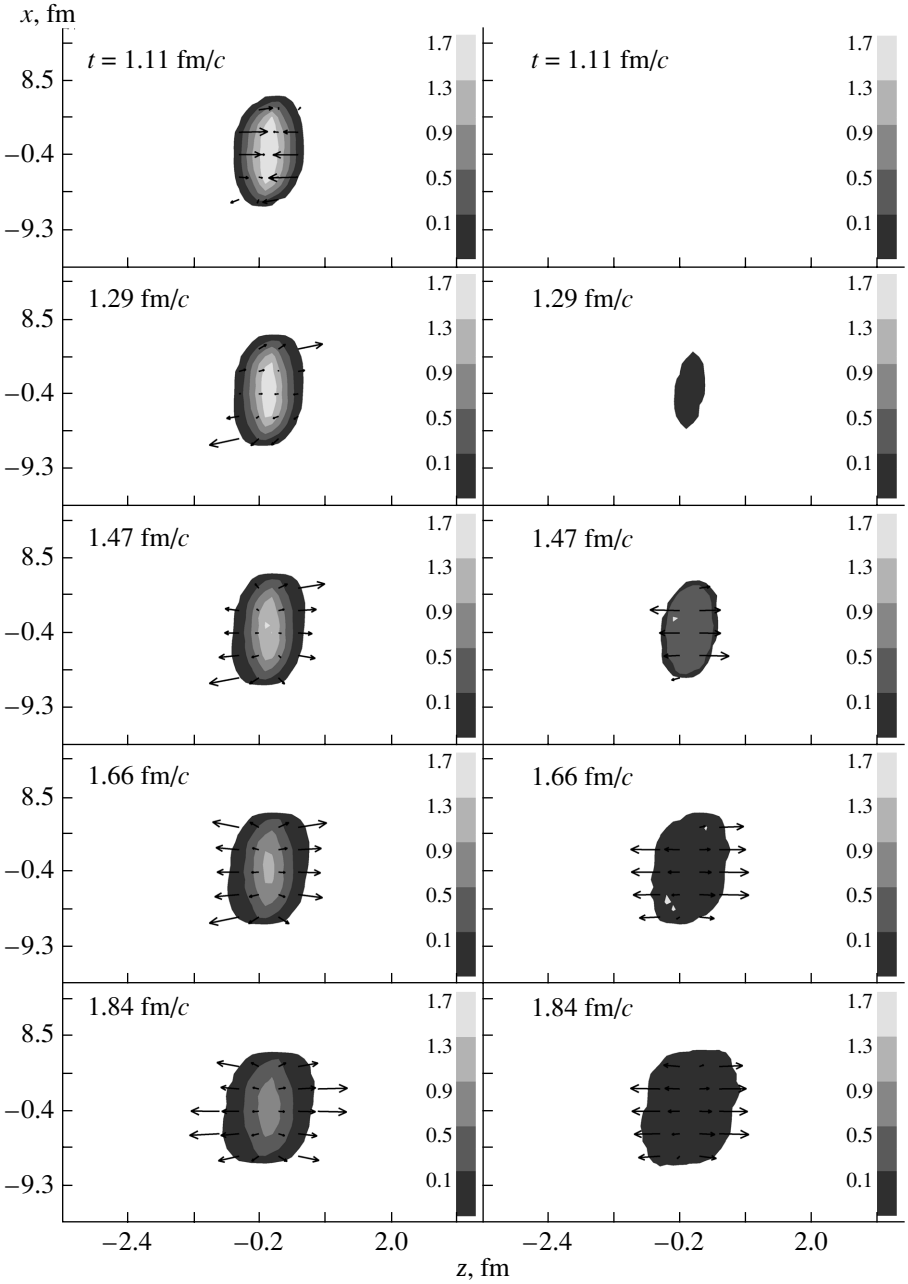

Fig. 2. The same as in Fig. 1, but for the fireball-energy density (ε_f in the c.m. frame of the colliding nuclei) for two formation times, $\tau = 0$ (the left column of panels) and 1 fm/c (the right column of panels).

fireball fluid occurs only during a short time of interpenetration of colliding nuclei. As was expected, at zero formation time $\tau = 0$, the interaction with the baryon-rich fluids strongly affects the fireball fluid: it reduces its total energy $E_f^{(\mathrm{tot})}$ as compared to the case without interaction (i.e., $\tau = 100$ fm/c). Even the released energy $E_f^{(\mathrm{released})}$ drops. This effect results from additional stopping of baryon-rich fluids associated with friction with the fireball fluid. Because of this additional stopping, the baryon-rich fluids produce less secondary particles (and those produced are less energetic). Naturally, this effect is more pronounced at the energy 158 A GeV, since the amount of produced secondary particles is much larger in this case than that at lower energies.

At realistic values of the formation times, $\tau = 0.5$ and 1 fm/c, the effect of the interaction is substantially reduced. This happens because the fireball fluid starts to interact only near the end of the interpenetration stage. As a result, by the end of the collision

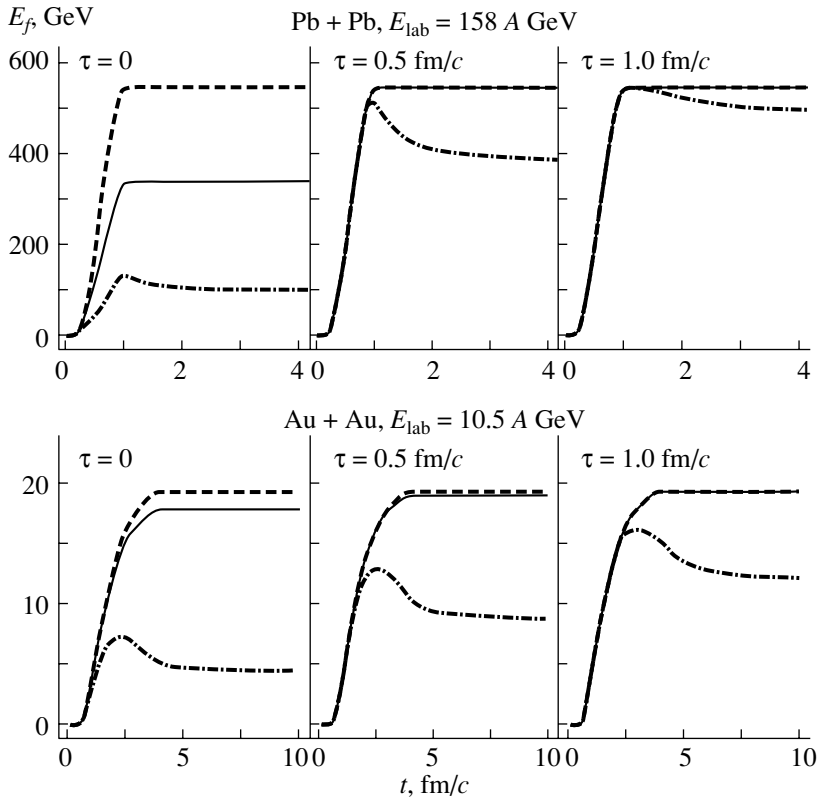

Fig. 3. Time evolution of the total energy released into the fireball fluid, $E_f^{(\mathrm{released})}$ (solid curves), and the total energy kept in the fireball fluid after interaction, $E_f^{(\mathrm{tot})}$ (dash-dotted curves). Two nucleus–nucleus collisions Pb + Pb at $E_{\mathrm{lab}} = 158\ A$ GeV (three upper panels) and Au + Au at $E_{\mathrm{lab}} = 10.5\ A$ GeV (three bottom panels), both at zero impact parameter, were calculated with different formation times τ indicated in the panels. The upper dashed curves in all six panels represent $E_f^{(\mathrm{released})}$ calculated with the formation time $\tau = 100$ fm/c.

process, it loses only 10% of its available energy $E_f^{(\mathrm{released})}$ at $E_{\mathrm{lab}} = 158\ A$ GeV and 30% at $E_{\mathrm{lab}} = 10.5\ A$ GeV. Certainly, this effect should be observable in mesonic quantities, in particular, in such fine observables as directed and elliptic flows. The global baryonic quantities stay practically unchanged at finite τ. Indeed, $E_f^{(\mathrm{released})}$ remains almost the same as at $\tau = 100$ fm/c.

The energy content of the baryon-rich fluids exceeds that of the fireball by an order of magnitude at $E_{\mathrm{lab}} = 158\ A$ GeV (3440 GeV) and even more at $E_{\mathrm{lab}} = 10.5\ A$ GeV (929 GeV). Therefore, the interaction with the fireball fluid does not substantially change the global baryonic quantities. As for refined baryonic observables, our preliminary calculations of the directed nucleon flow show no changes at $E_{\mathrm{lab}} = 10.5\ A$ GeV and only slight changes in the midrapidity region at $E_{\mathrm{lab}} = 158\ A$ GeV. This means that our previous results on the nucleon directed flow and its excitation function, obtained within the two-fluid model [9], are not affected by the interaction between the baryon-rich and fireball fluids.

5. CONCLUSION

In this paper, we have developed a three-fluid model for simulating heavy-ion collisions in the range of incident energies between a few to about 200 A GeV. In addition to two baryon-rich fluids, which constitute the two-fluid model [3, 4, 7–9], a delayed evolution of the produced baryon-free (fireball) fluid is incorporated. This delay is governed by a formation time, during which the fireball fluid neither thermalizes nor interacts with the baryon-rich fluids. After the formation, it thermalizes and comes into interaction with the baryon-rich fluids. This interaction is estimated from elementary pion–nucleon cross sections.

The hydrodynamic treatment of heavy-ion collisions is an alternative to kinetic simulations. The hydrodynamic approach has certain advantages and disadvantages. Lacking the microscopic feature of kinetic simulations, it overcomes their basic assumption, i.e., the assumption of binary collisions, which is quite unrealistic in dense matter. It directly addresses the nuclear EoS that is of prime interest

in heavy-ion research. Furthermore, our three-fluid model uses only friction forces instead of a vast body of differential cross sections of elementary processes, which are generally unknown experimentally. Naturally, we have to pay for all these pleasant features of hydrodynamics: the treatment assumes that the nonequilibrium stage of the collision can be described by the three-fluid approximation. However, all the assumptions used are quite transparent and can be tested numerically.

We have simulated relativistic nuclear collisions within the 3D code based on the relativistic three-fluid hydrodynamics combined with the EoS of the statistical mixed-phase model of the deconfinement phase transition, developed in [21–23]. We performed calculations of nucleus–nucleus collisions Pb + Pb at $E_{\rm lab} = 158$ A GeV and Au + Au at $E_{\rm lab} = 10.5$ A GeV. To reveal the role of the interaction between fireball and baryon-rich fluids, we examined the evolution of global quantities of the fireball fluid.

For zero formation time ($\tau = 0$), the interaction strongly affects the fireball fluid: it considerably reduces its total energy as compared to that without interaction. However, for realistic reasonable finite formation time, $\tau \approx 1$ fm/c, the effect of the interaction is substantially reduced. The fireball fluid loses only 10% of its available energy at $E_{\rm lab} = 158$ A GeV and 30% at $E_{\rm lab} = 10.5$ A GeV. Certainly, this effect should be observable in mesonic quantities, in particular, in such sensitive observables like directed and elliptic flows. Since the energy content of the baryon-rich fluids is much higher than that of the fireball fluid, global baryonic quantities remain insensitive to this interaction. As our preliminary calculations show, even directed nucleon flow remains practically unaffected by this interaction. In particular, this fact justifies our previous results on directed nucleon flow and its excitation function, obtained within the two-fluid model [9].

ACKNOWLEDGMENTS

We are grateful to L.M. Satarov for useful discussions and careful reading of the manuscript.

This work was supported in part by the Deutsche Forschungsgemeinschaft (DFG project 436 RUS 113/558/0-2), the Russian Foundation for Basic Research (project no. NS-03-02-04008), Russian Minpromnauki (grant no. NS-1885.2003.2), and the German BMBF (contract RUS-01/690).

REFERENCES

1. S. T. Belyaev and G. I. Budker, Dokl. Akad. Nauk SSSR **107**, 807 (1965).
2. V. V. Skokov, S. A. Smolyansky, and V. D. Toneev, hep-ph/0210099; V. V. Skokov, D. V. Vinnik, S. A. Smolyansky, and V. D. Toneev, JINR Communications P2-2002-215 (Dubna, 2002).
3. I. N. Mishustin, V. N. Russkikh, and L. M. Satarov, Yad. Fiz. **48**, 711 (1988) [Sov. J. Nucl. Phys. **48**, 454 (1988)].
4. I. N. Mishustin, V. N. Russkikh, and L. M. Satarov, Nucl. Phys. A **494**, 595 (1989).
5. Yu. B. Ivanov, I. N. Mishustin, and L. M. Satarov, Nucl. Phys. A **433**, 713 (1985).
6. Yu. B. Ivanov and L. M. Satarov, Nucl. Phys. A **446**, 727 (1985).
7. I. N. Mishustin, V. N. Russkikh, and L. M. Satarov, Yad. Fiz. **54**, 429 (1991) [Sov. J. Nucl. Phys. **54**, 260 (1991)].
8. I. N. Mishustin, V. N. Russkikh, and L. M. Satarov, in *Relativistic Heavy Ion Physics*, Ed. by L. P. Csernai and D. D. Strottman (World Sci., Singapore, 1991), p. 179.
9. Yu. B. Ivanov, E. G. Nikonov, W. Nörenberg, *et al.*, Heavy Ion Phys. **15**, 127 (2002); nucl-th/0011004.
10. J. Sollfrank, P. Huovinen, M. Kataja, *et al.*, Phys. Rev. C **55**, 392 (1997); P. Huovinen, P. V. Ruuskanen, and J. Sollfrank, Nucl. Phys. A **650**, 227 (1999).
11. C. M. Hung and E. V. Shuryak, Phys. Rev. Lett. **75**, 4003 (1995); Phys. Rev. C **57**, 1891 (1998); D. Teaney, J. Lauret, and E. V. Shuryak, nucl-th/0110037.
12. U. Katscher, D. H. Rischke, J. A. Maruhn, *et al.*, Z. Phys. A **346**, 209 (1993); U. Katscher, J. A. Maruhn, W. Greiner, and I. N. Mishustin, Z. Phys. A **346**, 251 (1993); A. Dumitru, U. Katscher, J. A. Maruhn, *et al.*, Phys. Rev. C **51**, 2166 (1995); hep-ph/9411358; Z. Phys. A **353**, 187 (1995); hep-ph/9503347.
13. J. Brachmann, A. Dumitru, J. A. Maruhn, *et al.*, Nucl. Phys. A **619**, 391 (1997); nucl-th/9703032; A. Dumitru, J. Brachmann, M. Bleicher, *et al.*, Heavy Ion Phys. **5**, 357 (1997); nucl-th/9705056; M. Reiter, A. Dumitru, J. Brachmann, *et al.*, Nucl. Phys. A **643**, 99 (1998); nucl-th/9806010; M. Bleicher, M. Reiter, A. Dumitru, *et al.*, Phys. Rev. C **59**, 1844 (1999); hep-ph/9811459; J. Brachmann, A. Dumitru, H. Stöcker, and W. Greiner, Eur. Phys. J. A **8**, 549 (2000); nucl-th/9912014; J. Brachmann, S. Soff, A. Dumitru, *et al.*, Phys. Rev. C **61**, 024909 (2000); nucl-th/9908010.
14. Conceptual Design Report *"An International Accelerator Facility for Beams of Ions and Antiprotons"*, http://www.gsi.de/GSI-Future/cdr/
15. F. Karsch, Lect. Notes Phys. **583**, 209 (2002); hep-lat/0106019.
16. C. Lourengo, Nucl. Phys. A **698**, 13c (2002).

17. F. Videbaek (BRAMS Collab.), Nucl. Phys. A **698**, 29c (2002); W. A. Zajac (PHENIX Collab.), Nucl. Phys. A **698**, 39c (2002); G. Roland (PHOBOS Collab.), Nucl. Phys. A **698**, 54c (2002); J. W. Harris (STAR Collab.), Nucl. Phys. A **698**, 64c (2002).
18. Yu. B. Ivanov, Nucl. Phys. A **474**, 669 (1987).
19. L. M. Satarov, Yad. Fiz. **52**, 412 (1990) [Sov. J. Nucl. Phys. **52**, 264 (1990)].
20. Madappa Prakash, Manju Prakash, R. Venugopalan, and G. Welke, Phys. Rep. **227**, 321 (1993).
21. E. G. Nikonov, A. A. Shanenko, and V. D. Toneev, Heavy Ion Phys. **8**, 89 (1998); nucl-th/9802018.
22. V. D. Toneev, E. G. Nikonov, and A. A. Shanenko, in *Nuclear Matter in Different Phases and Transitions*, Ed. by J.-P. Blaizot, X. Campi, and M. Ploszajczak (Kluwer Academic Publ., Dordrecht, 1999), p. 309.
23. E. G. Nikonov, V. D. Toneev, and A. A. Shanenko, Yad. Fiz. **62**, 1301 (1999) [Phys. At. Nucl. **62**, 1226 (1999)].

Physics of Atomic Nuclei, Vol. 67, No. 1, 2004, pp. 2–10. From Yadernaya Fizika, Vol. 67, No. 1, 2004, pp. 4–12.

On the Status of Very High Multiplicity Physics*

A. N. Sissakian**

Joint Institute for Nuclear Research, Dubna, Moscow oblast, 141980 Russia

Received April 30, 2003

Abstract—The paper contains a description of the main trends in very high multiplicity physics. The incident energy dissipation into the secondaries is considered as a thermalization phenomenon. An experimental fact is that the particle production process is stopped at such an early stage that the mean multiplicity is nothing but the logarithm of incident energy. This phenomenon is considered as an indication of the absence of complete thermalization in the most probable inelastic processes. A quantitative definition of thermalization phenomenon is offered and the very high multiplicity domain where the thermalization must occur is discussed. The physical consequences and model predictions of the thermalization effect are considered. A short review of the latest publications on very high multiplicity physics is also offered.

1. INTRODUCTION

The interest in very high multiplicity (VHM) hadron processes has become so many-sided that it is time to give a general description of the situation in this field. The trends can be divided into three sectors. They are purely theoretical, experimental, and intermediate, where the theoretical efforts are directed toward the VHM experiment.

The paper is based mainly on the talks presented at the VHM Physics Workshops held in Dubna in the years 2000–2002 [1]. It must be mentioned from the very beginning that there has been no experimental information concerning VHM high energy hadron reactions until now. Moreover, there are no theoretical predictions for such processes even on the model level either. For these reasons, the spectrum of efforts presented in [1] is broad.

We would like to start from the well-known experimental fact that high-energy hadron collisions are, for the most part, inelastic; see Fig. 1, where the experimental value of total and elastic cross sections are shown.

Having the multiparticle state, the idea to introduce thermodynamic methods for describing hadron interactions seems fruitful. It is important to notice here that the thermalization means the possibility of using the equilibrium thermodynamics phenomenology. Actually, one must be careful with this idea. The reason why this is not trivial will be the main subject of discussion.

Attempts to introduce thermodynamic notions into multiple production physics have a long history. The first so-called "thermodynamical model" was proposed by Fermi and Landau in the 1950s [2, 3]. It was assumed that particle production may be considered as the process of cooling of the incident high-temperature state. The reason for cooling is a tendency to equilibrium with the environment. Indeed, this process takes place in a "zero-temperature" vacuum and, therefore, the results of cooling should be the state with zero-momentum particles. In this case, the hadron mean multiplicity would be approximately equal to the total incident energy and, therefore, the multiplicity would have reached its maximal value $n_{\max} = \sqrt{s}/m$, where $\sqrt{s}$ is the total c.m. energy and $m \simeq 0.2$ GeV is the characteristic hadron mass.

But we know that the mean hadron multiplicity is only a logarithm or the second power of the logarithm of total incident energy (see Fig. 2), where the best fit of the power dependence, $\bar{n}(s) \sim \sqrt{s}$, is shown for comparison.

Therefore, something prevents the dissipation of the incident energy into the produced particle masses and, for this reason, the thermalization does not taken place. Here the term "thermalization" means the uniform distribution of perturbation over all degrees of freedom. At the same time, fluctuations must have a Gaussian character.

In other words, we would like to offer for discussion the most important question of hadron dynamics from our point of view: Why is the process of incident energy dissipation stopped at such an early stage that the mean multiplicity is comparably small and, for this reason, complete thermalization does not occur?

*This article was submitted by the author in English.

**e-mail: sisakian@jinr.ru

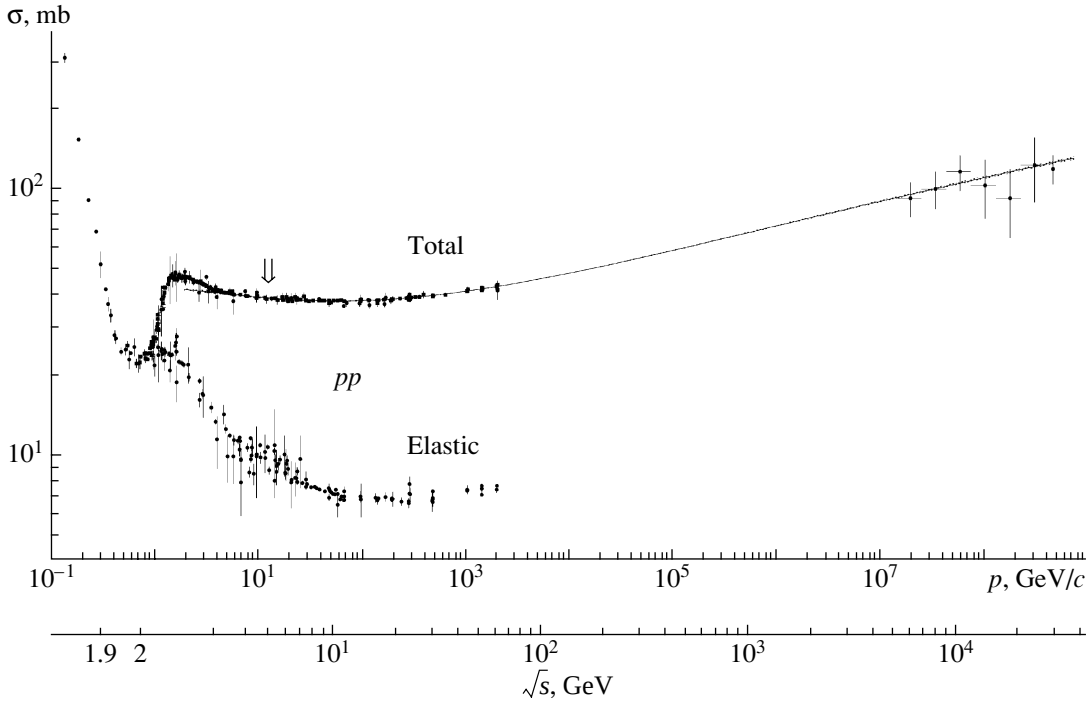

Fig. 1. Total cross section. It is remarkable that σ_{tot} is approximately constant in the interval of 10–100 GeV. The Froissart constraint: $\sigma_{\text{tot}} \lesssim \ln^2 s$.

1.1. Role of Symmetry Constraints

We know, at least qualitatively, the answer to this question: the reason why the mean hadron multiplicity is much smaller than $n_{\max}$ is hidden in the symmetry constraints. Namely, one may hope that this is an effect of underlying non-Abelian gauge symmetry recorded in Yang–Mills field theory.

Therefore, the purpose of the present paper is to discuss the most intriguing question of hadron physics: the dynamical consequence of the non-Abelian gauge symmetry of Yang–Mills field theory. One of the known consequences of this symmetry is the color charge confinement. Another one is the incomplete thermalization and, as a result, smallness of the total hadron multiplicity.

In the most inelastic hadron processes, thermalization is not produced and it is impossible to use the methods of thermodynamics for them. But it can be proved that, at VHM, the final state is completely thermalized. Thus, we would like to provide for the condition where the Fermi–Landau model works. It is evident that such a condition is realized in nature extremely rarely.

This also means that, in the VHM region, one may use "rough" thermodynamic parameters, "temperature," "chemical potential," etc., for a complete description of the system. For instance, in this case, one may completely describe the energy distribution of the system knowing only the mean energy of secondaries [4, 5].

Therefore, the confinement forces, as the symmetry constraints, should not act in the VHM region. This conclusion is crucial in our further considerations since it considerably simplifies the multiple production picture.

It is interesting to note that, on the other hand, the system of color charges must be considered as a plasma state in the case of absence of confinement forces.

Moreover, the thermalized state is calm. This means that the kinetic forces are not important in comparison with the potential ones. This situation is the best to observe collective phenomena.

1.2. References

The phenomenology of VHM events was formulated in the papers published in [6]. It includes two basic ideas. The first one gives the classification of asymptotics over multiplicity and the physical interpretation of the classes. This interpretation excludes from consideration final-state interactions, for instance, the Bose–Einstein correlation [7]. The papers [8, 9] fill this deficiency. It was shown [9] that final-state interaction can cardinally change the multiplicity distribution tail. The experimental investigation of this prediction will be performed during the

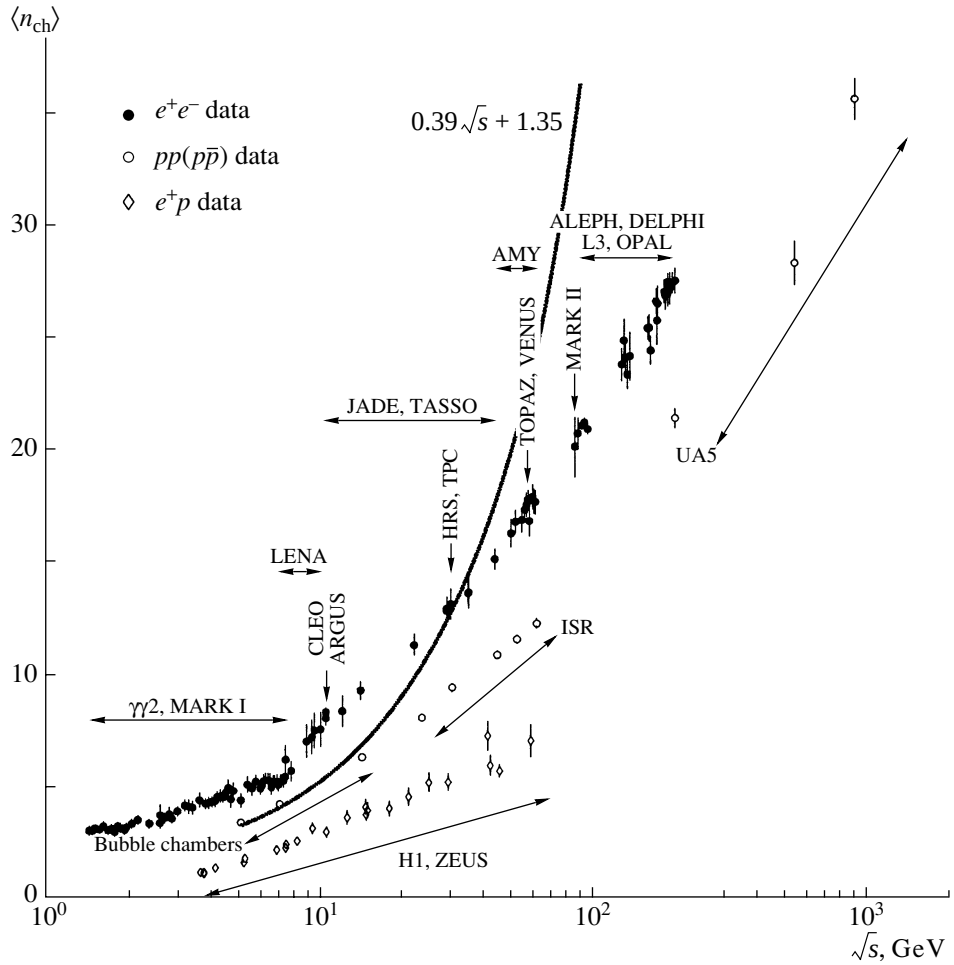

Fig. 2. Mean multiplicity. The mean multiplicity in QCD jet $\bar{n}(s)_j$ and in the e^+e^- annihilation processes is relatively high: $\ln \bar{n}(s)_j \sim \sqrt{\ln s}$.

experiment at U-70 (Protvino) (see [10]). We would also stress the efforts toward the experiment published in [11].

An idea was proposed [12] that measurements in the VHM region may be performed "roughly" (see also [13]). For instance, it is quite possible to have the multiplicity with some, but definite, error. One may also generalize the inclusive approach, combining particles into groups and considering the group as a "particle," and so on. The effectiveness of such a formulation of the experimental program was shown in [14].

The paper [4] contains a qualitative feature of VHM physics. The main question is: How much confidence may predictions of perturbative QCD and existing multiperipheral models in the VHM region have? We have found that pQCD cannot be used even if the VHM production process is hard. Experimental investigation of the range of validity of pQCD predictions has been performed in [15]. The point is that it is hard to use the leading logarithm approximation (LLA) ideology [16] in the VHM region. That is why a new perturbation theory has been built [17–20].

One can hope that the VHM domain is much "simpler" from the theoretical point of view than the traditional domain of $n \sim \bar{n}(s)$ [4]. Nevertheless, attempts to find new characteristics of inelastic collisions are extremely important. The "wavelet" analysis [21] is a corresponding example.

2. DEFINITION OF THE VHM REGION

It is natural that just the mean multiplicity defines the scale of multiplicities. Then, generally, we wish to consider the processes with multiplicity

$$n \gg \bar{n}(s),$$

where $\bar{n}(s)$ is the mean multiplicity. The VHM domain can be better specified while considering the details of production processes.

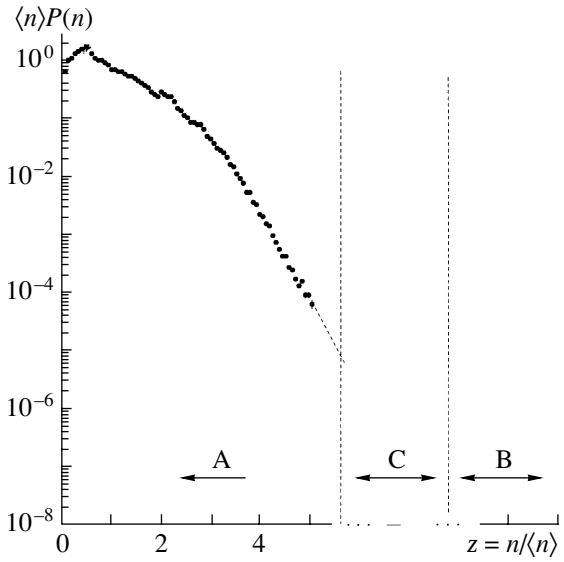

Fig. 3. Multiplicity distribution in terms of KNO variables: (A) the domain of multiperipheral models, (B) the deep asymptotics over multiplicity, (C) the very high multiplicity domain.

One may also introduce the inelasticity coefficient

$$\frac{E-\epsilon_{\max}}{E},$$

where E is the total energy in the c.m. frame and $\epsilon_{\max}$ is the energy of the fastest particle in the same frame. Then, VHM events mean

$$1-\frac{E-\epsilon_{\max}}{E}\ll 1.$$

Thus, the produced particle momentum would be comparatively small.

At the same time, we would like to exclude the influence of the phase space boundaries. For this reason, we would assume that the multiplicity cannot be too large:

$$n\ll n_{\max}=E/m,\qquad m\approx 0.2\ \text{GeV}.$$

From the experimental point of view, the VHM domain includes extremely rare processes (see Fig. 3). For this reason, the B range of multiplicity in Fig. 3 seems not to be attainable.

The fact that A is the multiperipheral dynamics domain and C represents the deep asymptotics over multiplicity must be noted. We will call the domain C the VHM domain and it is defined from the condition that thermalization is attained.

2.1. VHM Phenomenology

The kinematics conditions are changed with multiplicity and it is natural to expect a change in the particle production mechanism [22]. One may consider the result presented in [23] as experimental confirmation of this idea.

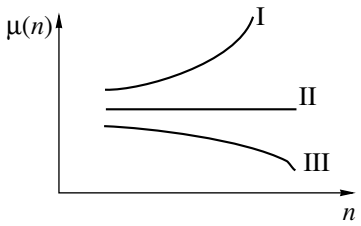

Fig. 4. "Chemical potential" $\mu=\langle\varepsilon\rangle\ln(\sigma_n/\sigma_{\text{tot}})$ vs. multiplicity. Case I corresponds to the multiperipheral model; case II is predicted by the QCD jet; III is a case where the vacuum is unstable against particle production. The latter case may include a situation with final-state interactions. To distinguish this possibility, one should investigate the analytical properties of μ over n.

It can be shown that only three classes of asymptotics can be realized:

The cross section falls faster than any power of the exponent of $(-n)$:

(I) *multiperipheral interactions*: $\sigma_n<O(e^{-n})$;

The cross section falls as the exponent:

(II) *hard processes*: $\sigma_n=O(e^{-n})$;

The cross section falls slower than any power of the exponent:

(III) *vacuum instability*: $\sigma_n>O(e^{-n})$.

Therefore, one may neglect the factors in front of $\exp\{-n\}$, and, since the cross section is extremely small at $n\gg\bar{n}(s)$, it is natural to estimate cross sections only with logarithmic accuracy. In other words, we propose measuring the quantity

$$\mu(n)=-\langle\varepsilon\rangle\frac{1}{n}\ln\frac{\sigma_n}{\sigma_{\text{tot}}},$$

where $\langle\varepsilon\rangle$ is the mean energy of secondaries. Then, one may distinguish the following possibilities in the region of large multiplicities (see Fig. 4):

$$\text{(I)}:\frac{\partial}{\partial n}\mu(n)>0,\quad \text{(II)}:\frac{\partial}{\partial n}\mu(n)=0,$$
$$\text{(III)}:\frac{\partial}{\partial n}\mu(n)<0.$$

Case (I) corresponds to the multiperipheral model; case (II) is predicted by the QCD jet; (III) is the case where the vacuum is unstable against particle production.

The latter may include the situation with final-state interactions. To distinguish this possibility, one should investigate the analytical properties of μ over n.

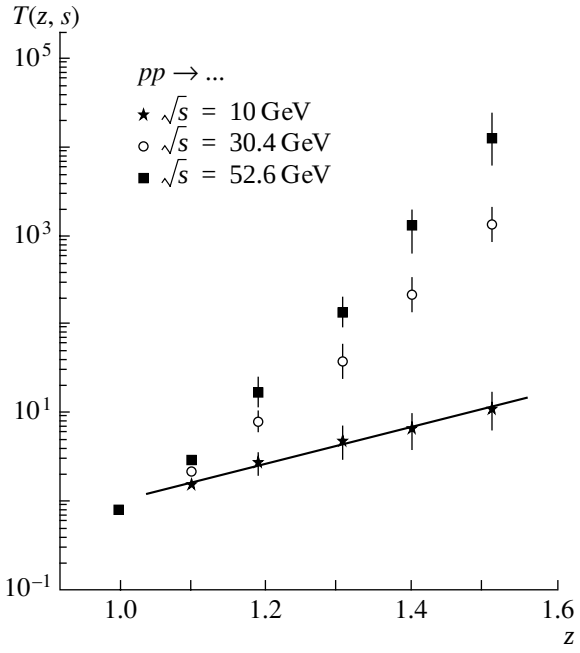

Fig. 5. Chemical potential vs. activity z. Straight line means the Poisson distribution.

3. THERMODYNAMICS

The multiple production amplitude, generally, is a function of $(3n-4)$ variables. This number is too high even if $n \sim \bar{n}(s)$ since at LHC energies $\bar{n}(s) \simeq 100$.

One may write

$$T(z,s) = \sum_n z^n \sigma_n(s)/\sigma_{\rm tot}(s) = e^{C(z,s)}.$$

Then, there exists the decomposition

$$C(z,s) = \sum_k (z-1)^k C_k(s)/k!,$$

where C_k is the binomial moment, $C_1(s) = \bar{n}(s)$.

Figure 5 shows that the higher multiparticle correlators become important with rising energy and multiplicity. Indeed, the straight line corresponds to the Poisson distribution. The deviation from the straight line means that the multiplicity distribution is wider than the Poissonian. In this case, the higher C_k should be taken into account and, accordingly, we lose the hope to describe the hadron dynamics completely.

Therefore, it is important to find conditions where the number of essential variables is sufficiently small. This condition will define the "thermalization" region. Now, one of the most important results of our investigations is the following: if

$$|K_l(E,n)| \ll |K_2(E,n)|^{l/2}, \quad l = 3,4,\ldots, \qquad (1)$$

where K_l is the ordinary l-particle energy correlator, then the energy spectrum of produced particles is defined by one parameter, $1/\beta$, which is the mean energy of produced particles. It is important that (1) be the criterion of thermalization. In practice, this means that, without checking this condition, it is impossible even to discuss the thermodynamic property of the system.

The correlation functions are usually defined as follows:

$$K_2(n,E) = \langle \varepsilon^2; n, E\rangle - \langle \varepsilon^1; n, E\rangle,$$
$$K_3(n,E) = \langle \varepsilon^3; n, E\rangle - 3\langle \varepsilon^2; n, E\rangle \times \langle \varepsilon^1; n, E\rangle + 2\langle \varepsilon^1; n, E\rangle^3,$$

etc., $E = \sqrt{s}$. Here,

$$\langle \varepsilon^l; n, E\rangle = \frac{\int \varepsilon(q_1) d^3q_1 \varepsilon(q_2) d^3q_2 \cdots \varepsilon(q_l) d^3q_l \{d^{3l}\sigma_n(E)/d^3q_1 d^3q_2 \cdots d^3q_l\}}{\int d^3q_1 d^3q_2 \cdots d^3q_l \{d^{3l}\sigma_n(E)/d^3q_1 d^3q_2 \cdots d^3q_l\}}$$

is the l-particle mean energy and

$$d^{3l}\sigma_n(E)/d^3q_1 d^3q_2 \cdots d^3q_l$$

is the corresponding differential cross section.

In conclusion, we can show that, if inequality (1) holds true, then the system of produced particles may be described using the formalism of thermodynamics. This important conclusion is general; it weakly depends on details of the dynamics. In other words, the proof of this statement is formal for the hadron system and uses only one fact that the fluctuations in the thermalized state must be Gaussian.

Having a quantitative definition of the equilibrium state, one may investigate predictions of the existing theories. First of all, we can prove that the system should be equilibrium in the domain B. It is easy to find what we have in the domain B:

$$\frac{|K_3(E,n)|}{|K_2(E,n)|^{3/2}} \sim \frac{1}{n}.$$

This estimate is a model-independent conclusion.

3.1. Theory

Now let us consider the question: Can we predict a tendency to the thermalized state? Considering the production as a process of thermalization, let us review the possible mechanisms of hadron production.

First of all, the most popular in hadron physics is the multiperipheral model. It describes the "soft" channel of hadron production. The phase space domain, corresponding to the Regge production mechanism, is shown in Fig. 6. It means that the longitudinal momenta of secondaries are large, but the transverse ones are small. Until now, there has been no well-established quantitative theory of these processes.

The second model is based on perturbative QCD and it describes the "hard" channel. The typical kinematics is the same as in deep inelastic scattering (DIS) processes. It means that, opposite to Regge, the DIS kinematics, shown in Fig. 6, assumes that the transverse momenta of secondaries are large and the longitudinal momenta are relatively small.

As has been explained above, the hard kinematics must dominate in the VHM region. But it is important to note that the VHM region does not overlap either Regge or DIS regions (see Fig. 6). This means that, for Regge and DIS theories, one cannot apply the ordinary formalism in the VHM domain.

We would like to explain the last conclusion in detail. This would also explain why the thermalization effect is important for hadron physics.

3.2. Multiperipheral Model

The main statement of the Regge multiperipheral model appears as the condition that the transverse momentum of secondaries is restricted.

Then the amplitude in the one-Pomeron Born approximation

$$A_{ab}(s,t) = ig_a g_b (s/s_0)^{\alpha(t)-1},$$

$$\alpha(t) = \alpha(0) + \alpha'(0)t, \quad 0 < \alpha(0) - 1 \ll 1,$$
$$\alpha'(0) = 1\ \text{GeV}^{-2}, \quad s_0 = 1\ \text{GeV}^2,$$

describes the experimental data well at intermediate energies.

Multiplicity distribution: In the Pomeron Born approximation, the topological cross section

$$\sigma_n(s) = \sigma_{\text{tot}} e^{-\bar{n}(s)} (\bar{n}(s))^n / n!$$

This distribution has a sharp maximum at $n \simeq \bar{n}(s) \approx a \ln(s/s_0)$. Thus, for the production of $n \gg \bar{n}(s)$ particles, one should consider the exchange of $\nu \sim n/\bar{n}(s)$ Pomeron.

But this production mechanism is restricted. Thus, the contribution of the diagram with ν Pomeron exchange gives, since the diffraction radii increase with s, a decrease with ν in the mean value of the impact parameter: $\bar{\mathbf{b}}^2 \simeq 4\alpha' \ln(s/s_0)/\nu \sim \alpha' \bar{n}(s)/\nu$. On the other hand, the number of necessary Pomeron exchanges $\nu \sim n/\bar{n}(s)$. As a result, $\bar{\mathbf{b}}^2/\alpha' \sim \bar{n}^2(s)/n$. Therefore, if the transverse momentum of created particles is a restricted quantity, i.e., $\bar{\mathbf{b}}^2/\alpha' \gtrsim 1$, then the Pomeron mechanism of the particle production is valid if $n \lesssim \bar{n}^2(s)$.

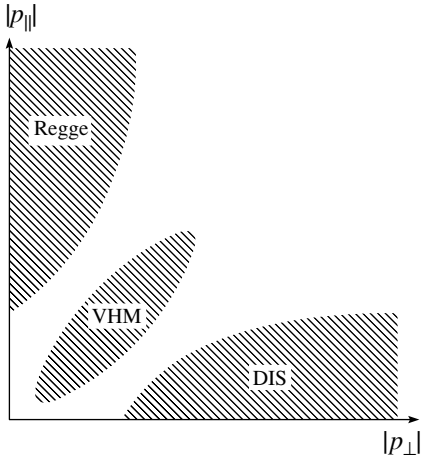

Fig. 6. Produced hadrons phase space.

In the framework of the multiperipheral model, the cross section must fall sharply at

$$n > \bar{n}^2(s)$$

since there is no interaction at $\bar{\mathbf{b}}^2 < \alpha'$ in this model.

Therefore, the multiperipheral picture is applicable if, and only if, the multiplicity is smaller than the square of the mean multiplicity. From outside of this region, the cross section must fall rapidly.

3.3. Perturbative QCD

Now let us consider the creation of n particles (gluons) in the DIS kinematics. We calculate $D_{ab}(x, q^2; n)$, where

$$\sum_n D_{ab}(x, q^2; n) = D_{ab}(x, q^2)$$

and $D_{ab}(x, q^2)$ is the probability of finding parton b with virtuality $q^2 < 0$ in the parton a of $\sim \lambda$ virtuality, $\lambda \gg \Lambda$ and $\alpha_s(\lambda) \ll 1$. One also should assume that x is sufficiently small, $(1/x) \gg 1$, to have the phase space of produced particles sufficiently large. Then $D_{ab}(x, q^2)$ is described by the ladder diagrams of Fig. 7.

One can conclude that the LLA is applicable in the VHM domain until the diffusion time τ is sufficiently large:

$$\tau = \ln(-q^2/\lambda) \gg \ln(1/x) \gg \omega(\tau, z), \qquad (2)$$

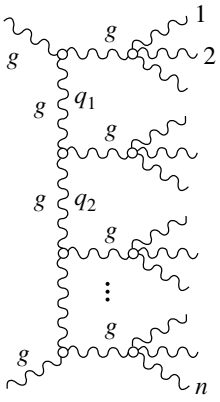

Fig. 7. Feynman ladder diagram: $-q_1^1 \gg -q_2^2 \gg \ldots$.

where

$$\omega(\tau, z) = \sum_n z^n \int_{\tau_0}^{\tau} \frac{d\tau'}{\tau'} w_n^g(\tau'), \quad \omega(\tau, 1) = \ln \tau/\tau_0,$$

is the generating function of the gluon jet multiplicity distribution. It is important to note here that all $w_n^g(\tau)$ are positive. It is a function with a sharp maximum at $\ln n \simeq \ln \bar{n}_j(\tau) \sim \sqrt{\tau}$. Therefore, to have $n \gg \bar{n}_j(\tau)$ jet mean multiplicity, one should choose $z > 1$.

For this reason, inequality (2) cannot be satisfied in the VHM region. Indeed, one always may find such large $n \gg \bar{n}_j(\tau)$ that, for fixed q^2, inequality (2) fails.

The reason why this DIS kinematics, based on the LLA assumption, cannot be considered in the VHM region leads to the evident conclusion that, in order to have the thermalized state, the mean values of the transverse and longitudinal momenta must be close to each other. Just this dynamical condition is in contradiction with LLA ideology.

4. SCENARIO FOR VHM PROCESS

Our multiple production scenario is the following:

The multiperipheral model is applicable for n less than n_s. Rough estimation gives $n_s \sim \bar{n}^2(s)$. One may expect that, at high energies, n_s is smaller than $\bar{n}^2(s)$.

When the multiplicity exceeds n_s (Fig. 8), one should take into account the hard processes. This means the production of (mini)jets and dominance of Fig. 7 diagrams. Thus, this contribution may be described in the framework of the LLA.

But in the VHM region, where the multiplicity exceeds $n_h > n_s$, the LLA cannot be used since all components of the particle momentum are comparable to each other in this domain.

We will define the VHM region as the multiplicity domain where one may use the thermodynamic description.

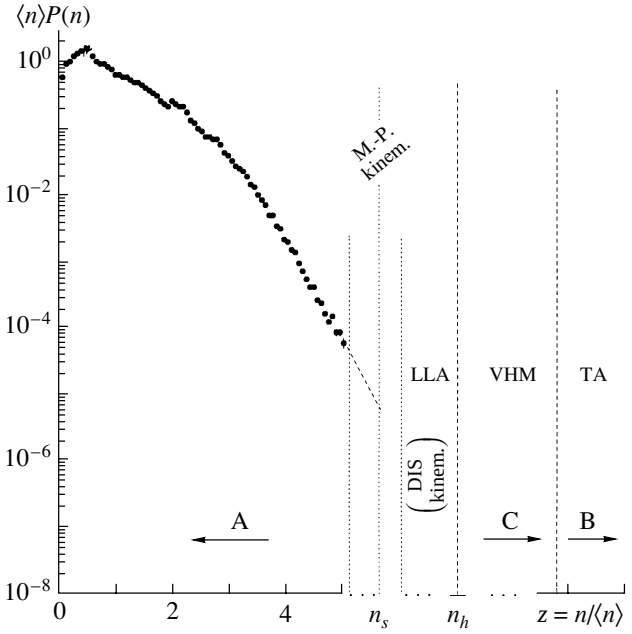

Fig. 8. (A) The range of multiperipheral models, $n < n_s$; (B) the range of deep asymptotics over n, where particle momentum $|p| \ll m$; (C) the VHM domain; $n_s < n < n_h$, the transition region into the VHM domain.

4.1. Prediction of Existing Generators of Events

It is evident that neither in the Regge nor in the DIS kinematics can one see the thermalization phenomena and the VHM state cannot be achieved by these production mechanisms. Let us consider the generator-of-events prediction to demonstrate this conclusion. It is enough to use the experience of existing generators of events since they absorb all known information for multiplicity smaller than n_h.

The PYTHIA prediction for ratio K_3 to K_2 is shown in Fig. 9. Notice that it does not predict even a tendency to equilibrium. This is no wonder since PYTHIA is based on the phenomenology of hadron peripheral interactions. We can conclude that the investigation in the VHM domain will allow us to define

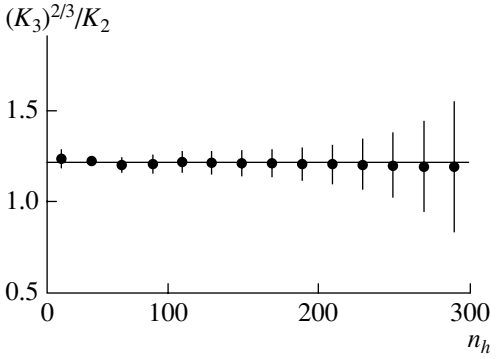

Fig. 9. PYTHIA: K_3/K_2.

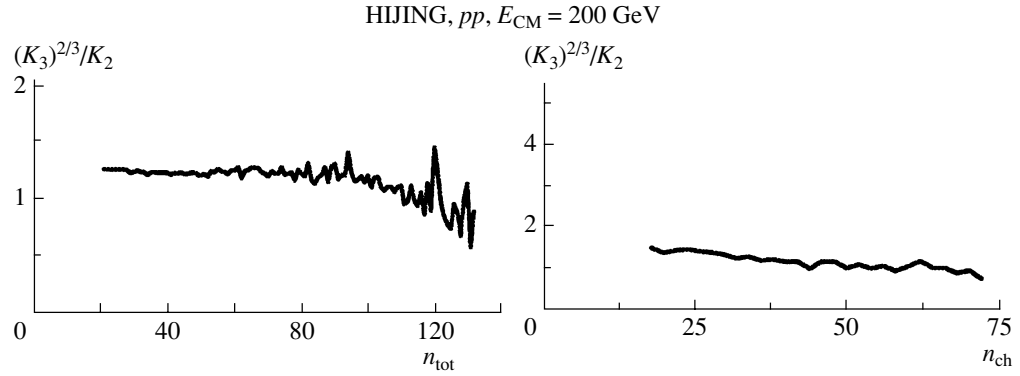

Fig. 10. HIJING: K_3/K_2. The soft tendency to thermalization is seen from this picture. From this point of view, the ion collisions, probably, are interesting.

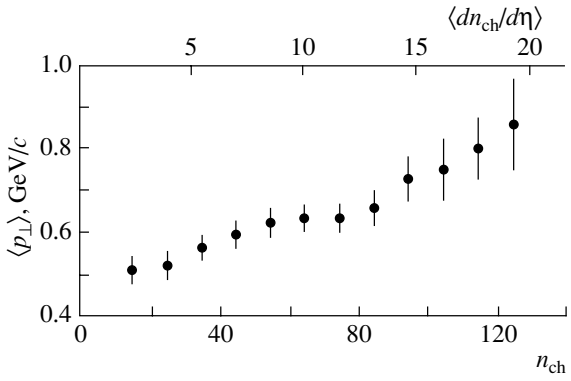

Fig. 11. Transverse momentum vs. multiplicity. The Tevatron data (E-735 Group) [24]. This result is in strong contradiction with the multiperipheral model.

the range of applicability of the peripheral picture of hadron interaction.

Figure 10 shows a prediction of the HIJING generator of events for the K_3/K_2 ratio. The slight tendency to equilibrium in this model is explained by the fact that this generator includes rescattering based on the possibility of taking into account more accurately the phenomena of scattering at the higher angles.

5. CONCLUSION

At the end, we would like to mention the following issues.

Rough Description

We adhere to the position that only rough measurements can be performed in the VHM domain. The reasons are as follows:

(i) The VHM cross sections are extremely small.

(ii) The multiplicity is hardly a measurable parameter.

(iii) It is practically impossible to restore the VHM kinematics completely.

These conditions will be taken into account in the VHM generator of events.

Experimental Program

Notice that our prediction that the VHM processes are "hard," i.e., that the VHM dynamics includes the production of highly virtual and extremely slow partons, has an immediate experimental confirmation (see Fig. 11), where the E-735 Group data from Tevatron show that the hadron-production processes become harder with rising multiplicity.

First of all, it seems important to investigate the following problems experimentally:

(i) The thermalization problem;

(ii) Quantitative definition of the range of validity of the LLA in the VHM domain.

It was mentioned that the VHM problem highlights the most sensitive questions of hadron physics.

(A) *Phase transition in the colored state.* The VHM gives a good chance for it, since the state is "calm" and "cold." The latter means that the interaction energy is larger than the kinetic one if we have the VHM final state.

(B) *The "preconfinement" VHM state represents equilibrium colored plasma.* This means that it can be characterized by a few global parameters. In this sense, it will be the "state."

(C) *Measurement of the ratio* $R = \langle p_\parallel \rangle / \langle p_\perp \rangle = \pi/4$. For the isotropic case, where the end of produced particle momenta is located on the sphere.

(D) *The process of VHM production must be "fast."* In this case, the isotope spin orientation may be frozen randomly. Experimentally, it looks like large fluctuations of the charge: if $C = n_{ch}/n_0$ is the ratio of the number of charged to neutral particles, then an

"anomalous" (non-Gaussian) distribution over C is expected.

It must be noted in the end that

(i) There is a definite indication that thermalization exists in heavy-ion collisions.

(ii) The estimate of the threshold value of multiplicity, n_h, exceeds the possibility of the LLA of perturbative QCD. Moreover, existing models are unable to find n_h.

(iii) The established S-matrix interpretation of a necessary and sufficient condition of thermalization is important from the experimental point of view. In addition, it allows one to show that thermalization occurs, at least, in the deep asymptotics over n.

(iv) New perturbation theory, topological QCD, which conserves the topology of Yang–Mills fields, was constructed. It is important that it includes pQCD as an approximation.

Various experimental approaches to VHM physics are widely discussed in the ATLAS, CDF, CMS [25], and STAR collaborations.

The construction of the "fast generator" of VHM events is the largest problem. It is also necessary to investigate the ideology of VHM triggers in detail.

It must be noted once more that only in the framework of a statistical approach is there any hope to describe completely the inelastic hadron reactions. But at the same time, we would like to stress that, generally speaking, actually not all that many-particle state can be described using thermodynamic methods. Such attempts may lead to a wrong conclusion: first of all, one must take into consideration the necessary and sufficient conditions of thermalization.

ACKNOWLEDGMENTS

I would like to take the opportunity to thank Yu. Budagov, I. Dremin, V. Kadyshevski, A. Korytov, E. Kuraev, L. Lipatov, V. Matveev, and V. Nikitin for fruitful discussions and constructive comments. I would like to mention especially the role of J. Manjavidze in the formulation of the VHM physics program.

REFERENCES

1. *Proceedings of the First, Second, and Third International Workshops on Very High Multiplicity Physics, Dubna, 2000–2002*; J. Manjavidze and A. N. Sissakian, in *Proceedings of the Bogolyubov Conference on Problems of Theoretical and Mathematical Physics, Moscow–Dubna–Kiev, Russia–Ukraine, 1999*; in *Proceedings of the XXXI International Symposium on Multiparticle Dynamics, Datong, China, 2001*; in *Proceedings of the XXXII International Symposium on Multiparticle Dynamics, Alushta, Ukraine, 2002*; in *Proceedings of the 31st International Conference on High Energy Physics, Amsterdam, The Netherlands, 2002*.
2. E. Fermi, Prog. Theor. Phys. **4**, 570 (1950); Phys. Rev. **81**, 683 (1951); **92**, 452 (1953).
3. L. D. Landau, Izv. Akad. Nauk SSSR, Ser. Fiz. **17**, 85 (1953).
4. J. Manjavidze and A. N. Sissakian, Phys. Rep. **346**, 1 (2001).
5. J. Manjavidze, this Proceedings; J. Manjavidze and A. N. Sissakian, this Proceedings.
6. J. Manjavidze and A. N. Sissakian, JINR Rapid Commun., No. 5[31]-88, 5 (1988).
7. R. Hanbury-Brown and R. Q. Twiss, Nature **178**, 1046 (1956); G. Goldhaber *et al.*, Phys. Rev. **120**, 300 (1960).
8. G. A. Kozlov, this Proceedings.
9. R. Lednický, this Proceedings.
10. P. F. Ermolov *et al.*, this Proceedings.
11. G. Chelkov, M. Gostkin, J. Manjavidze, *et al.*, JINR Rapid Commun., No. 4[96]-99, 45 (1999); G. Chelkov, J. Manjavidze, and A. Sissakian, JINR Rapid Commun., No. 4[96]-99, 35 (1999); J. Budagov, G. Chelkov, Y. Kulchitsky, *et al.*, *Talk at the Physics ATLAS Week, Lund, 2001*.
12. J. Manjavidze and A. Sissakian, JINR Rapid Commun., No. 2[28], 51 (1988).
13. V. A. Nechitailo, this Proceedings.
14. J. A. Budagov *et al.*, this Proceedings.
15. A. Korytov, this Proceedings.
16. L. N. Lipatov, this Proceedings.
17. J. Manjavidze and A. N. Sissakian, J. Math. Phys. (N.Y.) **41**, 5710 (2000); **42**, 641, 4158 (2001).
18. J. Manjavidze and A. N. Sissakian, Theor. Math. Phys. **123**, 776 (2000); **130**, 153 (2002).
19. J. Manjavidze and A. Sissakian, hep-ph/0201182.
20. J. Manjavidze and V. V. Voronyuk, this Proceedings.
21. I. M. Dremin, this Proceedings.
22. A. N. Sissakian and L. A. Slepchenko, Preprint No. P2-10651, JINR (Dubna, 1977); Fizika (Zagreb) **10**, 21 (1978).
23. F. Rimondi, this Proceedings.
24. T. Alexopoulos *et al.*, Phys. Rev. Lett. **64**, 991 (1990).
25. O. Kolobova, unpublished.

Physics of Atomic Nuclei, Vol. 67, No. 1, 2004, pp. 21–30. From Yadernaya Fizika, Vol. 67, No. 1, 2004, pp. 23–32.

VERY HIGH MULTIPLICITY PHYSICS

On Thermalization of Inelastic Processes*

J. Manjavidze[1)] and A. N. Sissakian[2)]

Received April 30, 2003

Abstract—The paper contains a discussion of the criteria of applicability of statistical methods in multiparticle-production processes. The main attention is devoted to thermalization phenomena, while the energy is uniformly distributed over the dynamical degrees of freedom and the energy correlators are relaxed. It is argued that this condition must be satisfied in the deep asymptotics over multiplicity, and the very high multiplicity (VHM) domain is defined as the region where this thermalization condition is satisfied but for moderate multiplicities. A model-independent classification of the multiplicity asymptotics and their physical content is proposed. It is shown explicitly that existing multiparticle-production models are not able to predict the range of the VHM domain. © *2004 MAIK "Nauka/Interperiodica".*

1. INTRODUCTION

It is now accepted that the main road of particle physics development is the Standard Model. However, it is obvious to expect the existence of other ways, less important at first sight, but permitting new interesting phenomena to be observed. The multiparticle-production phenomenon can be one of them.

But the multiparticle production phenomena seem to be uninteresting because of a very large number of involved degrees of freedom. This is definitely so and it must be mentioned also that, to all appearances, a gap between the strict theory based on the non-Abelian gauge symmetry and the obvious hadron multiple production phenomenology never would be surmounted for this reason. We will return to this question in Section 3.

Then the attempts to find the kinematical condition(s) where the multiparticle-production process becomes describable seem crucial. The most popular condition is based on the asymptotic freedom. It assumes hardness of the interaction. This allows one to investigate only the "local" properties of the hadron.

We discuss another possibility. In this connection, let us remember that statistical physics deals very well with the enormous number of degrees of freedom (particles). It is natural to engage this rich experience to describe the multiparticle-production phenomenon.

The main attention will be concentrated on equilibrium since, presumably, only it can be described completely. The appearance of such a state in hadron inelastic collisions will be considered as a phenomenon which can be examined experimentally and may be predicted theoretically.

Multiparticle production may be considered as the process of kinetic energy dissipation of colliding particles into the mass of produced particles. To use this interpretation, one must consider the final-state particles as the probes through which the measurement of the state of interacting fields is performed [1]. Then, one can consider the multiplicity as a measure of entropy $\mathcal{S}$. One may expect, therefore, that, in the very high multiplicity (VHM) domain, the entropy exceeds its maximum. For this reason, we will define here the VHM final state through the equilibrium condition.

Using thermodynamic terminology, we investigate in this case the production and properties of the comparatively cold final state of interacting fields. One may expect that, in this condition, the system becomes calm. This is one more argument why we expect equilibrium in the VHM domain.

In the Conclusion, we consider the VHM processes as the only ones whose complete theory can be constructed. Discussing the thermalization phenomenon, we actually try for the condition in the framework of which this theory would work.

The phenomenology and an idea of a rough (statistical) description of the VHM processes were formulated in our first publications [2]. Later on, we accumulated our main ideas on the VHM theory in the review paper [3]. The definite connection with the idea of N.N. Bogolyubov concerning transition to equilibrium was described in [4].

The preferable processes at $n \sim \bar{n}$ are saturated by excitation of the nonperturbative degrees of freedom.

*This article was submitted by the authors in English.

[1)]Institute of Physics, Georgia Academy of Sciences, Tbilisi, Georgia, and Joint Institute for Nuclear Research, Dubna, Moscow oblast, 141980 Russia; e-mail: joseph@nusun.jinr.ru

[2)]Joint Institute for Nuclear Research, Dubna, Moscow oblast, 141980 Russia; e-mail: sisakian@jinr.ru

1063-7788/04/6701-0021$26.00

These soft processes are described by the creation of quarks and gluons from the vacuum: the kinetic motion of partons leads to increasing, because of confinement phenomenon, polarization of the vacuum and in result to its instability concerning quark creation [5]. In other words, there is a long-range correlation among hadron constituents at $n \sim \bar{n}$.

The most popular field-theoretical description of statistical systems at a finite temperature is based on the formal analogy between imaginary time and inverse temperature β ($\beta = 1/T$) [6]. This approach is fruitful, if we do not want to clear up the dynamical aspects [7, 8]. The further attempts led to the real-time finite-temperature field theory [9–13].

2. CLASSIFICATION OF ASYMPTOTICS OVER MULTIPLICITY

We will use the following quantitative definition of the high-energy VHM hadron reactions under discussion. Let $\varepsilon_{\max}$ be the energy of the fastest particle in the given frame and let E be the total incident energy in the same frame. Then the difference $(E - \varepsilon_{\max})$ is the energy spent on the production of less energetic particles. It is useful to consider the inelasticity coefficient

$$\kappa = 1 - \frac{\varepsilon_{\max}}{E} \leq 1. \tag{2.1}$$

It defines the portion of spent energy. Therefore, we wish to consider processes with

$$1 - \kappa \ll 1, \tag{2.2}$$

and the particles produced would have comparatively small energies. Using the energy conservation law, the produced hadron multiplicity n is defined by the inequality

$$n(1 - \kappa) > 1. \tag{2.3}$$

Thus, (2.2) means roughly the VHM region.

Following the natural condition at finite CM energies, $\sqrt{s}$,

$$n \ll n_{\max} = \sqrt{s}/m_h, \quad m_h \simeq 0.2\ \text{GeV}, \tag{2.4}$$

we will assume that

$$1 - \kappa \gg m_h/E. \tag{2.5}$$

Therefore, the kinetic energy of produced particles in our processes would not be arbitrarily small.

It seems useful from the very beginning to elaborate a general point of view on the processes in the VHM domain. This would allow one, without going into details, to estimate the possibility of observing new phenomena.

2.1. The Thermodynamic Limit

We will introduce the generating function

$$T(s,z) = \sum_{n=1}^{n_{\max}} z^n \sigma_n(s), \tag{2.6}$$

$$s = (p_1 + p_2)^2 \gg m^2, \quad n_{\max} = \sqrt{s}/m.$$

This step is natural, since the number of particles is not conserved in our problem. Thus, the total cross section and the averaged multiplicity will be

$$\sigma_{\text{tot}}(s) = T(s,1) = \sum_n \sigma_n(s), \tag{2.7}$$

$$\bar{n}(s) = \sum_n n(\sigma_n(s)/\sigma_{\text{tot}}(s)) = \frac{d}{dz} \ln T(s,z)\Big|_{z=1}.$$

At the same time, the inverse Mellin transform gives

$$\sigma_n = \frac{1}{n!}\frac{\partial^n}{\partial z^n} T(s,z)\Big|_{z=0} \tag{2.8}$$

$$= \frac{1}{2\pi i}\oint \frac{dz}{z^{n+1}} T(s,z)$$

$$= \frac{1}{2\pi i}\oint \frac{dz}{z} \exp(-n \ln z + \ln T(s,z)).$$

The essential values of z in this integral are defined by the equation (of state)

$$n = z\frac{\partial}{\partial z} \ln T(z,s). \tag{2.9}$$

Taking into account the definition of the mean multiplicity $\bar{n}(s)$, given in (2.7), we can conclude that, in the solution to (2.9), z_c is equal to one at $n = \bar{n}(s)$. Therefore, $z > 1$ is essential in the VHM domain.

The asymptotics over n ($n \ll n_{\max}$ is assumed) are governed with exponential accuracy by the smallest solution z_c of (2.9) because of the asymptotic estimation of the integral (2.8):

$$\sigma_n(s) \propto e^{-n \ln z_c(n,s)}. \tag{2.10}$$

Let us assume that, in the VHM region and at high energies, $\sqrt{s} \to \infty$, there exists such a value of $z_c(n,s)$ that we can neglect in (2.6) the dependence on the upper boundary $n_{\max}$. This formal trick with the thermodynamic limit allows us to consider $T(z,s)$ as a nontrivial function of z for finite s.

Then, it follows from (2.9) that

$$z_c(n,s) \to z_s \quad \text{at} \quad n \in \text{VHM}, \tag{2.11}$$

where $z_s(s)$ is the leftmost singularity of $T(z,s)$ in the right-half plane of complex z. One can say that the singularity of $T(z,s)$ attracts $z_c(n,s)$ if $n \in$ VHM. We will put this observation in the basis of the phenomenology of VHM processes.

It must be emphasized once more that actually $T(z,s)$ is regular for arbitrary finite z if s is finite. But $z_c(n,s)$ behaves in the VHM domain as if it is attracted by the (imaginary) singularity z_s. And just this $z_c(n,s)$ defines σ_n in the VHM domain. We want to note that actually the energy $\sqrt{s}$ should be high enough to use such an estimation.

2.2. Classes and Their Physical Content

One can notice from the estimation (2.10) that σ_n weakly depends on the character of the singularity. Therefore, it is enough to classify only the possible positions of z_s. We may distinguish the following possibilities:

$$\begin{aligned} &\text{(A)} \qquad z_s = 1: \quad \sigma_n > O(e^{-n}), \qquad (2.12)\\ &\text{(B)} \qquad z_s = \infty: \quad \sigma_n < O(e^{-n}),\\ &\text{(C)} \qquad 1 < z_s < \infty: \quad \sigma_n = O(e^{-n}); \end{aligned}$$

i.e., following this classification, the cross section may decrease (A) slower than, (B) faster than, or (C) as an arbitrary power of e^{-n}. It is evident that, if all these possibilities may be realized in nature, then we should expect the asymptotics (A).

The cross section σ_n has a meaning of the n-particle partition function in the energy representation. Then $T(z,s)$ should be a grand partition function. Taking this interpretation into account, as follows from the Lee–Yang theorem, $T(z,s)$ cannot be singular at $|z| < 1$.

At the same time, direct calculations based on the physically acceptable interaction potentials give the following restriction from above:

$$\text{(D)} \qquad \sigma_n < O(1/n). \qquad (2.13)$$

This means that σ_n should decrease faster than any power of $1/n$. It should be noted that our classification predicts rough (asymptotic) behavior only.

One may notice (2.10) that

$$-\frac{1}{n}\ln\frac{\sigma_n(s)}{\sigma_{\text{tot}}(s)} = \ln z_c(n,s) + O(1/n). \qquad (2.14)$$

Using thermodynamic terminology, the asymptotics of σ_n is governed by the physical value of the activity $z_c(n,s)$. One can also introduce the chemical potential $\mu_c(n,s)$. It defines the work needed for creation of one particle, $\ln z_c(n,s) = \beta_c(n,s)\mu_c(n,s)$, where $\bar{\epsilon}(n,s) = 1/\beta_c(n,s)$ is the mean energy of produced particles. Thus, one may introduce the chemical potential if and only if $\beta_c(n,s)$ and $z_c(n,s)$ may be used as the "rough" variables.

Then the above-formulated classification has a natural explanation. Thus, the class (A) may be realized if and only if the system is unstable. In this case $z_c(n,s)$ is a decreasing function of n. The class (B) means that the system is stable against particle production and the activity $z_c(n,s)$ is an increasing function of n. The asymptotics (C) cannot be realized in equilibrium thermodynamics.

We will show that the asymptotics (B) reflects the kinematics of multiperipheral processes: created particles form a jet moving in the CM frame with different velocities along the directions of incoming particles, i.e., with restricted transverse momentum. The asymptotics (A) assumes condensation-like phenomena. The third-type asymptotics (C) is predicted by stationary Markovian processes with pQCD jets kinematics.

This interpretation of classes (2.12) allows us to conclude that we should expect reorganization of production dynamics in the VHM region: the soft channel (B) of particle production should yield to the hard dynamics (C) if the ground state of the investigated system is stable against particle production. Otherwise, we will have asymptotics (A).

Let us consider now in detail the physical content of this classification.

(A) $z_s = 1$. It is known that the singularity $z_s = 1$ reflects the first-order phase transition [14]. To find σ_n for this case, we will adopt Langer's analysis [15]. Introducing the temperature $1/\beta$ instead of total energy $\sqrt{s}$, we can use the isomorphism with the Ising model. For this purpose, we divide the space volume into cells, and if there is a particle in a cell, we will write (-1). In the opposite case, it will be $(+1)$. This is the model of "lattice gas" well described by the Ising model. We can regulate the number of down-looking spins, i.e., the number of created particles, by the external magnetic field $\mathbf{H}$. Therefore, $z = \exp\{-\beta H\}$ and $\mathbf{H}$ is the chemical potential.

One can find the energy representation using the Fourier transformation:

$$\rho(E,z) = \int\limits_{\Gamma} \frac{d\beta}{2\pi i} e^{E\beta} R(\beta,z), \qquad (2.15)$$

where the contour Γ is chosen along the complex axis.

The corresponding partition function in the continuous limit [15] (see also [16]) has the form

$$R(\beta,z) = \int D\mu \exp\left(-\int dx \right. \qquad (2.16)$$
$$\left. \times \left\{ \frac{1}{2}(\partial\mu)^2 - \epsilon\mu^2 + \alpha\mu^4 - \lambda\mu \right\} \right),$$

where $\epsilon \sim (1 - \beta_c/\beta)$ and $\lambda \sim H$, with critical temperature $1/\beta_c$.

If $\beta_c > \beta$, there is no phase transition and the potential has one minimum at $\mu = 0$. But if $\beta_c < \beta$,

there are two degenerate minima at $\mu_\pm = \pm\sqrt{\epsilon/2\alpha}$ if $\lambda = 0$. Switching on $H < 0$, the left minimum at $\mu_- \sim -\sqrt{\epsilon/2\alpha}$ becomes absolute and the system will tunnel into this minimum (see also [17]). This process describes particle creations as a process of spins overturnings.

Equation (2.9) gives at $n \to \infty$

$$\ln z_c \sim n^{-1/3} > 0.$$

As a result,

$$\sigma_n \sim e^{-an^{2/3}} > O(e^{-n}), \qquad a > 0,$$

i.e., decreases slower than e^{-n}. A semiclassical calculation shows that the functional determinant is singular at $\mathbf{H} = 0$. It must be emphasized that, in our use of the Ising model description, the chemical potential deforms the ground state. Consequently, the semiclassical approximation is applicable since $\ln z_c \ll 1$, i.e., since the processes of spin overturnings are rare in the high-multiplicity region. It is easy to show in this approximation [15] that the functional determinant is singular at $\mathbf{H} = 0$, i.e., at $z = 1$.

Note that z_c decreases to one with n. This unusual phenomenon must be explained. The mechanism of particle creation considered above describes "the fate of false vacuum" [17]. In the process of decay of the unstable state, clusters of a new phase of size X are created. If the cluster has dimension $X > X_c$, its size increases since the volume energy ($\sim X^3$) of the cluster becomes greater than the surface tension energy ($\sim X^2$). This condition defines the value of X_c. The wall of "critical" clusters will accelerate; i.e., the work needed to add one particle to the cluster decreases with $X > X_c$. This explains the reason why z_c decreases with n. Notice here that, at a given temperature, $\ln z_c$ is proportional to the Gibbs free energy per one particle.

The described mechanism of particle creation assumes that we have prepared the equilibrium system in the unstable phase at $\mu_+ \sim +\sqrt{\epsilon/2\alpha}$, and, going to another state at $\mu_- \sim -\sqrt{\epsilon/2\alpha}$, the system creates the particles. The initial state may be the QGP and the final state may be the hadron system. Therefore, we must describe the way how the quark system is prepared.

Following the Lee–Yang picture of the first-order phase transition [14, 16], there is no transition in a finite system (the partition function cannot be singular for finite $n_{\max}$). This means that the multiplicity (and the energy) must be high enough to see the described phenomena.

(B) $z_s = \infty$. Let us return to the integral (2.16) to investigate the case $\beta_c > \beta$. In this case, the potential has one minimum at $\mu = 0$. The external field $\mathbf{H}$ creates the mean field $\bar{\mu} = \bar{\mu}(\mathbf{H})$, and the integral (2.16) should be calculated expanding it near $\mu = \bar{\mu}$. As a result, in the semiclassical approximation ($\bar{\mu}$ increases with increasing n),

$$\ln R(\beta, z) \sim (\ln z)^{4/3}.$$

This gives $\ln \bar{z} \sim n^3$ and $\ln \sigma_n \sim -n^4$, i.e., $\sigma_n < O(e^{-n})$.

There is also another possible way to interpret the case (B). For this case, we can set

$$\ln T(z,s)/\sigma_{\text{tot}} = \bar{n}(s)(z-1) + O((z-1)^2) \quad (2.17)$$

at $|z-1| \ll 1$. The experimental distribution of $\ln T(z,s)$ for various energies shows that the contributions of $O((z-1)^2)$ terms increase with energy [1]. It is assumed in the Born approximation that

$$\ln t(z,s) = \bar{n}(s)(z-1).$$

There are various interpretations of this series, e.g., the multiperipheral model, the Regge pole model, the heavy color string model, the QCD multiperipheral models, etc. In all these models, $\bar{n}(s) = b_1 + b_2 \ln s$, $b_2 > 0$. The second ingredient of the hadron Standard Model is the assumption that the mean value of momentum transfer of created particles $\langle k \rangle = \text{const}$, i.e., is an energy- (and multiplicity) independent quantity. It can be shown that, under these assumptions,

$$\ln T(z,s)/\sigma_{\text{tot}} = \sum_n c_n(s)(z-1)^n, \qquad (2.18)$$
$$c_1 \equiv \bar{n},$$

is regular at finite values of z [1] and is able to give predictions confirmed by experiments. Inserting (2.18) into (2.9), we find, taking into account regularity of $T(z,s)$, that $\bar{z}(n,s)$ is an increasing function of n. Consequently,

$$\sigma_n < O(e^{-n}) \qquad (2.19)$$

for the hadron in the Standard Model.

Notice also that the Standard Model has a finite range of validity: beyond $n \sim \bar{n}^2$, the model must be changed since it is impossible to conserve $\langle k \rangle = \text{const}$ at higher multiplicities [18].

(C) $1 < z_s < \infty$. Let us assume now that, at $z > 1$,

$$T(z,s) \sim \left(1 - \frac{z-1}{z_c - 1}\right)^{-\gamma}, \quad \gamma > 0. \qquad (2.20)$$

Then, using the normalization condition $(\partial T(z,s)/\partial z)|_{z=1} = \bar{n}_j(s)$, we can find that $z_c(s) = 1 + \gamma/\bar{n}_j(s)$. The singular structure (2.20) is impossible in the "Standard Model" because of the condition $\langle k \rangle = \text{const}$. But if $|z-1| \ll 1$, we have

estimate (2.17). The difference between the Standard Model and (C) is seen only at $1-(z-1)/(z_c-1)\ll 1$, i.e., either the asymptotics over n or in the asymptotics over energy. The singular structure is familiar for logistic equations of QCD jets, e.g., [19].

In the considered case $z_s = z_c + O(\bar{n}_j/n)$ and at high energies ($\bar{n}_j(s)\gg 1$),

$$\sigma_n \sim e^{-\gamma n/\bar{n}_j} = O(e^{-n}). \qquad (2.21)$$

Therefore, comparing (2.19) and (2.21), we can conclude that, at sufficiently high energies, i.e., if $\bar{n}_j \gg \bar{n}$ and $\bar{n}_j \ll n_{\max}$, where $\bar{n}$ is the Standard Model mean multiplicity, the mechanism (C) must dominate in the asymptotics over n.

It is the general, practically model-independent, prediction. From the experimental point of view, it has the important consequence that, at high energies, there is a wide range of multiplicities where the Standard Model mechanism of hadron production is negligible. In other words, the cold colored final state of high multiplicity processes is the dynamical consequence of jets and Standard Model mechanisms. In the transition region between the "soft" of the Standard Model and "hard" of jets, one can expect the dominance of "semihard" processes of minijets.

The multiplicity distribution in jets has an interesting property noted many decades ago by Volterra in his mathematical theory of populations [20]. In our terms, if the one-jet partition function has the singularity at $z_c^{(1)}(s) = 1+\gamma/\bar{n}_j(s)$, then the two-jet partition function must be singular at

$$z_c^{(2)}(s) = 1 + \frac{\gamma}{\bar{n}_j(s/4)} > z_c^{(1)}(s),$$

and so on. Therefore, at high energies and $n > \bar{n}_j(s)$, the number of jets must be minimal (with exponential accuracy). This means that, at $n\to\infty$, the processes of hadron creation have a tendency to be Markovian (with increase in mean transverse momentum $\langle k\rangle$) and only in the last stage can the (first-order) phase transition (colored plasma) $\to$ (hadrons) be seen.

One can say that, in the asymptotics over n, we consider a process of thermalization which is so fast that the usual confinement forces are "frozen" and do not play an important role in the final colored state creation.

3. THERMALIZATION CONDITIONS

The following sign of "equilibrium" will be considered. First of all, it is intuitively evident that thermal equilibrium means the uniform distribution of energy over all degrees of freedom. Then the system is in a macroscopic thermal equilibrium if the energy flows in it are relaxed [1]. On the other hand, the condition of vanishing of the energy correlators and the condition of relaxation of the macroscopic energy flows seem equivalent since distant points of the macroscopic energy flow should be correlated. Then the relaxation of the flow would lead to the smallness of the mean value of the corresponding correlator. This conclusion reminds one of the Bogolyubov principle of vanishing of correlations.

Our idea may be illustrated by the following model. At the very beginning of the 20th century, the couple P. Ehrenfest and T. Ehrenfest proposed a model to visualize Boltzmann's interpretation of irreversibility phenomena in statistics. The model is extremely simple and fruitful [21]. It considers two boxes with $2N$ numerated balls. Choosing number $l = 1, 2, \ldots, 2N$ randomly, one must take the ball with the label l from one box and put it into the other. Starting from the highly nonequilibrium state with all balls in one box, there is tendency to the equalization of the number of balls in the boxes (see [21]). Thus, irreversible flow toward the preferable (equilibrium) state is seen. One can hope [21] that this model reflects a physical reality of nonequilibrium processes with the initial state very far from equilibrium. A theory of such processes with a (nonequilibrium) flow toward a state with maximal entropy should be sufficiently simple to give definite theoretical predictions.

The early models were based on the assumption that the final state of inelastic hadron processes has maximal entropy $\bar{n}(s)\sim n_{\max}$ [22]. But actually the hidden constraints stop the process of thermalization at comparably early stages. The result of this is a small value of the hadron mean multiplicity, $\bar{n}(s)$, i.e., $\bar{n}(s)\ll n_{\max}$.

3.1. Quantitative Definition of Equilibrium

Let us define the conditions when the fluctuations in the vicinity of β_c are Gaussian. Firstly, to estimate the integral (2.15) at $z = z_c$ in the vicinity of the extremum, β_c, we should expand $\ln\rho_n(\beta+\beta_c)$ over β:

$$\ln\rho_n(\beta+\beta_c) = \ln\rho_n(\beta_c) - \sqrt{s}\beta + \frac{\beta^2}{2!}\frac{\partial^2\ln\rho_n(\beta_c)}{\partial\beta_c^2} - \frac{\beta^3}{3!}\frac{\partial^3\ln\rho_n(\beta_c)}{\partial\beta_c^3} + \frac{\beta^4}{4!}\frac{\partial^4\ln\rho_n(\beta_c)}{\partial\beta_c^4} - \ldots. \qquad (3.1)$$

Secondly, let us expand the exponent in the integral (2.15) over the lth derivatives, $l = 3, 4, \ldots$, of $\ln\rho_n(\beta_c)$. As a result, if only the third derivative is taken into account, then the kth term of the perturbation series looks as follows:

$$\rho_{n,k} \sim \left\{\frac{\partial^3\ln\rho_n(\beta_c)/\partial\beta_c^3}{(\partial^2\ln\rho_n(\beta_c)/\partial\beta_c^2)^{3/2}}\right\}^k \Gamma\left(\frac{3k+1}{2}\right). \qquad (3.2)$$

Therefore, because of Euler's $\Gamma((3k+1)/2)$ function, the perturbation theory near β_c leads to the asymptotic series. Considering them as the asymptotic one, we may estimate it by the first term if and only if

$$\partial^3 \ln \rho_n(\beta_c)/\partial\beta_c^3 \ll (\partial^2 \ln \rho_n(\beta_c)/\partial\beta_c^2)^{3/2}. \quad (3.3)$$

One may write this condition as the approximate equality

$$\partial^3 \ln \rho_n(\beta_c)/\partial\beta_c^3 \approx 0. \quad (3.4)$$

If this condition is satisfied, then the fluctuations are Gaussian with dispersion

$$\sim \left|\partial^2 \ln \rho_n(\beta_c)/\partial\beta_c^2\right|^{1/2}$$

[see (3.1)].

Let us consider now (3.4) in detail. We will find that this condition means the following approximate equality:

$$\frac{\rho_n^{(3)}}{\rho_n} - 3\frac{\rho_n^{(2)}\rho_n^{(1)}}{\rho_n^2} + 2\frac{(\rho_n^{(1)})^3}{\rho_n^3} \approx 0, \quad (3.5)$$

where $\rho_n^{(k)}$ means the kth derivative over β. For identical particles,

$$\rho_n^{(k)}(\beta_c) = n^k(-1)^k \quad (3.6)$$
$$\times \int d\Gamma_n(\beta_c, q_1, q_2, \ldots, q_n) \prod_{i=1}^{k} \epsilon(q_i).$$

The left-hand side of (3.5) is the three-point correlator K_3 since $d\Gamma_n(\beta_c, q_1, q_2, \ldots, q_n)$ is a density of states for given β:

$$d\Gamma_n(\beta_c, q_1, q_2, \ldots, q_n)$$
$$= d\Omega_n(q)|a_n(q_1, q_2, \ldots, q_n)|^2 \prod_{i=1}^{n} e^{-\beta\epsilon(q_i)},$$

$$d\Omega_n = \prod_{i=1}^{n} \frac{d^3q_i}{(2\pi)^3 \cdot 2\epsilon(q_i)}, \quad \epsilon(q) = (q^2+m^2)^{1/2}, \quad (3.7)$$

and a_n is the n-particle amplitude. Then,

$$K_3 = \frac{1}{\rho_n(\beta_c)} \int_{\beta_c} d\Gamma_n \prod_{i=1}^{3} \epsilon(q_i) \quad (3.8)$$
$$- \frac{3}{\rho_n^2(\beta_c)} \int_{\beta_c} d\Gamma_n \prod_{i=1}^{2} \epsilon(q_i) \int_{\beta_c} d\Gamma_n \epsilon(q_3)$$
$$+ \frac{2}{\rho_n^3(\beta_c)} \prod_{i=1}^{3} \int_{\beta_c} d\Gamma_n \epsilon(q_i),$$

where the index β_c means that averaging is performed with the Boltzmann factor $\exp\{-\beta_c\epsilon(q)\}$.

As a result, to have all fluctuations in the vicinity of β_c Gaussian, we should have $K_m \approx 0$, $m \geq 3$. Note, as follows from (3.3), the set of minimal conditions actually looks as follows:

$$|K_l| \ll |K_2|^{l/2}, \quad l \geq 3. \quad (3.9)$$

If the experiment confirms these conditions, then, independently of the number of produced particles, the final-state energy spectrum is defined with sufficiently high accuracy by one parameter β_c and the energy spectrum of particles is Gaussian. Under these conditions, one may return to the statistical and hydrodynamical models.

But if the inequality does not hold, then one must take into account the third correlator K_3, fourth correlator K_4, etc. The corresponding series is asymptotic, with zero convergence radii. This means that, if (3.9) does not hold, then β_c loses its physical meaning in this case. Therefore, if β_c exists, then one may omit the K_l, $l = 3, 4, \ldots$, dependence. Otherwise, one must take them into account and the problem becomes nonintegrable. From all evidence, just this situation is realized at $n \sim \bar{n}(s)$ (see the next section).

3.2. Deep Asymptotics over Multiplicity: Dilute Gas Approximation

Let us consider the deep asymptotics over multiplicity, when produced particle momentum

$$|q_i| \ll m_h. \quad (3.10)$$

In this case, one may ignore the momentum dependence in the amplitudes. This reminds one of the dilute gas approximation considered in statistics.

In the dilute gas approximation,

$$\Delta\Gamma_n \sim |a_n|^2 \prod_{i=1}^{n} d\epsilon_i(\epsilon_i^2 - m_h^2)^{1/2} e^{-\beta\epsilon_i}. \quad (3.11)$$

Then,

$$K_l(E, n) = \frac{\partial^l}{\partial\beta_c^l} \quad (3.12)$$
$$\times \ln\left\{\int \prod_{i=1}^{n} d\epsilon_i(\epsilon_i^2 - m_h^2)^{1/2} e^{-\beta_c(E,n)\epsilon_i}\right\}.$$

The approximation (3.10) means that $0 < (\epsilon_i/m_h) - 1 \ll 1$. Then it is easy to find that the K_3-to-K_2 ratio is small in the dilute gas approximation. For example,

$$R_3 \sim 1/n. \quad (3.13)$$

This result proves our general statement that, at least, in the deep asymptotics over n, the produced particle system must obey the property of a completely thermalized state.

4. RELAXATION OF CORRELATIONS: MODEL PREDICTIONS

The symmetries may prevent equilibrium since they can lead to nonvanishing distant correlations if the symmetry is local. Following the terminology of Schwinger [3], there should not be special correlations among degrees of freedom of the system if the phenomenon of equilibrium is sought.

This question is important because of the hidden constraints of the underlined non-Abelian gauge symmetry. Nevertheless, existence of multiple production means that the colored parton system is not completely integrable, i.e., that the spacetime local non-Abelian gauge and attendant conformal symmetries are unable to produce enough constraints to depress the thermalization process completely. In other words, in hadron dynamics, the hidden constraints are weak in the sense that they may be switched off through the choice of special external kinematical conditions.

We will illustrate these ideas by considering the multiperipheral and deep inelastic scattering kinematics. The symmetry in both cases is realized in a different way, but the result is the same: particles are uniformly distributed (over rapidity in the multiperipheral model or over transverse momentum in the deep inelastic scattering kinematics).

4.1. Multiperipheral Kinematics

The leading energy asymptotics Pomeron contribution reflects the kinematics, where the longitudinal momentum of produced particles is large and is strictly ordered. Thus, in terms of rapidities $\xi_i \sim \ln \epsilon_i$, the multiperipheral kinematics means that

$$\xi_1 < \xi_2 < \ldots < \xi_m < \xi. \tag{4.1}$$

At the same time, particle transverse momentum is restricted: $q_\perp^2 \le 0.2\ \mathrm{GeV}^2$. The energy conservation law in this kinematics has the form:

$$\prod \epsilon_i \sim E: \quad \sum \xi_i = \xi, \tag{4.2}$$

where ξ is the total rapidity. For this reason, it is natural to consider the rapidity fluctuations instead of energy. So, we will introduce β as the Lagrange multiplier of the rapidity conservation law (4.2).

It was found that multiperipheral kinematics dominates inclusive cross sections $f(s, p_c)$. Moreover, the created particle spectra do not depend on s at high energies in the multiperipheral region:

$$f(s,p_c) = 2E_c\frac{d\sigma}{d^3p_c}$$
$$= \int \frac{dt_1 dt_2 s_1 s_2 \phi_1(t_1)\phi_2(t_2)}{(2\pi)^2 s (t_1-m^2)^2(t_2-m^2)^2},$$
$$s_1 s_2(-p_{c\perp}^2) = s t_1 t_2.$$

Here, $s_1 = (p_a + p_c)^2$, $s_2 = (p_b + p_c)^2$, $p_c = \alpha_c p_a + \beta_c p_b + p_{c\perp}$, and $\phi_i(t_i)$ are the impact factors of hadrons. Thus, the particle c forgets the details of its creation. It is found experimentally that the ratio

$$\frac{f(\pi^+ p \to \pi^- + \ldots)}{\sigma(\pi^+ p)} \tag{4.3}$$
$$= \frac{f(K^+ p \to \pi^- + \ldots)}{\sigma(K^+ + p)} = \frac{f(pp \to \pi^- + \ldots)}{\sigma(pp)}$$

is universal [23].

The total cross section is written in the multiperipheral model in the form

$$\sigma_{\mathrm{tot}}^{ab}(\xi) = g^a P(\xi) g^b, \tag{4.4}$$

where the Pomeron propagator

$$P(\xi) = e^{\Delta\xi} \tag{4.5}$$

and the LLA gives [24]

$$\Delta = \alpha(0) - 1 = \frac{12\ln 2}{\pi}\alpha_s \approx 0.55, \tag{4.6}$$
$$\alpha_s = 0.2.$$

But the subsequent correction gives $\Delta \approx 0.2$. The one-particle inclusive spectra of the particle c of rapidity ξ_1 produced in the collision of particles a and b can be written in the form

$$f_c^{ab}(\xi,\xi_1) = g^a P(\xi-\xi_1)\psi_c P(\xi_1) g^b = g^a \psi_c g^b e^{\Delta\xi}, \tag{4.7}$$

where the conservation law (4.2) and the definition (4.5) were used.

Upon the suppression of the indices, the two-particle spectra takes the form:

$$f_2 = gP(\xi_1)\psi P(\xi_2)\psi P(\xi_3) g, \tag{4.8}$$
$$\xi_1 + \xi_2 + \xi_3 = \xi, \qquad \xi_i \ge 0.$$

Generally,

$$f_k = g\left\{\prod_{i-1}^{k} P(\xi_i)\psi\right\} P(\xi_{k+1}) g, \quad \sum_{i=1}^{k+1}\xi_i = \xi. \tag{4.9}$$

Noting the normalization condition

$$\frac{1}{k!}\int \prod_{i=1}^{k+1} d\xi_i \delta\left(\xi - \sum_{i=1}^{k+1}\xi_i\right) f_k = \sum_{n=k}^{\infty}\frac{n!}{k!(n-k)!}\sigma_n,$$

one may use the Mellin transform to write

$$T(z,s) = g\mathcal{P}(0,\xi;z) g, \tag{4.10}$$

where the superpropagator

$$\mathcal{P}(0,\xi;z) = e^{(z-1)\bar{n}(s)}. \tag{4.11}$$

It is evident that (4.11) leads to the Poisson distribution:

$$\mathcal{P}_n(0,\xi) = e^{-\bar{n}(s)}\frac{\bar{n}(s)^n}{n!}, \quad \bar{n}(s) = \psi\xi. \qquad (4.12)$$

Therefore, we start the description by considering the production of noncorrelated particles. Indeed, $\omega(\xi,z) = \ln \mathcal{P}(0,\xi;z)$ can be considered as the generating function of particle number correlators: $C_l = \partial^l \omega(\xi,z)/\partial z^l$, where, if the inclusive correlators are considered, then one must take $z=1$ at the very end of calculations. Inserting $\mathcal{P}(0,\xi;z)$ from (4.11), we find that $C_l = 0$ for all $l > 1$.

But it must be mentioned that, nevertheless, the restrictions (4.1) introduce energy correlations of the produced particles. We will see as a result that the energy correlators $K_l, l \geq 3$, will be large as compared with $|K_2|$. Therefore, the condition of the uniform distribution of particles over the rapidity (4.1) creates strong correlations over rapidities, i.e., over the longitudinal momentum.

One may notice that just the Mellin transform is useful. Thus,

$$\mathcal{F}^1(\xi,z) = g\mathcal{P}(0,\xi-\xi_1;z)\psi\mathcal{P}(0,\xi_1;z)g \qquad (4.13)$$
$$= g^2\psi\mathcal{P}(0,\xi;z)$$

is the generating function of the one-particle exclusive spectrum. The inverse Mellin transform defines the one-particle spectrum in the n-particle environment:

$$\mathcal{F}^1_n(\xi) = g^2\psi\mathcal{P}_n(0,\xi). \qquad (4.14)$$

Consequently the two-particle spectrum generating function looks as follows:

$$\mathcal{F}^1(\xi,z) = g\mathcal{P}(0,\xi_3;z)\psi\mathcal{P}(0,\xi_2;z)\psi\mathcal{P}(0,\xi_1;z)g \qquad (4.15)$$
$$= g^2\psi^2\mathcal{P}(0,\xi;z), \qquad \xi_1+\xi_2+\xi_3 = \xi.$$

In conclusion,

$$\mathcal{F}^l(\xi,z) = g^2\psi^l\mathcal{P}(0,\xi;z), \quad \sum_{i=1}^{l+1}\xi_i = \xi, \qquad (4.16)$$

is the l-particle exclusive spectrum generating functional. Notice the ξ_i independence of $\mathcal{P}(0,\xi;z)$.

Let us calculate now

$$\rho^{(l)}_n(\xi) = \int_0^\infty d\Gamma^l_n(\xi)\prod_{i=1}^{l}\xi_i, \qquad (4.17)$$

where, as follows from (4.16),

$$d\Gamma^l_n(\xi) = \psi^l\mathcal{P}_n(0,\xi)\prod_{i=1}^{l+1}d\xi_i\delta\left(\sum_{i=1}^{l+1}\xi_i - \xi\right). \qquad (4.18)$$

Therefore,

$$\rho^{(l)}_n(\xi) = \frac{\psi^l\xi^{2l}}{(2l)!}\mathcal{P}_n(0,\xi) \qquad (4.19)$$

and

$$\rho_n(\beta_c) = \mathcal{P}_n(0,\xi). \qquad (4.20)$$

Having (4.19) and (4.20), one can find that, for example,

$$K_2 = \frac{\rho^{(2)}_n}{\rho_n} - \frac{\rho^{(1)2}_n}{\rho^2_n} = \frac{-5\psi^2\xi^4}{4!} \qquad (4.21)$$

and

$$K_3 = \frac{\rho^{(3)}_n}{\rho_n} - 3\frac{\rho^{(2)}_n}{\rho_n}\frac{\rho^{(1)}_n}{\rho_n} + 2\frac{\rho^{(1)2}_n}{\rho^3_n} = \frac{316\psi^3\xi^6}{6!}. \qquad (4.22)$$

Therefore, the K_3-to-K_2 ratio is large,

$$R_3 = \frac{K_3}{|K_2|^{3/2}} = \frac{316}{6!}\left(\frac{4!}{5}\right)^{3/2} > 1, \qquad (4.23)$$

and it is a ξ- and n-independent number. One may find that

$$R_l > 1 \qquad (4.24)$$

for all $l \geq 3$. Therefore, the multiperipheral models are not able to show even the tendency to equilibrium.

4.2. Deep Inelastic Scattering Kinematics

The deep inelastic scattering (DIS) structure function $\mathcal{D}_{ab}(x,q^2)$ is described in the LLA by the contribution of the ladder diagrams. From a qualitative point of view, this means the approximation of a random walk over the coordinate $\ln(1/x)$ and the time is $\ln|q^2|$. The leading contributions, which are able to compensate for the smallness of $\alpha_s(\lambda) \ll 1$, give the integration over a wide range over the mass $|k|$ of real, i.e., timelike gluons. At the same time, the masses are strongly ordered:

$$\lambda^2 \ll k^2_1 \ll \ldots \ll \kappa^2_\nu \ll -q^2, \qquad (4.25)$$

where ν is a number of steps (timelike gluons) of the ladder.

If the time needed to capture the parton into the hadron is $\sim(1/\lambda)$, then the gluon should decay if $k^2_i \gg \lambda^2$. This leads to the creation of QCD jets. The mean multiplicity $\bar{n}_j$ in the QCD jets is high if the gluon mass $|k|$ is high: $\ln\bar{n}_j \sim \sqrt{\ln(k^2/\lambda^2)}$.

Raising the multiplicity may (i) raise the number of jets ν and/or (ii) raise the mean value of the mass of jets $|\bar{k_i}|$. We will see that mechanism (ii) will be favorable. But raising the mean value of gluon masses, $|k_i|$,

decreases the range of integrability over k_i. For this reason, the LLA becomes invalid in the VHM domain and the next-to-leading-order corrections should be taken into account.

Indeed, let $\mathcal{F}_{ab}(x,q^2;\omega)$ be the generating functional:

$$\mathcal{F}_{ab}(x,q^2;\omega)=\sum_\nu\int d\Omega_\nu(k)$$
$$\times\prod_{i=1}^{\nu}\omega^{r_i}(k_i^2)\left|a_{ab}^{r_1r_2\ldots r_\nu}(k_1,k_2,\ldots,k_\nu)\right|^2,$$

where $a_{ab}^{r_1r_2\ldots r_\nu}$ is the production amplitude of ν partons ($r_i=(q,\bar q,g)$) with momenta $(k_1,k_2,\ldots,k_\nu)$ in the process of scattering of parton a on parton b; $d\Omega_\nu(k)$ is the phase space element; and $\omega^r(k^2)$ is the "probe function," i.e., the correlation functions

$$N_{ab}^{r_1r_2\ldots r_\nu}(k_1^2,k_2^2,\ldots,k_\nu^2;x,q^2)$$
$$=\prod_{i=1}^{\nu}\frac{\delta}{\delta\omega^{r_i}(k_i^2)}\ln\mathcal{F}_{ab}(x,q^2;\omega)\Big|_{\omega=1}.$$

The generating functional is normalized on the DIS structure function $\mathcal{D}_{ab}(x,q^2)$,

$$\mathcal{F}_{ab}(x,q^2;\omega=1)=\mathcal{D}_{ab}(x,q^2).$$

We will consider the approximation when the cutting line passes only through the steps of the ladder diagram. In this case, $\mathcal{D}_{ab}(x,q^2)$ has a meaning of the probability of finding parton a in parton b.

It is useful to consider the Laplace image over $\ln(1/x)$:

$$\mathcal{F}_{ab}(x,q^2;\omega)=\int\frac{dj}{2\pi i}\left(\frac{1}{x}\right)^j\mathbf{F}_{ab}(j,q^2;\omega). \quad (4.26)$$

Then, taking into account the above-mentioned conditions, one may find the DGLAP evolution equation:

$$t\frac{\partial}{\partial t}\mathbf{F}_{ab}(j,t;\omega)=\sum_{c,r}\varphi_{ac}^r(j)\omega^r(t)\mathbf{F}_{cb}(j,t;\omega), \quad (4.27)$$

where $t=\ln(|q^2|/\Lambda^2)$,

$$\varphi_{ac}^r(j)\equiv\varphi_{ac}(j)=\int_0^1 dx\,x^{j-1}\,P_{ac}^r(x),$$

and $P_{ac}^r(x)$ are the regular kernels of the Bethe–Salpeter equation for pQCD [18]. Equation (4.27) coincides at $\omega^r=1$ with the habitual equation for the Laplace transform of the structure function $\mathcal{D}_{ab}(x,q^2)$. When Eq. (4.27) was being derived, only one additional assumption was used for our problem, $\omega^r=\omega^r(k^2)$.

The dominance of gluon contributions for the case $x\ll 1$ must be taken into account, and for this reason, we will omit all parton indices. One may find the solution to (4.27) in terms of the ν-gluon correlation functions $N^{(\nu)}$. Omitting the t dependence in the renormalized constant α_s, let us write

$$\mathbf{F}(j,t;\omega)=\mathbf{D}(j,t)\exp\left\{\sum_\nu\frac{1}{\nu!}\int\prod_{i=1}^{\nu}dt_i(\omega(t_i)-1)\right.$$
$$\left.\times N^{(\nu)}(t_1,t_2,\ldots,t_\nu;x,t)\right\},$$

where $t_i=\ln(k_i^2/\lambda_i^2)$. In the VHM domain, where $x\ll 1$ is important, one must consider $(j-1)\ll 1$. Then,

$$N^{(1)}(t_1;j,t)=\varphi(j)\sim\frac{1}{j-1}\gg 1.$$

The second correlator

$$N^{(2)}(t_1,t_2;j,t)$$
$$=O\left(\max\left\{\left(\frac{t_1}{t}\right)^{\varphi(j)},\left(\frac{t_2}{t}\right)^{\varphi(j)},\left(\frac{t_1}{t_2}\right)^{\varphi(j)}\right\}\right)$$

is negligible at $(j-1)\ll 1$ since [see (4.25)] $t_1<t_2<t$. Therefore, in the LLA,

$$\mathbf{F}(j,t;\omega)=\mathbf{D}(j,t)\exp\left\{\varphi(j)\int_{t_0}^{t}dt_1(\omega(t_1)-1)\right\}.$$

Taking $\omega(t)=\text{const}$, one finds that $\mathbf{F}(j,t;\omega)$ has the Poisson distribution with the mean multiplicity $\sim\varphi(j)t$.

If the quantity

$$\omega(t,z),\quad \omega(t,1)=1,\quad t=\ln(k^2/\lambda^2),$$

is the generating function of the preconfinement (close to the mass shell $\simeq\lambda$) parton multiplicity distribution

$$\omega_n(t)=\frac{\partial^n}{\partial z^n}\omega(t,z)\Big|_{z=0},$$

then, using the parton–hadron correspondence idea, as follows from derivation of $\mathbf{F}(j,t;\omega)$, the quantity

$$\mathbf{F}(j,t;\omega)=\mathbf{D}(j,t) \quad (4.28)$$
$$\times\exp\left\{\frac{1}{j-1}\int_{t_0}^{t}dt(\omega(t,z)-1)\right\}$$

is the generating function for the hadron multiplicity distribution in the DIS processes calculated in the framework of the LLA.

Inserting (4.28) into the integral (4.26), one can find that, if

$$\bar{\omega}(t,z) \equiv \int\limits_{t_0}^{t} dt\, \omega(t,z),$$

then

$$j-1 = \{\bar{\omega}(t,z)/\ln(1/x)\}^{1/2}$$

are essential. Thus, the mobility

$$\{\ln(1/x)/\bar{\omega}(t,z)\} \gg 1 \qquad (4.29)$$

decreases with z or, what is the same, with the multiplicity n. This is the reason why the LLA for the considered DIS kinematics has a restricted range of validity in the VHM region.

Nevertheless, in the frame of LLA conditions, as follows from (4.28), the generating functional $\mathcal{F}_{ab}(x,t;z)$ has the following estimate:

$$\ln \mathcal{F}_{ab}(x,t;z) \propto \{\ln(1/x)\bar{\omega}(t,z)\}^{1/2}. \qquad (4.30)$$

Therefore, since the coupling is a constant,

$$\ln \mathcal{F}_{ab}(x,t;z=1) = \ln \mathcal{D}_{ab}(x,t) \propto (t\ln(1/x))^{1/2}.$$

This is a well-known result. Therefore, one should take into account the screening effects (see [18]).

Nevertheless, the kinematics described by (4.30) cannot predict tendency to equilibrium.

5. CONCLUSION

Summarizing the results, one may conclude the following:

(i) If the hadron amplitudes are regular in the zero momentum limit, then, at least, in the deep asymptotics over multiplicity, i.e., in the nonrelativistic limit, one must see complete thermalization.

(ii) Existing multiple production models are not able to predict even tendency to thermalization. But it must be noted that the models have a finite range of application in the VHM domain. Experimental information in the VHM domain seems crucial for this reason.

(iii) The description of multiparticle-production processes in a finite neighborhood of the mean multiplicity $\bar{n}(s)$ requires a large number of correlators. For this reason, the VHM domain, where the correlators vanish, is important.

ACKNOWLEDGMENTS

We would like to take the opportunity to thank Yu. Budagov, V. Kadyshevski, A. Korytov, E. Kuraev, L. Lipatov, V. Matveev, and V. Nikitin for fruitful discussions and constructive comments.

REFERENCES

1. J. Manjavidze, Fiz. Élem. Chastits At. Yadra **16**, 101 (1985) [Sov. J. Part. Nucl. **16**, 44 (1985)].
2. J. Manjavidze and A. Sissakian, JINR Rapid Commun., No. 5[31]-88, 5 (1988); G. Chelkov, J. Manjavidze, and A. Sissakian, JINR Rapid Commun., No. 4[96]-99, 35 (1999); hep-ph/9811360.
3. J. Manjavidze and A. Sissakian, Phys. Rep. **346**, 1 (2000).
4. J. Manjavidze and A. Sissakian, Part. Nucl. **31**, 104 (2000).
5. A. Casher, H. Neuberger, and S. Nassinov, Phys. Rev. D **20**, 179 (1979); E. Gurvich, Phys. Lett. B **87B**, 386 (1979).
6. F. Bloch, Z. Phys. **74**, 295 (1932).
7. T. Matsubara, Prog. Theor. Phys. **14**, 351 (1955).
8. N. P. Landsman and Ch. G. van Weert, Phys. Rep. **145**, 141 (1987).
9. L. Dolan and R. Jackiw, Phys. Rev. D **9**, 3320 (1974).
10. A. J. Niemi and G. Semenoff, Ann. Phys. (N.Y.) **152**, 105 (1984).
11. J. Schwinger, J. Math. Phys. A **9**, 2363 (1994).
12. L. V. Keldysh, Zh. Éksp. Teor. Fiz. **47**, 1612 (1964) [Sov. Phys. JETP **20**, 1018 (1964)].
13. H. Umezawa, H. Matsumoto, and M. Tachiki, *Thermo-Field Dynamics and Condensed States* (North-Holland, Amsterdam, 1982).
14. T. D. Lee and C. N. Yang, Phys. Rev. **87**, 404, 410 (1952).
15. J. S. Langer, Ann. Phys. (N.Y.) **41**, 108 (1967).
16. M. Kac, G. E. Uhlenbeck, and P. C. Hemmer, J. Math. Phys. (N.Y.) **4**, 216 (1963); **5**, 60 (1964).
17. S. Coleman, Phys. Rev. D **15**, 2929 (1977).
18. L. V. Gribov, E. M. Levin, and M. G. Ryskin, Phys. Rep. **100**, 1 (1983).
19. K. Konishi, A. Ukawa, and G. Veneziano, Phys. Lett. B **80B**, 259 (1979); A. Basseto, M. Ciafaloni, and G. Marchesini, Nucl. Phys. B **163**, 477 (1980).
20. V. Volterra, *Lecons sur la Theoreie Mathematique de la Lutte Pour La Vie* (Paris, 1931).
21. M. Kac, *Probability and Related Topics* (Intersci., London, 1957).
22. L. D. Landau, Izv. Akad. Nauk SSSR, Ser. Fiz. **17**, 85 (1953).
23. M. G. Ryskin, in *Proceedings of the VII Winter School* (LIYaPh, Leningrad, 1972).
24. E. A. Kuraev, L. N. Lipatov, and V. S. Fadin, Zh. Éksp. Teor. Fiz. **71**, 840 (1976) [Sov. Phys. JETP **44**, 443 (1976)]; L. N. Lipatov, Yad. Fiz. **20**, 181 (1975) [Sov. J. Nucl. Phys. **20**, 94 (1975)]; V. N. Gribov and L. N. Lipatov, Sov. J. Nucl. Phys. **15**, 438, 675 (1972); G. Altarelli and G. Parisi, Nucl. Phys. B **126**, 298 (1977).

Physics of Atomic Nuclei, Vol. 67, No. 1, 2004, pp. 31–40. From Yadernaya Fizika, Vol. 67, No. 1, 2004, pp. 33–41.

Development and Application of the Hadronic Event Generators in HEP*

N. S. Amelin** and **M. E. Komogorov**

Joint Institute for Nuclear Research, Dubna, Moscow oblast, 141980 Russia
Jyväskylä University, Jyväskylä, Finland

Received April 30, 2003

Abstract—We have suggested a new approach to the development and use of Monte Carlo event generators in high-energy physics (HEP). It is a component approach where a complex numerical model is composed from standardized components. Our approach opens a way to organize a library of HEP model components and provides a great deal of flexibility for the construction of powerful and realistic numerical models. To support this approach, we have designed the NiMax software system (framework) that is written in C++. © *2004 MAIK "Nauka/Interperiodica".*

1. INTRODUCTION

The full description of high-energy hadronic and nuclear interactions from first principles of quantum chromodynamics (QCD) is rather limited. As a rule, we are able to obtain the QCD predictions for the short-distance processes, where interaction takes place with large momentum transfer. It makes the task of development and use of the QCD motivated phenomenological models very important. Such models are extremely popular for predictions of new phenomena and analysis of obtained experimental data. In addition, the design, construction, and performance of experimental detectors require careful numerical simulations. The Monte Carlo (MC) phenomenological models often referred to as MC event generators are standard tools to perform such simulations [1].

The most widely used model codes were written in Fortran. Nevertheless, many physics centers have turned now to using object-oriented languages (C++, Java) for the development of physics-related software, because object-oriented programming has many advantages as compared with traditional procedural coding (see, e.g., [2]).

In this paper, we present an object-oriented system to use and develop numerical models. We refer to our system as the NiMax system. The main idea of this software system is to support the component approach to the development and use of numerical models [3]. The component can represent either a model of single physical process, e.g., hadron elastic scattering, or a model of a very complicated physical phenomenon, e.g., ultrarelativistic heavy-ion collision.

For the NiMax system, we distinguish two categories: component developers and component users. We consider a component user as the person who interacts with the components by means of a user interface without writing and modifying the component codes. Thus, the created components are required to allow productive user work without touching component codes and, therefore, without learning any programming languages. On the other hand, we require that the built components have the ability to be used as usual C++ classes by the component developers without any limitations as compared with normal C++ programming. A component developer needs detailed knowledge of the component structure, component life cycle, and data event configurations. In this talk, we would like to provide a brief explanation of the system as well as the work of the component users and component developers. The interested reader can find a more detailed explanation in [3], which served as an early release of the system manual.

2. SYSTEM UNDERSTANDING

The component concept is a central concept of the NiMax system (see Fig. 1). We made an attempt to formalize numerical components as construction blocks for numerical applications that are stored as extendable collections.

Any numerical component could be divided into an interface part and the part implementing the component algorithm. The interface parts include different methods and related data that allow collaboration among components and component collaborations with users. The interface methods and data are divided into five standard groups and are referred to

*This article was submitted by the authors in English.

**e-mail: Nikolai.Ameline@phys.jyu.fi

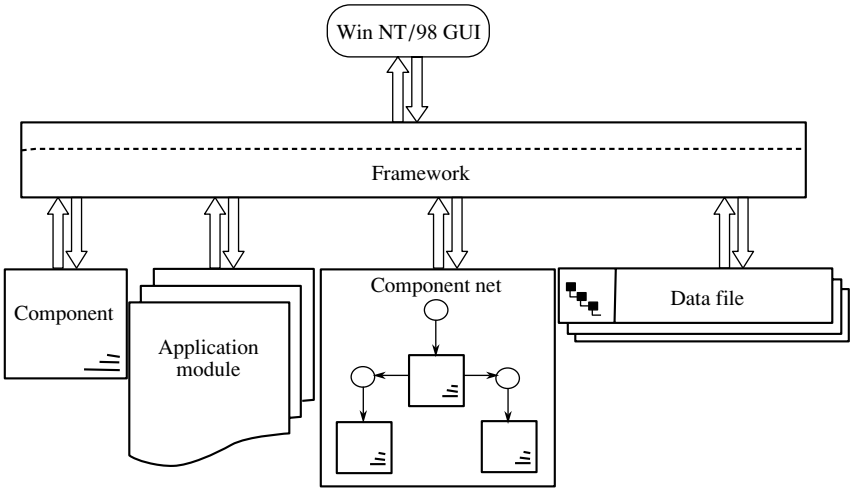

Fig. 1. An architectural overview of the NiMax system.

as the input, tuning, output, matching, and runtime interfaces. By means of the input, tuning, and runtime interfaces, a user can request components to fulfill some actions, handle their parameters, and control their execution processes, respectively. By means of the output and matching interfaces, the components are able to write and read data in data files and exchange data with other components. Thus, only through the outlined standard interfaces does a component communicate with the system users. Therefore, it offers for the users only a limited number of standard operations.

Such a situation dictates a component developer to follow definite rules during a component implementation. On the other hand, these rules can easily be taken into account by means of the component wizards that facilitate writing of the component interface parts and interface documentation. The component developers should mostly work on the implementation of particular component algorithms. In the case of developing composite components, there are very important questions about the subcomponent control, their collaboration, and their collaboration with the users. Particularly, the subcomponent collaboration should allow substitution of variable implementation of different algorithms (e.g., alternative components) via a graphical user interface. Thus, it is essential that suggested interfaces support the mechanisms for subcomponent control and their collaboration and do not pose limitations for normal C++ programming during the development of the composite component algorithms.

To increase the productivity of component developers, the components that are related to a particular application domain and some software such as common classes, functions, and data that are shared by these components are packaged into application modules. For the component developers, it is more natural and efficient to work on the codes of component algorithms within a component-related software environment than on the isolated codes. On the other hand, the components from an application module are only visible and accessible to system users. Thus, the application modules fulfill a twofold function: they offer useful software for component developers and hide it from component users.

We can classify different types of components according to the presence or absence of a particular interface or interfaces. For example, we distinguish so-called executable components with input or matching interfaces from general components that have neither input nor matching interfaces and cannot be executed. Particularly, it is important that the system user be able to assemble the executable components into pipeline component nets for common execution.

In spite of the different algorithms, any component belongs to either data event generator or data event processor or data event converter groups. A data event is a configured portion of data that can be generated by a component to be stored on disk or sent to other components. A data event can also be received by a component for converting or further processing (analytical analysis of data). Thus, data events are considered as units of data for data exchanges. Any data event consists of data event channels (at least one) that are considered as units for data processing.

The system includes a data file. Thus, a component can write and read the data events in the data file. The data file has several views. The most important of them are the view of data event configurations that allows structural data analysis to be performed and the view of data from data events. Some data events and groups of data event channels are considered

by the system as predefined data events and predefined data event channels. The system offers special services for the user to deal with such events and groups of channels. Particularly, it allows for users to perform graphical analysis of the data. The idea of predefined data events opens a possibility to create special graphical user interfaces for particular application domains.

The component user works by means of the graphical user interface (GUI) that is developed in accordance with the document—view technology (see [4]). Each document object (component, data file, component net, etc.) is connected with one or several views that display data and allow editing.

We have developed a large set of classes to support component control, management, and development and data management and visualization. This set of classes is thought of as a framework. Its application programming interface (open arrows in Fig. 1) links together the components, application modules, data files, component nets, and GUI.

3. NiMax APPLICATION LAYERS

Within the NiMax system, all application software is organized into three abstraction layers: the application data types, application components, and application modules. Each layer of the application software partially builds upon the layers below. The uppermost layer consists of the application modules that are complete user applications and considered as distribution units. The modules can either be completely independent and self-sufficient on the level of source codes (i.e., no external implementations are required to execute their components) or be connected with other modules for some applications. For system users, the modules are prepared as dynamically linked libraries. As we have already stated, with the exception of the components, all module software, as well as the application data types, is hidden from the system users. The components from a module or different modules can be composed into composite components or component nets in a variety of ways. The component algorithm of each particular application module can be tuned and different implementations of it can be interchanged at runtime, enabling the component user to obtain the required algorithm properties. This provides a great degree of flexibility for the construction of powerful and realistic numerical applications.

We consider the application modules as development units. They are parts of component projects that include in addition the module and component development tools. Component related software that can be used by many components substantially facilitates the component development process, increases the developer's productivity, and also has the benefit of efficient use of computer resources. Thus, new components with their own peculiarities can more easily be developed. The application module idea makes it possible to create scalable systems from separate blocks as well.

The lowermost layer contains the application data type (ADT) classes. For the developers of the component algorithms, application data type classes are the most important ingredients of the modules. They represent real objects and many operations on them from application domains and allow rapid development of robust component algorithms. The subset of ADT classes is the so-called data transfer classes. They include methods to write and read configured data events and facilitate the development of the component input and output. We are working on a library of the application data type classes that will include particle, field, material, solid, and tracer classes. These classes will allow developers to work efficiently on different component algorithms from many problem domains related to radiation transport in composite media.

4. COMPONENT INTERFACES

We consider any component as a set of standardized interfaces between its numerical algorithm and the outside world. An interface includes several methods and some related data.

By means of the input interface, a user sends a request for a component and provides necessary input data to fulfill this request. The request, as well as input data, is provided in the form of an input map [3]. On the other hand, an input map can be understood as the user request on some action that is completed by a list of parameters that must be specified by users before the component execution.

The tuning interface makes it possible for component users to tune the component with the aim of obtaining reliable results from its execution. By means of this interface, the user has access to component parameters. In the present version of the system, any component parameters are presented by a list of simple data types. The input interface and tuning interface have many similarities from the developer's point of view (the same classes in use [3], the same data structures in use).

The result of component execution is obtained by means of the output interface. This interface assists either in writing component output data in the data file or in sending component output data to other components. The output data are produced as configured data events and have a tree structure in the common case [3].

A component can also read necessary input data from the data file or receive it from another component by means of the matching interface. It allows a component to select data according to its matching configuration [3]. A particular matching configuration is realized as a matching map.

We have also developed a runtime information interface. It is used to obtain and control component runtime messages [3]. By means of such messages, the numerical components inform about their execution processes during the run session. The runtime information is simple text-based information. There are three types of runtime messages: information messages, warning messages, and error messages. The information messages are used to tell about the normal execution process. The warning messages inform a user about potential errors or other situations that are able to destroy the normal execution process. The execution process will continue after the appearance of the warning messages. The error messages appear when the execution process is aborted.

The system allows an extension of the existing interfaces as well as addition of new ones. By adding more standard component interfaces, we can extend the application area of the NiMax system.

In addition to the outlined standard interfaces, each particular component has its application programming interface (API), which implements the component functionality and can be called directly or indirectly by means of the component interface methods.

Each component interface is complemented by at least one view. These views help a component user to perform many actions on the component state (see the graphical user interface section).

5. COMPONENT PROPERTIES

Besides standardized interfaces and views, the system components have other common elements. Each component has its own component factory to create the component objects and includes the component static information, which is needed for component object creation. Any component has its unique identifier. The knowledge of a component's identifier helps us to obtain full information about the component. Particularly, the composite component aggregating (see below) other components should include their proxies [3].

The observation of many common component elements allowed us to develop the component frames [3] with aim of producing so-called skeleton components simply by editing a particular component frame. Such a frame can be thought of as the component template that is supporting a correct programming style. Thus, a component developer needs to design only the component application algorithm. To help a component developer, we created a component wizard similar to the Microsoft Visual C++ 6.0 class wizard [4]. The component wizard is the code generator that produces a component skeleton by means of the dialog windows.

A component developer can extend the functionality of a ready component by applying the inheritance mechanism [3] that is supported by our system. The interfaces of a base component and derived component are joined as well as their public APIs. For example, the component inheritance is a convenient way to add either new input maps or new matching maps.

A new composite component can be developed by the aggregation of existing components [3]. A composite component can include several aggregated components. A particular component can include the tree of aggregated components. The tuning and output interfaces of aggregated components are simply joined to the relevant aggregating component interfaces.

There are several important features of the suggested aggregation mechanism. The component user is able to see the composite component structure and has access to any subcomponents by means of the GUI. There are no limitations to creating an efficient component code, e.g., as compared with the standard C++ coding for the developer, which is working on the creation of a component by aggregation of other components. The APIs of aggregated components are called directly. In this case, the component coding is even simplified; e.g., no efforts are required to create and destroy the aggregated component objects.

The inheritance and aggregation mechanisms provide a unique possibility for the composite component users to change its algorithm without touching the component source code and its recompilation. We refer to this possibility as the runtime substitution of subcomponents in the aggregating components.

Each component should be accompanied with its documentation. The component documentation includes the names of component authors, descriptions of component applicability, its input maps, parameters, subcomponents in use, numerical algorithm, etc. The component documentation is realized as a set of html files.

Writing of the component documentation is a very important part of the component development process. We offer documentation frames and a documentation wizard (for the Windows platform only) for the component developers. The component documentation frames allow a developer to present information with the standard appearance. They are similar to the

component frames discussed below and developed in the complement of model component frames.

6. APPLICATION MODULES

Several implemented components can share common data, functions, and classes that are related to a particular application domain. For a component developer, it is more natural and more efficient to work on the component code within some component-related software environment than on an isolated component code. It allows more efficient use of the computer resources by the developer. We suggest packaging of built components with their related software into modules [3] that are referred to as application domain modules. We consider these modules as developer's units. In addition to the components, application data types and data transfer classes (see below) are the most important members of the application modules. The application data types represent key abstractions from the problem domain and operations on that are used to manipulate the types. The development of MC event generators is our problem domain. Thus, most of the ADT objects are counterparts of real high-energy physics objects (particle, parton, nucleus, string, etc.). We have also created module frames that are similar to the component frames to support implementation of the module structures.

The application modules can be self-sufficient on the level of source code; i.e., no external methods, external implementations, etc., are required to compile and execute module components. It allows us to use these modules as the units for distribution. By compilations, they are prepared as dynamically linked libraries (DLLs) for the users of our system. Only the components from an application module are visible and accessible to the users. The module independence does not forbid use of components from other modules. It does not pose any limitation on the inheritance and aggregation mechanisms. For example, it does not forbid subcomponent substitution if an aggregated subcomponent and its alternative subcomponent belong to different DLLs.

A large set of hadronic model components have already been implemented and included in the hadronic modules [3]. It allows their users to perform simulation of particle and nuclear interactions in a wide high-energy range and for a large set of projectiles and targets.

7. DATA EVENTS

Any numerical component deals with data. It can generate a very large bulk of data and store it on a disk for further analysis and visualization. It can read data from a disk and process it. The collaborative work of several components requires data exchange. To fulfill these needs, we have suggested the idea of a data event [3].

A data event is a portion of data that only consists of values of simple data types (int, float, double, etc.). Any data event has its own definition. The definition includes a unique identifier and describes data event configuration.

The data event definition is a tree of data channel definitions. The data channel definition includes the channel identifier, its type, and its name, and more information can be added. A data event is not a C++ object; i.e., it is not an instance of a definite class. The data of a data event can be placed into memory or stored on disk according to the data event definition.

We have suggested [3] the concept of predefined data events and channels. These events and channels are associated with definite services that are offered to the system users. The predefined channels and predefined group of channels have fixed configurations (similarity with C++ objects) and the system user is not able to change their configurations. To deal with such data events, the framework needs to know only their identifiers; e.g., the framework knows (due to the unique identifier) how to display table and graphical views for the predefined histogram and plot channels. The component parameters, input maps, and proxy sets are other examples of the predefined data events representing component states. The framework knows how to display and execute such predefined data events.

7.1. Data File

A component can write and read data events in the data file. The data file has its header, which is needed to identify the file and facilitate the navigation through it. The data file is separated into two parts: the data event configuration part and the data part. The presence of the data event configurations in the data file allows a system user or a component to perform a very flexible selection of data. We refer to it as structural data selection. The data event configuration part has its own header and includes the list of event definitions with their unique identifiers. The event configuration header keeps some statistical information about the data events. The data part consists of the data records, where the tree-structured data are written. Each data record has its own header, where the information to help for navigation through the data is stored.

For system users, we have created several views for the data file. The most important of them is the data configuration view and data view.

8. DATA TRANSFER CLASSES

Many of the implemented components can be considered as generators or converters of the data events. The data transfer classes (DTC) help the component developers to facilitate design and implementation of the component outputs and inputs and, hence, to pay more attention to development of the component algorithms.

The DTC library has a hierarchical structure, because it is very convenient to have base classes that either factorize common properties of all objects of this hierarchy or collect most of the operations needed to manage these objects. These classes help to implement universal numerical algorithms. The degree of universality of an algorithm is determined by the amount of needed input/output information. The most universal algorithms are those that use objects of the node data transfer class as input and output.

We should note that data transfer classes are essentially the same as ADT classes, which we discussed before. By introducing the data transfer term for a subset of ADT classes, we should stress their importance for data management. Within our system, we have no strict recommendations on how to build such classes. The most important thing is that any object of a data transfer class should support a serialization, i.e., this class needs methods to write in the data file and read from the data file its object states.

9. COMPONENT NETS

A component could receive the data events produced and sent by other components. Thus, several components can be assembled into an event-oriented net to perform collaborative work.

The produced data events have tree structures that are described by data event configurations. The framework analyzes event configurations and searches the necessary data configuration for a component. We refer to this process as the matching of a data configuration [3]. If the necessary configuration is found, we refer to this situation as observation of an entry point into the component input data.

The necessary data configurations for a given component are described by the component matching configurations or matching maps. The component developer can offer several matching maps. It provides room for the component user to tune this component by registering a chosen matching map as the default one.

It is important to stress the following. The ability of a component to recognize necessary data obtained from the data file or from other components does not require the component developer either to learn or use system classes (objects) or to have knowledge about the data source (the data file, other components). The component developer does not need to learn the configurations of data events that can be received by the component. He or she has to know how to create the configurations of the required input data.

We distinguish two different situations for component collaboration through standard output and matching interfaces [3]. The first one is that a component writes its output data events in the data file and another component reads these data from the data file. We consider this situation as component collaboration through the data file bus, having in mind a hardware analogy. For this type of interaction, the component objects are completely isolated from each other.

The second situation is that one component produces a data event output, which will be received by another component as an input. We consider this situation as component collaboration by the data event bus. For this type of interaction, the components are executed inside a common process.

A set of components that collaborate through the standard output and matching interfaces by sending and receiving data event messages and are connected in sequence to process numerical data is referred to as an event-oriented net [3].

Figure 2 demonstrates an example of a net. Here, component $C1$ produces two events having configurations $C1_{E1}$ and $C1_{E2}$; then, components $C2$ and $C3$ receive data of those events that are selected in accordance with the matching configurations $C2_{M1}$ and $C3_{M1}$, respectively. These components produce new data events configured as $C2_{E1}$ and $C3_{E1}$, respectively. The last events are written in the data file.

We consider only nets whose component execution order is defined by data flows; i.e., we consider only so-called pipeline nets. For pipeline nets, a system user does not need to write and compile the event control procedure. Any net includes the component that is executed first. We refer to this component as the start or main component. It reads its input by the input or matching interface. Thus, during a net assembly, the system user has to outline participating components, point out the start component, and provide information about pairs of collaborating (connected) components. Any component or subcomponent from the net could write its output in the data file.

Any net is presented by the NiMax system file. The file consists of two parts. The first part can be considered as a net definition part. The second part includes the event control procedure. This file is constructed on the basis of the information obtained from a user through a net view.

We should note that very often a net consists of only one component and, if we are going to perform

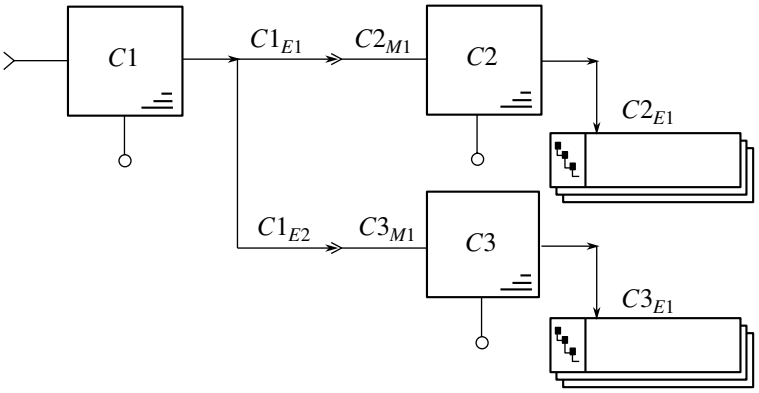

Fig. 2. An event-oriented net.

a component execution, we always deal with the net file.

10. NiMax FRAMEWORK METHODS

The full description of the framework and other classes that belong to the NiMax system requires a separate paper or manual. Here, we would like to explain in brief the framework functionality offered by the control and navigation methods.

There are many methods to control the component life cycle. In spite of the fact that the component life cycle consists mostly of internal framework processes, which are hidden from the system users, we would like to share an idea about it. There are many possibilities for the user to influence the component life cycle. It includes several phases: the component instance creation phase, editing phase, execution phase, and destruction phase.

Before starting the component object creation procedure, the framework creates an environment for the component object. The context of this environment defines the optional variables, which are set to default values, and output and input files, if they will be used. The user is able to modify these optional variables by means of the user interface; e.g., the user can either set his own default parameters and input and matching maps or suppress the output of some data events or suppress the runtime information output. In the case of a composite component, the aggregating component instance is created first. Then, the framework creates aggregated component instances. In order to create any component object, the framework needs to know only the component's identifier. It uses aggregated component identifiers to look for their factories. If a factory is not found, the framework tries to find an alternative component according to the component proxy definitions and the component hierarchy. The user is able to control this process by changing the context object and enabling or disabling component substitution.

The destruction phase for the created component objects is fulfilled in the reverse order as compared to the construction phase without user influence.

During the component editing phase, the user is able to edit parameters and input maps as well as reconfigure the component's output. The check methods are called to control the editing consistency. In the case of inconsistency, these methods send warning messages and set the inconsistent variables back to the default values.

The framework helps the system users to execute net files and controls these processes. The framework allows the user to execute several nets as different processes at the same time or can have several execution processes of one net, e.g., different component parameters in use, at the same time.

The framework helps to fulfill component librarian functions. Particularly, it allows the user to see the total list of components included in the system and to register a required component. This component view shows static information, because the component objects are not created yet. The framework allows the user to look through net files as well.

Tree structures are heavily used in our system, e.g., the tree structure of composite components and tree structure of data events. Thus, the methods to navigate through a composite component and through a data file are very similar.

Using file navigation methods, a model developer is also able to write adapter or driver tools to transform the format of the data written to the system data file into data formats that are acceptable for external packages.

Besides the runtime information and different information messages that can appear during a component life cycle, the system user could be offered more detailed help information. Any object of our

framework, such as a component, parameter, and error message, has its own unique identifier. It opens a possibility to bind these identifiers with HTML files describing the objects. Thus, the user can get help from "inside" a code by means of a unique identifier, e.g., through warning and error message identifiers, the framework finds and opens the HTML files related to the detailed descriptions of these messages.

11. NiMax GRAPHICAL USER INTERFACE

When the NiMax system is started, the main window will appear. This window includes many views. These views allow a user to work on model components, nets, and data files, as well as to obtain necessary help.

11.1. Component and Net Navigation

The available model components and component nets are displayed for the system users. There are three different views of the total component list for the users: by categories (default view) to see the components from different application categories, by modules (DLLs) to see the DLL component contents, and by hierarchies to see the component inheritance relations. The component views also show the component types that are defined by the presence or absence of particular standard interfaces [3]. The icons mark the component types. A file browser and selector fulfills the net navigation and offers access to component nets by the open command from the file menu.

11.2. Working on Component States

By means of the component interface views, the framework offers the component user the option to change a component state. The user can see, register (instead of the default input map), and edit component input maps, as well as see and edit component parameters. The user always has the option to use the default parameter values. The user also has access to any parameter of any subcomponent inside a composite component.

A subcomponent can be substituted by another subcomponent if they have a common base component. To see that components have a common base component, the user can use the component hierarchy view. Thus, inside a composite component, an aggregated component can be substituted by an alternative component without coding, i.e., using the user interface. The component user can perform substitution inside any subcomponent. It is a way to change and update the application algorithm of a composite component.

If a component is expected to produce output, the component user has the option to reconfigure the output. The total events or only some selected channels can be disabled for this output. In the case of a composite component, the output reconfiguration can be performed for any subcomponent.

If a component is expected to receive data either from another component or from the data file, the component user has the option to choose and register a suitable matching map. There is also the option to check if a matched data configuration will be produced by another collaborated component or if it really exists in the attached data file.

11.3. Net Assembling and Editing

The user can open a component net file for editing. He or she can create a new component net file as a starting point of the component net assembly. The system provides an environment, e.g., the name of the output file, for the net assembly and execution.

All available components are displayed and the user can launch several of them in a net for collaborative work. Then the user should connect them one by one to their output and matching connectors. The nets are arranged so that the data stream flows from left to right across the screen. Providing the links between the component connectors, the user is able to reconfigure component outputs and to choose suitable matching maps. Some components can be removed from the net file as well. Finally, the user can save the net file by giving it a particular name.

11.4. Net Execution Control

The net user has the option to reset an execution environment for a net before its execution.

The user can obtain information about current states of the execution processes, select a process, and perform some actions on it, e.g., kill a selected process and save its runtime information.

By means of runtime messages, the net components inform about their execution processes during the run session. The user has the option to control the runtime information output.

11.5. Working on Data Files

It is possible to visualize data file content by means of the data file views. The data events as well as their channels can be selected through the data configuration view. After selection, one can perform different operations on data, e.g., copy, cut, and protect against component access.

11.6. Working on Histograms and Plots

One- and two-dimensional histograms with fixed partitions and two-dimensional plots can be created and visualized. Histogram statistics are implemented as bin content statistics. The average and root-mean-square values are calculated as well. Bin errors are always computed taking weights into account. All histogram objects can store bin values and errors as different types, and the user has the option to make some choice among these types. For any histogram object, the user can work on its table view. One-dimensional histograms also have a graphical view. Two-dimensional histograms have the cell graphical view. The plots are presented by the table and scatter plot graphical views.

The user can apply different operations on the selected data of any view. Selection methods are different for different views. For example, the user can use a mouse to select the content of bins for table view of a histogram object, and for graphical views, we offer a brush tool.

11.7. Obtaining Help

The help subsystem based on the HTML Help Workshop has been developed for the Windows platforms [4]. There are two types of help: system help, i.e., help information to assist in the system usage, and component help. Help topics related to the NiMax system describe how to handle a component, how to process data, etc. Help topics related to a particular component include information about component parameters, its input maps, its output events, etc. Navigation through the help can be done using contents and keywords.

12. CONCLUSION

We have suggested a new approach to develop, assemble, and use numerical models in high-energy physics. It is a component approach where a complex numerical model is composed of simpler components that are included in application modules.

We have formulated a standard component by separating the component interface part and component numerical algorithm part. Any component is considered as a set of standard interfaces between its algorithm and the outside world.

We have suggested a unit of configured data: the data event. A component can produce data events, write them in a data file for further analysis and visualization, read data events from a data file, and receive data events from other components. The developed data file allows the storage of a very large quantity of differently structured data and fast navigation through these data.

Several components can be composed into a composite model component or a component net in a variety of ways, and new components with their own peculiarities can be added. It offers a great deal of flexibility for the construction of a powerful numerical model. Each particular component can be tuned and different implementations of the component algorithm can be interchanged at runtime, enabling a model user to obtain the needed model properties without redesigning a model and writing the model code.

To support this approach, we have developed the NiMax software system. The NiMax system is an object-oriented program written in C++. Its central part is the framework that controls all the system's internal processes and provides interaction between the graphical user interface and the rest parts.

The framework supports many GUI services to provide convenient and productive user sessions. For example, the user is able to launch required components and component nets. He or she is able to perform a controlled editing of component and subcomponent parameters, substitution of subcomponents within a composite component, and reorganization of component and subcomponent outputs. The user can assemble and edit different component nets and execute them as separate processes. The user is able to perform structural, analytical, and graphical selections of the data produced and written in the data files. He or she can build and visualize histograms and plots.

We have developed different component and module frames, application data types, and data transfer class libraries to facilitate creation and distribution of component codes. Component functionality is extendable by the inheritance mechanism and reusable by the component aggregation mechanism.

We have applied the NiMax system for a particular class of numerical models: MC event generators. Many MC model components that are parts of the hadronic modules have been implemented.

In addition to fundamental studies, the NiMax system could be a laboratory for the development and use of specific engineering modules for simulations to find solutions of practical radiation transport problems as well as for specific educational modules that are essential to teach particle, nuclear, and radiation physics. We could also apply it for analytical, structural, and graphical analysis of generated and acquired data, where the data file, data file views and data file control, and navigation methods can be considered as an independent data file system having its own applications.

ACKNOWLEDGMENTS

We would like to thank the organizers of this workshop for the invitation to present a talk and the Academy of Finland for financial support under grant no. 48477.

REFERENCES

1. N. Amelin, CERN/IT/99/6.
2. T. Wenaus *et al.*, CERN/LHCC/97-40.
3. N. Amelin and M. Komogorov, JINR Commun. No. D11/175, 1 (Dubna, 2001).
4. D. J. Kruglinski, G. Shepherd, and S. Wingo, *Programming Microsoft Visual C++* (Microsoft Press, 1998).

Physics of Atomic Nuclei, Vol. 67, No. 1, 2004, pp. 41–46. From Yadernaya Fizika, Vol. 67, No. 1, 2004, pp. 42–47.

Wavelets Applied to Very High Multiplicity Events*

I. M. Dremin**

Lebedev Institute of Physics, Russian Academy of Sciences, Leninskiĭ pr. 53, Moscow, 117924 Russia

Received April 30, 2003

Abstract—Wavelets are widely used now for the analysis of local scales (or frequencies) important in physical events, biological objects, natural phenomena, etc. They provide unique information about scales at different locations. In particular, they are used for analysis of patterns in the phase space of very high multiplicity events. © *2004 MAIK "Nauka/Interperiodica".*

1. INTRODUCTION

Wavelets have become a necessary mathematical tool in many investigations. They are used in those cases where the result of the analysis of a particular signal[1)] should contain not only the list of its typical frequencies (scales) but also knowledge of the definite local coordinates where these properties are important, i.e., the size and location of its fluctuations. In particular, the secondary particle distributions within the available phase space for the very high multiplicity events can be studied and the corresponding patterns defined by the particle correlations found.

The wavelet basis is formed by using dilations and translations of a particular function defined on a finite interval. Its finiteness is crucial for the locality property of the wavelet analysis. Commonly used wavelets generate a complete orthonormal system of functions with a finite support. That is why, by changing the scale (dilations), they can distinguish the local characteristics of a signal at various scales, and by translations they cover the whole region in which it is studied. Due to the completeness of the system, they also allow for the inverse transformation to be properly done. That is why, e.g., one can ask such a question as how the high-multiplicity event would look if only correlations of a definite scale are left in this event. This is demonstrated below.

The locality property of wavelets gives a substantial advantage over the Fourier transform, which provides us only with knowledge of the global frequencies (scales) of the object under investigation because the system of basic functions used (sine, cosine, or imaginary exponential functions) is defined over an infinite interval.

It has been proven that any function can be written as a superposition of wavelets, and there exists a numerically stable algorithm to compute the coefficients for such an expansion. Moreover, these coefficients completely characterize the function, and it is possible to reconstruct it in a numerically stable way by knowing these coefficients. The discrete wavelets cannot be represented by analytical expressions (except for the simplest one) or by solutions of some differential equations, and instead are given numerically as solutions of definite functional equations containing rescaling and translations. Moreover, in practical calculations, their direct form is not even required, and only the numerical values of the coefficients of the functional equation are used. This is a very important procedure, called multiresolution analysis, which gives rise to the multiscale local analysis of the signal and fast numerical algorithms. Each scale contains an independent nonoverlapping set of information about the signal in the form of wavelet coefficients, which are determined from an iterative procedure called the fast wavelet transform. In combination, they provide its complete analysis and simplify the diagnosis of the underlying processes. See the extended review on wavelets in [1].

2. WAVELETS FOR BEGINNERS

Each signal can be characterized by its averaged (over some intervals) values (trend) and by its variations around this trend. Actually, physicists dealing with experimental histograms analyze their data at different scales when averaging over different size intervals. This is a particular example of a simplified wavelet analysis treated in this section. To be more definite, let us consider the situation where an experimentalist measures some function $f(x)$ within the

*This article was submitted by the author in English.

** e-mail: dremin@lpi.ru

1)The notion of a signal is used here for any ordered set of numerically recorded information about some processes, objects, functions, etc. The signal can be a function of some coordinates, be it the time, the space, or any other (in general, n dimensional) scale.

interval $0 \le x \le 1$, and the best resolution obtained with the measuring device is limited to 1/16th of the whole interval. Thus, the result consists of 16 numbers representing the mean values of $f(x)$ in each of these bins and can be plotted as a 16-bin histogram. It can be represented by the formula

$$f(x) = \sum_{k=0}^{15} s_{4,k}\varphi_{4,k}(x), \qquad (1)$$

where $s_{4,k} = f(k/16)/4$, and $\varphi_{4,k}$ is defined as a steplike block of the unit norm (i.e., of height 4 and widths 1/16) different from zero only within the kth bin. For an arbitrary j, one imposes the condition $\int dx|\varphi_{j,k}|^2 = 1$, where the integral is taken over the intervals of the lengths $\Delta x_j = 1/2^j$ and, therefore, $\varphi_{j,k}$ have the form $\varphi_{j,k} = 2^{j/2}\varphi(2^j x - k)$ with φ denoting a steplike function of the unit height over such an interval. The label 4 is related to the total number of such intervals in our example. At the next coarser level, the average over the two neighboring bins is taken. Up to the normalization factor, we will denote it as $s_{3,k}$ and the difference between the two levels as $d_{3,k}$. To be more explicit, let us write the normalized sums and differences for an arbitrary level j as

$$s_{j-1,k} = \frac{1}{\sqrt{2}}[s_{j,2k} + s_{j,2k+1}], \qquad (2)$$
$$d_{j-1,k} = \frac{1}{\sqrt{2}}[s_{j,2k} - s_{j,2k+1}],$$

or for the backward transform (synthesis)

$$s_{j,2k} = \frac{1}{\sqrt{2}}(s_{j-1,k} + d_{j-1,k}), \qquad (3)$$
$$s_{j,2k+1} = \frac{1}{\sqrt{2}}(s_{j-1,k} - d_{j-1,k}).$$

Since, for the dyadic partition considered, this difference has opposite signs in the neighboring bins of the previous fine level, we introduce the function ψ which is 1 and -1, respectively, in these bins and the normalized functions $\psi_{j,k} = 2^{j/2}\psi(2^j x - k)$. This allows us to represent the same function $f(x)$ as

$$f(x) = \sum_{k=0}^{7} s_{3,k}\varphi_{3,k}(x) + \sum_{k=0}^{7} d_{3,k}\psi_{3,k}(x). \qquad (4)$$

One proceeds further in the same manner to the sparser levels 2, 1, and 0 with averaging done over the interval lengths 1/4, 1/2, and 1, respectively. The sparsest level with the mean value of f over the whole interval denoted as $s_{0,0}$ provides

$$f(x) = s_{0,0}\varphi_{0,0}(x) + d_{0,0}(x)\psi_{0,0}(x) \qquad (5)$$
$$+ \sum_{k=0}^{1} d_{1,k}\psi_{1,k}(x) + \sum_{k=0}^{3} d_{2,k}\psi_{2,k}(x)$$
$$+ \sum_{k=0}^{7} d_{3,k}\psi_{3,k}(x).$$

The functions $\varphi_{j,k}(x)$ and $\psi_{j,k}(x)$ are normalized by the conservation of the norm, dilated and translated versions of them. In the next section, we will give explicit formulas for them in a particular case of Haar scaling functions and wavelets. In practical signal processing, these functions (and more sophisticated versions of them) are often called low- and high-pass filters, respectively, because they filter the large- and small-scale components of a signal. The subsequent terms in Eq. (5) show the fluctuations (differences $d_{j,k}$) at finer and finer levels with larger j. In all the cases (1)–(5), one needs exactly 16 coefficients to represent the function. In general, there are 2^j coefficients $s_{j,k}$ and $2^{j_n} - 2^j$ coefficients $d_{j,k}$, where j_n denotes the finest resolution level (in the above example, $j_n = 4$).

All the above representations of the function $f(x)$ [Eqs. (1)–(5)] are mathematically equivalent. However, the latter one representing the wavelet analyzed function directly reveals the fluctuation structure of the signal at different scales j and various locations k present in a set of coefficients $d_{j,k}$, whereas the original form (1) hides the fluctuation patterns in the background of a general trend. In practical applications, the latter wavelet representation is preferred because, for rather smooth functions, strongly varying only at some discrete values of their arguments, many of the high-resolution d coefficients in relations similar to Eq. (5) are close to zero (compared to the "informative" d coefficients) and can be discarded. Bands of zeros (or close to zero values) indicate those regions where the function is fairly smooth.

At first sight, this simplified example looks somewhat trivial. However, for more complicated functions and more data points with some elaborate forms of wavelets, it leads to a detailed analysis of a signal and to possible strong compression with subsequent good quality restoration. This example also provides an illustration of the very important feature of the whole approach with successive coarser and coarser approximations to f called multiresolution analysis and discussed in more detail below.

3. BASIC NOTIONS AND HAAR WAVELETS

To analyze any signal, one should, first of all, choose the corresponding basis, i.e., the set of functions to be considered as "functional coordinates." In most cases, we will deal with signals represented by

square integrable functions defined on the real axis. For nonstationary signals, for example, the location of that moment when the frequency characteristics have abruptly been changed is crucial. Therefore, the basis should have a compact support; i.e., it should be defined on a finite region. Wavelets have this property. Nevertheless, with them it is possible to span the whole space by translation of the dilated versions of a definite function. That is why every signal can be decomposed in a wavelet series (or integral). Each frequency component is studied with a resolution matched to its scale.

Let us try to construct functions satisfying the above criteria. An educated guess would be to relate the function $\varphi(x)$ to its dilated and translated version. The simplest linear relation with $2M$ coefficients is

$$\varphi(x) = \sqrt{2}\sum_{k=0}^{2M-1} h_k \varphi(2x-k) \tag{6}$$

with the dyadic dilation 2 and integer translation k. At first sight, the chosen normalization of the coefficients h_k with the "extracted" factor $\sqrt{2}$ looks somewhat arbitrary. Actually, it is defined a posteriori by the traditional form of fast algorithms for their calculation [see Eqs. (20) and (21) below] and normalization of functions $\varphi_{j,k}(x), \psi_{j,k}(x)$. It is used in all the books and papers.

For discrete values of the dilation and translation parameters, one gets discrete wavelets. The value of the dilation factor determines the size of cells in the lattice chosen. The integer M defines the number of coefficients and the length of the wavelet support. They are interrelated because, from the definition of h_k for orthonormal bases

$$h_k = \sqrt{2}\int dx \varphi(x)\bar{\varphi}(2x-k), \tag{7}$$

it follows that only finitely many h_k are nonzero if φ has a finite support. The normalization condition is chosen as

$$\int_{-\infty}^{\infty} dx \varphi(x) = 1. \tag{8}$$

The function $\varphi(x)$ obtained from the solution of this equation is called a scaling function.[2)] If the scaling function is known, one can form a "mother wavelet" (or a basic wavelet) $\psi(x)$ according to

$$\psi(x) = \sqrt{2}\sum_{k=0}^{2M-1} g_k \varphi(2x-k), \tag{9}$$

where

$$g_k = (-1)^k h_{2M-k-1}. \tag{10}$$

The simplest example would be for $M = 1$ with two nonzero coefficients h_k equal to $1/\sqrt{2}$, i.e., the equation leading to the Haar scaling function $\varphi_{\rm H}(x)$:

$$\varphi_{\rm H}(x) = \varphi_{\rm H}(2x) + \varphi_{\rm H}(2x-1). \tag{11}$$

One easily gets the solution of this functional equation

$$\varphi_{\rm H}(x) = \theta(x)\theta(1-x), \tag{12}$$

where $\theta(x)$ is the Heaviside step function equal to 1 at positive arguments and 0 at negative ones. The additional boundary condition is $\varphi_{\rm H}(0) = 1$, $\varphi_{\rm H}(1) = 0$. This condition is important for the simplicity of the whole procedure of computing the wavelet coefficients when two neighboring intervals are considered.

The "mother wavelet" is

$$\psi_{\rm H}(x) = \theta(x)\theta(1-2x) - \theta(2x-1)\theta(1-x), \tag{13}$$

with boundary values defined as $\psi_{\rm H}(0) = 1$, $\psi_H(1/2) = -1$, $\psi_{\rm H}(1) = 0$. This is the Haar wavelet known since 1910 and used in functional analysis. Namely, this example has been considered in the previous section for the histogram decomposition. This is the first one of a family of compactly supported orthonormal wavelets ${}_M\psi : \psi_{\rm H} = {}_1\psi$. It possesses the locality property since its support $2M-1 = 1$ is compact.

The dilated and translated versions of the scaling function φ and the "mother wavelet" ψ

$$\varphi_{j,k} = 2^{j/2}\varphi(2^j x - k), \tag{14}$$

$$\psi_{j,k} = 2^{j/2}\psi(2^j x - k) \tag{15}$$

form the orthonormal basis, as can be (easily for Haar wavelets) checked.[3)]

The Haar wavelet oscillates, so that

$$\int_{-\infty}^{\infty} dx \psi(x) = 0. \tag{16}$$

This condition is common for all the wavelets. It is called the oscillation or cancellation condition. From it, the origin of the name wavelet becomes clear. One can describe a "wavelet" as a function that oscillates within some interval like a wave but is then localized by damping outside this interval. This is a necessary

[2)] It is often also called a "father wavelet," but we will not use this term.

[3)] We return back to the general case and therefore omit the index H because the same formula will be used for other wavelets.

condition for wavelets to form an unconditional (stable) basis. We conclude that, for special choices of coefficients h_k, one gets the specific forms of "mother" wavelets, which give rise to orthonormal bases.

The wavelet coefficients $s_{j,k}$ and $d_{j,k}$ can be calculated as

$$s_{j,k} = \int dx f(x)\varphi_{j,k}(x), \tag{17}$$

$$d_{j,k} = \int dx f(x)\psi_{j,k}(x). \tag{18}$$

However, in practice their values are determined from the fast wavelet transform described below.

These coefficients are referred to as sums (s) and differences (d), thus being related to mean values and fluctuations. If only the terms with d coefficients in (5) are considered, the result is called the wavelet expansion. For the histogram interpretation, this procedure would imply that one is not interested in average values but only in the histogram shape determined by fluctuations at different scales.

4. MULTIRESOLUTION ANALYSIS AND DAUBECHIES WAVELETS

Though the Haar wavelets provide a good tutorial example of an orthonormal basis, they suffer from several deficiencies. One of them is the bad analytic behavior with an abrupt change at the interval bounds, i.e., their bad regularity properties. By this, we mean that all finite rank moments of the Haar wavelet are different from zero—only its zeroth moment, i.e., the integral (16) of the function itself, is zero. This shows that this wavelet is not orthogonal to any polynomial apart from a trivial constant. The Haar wavelet does not have good time-frequency localization. Its Fourier transform decays like $|\omega|^{-1}$ for $\omega \to \infty$.

The goal is to find a general class of those functions which would satisfy the requirements of locality, regularity, and oscillatory behavior. Note that, in some particular cases, the orthonormality property sometimes can be relaxed. They should be simple enough in the sense that they are sufficiently explicit and regular to be completely determined by their samples on the lattice defined by the factors 2^j.

The general approach that respects these properties is known as the multiresolution approximation. This works in practice when applied to the problem of finding the coefficients of any filter h_k and g_k. They can be directly obtained from the definition and properties of the discrete wavelets. These coefficients are defined by relations (6) and (9). The orthogonality of the scaling functions, of wavelets to the scaling functions, and of wavelets to all polynomials up to the power $(M-1)$ and the normalization condition can be written as equations for h_k which uniquely define them (see [1]). For $M = 2$, they lead to the following values of coefficients:

$$h_0 = \frac{1}{4\sqrt{2}}(1+\sqrt{3}), \quad h_1 = \frac{1}{4\sqrt{2}}(3+\sqrt{3}), \tag{19}$$
$$h_2 = \frac{1}{4\sqrt{2}}(3-\sqrt{3}), \quad h_3 = \frac{1}{4\sqrt{2}}(1-\sqrt{3}).$$

These coefficients define the simplest D^4 (or ${}_2\psi$) wavelet from the famous family of orthonormal Daubechies wavelets (D^{2M}) with finite support. For filters of higher order in M, i.e., for higher rank Daubechies wavelets, the coefficients can be obtained in the same manner. The wavelet support is equal to $2M-1$. It is wider than for the Haar wavelets. However, the regularity properties are better. The higher order wavelets are smoother compared to D^4.

5. FAST WAVELET TRANSFORM

The fast wavelet transform allows one to proceed with the entire computation within a short time interval because it uses a simple iterative procedure. Therefore, it is crucial for all work with wavelets.

The coefficients $s_{j,k}$ and $d_{j,k}$ carry information about the content of the signal at various scales and can be calculated directly using formulas (17), (18). However, this algorithm is inconvenient for numerical computations because it requires many (N^2) operations, where N denotes the number of sampled values of the function. We will describe a faster algorithm. In practical calculations, only the coefficients h_k are used, without referring to the shapes of wavelets.

In real situations with digitized signals, we have to deal with finite sets of points. Thus, there always exists the finest level of resolution where each interval contains only a single number. Correspondingly, the sums over k will get finite limits. It is convenient to reverse the level indexation under the assumption that the label of this fine scale is $j = 0$. It is then easy to compute the wavelet coefficients for sparser resolutions $j \geq 1$. Multiresolution analysis naturally leads to a hierarchical and fast scheme for the computation of the wavelet coefficients of a given function. In general, one can get the iterative formulas of the fast wavelet transform

$$s_{j+1,k} = \sum_m h_m s_{j,2k+m}, \tag{20}$$

$$d_{j+1,k} = \sum_m g_m s_{j,2k+m}, \tag{21}$$

where

$$s_{0,k} = \int dx f(x)\varphi(x-k). \tag{22}$$

These equations yield fast algorithms (so-called pyramid algorithms) for computing the wavelet coefficients, asking now just for $O(N)$ operations to be done. Starting from $s_{0,k}$, one computes by iteration all other coefficients provided the coefficients h_m, g_m are known. The explicit shape of the wavelet is not used in this case anymore.

The remaining problem lies in the initial data. If an explicit expression for $f(x)$ is available, the coefficients $s_{0,k}$ may be evaluated directly according to (22). But this is not so in the situation where only discrete values are available. In the simplest approach, they are chosen as $s_{0,k} = f(k)$.

6. THE FOURIER AND WAVELET TRANSFORMS

As has been stressed already, the wavelet transform is superior to the Fourier transform, first of all, due to the locality property of wavelets. The Fourier transform uses sine, cosine, or imaginary exponential functions as the main basis. It is spread over the entire real axis, whereas the wavelet basis is localized. An attempt to overcome these difficulties and improve time localization while still using the same basis functions is made by the so-called windowed Fourier transform. The signal $f(t)$ is considered within some time interval (window) only. However, all windows have the same width.

In contrast, the wavelets ψ automatically provide the time (or spatial location) resolution window adapted to the problem studied, i.e., to its essential frequencies (scales). Namely, let t_0, δ and ω_0, δ_ω be the centers and the effective widths of the wavelet basic function $\psi(t)$ and its Fourier transform. Then, for the wavelet family $\psi_{j,k}(t)$ (15) and, correspondingly, for wavelet coefficients, the center and the width of the window along the t axis are given by $2^j(t_0 + k)$ and $2^j\delta$. Along the ω axis, they are equal to $2^{-j}\omega_0$ and $2^{-j}\delta_\omega$. Thus, the ratios of widths to the center position along each axis do not depend on the scale. This means that the wavelet window resolves both the location and the frequency in fixed proportions to their central values. For the high-frequency component of the signal, it leads to quite a large frequency extension of the window, whereas the time location interval is squeezed so that the Heisenberg uncertainty relation is not violated. That is why wavelet windows can be called Heisenberg windows. Correspondingly, the low-frequency signals do not require small time intervals and admit a wide window extension along the time axis. Thus, wavelets localize well the low-frequency "details" on the frequency axis and the high-frequency ones on the time axis. This ability of wavelets to find a perfect compromise between the time localization and the frequency localization by automatically choosing the widths of the windows along the time and frequency axes well adjusted to the location of their centers is crucial for their success in signal analysis. The wavelet transform cuts up the signal (functions, operators, etc.) into different frequency components and then studies each component with a resolution matched to its scale, providing a good tool for time-frequency (position-scale) localization. That is why wavelets can zoom in on singularities or transients (an extreme version of very short lived high-frequency features!) in signals, whereas the windowed Fourier functions cannot. In terms of traditional signal analysis, the filters associated with the windowed Fourier transform are constant bandwidth filters, whereas the wavelets may be seen as constant relative bandwidth filters whose widths in both variables linearly depend on their positions.

The wavelet coefficients are negligible in the regions where the function is smooth. That is why wavelet series with plenty of nonzero coefficients represent really pathological functions, whereas "normal" functions have "sparse" or "lacunary" wavelet series and are easy to compress. On the other hand, the Fourier series of the usual functions have a lot of nonzero coefficients, whereas "lacunary" Fourier series represent pathological functions.

Thus, these two types of analysis can be considered as complementary rather than overlapping.

One can already start the signal analysis with above procedures. However, there are several technical problems that will not be mentioned here. They are described at some length in the cited review paper.

7. APPLICATIONS

Wavelets have become widely used in pure and applied science. Here, we describe just two examples of wavelet application to analysis of one- and two-dimensional objects (see [1]).

The single-variable example is provided by the time variation of the pressure in an aircraft compressor. The goal of the analysis of this signal is motivated by the desire to find the precursors of a very dangerous effect (stall + surge) in engines leading to their destruction. It turns out that the dispersion of the wavelet coefficients can serve as a precursor of this effect. Let us mention that a similar procedure has been quite successful in analysis of other engines and of heartbeat intervals and in diagnosis of a disease.

Two-dimensional wavelet analysis can be used for recognition of shapes of objects. It has been applied, e.g., to pattern recognition of fingerprints (this helps to save a lot of computer memory, in particular) and of erythrocytes and their classification. It was also used for analysis of patterns in very high multiplicity

events. Lead–lead collisions at 158 GeV/c with multiplicities exceeding 1000 charged particles were analyzed in two-dimensional phase space and wavelet coefficients for low scales $j < 6$ were omitted. Then, the long-range images of events were obtained by the inverse transform. They showed some quite peculiar features of long-range correlations, in particular, the ringlike structure reminding one of Cherenkov rings.

Many other examples can be found in the cited paper and on Web sites.

8. CONCLUSIONS

The beauty of the mathematical construction of the wavelet transformation and its utility in practical applications attract researchers from both pure and applied science. Moreover, the commercial outcome of this research has become quite important. We have outlined a minor part of the activity in this field.

REFERENCES

1. I. M. Dremin, O. V. Ivanov, and V. A. Nechitailo, Usp. Fiz. Nauk **171**, 465 (2001) [Phys. Usp. **44**, 447 (2001)].

Physics of Atomic Nuclei, Vol. 67, No. 1, 2004, pp. 47–49. From Yadernaya Fizika, Vol. 67, No. 1, 2004, pp. 48–50.

VERY HIGH MULTIPLICITY PHYSICS

Very High Energy Multiplicity Distributions*

L. L. Jenkovszky** **and B. V. Struminsky**†

Bogolyubov Institute for Theoretical Physics, National Academy of Sciences of Ukraine, Kiev, 03143 Ukraine

Received April 30, 2003

Abstract—Within a geometrical model developed in earlier papers, a change of regime, or a "knee," is predicted in the multiplicity distributions at large multiplicities. The position and motion of this knee is related to geometrical and KNO scaling and their violation, in particular, the rise of the ratio $\sigma_{\rm el}/\sigma_t$, as well as to the transition from shadowing to antishadowing, expected at LHC energies. © *2004 MAIK "Nauka/Interperiodica".*

As pointed out in a series of recent papers [1], the dynamics of rare processes with very high multiplicities (VHM) may be quite different from the rest of the events. In this paper, we present our predictions concerning the behavior of the multiplicity distributions $\Psi(z)$ near their high-z border. Our model, in principle, is applicable to any z, but here we ignore the shape of the small and moderate z, concentrating on the rightmost edge of $\Psi(z)$.

Our knowledge about high-energy multiplicity distributions comes from the data collected at ISR, the $Sp\bar{p}S$ collider (UA1, UA2, and UA5 experiments) and the Tevatron collider (CDF and E735 experiments). It should be noted that the recent results from the E735 collaboration taken at the Tevatron [2] do not completely agree with those obtained by the UA5 collaboration at comparable energies at the $Sp\bar{p}S$ collider [3].

Note that the delicate features of $\Psi(z)$ at very large multiplicities near the large-z edge can be better seen if the variable z is used instead of n.

On the theoretical side, it became common [4–7] to approximate the observed distributions by the convolution of two binomial distributions, accounting for the general bell-like shape of $P(n)$ with the observed structures (knee and possible oscillations) superimposed.

One of the hottest issues in this field is the dynamics of the VHM [8], which is close to the kinematical limit imposed by the phase space. The VHM events are very rare, making up only about 10^{-7} of the total cross sections at the LHC energy, which makes their experimental identification very difficult. An intriguing question is the possible existence of a cutoff in the VHM region, beyond $z = n/\langle n\rangle \approx 5$, where $\langle n\rangle$ is the mean multiplicity. In our opinion, a better understanding of the underlying physics can be inferred only in a model involving both elastic and inelastic scattering related by unitarity. Such an approach has been advocated in a series of papers [9–11], summarized in [12].

After a brief summary of the main ideas within this approach, we analyze the relation of the distribution of secondaries and the behavior of the elastic and total cross sections with the possible transition from shadowing to antishadowing [13].

We show that the existence of the cutoff at high multiplicities in the distribution of $\Psi(z)$ is related to the validity of the GS and KNO scaling.

The basic idea of the geometrical approach to the multiple production used in the present paper is that the number of the secondaries at a given impact parameter ρ, $n(\rho, s)$ is proportional to the amount of the hadronic matter in the collision or the overlap function $G(\rho, s)$,

$$\langle n(\rho, s)\rangle = N(s)G(\rho, s), \tag{1}$$

where $N(s)$ is related to the mean multiplicity, not specified in this approach, and $G(\rho, s)$ is the overlap function related to the elastic scattering by unitarity,

$$\mathrm{Im}h(\rho, s) = |h(\rho, s)|^2 + G(\rho, s), \tag{2}$$

where $h(\rho, s)$ is the elastic amplitude in the impact parameter representation. Unitarity, a key issue in this approach, enters in the definition of both the elastic amplitude and the inelastic overlap function.

In u-matrix unitarization (see [12] and references therein),

$$G_{\rm in} = \frac{\mathrm{Im}u}{1 + 2\mathrm{Im}u + |u|^2}, \tag{3}$$

*This article was submitted by the authors in English.

†Deceased.

** e-mail: jenk@gluk.org

where u is the elastic amplitude (input, or the "Born term").

We use a dipole (DP) model for the elastic scattering amplitude, exhibiting geometrical features and fitting the data. After u-matrix unitarization, the elastic amplitude reads (see [12])

$$h(\rho,s)=\frac{u}{1-iu}, \tag{4}$$

where $u(y,s)=ige^{-y}$, $y=\dfrac{\rho^2}{4\alpha' L}$, and $L\equiv\ln s$.

Remarkably, the ratio of the elastic to total cross sections in this model,

$$\frac{\sigma_{\rm el}}{\sigma_t}=1-\frac{g}{(1+g)\ln(1+g)}, \tag{5}$$

fixes the (energy-dependent) values of the parameter g. Typical values of g for several representative energies are quoted in [12].

Rescattering corrections to $G_{\rm in}(\rho,s)$ here will be accounted for phenomenologically according to the following prescription (see [12] and earlier reference therein):

$$G_{\rm in}(\rho,s)=|S(\rho,s)|\tilde{G}_{\rm in}(\rho,s), \tag{6}$$

where $S(\rho,s)$ is the elastic scattering matrix related to the u matrix by

$$S(\rho,s)=\frac{1+iu(\rho,s)}{1-iu(\rho,s)}. \tag{7}$$

This procedure is not unique. For example, it allows the following generalization (see [12] and the earlier reference therein):

$$G_{\rm in}(\rho,s)=|S(\rho,s)|^{\alpha}\tilde{G}^{\alpha}(\rho,s), \tag{8}$$

where α is a parameter, varying between 0 and 1.

We assume

$$\langle n(\rho,s)\rangle=N(s)\tilde{G}^{\alpha}_{\rm in}(\rho,s). \tag{9}$$

The moments are defined by (see [12] and earlier references therein)

$$\langle n^k(s)\rangle=\frac{N^k(s)\int G_{\rm in}(\rho,s)(G^{\alpha}_{\rm in}(\rho,s))^k d^2\rho}{\int G_{\rm in}(\rho,s)d^2\rho}. \tag{10}$$

Now, we insert the expression for the DP with the u-matrix unitarization (4) into (10) to get

$$\langle n^k(s)\rangle=\frac{N^k(s)(1+g)}{g} \times\int\limits_0^g\frac{dx}{(1+x)^2}\left(\Big(\frac{1+x}{1-x}\Big)^{\alpha}\frac{x}{(1+x)^2}\right)^k. \tag{11}$$

The mean multiplicity $\langle n(s)\rangle$ is defined as

$$\langle n(s)\rangle=\frac{N(s)(1+g)}{g} \times\int\limits_0^g\frac{xdx}{(1+x)^4}\Big(\frac{1+x}{1-x}\Big)^{\alpha}=\frac{N(s)}{a}. \tag{12}$$

For the distributions, we have

$$P(n)=\frac{1+g}{g}\int\limits_0^g\frac{dx}{(1+x)^2} \times\delta\left(n-N\Big(\frac{1+x}{1-x}\Big)^{\alpha}\frac{x}{(1+x)^2}\right). \tag{13}$$

The integration in (13) gives

$$\psi(z)=\langle n\rangle P(n)=\frac{1+g}{g}\frac{x(1-x)}{z(1+x)[(1-x)^2+2\alpha x]},$$

where $z=n/\langle n\rangle$.

Since the above integral is nonzero only when the argument of the δ function vanishes,

$$n=N\left(\frac{1+x}{1-x}\right)^{\alpha}\frac{x}{(1+x)^2},$$

one gets a remarkable relation

$$z=\frac{\alpha x}{(1+x)^{2-\alpha}(1-x)^{\alpha}}. \tag{14}$$

To calculate the distribution $\Psi(z)$, one needs the solution to (14). It can be found explicitly for two extreme cases, namely, $\alpha=0$ and $\alpha=1$. Otherwise, it can be calculated numerically.

The maximal value of z, corresponding to $x=g$ (x varies between 0 and g), can be found as

$$z_{\rm max}=\frac{\alpha g}{(1+g)^{2-\alpha}|1-g|^{\alpha}}. \tag{15}$$

It can be seen from (15) that $z_{\rm max}$ is a constant if g is energy independent. In the interval between 53 and 900 GeV, the experimentally observed ratio $\sigma_{\rm el}/\sigma_t$ varies from 0.174 to 0.225, implying the variation of g from 0.489 to 0.702, and is uniquely determined by the above ratio. This monotonic increase in $g(s)$ in turn pushes $z_{\rm max}(s)$ outwards, terminating when g reaches unity (according to [12], this will happen around 10 TeV, i.e., at the future LHC), beyond which the term $|1-g|$ in (15) will start rising again, pulling $z_{\rm max}(s)$ back to smaller values (i.e., $z_{\rm max}(s)$ has its own maximum in s at $g=1$).

The unusual behavior of $z_{\rm max}(s)$ is not the only interesting feature of the present approach. This effect can be related to the behavior of the ratio $\sigma_{\rm el}/\sigma_t$.

As argued by Troshin and Tyurin (see [13]), σ_{el}/σ_t may pass the so-called black disc limit and continue rising in a new "antishadowing" mode of the u-matrix unitarity approach (multiplicity distributions were not considered in that paper). According to recent calculations [14], the transition from shadowing to antishadowing will also occur in the LHC energy region.

To summarize, we found a regularity connecting the geometrical properties in high-energy dynamics (GS and KNO scaling) with the dynamics of the high-multiplicity processes. We showed, in particular, that the exact geometrical or KNO scaling, implying constant g in our model, results in a cutoff at large z of the distribution function $\Psi(z)$. Any departure from scaling (energy dependence of g in our model) shifts the point z_{max} according to Eq. (15). Within the present accelerator energy domain (ISR, SPS, Tevatron), g varies from about 0.5 to about 0.8. It will reach the critical value $g = 1$ at LHC, where we predict a change of the regime: $z_{max}(s)$ will start decreasing and the black disc limit will be exceeded (which, as shown in [13, 14], is not equivalent to the violation of the unitarity limit, but means transition from shadowing to antishadowing).

Finally, it should be noted that we use many model assumptions that decrease the predictive power of our calculations. These assumptions mostly concern the way absorption corrections are introduced and the assumption of the local (δ function) dependence of multiplicities on the impact parameter. Both assumptions as well as others can be modified. As a result, we expect quantitative rather than qualitative changes in the results.

The most drastic approximation used in our calculations was the use in Eq. (13) of a delta-function distribution in the impact parameter, making possible explicit calculations. The sharp (delta-function) dependence of the multiplicity on the impact parameter resulted in an equally sharp and unrealistic cutoff in the multiplicity distributions at the largest z. It is obvious that physics (multiplicity distributions) cannot be discontinuous. Actually, this cutoff is expected to transform, after smoothing of the delta function in Eq. (13), into a change of the regime in the distribution $\Psi(z)$. In other words, after replacement of the delta function in (13) by a Gaussian or a Breit–Wigner-like dependence on the impact parameter, a mild asymptotic tail will appear in $\Psi(z)$. The relevant integrals are to be calculated numerically.

Thus, we predict an experimentally measurable change of $\Psi(z)$'s slope near $z_{max}(s)$. This effect can be revealed by measuring the local slope $\dfrac{d\ln\Psi(z)}{d\ln z}$ within finite bins in z, close to $z_{max}(s)$.

ACKNOWLEDGMENTS

L.J. thanks Prof. A.N. Sissakian and his staff for their hospitality at this inspiring meeting.

REFERENCES

1. J. Manjavidze and A. Sissakian, Phys. Rep. **346**, 1 (2001); hep-ph/0204281.
2. T. Alexopoulos *et al.* (E735 Collab.), Phys. Lett. B **435**, 453 (1998).
3. G. J. Alner *et al.* (UA5 Collab.), Phys. Rep. **154**, 247 (1987); R. E. Ansorge *et al.* (UA5 Collab.), Z. Phys. C **43**, 357 (1989).
4. I. Dremin and J. W. Gary, Phys. Rep. **349**, 301 (2001).
5. A. Giovannini and R. Ugoccioni, hep-ph/0203215 and references therein.
6. L. Jenkovszky, V. Kuvshinov, Z. Cicovani, *et al.,* Preprint No. 28/89, DFTT (Torino Univ., 1989).
7. V. D. Rusov *et al.*, Phys. Lett. B **504**, 213 (2001).
8. N. Giokaris, CERN Courier **41** (10), 12 (2001).
9. M. K. Aliev *et al.,* Preprint No. 84-74R, ITP (Kiev, 1984).
10. L. L. Jenkovszky, B. V. Struminsky, and Z. E. Chikovani, Preprint No. 86-55P, ITP (Kiev, 1986).
11. Z. E. Chikovani *et al.*, Preprint No. 87-145, ITP (Kiev, 1987).
12. A. N. Vall, L. L. Jenkovszky, and B. V. Struminsky, Fiz. Élem. Chastits At. Yadra **19**, 180 (1988) [Sov. J. Part. Nucl. **19**, 77 (1988)].
13. S. M. Troshin and N. E. Tyurin, Phys. Lett. B **316**, 175 (1993).
14. P. Desgrolard, L. L. Jenkovszky, and B. V. Struminsky, Eur. Phys. J. C **11**, 145 (1999).

Physics of Atomic Nuclei, Vol. 67, No. 1, 2004, pp. 50–61. From Yadernaya Fizika, Vol. 67, No. 1, 2004, pp. 51–62.

VERY HIGH MULTIPLICITY PHYSICS

QCD Physics at Tevatron and LHC*

A. Korytov**

University of Florida, USA

Received May 28, 2003

Abstract—Presented are the Tevatron Run I QCD results that have been known for the degree of controversy associated with them. Also, the prospects for the QCD-motivated studies at Tevatron Run II and LHC are briefly discussed. © *2004 MAIK "Nauka/Interperiodica".*

INTRODUCTION

QCD is extremely rich in various phenomena and very challenging both theoretically and experimentally. Within the hard QCD domain (processes involving large momentum transfers), one deals with production of jets, photons, W and Z bosons, and heavy flavor quarks. Perturbative QCD calculations are straightforward, but, if precision better than 10% is desired, they must typically go beyond the leading order and soon become very difficult. The soft QCD phenomena are usually associated with jet fragmentation, hadronization, diffractive processes, underlying event structure, etc. Perturbative calculations here are even more problematic, if possible at all, and, often, one needs to make a leap to new, preferably QCD-motivated, constructs (e.g., Pomeron) or come up with approximate methods of resummation of perturbative terms in all orders [e.g., MLLA (modified leading log approximation) and BFKL] or, as a last resort, develop completely phenomenological tools such as hadronization schemes in various Monte Carlo models.

Also, QCD can be viewed in a broader context of the Standard Model (SM) and its various extensions. Measurements of the key SM parameters, at first glance not directly connected to QCD, are, nevertheless, often limited by the level of our understanding of QCD processes (e.g., M_W, $(g-2)$, ε'/ε). Even more intriguing, the new physics at hadron colliders, if any, is likely to be born via QCD processes (e.g., consider production mechanisms for Higgs and SUSY particles), and, at the same time, the background to this new physics is likely to be from QCD processes as well. So learning and understanding details of the QCD phenomena is vital in searching for signs of what might be beyond the SM.

*This article was submitted by the author in English.

**e-mail: korytov@phys.ufl.edu

TEVATRON RUN I

I will start from the b-quark production cross section in proton–antiproton collisions. Figure 1 shows the CDF results and the theoretical prediction as they stood in 2001 [1]. The discrepancy between experiment and the NLO QCD calculations was a factor of $2.9 \pm 0.2 \pm 0.4$, or $\sim 4.2\sigma$, which, naturally, prompted searching for explanations beyond the SM [2]. Since then, the NLO calculations of the b-quark production were extended to include the NLL resummation as well as the improved B-meson fragmentation function as obtained at LEP. The net result is shown in Fig. 2 [3]. One can see that the data points remain where they were two years ago, while the theoretical curve has moved up and the discrepancy is now 1.7.

Another highly controversial result that even made newspaper headlines was the apparent excess of high-E_T jets reported by CDF. The inclusive jet cross section $d\sigma/dE_T$ agreed with the pQCD calculation for $E_T = 50$–300 GeV (over six orders of magnitude in cross section), but seemed to start departing from the theory at higher transverse jet energies—Fig. 3 [4]. To make the situation even more entangled, the D0 data [5] fell right in between the CDF and theory points and were consistent with the theory and, at the same time, with CDF. Immediately, it was pointed out that the angular distributions of dijets (Fig. 4 [6]) did not call for the presence of any, albeit very exotic, new physics such as quark compositeness. At the same time, it was also shown that the poor knowledge of gluon PDF at large x might be responsible for the discrepancy. Recently, the CTEQ Collaboration released a new set of PDF fits, CTEQ6M, that included H1, ZEUS, CDF, and η-dependent D0 results, and, also, new methods of treating the experimental systematic errors. As a result, both the D0 and CDF data from Run I are now in an amazingly good agreement with the theory and with each other (Figs. 5 and 6 [7]).

Now, I will turn to a few examples of QCD results still awaiting resolution. The first example is a large

1063-7788/04/6701-0050$26.00

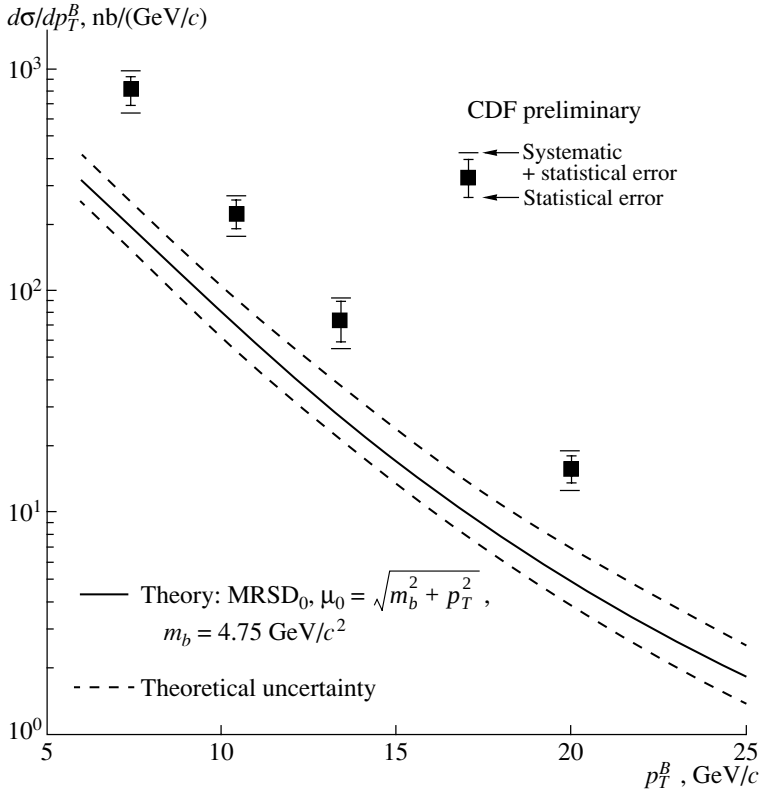

Fig. 1. B^+ meson cross section and theoretical predictions as of 2001 [1].

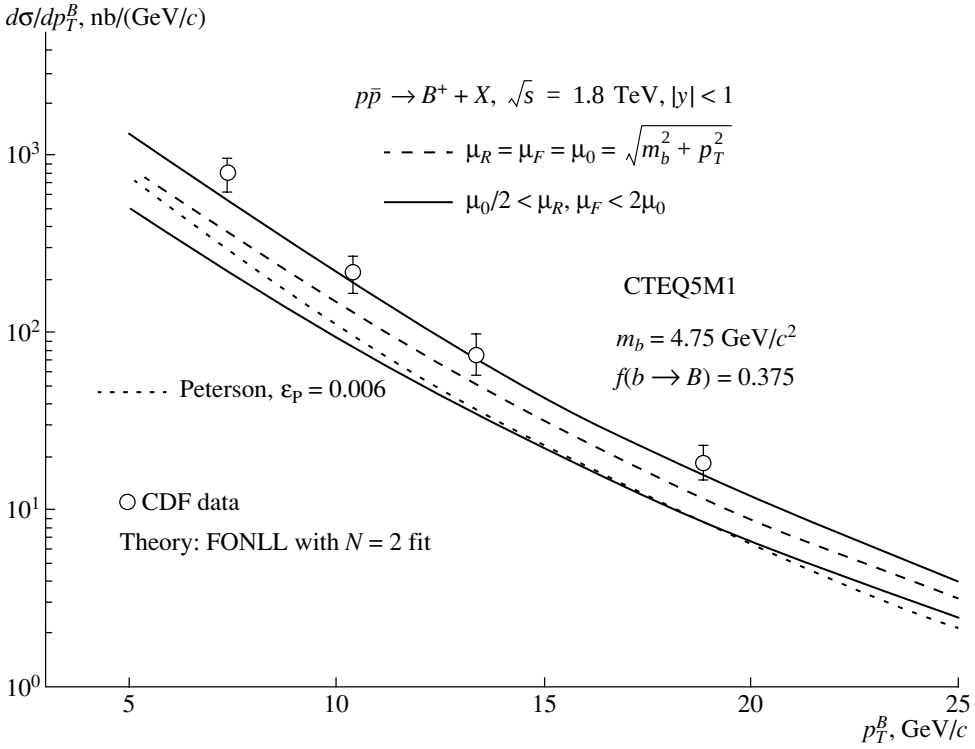

Fig. 2. B^+ meson cross section and theoretical predictions as of 2002 [3].

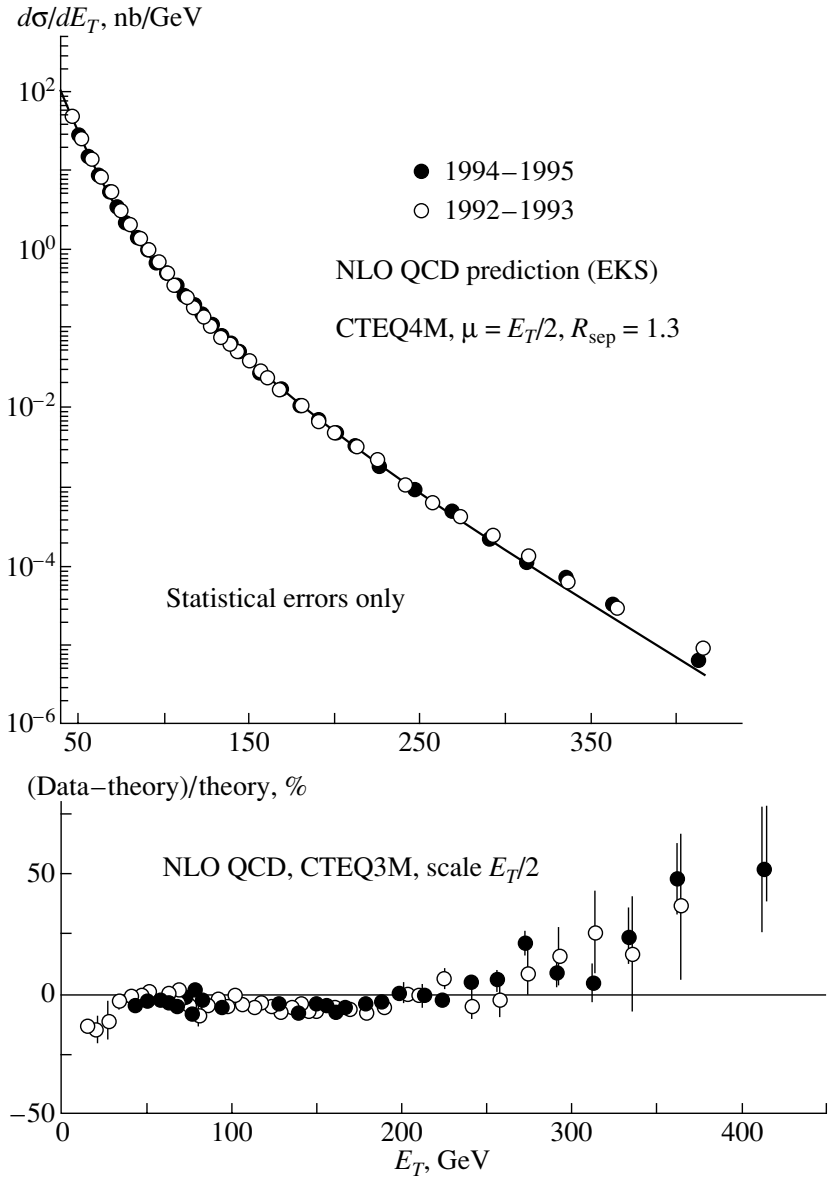

Fig. 3. Inclusive differential jet cross section and the NLO predictions as of 2001 [4].

excess of three- and four-jets events with all jets being relatively soft as reported by D0 (Fig. 7 [8]). In addition to the excess, the jets seem to have a different spectrum of the overall misbalance in comparison to Monte Carlo predictions (Fig. 8 [8]). However, these discrepancies apparently can be removed by tweaking some of the Monte Carlo parameters [9], but there are no guarantees that such tuning would not cause problems somewhere else.

Another troublesome measurement is too small an inclusive jet cross section in proton–antiproton collisions with a c.m. energy of 630 GeV. To reduce the sensitivity to PDFs, one can consider a ratio of inclusive cross sections at $\sqrt{s} = 630$ and 1800 GeV $r = [d\sigma/dx_T(630)]/[d\sigma/dx_T(1800)]$, where $x_T = E_T/(\sqrt{s}/2)$ (Fig. 9 [10]). In addition to being systematically ~15% below the theory, the CDF and D0 data seem to have very different trends at $x_T < 0.1$.

These two last discrepancies might be linked to the uncertainties in relating the experimental and theoretical definitions of jets—inherently different entities, given our limited abilities in handling multiparton states within the pQCD framework. A good illustration for this issue is the recent CDF and D0 attempts to switch to the k_T-jet-finding algorithm [11] as an alternative to the cone algorithm [12] commonly used for Run I data analyses. The k_T algorithm was a standard at LEP and HERA and proved to be very successful. Unexpectedly, both CDF and D0 encountered a problem that still remains: despite the fact

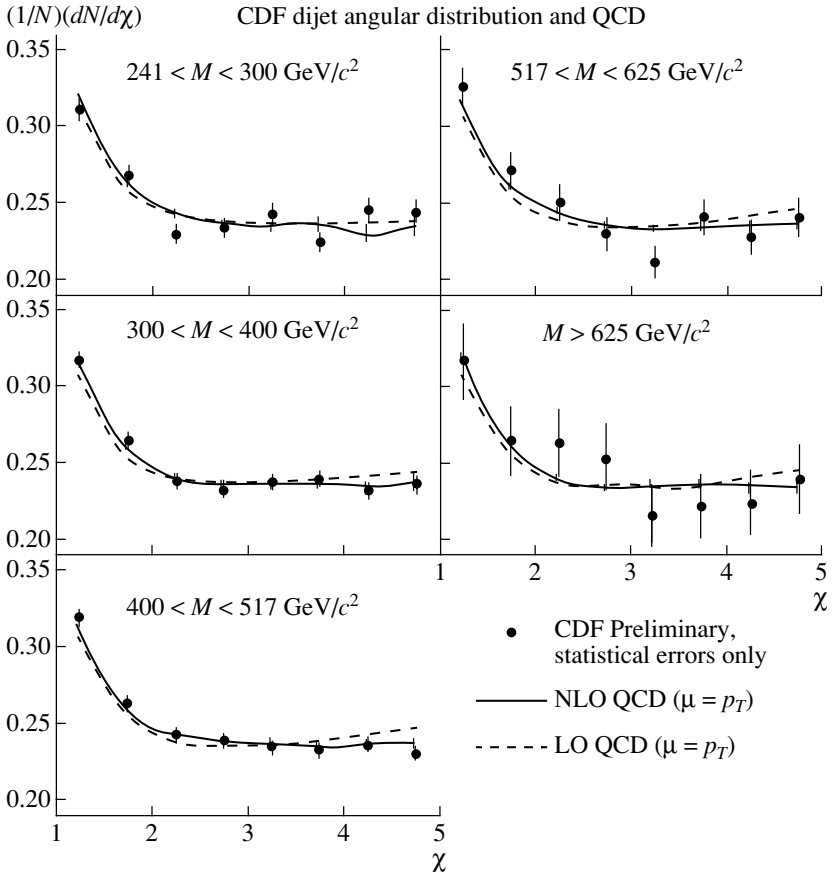

Fig. 4. Angular distribution of the leading jet in the dijet c.m. frame, $d\sigma/d\chi$, where $\chi = (1 - \cos\theta_{\text{c.m}})/(1 + \cos\theta_{\text{c.m}})$ [6].

that both the k_T algorithm with $D = 1$ and the cone algorithm with $R = 0.7$ give nearly identical inclusive jet cross sections within the NLO framework, when applied to data, the k_T algorithm gives a substantially larger cross section and strongly disagrees with NLO QCD (Fig. 10 [13]). The work on understanding this setback is in progress.

The inclusive photon cross section provides for means to study QCD physics without having to deal with the problems associated with the jet-finding algorithms. However, the results here do not seem to follow the theory either. Both CDF and D0 data indicate that the photon E_T spectrum is noticeably steeper than predicted by the theory (Fig. 11 [14])—a fact also observed way back by the UA2 Collaboration [15]. Varying PDFs and renormalization/factorization scales does not seem to help in this case. New ad hoc ideas (e.g., k_T smearing of the primary partons due to soft-gluon radiation) have been put forward to help consolidate the theory and experiment. Nevertheless, it is clear that more work needs to be done.

Switching gears to soft QCD physics, I will continue with jet fragmentation phenomena, the inherently soft process largely driven by gluon emissions off a primary parton and giving rise to a jet. Such gluons typically have transverse momenta of 200–300 MeV with respect to the jet direction. The controversy here is just the opposite to the examples discussed earlier—it is in amazingly good agreement with the experiment and the resumed pQCD calculations, also known as MLLA. The fit of data yields a value for the MLLA phenomenological k_T-cutoff scale as low as ~200 MeV (Figs. 12 and 13 [16])—the scale at which pQCD language is hardly applicable at all.

The ratio of hadron multiplicities in gluon and quark jets is yet another example of the 10-year-long odyssey that began at LEP in 1991 [17] and has lasted since then with more than ten papers published, the most recent one after the closing of LEP [18]. The measurements were inconsistent and ranged from $r \sim 1.1$ to ~ 1.5 (with typically very small errors). The CDF result, $r = 1.6 \pm 0.2$ (Fig. 14 [19]), coming from a completely different environment and obtained using different techniques, will help settle the ordeal related to this measurement.

The next example that I have selected for this note is the diffractive phenomena. There have been a number of various subprocesses measured at Tevatron

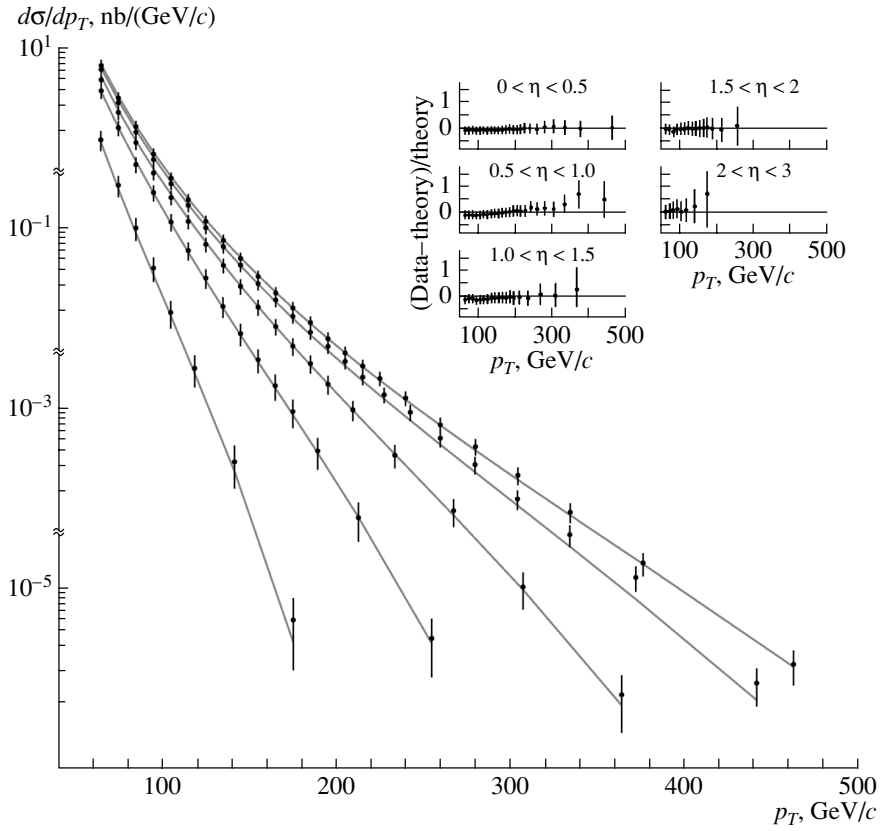

Fig. 5. Inclusive differential jet cross section for five η bins and the NLO predictions with CTEQ6M PDFs (D0 data [7]). The inset shows the relative discrepancy of data and theory: (data–theory)/theory.

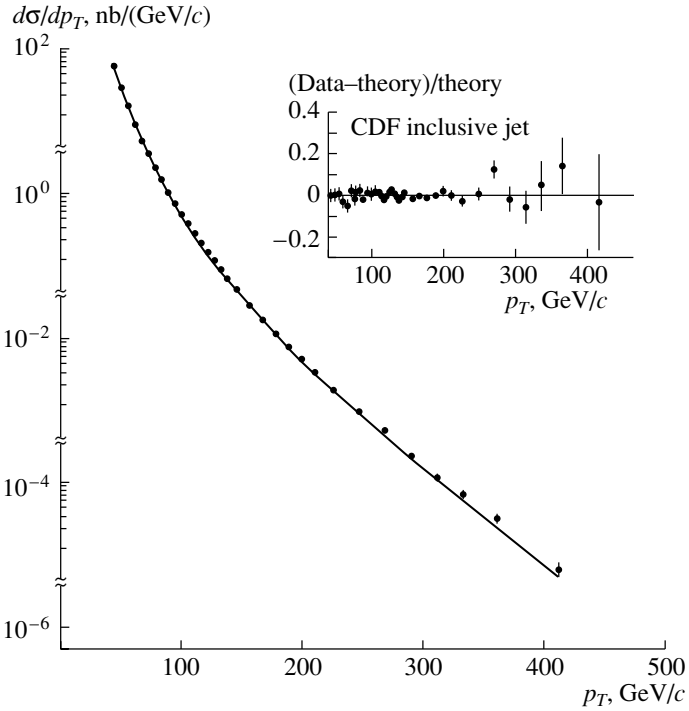

Fig. 6. Inclusive differential jet cross section and the NLO predictions with CTEQ6M PDFs (CDF data [7]). The inset shows the relative discrepancy of data and theory: (data–theory)/theory.

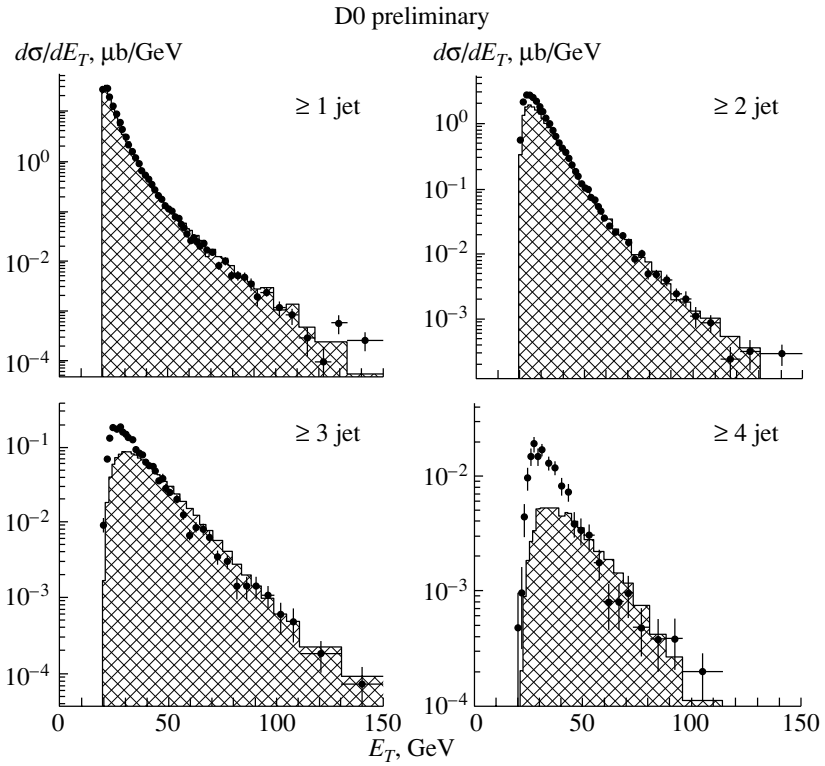

Fig. 7. Differential leading jet cross sections in multijet events (filled circles) and the PYTHIA predictions (hatched histogram; PYTHIA is normalized on the inclusive dijet sample) [8].

both by CDF and D0 (single and double diffraction, hard diffraction, double-Pomeron exchange, etc.), all indicating that the diffractive cross sections at Tevatron were substantially smaller than one would naively expect by extrapolating the results obtained

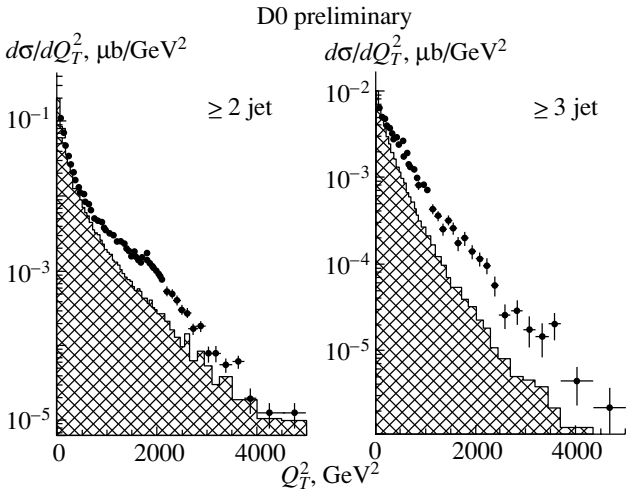

Fig. 8. Distribution in the square of the summed vector transverse momenta in inclusive two- and three-jet events: data (jet $E_T > 20$ GeV)—filled circles; PYTHIA Monte Carlo—hatched histogram [8].

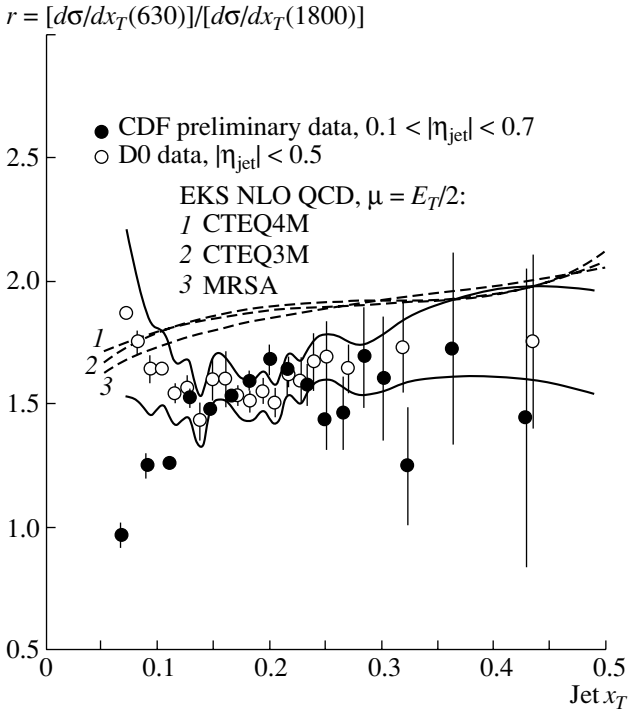

Fig. 9. Ratio of scaled inclusive differential jet cross sections at $\sqrt{s} = 630$ and 1800 GeV (circles) and the NLO QCD predictions for different PDFs (numbered curves) [10].

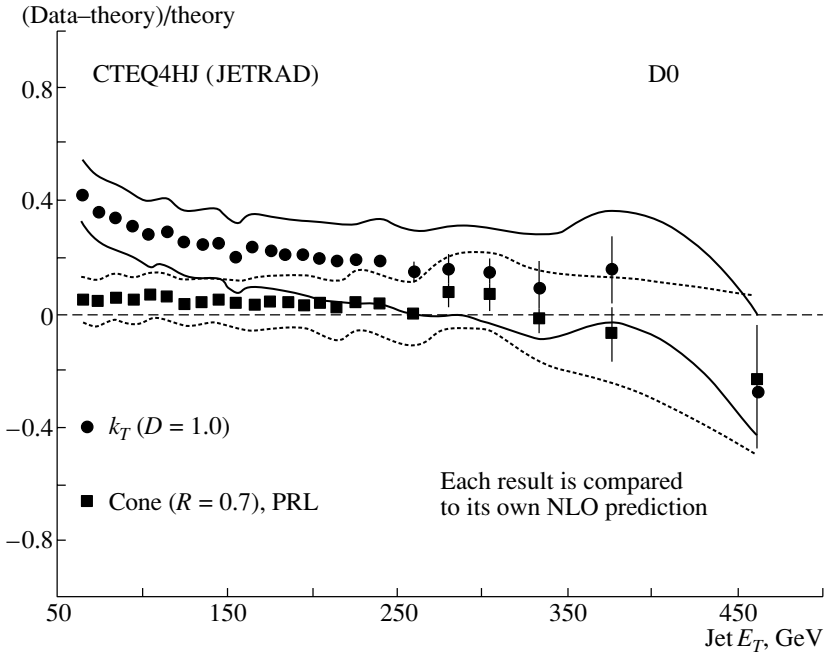

Fig. 10. Inclusive jet cross section compared to theory (data–theory)/theory for two different jet-finding algorithms: squares—cone algorithm; circles—k_T algorithm [13].

at smaller energies. Figure 15 is a representative example illustrating this discrepancy [20]. A number of models have been suggested to account for the difference, but there does not seem to be a common agreement on how to deal with this issue.

Another soft QCD example is the structure of the underlying event, for which there is not any quantitative theory—all one has at hand is just a few Monte Carlo generators with various knobs to tune, and it is not uncommon that the default parameters fail to describe data (Fig. 16 [21]). As will be discussed below, the underlying event process will be of special importance at LHC, and the lack of a theory becomes ever more frustrating.

TEVATRON RUN II AND LHC

Tevatron Run II has a c.m. energy $\sqrt{s} = 2.0$ TeV (up from 1.8 TeV in Run I). The design luminosity (to peak by 2006 at $\sim 5 \times 10^{32}$ cm^{-2} s^{-1}) should allow collecting 15 000 pb^{-1} worth of data by the year 2008 (Run I total was about 100 pb^{-1}). The short-term goal of 2000 pb^{-1} is often referred to as Run IIa. The CDF and D0 detectors were substantially upgraded. By the time of the conference, the accumulated luminosity remained below 50 pb^{-1} per detector and, therefore, significantly new results were still in the domain of the future.

To give sense to what kind of QCD results one might expect from Tevatron Run II, I give below just a few examples. With Run IIa statistics, one should be able to measure the jet inclusive spectra well beyond 400 GeV. The number of events with jet $E_T >$ 400 GeV will be on the order of 500 (cf. 11 in Run I). The factor of 20 in the statistics comes from the luminosity and the additional factor of 2.5 comes from the increase in the c.m. energy (Fig. 17 [22]). With the full 15 fb^{-1} statistics (all Run II), one can advance in the diphoton cross section up to $E_T \sim 600$ GeV (cf. $\sim$200 GeV in Run I) (Fig. 18 [22]). The B physics will doubly benefit: first, from the large luminosity and,

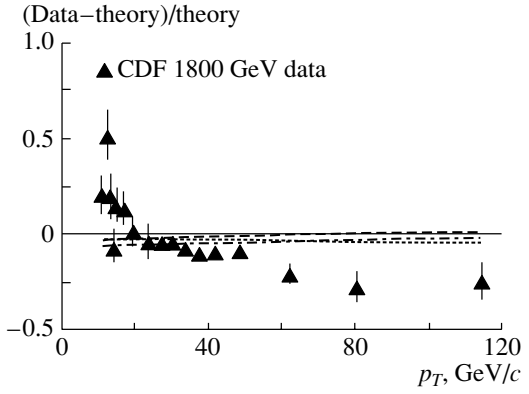

Fig. 11. Inclusive photon cross section vs. photon energy normalized on the NLO calculations performed with CTEQ4M PDFs. Also shown are variations arising from using other PDFs: CTEQ5HJ, MRST99, MRST99 ($g \uparrow$) [14].

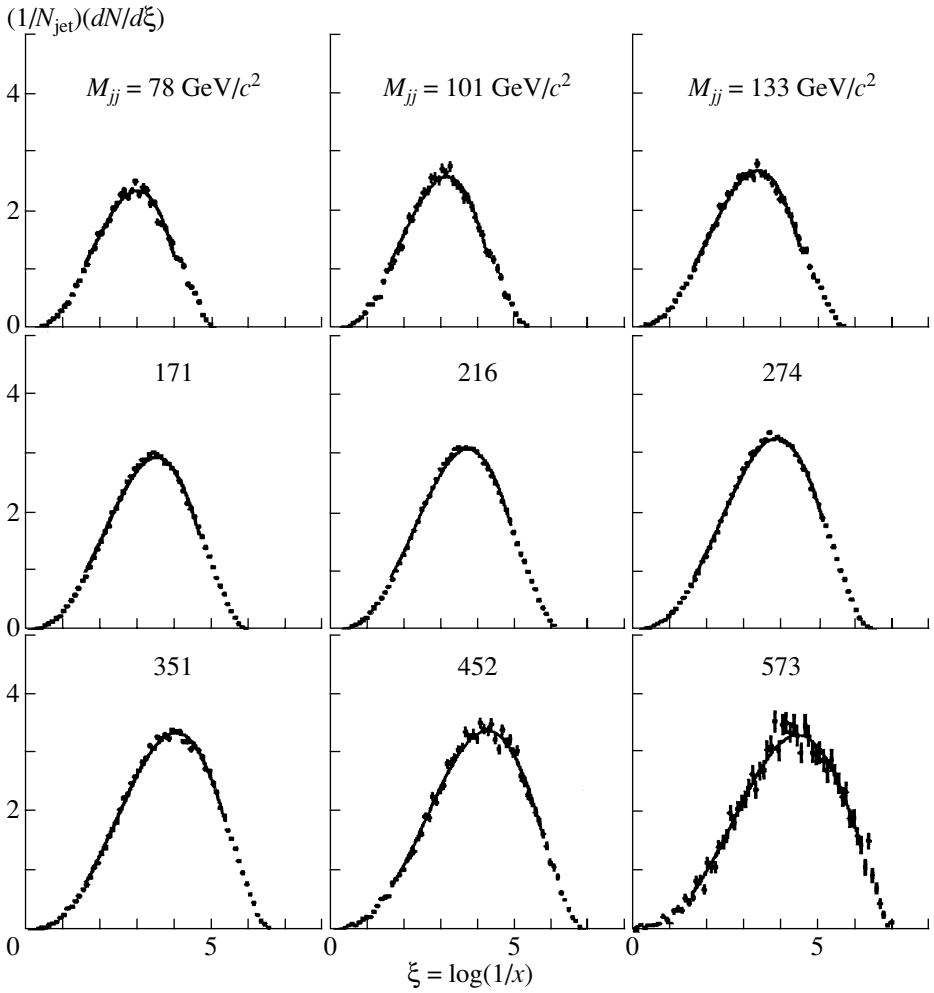

Fig. 12. Inclusive momentum distribution of charged particles in jets (within an opening angle around the jet axis $\theta = 0.47$ rad) for different dijet masses [16]. The data points are fit with the MLLA curves for partons.

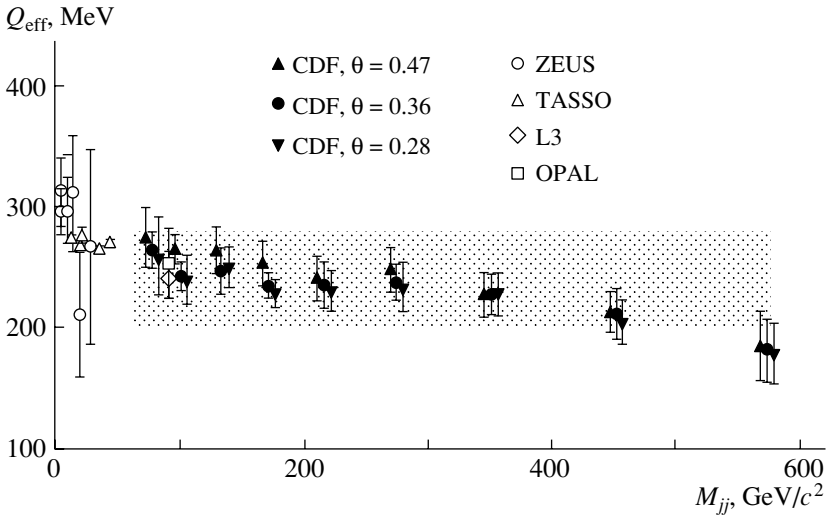

Fig. 13. The MLLA cutoff parameter Q_{eff} obtained from fitting inclusive momentum distributions of charged particles in jets of various energies (dijet masses) and within different opening angles around the jet axis [16].

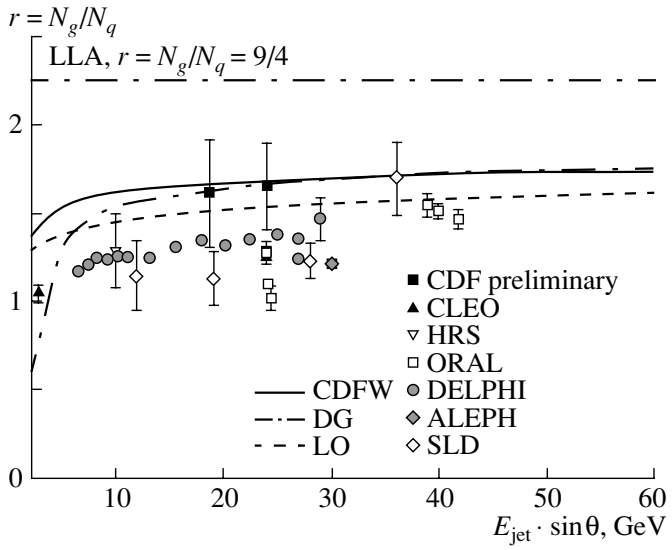

Fig. 14. Ratio of charged particle multiplicities in gluon and quark jets [19].

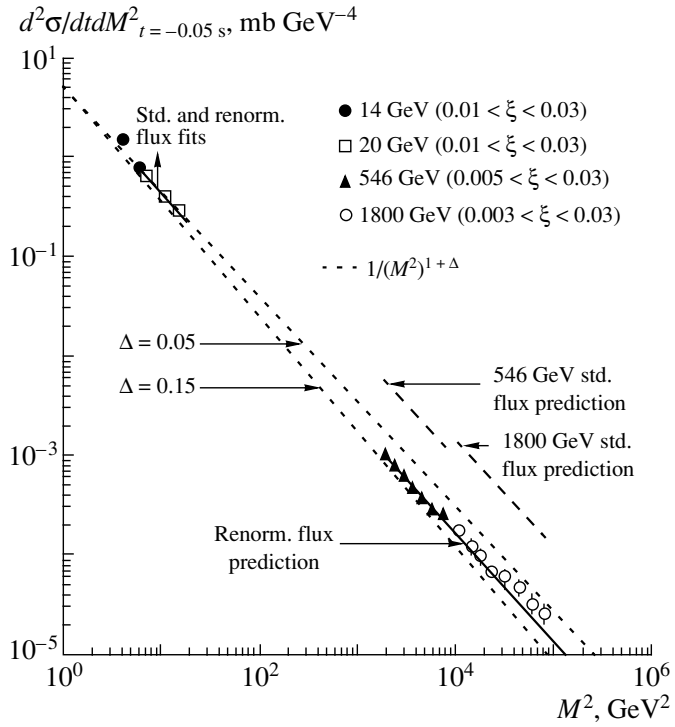

Fig. 15. Differential single diffractive cross sections for different $\sqrt{s}$ energies [20].

second, from detector upgrades (a much improved vertex detector at CDF; a newly added vertex detector and a new magnetic field tracker at D0). All statistically limited results from Run I will be substantially improved over the next few years.

LHC will deliver 14-TeV proton–proton collisions with the target luminosity of 10^{34} cm^{-2} s^{-1} and is to become the facility for precision QCD studies—what LEP was for the electroweak theory. Figures 19 [23] and 20 [24] are just two illustrations of the fantastic prospects. However, to take full advantage of these opportunities, the ATLAS and CMS experimentalists must push the limits of detector technology and have set goals to achieve ~2% jet energy resolution (cf. ~10% at Tevatron Run I) and ~1% energy scale accuracy (cf. ~5% at Tevatron Run I). In addition,

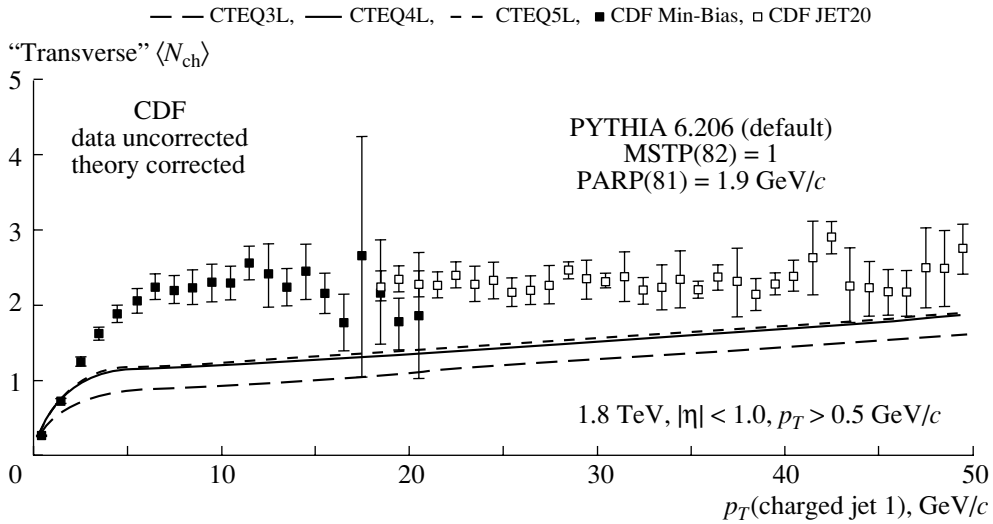

Fig. 16. Multiplicity of charged particles in direction transverse to jet direction compared to PYTHIA Monte Carlo predictions [21].

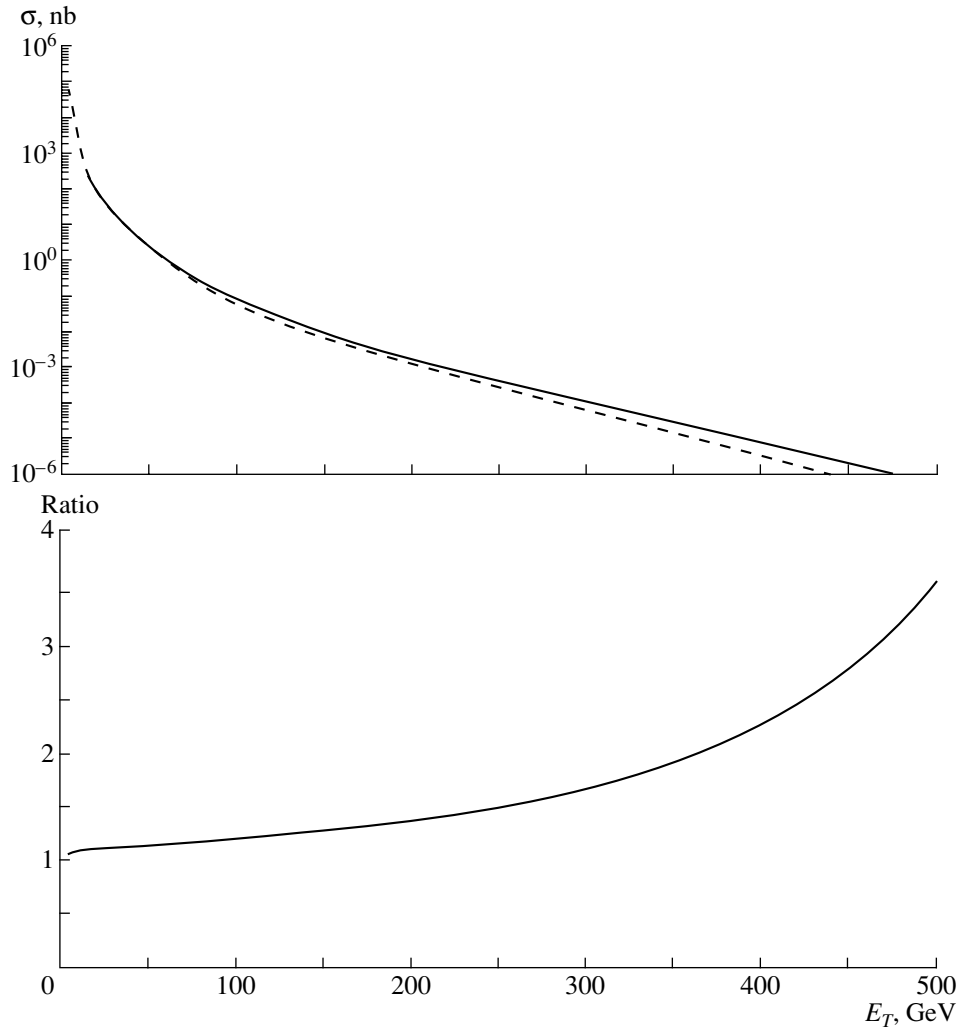

Fig. 17. Inclusive differential jet cross sections (top) and their ratio (bottom) at $\sqrt{s} = 1.8$ and 2 TeV (CTEQ4HJ) [22].

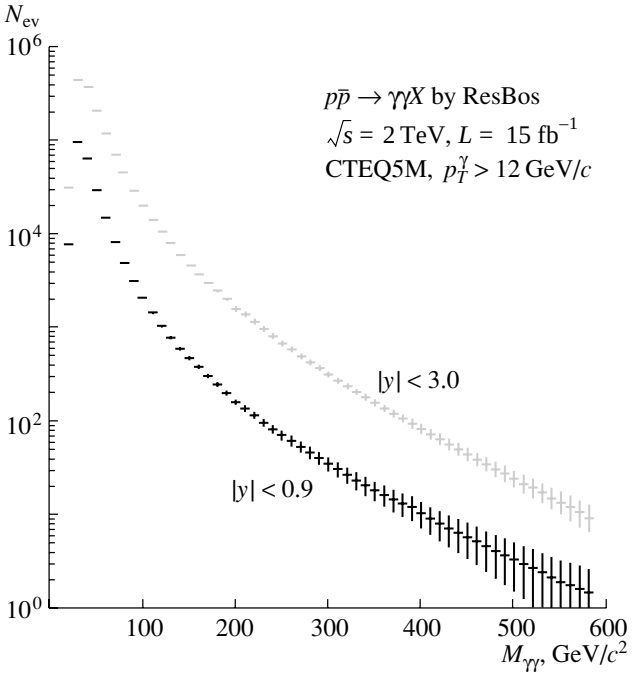

Fig. 18. Differential diphoton cross section at $\sqrt{s} =$ 2 TeV [22].

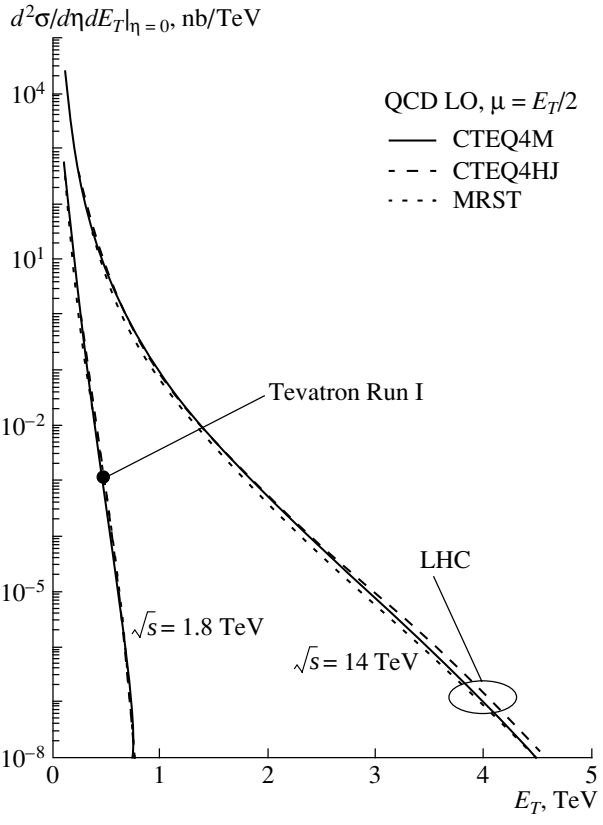

Fig. 19. Inclusive differential jet cross sections at Tevatron Run I for $\sqrt{s} = 1.8$ and LHC for $\sqrt{s} = 14$ TeV [23].

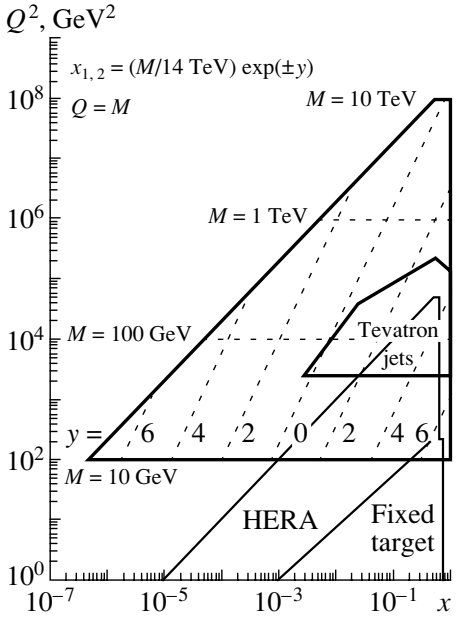

Fig. 20. Probing proton structure at LHC [24].

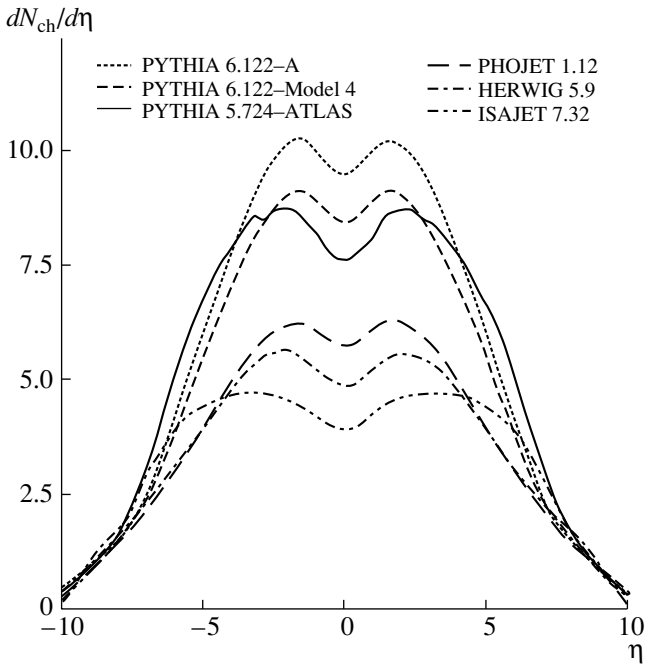

Fig. 21. Multiplicity of charged particles per unit of rapidity in min-bias events at LHC as predicted by different Monte Carlo generators [25].

one should realize that, once the full luminosity is achieved, there will be on average 20 minimum bias events in each bunch crossing and this will imply substantial experimental challenges for QCD studies: the multiple collision background will sum up

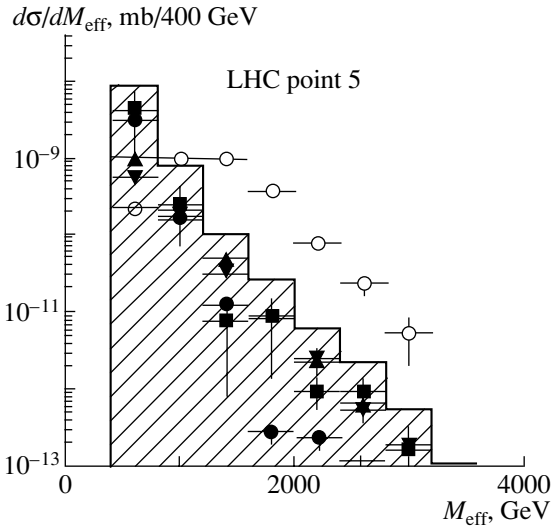

Fig. 22. M_{eff} distribution in multijet ($\geq$4) events with large missing E_T at LHC. M_{eff} is defined as sum of E_T of four leading jets and missing E_T. The SM is presented by the hatched histogram (with various QCD-driven process given by filled symbols). The additional contribution from the presence of squarks and sgluons ($M_{\text{squark}} \sim 680$ GeV, $M_{\text{sgluon}} \sim 770$ GeV) is shown in open circles [27].

to about 10 charged tracks and ~15 GeV of energy flow within a jet cone of $R \sim 0.5$. Unfortunately, the poor understanding of the underlying and minimum bias events results in large uncertainties in current modeling of this background at LHC (Fig. 21 [25]).

As discussed in the Introduction, any search for new physics is intimately connected to QCD. Accurate measurement of the jet inclusive cross sections will allow one to set ~30–40 TeV limits [26] on quark compositeness (or discover it!). Figure 22 [27] gives a representative example of how ~700-GeV squarks and sgluons would manifest themselves in multijet events with large missing E_T.

CONCLUSIONS

Hadron colliders provide us with a wealth of data for studying hard and soft QCD processes. Although some of the questions that emerged from the Tevatron Run I data analyses seem to have found explanations over the last few years, there are still a few remaining controversies awaiting their resolution. The Tevatron Run II is ramping up now and soon will provide many more insights, while LHC, once turned on, will become the ultimate machine for precision tests of QCD. Searches for new physics at both Tevatron Run II and LHC will not be possible without good understanding of QCD that, very likely, will give rise to these new phenomena and, at the same time, be the major source of the background to them.

REFERENCES

1. CDF Collab., hep-ph/0111359.
2. E. L. Berger *et al.*, Phys. Rev. Lett. **86**, 4231 (2001).
3. C. Paus, in *Proceedings of the ICHEP 2002, Amsterdam.*
4. CDF Collab., Phys. Rev. D **64**, 032001 (2001).
5. D0 Collab., Phys. Rev. Lett. **82**, 2451 (1999).
6. CDF Collab., Phys. Rev. Lett. **77**, 5336 (1996); **78**, 4307(E) (1997).
7. D. Stump, in *Proceedings of the ICHEP 2002, Amsterdam.*
8. D0 Collab., hep-ex/0106072.
9. D0 Collab., hep-ex/0207046.
10. J. Dittmann, in *Proceedings of the ICHEP 2002, Amsterdam, The Netherlands, July 2002.*
11. S. D. Ellis and D. E. Soper, Phys. Rev. D **48**, 3160 (1993); S. Catani, Yu. L. Dokshitzer, M. H. Seymour, and B. R. Webber, Nucl. Phys. B **406**, 187 (1993).
12. J. Huth *et al.*, in *Proceedings of Research Directions for the Decade, Snowmass, 1990,* Ed. by E. L. Berger (World Sci., Singapore, 1992).
13. U. Bassler, in *Proceedings of the ICHEP2002, Amsterdam.*
14. CDF Collab., Phys. Rev. D **65**, 112003 (2002).
15. UA2 Collab., Phys. Lett. B **263**, 544 (1991).
16. CDF Collab., FERMILAB-PUB-02-096 (to be published in Phys. Rev. D).
17. OPAL Collab., Phys. Lett. B **265**, 462 (1991).
18. OPAL Collab., Eur. Phys. J. C **23**, 597 (2002).
19. A. Pronko, *APS Meeting, Albuquerque, New Mexico, 2002.*
20. K. Goulianos and J. Montanha, Phys. Rev. D **59**, 114017 (1999).
21. R. Filed, in *Proceedings of the Workshop on TeV-Scale Physics, Cambridge, UK, 2002.*
22. J. Huston, in *Proceedings of the Workshop on TeV-Scale Physics, Cambridge, UK, 2002.*
23. J. Proudfoot, in *Proceedings of the ICHEP 2002, Amsterdam.*
24. *ATLAS Detector and Physics Performance TDR,* 25 May 1999, Fig. 15-2.
25. *ATLAS Detector and Physics Performance TDR,* 25 May 1999, Fig. 15-12.
26. *ATLAS Detector and Physics Performance TDR,* 25 May 1999, p. 939.
27. *ATLAS Detector and Physics Performance TDR,* 25 May 1999, Fig. 20-4.

Physics of Atomic Nuclei, Vol. 67, No. 1, 2004, pp. 62–68. From Yadernaya Fizika, Vol. 67, No. 1, 2004, pp. 63–69.

Finite-Temperature Bose–Einstein Distribution Functions of Identical Particles*

G. A. Kozlov**

Joint Institute for Nuclear Research, Dubna, Moscow oblast, 141980 Russia

Received April 30, 2003

Abstract—We study the evolution properties of propagating identical particles produced at a finite temperature in a randomly distributed environment. The lower bound on the spacetime size of the multiparticle production region and the correlation chaoticity are derived. © *2004 MAIK "Nauka/Interperiodica".*

1. INTRODUCTION

The investigation of particle collisions with high multiplicity is a central feature of modern particle physics. An interest in (charged) particles "moving" in an environment of quantum fields taking into account the relations between quantum fluctuations and chaoticity is expressed by particle physicists.

One of the most important tasks of multiparticle studies is to analyze fluctuations and correlations such as the Bose–Einstein correlation (BEC) [1, 2] of produced particles. This is a rather instructive tool to study high-multiplicity hadron processes in detail. The most recent reviews on BEC can be found in [3]. We understand the multiparticle production as the process of colliding particles where the kinetic energy is dissipated into the mass of produced particles [4]. We consider the incident energy $\sqrt{s} \gg \Lambda$, where Λ means the quantum chromodynamics scale. Phenomenological models [5–9] describing the crucial properties of multiparticle correlations are very useful for systematic investigations of the properties caused by the fluctuations and correlations. By considering them, one can obtain the characteristic properties of the internal structure of the disordering of produced particles in order to extract information on the spacetime size of the multiparticle production region, to estimate the lifetime of the particle emitter, etc. The analysis of the correlation and distribution functions was used in [7] to understand the possible views on quark–gluon plasma formation.

In this paper, we present a model to describe high-multiplicity effects at finite temperature. The most distinctive point of our model is that both the distribution and the correlation functions are taken into account at a quantum level (the operators of production and annihilation are used) with the random source contributions coming from the environment. It is well known that the cross section of the production of N particles at a given c.m. energy $\sqrt{s}$ of two colliding particles with momenta p and $\bar{p}$ is defined as

$$\sigma_N(s) = \int d\Omega_N \delta^4 \left(p + \bar{p} - \sum_{j=1}^{N} q_j \right) |A_N(p,q)|^2,$$

where A_N is the N-particle production amplitude, q_j are the 4-momenta of produced particles, and Ω_N is a phase space. In a simple nonrelativistic case, the multiplicity N depends on the mean kinetic energy $\epsilon = \frac{3}{2}kT$ at temperature T as $N = (\sqrt{s} + \epsilon)/(m + \epsilon)$, where k is the Boltzmann constant and m is the mass of a particle. We define the average mean multiplicity $\langle \bar{N} \rangle$ (as a natural scale of the produced particle multiplicity N) via the multiparticle correlation function $w(\mathbf{k})$ as $\langle \bar{N} \rangle = \int d\mathbf{k} w(\mathbf{k})$, where $\mathbf{k}$ is the spatial momentum of a particle. Following a natural way, we suppose $\langle \bar{N} \rangle \ll N$, while $N \ll N_0 = \sqrt{s}/M$, where $M \sim O(0.1\ \mathrm{GeV})$. The main object in this investigation is the multiparticle thermal distribution function $\tilde{W}(k_\mu)$ related to $\langle N \rangle$ as

$$\tilde{W}(k_\mu) = \langle N \rangle f(k_\mu) = \langle N \rangle \langle b^+(k_\mu) b(k_\mu) \rangle_\beta, \quad (1)$$

where $\langle N \rangle$ is defined as the scale of the multiplicity N at four-momentum k_μ (μ is the Lorenz index); the normalized distribution function $f(k_\mu)$ is finite, i.e., $\int d^4k f(k_\mu) < \infty$; and the label β in (1) means the temperature T (of the phase space occupied by operators $b^+(k_\mu)$ and $b(k_\mu)$) inverse. The nature of

*This article was submitted by the author in English.

** e-mail: kozlov@thsun1.jinr.ru

the operators $b^+(k_\mu)$ and $b(k_\mu)$ will be clarified in Section 3.

At present no (phenomenological) model can fit the experimental data and no analysis from first principles is in sight for BEC. As a new theoretical idea, we use a method that combines different fields of physics to describe BEC in the multiparticle production processes:

(i) a semiphenomenological transport theory that is formulated by means of an operator-field evolution equation of the Langevin type [7–10];

(ii) an axiomatic quantum field theory [11] in terms of distributions (generalized functions) [12];

(iii) a statistical distribution theory.

We formulate an evolution model of dual representation in Section 2. In this paper, we claim that the observation of the spacetime size effect in the multiparticle production is derived via the multiparticle correlation and distribution functions as well as the so-called chaoticity which will be introduced in Section 3. The multiparticle correlation function formalism concerns the statistical physics based on the Langevin-type equation. This equation, introduced in Section 3, is considered as a basis for studying the approach to the equilibrium of the particle(s). It is assumed that a heat bath being in essence infinite in size for all times remains in equilibrium as well. We use a method applied to the model where a relativistic particle moving in the Fock space is described by a number of representations underlying the second quantization formulation of the canonical field theory. We deal with a microscopic look at the problem with the elements of quantum field theory at a stochastic level with the semiphenomenological noise embedded into the evolution dissipative equation of motion. The statistical distribution of the particles will be discussed in Section 4. We conclude in Section 5.

2. THE MODEL OF DUAL REPRESENTATION WITHIN THE DISSIPATIVE DYNAMICS

Let us suppose that the evolution of particles produced at high energies is described by the solutions of the model Hamiltonian where any physical system of particles is described by the doublet of field operators. We introduce the dual states in the eigenbasis $\{|k\rangle, |k(\epsilon)\rangle\}$ of the Hamiltonian H, where $0 \le \epsilon < \infty$ is identified as the frequency representing the energy of the object and $|k\rangle$ is a discrete eigenstate. We consider the simple dual model where H is given within the damped harmonic oscillator

$$H = H_0 + H_i, \tag{2}$$

where

$$H_0 = \epsilon_0 |k\rangle\langle k| + \int_0^\infty d\epsilon \epsilon |k(\epsilon)\rangle\langle k(\epsilon)|, \tag{3}$$

$$H_i = \rho \int_0^\infty d\epsilon g(\epsilon)[|k(\epsilon)\rangle\langle k| + |k\rangle\langle k(\epsilon)|], \tag{4}$$

$$\langle k|k\rangle = 1, \quad \langle k|k(\epsilon)\rangle = \langle k(\epsilon)|k\rangle = 0,$$
$$\langle \epsilon|\epsilon'\rangle = \delta(\epsilon - \epsilon').$$

Here, we identify $|k\rangle$, $|k(\epsilon)\rangle$ and $\langle k|$, $\langle k(\epsilon)|$ with the special mode operators of annihilation $a, b(\epsilon)$ and creation $a^+, b^+(\epsilon)$, respectively, e.g., for "quarks" and "gluons" or their combinations. In the interaction Hamiltonian (4), ρ is the coupling constant, while $g(\epsilon)$ provides the transition between discrete and continuous states.

The equations of motion obeying (2) with (3) and (4) are

$$i d_t a_k(t) = \epsilon_0 a_k(t) + \rho \int_0^\infty d\epsilon g(\epsilon) b_k(\epsilon, t),$$

$$i d_t b_k(\epsilon, t) = \epsilon b_k(\epsilon, t) + \rho g(\epsilon) a_k(t),$$

where the label k means $|\mathbf{k}|$ as the momentum. We demand that $a_k(t)$ and $b_k(\epsilon, t)$ meet the following natural conditions:

$$a_k(t) a_k^+(t) + \int_0^\infty d\epsilon b_k(\epsilon, t) b_k^+(\epsilon, t) < \infty,$$

$$[a_k^+(t)]^+ = a_k(t), \quad [b_k^+(\epsilon, t)]^+ = b_k(\epsilon, t).$$

The next step is to establish relations between the variables and couplings of the model (2) and the phenomenological constants, e.g., the frequency E and the damping constant κ involved in the dissipative dynamics given by the Boltzmann-type equations in the relaxation time approximation:

$$\frac{d_t \langle a_k(t)\rangle}{\langle a_k(t)\rangle} = -(iE + \kappa), \tag{5}$$

$$d_t w_k(t) = d_t \langle a_k^+(t) a_k(t)\rangle = -2\kappa[w_k(t) - n(\beta)]. \tag{6}$$

Here,

$$d_t \langle a_k(t)\rangle = -i\epsilon_0 \langle a_k(t)\rangle - \rho^2 \int_0^\infty d\epsilon g^2(\epsilon)$$

$$\times \int_\tau^t ds \langle a_k(s)\rangle \exp[-i\epsilon(t - s)],$$

$$\langle a_k(z)\rangle = -i\rho\int\limits_{\tau}^{z} dx\langle\sigma_k(x)\rangle\exp[-i\epsilon_0(z-x)],$$

$$\sigma_k(t) = \int\limits_{0}^{\infty} d\epsilon g(\epsilon) b_k(\epsilon,t),$$

$$n(\beta) = [\exp(\epsilon_0\beta)\pm 1]^{-1}$$

as $\tau\to-\infty$. One can conclude that the phenomenological constants E and κ in (5) and (6) are nothing else but ϵ_0 and $2\pi\rho^2 g^2(\epsilon_0)$, respectively, i.e., the microscopic parameters coming from the model Hamiltonian (2).

3. THE MODEL

The investigation of BEC is one of the most challenging topics in modern physics to analyze theoretically such phenomena based on the general principles of quantum field theory (QFT) at finite temperature. However, such complicated phenomena are rather far from the basic features of QFT to be connected together. Hence, one needs to introduce an approximate semiphenomenological model that enables one to clarify the details of correlations in terms of basic variables and some parameters embedded into this model.

Suppose the phase space of produced hadrons consists of many "quantum" cells where a number of the (canonical) operators $a(k_\mu)$ and its Hermitian conjugate $a^+(k_\mu)$ are localized. Since the nature of the operators $a(k_\mu)$ and $a^+(k_\mu)$ is unknown, one can consider them as some mode operators which can in principle be composed of any other operators. Hence, the operator $a(k_\mu)$ ($a^+(k_\mu)$) describes a special matter mode that is excited in a cell. For simplicity, one can identify the operator $a(k_\mu)$ with a single boson or fermion operator. The system of "quantum" cells interacts with a more extended system that is supposed to be a thermal bath in which the energy of a system containing "quantum" cells is dissipated. In a simple version, the heat bath is considered as a large number of independent harmonic oscillators given by the operators $\hat{c}$ ($\hat{c}^+$) obeying the standard Hamiltonian $H_\beta = \sum_i \omega_i(\hat{c}_i^+\hat{c}_i + 1/2)$. On the semiphenomenological level, we suppose that the rather complicated multiparticle interaction process is replaced with a single-particle operator $b = a + R$ propagation derived by a systematic operator A and disturbed by a random force $F_1 = F + P$. R is a random source operator, while P gives a stationary external force.

Considering the "propagation" of a particle with momentum $\mathbf{k}$ in the quantum equilibrium phase space under the influence of a random force coming from surrounding particles, the dissipative dynamics of the relevant system is described by an equation containing only the first-order time derivatives of the dynamic degrees of freedom, the operators $b(\mathbf{k},t)$ and $b^+(\mathbf{k},t)$ [7–9]:

$$i\partial_t b(\mathbf{k},t) = F_1(\mathbf{k},t) - A(\mathbf{k},t). \qquad (7)$$

Here, the interaction of particles under consideration with the surroundings as well as providing the propagation is given by the operator $A(\mathbf{k},t)$ defined as the one closely related to the dissipation force:

$$A(\mathbf{k},t) = \int\limits_{-\infty}^{+\infty} K(\mathbf{k},t-\tau)b(\mathbf{k},\tau)d\tau.$$

An interplay of particles with the surroundings is embedded into the interaction complex kernel $K(\mathbf{k},t)$, while the real physical transitions are provided by the random source operator $F(\mathbf{k},t)$ with the zeroth value of the statistical average, $\langle F\rangle = 0$. The random evolution field operator $K(\mathbf{k},t)$ stands for the random noise and it is assumed to vary stochastically with a δ-like equal time correlation function

$$\langle K^+(\mathbf{k},\tau)K(\mathbf{k}',\tau)\rangle = 2(\pi l)^{1/2}\xi\delta(\mathbf{k}-\mathbf{k}'),$$

where both the strength of the noise ξ and the positive constant $l\to\infty$ define the effect of the Gaussian noise on the evolution of particles in the thermalized environment.

The formal solution to Eq. (7) in the operator form in the four-momentum spacetime $S(\mathfrak{R}_4)$ ($k^\mu = (\omega = k^0, k_j)$) is $\tilde{b}(k_\mu) = \tilde{a}(k_\mu) + \tilde{R}(k_\mu)$, where the operator $\tilde{a}(k_\mu)$ is expressed via the Fourier-transformed operator $\tilde{F}(k_\mu)$ and the Fourier-transformed kernel function $\tilde{K}(k_\mu)$ as $\tilde{a}(k_\mu) = \tilde{F}(k_\mu)[\tilde{K}(k_\mu)-\omega]^{-1}$, while the function $\tilde{R}(k_\mu)\sim P[\tilde{K}(k_\mu)-\omega]^{-1}$. We suppose in our model that the heat bath (an environment) is an assembly of damped oscillators coupled to the produced particles, which in turn are distributed by the random force $\tilde{F}(k_\mu)$. In addition, there is the assumption that the heat bath is statistically distributed. The random force operator $F(\mathbf{k},t)$ can be expanded by using the Fourier integral

$$F(\mathbf{k},t) = \int\limits_{-\infty}^{+\infty}\frac{d\omega}{2\pi}\psi(k_\mu)\hat{c}(k_\mu)e^{-i\omega t},$$

where the form $\psi(k_\mu)\hat{c}(k_\mu)$ is just the Fourier operator $\tilde{F}(k_\mu) = \psi(k_\mu)\hat{c}(k_\mu)$, and the canonical operator

$\hat{c}(k_\mu)$ obeys the commutation relation

$$\left[\hat{c}(k_\mu), \hat{c}^+(k'_\mu)\right]_\pm = \delta^4(k_\mu - k'_\mu).$$

The function $\psi(k_\mu)$ is determined by the condition (the canonical commutation relation with the operators $\hat{c}(k_\mu), \hat{c}^+(k'_\mu)$ is taken into account)

$$\int_{-\infty}^{+\infty} \frac{d\omega}{2\pi} \left[\frac{\psi(k_\mu)}{\tilde{K}(k_\mu) - \omega}\right]^2 = 1.$$

We formulate distribution functions of the produced particles in terms of a point-to-point equal-time temperature-dependent thermal correlation function of the two operators

$$w(\mathbf{k}, \mathbf{k}', t; T) = \langle a^+(\mathbf{k}, t) a(\mathbf{k}', t)\rangle_\beta$$
$$= \mathrm{Tr}[a^+(\mathbf{k}, t) a(\mathbf{k}', t) e^{-H\beta}]/\mathrm{Tr}(e^{-H\beta}).$$

The standard canonical commutation relation

$$\left[a(\mathbf{k}, t), a^+(\mathbf{k}', t)\right]_\pm = \delta^3(\mathbf{k} - \mathbf{k}')$$

at every time t is used as usual for Bose $(-)$ and Fermi $(+)$ operators.

The probability of finding the particles in the multiparticle production region with momenta $\mathbf{k}$ and $\mathbf{k}'$ in the same event at time t is

$$C_2(\mathbf{k}, \mathbf{k}', t) = W(\mathbf{k}, \mathbf{k}', t)/[W(\mathbf{k}, t) W(\mathbf{k}', t)].$$

Here, the one-particle thermal distribution function in a simple version fluctuates only its normalization, e.g., the mean multiplicity $\langle N\rangle$, $W(\mathbf{k}, t) = \langle N\rangle f(\mathbf{k}, t)$ defining the single spectrum, while $W(\mathbf{k}, \mathbf{k}', t) = \langle N(N' - \delta_{ij})\rangle f(\mathbf{k}, \mathbf{k}', t)$ for i and j types of particles. Here, $\delta_{ij} = 1$ if $i = j$ and 0 otherwise. Distribution functions $f(\mathbf{k}, t)$ and $f(\mathbf{k}, \mathbf{k}', t)$ look like

$$f(\mathbf{k}, t) = \langle b^+(\mathbf{k}, t) b(\mathbf{k}, t)\rangle$$

and

$$f(\mathbf{k}, \mathbf{k}', t) = \langle b^+(\mathbf{k}, t) b^+(\mathbf{k}', t) b(\mathbf{k}, t) b(\mathbf{k}', t)\rangle,$$

respectively.

The ratio function C_2 leads to enhanced probability for emission of identical particles, which is given in $S(\mathfrak{R}_4)$ [11, 12] as follows:

$$C_2(k_\mu, k'_\mu; T) = \xi(N)[1 + D(k_\mu, k'_\mu; T)], \quad (8)$$

where

$$\xi(N) = \frac{\langle N(N' - \delta_{ij})\rangle}{\langle N\rangle\langle N'\rangle}.$$

The two-particle BEC function $\Xi(k_\mu, k'_\mu)$ looks like

$$\Xi(k_\mu, k'_\mu) = \langle \tilde{a}^+(k_\mu) \tilde{a}(k'_\mu)\rangle$$
$$= \frac{\psi^*(k_\mu)\psi(k'_\mu)}{[\tilde{K}^*(k_\mu) - \omega][\tilde{K}(k'_\mu) - \omega']} \langle \hat{c}^+(k_\mu) \hat{c}(k'_\mu)\rangle.$$

Taking into account the trick with the $\delta^4(k_\mu - k'_\mu)$ function being replaced by a δ-like consequence like $\Omega(r)\exp[-(k - k')^2 r^2]$ [12], one can get the following expression for the D function:

$$D(k_\mu, k'_\mu; T) = \lambda(k_\mu, k'_\mu; T)\exp(-q^2/2) \quad (9)$$
$$\times [n(\bar{\omega}, T)\Omega(r)\exp(-q^2/2) + \tilde{R}^*(k'_\mu)\tilde{R}(k_\mu)$$
$$+ \tilde{R}^*(k_\mu)\tilde{R}(k'_\mu)],$$

where

$$\lambda(k_\mu, k'_\mu; T) = \frac{\Omega(r)}{\tilde{f}(k_\mu)\tilde{f}(k'_\mu)} n(\bar{\omega}, T),$$
$$\bar{\omega} = \frac{1}{2}(\omega + \omega'),$$

while $q^2 \equiv Q^2 r^2$ and the function $\Omega(r) n(\omega; T) \times \exp(-q^2/2)$ in (9) describes the spacetime size of the multiparticle production region. Choosing the z axis along the pp or $\bar{p}p$ collision axis, one can set

$$q^2 = (r_0 \cdot Q_0)^2 + (r_z \cdot Q_z)^2 + (r_t \cdot Q_t)^2,$$
$$Q_\mu = (k - k')_\mu, \quad Q_0 = \epsilon_{\mathbf{k}} - \epsilon_{\mathbf{k}'}, \quad Q_z = k_z - k'_z,$$
$$Q_t = [(k_x - k'_x)^2 + (k_y - k'_y)^2]^{1/2},$$
$$\Omega(r) = \frac{1}{\pi^2} r_0 \cdot r_z \cdot r_t^2,$$

where r_0, r_z, and r_t are timelike, longitudinal, and transverse "size" components of the multiparticle production region. To derive (9), the Kubo–Martin–Schwinger condition

$$\langle a(\mathbf{k}', t') a^+(\mathbf{k}, t)\rangle$$
$$= \langle a^+(\mathbf{k}, t) a(\mathbf{k}', t - i\beta)\rangle \exp(-\beta\mu)$$

has been used (μ is the chemical potential), and the thermal statistical averages for the $\hat{c}(k_\mu)$ operator should be represented in the form

$$\langle \hat{c}^+(k_\mu)\hat{c}(k'_\mu)\rangle = \delta^4(k_\mu - k'_\mu) n(\omega, T),$$
$$\langle \hat{c}(k_\mu)\hat{c}^+(k'_\mu)\rangle = \delta^4(k_\mu - k'_\mu)[1 \pm n(\omega, T)]$$

for Bose $(+)$ and Fermi $(-)$ statistics, respectively; $n(\omega, T) = \{\exp[(\omega - \mu)\beta] \pm 1\}^{-1}$. Formula (9) indicates that the chaotic multiparticle source emanating from the thermalized multiparticle production region exists. It is easy to see that the correlation functions containing the random force functions $F(\mathbf{k}, t)$ carry quantum features in the thermalized stationary equilibrium, namely,

$$\langle F(\mathbf{k}, t) F^+(\mathbf{k}', t')\rangle = \delta^3(\mathbf{k} - \mathbf{k}')\Gamma_1(\mathbf{k}, -\Delta t),$$

$$\Gamma_1(\mathbf{k},-\Delta t)=\int\frac{d\omega}{2\pi}|\psi(k_\mu)|^2[1\pm n(\omega,\beta)]\times\exp(-i\omega\Delta t),$$
$$\Delta t=t-t';$$
$$\langle F^+(\mathbf{k},t)F(\mathbf{k}',t')\rangle=\delta^3(\mathbf{k}-\mathbf{k}')\Gamma_2(\mathbf{k},\Delta t),$$
$$\Gamma_2(\mathbf{k},\Delta t)=\int\frac{d\omega}{2\pi}|\psi(k_\mu)|^2 n(\omega,\beta)\exp(i\omega\Delta t).$$

Quantitative information (longitudinal r_z and transverse r_t components of the multiparticle production region, the temperature T of the environment) could be extracted by fitting theoretical formula (9) to the measured D function and estimating the errors of the fitted parameters. Hence, the measurement of the spacetime evolution of the multiparticle source would provide information on the multiparticle process and the general reaction mechanism. The temperature of the environment enters into formula (9) through the two-particle correlation function $\Xi(k_\mu,k'_\mu;T)$. Formula (8) looks like the fitting $C_{\rm F}$ ratio using a source parametrization:

$$C_{\rm F}(r)=\mathrm{const}[1+\lambda_{\rm F}(r)\times\exp(-r_t^2\cdot Q_t^2/2-r_z^2\cdot Q_z^2/2)],$$

where $r_t(r_z)$ is the transverse (longitudinal) radius parameter of the source with respect to the beam axis and $\lambda_{\rm F}$ stands for the effective intercept parameter (chaoticity parameter) which has a general dependence of the mean momentum of the observed particle pair. Here, the dependence on the source lifetime is omitted. The chaoticity parameter $\lambda_{\rm F}$ is temperature-dependent and positive and is defined by

$$\lambda_{\rm F}(r)=\frac{|\Omega(r)n(\bar\omega;T)|^2}{\tilde f(k_\mu)\tilde f(k'_\mu)}.$$

The correlation function $\Xi(k_\mu,k'_\mu)$,

$$\Xi(k_\mu,k'_\mu)=\Omega(r)n(\bar\omega;T)\exp(-q^2/2),$$

defines uniquely the size r of the multiparticle production region. There is no satisfactory tool to derive the precise analytic form of the random source function $\tilde R(k_\mu)$, but one can set [8, 9, 13]

$$\tilde R(k_\mu)=[\alpha\langle\tilde a^+(k_\mu)\tilde a(k_\mu)\rangle]^{1/2},$$

where α is of the order $O(P^2/n(\omega,T)|\psi(k_\mu)|^2)$. Finally, one can obtain

$$D(q^2;T)=\frac{\tilde\lambda^{1/2}(\bar\omega;T)}{(1+\alpha)(1+\alpha')}e^{-q^2/2}\times\left[\tilde\lambda^{1/2}(\bar\omega;T)e^{-q^2/2}+2(\alpha\alpha')^{1/2}\right],\qquad(10)$$

where $\tilde\lambda(\bar\omega;T)=n^2(\bar\omega;T)/[n(\omega;T)n(\omega';T)]$. It is easy to see that, in the vicinity of $q^2\approx0$, one can get the full correlation if $\alpha=\alpha'=0$ and $\tilde\lambda(\bar\omega;T)=1$. Setting $\alpha=\alpha'$ in (10), we find the formal lower bound on the spacetime dimensionless size of the multiparticle production region of the bosons

$$q^2\geq\left(\frac{1}{1+\frac{1}{2}\sqrt{\frac{\tilde\lambda}{\alpha\cdot\alpha'}}}\right)\times\left\{\ln\left[\frac{2\sqrt{\tilde\lambda\alpha\alpha'}}{B(1+\alpha)(1+\alpha')}\right]^2+\sqrt{\frac{\tilde\lambda}{\alpha\alpha'}}\right\}$$

at $(k-k')^2\leq2/r^2$, where B means the maximal value of C_2 at $Q=0$, otherwise

$$q^2\geq2\ln\left[\frac{2\sqrt{\tilde\lambda\alpha\alpha'}}{B(1+\alpha)(1+\alpha')}\right]$$

at $(k-k')^2\gg2/r^2$.

4. STATISTICAL DISTRIBUTIONS

From a widely accepted point of view at high energies, there are two channels, at least, for the multiparticle production where produced particles occupy the multiparticle production region consisting of i elementary cells. These main channels are (a) a direct channel, which assumes that all particles p_j are produced directly within quark (q)–antiquark ($\bar q$) annihilation or gauge-boson fusion, e.g., $q\bar q\to p_jp_j\ldots$; (b) an indirect channel, which means that the particles are produced via the decays of intermediate vector bosons χ^* in both heavy and light sectors in the kinematically allowed region, e.g., $q\bar q\to\chi^*\chi^*,\ldots\to p_jp_j,\ldots$. All the produced particles are classified by the like-sign constituents that are labeled as p^+,p^-,p^0 subsystems, where p: $\mu,\pi,K\ldots$. The mean multiplicity $\langle N\rangle$ and the mean energy $\langle E\rangle$ of the p_j subsystem are defined as [5] $\langle N\rangle=\sum_j\sum_{m_j}m_j\zeta_j^{(m_j)}$ and $\langle E\rangle=\sum_j\sum_{m_j}m_j\epsilon_j\zeta_j^{(m_j)}$, where ϵ_j is the energy of a p particle in the jth elementary cell and $\zeta_j^{(m_j)}$ stands for the probability of finding m_j p particles in the jth cell and is normalized as $\sum_{m_j=0}^{\infty}\zeta_j^{(m_j)}=1$. In the direct channel for produced charged mesons, $\langle N\rangle$ is defined uniquely for a given β as

$$\langle N\rangle=2\sum_j[\exp(\epsilon_j\beta)-1]^{-1},$$

while $\langle E\rangle$ looks like

$$\langle E\rangle = \frac{1}{3}\sqrt{s} = \sum_j \frac{\epsilon_j}{\exp(\epsilon_j\beta) - 1}.$$

Going into y-rapidity space in the longitudinal phase space with a lot of cells of equal size δy, the energy ϵ_j should be expressed in terms of the transverse mass $m_t = \sqrt{\langle k_t\rangle^2 + m_p^2}$ ($\langle k_t\rangle$ and m_p are the transverse average momentum and the mass of the p particle):

$$\epsilon_j(s) = \frac{m_t}{2}[g_j(\tilde{s}) + g_j^{-1}(\tilde{s})],\ \tilde{s} = \frac{s}{4m_t^2},$$

$$g_j(\tilde{s}) = (\sqrt{\tilde{s}} + \sqrt{\tilde{s}-1})\exp[-(j-1/2)\delta y].$$

Here, the four-momentum of the p particle is given as

$$k^\mu = \left(\sqrt{\langle k_t\rangle^2 + m_p^2}\cosh y, k_t\cos\varphi, k_t\sin\varphi, \sqrt{\langle k_t\rangle^2 + m_p^2}\sinh y\right),$$

where the azimuthal angle is in the range $0 < \varphi < 2\pi$. Our model produces an enhancement of $C_2(Q,\beta)$ in the sufficiently small region of Q where C_2 is defined only by the model parameters α and α' and the mean multiplicity $\langle N(s)\rangle$ at the fixed value of β, namely, ($\alpha = \alpha'$):

$$C_2(Q,\beta) \simeq \xi(\langle N\rangle)\left\{1 + \frac{\sqrt{\tilde{\lambda}(\bar{\omega},\beta)}}{(1+\alpha)^2}\right. \qquad (11)$$

$$\left.\times\left[\sqrt{\tilde{\lambda}(\bar{\omega},\beta)} + 2\alpha - \left(\sqrt{\tilde{\lambda}(\bar{\omega},\beta)} + \alpha\right)Q^2r^2\right]\right\}.$$

It is clear that the $C_2(Q,\beta)$ function at $Q^2 = 0$,

$$C_2(Q,\beta) \simeq \xi(\langle N(s)\rangle)\left[2 - \left(\frac{\alpha}{1+\alpha}\right)^2\right],$$

cannot exceed 2 because of $\alpha \neq 0$ and $\xi(N(s)) < 1$ even at large multiplicity. The Boltzmann behavior should be realized in the case where $\alpha \to \infty$; i.e., the main contribution to the fluctuating behavior of the $C_2(Q,\beta)$ function should come from the random source contribution [see (9) and (10)]. We have found that the enhancement of the $C_2(Q,\beta)$ function, mainly the shape of this function, strongly depends on the transverse size r_t of the phase space and has a very weak dependence on the δy size of a separate elementary cell. Increasing r_t makes the shape of the $C_2(Q,\beta)$ function more crucial.

Obviously, $\xi(\langle N(s)\rangle)$ is the normalization constant in (8), where $\langle N(s)\rangle$ should be derived at the origin of Q^2 precisely from $C_2(Q=0,\beta) \equiv C_{2_0}(s)$ as $\langle N(s)\rangle \simeq \dfrac{1}{\varepsilon}$, where

$$\varepsilon = 1 - \frac{C_{2_0}(s)}{2 - \left(\dfrac{\alpha}{1+\alpha}\right)^2}$$

can be extracted from the experiment at some chosen value of α ($\alpha = 0$ should be taken into account as well). On the other hand, the $C_2(Q,\beta)$ function allows one to measure $\alpha = \alpha'$ which parameterizes the random source contribution as well as the splitting between α and α'. Neglecting the random source contribution (i.e., setting $\alpha = \alpha' = 0$), we can estimate the chaoticity $\tilde{\lambda}(\bar{\omega},\beta)$ by measuring $C_2(Q,\beta)$ as $Q^2 \to 0$.

In fact, the theoretical prediction that $D(Q,\beta) > 0$ means that, in the multiparticle production region, one should select the single boson "dressing" of some quantum numbers, and the particles near it in the phase space will be "dressed" with the same set of quantum numbers. The amount of such neighboring particles has to be as high as possible. This allows a cell to be formed in the spacetime occupied by the equal-statistics particles only. Such a procedure can be repeated while all the particles occur in the multiparticle production region. This leads to the spacetime distribution of produced particles in the phase-space cells formed only for bosons. In fact, there is no restriction of the number of bosons occupying the chosen elementary cells. It means that the $D(Q,\beta)$ function is defined for all orders.

5. SUMMARY AND DISCUSSION

We investigated the finite temperature BEC of identical particles in multiparticle production using the solutions to the operator field Langevin-type equation in $S(\mathfrak{R}_4)$, the quantum version of the Nyquist theorem, and quantum statistical methods. We presented the crucial role of the model in describing BEC via calculations of the distribution functions as functions of the mean multiplicity and chaoticity at each four-momentum $\sqrt{Q_\mu^2}$. Based on this model, one can compare the effects on single particle spectra and the multiparticle distribution

caused by the multiparticle correlations. There are several parameters in the model: $\beta, \delta y, \alpha(\alpha')$. One can focus on the statement that the deviation of the $D(Q,\beta)$ function from zero at finite values of the physical variables q^2 and the model parameter α indicates that the multiparticle production region should be considered as the phase space consisting of elementary cells (each with the size δy) which are occupied by particles of identical statistics. The Boltzmann behavior of the C_2 function (11) is available only at sufficiently large values of α, which means the leading role of the random source contribution to the distribution function. An important feature of the model is getting information on the spacetime structure of the multiparticle production region. We are able to predict the source size as well as the intercept parameter—the chaoticity λ. We have found that the distribution function $C_2(Q,\beta)$ depends on the number of elementary cells defined by equal size δy in the rapidity y space.

There is no doubt that the best check of any model could be made if various kinds of high-energy experimental data on multiparticle correlations were well reproduced by the model under consideration.

ACKNOWLEDGMENTS

I gratefully acknowledge G. Wilk for a useful discussion concerning the nature of the Bose–Einstein correlation.

REFERENCES

1. R. Hanbury-Brown and R. Q. Twiss, Nature **178**, 1046 (1956).
2. G. Goldhaber *et al.*, Phys. Rev. **120**, 300 (1960).
3. U. A. Wiedemann and U. Heinz, Phys. Rep. **319**, 145 (1999); R. M. Weiner, Phys. Rep. **327**, 249 (2000).
4. J. D. Manjavidze and A. N. Sissakian, Phys. Rep. **346**, 1 (2001).
5. T. Osada, M. Maruyama, and F. Tagaki, Phys. Rev. D **59**, 014024 (1999).
6. O. V. Utyuzh, G. Wilk, and Z. Wlodarczyk, hep-ph/0102275; Phys. Rev. C **64**, 027901 (2001); Phys. Lett. B **522**, 273 (2001).
7. G. A. Kozlov, Phys. Rev. C **58**, 1188 (1998).
8. G. A. Kozlov, J. Math. Phys. **42**, 4749 (2001).
9. G. A. Kozlov, New J. Phys. **4**, 23 (2002).
10. M. Mizutani, S. Muroya, and M. Namiki, Phys. Rev. D **37**, 3033 (1988).
11. N. N. Bogoliubov, A. A. Logunov, A. I. Oksak, and I. T. Todorov, *General Principles of Quantum Field Theory* (Nauka, Moscow, 1987) [in Russian].
12. M. Gelfand and G. E. Shilov, *Generalized Functions* (Acad. Press, New York, 1964), Vol. 1.
13. M. Namiki and S. Muroya, in *Proceedings of RIKEN Symposium on Physics of High Energy Heavy Ion Collisions, 1992,* Ed. by S. Date and S. Ohta (Saitama, Japan), p. 91.

Physics of Atomic Nuclei, Vol. 67, No. 1, 2004, pp. 69–71. From Yadernaya Fizika, Vol. 67, No. 1, 2004, pp. 70–72.

On Correlators for High Multiplicity Events*

J. A. Budagov, Yu. A. Kulchitsky[1)], J. Manjavidze, N. A. Russakovich, and A. N. Sissakian**

Joint Institute for Nuclear Research, Dubna, Moscow oblast, 141980 Russia

Received May 21, 2003

Abstract—We present the results of the study of the energy correlators $K_2(n)$ and $K_3(n)$ and their ratio $R_3(n)$ as a function of the hadron multiplicity at the LHC. The PYTHIA generator has been used. PYTHIA predicts that $R_3(n)$ is not dependent on multiplicity. $K_2(n)$, $K_3(n)$, and the $R_3(n)$ ratio can be studied at ATLAS. © *2004 MAIK "Nauka/Interperiodica".*

The investigation of very high multiplicity (VHM) events is a very important task for high-energy physics [1]. The purpose of this study is to calculate the energy correlators $K_2(n,s)$ and $K_3(n,s)$ and the ratio $R_3(n,s) = |K_3(n,s)|^{2/3}/|K_2(n,s)|$ as a function of hadron multiplicity at ATLAS [2]. The theory predicts that the $R_3(n,s)$ ratio tends to equilibrium for VHM events [1].

We will call very high multiplicity events ones for which the condition $n(s) \gg \bar{n}(s)$ is fulfilled, where n is the number of hadrons in an event, $\bar{n}$ is the mean multiplicity of hadrons, and $\sqrt{s}$ is the c.m.s. energy. Figure 1 shows the distribution of $\langle n\rangle P(n)$, where $P(n) = \sigma_n/\sigma_{\rm tot}$, as a function of the secondary particle multiplicity represented in units of the mean multiplicity. The points are the results of the E735 (FNAL) experiment at 1.8 TeV with $\langle n\rangle = 44$ [3]. The A region corresponds to multiperipheral kinematics where $n \sim \bar{n}(s)$. The B region is the thermodynamical region corresponding to the approximation of the noninteracting gas where $n \to n_{\max}(s)$. The maximum possible number of hadrons is equal to $n_{\max}(s) = \sqrt{s}/m_\pi$, where m_π is the pion mass. The C region corresponds to VHM events. The cross section of such a process is significantly smaller than $10^{-7}\sigma_{\rm tot}$ at 2 TeV. The thermodynamical description of the final-state events in high-energy physics is possible upon fulfillment of the condition of Bogolyubov's principle of vanishing correlators [4]: $R_l(n,s) = |K_l(n,s)|^{2/l}/|K_2(n,s)| \ll 1$, where $l = 3,4,\ldots$, $K_l(n,s)$ is the l-particle energy correlator for the n-particle event. Two- and three-particle correlators are defined as

$$K_2(n,s) = \langle([\varepsilon_1;n,s] - \langle\varepsilon;n,s\rangle)([\varepsilon_2;n,s] - \langle\varepsilon;n,s\rangle)\rangle$$

and

$$K_3(n,s) = \langle([\varepsilon_1;n,s] - \langle\varepsilon;n,s\rangle)([\varepsilon_2;n,s] - \langle\varepsilon;n,s\rangle)([\varepsilon_3;n,s] - \langle\varepsilon;n,s\rangle)\rangle,$$

where ε_i is the energy of the ith particle and $\langle\varepsilon;n,s\rangle$ is the mean energy.

PYTHIA has been used for this investigation [5]. For the simulation of the trigger events, the hard processes have been used: $q_iq_j \to q_iq_j$, $q_i\bar{q}_i \to q_j\bar{q}_j$, $q_i\bar{q}_i \to gg$, $q_ig \to q_ig$, $gg \to q_i\bar{q}_i$, $gg \to gg$, where q are quarks and g are gluons. The main background for the VHM events at the LHC will be the soft processes. There will be $\approx 23pp$ interactions in the 25 ns of one interaction of bunches at the full LHC luminosity (10^{34} cm^{-2} s^{-1}). The time of the data collection will be 125 ns, for example, for the electromagnetic calorimeter. Therefore, about 115 soft background events will be written, which are called "pileup," simultaneously with the trigger event. The inelastic processes have been used for the simulation of pileup events.

Figure 2 (left) shows the results of calculations of the average energy and the correlators $\sqrt{K_2(n)}$ and $\sqrt[3]{K_3(n)}$ on the GeV scale as a function of the hadron multiplicity at 14 TeV. The values of $\sqrt{K_2(n)}$ have signs of $K_2(n)$. As can be seen, $K_2(n)$ and $K_3(n)$ tend to zero at $n_h \to 500$. The dependence of the $R_3(n)$ ratio on n_h is given in Fig. 2 (right). The PYTHIA predictions are given for the A region shown in Fig. 1. The average value of the $R_3(n)$ ratio does not depend on the hadron multiplicity and is equal to 1.23. There is no tendency to equilibrium in this

*This article was submitted by the authors in English.

1)Joint Institute for Nuclear Research, Dubna, Moscow oblast, 141980 Russia, and Institute of Physics, National Academy of Sciences of Belarus, Minsk, Belarus.

**e-mail: Iouri.Koultchitski@cern.ch

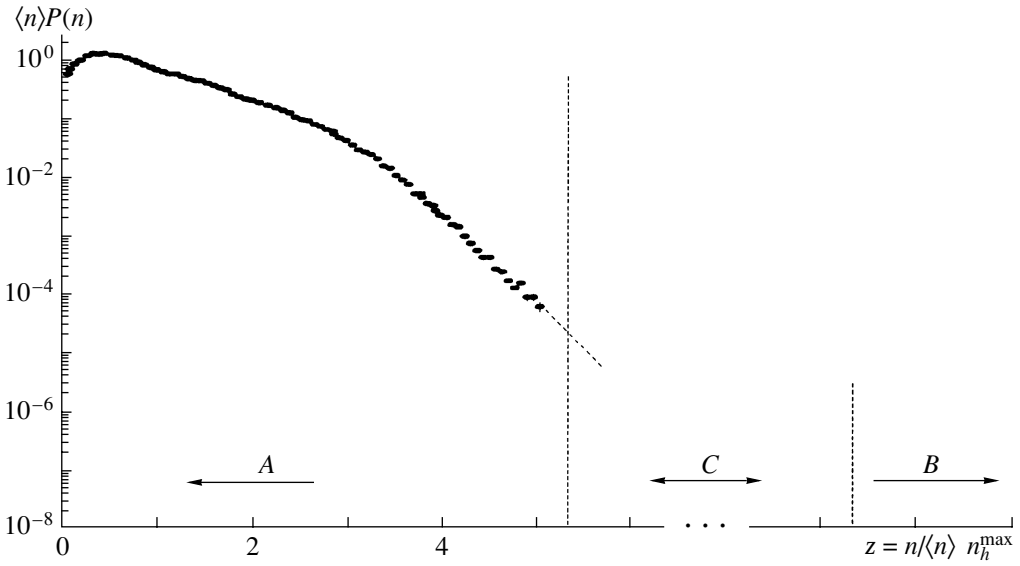

Fig. 1. Multiplicity distribution $\langle n\rangle P(n)$ in the KNO scaling form at 1.8 TeV.

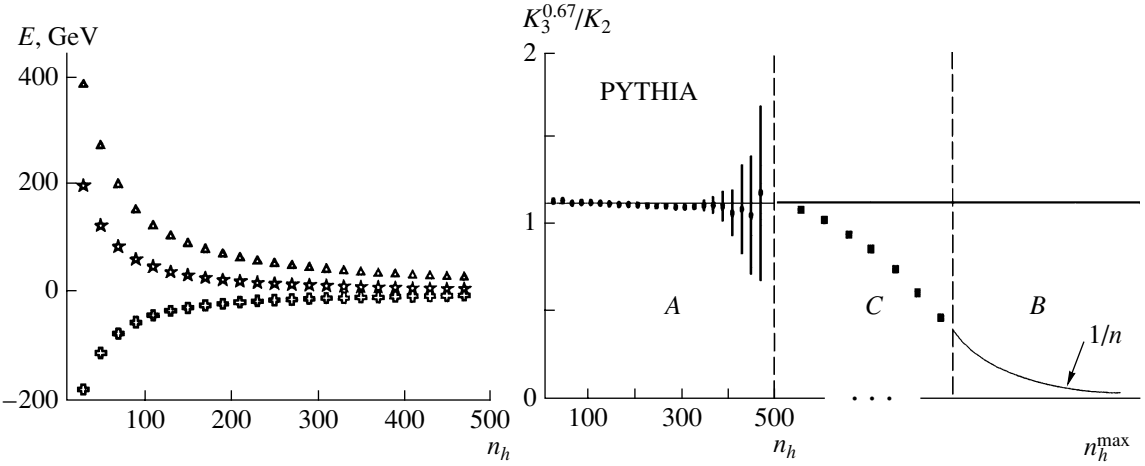

Fig. 2. The average energy (triangles), the correlators $\sqrt{K_2(n)}$ (crosses) and $\sqrt[3]{K_3(n)}$ (stars) on the left side, and the $R_3(n)$ ratio (black circles) on the right side as a function of the multiplicity at 14 TeV. The black squares on the right side are the theory supposition for the very high multiplicity region.

region. This can be understood as PYTHIA is based on the multiperipheral model [1].

Harder events have been selected taking into account the experimental trigger conditions. The requirement on the transverse parton momentum $p_t^q \geq p_t^{q,\min}$ has been used, where $p_t^{q,\min} \geq 500$ GeV. This has led to the multiplicity increasing to ≈ 800. However, no tendency to equilibrium is observed, although the $R_3(n)$ ratio decreases to 1.1 for $p_t^q \geq 2000$ GeV.

The investigation of behavior of the VHM events is planned for ATLAS (LHC) [2] by using its calorimeter [6]. This calorimeter has beautiful energy resolution $\sigma/E = (42\%/\sqrt{E} + 1.8\%) \oplus 1.8/E$ in the barrel region [7]. Only charged particles with transverse momentum more than ≈ 1.5–2 GeV reach the calorimeter because of the strong magnetic field (2 T) of the solenoidal magnet. Therefore, only hadrons with $p_t \geq 2$ GeV in the region $|\eta| \leq 2.5$ have been selected. The physics events satisfying the condition $p_t^q \geq p_t^{q,\min}$ for partons have been simulated for decreasing background pileup events. The obtained distributions of the correlators $K_2(n)$ and $K_3(n)$ as a function of multiplicity taking into account the pileup are similar to the ones shown in Fig. 2 (left). As a result of using the cuts $p_t \geq 2$ GeV and $|\eta| \leq 2.5$, the maximum multiplicity decreases to ≈ 300 hadrons per event. As before, there is no tendency to equi-

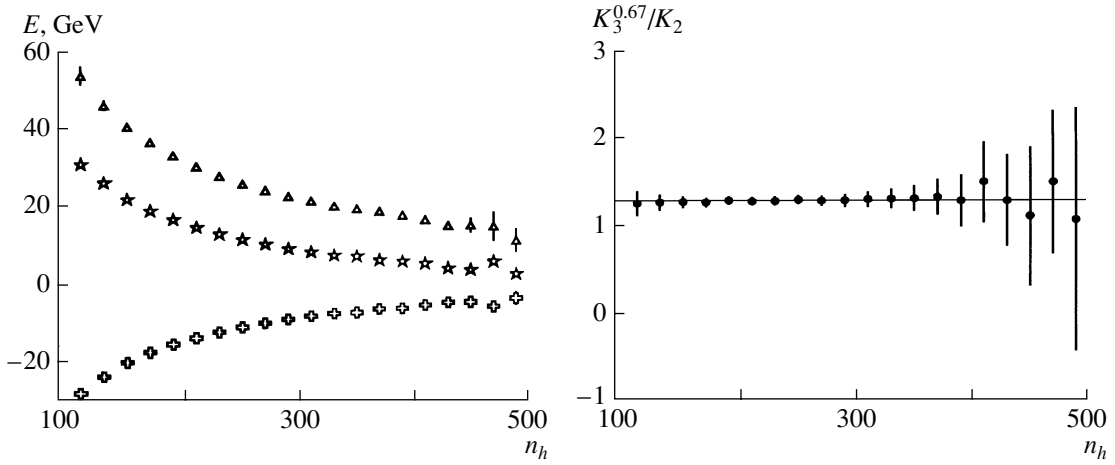

Fig. 3. The average energy (triangles), the correlators $\sqrt{K_2(n)}$ (crosses) and $\sqrt[3]{K_3(n)}$ (stars) on the left side, and the $R_3(n)$ ratio (black circles) on the right side for energies in calorimeter towers as a function of the multiplicity at 14 TeV.

librium for the $R_3(n)$ ratio, $R_3(n) = 1.21$ for $p_t^q \geq 2000$ GeV. It is important to note that it is not necessary to take into account the detector acceptance because the correlations are small and equal for all particles in the VHM region.

Use of calorimetric information is assumed for determining the energy correlators in the ATLAS experiment. There is the projective geometry for calorimeter towers. The initial transverse dimension of a hadronic calorimeter tower is equal to $\eta \times \phi = 0.1 \times 0.1$. The hadronic shower size is larger than one calorimeter tower size [8]. Signals from each tower have been used in the calculations separately. The ATLFAST program [9] has been used for the simulation.

Figure 3 (left) shows the dependence of the average energy and the energy correlators $\sqrt{K_2(n)}$ and $\sqrt[3]{K_3(n)}$ for energy in calorimeter towers as a function of multiplicity of working towers and using the cuts $p_t \geq 1.5$ GeV and $|\eta| \leq 3.5$. The values of the correlators lead to 5 GeV for $n_h \to 500$. The obtained distributions are also similar to the ones shown in Fig. 2 (left). The dependence of the $R_3(n)$ ratio as a function of working towers is shown in Fig. 3 (right). There is no tendency for the $R_3(n)$ ratio to decrease when n_h increases. The value of this ratio is equal to 1.28 and coincides with the above results [Fig. 2 (right)].

The results of the study of the energy correlators $K_2(n)$ and $K_3(n)$ and their ratio $R_3(n)$ as a function of the hadron multiplicity at 14 TeV are presented. It is shown that the value of the ratio does not depend on multiplicity and it is slightly more than unity. Thus, PYTHIA does not predict tendency to equilibrium, $R_3(n) \ll 1$, at high multiplicity. It is shown that the pileup background and the change in the particle energy to the detected ones in the ATLAS calorimeter towers have a negligible effect on $R_3(n)$.

REFERENCES

1. J. Manjavidze and A. Sissakian, Phys. Rep. **346**, 1 (2001).
2. ATLAS Collab., CERN-LHCC-99-014; CERN-LHCC-99-015.
3. T. Alexopoulos *et al.*, Nucl. Phys. A **544**, 343 (1992).
4. N. N. Bogolyubov, *Studies in Statistical Mechanics* (Amsterdam, 1962).
5. T. Sjöstrand *et al.*, Comput. Phys. Commun. **135**, 238 (2001).
6. ATLAS Collab., CERN-LHCC-96-040; CERN-LHCC-96-042.
7. S. Akhmadaliev *et al.*, Nucl. Instrum. Methods Phys. Res. A **449**, 461 (2000).
8. P. Amaral *et al.*, Nucl. Instrum. Methods Phys. Res. A **443**, 51 (2000).
9. E. Richter-Was *et al.*, ATL-PHYS-98-131, CERN (Geneva, 1998).

Physics of Atomic Nuclei, Vol. 67, No. 1, 2004, pp. 72–82. From Yadernaya Fizika, Vol. 67, No. 1, 2004, pp. 73–83.

Correlation Femtoscopy of Multiparticle Processes*

R. Lednický**

Joint Institute for Nuclear Research, Dubna, Moscow oblast, 141980 Russia
Institute of Physics, ASCR, Prague, Czech Republic

Received May 21, 2003

Abstract—Recent results on particle momentum and spin correlations are discussed in view of the role played by the effects of quantum statistics, including multiboson and coherence phenomena, and final-state interaction. Particularly, it is demonstrated that the latter allows for (i) correlation femtoscopy with unlike particles; (ii) study of the relative spacetime asymmetries in the production of different particle species (e.g., relative time delays or spatial shifts due to collective flows); and (iii) study of the particle strong interaction hardly accessible by other means (e.g., in $\Lambda\Lambda$ system). © *2004 MAIK "Nauka/Interperiodica".*

1. INTRODUCTION

The momentum correlations of particles at small relative velocities are widely used to study spacetime characteristics of the production processes, thus serving as a correlation femtoscope. Particularly, for noninteracting identical particles, like photons or, to some extent, pions, these correlations result from the interference of the production amplitudes due to the symmetrization requirement of quantum statistics (QS) [1, 2]. There exists [3] a deep analogy of the momentum QS correlations of photons with the spacetime correlations of the intensities of classical electromagnetic fields used in astronomy to measure the angular radii of stellar objects based on the superposition principle—so-called HBT intensity interferometry [4].[1)]

The momentum QS correlations were first observed as an enhanced production of the pairs of identical pions with small opening angles (GGLP effect [1]). Later on, Kopylov and Podgoretsky [2] settled the basics of correlation femtoscopy; particularly, they suggested studying the interference effect in terms of the correlation function and clarified the role of the spacetime characteristics of particle production in various physical situations.

The momentum correlations of particles emitted at nuclear distances are also influenced by the effect of final-state interaction (FSI) [6–8]. Thus the effect of the Coulomb interaction dominates the correlations of charged particles at very small relative momenta (of the order of the inverse Bohr radius of the two-particle system), respectively suppressing or enhancing the production of particles with like or unlike charges. Though the FSI effect complicates the correlation analysis, it is an important source of information allowing for the coalescence femtoscopy (see, e.g., [9–12]), the correlation femtoscopy with unlike particles [8, 13] including access to the relative spacetime asymmetries in particle production [14] and a study of particle interaction hardly accessible by other means.

We do not touch here the fluctuation measures that are closely related to particle correlations in momentum space and carry important information on the dynamics and spacetime evolution of the production process (see [15] for a recent review).

The rest of the paper is organized as follows. In Section 2, we briefly review the formalism of particle correlations at small relative velocities. The basic concepts of femtoscopy with identical and nonidentical particles, including access to the relative spacetime shifts in the emission of various particle species, and some recent results are reviewed in Sections 3,

*This article was submitted by the author in English.

** e-mail: lednicky@fzu.cz

1)This analogy is sometimes misunderstood and the momentum correlations are mixed up with the spacetime HBT correlations in spite of their orthogonal character and the failure of the superposition principle for correlations of identical fermions. In fact, in spite of the common QS origin of the momentum correlations of identical particles and the spacetime HBT correlations (allowing for a generalization of the latter to any type of identical bosons or fermions), the corresponding correlation measurements differ in principle [3] (see also [5]). The former, being the momentum–energy measurement, yields the spacetime picture of the source, while the latter does the opposite. In particular, the dependence of the number of coincident two-photon counts on the distance between detectors (a quantum analogy of the HBT measurement) provides information on the characteristic relative three-momenta of emitted photons and so, when divided by the mean detected momentum, on the angular size of a star, but, of course, no information on the star radius or lifetime.

5, and 7. In Section 4, we discuss the present theoretical and experimental status of the multiboson and coherence phenomena in multiparticle production. Recent results from correlation measurements of the strong interaction in various two-particle systems are reviewed in Section 6. In Section 8, we briefly discuss spin correlations as a new femtoscopy tool. We conclude in Section 9.

2. FORMALISM

The ideal two-particle correlation function $\mathcal{R}(p_1, p_2)$ is defined as a ratio of the measured two-particle distribution to the reference one which would be observed in the absence of the effects of QS and FSI. In practice, the reference distribution is usually constructed by mixing the particles from different events of a given class, normalizing the correlation function to unity at sufficiently large relative velocities.

Usually, it is assumed that the correlation of two particles emitted with a small relative velocity is influenced by the effects of their mutual QS and FSI only[2)] and that the momentum dependence of the one-particle emission probabilities is inessential when varying the particle four-momenta p_1 and p_2 by an amount characteristic for the correlation due to QS and FSI (smoothness assumption). Clearly, the latter assumption, requiring the components of the mean spacetime distance between particle emitters much larger than those of the spacetime extent of the emitters, is well justified for heavy-ion collisions.

The correlation function is then given by a square of the properly symmetrized Bethe–Salpeter amplitude in the continuous spectrum of the two-particle states, averaged over the four-coordinates $x_i = \{t_i, \mathbf{r}_i\}$ of the emitters and over the total spin S of the two-particle system [8]. After the separation of the unimportant phase factor due to the c.m.s. motion, this amplitude reduces to one depending only on the relative four-coordinate $\Delta x \equiv x_1 - x_2 = \{t, \mathbf{r}\}$ and the generalized relative momentum $\widetilde{q} = q - P(qP)/P^2$, where $q = p_1 - p_2$, $P = p_1 + p_2$, and $qP = {m_1}^2 - {m_2}^2$; in the two-particle c.m.s., $\mathbf{P} = 0$, $\widetilde{q} = \{0, 2\mathbf{k}^*\}$, and $\Delta x = \{t^*, \mathbf{r}^*\}$. At equal emission times of the two particles in their c.m.s. ($t^* \equiv t_1^* - t_2^* = 0$), the reduced nonsymmetrized amplitude coincides with a stationary solution $\psi^{S(+)}_{-\mathbf{k}^*}(\mathbf{r}^*)$ of the scattering problem having, at large distances r^*, the asymptotic form of a superposition of the plane and outgoing spherical waves (the minus sign of the vector $\mathbf{k}^*$ corresponds to the reverse in time direction of the emission process). The Bethe–Salpeter amplitude can usually be replaced by this solution (equal time approximation),[3)] so, for nonidentical particles,

$$\mathcal{R}(p_1, p_2) \doteq \sum_S \widetilde{\rho}_S \langle |\psi^{S(+)}_{-\mathbf{k}^*}(\mathbf{r}^*)|^2 \rangle_S; \qquad (1)$$

for identical particles, the amplitude in Eq. (1) enters in a symmetrized form:

$$\psi^{S(+)}_{-\mathbf{k}^*}(\mathbf{r}^*) \to [\psi^{S(+)}_{-\mathbf{k}^*}(\mathbf{r}^*) + (-1)^S \psi^{S(+)}_{\mathbf{k}^*}(\mathbf{r}^*)]/\sqrt{2}. \qquad (2)$$

The averaging in Eq. (1) is done over the four-coordinates of the emitters at a given total spin S of the two-particles; $\widetilde{\rho}_S$ is the corresponding population probability, $\sum_S \widetilde{\rho}_S = 1$. For unpolarized particles with spins s_1 and s_2, the probability $\widetilde{\rho}_S = (2S + 1)/[(2s_1 + 1)(2s_2 + 1)]$. Generally, the correlation function is sensitive to particle polarization. For example, if two spin-1/2 particles are initially emitted with polarizations $\boldsymbol{\mathcal{P}}_1$ and $\boldsymbol{\mathcal{P}}_2$, then [8]

$$\widetilde{\rho}_0 = (1 - \boldsymbol{\mathcal{P}}_1 \cdot \boldsymbol{\mathcal{P}}_2)/4, \quad \widetilde{\rho}_1 = (3 + \boldsymbol{\mathcal{P}}_1 \cdot \boldsymbol{\mathcal{P}}_2)/4. \qquad (3)$$

3. FEMTOSCOPY WITH IDENTICAL PARTICLES

For identical pions or kaons, the effect of the strong FSI is usually small and the effect of the Coulomb FSI can be in the first approximation simply corrected for (see [17] and references therein). The corrected correlation function is determined by the QS symmetrization only [see Eq. (2) and replace the nonsymmetrized amplitude with the plane wave $\mathrm{e}^{iq\Delta x/2}$]:

$$\mathcal{R}(p_1, p_2) = 1 + \langle \cos(q\Delta x) \rangle. \qquad (4)$$

Its characteristic feature is the presence of the interference maximum at small components of the relative four-momentum q with the width reflecting the inverse spacetime extent of the effective production

[2)] Besides events with large phase-space density fluctuations, this assumption also may not be justified in low-energy heavy-ion reactions when the particles are produced in a strong Coulomb field of residual nuclei. To deal with this field, a quantum adiabatic (factorization) approach can be used [16].

[3)] For noninteracting particles, the nonsymmetrized Bethe–Salpeter amplitude reduces to the plane wave $e^{i\widetilde{q}\Delta x/2} \equiv e^{-i\mathbf{k}^* \cdot \mathbf{r}^*}$, which is independent of the relative time in the two-particle c.m.s. and so coincides with the corresponding equal-time amplitude. For interacting particles, the equal time approximation is valid under the condition [8] $|t^*| \ll m_{2,1} r^{*2}$ for $\mathrm{sgn}(t^*) = \pm 1$, respectively. This condition is usually satisfied for heavy particles like kaons or nucleons. But even for pions, the $t^* = 0$ approximation merely leads to a slight overestimation (typically $< 5\%$) of the strong FSI effect and it doesn't influence the leading zero-distance ($r^* \ll |a|$) effect of the Coulomb FSI.

region. For example, assuming that, for a fraction λ of the pairs, the pions are emitted independently according to one-particle amplitudes of a Gaussian form characterized by the spacetime dispersions r_0^2 and τ_0^2, while, for the remaining fraction $(1-\lambda)$ related to very long-lived sources (η, η', K_s^0, Λ, ...), the relative distances r^* between the emitters in the pair c.m.s. are extremely large, one has

$$\mathcal{R}(p_1,p_2) = 1+\lambda\exp\left(-r_0^2\mathbf{q}^2-\tau_0^2 q_0^2\right) \qquad (5)$$
$$= 1+\lambda\exp\left(-r_0^2\mathbf{q}_T^2-(r_0^2+v^2\tau_0^2)q_L^2\right),$$

where $\mathbf{q}_T$ and q_L are the transverse and longitudinal components of the three-momentum difference $\mathbf{q}$ with respect to the direction of the pair velocity $\mathbf{v} = \mathbf{P}/P_0$. One may see that, due to the on-shell constraint [2] $q_0 = \mathbf{v}\cdot\mathbf{q} \equiv vq_L$ (following from the equality $qP = 0$), strongly correlating the energy difference q_0 with the longitudinal momentum difference q_L, the correlation function at $v\tau_0 > r_0$ depends substantially on the direction of the vector $\mathbf{q}$ even in the case of a spherically symmetric spatial form of the production region.

Note that the on-shell constraint makes the q dependence of the correlation function essentially three-dimensional (particularly, in pair c.m.s., $q\Delta x = -2\mathbf{k}^*\cdot\mathbf{r}^*$) and thus makes impossible a unique Fourier reconstruction of the spacetime characteristics of the emission process. However, within realistic models, the directional and velocity dependence of the correlation function can be used to determine both the duration of the emission and the form of the emission region [2], as well as to reveal the details of the production dynamics (such as collective flows; see, e.g., [18, 19] and the reviews [20, 21]). For this, the correlation functions can be analyzed in terms of the out (x), side (y), and longitudinal (z) components of the relative momentum vector $\mathbf{q} = \{q_x, q_y, q_z\}$ [22, 23]; the out and side denote the transverse, with respect to the reaction axis, components of the vector $\mathbf{q}$; the out direction is parallel to the transverse component of the pair three-momentum. The corresponding correlation widths are usually parametrized in terms of the Gaussian correlation radii R_i,

$$\mathcal{R}(p_1,p_2) = 1+\lambda \qquad (6)$$
$$\times\exp(-R_x^2q_x^2-R_y^2q_y^2-R_z^2q_z^2-R_{xz}^2q_xq_z),$$

and their dependence on pair rapidity and transverse momentum is studied. The form of Eq. (6) assumes azimuthal symmetry of the production process [20, 22]. Generally, e.g., in the case of correlation analysis with respect to the reaction plane, all three cross terms q_iq_j contribute [24].

It is well known that particle correlations at high energies usually measure only a small part of the spacetime emission volume, being only slightly sensitive to its increase related to the fast longitudinal motion of particle sources. In fact, due to limited source decay momenta $p^{(s)}$ of a few hundred MeV/c, the correlated particles with nearby velocities are emitted by almost comoving sources and thus at nearby spacetime points. In other words, the maximal contribution of the relative motion to the correlation radii in the two-particle c.m.s. is limited by the moderate source decay length $\tau p^{(s)}/m$. The dynamical examples are sources-resonances, color strings, or hydrodynamic expansion. To substantially eliminate the effect of the longitudinal motion, the correlations can be analyzed in terms of the invariant variable $q_{\rm inv} \equiv Q = (-\widetilde{q}^2)^{1/2} = 2k^*$ and the components of the momentum difference in pair c.m.s. ($\mathbf{q}^* \equiv \mathbf{Q} = 2\mathbf{k}^*$) or in the longitudinally comoving system (LCMS) [25]. In the LCMS, each pair is emitted transverse to the reaction axis so that the generalized relative momentum $\widetilde{\mathbf{q}}$ coincides with $\mathbf{q}^*$ except for the component $\widetilde{q}_x = \gamma_t q_x^*$, where γ_t is the LCMS Lorentz factor of the pair.

Particularly, in the case of one-dimensional boost invariant expansion, the longitudinal correlation radius in the LCMS reads [19] $R_z \approx (T/m_t)^{1/2}\tau$, where T is the freeze-out temperature, τ is the proper freeze-out time, and m_t is the transverse particle mass. In this model, the side radius measures the transverse radius of the system, while, similar to Eq. (5), the square of the out radius gets an additional contribution $(p_t/m_t)^2\Delta\tau^2$ due to the finite emission duration $\Delta\tau$. The additional transverse expansion leads to a slight modification of the p_t dependence of the longitudinal radius and to a noticeable decrease in the side radius and the spatial part of the out radius with p_t. Since the freeze-out temperature and the transverse flow also determine the shapes of the m_t spectra, the simultaneous analysis of correlations and single-particle spectra for various particle species allows one to disentangle all the freeze-out characteristics (see [20] for a review). It appears that, with increasing energy of heavy-ion collisions from AGS and SPS up to the highest energies at RHIC, the data show rather weak energy dependence [26] and point to a kinetic freeze-out temperature somewhat below the pion mass, a strong transverse flow (with the mean transverse flow velocity at RHIC exceeding half the velocity of light [27]), a short evolution time of 8–10 fm/c, and a very short emission duration of about 2 fm/c. The short evolution and emission duration at RHIC are also supported by the correlation analysis with respect to the reaction plane [28]. The small time scales at RHIC were not expected in transport and hydrodynamic models [29, 30] and may indicate an explosive character of particle production (see, e.g., [31, 32]). In fact, the RHIC data can be

described in the so-called blast wave model [33, 34] assuming a strong three-dimensional expansion with a sharp boundary of the freeze-out density profile in transverse plane. The same model with $\sim 15\%$ lower mean transverse flow velocity is also consistent with the SPS data [35].

4. MULTIBOSON AND COHERENCE EFFECTS

In present and future heavy-ion experiments at SPS, RHIC, and LHC, many hundreds or thousands of pions can be produced per unit rapidity interval. Since pions are bosons, there can be multiboson effects enhancing the production of pions with low relative momenta, thus increasing the pion multiplicities, softening their spectra, and modifying the correlation functions (see [36–38] and references therein). In particular, it was shown [37] that the width of the low-p_t enhancement due to Bose–Einstein (BE) condensation decreases with the system size as $r_0^{-1/2}$ and this narrowing makes easier the identification of this effect among others. For events of approximately fixed multiplicity, the multiboson effects can be triggered by decreasing correlation strength and a dip in the two-pion correlation function at intermediate relative momenta [37, 38].

Though the present data do not point to any spectacular multiboson effects, one can hope to observe new interesting phenomena like boson condensation or speckles in some rare events or in eventually overpopulated kinematic regions with the pion density in six-dimensional phase space, $f = (2\pi)^3 d^6n/d^3\mathbf{p}d^3\mathbf{x}$, of the order of unity. An example is a rapidly expanding system with the entropy much smaller than in the case of total equilibrium. Then a strong transverse flow can lead to rather dense gas of soft pions in the central part of the hydrodynamic tube at the final expansion stage (see, e.g., [39]). Another reason can be the expected formation of a quark–gluon plasma or mixed phase. Due to large gradients of temperature or velocity, the hydrodynamic layer near the boundary with vacuum can decay at a large phase space density and lead to pion speckles even at moderate transverse momenta [40].

In the low-density limit ($f \ll 1$), the mean phase space density at a given momentum $\mathbf{p}$ can be estimated as the mean number of pions interfering with a pion of momentum $\mathbf{p}$ (rapidity y and transverse momentum $\mathbf{p}_t$) and building the BE enhancement in the two-pion correlation function [41, 42]: $\langle f\rangle_{\mathbf{p}} \sim \pi^{3/2} N(\mathbf{p})/V$, where $N(\mathbf{p}) = d^3n/d^3\mathbf{p}$ and $V = r_x r_y r_z$ is the interference volume defined in terms of the outward (r_x), sideward (r_y), and longitudinal (r_z) interferometry radii. Typically, $\langle f\rangle_{\mathbf{p}} \sim 0.1$ for midrapidities and $p_t \sim \langle p_t\rangle$ [41]. The data are also consistent with the phase space density of pions near the local thermal equilibrium [43, 44].

At AGS and SPS energies, the interference volume V seems to scale with dn/dy (see, e.g., [44, 45]), pointing to the freeze-out of pions at a constant phase space density. This trend is, however, questioned by recent STAR data from RHIC, indicating an increase in the freeze-out phase space density with energy (a slight increase in V is not sufficient to balance $\sim 50\%$ increase in dn/dy as compared with SPS) and centrality [46]. Extrapolation of the RHIC phase space density measurements to low transverse momenta predicts $\langle f\rangle_{\mathbf{p}}$ close to unity for central events, suggesting that significant multiboson effects can be present at low p_t at RHIC.

According to lattice Monte Carlo calculations including dynamical fermions, deconfining phase transition leading to a quark–gluon plasma (QGP) phase of matter is accompanied by restoration of chiral symmetry. Subsequent phase transition into the hadronic phase can be revealed, particularly, through substantial delays in particle emission and/or through the coherent component of the pion radiation. This component would be characterized by a narrow Poisson multiplicity distribution, contrary to wide multiplicity fluctuations in the usual BE condensate. The pions in the coherent state may appear from the decay of a quasi-classical pion field (the order parameter of the phase transition), the latter possibly being related to the spontaneous chiral symmetry breaking via the formation of the disoriented chiral condensate (DCC) (see [47] and [48] for a review).

The most plausible mechanism of DCC formation is a fast expansion of hot QGP resulting in a rapid suppression of thermal fluctuations (quenching), which in turn triggers a dramatic amplification of soft pion modes. The detection and study of DCC are expected to provide valuable information about the chiral phase transition and vacuum structure of strong interactions. DCC formation is usually expected to be associated with large event-by-event fluctuations in the ratio of neutral to charged pions in a certain phase-space domain. The search for these fluctuations at CERN SPS has so far resulted in setting only an upper limit on the production of a single DCC domain [49]. The absence of experimental evidence for isospin fluctuations has been, however, recently claimed to be in agreement with a presumably more realistic picture of an "unpolarized" DCC with the Fourier modes of the field randomly oriented in isospin space (instead of being aligned as in the original DCC scheme) [50]. The search for other DCC signatures like low-momentum pion clusters is therefore important. Particularly, one can exploit

the impact of the admixture of coherent radiation on the QS and Coulomb correlations of like and unlike pions [51]. Other possibilities of experimental investigations of BE condensate and DCC phenomena have been discussed, e.g., in [52, 53].

The presence of the coherent pions (or pions emitted in the same quantum state) manifests itself also as a suppression of the BE correlations of two or more identical pions [7, 54–56]. Unfortunately, there are also other reasons leading to the suppression of particle correlations. Besides the experimental effects like finite resolution and particle misidentification (which can be corrected for), presumably the most important one is the contribution of the particles emitted by long-lived sources [57], leading to the appearance of the parameter $\lambda < 1$ in Eqs. (5) and (6). Also, the usual Gaussian parametrizations of the QS correlation functions may be inadequate and lead to $\lambda < 1$ in the presence of sources with moderate but very different spacetime characteristics [57–59].

In principle, the effect of long-lived sources can be eliminated in a combined analysis of two-pion and three-pion correlation functions. The measured quantity is the genuine three-pion correlation normalized with the help of the three two-pion contributions—its intercept measures the chaotic or coherent fraction [60]. The first such measurements have been performed only recently in heavy-ion experiments at CERN SPS [61, 62] and RHIC [63] and in e^+e^- collisions at LEP [64]. The most accurate ones at RHIC and LEP indicate a dominant chaotic fraction, though the systematic errors allow for a substantial coherent component. Some sources of the systematic errors, e.g., the simplified treatment of the two-body Coulomb and strong FSI, can be overcome. However, others, e.g., the approximate (factorization) treatment of the multiparticle FSI or the insufficiently differential analysis of the three-pion correlation function, can hardly be avoided at present computational and experimental possibilities.

5. FEMTOSCOPY WITH UNLIKE PARTICLES

The complicated dynamics of particle production, including resonance decays and particle rescatterings, leads to an essentially non-Gaussian tail of the distribution of the relative distances r^* of the particle emitters in the pair rest frame. Therefore, due to different r^* sensitivity of the QS and strong and Coulomb FSI effects, one has to be careful when analyzing the correlation functions in terms of simple models. Thus, the QS and strong FSI effects are influenced by the r^* tail mainly through the suppression parameter λ already for distances of the order of the inverse q resolution (typically, some tens of fm), while the Coulomb FSI is sensitive to distances as large as the pair Bohr radius $|a|$; for $\pi\pi$, πK, πp, KK, Kp, and pp pairs, $|a| = 387.5$, 248.6, 222.5, 109.6, 83.6, and 57.6 fm, respectively. Clearly, the usual Gaussian parametrizations of the distributions of the components of the distance vector $\mathbf{r}^*$ may lead to inconsistencies in the treatment of QS and FSI effects (the Coulomb FSI contribution requiring larger effective radii). These problems can be at least partially overcome with the help of transport code simulations accounting for the dynamical evolution of the emission process and providing the phase space information required to calculate the QS and FSI effects on the correlation function.

Thus, in a preliminary analysis of the NA49 correlation data from central Pb + Pb 158 A GeV collisions [65, 66], the freeze-out phase space distribution was simulated with the RQMD v. 2.3 code [67]. The correlation functions were calculated using the code of [8], weighting the simulated pairs by squares of the corresponding wave functions. The dependence of the correlation function on the invariant relative momentum $Q = 2k^*$ was then fitted according to the formula [65]

$$\mathcal{R}(Q) = \text{norm} \cdot [\text{purity} \cdot \text{RQMD}(r^* \to \text{scale} \cdot r^*) + (1 - \text{purity})]; \quad (7)$$

to account for a possible mismatch in $\langle r^* \rangle$, the dependence on the r^*-scale parameter was introduced using the quadratic interpolation of the points simulated at three scales chosen at 0.7, 0.8, and 1. The fitted values of the purity parameter are in reasonable agreement with the expected contamination of $\sim 15\%$ from strange particle decays and particle misidentification. The fitted values of the scale parameter indicate that RQMD overestimates the distances r^* by 10–20%. Similar overestimation has also been observed when RQMD predictions are compared with the NA49 data on pp and $\pi^\pm\pi^\pm$ correlations [68–70].

Recently, there appeared data on $p\Lambda$ correlation functions from Au + Au experiment E895 at AGS [71] and Pb + Pb experiment NA49 at SPS CERN [72]. As the Coulomb FSI is absent in the $p\Lambda$ system, one avoids here the problem of its sensitivity to the r^* tail. Also, the absence of the Coulomb suppression of small relative momenta makes this system more sensitive to the radius parameters as compared with pp correlations [73]. In spite of rather large statistical errors, a significant enhancement is seen at low relative momentum, consistent with the known singlet and triplet $p\Lambda$ s-wave scattering lengths. In fact, the fits using the analytical expression for the correlation function (originally derived for the pn system [8]) yield for the AGS data [66] the purity of 0.5 ± 0.2 and the Gaussian radius of 4.5 ± 0.7 fm. For the NA49 data, the fitted parameters are [72] 0.17 ± 0.11 and $2.9 \pm$

0.7 fm. The fitted AGS purity is consistent with the product of the estimated one, while the NA49 purity is about one standard deviation too low. When the NA49 purity is fixed at the estimated value of 0.33, the Gaussian radius increases by about 1 fm and becomes 3.8 ± 0.4 fm [72]. The fitted AGS and NA49 radii are in agreement with the radii of 3–4 fm obtained from pp correlations in heavy-ion collisions at GSI, AGS, and SPS energies.

6. CORRELATION MEASUREMENT OF STRONG INTERACTION

In the case of poor knowledge of the two-particle strong interaction, which is the case for meson–meson, meson–hyperon, or hyperon–hyperon systems,[4)] it can be improved with the help of correlation measurements.

In heavy-ion collisions, the effective radius r_0 of the emission region can be considered much larger than the range of the strong-interaction potential. The FSI contribution is then independent of the actual potential form [75]. At small $Q = 2k^*$, it is determined by the s-wave scattering amplitudes $f^S(k^*)$ [8]. For $|f^S| > r_0$, this contribution is of the order of $|f^S/r_0|^2$ and dominates over the effect of QS. In the opposite case, the sensitivity of the correlation function to the scattering amplitude is determined by the linear term f^S/r_0.

The possibility of a correlation measurement of scattering amplitudes has been demonstrated [66] in a recent analysis of the NA49 $\pi^+\pi^-$ correlation data within the RQMD model. For this, the strong-interaction scale has been introduced (similar to the r^* scale), redefining the original s-wave $\pi^+\pi^-$scattering length $f_0 = 0.232$ fm: $f_0 \to \mathrm{sisca} \cdot f_0$. The fitted parameter $\mathrm{sisca} = 0.63 \pm 0.08$ appears to be significantly lower than unity. Recent BNL data on K_{l4} decays also point to a similar shift ($\sim 20\%$) [76]. These results are in agreement with the two-loop calculation in the chiral perturbation theory with a standard value of the quark condensate [77].

Recently, also the singlet $\Lambda\Lambda$ s-wave scattering length f_0 has been estimated [66, 72] on the basis of fits of the NA49 $\Lambda\Lambda$ data. Using the analytical expression for the correlation function [78] (originally derived for the nn system [8]) and fixing the purity of direct Λ pairs at the estimated value of 0.16 and varying the effective radius r_0 in the acceptable range of several fm, one gets [72], e.g., $f_0 = 2.4 \pm 2.1$ and 3.2 ± 5.7 fm for $r_0 = 2$ and 4 fm, respectively (we use the same sign convention as for meson–meson and meson–baryon systems). Though the fitted results are not very restrictive, they likely exclude the possibility of a large positive singlet scattering length comparable to that of $\sim$20 fm for the two-nucleon system.

Important information also comes from $\Lambda\Lambda$ correlations at LEP [79]. Here, the effective radius r_0 is substantially smaller than the range of the strong interaction potential, so the $\Lambda\Lambda$ correlation function is sensitive to the potential form and requires one to account for waves with orbital angular momentum up to $l \sim 20$ [80]. In [79], the strong interaction has been neglected and the observed decrease of the $\Lambda\Lambda$ correlation function at small Q has been attributed solely to the effect of the QS (Fermi–Dirac) suppression. The correlation function has been fitted by the expression[5)]

$$\mathcal{R} = 1 - \frac{1}{2}\lambda(1 + \boldsymbol{\mathcal{P}}^2)\exp(-r_0^2Q^2), \qquad (8)$$

corresponding to the simple Gaussian distribution of the components of the relative distance vector $\mathbf{r}^*$ characterized by a dispersion $2r_0^2$. The fitted results are, however, unsatisfactory for two reasons [80]: (i) the parameter $\lambda = 1.2 \pm 0.2$ [neglecting in Eq. (8) the $\boldsymbol{\mathcal{P}}^2$ polarization term on a percent level] is significantly higher than the value of ~ 0.5 expected due to the feed-down from Σ^0 and weak decays; (ii) the parameter $r_0 = 0.11 \pm 0.02$ fm appears to be smaller than the string model lower limit of ~ 0.2 fm. Therefore, the observed anticorrelation at small Q can be considered as direct evidence for a repulsive core in the $\Lambda\Lambda$ interaction potential.[6)] In fact, reasonable fits can be achieved using the Nijmegen singlet potential NSC97e [81], rescaling the triplet one from [82], and neglecting spin–orbit and tensor couplings. For example, at a fixed $\lambda = 0.6$, the fitted radius takes an acceptable value $r_0 = 0.29 \pm 0.03$ fm [80].

7. ACCESSING RELATIVE SPACETIME ASYMMETRIES

The correlation function of two nonidentical particles, compared with identical ones, contains a fundamentally new piece of information on the relative

[4)] The $\Lambda\Lambda$ system is of particular interest in view of an experimental indication of the enhanced $\Lambda\Lambda$ production near threshold [74] and its possible connection with the six-quark H dibaryon problem.

[5)] The singlet and triplet contributions to the correlation function $\mathcal{R} = \mathcal{R}_s + \mathcal{R}_t$ are $\mathcal{R}_{s,t} = \widetilde{\rho}_{s,t}[1 \pm \lambda\exp(-r_0^2Q^2)]$, where $\widetilde{\rho}_{s,t}$ depend on the Λ polarization $\mathcal{P}$ according to Eq. (3) with $\boldsymbol{\mathcal{P}}_1 = \boldsymbol{\mathcal{P}}_2 = \boldsymbol{\mathcal{P}}$.

[6)] The repulsive core arises due to the exchange of vector mesons and is present, e.g., in various Nijmegen potentials used for the analysis of the double Λ hypernuclei. The core height and width are about 9 GeV and 0.4 fm, respectively. The s-wave scattering length (effective radius) ranges from about 0.3 (15) to 11 (2) fm.

spacetime asymmetries in particle emission such as mean relative time delays in the emission of various particle species [14]. It can be particularly useful in searches for the effects of the quark–gluon plasma phase transition like delays between the emission of strange and antistrange particles due to the process of strangeness distillation from the mixed phase. Important information is also contained in the spatial part of the asymmetry related, in particular, to the intensity of the collective flow [66].

Since the information on the relative spacetime shifts enters the two-particle wave function through the terms odd in $\mathbf{k}^* \cdot \mathbf{r}^* \equiv \mathbf{p}_1^* \cdot (\mathbf{r}_1^* - \mathbf{r}_2^*)$, it can be accessed by studying the correlation functions $\mathcal{R}_{+i}$ and $\mathcal{R}_{-i}$ with, respectively, positive and negative projection k_i^* of the momentum $\mathbf{k}^* = \mathbf{p}_1^* = -\mathbf{p}_2^*$ onto a given direction i, or the ratio $\mathcal{R}_{+i}/\mathcal{R}_{-i}$. For example, i can be the direction of the pair velocity or any of the out (x), side (y), and longitudinal (z) directions. Note that, in the LCMS system,

$$r_x^* \equiv \Delta x^* = \gamma_t(\Delta x - v_t \Delta t), \qquad (9)$$
$$r_y^* \equiv \Delta y^* = \Delta y, \quad r_z^* \equiv \Delta z^* = \Delta z,$$

where $\gamma_t = (1 - {v_t}^2)^{1/2}$ and $v_t = P_t/P_0$ are the pair LCMS Lorentz factor and velocity. One may see that the asymmetry in the out (x) direction depends on both space and time asymmetries $\langle \Delta x \rangle$ and $\langle \Delta t \rangle$. In the case of a dominant Coulomb FSI, the intercept of the correlation function ratio is directly related to the asymmetry $\langle r_i^* \rangle$ [83, 84] (see also [85]):

$$\mathcal{R}_{+i}/\mathcal{R}_{-i} \approx 1 + 2\langle r_i^* \rangle / a, \qquad (10)$$

where $a = (\mu z_1 z_2 e^2)^{-1}$ is the Bohr radius of the two-particle system taking into account the sign of the interaction ($z_i e$ are the particle electric charges and μ is their reduced mass).

At low energies, the particles in heavy-ion collisions are emitted with characteristic emission times of tens to hundreds of fm/c, so that the observable time shifts should be of the same order [14]. Such shifts have indeed been observed with the help of the $\mathcal{R}_+/\mathcal{R}_-$ correlation ratios for proton–deuteron systems in several heavy-ion experiments at GANIL [86], indicating, in agreement with the coalescence model, that deuterons are on average emitted earlier than protons.

For ultrarelativistic heavy-ion collisions, the sensitivity of the $\mathcal{R}_+/\mathcal{R}_-$ correlation ratio to the relative time shift $\langle \Delta t \rangle$ (introduced ad hoc) was studied for various two-particle systems simulated using transport codes [85]. The scaling of the effect with the spacetime asymmetry and with the inverse Bohr radius a was clearly illustrated. It was concluded that the $\mathcal{R}_+/\mathcal{R}_-$ ratio can be sensitive to shifts in particle emission times of the order of a few fm/c. Motivated by this result, the correlation asymmetry for the K^+K^- system has been studied in a two-phase thermodynamic evolution model and the sensitivity to the production of the transient strange quark-matter state has been demonstrated even if it decays on strong-interaction time scales [87]. The method's sensitivity to the spacetime asymmetries arising also in the usual multiparticle production scenarios was demonstrated for AGS and SPS energies using the transport code RQMD [65, 83, 84]. At AGS energy, Au + Au collisions have been simulated and πp correlations have been studied in the projectile fragmentation region where proton directed flow is most pronounced and where the proton and pion sources are expected to be shifted relative to each other both in the longitudinal and in the transverse directions in the reaction plane. It was shown [84] that the corresponding $\mathcal{R}_+/\mathcal{R}_-$ ratios are sufficiently sensitive to reveal the shifts; they were confirmed in the directional analysis of the experimental AGS correlation data [88].

At SPS energy, the simulated central Pb + Pb collisions yield practically zero asymmetries for the $\pi^+\pi^-$ system, while, for $\pi^\pm p$ systems, the LCMS asymmetries are $\langle \Delta x \rangle = -6.2$ fm, $\langle \Delta y \rangle = \langle \Delta z \rangle = 0$, $\langle \Delta t \rangle = -0.5$ fm/c, and $\langle \Delta x^* \rangle = -7.9$ fm in the symmetric midrapidity window[7] [83] and $\langle \Delta x \rangle = -5.2$ fm, $\langle \Delta y \rangle = 0$, $\langle \Delta z \rangle = -6.5$ fm, $\langle \Delta t \rangle = 2.9$ fm/c, and $\langle \Delta x^* \rangle = -8.5$ fm for the NA49 acceptance (shifting the rapidities into the forward hemisphere) [65]. In addition, $\langle x \rangle$ increases with particle p_t or $u_t = p_t/m$ starting from zero due to kinematic reasons. The asymmetry arises because of a faster increase with u_t for heavier particles. The nonzero positive value of $\langle x \rangle = \langle \mathbf{r}_t \hat{\mathbf{x}} \rangle$ ($\hat{\mathbf{x}} = \mathbf{p}_t/p_t$ and $\mathbf{r}_t$ is the transverse radius vector of the emitter) along with the hierarchy $\langle x_\pi \rangle < \langle x_K \rangle < \langle x_p \rangle$ is a signal of a universal transversal collective flow [65, 66]. To see this, one should simply take into account that the thermal transverse velocity β_T is smaller for heavier particles and thus washes out the positive shift due to the transversal collective flow velocity β_F to a lesser extent. More explicitly, in the nonrelativistic approximation, the transverse velocity $\boldsymbol{\beta}_t = \boldsymbol{\beta}_F + \boldsymbol{\beta}_T$; in the out-side decomposition, $\boldsymbol{\beta}_t = \beta_t\{1, 0\}$, $\boldsymbol{\beta}_F = \beta_F\{\cos\phi_r, \sin\phi_r\}$, and $\boldsymbol{\beta}_T = \beta_T\{\cos\phi_T, \sin\phi_T\}$. Due to the azimuthal symmetry, the angles ϕ_r and ϕ_T are uniformly distributed, and the vector of the transversal collective flow velocity $\boldsymbol{\beta}_F$ is parallel to the transverse radius vector $\mathbf{r}_t = r_t\{\cos\phi_r, \sin\phi_r\}$ and its magnitude depends only on r_t: $\boldsymbol{\beta}_F = \boldsymbol{\beta}_F(r_t)$. To

[7] $\langle \Delta y \rangle = 0$ due to the azimuthal symmetry and $\langle \Delta z \rangle = 0$ in a symmetric midrapidity window due to the symmetry of the initial system.

calculate $\langle x\rangle$, one has to average over four variables r_t, ϕ_r, β_T, and ϕ_T. At a fixed transverse velocity vector $\boldsymbol{\beta}_t$, only two of them (e.g., r_t, ϕ_r or r_t, β_T) are independent. In particular, $\beta_T^2 = \beta_t^2 + \beta_F^2 - 2\beta_t\beta_F\cos\phi_r$, so the destructive effect of the thermal velocity β_T on the out shift is clearly seen:

$$\langle x\rangle = \langle r_t\cos\phi_r\rangle = \left\langle r_t\frac{\beta_t^2+\beta_F^2-\beta_T^2}{2\beta_t\beta_F}\right\rangle. \qquad (11)$$

The maximal out shift $\langle x\rangle_{\max} = \langle r_t\rangle$ corresponds to zero thermal velocity. The shift vanishes when the width of the contributing interval $|\beta_t - \beta_F| \le \beta_T \le \beta_t + \beta_F$ becomes negligible compared with the characteristic width of the thermal distribution, e.g., at $\beta_t \to 0$ or $\beta_F \to 0$, or for very light particles; the angle ϕ_r is then decorrelated from β_T and so distributed uniformly in the full angular interval $(-\pi, \pi)$.[8] As a result, in the case of a locally equilibrated expansion process, one expects a negative asymmetry $\langle\Delta x\rangle \equiv \langle x_1 - x_2\rangle$ provided $m_1 < m_2$. Moreover, this asymmetry vanishes in both limiting cases: $\beta_F \ll \beta_T$ and $\beta_F \gg \beta_T$.

These conclusions agree with the calculations in the longitudinal-boost invariant hydrodynamic model. Thus, assuming a linear nonrelativistic transversal flow velocity profile $\beta_F = \beta_0 r_t/r_0$, the local thermal momentum distribution characterized by the kinetic freeze-out temperature T, and the Gaussian density profile $\exp(-r_t^2/(2r_0^2))$, one confirms a faster rise of $\langle x\rangle$ with β_t for heavier particles {see the nonrelativistic limit of Eq. (30) in [89]}:

$$\langle x\rangle = r_0\frac{\beta_t\beta_0}{\beta_0^2 + T/m_t}. \qquad (12)$$

The maximal magnitude of the asymmetry $\langle x_1 - x_2\rangle$ at $\beta_{1t} = \beta_{2t} = v_t$ is achieved for an optimal value of the flow parameter $\beta_0 = T/(m_{1t}m_{2t})^{1/2} = T/(\gamma_t^2 m_1 m_2)^{1/2}$; e.g., for πp pairs at $v_t = 0.6$ (close to a mean LCMS velocity of low-Q πp pairs in the NA49 experiment at SPS [65]) and $T = 120$ MeV, the optimal value $\beta_0 = 0.27$. The SPS data on particle spectra and interferometry radii in central Pb + Pb collisions at 158 A GeV are consistent with the parameters $\beta_0 \approx 0.35$, $r_0 \approx 6$ fm, and $T \approx 120$ MeV with uncertainties of 10–20% [20, 35, 90]. The corresponding out asymmetry for πp pairs $\langle\Delta x\rangle = \langle x_\pi - x_p\rangle \approx -4$ fm at $v_t = 0.6$. As for the longitudinal and time shifts, in the longitudinal-boost invariant hydrodynamic model, $z = \tau\sinh\eta$ and $t = \tau\cosh\eta$, where τ is the proper freeze-out time and η is the emitter rapidity. At a given p_t, the LCMS η distribution of the contributing emitters is given by the thermal law $\exp(-m_t\cosh\eta/T)$. Being symmetric, it predicts vanishing longitudinal shift: $\langle z\rangle = \langle\tau\sinh\eta\rangle = 0$. To estimate the time shift, for $m_t > T$, one can write $\cosh\eta \approx 1 + \eta^2/2$ and get $\langle t\rangle \approx \tau\left(1 + \frac{1}{2}T/m_t\right)$.[9] For central Pb + Pb collisions at SPS, $\tau \sim 8$ fm/c and the relative time shift $\langle\Delta t\rangle = \langle t_\pi - t_p\rangle \approx 3$ fm/c. This shift is about the same as predicted by RQMD for the asymmetric NA49 rapidity acceptance. The magnitude of the relative out shift in the pair rest frame (determining the observable asymmetry), $\langle\Delta x^*\rangle \approx -7$ fm, is, however, lower than in RQMD due to $\sim 20\%$ lower magnitude of $\langle\Delta x\rangle$.

In fact, the NA49 data on the $\mathcal{R}_{+x}/\mathcal{R}_{-x}$ ratio for π^+p and π^-p systems show consistent mirror symmetric deviations from unity, their size of several percent, and the Q dependence being in agreement with RQMD calculations corrected for the resolution and purity [66, 70, 72]. A similar pattern of correlation asymmetries has been reported also for $\pi^\pm K^\pm$ and $\pi^\pm K^\mp$ systems in the STAR experiment at RHIC. They seem to be in agreement with hydrodynamic-type calculations with a stronger transverse flow than at SPS and a boxlike density profile (blast wave), and somewhat lower than RQMD predictions [34, 46].

The finite widths of particle rapidity distributions require, however, a violation of the boost invariance. It can be parametrized by a Gaussian dispersion $\Delta\eta^2$ of the LCMS η distribution centered at $-Y$, where Y is the CMS pair rapidity; e.g., the data on central Pb + Pb collisions at 158 A GeV are consistent with $\Delta\eta = 1.3$ [20]. As a result,

$$\langle z\rangle \approx -\tau Y(1 + \Delta\eta^2 m_t/T)^{-1} \qquad (13)$$

and $\langle t\rangle$ acquires a Y-dependent contribution $\frac{1}{2}\tau Y^2(1 + \Delta\eta^2 m_t/T)^{-2}$. For the asymmetric NA49 rapidity acceptance, the mean πp pair rapidity $Y \sim 1.5$, $\langle z_\pi - z_p\rangle \approx -2.8$ fm, and the πp time shift at $Y = 0$ is increased by ~ 0.7 fm/c. This is in qualitative agreement with the RQMD predictions for the rapidity dependence of the longitudinal and time shifts. The magnitude of the Y-dependent shifts in the hydrodynamic model is, however, substantially smaller. In addition, the LCMS emission times in RQMD are a factor of 2–3 larger and show substantial dependence on the transverse velocity [65]. These differences may

[8] Note that, irrespective of the thermal width, the side shift $\langle y\rangle = \langle r_t\sin\phi_r\rangle = 0$, since, due to azimuthal symmetry, the angles ϕ_r and $-\phi_r$ contribute with the same weights.

[9] One also recovers the expression for the LCMS interferometry longitudinal radius squared [19]: $R_z^2 = \langle(z - \langle z\rangle)^2\rangle \approx \tau^2 T/m_t$ up to a relative correction $\mathcal{O}(T/m_t)$.

point to the oversimplified spacetime evolution picture in the hydrodynamic model. Particularly, the neglect of the r_t dependence of the proper freeze-out time and of the longitudinal acceleration during the evolution may not be justified [20, 89].

8. SPIN CORRELATIONS

Information on the system size and the two-particle interaction can also be acquired with the help of spin correlation measurements using as a spin analyzer the asymmetric (weak) particle decay [65, 91, 92]. Since this technique requires no construction of the uncorrelated reference sample, it can serve as an important consistency check of the standard correlation measurements. Particularly, for two Λ particles decaying into the $p\pi^-$ channel characterized by the asymmetry parameter $\alpha = 0.642$, the distribution of the cosine of the relative angle θ between the directions of the decay protons in the respective Λ rest frames allows one to determine the triplet fraction $\rho_t = \mathcal{R}_t/\mathcal{R}$, where $\mathcal{R}_t$ is the triplet part of the correlation function [see the footnote in connection with Eq. (8)]:

$$dN/d\cos\theta = \frac{1}{2}\left[1 + \alpha^2\left(\frac{4}{3}\rho_t - 1\right)\cos\theta\right]. \quad (14)$$

Both correlation and spin composition measurements were recently performed for two-Λ systems produced in multihadronic Z^0 decays at LEP [79, 93]. Except for a suppression at $Q < 2$ GeV/c, the triplet fraction ρ_t was found to be consistent with the value 0.75, as expected from a statistical spin mixture. Such a suppression, as well as similar suppression of the usual correlation function, is expected due to the effects of QS and a repulsive potential core and points to a small correlation radius $r_0 < 0.5$ fm [80].

The spin correlations also allow for a relatively simple test of the quantum-mechanical coherence, based on Bell-type inequalities derived from the assumption of the factorizability of the two-particle density matrix, i.e., its reduction to a sum of the direct products of one-particle density matrices with the nonnegative coefficients [92]. Clearly, such a form of the density matrix corresponds to a classical probabilistic description and cannot account for the coherent quantum-mechanical effects, particularly, for the production of two Λ particles in a singlet state. Thus, the suppression of the triplet $\Lambda\Lambda$ fraction observed in multihadronic Z^0 decays at LEP indicates a violation of one of the Bell-type inequalities $\rho_t \geq 1/2$.

9. CONCLUSION

Thanks to the effects of quantum statistics and final-state interaction, the particle momentum and, recently, also spin correlations give unique information on the spacetime production characteristics and the collective phenomena like multiboson and coherence effects and collective flows. Besides the flow signals from single-particle spectra and like-meson interferometry, rather direct evidence for a strong transverse flow in heavy-ion collisions at SPS and RHIC comes from unlike particle correlation asymmetries. Being sensitive to relative time delays and collective flows, the correlation asymmetries can be especially useful to study the effects of the quark–gluon plasma phase transition. The correlations also yield valuable information on the particle strong interaction hardly accessible by other means.

ACKNOWLEDGMENTS

This work was supported by grant no. 202/01/0779 of the Grant Agency of the Czech Republic.

REFERENCES

1. G. Goldhaber *et al.*, Phys. Rev. **120**, 300 (1960).
2. G. I. Kopylov and M. I. Podgoretsky, Yad. Fiz. **15**, 392 (1972) [Sov. J. Nucl. Phys. **15**, 219 (1972)]; G. I. Kopylov, Phys. Lett. **50**, 472 (1974); M. I. Podgoretsky, Fiz. Élem. Chastits At. Yadra **20**, 628 (1989) [Sov. J. Part. Nucl. **20**, 266 (1989)].
3. G. I. Kopylov and M. I. Podgoretsky, Zh. Éksp. Teor. Fiz. **69**, 414 (1975) [Sov. Phys. JETP **42**, 211 (1975)].
4. R. Hanbury-Brown and R. Q. Twiss, Philos. Mag. **45**, 663 (1954); Nature **178**, 1046 (1956).
5. V. L. Lyuboshitz, in *Proceedings of CRIS'98, Acicastello, 1998*, p. 213.
6. S. E. Koonin, Phys. Lett. B **70B**, 43 (1977).
7. M. Gyulassy, S. K. Kauffmann, and L. W. Wilson, Phys. Rev. C **20**, 2267 (1979).
8. R. Lednicky and V. L. Lyuboshitz, Sov. J. Nucl. Phys. **35**, 770 (1982); in *Proceedings of Corinne Workshop, Nantes, France, 1990*, Ed. by D. Ardouin (World Sci., Singapore, 1990), p. 42; Heavy Ion Phys. **3**, 93 (1996).
9. H. Sato and K. Yazaki, Phys. Lett. B **98B**, 153 (1981).
10. V. L. Lyuboshits, Yad. Fiz. **48**, 1501 (1988) [Sov. J. Nucl. Phys. **48**, 956 (1988)].
11. S. Mrowczynski, Phys. Lett. B **277**, 43 (1992); **308**, 216 (1993).
12. R. Scheibl and U. Heinz, Phys. Rev. C **59**, 1585 (1999).
13. D. H. Boal and J. C. Shillcock, Phys. Rev. C **33**, 549 (1986); D. H. Boal, C.-K. Gelbke, and B. K. Jennings, Rev. Mod. Phys. **62**, 553 (1990).
14. R. Lednicky *et al.*, Phys. Lett. B **373**, 30 (1996); Report SUBATECH-94-22, Nantes, 1994.
15. S. Jeon and V. Koch, hep-ph/0304012.

16. B. Erazmus *et al.*, Nucl. Phys. A **583**, 395 (1995); L. Martin *et al.*, Nucl. Phys. A **604**, 69 (1996); R. Lednicky, Nukleonika **43**, 345 (1998).
17. Yu. M. Sinyukov *et al.*, Phys. Lett. B **432**, 248 (1998).
18. S. Pratt, Phys. Rev. Lett. **53**, 1219 (1984); Phys. Rev. D **33**, 1314 (1986); S. Pratt, T. Csörgö, and J. Zimanyi, Phys. Rev. C **42**, 2646 (1990).
19. A. N. Makhlin and Yu. M. Sinyukov, Yad. Fiz. **46**, 637 (1987) [Sov. J. Nucl. Phys. **46**, 354 (1987)]; Z. Phys. C **39**, 69 (1988); Yu. M. Sinyukov, Nucl. Phys. A **498**, 151c (1989).
20. U. A. Wiedemann and U. Heinz, Phys. Rep. **319**, 145 (1999).
21. T. Csörgö, Heavy Ion Phys. **15**, 1 (2002).
22. M. I. Podgoretskii, Yad. Fiz. **37**, 455 (1983) [Sov. J. Nucl. Phys. **37**, 272 (1983)]; R. Lednicky, Report No. B2-3-11460, JINR (Dubna, 1978).
23. G. F. Bertsch, P. Danielewicz, and M. Herrmann, Phys. Rev. C **49**, 442 (1994); S. Pratt, in *Proceedings on Quark Gluon Plasma 2*, Ed. by R. C. Hwa (World Sci., Singapore, 1995), p. 700; S. Chapman, P. Scotto, and U. Heinz, Phys. Rev. Lett. **74**, 4400 (1995).
24. U. A. Wiedemann, Phys. Rev. C **57**, 266 (1998).
25. T. Csörgö and S. Pratt, in *Proceedings of the Workshop on Heavy Ion Physics*, KFKI-1991-28/A, p. 75.
26. C. Adler *et al.* (STAR Collab.), Phys. Rev. Lett. **87**, 082301 (2001).
27. N. Xu and M. Kaneta, Nucl. Phys. A **698**, 306c (2002).
28. M. Lisa *et al.* (STAR Collab.), in *Proceedings of XXXII ISMD'02*; nucl-ex/0301005.
29. S. Soff, S. A. Bass, and A. Dumitru, Phys. Rev. Lett. **86**, 3981 (2001).
30. U. Heinz and P. Kolb, Nucl. Phys. A **702**, 269 (2002).
31. T. Csörgö and L. P. Csernai, Phys. Lett. B **333**, 494 (1994).
32. A. Dumitru and R. D. Pisarski, Nucl. Phys. A **698**, 444 (2002).
33. C. Adler *et al.* (STAR Collab.), Phys. Rev. Lett. **87**, 182301 (2001).
34. F. Retiere *et al.* (STAR Collab.), in *Proceedings of CIPPQG'01, Palaiseau*; nucl-ex/0111013; Nucl. Phys. A **715**, 591c (2003).
35. B. Tomasik, U. A. Wiedemann, and U. Heinz, nucl-th/9907096; U. A. Wiedemann, Nucl. Phys. A **661**, 65c (1999).
36. S. Pratt, Phys. Lett. B **301**, 159 (1993); Phys. Rev. C **50**, 469 (1994).
37. R. Lednicky *et al.*, Phys. Rev. C **61**, 034901 (2000).
38. U. Heinz, P. Scotto, and Q. H. Zhang, Ann. Phys. (N.Y.) **288**, 325 (2001).
39. S. V. Akkelin and Yu. M. Sinyukov, Phys. Lett. B **356**, 525 (1995).
40. Yu. M. Sinyukov, B. Lorstad, and V. A. Averchenkov, Z. Phys. C **49**, 417 (1991).
41. G. F. Bertsch, Phys. Rev. Lett. **72**, 2349 (1994).
42. Yu. M. Sinyukov and B. Lorstad, Z. Phys. C **61**, 587 (1994).
43. J. Barrette *et al.* (E877 Collab.), Phys. Rev. Lett. **78**, 2916 (1997).
44. D. Ferenc *et al.*, Nucl. Phys. A **661**, 374c (1999); Phys. Lett. B **457**, 347 (1999).
45. M. Gazdzicki, Nucl. Phys. A **590**, 197c (1995).
46. R. L. Ray *et al.* (STAR Collab.), Nucl. Phys. A **715**, 45c (2003).
47. J. D. Bjorken, Acta Phys. Pol. B **23**, 637 (1992); **28**, 2773 (1997); G. Amelino-Camelia, J. D. Bjorken, and S. E. Larsson, Phys. Rev. D **56**, 6942 (1997).
48. J. P. Blaizot and A. Krzywicki, Acta Phys. Pol. B **27**, 1687 (1996).
49. M. Aggarwal *et al.* (WA98 Collab.), Phys. Lett. B **420**, 169 (1998).
50. J. Serreau, hep-ph/0304011.
51. S. V. Akkelin, R. Lednicky, and Yu. M. Sinyukov, Phys. Rev. C **65**, 064904 (2002).
52. S. V. Akkelin and Yu. M. Sinyukov, Nucl. Phys. A **661**, 613c (1999).
53. A. Bialas and K. Zalewski, Phys. Rev. D **59**, 097502 (1999).
54. G. N. Fowler and R. M. Weiner, Phys. Lett. B **70B**, 201 (1977); Phys. Rev. D **17**, 3118 (1978).
55. R. Lednicky, V. L. Lyuboshitz, and M. I. Podgoretsky, Yad. Fiz. **38**, 251 (1983) [Sov. J. Nucl. Phys. **38**, 147 (1983)].
56. V. L. Lyuboshitz, Yad. Fiz. **53**, 823 (1991) [Sov. J. Nucl. Phys. **53**, 514 (1991)].
57. R. Lednicky and M. I. Podgoretsky, Yad. Fiz. **30**, 837 (1979) [Sov. J. Nucl. Phys. **30**, 432 (1979)].
58. R. Lednicky and T. B. Progulova, Z. Phys. C **55**, 295 (1992).
59. T. Csörgö, B. Lorstadt, and J. Zimanyi, Z. Phys. C **71**, 491 (1996).
60. U. Heinz and Q. H. Zhang, Phys. Rev. C **56**, 426 (1997).
61. I. G. Bearden *et al.* (NA44 Collab.), Phys. Lett. B **455**, 77 (1999).
62. M. Aggarwal *et al.* (WA98 Collab.), Phys. Rev. Lett. **85**, 2895 (2000).
63. R. L. Willson *et al.* (STAR Collab.), Nucl. Phys. A **715**, 619c (2003).
64. P. Achard *et al.* (L3 Collab.), Phys. Lett. B **540**, 185 (2002).
65. R. Lednicky, NA49 Note 210, CERN (1999).
66. R. Lednicky, in *Proceedings of CIPPQG'01, Palaiseau, France*; nucl-th/0112011; in *Proceedings of XXXII ISMD'02, Alushta, Ukraine*; nucl-th/0212089.
67. H. Sorge *et al.*, Phys. Lett. B **243**, 7 (1990).
68. H. Appelshauser *et al.* (NA49 Collab.), Phys. Lett. B **467**, 21 (1999).
69. R. Ganz *et al.* (NA49 Collab.), Nucl. Phys. A **661**, 498 (1999).
70. P. Seyboth *et al.* (NA49 Collab.), Nucl. Phys. B (Proc. Suppl.) **92**, 7 (2001).
71. M. Lisa *et al.* (E895 Collab.), Nucl. Phys. A **698**, 185 (2002).
72. Ch. Blume *et al.* (NA49 Collab.), Nucl. Phys. A **715**, 55c (2003).

73. F. Wang and S. Pratt, Phys. Rev. Lett. **83**, 3138 (1999).
74. J. K. Ahn *et al.*, Phys. Lett. B **444**, 267 (1998).
75. M. Gmitro *et al.*, Czech. J. Phys. B **36**, 1281 (1986).
76. S. Pislak *et al.*, Phys. Rev. Lett. **87**, 221801 (2001).
77. G. Colangelo, J. Gasser, and H. Leutwyler, Phys. Lett. B **488**, 261 (2000).
78. R. Lednicky, Report No. 99-10, PhE (Munich, 1999).
79. ALEPH Collab., Phys. Lett. B **475**, 395 (2000).
80. R. Lednicky, *Poster QM'02, Nantes, France*.
81. I. N. Filinkin and A. Gal, Nucl. Phys. A **707**, 491 (2002).
82. E. Hiyama *et al.*, nucl-th/0204059.
83. R. Lednicky, S. Panitkin, and N. Xu, nucl-th/0304062; R. Lednicky, in *Proceedings on Correlations and Fluctuations'98, Matrahaza*, p. 148; nucl-th/0304063; in *Proceedings on Hadron Structure'98, Stara Lesna*, p. 293; nucl-th/0304064.
84. S. Voloshin *et al.*, Phys. Rev. Lett. **79**, 4766 (1997).
85. B. Erazmus *et al.*, CERN Note ALICE-INT-1995-43; R. Lednicky, Nukleonika **43**, 345 (1998).
86. C. Ghisalberti, PhD Thesis (Nantes, 1996); D. Nouais, PhD Thesis (Nantes, 1996); D. Gourio, PhD Thesis (Nantes, 1996).
87. S. Soff *et al.*, J. Phys. G **12**, 2095 (1997); D. Ardouin *et al.*, Phys. Lett. B **446**, 191 (1999).
88. D. Miskowiec *et al.* (E877 Collab.), in *Proceedings of CRIS'98, Acicastello*; nucl-ex/9808003.
89. S. V. Akkelin and Yu. M. Sinyukov, Z. Phys. C **72**, 501 (1996).
90. S. V. Akkelin, P. Braun-Munzinger, and Yu. M. Sinyukov, Nucl. Phys. A **710**, 439 (2002).
91. G. Alexander and H. J. Lipkin, Phys. Lett. B **352**, 162 (1995).
92. R. Lednicky and V. L. Lyuboshitz, Phys. Lett. B **508**, 146 (2001).
93. OPAL Collab., Phys. Lett. B **384**, 377 (1996); DELPHI Collab., in *Proceedings of ICHEP'98, Vancouver, 1998*, Ref. No. 154.

Physics of Atomic Nuclei, Vol. 67, No. 1, 2004, pp. 83–89. From Yadernaya Fizika, Vol. 67, No. 1, 2004, pp. 84–89.

VERY HIGH MULTIPLICITY PHYSICS

Leading Logarithmic Approximation in QCD*

L. N. Lipatov**

Petersburg Nuclear Physics Institute, Gatchina, 188350 Russia

Received April 30, 2003

Abstract—The leading logarithmic approximation (LLA) for the scattering amplitudes in QCD is reviewed. The double-logarithmic asymptotics of scattering amplitudes is obtained as a solution to nonlinear evolution equations in the infrared cutoff. The DGLAP equation describes an evolution of parton distributions with increasing parton virtuality. The evolution of the amplitudes with respect to the scale in the longitudinal subspace is given by the BFKL equation. The gluon and quarks in QCD lie on the Regge trajectories calculable in perturbation theory. Mesons and baryons are composite states of Reggeized quarks. Similarly the Pomeron and Odderon are colorless ground states of Reggeized gluons. In the case of multicolor QCD, the Reggeon field theory in LLA is completely integrable. The Reggeon interactions in QCD are derived from a gauge-invariant effective action. In particular, next-to-leading corrections to the BFKL equation in QCD and in supersymmetric gauge models are obtained in this way.

EQUATIONS FOR THE AMPLITUDES WITH INFRARED AND ULTRAVIOLET CUTOFFS

Both DGLAP [1] and BFKL [2] equations are used now to describe an experimentally observed growth of partonic distributions at small x. The small-x asymptotics of structure functions is related to the behavior of scattering amplitudes in the Regge limit of large energies $\sqrt{s} \sim 1/x$ and fixed momentum transfers $\sqrt{-t}$. In the leading logarithmic approximation (LLA), the high-energy scattering amplitude is obtained by summing the asymptotic contributions of the Feynman diagrams in all orders of perturbation theory.

In the case of double-logarithmic asymptotics (DLA), we have

$$A(s,t) = \sum_{k=0}^{\infty} c_k(t)(g^2 \ln^2 s)^k. \qquad (1)$$

The simplest example of DLA is the Sudakov form factor of the quark

$$\Gamma(q^2) = \exp\left(-\frac{g^2}{12\pi^2}\ln^2(q^2/m^2)\right).$$

Due to the asymptotic freedom in QCD, one can verify the predictions of LLA in the region where the effective coupling constant g is small for fixed values of the DLA parameter $g^2 \ln^2 s$. The colliding particle momenta p_A and p_B at high $s = 2p_Ap_B$ satisfy the condition $p_r^2 = 0$. The momenta of the virtual particles can be parametrized with the Sudakov parameters

$$k = \beta p_A + \alpha p_B + k_\perp.$$

The double-logarithmic asymptotics of amplitudes of various processes of the quark scattering can be obtained with the use of the method of infrared evolution equations [3]. In the framework of this method, an infrared cutoff μ over transverse momenta of the virtual particles is introduced. Further, instead of summing contributions of the Feynman diagrams, one extracts in these diagrams the particle with the smallest transverse momentum $k_\perp$. In the case where this particle is a gluon, it is possible to show with the use of gauge invariance that the integration over the momentum of the extracted gluon is factorized in front of the same amplitude, but with the infrared cutoff replaced by $|k_\perp|$. In the case where the soft particles are quarks, the amplitude is written as a product of three factors: the integral over momenta of the extracted quarks and two scattering amplitudes with smaller energies $\sqrt{s_r}$ ($r = 1, 2$, $s_1 s_2 \sim s$) and with a new infrared cutoff $\mu \to |k_\perp|$. Thus, one can obtain nonlinear equations for the scattering amplitudes on mass shell [3]. This method can also be used in the weak interaction theory, for example, to calculate the amplitude of the backward lepton scattering [3]

$$A = \int_{-i\infty}^{i\infty} \frac{dj}{2\pi i}\frac{1}{a}\frac{d}{dj}\ln\left(\exp\left(-a\frac{\omega^2}{4}\right)D_a(\omega\sqrt{-a})\right),$$

*This article was submitted by the author in English.

** e-mail: lipatov@thd.pnpi.spb.ru

where $D_a(x)$ is the parabolic cylinder function, $a = -2g'^2/(3g^2+9g'^2), \omega = 4\pi j/g'$, and g, g' are the electroweak constants.

The DGLAP equation [1] is related to the renormalization group approach. Again, instead of calculating and adding contributions of the Feynman diagrams $\sim(g^2\ln(q^2/m^2))^n$, one extracts from all diagrams the particles with the biggest virtuality k^2 playing the role of the ultraviolet cutoff for the 4-momenta of all other virtual particles. The time parameter in the evolution equations here is the logarithm of the particle virtuality. For matrix elements of the twist-2 operators, we have a simple physical interpretation in terms of the distributions $n^i(x)$ of the partons i with the fixed Feynman parameter $x = k_0/E$ in the infinite momentum frame $E \to \infty$. The DGLAP evolution equations have a clear probabilistic interpretation similar to the equations of dynamical balance in chemistry. It is possible to introduce so-called quasi-partonic operators generalizing the twist-2 operators [4]. Their matrix elements between hadron states can be expressed in terms of the matrix elements between partonic states averaged with the parton correlation functions. The evolution equations for the matrix elements of the quasi-partonic operators contain integral kernels for the twist-2 operators and are similar to the Schrödinger equation for n particles in one-dimensional space.

GLUON REGGEIZATION AND MULTI-REGGE PROCESSES

In gauge theories, the dispersion method developed in [2] turns out to be the most powerful. Using this approach, an approximate solution to the nonlinear bootstrap equations corresponding to S-matrix unitarity was found in LLA. In multi-Regge kinematics, where the squared pair energies $s_i = (k_{i-1}-k_i)^2$ of produced particles are significantly bigger than the squared momentum transfers $-t_i$, the production amplitudes have the form [2]

$$A^{\mathrm{LLA}}_{2\to 2+n} = 2gT^{c_1}_{A'A}\Gamma_1\frac{s_1^{\omega_1}}{t_1}gT^{d_1}_{c_2c_1} \times \Gamma^1_{2,1}\frac{s_2^{\omega_2}}{t_2}\times\ldots\times gT^{d_n}_{c_{n+1}c_n}\Gamma^n_{n+1,n}\frac{s_{n+1}^{\omega_{n+1}}}{t_{n+1}}gT^{c_{n+1}}_{B'B}\Gamma_2. \quad (2)$$

Here, $j_i = 1+\omega_i = 1+\omega(t_i)$ are the gluon Regge trajectories and

$$\omega(t) = -\frac{g^2N_c}{16\pi^3}\int d\mathbf{k}\frac{\mathbf{q}^2}{\mathbf{k}^2(\mathbf{q}-\mathbf{k})^2}, \quad t=-\mathbf{q}^2. \quad (3)$$

Infrared divergences in the Regge factors are canceled in σ_{tot} with analogous divergences in contributions of real gluons. A, B and A', B', d_r ($r = 1,2,\ldots,n$) are color indices for initial and final gluons, respectively. $T^c_{ab} = -if_{abc}$ are generators of the gauge group $SU(N_c)$ and g is the Yang–Mills coupling constant. Further,

$$\Gamma_1 = \frac{1}{2}e^\lambda_\nu e^{\lambda'*}_{\nu'}\Gamma^{\nu\nu'}, \quad \Gamma^r_{r+1,r} = -\frac{1}{2}\Gamma_\mu(q_{r+1},q_r)e^{\lambda_r*}_\mu(k_r) \quad (4)$$

are the Reggeon–particle–particle (RPP) and Reggeon–Reggeon–particle (RRP) vertices, respectively. The s-channel helicities are conserved for each of two colliding particles.

The tensor $\Gamma^{\nu\nu'}$ can be written as the sum of two terms [2]:

$$\Gamma^{\nu\nu'} = \gamma^{\nu\nu'+} - q^2(n^+)^\nu\frac{1}{p_A^+}(n^+)^{\nu'}, \quad (5)$$

where we introduced the light-cone vectors

$$n^- = \frac{p_A}{E}, \quad n^+ = \frac{p_B}{E}, E=\sqrt{s}/2, n^+n^- = 2, \quad (6)$$

and the light-cone projections $k^\pm = k^\sigma n^\pm_\sigma$ of the Lorentz vectors k^σ. The first term is the light-cone component of the Yang–Mills vertex. The second (induced) term is a coherent contribution of the Feynman diagrams in which there are no particles in the t channel.

Similarly, the effective RRP vertex $\Gamma\ (q_2,q_1)$ can be represented as follows [2]:

$$\Gamma^\sigma(q_2,q_1) = \gamma^{\sigma-+} - 2q_1^2\frac{(n^-)^\sigma}{k_1^-} + 2q_2^2\frac{(n^+)^\sigma}{k_1^+}. \quad (7)$$

Again, the last two terms appear as coherent contributions of the diagrams without any particles in t_1 and t_2 channels.

The total hadron cross section is obtained from the square of $A^{\mathrm{LLA}}_{2\to 2+n}$ by summing over all final states and integrating over the produced particle momenta. According to the optical theorem, it can be expressed through the imaginary part of the forward scattering amplitude with the vacuum quantum numbers in the t channel. It is convenient to write this amplitude in terms of the t-channel partial wave $f_\omega(t)$:

$$A(s,t) = i\,|s|\int\frac{d\,\omega}{2\pi i}s^\omega f_\omega(t), \quad t=-q^2. \quad (8)$$

In turn, the hadron amplitude $f_\omega(t)$ in QCD can be expressed through the product of the impact factors $\Phi_{A,B}$ describing the inner structure of the colliding particles and the gluon–gluon partial wave f_ω depending on the impact parameters ρ_1, ρ_2 and $\rho_{1'}, \rho_{2'}$

of the initial and final gluons in the t channel. The homogeneous BFKL equation for the Pomeron as a compound state of two Reggeized gluons can be written as a Schrödinger equation with the Hamiltonian:

$$H_{12} = \frac{1}{p_1 p_2^*} \ln|\rho_{12}|^2 \, p_1 p_2^* + \ln|p_1|^2 + 2\gamma + (1 \leftrightarrow 2),$$

where γ is the Euler constant and $\rho_{12} = \rho_1 - \rho_2$. We introduced here the complex coordinates $\rho_k = x_k + iy_k$ and their canonically conjugated momenta $p_k = i\dfrac{\partial}{\partial \rho_k}$. The kinetic energy $\sum_i \ln|p_i|^2$ is proportional to the Regge trajectories of the gluons, and the potential energy coincides with the Green's function $\ln|\rho_{12}|^2$ (up to a similarity transformation). It is obtained by the Fourier transform from the bilinear combination of the RRP effective vertices [2]. The eigenvalues E of the Hamiltonian H_{12} are related to the Pomeron intercept ω governing the high-energy asymptotics $\sim s^{1+\omega}$ of $A(s,t)$:

$$E = -\frac{8\omega\pi^2}{g^2 N_c}. \tag{9}$$

It turns out [2] that, for the ground-state energy, we have $E_0 = -8\ln 2$ and, therefore, the total cross section grows at large energies as s^{ω_0}, where $\omega_0 = g^2 N_c \ln 2/\pi^2$. Thus, in LLA, we obtain the violation of the Froissart theorem $\sigma_{\text{tot}} < c(\ln s)^2$, which is a consequence of the fact that the scattering amplitudes in this approximation do not satisfy all requirements following from the s-channel unitarity [2]. We shall discuss below various methods to overcome this drawback of LLA.

POMERON IN THE IMPACT-PARAMETER SPACE

The amplitude for the hadron–hadron scattering can be expressed in LLA in terms of the gluon–gluon scattering amplitude whose t-channel partial wave $f_\omega(\rho_1, \rho_2; \rho_{1'}, \rho_{2'})$ in the impact-parameter representation ρ is invariant under the conformal (Möbius) transformations [5]

$$\rho_k \to \frac{a\rho_k + b\rho_k}{c\rho_k + d\rho_k} \tag{10}$$

for arbitrary complex parameters a, b, c, and d provided that we use the complex coordinates ρ and ρ^*.

It can be written in the form [5]

$$f_\omega(\rho_1, \rho_2; \rho_{1'}, \rho_{2'}) \tag{11}$$
$$= \sum_{n=-\infty}^{+\infty} \int_{-\infty}^{+\infty} \frac{(\nu^2 + n^2/4)d\nu}{[\nu^2 + (n-1)^2/4]\,[\nu^2 + (n+1)^2/4]} \times \frac{G_{\nu n}(\rho_1, \rho_2; \rho_{1'}, \rho_{2'})}{\omega - \omega(\nu, n)},$$

where the quantity $\omega(\nu, n)$ is the eigenvalue of the BFKL equation [2]:

$$\omega(\nu, n) = -\frac{N_c g^2}{2\pi^2} \mathrm{Re}\left(\psi\left(\frac{1+|n|}{2} + i\nu\right) - \psi(1)\right), \tag{12}$$
$$\psi(x) = \Gamma'(x)/\Gamma(x).$$

The Green's function $G_{\nu n}(\rho_1, \rho_2; \rho_{1'}, \rho_{2'})$ can be expressed in terms of products of hypergeometric functions [6].

The composite field describing the BFKL Pomeron has the conformal weights

$$m = \frac{1}{2} + i\nu + \frac{n}{2}, \quad \widetilde{m} = \frac{1}{2} + i\nu - \frac{n}{2} \tag{13}$$

with real ν and integer conformal spin n in accordance with the fact that it belongs to the principal series of irreducible unitary representations.

If we take into account the fact that the QCD coupling constant decreases in the region of large gluon virtualities $k^2 \sim \rho^{-2} \gg q^2$, we can calculate from the BFKL equation the trajectories for an infinite set of Regge poles situated at small ω [5].

INTEGRABILITY IN MULTICOLOR QCD

The Hamiltonian for the BFKL Pomeron has the property of holomorphic separability [7]:

$$H_{12} = h_{12} + h_{12}^*, \tag{14}$$

where the holomorphic Hamiltonian is [7]

$$h_{12} = \frac{1}{p_1}\ln(\rho_{12})p_1 + \frac{1}{p_2}\ln(\rho_{12})p_2 + \ln(p_1 p_2) - 2\psi(1). \tag{15}$$

One of the possible ways to unitarize the results of LLA is to take into account the Feynman diagrams with an arbitrary number of Reggeized gluons in the t channel. In a generalized LLA, this problem is reduced to the solution to the Schrödinger equation for compound states of n gluons. Because the color structure of their eigenfunctions at large N_c is unique, the total Hamiltonian H can be written as a sum of the mutually commuting holomorphic and antiholomorphic operators $H = (h + h^*)/2$ [7], where

$$h = \sum_{i=1}^{n} h_{i,i+1}. \tag{16}$$

The eigenfunction has the property of holomorphic factorization:

$$\Psi = \sum c_{kr} \psi_k(\rho_1, \ldots, \rho_n) \widetilde{\psi}_r(\rho_1^*, \ldots, \rho_n^*), \tag{17}$$

where ψ_k and $\widetilde{\psi}_r$ are the solutions to the Schrödinger equations in the holomorphic and antiholomorphic subspaces corresponding to the same energies ϵ and $\widetilde{\epsilon}$,

$$E = \frac{1}{2}(\epsilon + \widetilde{\epsilon}).$$

These equations have the nontrivial integrals of motion [7]

$$t(\theta) = \mathrm{tr}T(\theta), \quad [t(u), t(v)] = [t(\theta), h] = 0, \quad (18)$$

where θ is the spectral parameter of the transfer matrix $t(\theta)$. The monodromy matrix $T(\theta)$ is constructed from the product of the L operators

$$T(\theta) = L_1(\theta)L_2(\theta) \times \ldots \times L_n(\theta) \quad (19)$$

expressed in terms of the Möbius group generators

$$L_k(\theta) = \begin{pmatrix} \theta + i\rho_k\partial_k & -i\partial_k \\ i\rho_k^2\partial_k & \theta - i\rho_k\partial_k \end{pmatrix}. \quad (20)$$

The Hamiltonian and the integrals of motion are invariant under the duality transformation [8]

$$p_r \to \rho_{r,r+1} \to p_{r+1}$$

combined with the transposition of operator multiplication. The monodromy matrix parametrized as

$$T(\theta) = \begin{pmatrix} A(\theta) & B(\theta) \\ C(\theta) & D(\theta) \end{pmatrix}$$

satisfies the Yang–Baxter bilinear equations. One can apply the Bethe ansatz technique to find the representation of the corresponding commutation relations [7]. For the transposed operator $C^T(\theta)$, there exists the pseudovacuum eigenstate [9]

$$C^T(\theta)\Omega_0 = 0, \quad \Omega_0 = \prod_{k=1}^{n} \rho_{k0}^{-2}.$$

According to E. Sklyanin, the physical states can be constructed according to the following prescription:

$$\Psi = -PQ(\lambda_1) \times \ldots \times Q(\lambda_{n-1})\Omega_0,$$

where P is the total momentum of the n-Reggeon state, λ_k are the operator roots of the equation

$$B^T(\lambda_k) = 0,$$

$Q(u)$ is the Baxter function satisfying the Baxter equation

$$\Lambda(u)Q(u) = (u+i)^n Q(u+i) + (u-i)^n Q(u-i),$$

and $\Lambda(u)$ is a polynomial of rank $(n-1)$ being an eigenvalue of the transfer matrix $t(u)$. The Baxter function has poles at the imaginary integer points $u = il$, and for the residues in these poles, one can write a recursion relation [10]. The energy of the physical state is expressed through the behavior of $Q(u)$ near the pole with $l = 1$. Lastly, the quantization of the energy is related to the condition that the energy should be the same for all solutions to the Baxter equation having the same integrals of motion [10].

For the case of the Odderon ($n = 3$), one can use the conformal ansatz [7]

$$\psi(\rho_1, \rho_2, \rho_3; \rho_0) = \left(\frac{\rho_{23}}{\rho_{20}\rho_{30}}\right)^m \phi(x), \quad (21)$$

where

$$x = \frac{\rho_{12}\rho_{30}}{\rho_{13}\rho_{20}}. \quad (22)$$

In the x representation, the eigenvalue equation for the integral of motion is the ordinary differential equation of the third order [7]

$$a_{1-m}a_m\phi(x) = A\phi(x),$$

where a_m is the duality operator [9]:

$$a_m = x(1-x)(i\partial)^{1+m}.$$

For the most interesting case $m = 1/2$, the duality equation can be reduced to a one-dimensional Schrödinger equation with the potential $1/r^{3/2}$ [8]. By imposing the single-valuedness condition on the Odderon wave function (18) in the two-dimensional space $\mathbf{x}$, one can obtain the quantization of the eigenvalues of A and the Odderon energy, corresponding to the negative values of the Odderon intercept [11].

In [12], a new solution to the Schrödinger equation for the Odderon wave function with the intercept $\omega_0 = 0$ was found. Physically, the new Odderon is a composite state of a usual Reggeized gluon and the Reggeon state with the same quantum numbers but with an opposite signature. The duality symmetry of the Reggeon interactions appearing at the large-N_c limit can be interpreted as the symmetry between these two-Reggeon states. The new solution has a more singular behavior at small relative distances than the old solutions. On such functions, the holomorphic separability of the Hamiltonian is broken, which can be considered as a quantum anomaly.

EFFECTIVE ACTION FOR SMALL-x PHYSICS IN QCD

The next-to-leading corrections to the BFKL equation are important for finding the region of its applicability including the intervals of energies and momentum transfers fixing the scale for the QCD coupling constant. Such corrections appear from the quasi-multi-Regge processes in which the final-state particles are separated in several clusters consisting of an arbitrary number of gluons and quarks with a

fixed invariant mass; each group is produced with respect to the others in multi-Regge kinematics. The gauge-invariant effective action S_{eff} local in a rapidity interval $(y_0-\eta, y_0+\eta)$ was constructed in [13]:

$$S_{\text{eff}}(v,A_\pm) = -\int d^4x \mathrm{tr}\left[\frac{1}{2}G^2_{\mu\nu}(v) \right. \quad (23)$$

$$\left. + (A_-(v)-A_-)j_+^{\text{Reg}} + (A_+(v)-A_+)j_-^{\text{Reg}}\right],$$

where the anti-Hermitian $SU(N_c)$ matrices v_σ and $A_\pm$ describe, respectively, the usual and Reggeized gluons. The Reggeon current $j_\pm^{\text{Reg}}$ is

$$j_\pm^{\text{Reg}} = \partial_\sigma^2 A_\pm, \quad (24)$$

which guarantees that the gluon–Reggeon interaction disappears on the mass shell $k^2=0$. Moreover, it makes it possible to interpret the composite fields $A_\pm(v)$ as the quantities describing the emission of gluons in the given interval of rapidity by particles with different rapidities.

The fields $A_\pm$ are invariant,

$$\delta A_\pm = 0, \quad (25)$$

under the infinitesimal gauge transformation

$$\delta v_\sigma = [D_\sigma, \chi], \quad D_\sigma = \partial_\sigma + g v_\sigma, \quad (26)$$

with the gauge parameter χ decreasing at $x\to\infty$, but they belong to the adjoint representation of the global $SU(N_c)$ group.

The fields $A_\pm$ obey the additional kinematical constraints

$$\partial_+ A_- = 0, \quad \partial_- A_+ = 0 \quad (27)$$

in the quasi-multi-Regge kinematics where the neighboring clusters differ significantly in their rapidities: $y_{k-1}-y_k \gg \eta$. The effective action describes the self-interaction of real and virtual particles inside each cluster and their coupling with neighboring Reggeized gluons. The composite Reggeon field $A_\pm(v)$ can be written in the explicit form

$$A_\pm(v) = v_\pm D_\pm^{-1}\partial_\pm = -\frac{1}{g}\partial_\pm U(v_\pm), \quad (28)$$

$$U(v_\pm) = \frac{P}{2} e^{-\frac{g}{2}\int\limits_{-\infty}^{x^\pm} dx'^\pm v_\pm} + \frac{\bar{P}}{2} e^{\frac{g}{2}\int\limits_{x^\pm}^{\infty} dx'^\pm v_\pm},$$

where the integral operator $D_\pm^{-1}\partial_\pm$ is implied to act on a unit constant matrix from the left-hand side and the symbol P means the ordering of the fields v in the matrix product in accordance with an increase in their arguments $x'^\pm$. Because j^{Reg} in the momentum representation contains the factor $t=q^2$ killing the pole in the neighboring Reggeon propagator, the corresponding scattering amplitudes do not have simultaneous singularities in the overlapping channels t and s.

Further, the physical results do not depend on η due to cancellations between the integrals over the invariant masses of the produced clusters and the integrals over their relative rapidities [6]. By expanding the functional integral in g, one can reproduce the above effective vertices for gluon–Reggeon interactions.

The effective action S_{eff} has a nontrivial stationary point $v=\bar{v}$ satisfying the classical equations. In the Landau gauge in the first approximation of perturbation theory, the classical solution coincides with $A_\pm$.

To obtain the Reggeon action in the tree approximation, we should substitute $v_\sigma \to \overline{v}_\sigma$ in S_{eff}. Further, one can write the field v as a sum of its classical component $\overline{\nu}$ and the small variation ϵ describing its fluctuations near the classical solution. The Reggeon action in the semiclassical approximation can be obtained if one would calculate the functional integral over the quantum fluctuations ϵ (taking into account the Faddeev–Popov ghosts). In particular, one can find next-to-leading corrections to the BFKL Pomeron.

The subsequent functional integration over $A_\pm$ corresponds to the solution of the Reggeon field theory defined in the two-dimensional impact-parameter subspace with the rapidity playing the role of time. It is important that, in the functional approach, the t-channel dynamics of the Reggeon interactions turns out to be in agreement with the s-channel unitarity of the S matrix in the initial Yang–Mills model. In the Hamiltonian formulation of the Reggeon calculus, the wave function will contain components with an arbitrary number of Reggeized gluons. Nevertheless, one can hope that at least some of the remarkable properties of the BFKL equation will remain in the general case of the nonconserved number of Reggeized gluons.

The effective action can also be constructed for the Reggeized quarks interacting with the usual quarks and gluons [14]. It can be used for the calculation of the next-to-leading corrections to the quark Regge trajectory and to other Reggeized quark vertices.

NEXT-TO-LEADING CORRECTIONS TO THE BFKL POMERON IN QCD AND IN SUPERSYMMETRIC MODELS

The generalized BFKL equation for the total cross section can be written in the integral form as follows [15]:

$$\sigma(\mathbf{q}_1, q_1^+) = \sigma_0(\mathbf{q}_1, q_1^+) \quad (29)$$

$$+\int\frac{dq_2^+}{q_2^+}\mu^{4-D}\int d\mathbf{q}_2 K_\delta(\mathbf{q}_1,\mathbf{q}_2)\sigma(\mathbf{q}_2,q_2^+).$$

Here, the integration region for the longitudinal momentum q_2^+ is restricted from above by a value proportional to q_1^+:

$$q_2^+ < \delta q_1^+. \tag{30}$$

The intermediate infinitesimal parameter $\delta 0$ is introduced instead of the above parameter η to arrange the particles in the groups with strongly different rapidities. The integral kernel $K_\delta(\mathbf{q}_1,\mathbf{q}_2)$ takes into account the interaction among the particles inside each group where δ plays role of the ultraviolet cutoff in their relative rapidities. The kernel K_δ is calculated in perturbation theory [15].

The next-to-leading term in K_δ related to two-gluon or two-quark production is proportional to the square of the RRP vertices ψ integrated over the invariant mass of the produced particles. It enters the amplitude of the pair production in the central rapidity region:

$$A^{\nu_1\nu_2\ldots\nu_n+-}_{d_1d_2\ldots.d_nA'AB'B} = -gp_A^+T^{c_1}_{A'A}\delta_{\lambda_A\lambda_{A'}} \tag{31}$$
$$\times\frac{1}{t_1}\psi^{\nu_1\nu_2\ldots\nu_n+-}_{d_1d_2\ldots d_nc_2c_1}\frac{1}{t_2}gp_B^-T^{c_2}_{B'B}\delta_{\lambda_B\lambda_{B'}}.$$

The Reggeon–particle vertex ψ can be calculated using the Feynman rules for the above effective action [13].

All other next-to-leading terms are related to the virtual corrections to the gluon production amplitudes in the multi-Regge kinematics. These contributions are a one-loop correction to the RRP vertex and a two-loop correction to the Regge trajectory. It was verified that infrared divergences in the sum of all contributions to the BFKL kernel are canceled. Finally, the next-to-leading corrections to the BFKL kernel were expressed in terms of dilogarithm integrals [15]. The BFKL equation with next-to-leading corrections to its integral kernel was solved with the use of the BLM procedure for fixing the argument of the QCD running coupling constant, and the results were compared with the experimental data on the hadron production in the virtual photon collisions obtained by the L3 group at CERN [16]. The theoretical predictions for the total cross section are in agreement with the experimental data.

The integral kernel for the BFKL equation in the next-to-leading approximation is diagonalized in [17]. It turns out that its eigenvalue contains nonanalytic terms proportional to Kronecker symbols δ_{n0} and δ_{n2}, where n is the conformal spin of the representation of the Möbius group.

In supersymmetric gauge theories, the term δ_{n2} is canceled. Moreover, in the extended $N=4$ super-Yang–Mills model, both Kronecker symbols disappear and the eigenvalue is an analytic function of n [17]. The anomalous dimensions of local operators can be calculated from this eigenvalue as functions of parameters $\omega\sim g^2$ and n. In [17], it was argued that the analytic continuation of the eigenvalue of the BFKL kernel to negative values $n=-k$ makes it possible to calculate the residues of the anomalous dimensions of the twist-2 operators in the poles situated at $j=-k$.

Therefore, all information about the DGLAP equation in $N=4$ supersymmetric gauge theory is presumably contained inside the BFKL equation. Moreover, it turns out that the Bukhvostov–Frolov–Kuraev–Lipatov equation [4] for the anomalous dimensions of the quasi-partonic operators coincides in this theory with the Schrödinger equation for the integrable Heisenberg spin model [17]. Probably, these properties are related to the Maldacena guess that the $N=4$ model is dual to the superstring theory on the anti–de Sitter space.

REFERENCES

1. V. N. Gribov and L. N. Lipatov, Yad. Fiz. **15**, 781 (1972) [Sov. J. Nucl. Phys. **15**, 438 (1972)]; L. N. Lipatov, Yad. Fiz. **20**, 181 (1975) [Sov. J. Nucl. Phys. **20**, 94 (1975)]; G. Altarelli and G. Parisi, Nucl. Phys. B **26**, 298 (1971); Yu. L. Dokshitzer, Zh. Éksp. Teor. Fiz. **73**, 1216 (1977) [Sov. Phys. JETP **46**, 641 (1977)].
2. E. A. Kuraev, L. N. Lipatov, N. P. Merenkov, and M. I. Strikman, Yad. Fiz. **23**, 163 (1976) [Sov. J. Nucl. Phys. **23**, 85 (1976)]; V. S. Fadin, E. A. Kuraev, and L. N. Lipatov, Phys. Lett. B **60B**, 50 (1975); E. A. Kuraev, L. N. Lipatov, and V. S. Fadin, Zh. Éksp. Teor. Fiz. **71**, 88 (1976) [Sov. Phys. JETP **44**, 443 (1976)]; **72**, 377 (1977) [**45**, 199 (1977)]; Ya. Ya. Balitskii and L. N. Lipatov, Yad. Fiz. **28**, 1597 (1978) [Sov. J. Nucl. Phys. **28**, 822 (1978)].
3. R. Kirshner and L. N. Lipatov, Zh. Éksp. Teor. Fiz. **83**, 488 (1982) [Sov. Phys. JETP **56**, 266 (1982)]; B. I. Ermolaev and L. N. Lipatov, Yad. Fiz. **47**, 1320 (1988) [Sov. J. Nucl. Phys. **47**, 841 (1988)]; Int. J. Mod. Phys. A **4**, 3147 (1989); J. Bartels, B. I. Ermolaev, and M. G. Ryskin, Z. Phys. C **70**, 273 (1996); V. S. Fadin, L. N. Lipatov, A. D. Martin, and M. Milles, Phys. Rev. D **61**, 094002 (2000).
4. A. P. Bukhvostov, G. V. Frolov, E. A. Kuraev, and L. N. Lipatov, Nucl. Phys. B **258**, 601 (1985).
5. L. N. Lipatov, Zh. Éksp. Teor. Fiz. **90**, 1536 (1986) [Sov. Phys. JETP **63**, 904 (1986)].
6. L. N. Lipatov, Phys. Rep. **286**, 97 (1997).
7. L. N. Lipatov, Phys. Lett. B **309**, 394 (1993); Preprint No. DFPD/93/TH/70, Padova Univ.
8. L. N. Lipatov, Nucl. Phys. B **548**, 327 (1999).

9. L. N. Lipatov, Pis'ma Zh. Éksp. Teor. Fiz. **59**, 596 (1994) [JETP Lett. **59**, 596 (1994)]; L. D. Faddeev and G. P. Korchemsky, Phys. Lett. B **342**, 311 (1995).
10. H. de Vega and L. N. Lipatov, Phys. Rev. D (in press); hep-ph/0107225.
11. R. E. Janik and J. Wosiek, Phys. Rev. Lett. **82**, 1092 (1999).
12. J. Bartels, L. N. Lipatov, and G. P. Vacca, Phys. Lett. B **477**, 178 (2000).
13. L. N. Lipatov, Nucl. Phys. B **452**, 369 (1995).
14. L. N. Lipatov and M. I. Vyazovsky, Nucl. Phys. B **597**, 399 (2001).
15. L. N. Lipatov and V. S. Fadin, Yad. Fiz. **50**, 1141 (1989) [Sov. J. Nucl. Phys. **50**, 712 (1989)]; V. S. Fadin and L. N. Lipatov, Phys. Lett. B **429**, 127 (1998).
16. S. J. Brodsky, V. S. Fadin, V. T. Kim, *et al.*, Pis'ma Zh. Éksp. Teor. Fiz. **70** (3), 161 (1999) [JETP Lett. **70**, 155 (1999)]; V. T. Kim, L. N. Lipatov, and G. B. Pivovarov, hep-ph/9911228; hep-ph/9911242.
17. A. V. Kotikov and L. N. Lipatov, Nucl. Phys. B **582**, 19 (2000).

Physics of Atomic Nuclei, Vol. 67, No. 1, 2004, pp. 90–99. From Yadernaya Fizika, Vol. 67, No. 1, 2004, pp. 90–99.

Total Cross Section, Inelasticity, and Multiplicity Distributions in Proton–Proton Collisions*

G. Musulmanbekov**

Joint Institute for Nuclear Research, Dubna, Moscow oblast, 141980 Russia

Received April 30, 2003

Abstract—Multiparticle production in high-energy proton–proton collisions has been analyzed in the framework of the strongly correlated quark model of the hadron structure elaborated by the author. It is shown that inelasticity decreases at high energies and the violation of KNO scaling is a consequence of total cross-section growth and increases with collision energy masses of intermediate clusters.

1. INTRODUCTION

In inelastic hadronic interactions with multiparticle production, only a fraction of collision energy is converted into the production of secondaries. For the quantitative estimation of this fraction, one can use for a given interaction a characteristic, originating from cosmic-ray physics, inelasticity, which can be defined as

$$k_1(s) = \frac{M}{\sqrt{s}}, \qquad (1)$$

where s is square of c.m. energy and M is the mass of intermediate system which decays into final produced particles. The remaining part of the incident energy is carried away by the participant's remnants—so-called leading particles. From the experimental point of view, more suitable is another definition of inelasticity

$$k_2(s) = \frac{1}{\sqrt{s}} \sum_i \int dy \mu_i \frac{dn_i}{dy} \cosh y, \qquad (2)$$

where $\mu_i = \sqrt{p_{T_i}^2 + m_i^2}$ is transverse mass of a produced particle of type i and dn_i/dy is its measured rapidity distribution. Fluctuation of inelasticity from event to event leads to the distribution $P(k)$ with mean inelasticity $\langle k(s) \rangle$. The energy dependence of inelasticity is a problem of great interest from both theoretical and experimental points of view. There is no consensus in the physical community on the energy dependence of $\langle k(s) \rangle$. The decrease in inelasticity with energy is advocated by some authors [1–4], while others believe that inelasticity is an increasing function of energy [5–8]. The question cannot be answered by collider experiments. At ISR energies (23–60 GeV), where the leading particle spectrum could be measured, the inelasticity is defined to be about 0.5. In the collider experiments at higher energies (SPS and Tevatron), leading particles are emitted in an extremely forward cone and could not be measured due to the presence of the beam pipe. Obviously, multiplicity distributions are connected with inelasticity distributions, and so one can study features of multiplicity distributions, deriving information on inelasticity or fraction of the initial energy converted into particle production. As we know, scaled multiplicity distributions exhibit KNO [9] scaling up to ISR energies, which is violated for higher energy data (SPS), where they can be described approximately by a negative binomial distribution (NBD). And again, at the highest SPS energy, 900 GeV, there is an evident deviation of multiplicity distributions from the NBD. In this paper, we demonstrate that there is a connection between the energetic behavior of the shapes of scaled multiplicity distributions and inelasticity distributions, which, in turn, is related to the effect of the total cross-section growth. For this purpose, we use geometrical considerations that are justified by the following arguments. First, hadrons are extended objects with a size of about 1 fm, and, second, at high energies, the de Broglie wavelength becomes small.

Our analysis is based on a model of hadron structure called the strongly correlated quark model (SCQM) [10], which is described in Section 2. In Section 3, the model is applied to the calculation of proton–proton total cross sections and the analysis of multiparticle production.

*This article was submitted by the author in English.

** e-mail: genis@jinr.ru

2. STRONGLY CORRELATED QUARK MODEL

The ingredients of the model are the following. A single quark of a definite color embedded in a vacuum starts to polarize its surroundings, resulting in the formation of a quark and a gluon condensate. At the same time, it experiences the pressure of vacuum because of a zero point radiation field or vacuum fluctuations that act on the quark, tending to destroy the ordering of the condensate. Suppose that we place the corresponding antiquark in the vicinity of the first one. Owing to their opposite signs, color polarization fields of the quark and antiquark interfere destructively in the overlapped space regions, eliminating each other maximally at the midpoint between the quarks. This effect leads to the decrease in condensate density in the same space region and overbalancing of the vacuum pressure acting on the quark and antiquark from outer space regions. As a result, an attractive force between the quark and antiquark emerges and the quark and antiquark start to move towards each other. The density of the remaining condensate around the quark (antiquark) is identified with the hadronic matter distribution. At maximum displacement in the $\bar{q}q$ system corresponding to small overlapping of polarization fields, the hadronic matter distributions have maximum extent and magnitude. The closer they are to each other, the larger the effect of mutual destruction and the smaller the hadronic matter distributions around the quarks and the larger their kinetic energies. In that way, the quark and antiquark start to oscillate around their midpoint. For such interacting $\bar{q}q$ pair located on the X axis at a distance of $2x$ from each other, the total Hamiltonian is

$$H = \frac{m_{\bar{q}}}{(1-\beta^2)^{1/2}} + \frac{m_q}{(1-\beta^2)^{1/2}} + V_{\bar{q}q}(2x), \quad (3)$$

where $m_{\bar{q}}$ and m_q are the current masses of the valence antiquark and quark, $\beta = \beta(x)$ is their velocity depending on displacement x, and $V_{\bar{q}q}$ is the quark–antiquark potential energy at separation $2x$. It can be rewritten as

$$H = \left[\frac{m_{\bar{q}}}{(1-\beta^2)^{1/2}} + U(x)\right] + \left[\frac{m_q}{(1-\beta^2)^{1/2}} + U(x)\right] = H_{\bar{q}} + H_q, \quad (4)$$

where $U(x) = \frac{1}{2}V_{\bar{q}q}(2x)$ is the potential energy of the quark or antiquark. The quark (antiquark) with the surrounding cloud (condensate) of quark–antiquark pairs and gluons, or hadronic matter distribution, forms the constituent quark (CQ). It is natural to assume that the potential energy of the quark (antiquark), $U(x)$, corresponds to the mass M_Q of the CQ:

$$2U(x) = C_1 \int_{-\infty}^{\infty} dz' \int_{-\infty}^{\infty} dy' \int_{-\infty}^{\infty} dx' \rho(x, \mathbf{r}') \approx 2M_Q(x), \quad (5)$$

where C_1 is a dimensional constant and hadronic matter density distribution $\rho(x, \mathbf{r}')$ is defined as

$$\rho(x, \mathbf{r}') = C_2 \left|\varphi(x, \mathbf{r}')\right| = C_2 \left|\varphi_Q(x' + x, y', z') - \varphi_{\bar{Q}}(x' - x, y', z')\right|. \quad (6)$$

Here, C_2 is a constant, φ_Q and $\varphi_{\bar{Q}}$ are density profiles of the condensates around the quark and antiquark located at distance $2x$ from each other. Here, we consider that the condensates around the quark and antiquark have opposite color charges. They are similar to compressive stress and tensile stress (around defects) in solids. The generalization to a three-quark system in baryons is performed according to $SU(3)_{\text{color}}$ symmetry: in general, a pair of quarks have coupled representations

$$3 \otimes 3 = 6 \oplus \bar{3} \quad (7)$$

in $SU(3)_{\text{color}}$, and for quarks within the same baryon, only the $\bar{3}$ (antisymmetric) representation occurs. Hence, the antiquark can be replaced by two correspondingly colored quarks to get a color singlet baryon, and destructive interference takes place between color fields of three valence quarks (VQs). Putting aside the mass and charge differences and spins of VQs, we may say that, inside the baryon, three quarks oscillate along the bisectors of an equilateral triangle. Therefore, keeping in mind that the quark and antiquark in mesons and three quarks in baryons are strongly correlated, we can consider each of them separately as undergoing oscillatory motion under the potential (5) in $1+1$ dimension. Hereinafter, we consider that the VQ oscillates along the X axis, and the Z axis is perpendicular to the plane of oscillation XY. Density profiles of condensates around VQs are taken in the Gaussian form. It has been shown in papers [11] that the wave packet solutions to the time-dependent Schrödinger equation for a harmonic oscillator move in exactly the same way as corresponding classical oscillators. These solutions are called "coherent states." This relationship justifies our semiclassical treatment of quark dynamics.

We specify the mass of the CQ at maximum displacement as

$$M_{Q(\bar{Q})}(x_{\max}) = \frac{1}{3}\frac{m_\Delta + m_N}{2} \approx 360 \text{ MeV},$$

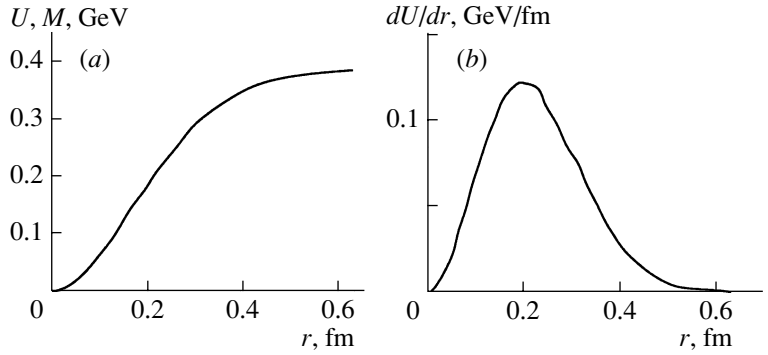

Fig. 1. (a) Potential energy of valence quark and mass of constituent quark; (b) "confinement" force.

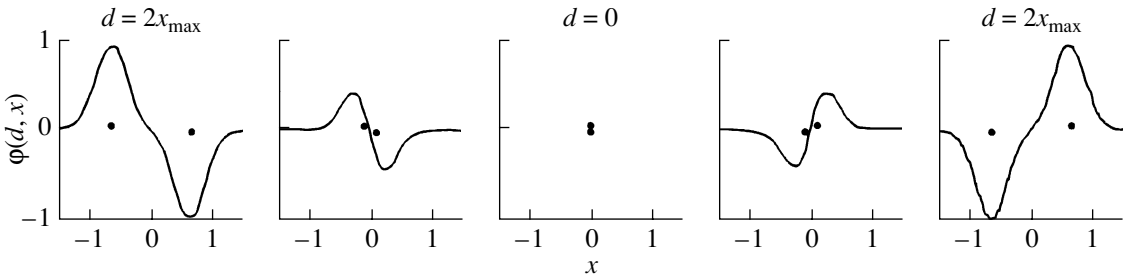

Fig. 2. Evolution of color charge density profile φ in the quark–antiquark system during half-period of oscillations; $d = 2x$ is a distance (in fm) between quark and antiquark depicted as dots.

where m_Δ and m_N are the delta–isobar and nucleon masses, respectively. The parameters of the model, namely, maximum displacement $x_{\max}$ and parameters of the Gaussian function $\sigma_{x,y,z}$ for the hadronic matter distribution around the VQ, are chosen inside the following corridors:

$$x_{\max} = 0.64\text{–}0.66 \text{ fm}, \qquad (8)$$
$$\sigma_{x,y} = 0.24\text{–}0.28 \text{ fm}, \quad \sigma_z = 0.12\text{–}0.20 \text{ fm}.$$

They are estimated by comparison of calculated and experimental values of inelastic cross sections $\sigma_{\text{in}}(s)$ and the inelastic overlap function $G_{\text{in}}(s,b)$ for pp and $\bar{p}p$ collisions (see the next section). The current mass of the VQ is taken to be 5 MeV. The behavior of potential (5) evidently demonstrates the relationship between constituent- and current-quark states inside a hadron (Fig. 1). At maximum displacement, the quark is a nonrelativistic, constituent one (VQ surrounded by the condensate), since the influence of polarization fields of other quarks becomes minimal and the VQ possesses the maximal potential energy corresponding to the mass of the CQ. At the origin of oscillation, $x = 0$, the antiquark and quark in mesons and three quarks in baryons, being close to each other, have maximum kinetic energy and correspondingly minimum potential energy and mass: they are relativistic, current quarks (bare VQs). This configuration corresponds to so-called "asymptotic freedom." In the intermediate region, there is an increase (decrease) in the CQ mass by dressing (undressing) of VQs due to a decrease (increase) in the destructive interference effect. The evolution of color charge density profiles of the quark–antiquark pair during the half-period of oscillation is shown in Fig. 2. Here, we suppose that the quark color charge is positive and the antiquark color charge is negative.

The proposed dynamical picture meets the local gauge invariance principle. Indeed, destructive interference of color fields of the quark and antiquark in mesons and three quarks in baryons depending on their displacements can be treated as a phase rotation of the wave function of a single VQ in color space ψ_c on angle θ depending on the displacement x of the VQ in the coordinate space:

$$\psi_c(x) \to e^{ig\theta(x)}\psi_c(x). \qquad (9)$$

The color phase rotation, in turn, leads to VQ dressing (undressing) by quark and gluon condensate that corresponds to the transformation of a gauge field

$$A_\mu(x) \to A_\mu(x) + \partial_\mu\theta(x). \qquad (10)$$

Here, we drop color indices of $A_\mu(x)$ and consider each quark of specific color separately as changing its effective color charge, $g\theta(x)$, in color fields of other quarks (antiquark) due to the destructive interference. Thus, gauge transformations (9), (10) map internal

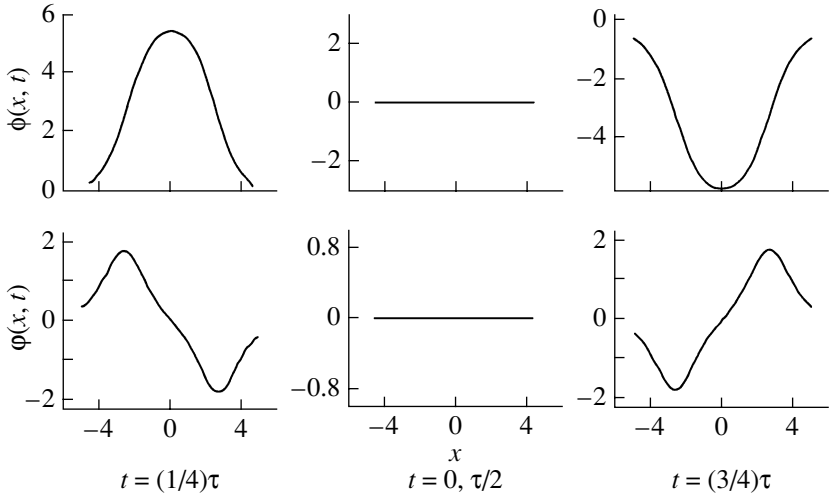

Fig. 3. Evolution of a breather ϕ and its energy density profile φ during a half-period of oscillation. Scales are arbitrary.

(isotopic) space of a colored quark onto the coordinate space. On the other hand, this dynamical picture of VQ dressing (undressing) corresponds to chiral symmetry breaking (restoration). Due to this mechanism of VQ oscillations, the nucleon runs over the states corresponding to specific terms of the infinite series of Fock space

$$|B\rangle = c_1|q_1q_2q_3\rangle + c_2|q_1q_2q_3\bar{q}q\rangle + c_3|q_1q_2q_3g\rangle \ldots . \quad (11)$$

The proposed model has some important consequences. Inside hadrons, the VQs and gluons and quark–antiquark pairs accompanying them, as well, are strongly correlated. Nucleons are nonspherical objects: they are flattened along the axis perpendicular to the plane of quark oscillations.

From the form of the quark potential (Fig. 1), one can conclude that the dynamics of a VQ corresponds to a nonlinear oscillator and VQ in which its surroundings can be treated as a nonlinear wave packet. Moreover, our quark–antiquark system turned out to be identical to the so-called "breather" solution to the (nonlinear) sine-Gordon (SG) equation [12]. The SG equation in $1+1$ dimension in the reduced form for scalar function $\phi(x,t)$ is given by

$$\Box\phi(x,t) + \sin\phi(x,t) = 0, \quad (12)$$

where x and t are dimensionless. The breather is a periodic solution representing a bound state of a soliton–antisoliton pair that oscillates around its center of mass:

$$\phi_{\rm br}(x,t) = 4\tan^{-1}\left[\frac{\sinh\left(ut/\sqrt{(1-u^2)}\right)}{u\cosh\left(x/\sqrt{(1-u^2)}\right)}\right], \quad (13)$$

where u is 4-velocity. During the oscillations of the soliton–antisoliton pair, their density profile

$$\varphi_{\rm br}(x,t) = \frac{d\phi_{\rm br}(x,t)}{dx} \quad (14)$$

evolves like our quark–antiquark system; i.e., at the maximal displacement, the soliton and antisoliton are emphasized maximally, and at the minimum displacement, they "annihilate" (Fig. 3). This similarity is not surprising because our quark–antiquark system was formulated in close analogy with the model of dislocation–antidislocation, which in the continuous limit is described by the breather solution to the SG equation [13]. It can be shown that the soliton, antisoliton, and breather obey relativistic kinematics, i.e., their energies, momenta, and shapes are transformed according to Lorentz transformations. Since the above consideration of quarks as solitons is purely classical, the important problem is to construct quantum states around them. Although the soliton solution to the SG equation looks like an extended (quantum) particle, the relationship between classical solitons and quantum particles is not so trivial. The technique of quantization of classical solitons with the use of various methods has been developed by many authors. The best known of them is the semiclassical method of quantization (WKB), which allows one to relate classical periodic orbits (breather solution to the SG) with the quantum energy levels [14].

Hereinafter, we adhere to our semiclassical model (SCQM), applying it for analysis of cross sections and multiparticle production in hadron–hadron collisions.

3. HADRON–HADRON COLLISIONS

Different configurations of the quark content inside a hadron realized at the instant of collision re-

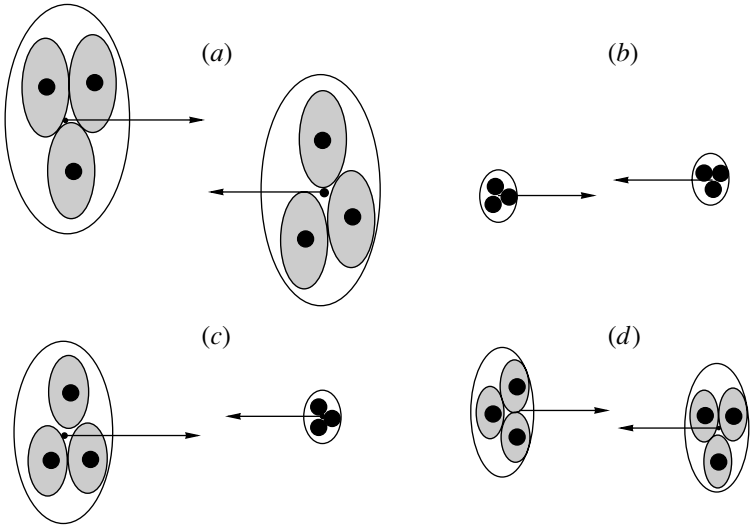

Fig. 4. Different quark configurations realized inside colliding nucleons at the instant of a collision.

sult in different types of reactions. The probability of finding any quark configuration inside the hadron is defined by the probability of VQ displacement in a proper frame of the hadron:

$$P(x)dx = \frac{Adx}{\sqrt{1 - m_q^2/\left[E_q - U(x)\right]^2}}, \qquad (15)$$

where E_q is the total energy of the valence quark (antiquark) and the constant A can be derived from the normalization condition

$$\int_{-\infty}^{\infty} P(x)dx = 1. \qquad (16)$$

Configurations with nonrelativistic CQs ($x \simeq x_{\max}$) in both colliding hadrons lead to soft interactions with the nondiffractive multiparticle production in central and fragmentation regions (Fig. 4*a*). Hard scattering with jet production and large-angle elastic scattering take place when configurations with current VQs ($x \simeq 0$) in both colliding hadrons are realized (Fig. 4*b*). The near current quark configuration inside one of the hadrons and CQ configuration inside the second one result in single diffractive scattering (Fig. 4*c*). And finally, intermediate configurations inside one or both hadrons are responsible for semihard and double diffractive scattering (Fig. 4*d*). The same geometrical consideration can be applied to deep-inelastic scattering (DIS) processes if one assumes that a real or virtual photon converts into a vector meson according to the vector dominance model.

We apply our model to the calculation of proton–proton and antiproton–proton cross sections at high energies and demonstrate that the growth of the cross section with energy is caused by a predominantly increasing contribution of peripheral interactions, which, in turn, leads to decreasing inelasticity of collisions. Then, we will show that the energetic behavior of inelasticity distributions governs the energetic behavior of scaled multiplicity distributions.

3.1. Cross Sections

To calculate cross sections, we used an impact parameter representation, namely, the inelastic overlap function (IOF), which can be specified via the unitarity equation

$$2\mathrm{Im}f(s,b) = |f(s,b)|^2 + G_{\mathrm{in}}(s,b), \qquad (17)$$

where $f(s,b)$ is the elastic scattering amplitude and $G_{\mathrm{in}}(s,b)$ is the IOF. The IOF is connected with inelastic differential cross sections in impact parameter space:

$$\frac{1}{\pi}(d\sigma_{\mathrm{in}}/db^2) = G_{\mathrm{in}}(s,b). \qquad (18)$$

Then the inelastic, elastic, and total cross sections can be expressed via the IOF as

$$\sigma_{\mathrm{in}}(s) = \int G_{\mathrm{in}}(s,\mathbf{b})d^2b, \qquad (19)$$

$$\sigma_{\mathrm{el}}(s) = \int \left[1 - \sqrt{1 - G_{\mathrm{in}}(s,\mathbf{b})}\right]^2 d^2b, \qquad (20)$$

$$\sigma_{\mathrm{tot}}(s) = 2\int \left[1 - \sqrt{1 - G_{\mathrm{in}}(s,\mathbf{b})}\right] d^2b. \qquad (21)$$

Since the IOF is related to the probability of inelastic interaction at a given impact parameter, we carried out Monte Carlo simulation of inelastic nucleon–nucleon interactions. Inelastic interaction takes place

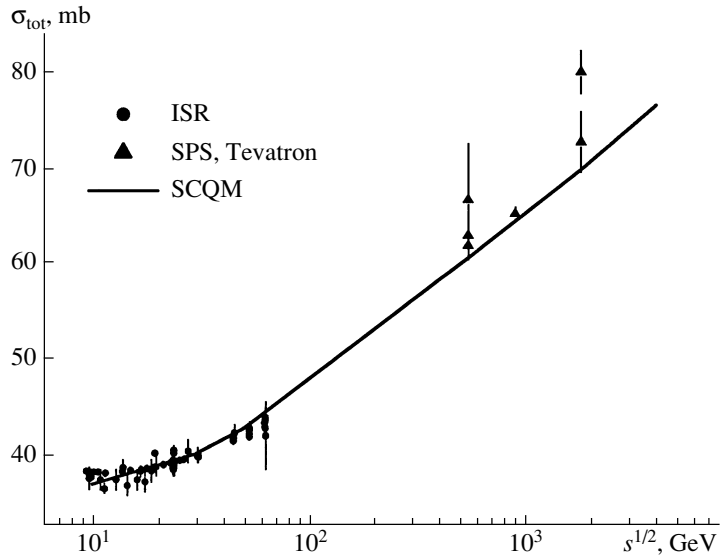

Fig. 5. Total cross section for pp and $\bar{p}p$ collisions. Data are taken from electronic database HEPDATA [16].

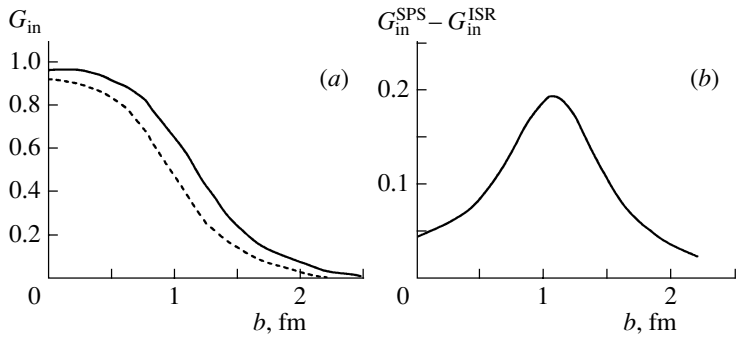

Fig. 6. Plots of (a) overlap functions at ISR and SPS energies and (b) the difference of overlap functions $G_{\rm in}^{\rm SPS} - G_{\rm in}^{\rm ISR}$ as functions of impact parameter b.

at a definite value of impact parameter b if the produced mass meets the following requirement:

$$M_{\rm CF}^2 = 4M_P\gamma_P M_T\gamma_T \times \int \rho_P(\mathbf{r})\rho_T(\mathbf{r}-\mathbf{b})d\mathbf{r} \geq (M_{\rm CF}^2)_{\rm min}, \quad (22)$$

where $M_{\rm CF}$ is the mass of the central "fireball" (CF) produced in the overlapped region, ρ_P and ρ_T are hadronic matter density distributions in projectile and target hadrons, M_P and M_T are their masses, γ_P and γ_T are gamma factors of the colliding hadrons, and $(M_{\rm CF}^2)_{\rm min}$ is the minimal mass of a fireball that results in an inelastic event. This expression is a modification of the Heisenberg assumption [15] on the interaction of extended particles: we replaced in his original formula the pion mass squared (on the right-hand side) by $(M_{\rm CF}^2)_{\rm min}$. In our previous papers, this quantity corresponded to the transverse mass of the pion: $m_{\pi_\perp}^2 = p_\perp^2 + m_\pi^2$. Taking into account the energy dependence of the average momentum of produced particles and the increasing yield of minijets (as treated in what follows), we parametrize the minimal fireball mass as

$$(M_{\rm CF})_{\rm min} = 0.3 + 0.03s^{1/4}. \quad (23)$$

Specifying the quark configurations in each colliding hadron according to (15), we calculated $G_{\rm in}(s,b)$ for particular values of the impact parameter b and then, according to (21), total cross sections $\sigma_{\rm tot}$. Figure 5 shows the results of the calculation for total cross sections for proton–proton and antiproton–proton collisions in a wide range of collision energies. One can see that the model with fixed parameters characterizing the geometrical size of hadrons describes the energetic behavior of $\sigma_{\rm tot}$ rather well. The growth of the total cross section with energy coming from the growth of the inelastic cross section is due to the continuous tails of condensates (hadronic matter distributions) around VQs not compensated by the

destructive interference effect inside each interacting particle. With rising collision energy, the overlap of more peripheral parts of these tails makes it possible to meet the requirement in (22) and consequently results in an increasing effective size of the hadronic matter distribution inside nucleons and, correspondingly, an increasing radius of interactions. It can be seen from the comparison of IOFs for ISR and SPS energies that is given in Fig. 6. According to Eq. (18), the difference $G_{\rm in}^{\rm SPS} - G_{\rm in}^{\rm ISR}$ exhibits a predominantly peripheral increase in the inelastic cross section (and thus in the total cross section, since $\sigma_{\rm el}/\sigma_{\rm tot}$ is only about 20%) that is centered around 1 fm (Fig. 6*b*). As noted by the authors of the paper [17], at high energies, colliding nucleons become blacker, edgier, and larger ("BEL effect"). The model gives the linear logarithmic energy dependence for total cross sections. At energies $\sqrt{s} < 30$ GeV, the calculated cross sections were corrected for contributions of Regge pole exchange by using the Donnachie and Landshoff parametrization [18]. An oscillatory motion of VQs appearing as an interplay between constituent and bare (current) quark configurations results in fluctuations of the hadronic matter distribution inside colliding nucleons. The manifestation of these fluctuations is a variety of scattering processes, hard and soft, in particular, the process of single diffraction (SD). SD events correspond to the CQ configuration inside one colliding hadron and (semi)bare quark configuration inside the other one. Our unified geometrical explanation of diffractive, nondiffractive, and DIS processes could give an answer to the long-standing question: What is a Pomeron? Historically, the concept of a Pomeron originating from a simple Regge pole with the intercept $a_0 = 1$ transformed into a rather complicated object with relatively arbitrary features and smooth meaning. To produce the rising cross sections, it must have an intercept such that $a_0 = 1 + \varepsilon$. The fact that the parameter ε is universal, independent of particles being scattered in hadronic and DIS interactions, could tell us that the nature of the cross-section growth is the same for all processes. Our interpretation of the Pomeron is a geometrical one. Both diffractive and nondiffractive particle productions emerge from the disturbance (excitation) of overlapped continuous vacuum polarization fields (gluon and $\bar{q}q$ condensate) around VQs of colliding hadrons, followed by the fragmentation process. The type of interaction depends on quark configurations inside a colliding hadron occurring at the instant of the interaction and the value of the impact parameter. Thus, what we used to call the Pomeron in the t channel is solely continuum states in the s channel and we claim that the Pomeron is unique in elastic, inelastic (diffractive and nondiffractive), and DIS processes.

3.2. Multiparticle Production in Hadronic Collisions

According to our model, the configurations with nonrelativistic constituent quarks ($x \simeq x_{\max}$) inside both colliding hadrons lead to soft interactions with multiparticle production in central and fragmentation regions. The additional restriction by small impact parameters selects central collisions when hadronic matter distributions of colliding hadrons (quarks) overlap totally. In this case, kinetic energies of colliding hadrons dissipate totally, converting into the production of secondary particles that corresponds to collision inelasticity close to 1 and very high multiplicity in comparison with the mean one. We will consider soft interactions and nondiffractive multiparticle production, in particular. According to the KNO hypothesis, the scaled multiplicity distributions, $\langle n\rangle P_n(s)$, depend on the ratio of the number of particles to the average multiplicity $z = n/\langle n\rangle$ and they are energy independent. From our geometrical point of view, such behavior could be explained as a superposition of relatively narrow distributions corresponding to the particular impact parameters of the collisions. Indeed, the multiplicity distribution can be defined as

$$P_n(s) = \int_0^1 P(n|k)P[k(s)]dk, \qquad (24)$$

where $P[k(s)]$ is inelasticity distribution and $P(n|k)$ is the probability of the production of n particles at the given inelasticity k. Thus, if the conditional probability $P(n|k)$ is sufficiently narrow, then the shape of the distribution P_n is defined by the shape of the inelasticity distribution $P[k(s)]$. The inelasticity distributions are strictly connected with the impact parameter distributions. KNO scaling holds (at least, approximately) if the impact parameter distributions and, consequently, inelasticity distributions are energy-independent. As shown in the previous subsection, the growth of inelastic and total cross sections with energy in hadronic collisions is due to increasing effective sizes of interacting hadrons. To make a quantitative analysis of energetic dependence of multiplicity distributions, we performed, in the framework of the SCQM, Monte Carlo simulation of inelastic proton–proton interactions selecting nondiffractive events. The process of simulation includes the following steps:

(i) Applying Heisenberg prescription (22), we define the mass of CF (Fig. 7) produced in the proton–proton collision at a particular impact parameter. Quark configurations inside each proton at the instant of the collision are specified randomly according to the probability (15) that allows one to fix energies and momenta of quarks inside both protons. Since

the mass of CF is formed by the overlap of hadronic densities of individual CQs of colliding protons, we know the energies and momenta of quarks in both remnants, which we call, by convention, forward and backward fireballs (FF and BF). The notion fireball is applied by convention only because all fireballs, CF, FF, and BF, can decay in a string-like manner and there is no sharp boundary between secondaries emitted from fireballs in the rapidity space for nondiffractive events. Then we calculate the effective masses of FF and BF (Fig. 7):

$$M_{\mathrm{FF}} = \sqrt{\left(\sum_{i=1}^{3} E_i'\right)^2 - \left(\sum_{i=1}^{3} \mathbf{k}_i\right)^2}, \qquad (25)$$

$$M_{\mathrm{BF}} = \sqrt{\left(\sum_{i=4}^{6} E_i'\right)^2 - \left(\sum_{i=4}^{6} \mathbf{k}_i\right)^2}, \qquad (26)$$

where E_i' and $\mathbf{k}_i$ are energies and momenta of CQs after the collision.

(ii) We assume that each fireball breaks up, in general, into clusters. Here, the bremsstrahlung analogy is used; namely, at the instant of the collision, a proton (electron) loses the energy dumping fraction of its hadronic (electromagnetic) field by means of the emission of clusters (photons). To simulate the masses of the clusters, we apply the result of [19] for a cluster mass spectrum

$$P(m_{\mathrm{cl}}) = (m_{\mathrm{cl}}/m_0)\exp(-m_{\mathrm{cl}}/m_0), \qquad (27)$$

following from the statistical nature of the cluster emission. Our next assumption is that masses of clusters increase with the collision energy. This is dictated by the necessity to take into account such peculiarities of multiparticle production as the growth of a rapidity distribution plateau, the increasing transverse momenta of secondaries, and the increasing yield of minijets. We parametrize the energy dependence of the average mass of clusters as

$$\langle m_{\mathrm{cl}}\rangle = 0.3 + 0.09 s^{1/4}. \qquad (28)$$

Notice that we have chosen the same energetic dependence for the minimal fireball mass in Heisenberg prescription (23) except for the value of the slope parameter.

(iii) Given the positions of the centers of mass of each fireball in rapidity space and kinematically allowed rapidity (sub)spaces for the breaking up of each fireball into clusters, we simulate the momenta for each generated cluster in the proper frame of the corresponding fireball. The bremsstrahlung mechanism of the fireball fragmentation corresponds to statistically independent emission of clusters with limited transverse momenta. Therefore, we apply the cylindrical phase-space model according to which the rapidity of the ith cluster is defined as

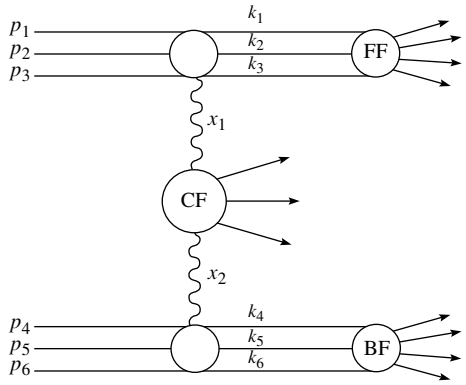

Fig. 7. Fireball picture of multiparticle production in proton–proton collision; p_i and k_i are momenta of constituent quarks before and after collision, respectively; x_1 and x_2 are fractions of protons momenta forming the central fireball.

$$y_i = \xi Y_i, \qquad (29)$$

where ξ is random number uniformly distributed in the interval $[0,1]$. The allowed rapidity interval, Y_i, is given by

$$Y_i = \ln(M_F^2/(\mu_{\mathrm{cl}})_i^2),$$

where $(\mu_{\mathrm{cl}})_i^2 = (m_{\mathrm{cl}})_i^2 + p_{\perp i}^2$, the transverse mass of the cluster i. Moreover, the rapidity interval for fragmentation of the CF, Y_i^{CF}, is restricted by the requirement

$$Y_i^{\mathrm{CF}} \le Y^{\mathrm{FF}} - Y^{\mathrm{BF}}, \qquad (30)$$

where Y^{FF} and Y^{BF} are rapidities of FF and BF, respectively. The transverse momenta of the clusters are generated according to the distribution

$$f(p_\perp^2) \propto \exp(-b p_\perp^2). \qquad (31)$$

The energy of the remnant baryon in the proper frame of FF (BF) is defined by the total energy of two quarks closest to each other in rapidity space; i.e., the kinematic characteristics of the baryon are connected to those of the diquark.

(iv) Since our clusters are identified with minijets, they should decay in a jetlike manner. One could assume that these minijets are formed by the fragmentation of the excited sea quark–antiquark pair. Hence, we can approximate the spectrum of cluster decay using data on the electron–positron annihilation provided that the cluster mass is identified with the c.m. energy of an electron and positron: $m_{\mathrm{cl}} = \sqrt{s_{e^+e^-}}$. One can apply for this purpose any of the appropriate Monte Carlo generators. The axis of the decaying jet is generated to be directed isotropically. And, finally,

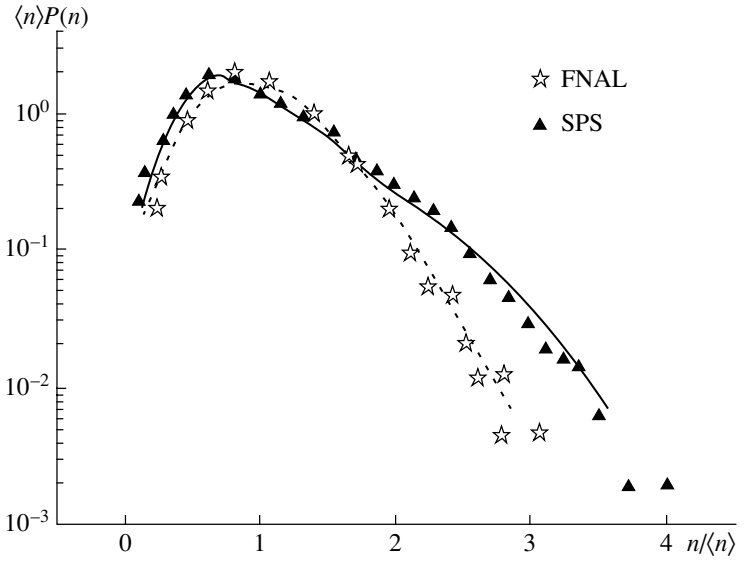

Fig. 8. The multiplicity distributions of charged particles in pp and $\bar{p}p$ collisions. Data are taken from electronic database HEPDATA [16].

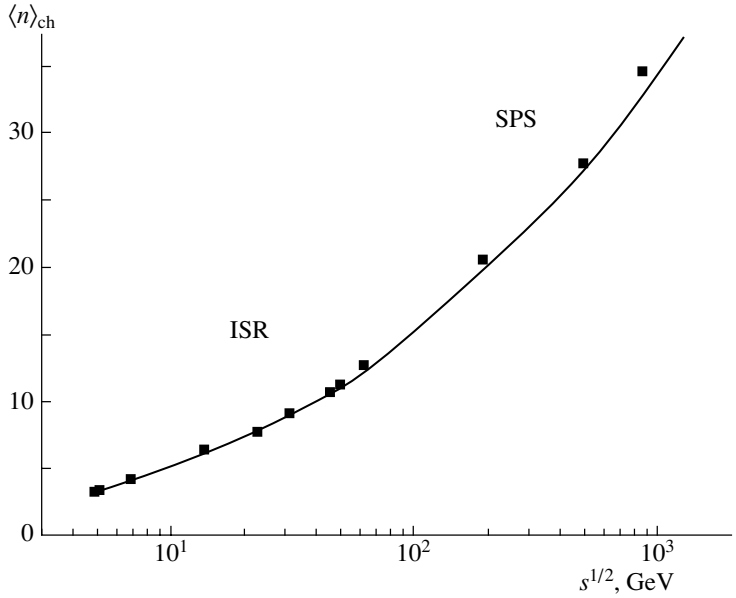

Fig. 9. The energetic dependence of the average multiplicity of charged particles in pp and $\bar{p}p$ collisions. Data are taken from electronic database HEPDATA [16].

the model meets energy–momentum conservation requirements for all products of a reaction.

Calculated in such a manner, the multiplicity distributions in the KNO form and the energetic dependence of the mean multiplicity for charged particles are shown in Figs. 8 and 9. Given all characteristics of produced particles in the event, we can calculate inelasticity k_2 (2). Its distributions for pp interactions at different collision energies are shown in Fig. 10. The inelasticity distribution evolves with energy in such a way that its maximum position shifts to lower values of inelasticity at higher collision energies. It means that the higher the collision energy, the lower the average inelasticity (Fig. 11). Analyzing the multiplicity distribution at different energies, one can see that the position of its maximum shifts to lower values of scaled multiplicities and the contribution of high multiplicities increases, while the collision energy increases. According to Eq. (24), the multiplicity distribution can be expressed via the conditional multi-

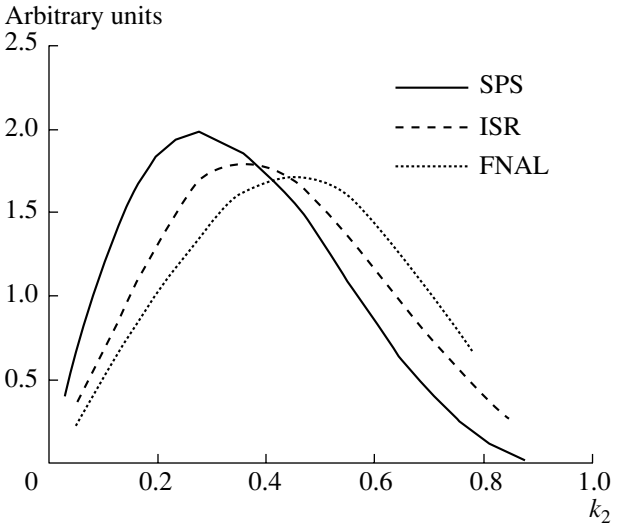

Fig. 10. Inelasticity distributions for pp and $\bar{p}p$ collisions calculated according to Eq. (2).

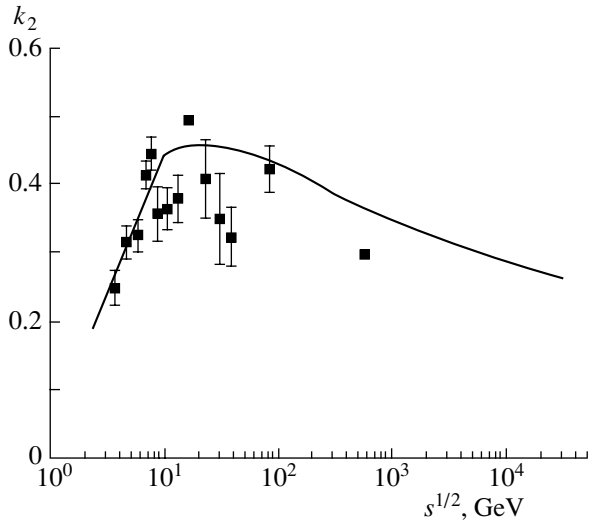

Fig. 11. The average inelasticity plotted as a function of the energy for pp and $\bar{p}p$ collisions. Squares are compilation of data given in paper [20].

plicity distribution at a particular inelasticity and the inelasticity distribution. The conditional multiplicity distribution at the particular inelasticity, in turn, is built from multiplicities of clusters emitted from FF, BF, and CF and multiplicities going from the clusters' fragmentation. If the inelasticity distribution and (average) mass of the clusters do not depend on the collision energy, then the scaled multiplicity distributions will not depend on energy either and KNO scaling will take place. The shift of the position of the maximum of the inelasticity distribution with the energy growth shifts the position of the scaled multiplicity distribution. On the other hand, masses of clusters growing with collision energy lead to the narrowing of available rapidity space and, consequently, to the violation of Feynman scaling. This effect is most obviously exhibited at inelasticities close to 1 and causes the tail of the multiplicity distribution to shift upward at high multiplicities. To summarize, we claim that the mean inelasticity decreases with energy, and the violation of KNO scaling is a consequence of the growth of inelastic and total cross sections and of masses of emitted clusters with energy.

ACKNOWLEDGMENTS

This research was partly supported by the Russian Foundation for Basic Research, project no. 01-07-90144.

REFERENCES

1. G. Fowler, R. M. Weiner, and G. Wilk, Phys. Rev. Lett. **55**, 173 (1985).
2. Z. Wlodarczyk, J. Phys. G **19**, L128 (1993).
3. Yu. A. Shabelski *et al.*, J. Phys. G **18**, 1281 (1992).
4. Y. D. He, J. Phys. G **19**, 1953 (1993).
5. J. Dias de Deus, Phys. Rev. D **32**, 2334 (1985).
6. T. K. Gaisser and T. Stanev, Phys. Lett. B **219**, 375 (1989).
7. B. Z. Kopeliovich, N. N. Nikolaev, and I. K. Potashikova, Phys. Rev. D **39**, 769 (1989).
8. F. S. Duraes, F. O. Navarra, and G. Wilk, Phys. Rev. D **47**, 3049 (1993).
9. Z. Koba, N. B. Nielsen, and P. Olesen, Nucl. Phys. B **40**, 317 (1972).
10. G. Musulmanbekov, in *Proceedings of the VIII Blois Workshop,* Ed. by V. A. Petrov (World Sci., Singapore, 2000), p. 341 (and references therein).
11. E. Schrödinger, Naturwissenschaften **14**, 664 (1926).
12. G. Musulmanbekov, in *Frontiers of Fundamental Physics 4*, Ed. by B. G. Sidharth (Kluwer Acad. Plenum, New York, 2001), p. 109.
13. R. Rajaraman, Phys. Rep. **21C**, 229 (1975).
14. R. Dashen, B. Hasslacher, and A. Neveu, Phys. Rev. D **10**, 4114 (1974).
15. W. Heisenberg, Z. Phys. **133**, 65 (1952).
16. http://durpdg.durham.ac.uk/HEPDATA
17. R. Henzi and P. Valin, Phys. Lett. B **132B**, 443 (1983); R. Henzi, in *Proceedings of the 4th Topical Workshop on $\bar{p}p$ Collider Physics, Bern, Switzerland, 1984*.
18. A. Donnachie and P. V. Landshoff, CERN-TH 6635/92.
19. Kuang-Chao Chou, Lian-Son Liu, and Ta-Chung Meng, Phys. Rev. D **28**, 1080 (1983).
20. V. S. Barashenkov and N. B. Slavin, Acta Phys. Pol. B **12**, 563 (1981).